LBL-22090
UC-13

RECEIVED
LAWRENCE
BERKELEY LABORATORY
NOV 10 1987
LIBRARY AND
DOCUMENTS SECTION

Annual Report 1986

TWO-WEEK LOAN COPY
This is a Library Circulating Copy
which may be borrowed for two weeks.

Earth Sciences Division

August 1987

LAWRENCE BERKELEY LABORATORY
UNIVERSITY OF CALIFORNIA
BERKELEY, CALIFORNIA 94720

Prepared for the U.S. Department of Energy under Contract No. DE-AC03-76SF00098

LBL-22090
c.2

DISCLAIMER

This document was prepared as an account of work sponsored by the United States Government. While this document is believed to contain correct information, neither the United States Government nor any agency thereof, nor the Regents of the University of California, nor any of their employees, makes any warranty, express or implied, or assumes any legal responsibility for the accuracy, completeness, or usefulness of any information, apparatus, product, or process disclosed, or represents that its use would not infringe privately owned rights. Reference herein to any specific commercial product, process, or service by its trade name, trademark, manufacturer, or otherwise, does not necessarily constitute or imply its endorsement, recommendation, or favoring by the United States Government or any agency thereof, or the Regents of the University of California. The views and opinions of authors expressed herein do not necessarily state or reflect those of the United States Government or any agency thereof or the Regents of the University of California.

EARTH SCIENCES DIVISION ANNUAL REPORT 1986

Lawrence Berkeley Laboratory
University of California
Berkeley, California 94720

August 1987

Prepared for the U.S Department of Energy under Contract No. DE-AC03-76SF00098

ACKNOWLEDGMENTS

This work was supported through U.S. Department of Energy Contract No. DE-AC03-76SF00098 by (1) the DOE Assistant Secretary for Energy Research, Office of Basic Energy Sciences, Division of Engineering and Geosciences; (2) the DOE Office of Civilian Radioactive Waste Management, Office of Geologic Repositories, Divisions of Repository Coordination and Engineering & Geotechnology; (3) the DOE Assistant Secretary for Conservation and Renewable Energy, Office of Renewable Technology, Division of Geothermal Technology; (4) the DOE Assistant Secretary for Conservation and Renewable Energy, Office of Advanced Conservation Technology, Division of Thermal and Mechanical Storage Systems; (5) the DOE Assistant Secretary for Fossil Energy, Office of Petroleum Resources, Division of Enhanced Oil Recovery; (6) the Waste Management Research Branch, Division of Health, Siting and Waste Management, Office of Nuclear Regulatory Research, U.S. Nuclear Regulatory Commission; (7) the Office of Drinking Water, the Environmental Monitoring Systems Laboratory, and the Robert S. Kerr Laboratory of the Environmental Protection Agency; (8) the Bureau of Mines, the Bureau of Reclamation, and the Geological Survey, U.S. Department of Interior; (9) the Army Corps of Engineers, the Air Force Ballistic Missile Operation, the Defense Advanced Research Projects Agency, and the Naval Research Office of the U.S. Department of Defense; (10) the California State Lands Commission and the University of California; (11) The California Consortium for Crustal Studies, the University of Southern California, and the University of California at Berkeley under National Science Foundation sponsorship; and (12) the Gas Research Institute.

CONTENTS

INTRODUCTION

Scientists and engineers of the Earth Sciences Division, following the mission of a multipurpose National Laboratory, conduct research on a wide variety of topics relevant to the nation's energy development programs. This report summarizes the activities for 1986. The Earth Sciences Division has developed unique expertise in several research areas. This expertise is due in part to the special resources and facilities available to researchers at the Lawrence Berkeley Laboratory and in part to the Laboratory's commitment to technical and scientific excellence. In addition to the permanent Laboratory staff, University faculty members, postdoctoral fellows, students, and visiting scientists participate in many investigations. Each year, several Ph.D. and Masters theses are founded in research within the Division. Interlaboratory cooperation within the U.S. Department of Energy system and collaboration with other research institutions provide access to unmatched intellectual and technological resources for the study of complex problems.

Much of the Division's research deals with the physical and chemical properties and processes in the Earth's crust, from the partially saturated, low-temperature near-surface environment to the high-temperature environments characteristic of regions where magmatic-hydrothermal processes are active. Strengths in laboratory and field instrumentation, numerical modeling, and in situ measurement allow study of the transport of mass and heat through geologic media—studies that now include the appropriate chemical reactions and the hydraulic-mechanical complexities of fractured rock systems. Related and parallel laboratory and field investigations address the effects of temperature, pressure, stresses, pore fluids, and fractures on the elastic and electrical properties of rock masses. These studies are concerned with rock behavior in the brittle and ductile crustal regimes, and they drive the development of improved geomechanical and geophysical tools and techniques for mapping and characterizing fractures in the subsurface. Prompted by Congressional concern over the decline in basic research in the petroleum industry due to the low price of oil, the Division has increased its emphasis on the application of fluid transport modeling and subsurface imaging methods to problems related to discovery and recovery of petroleum.

This Annual Report presents summaries of research activities grouped according to the principal disciplines of the Earth Sciences Division: Reservoir Engineering and Hydrogeology, Geochemistry, Geomechanics, and Geophysics. We are proud to be able to bring you this report, which we hope will convey not only a description of the Division's scientific activities but also a sense of the enthusiasm and excitement present today in the Earth Sciences.

RESERVOIR ENGINEERING AND HYDROGEOLOGY

The scientists and engineers in the Reservoir Engineering and Hydrogeology group are primarily concerned with several different approaches to the fundamental problem of the movement of mass and energy through rocks. For a number of years, we have been striving to understand geothermal systems and to unravel the complex physics that controls such systems. This has required the perfection of mathematical models and their application to rather large and complicated field projects. Several articles in this section present the results of recent developments and serve to illustrate the level of sophistication that has been attained in modeling geothermal reservoirs.

Several years ago we began to investigate the phenomenon of flow in fractured rocks, and this has now become a major effort. The importance of fractures in fluid flow arose in connection with our work on geothermal systems and has become a central theme in our investigations of problems related to the isolation of radioactive and toxic wastes. One of these problems is to be able to characterize the fracture system of a rock mass; several articles discuss the difficulties in the evaluation of field data and the use of well tests. Another problem is to develop a model that is appropriate to use in evaluating the factors that control fluid movement in fractures; several approaches are presented here.

High-level radioactive waste generates substantial amounts of heat, and once the waste is placed underground the dissipation of this thermal energy and its effects on the rock mass must be understood. Our previous work on geothermal systems has provided us with an excellent background for confronting this problem; the results of several investigations are included here. Another problem concerns the reactions that can take place between dissolved chemicals in the groundwater and the minerals of the rock surfaces. We are developing numerical methods of handling this geochemical problem, and the results are discussed in several articles. Still another problem under investigation is that of the migration of gas and water in the unsaturated region; this subject is treated in several articles.

Long-Term Infiltration at Yucca Mountain, Nevada Test Site

M. Alavi and T.N. Narasimhan

Geologic burial is considered to be the primary means for disposing of high-level nuclear waste. The Nevada Nuclear Waste Storage Investigation project (NNWSI), managed by the Nevada Operation Office of the U.S. Department of Energy, has chosen Yucca Mountain as a possible site for the construction of a repository. Prior to the construction process, it is necessary to study the effects of radionuclide containments on the hydrologic and geochemical systems at Yucca Mountain. This study requires use of computer codes capable of simulating these effects over time. These codes should be able to produce numerically accurate and physically valid results for the geologic conditions that prevail at Yucca Mountain. The accuracy of the various computer codes can be partially demonstrated by comparing the results of those codes with each other—a procedure called benchmarking. As a first step in certifying the codes to be used in the NNWSI performance assessment, 12 one-dimensional cases have been proposed and labeled as COVE2A benchmarking studies by the NNWSI.

PROBLEM DEFINITION

The cases under consideration in the COVE2A benchmarking studies are concerned with one-dimensional downward flow of water in an isothermal, multilayered representation of the Yucca Mountain site (Fig. 1). Water enters the system by infiltration at its upper boundary, flows downward, and discharges at the lower boundary water into a static water table. Each layer of the system is a fractured porous medium. For the COVE2A benchmarking studies, each layer is treated as an equivalent porous medium. More specifically, the Mualem and van Genuchten models for the pressure head dependence of saturation, S, and hydraulic conductivity, K, are applied to both the rock matrix and the fractures. Composite S and K relations for the bulk rock are then obtained from porosity-weighted averaging of rock matrix and fracture contributions (van Genuchten, 1980; Peters et al., 1985)

MODELING DETAILS

The COVE2A benchmarking effort consists of 12 cases, 6 of which are steady-state cases and the other 6 transient. To accomplish the COVE2A benchmarking, code TRUST was used to model all 12 cases. TRUST is a three-dimensional isothermal fluid-flow code that can be used as a tool to solve fluid-flow problems in variably saturated deformable porous media. All 12 cases utilize prescribed flux boundary conditions at the upper surface and a water-table (prescribed potential) boundary condition at the lower boundary of the system. We use a small computer program that is based on path integration to obtain the initial estimate of pressure distribution.

RESULTS

The TRUST program solves for the steady-state problem by treating it as the limiting case of a non-steady problem after a sufficiently long time has passed. In our calculations the steady-state condition was assumed to have been attained when the maximum error in local fluxes was less than 3% of the infiltration flux at the top. Figures 2 and 3

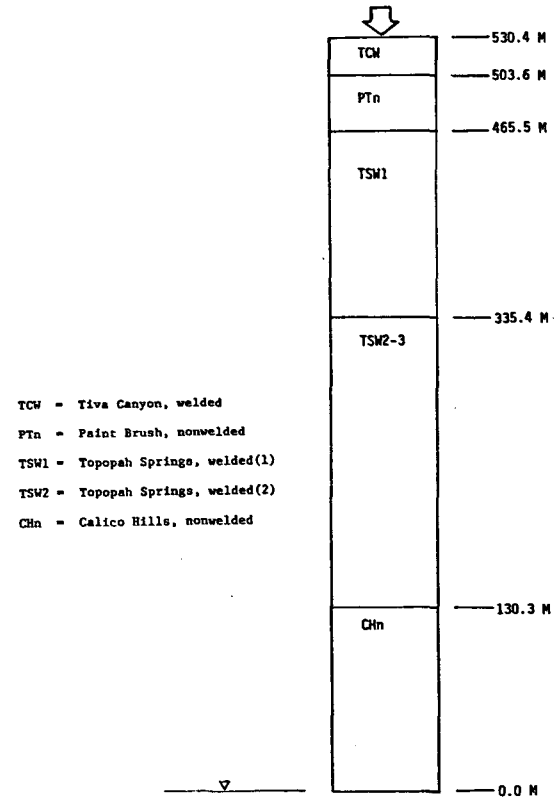

Figure 1. Idealized vertical column through the Yucca Mountain site. [XBL 871-212]

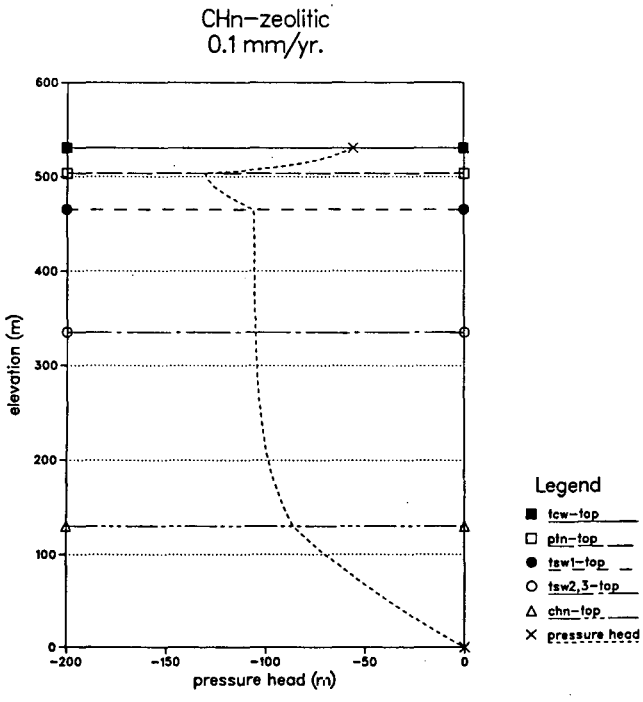

Figure 2. Pressure head versus distance above the water table. [XBL 871-213]

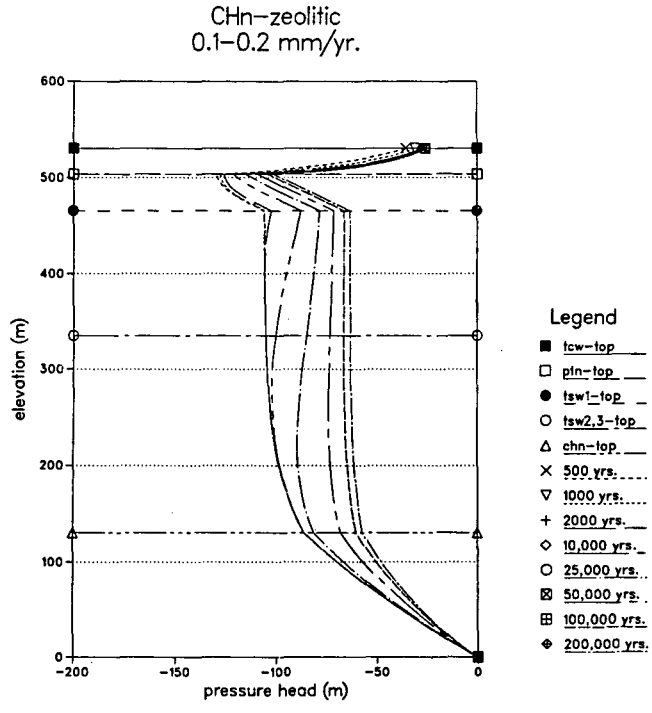

Figure 4. Pressure head versus distance above the water table at progressive times. [XBL 871-215]

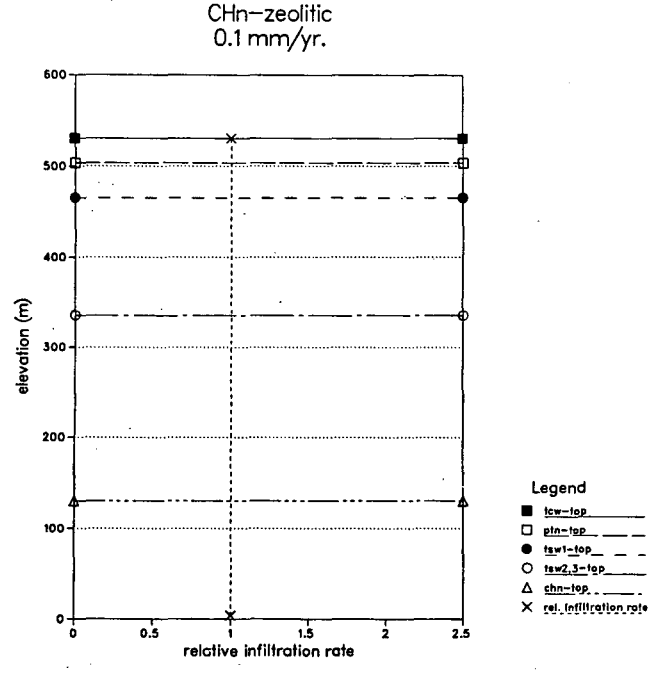

Figure 3. Normalized flux (calculated flux divided by imposed flux) versus distance above the water table. [XBL 871-214]

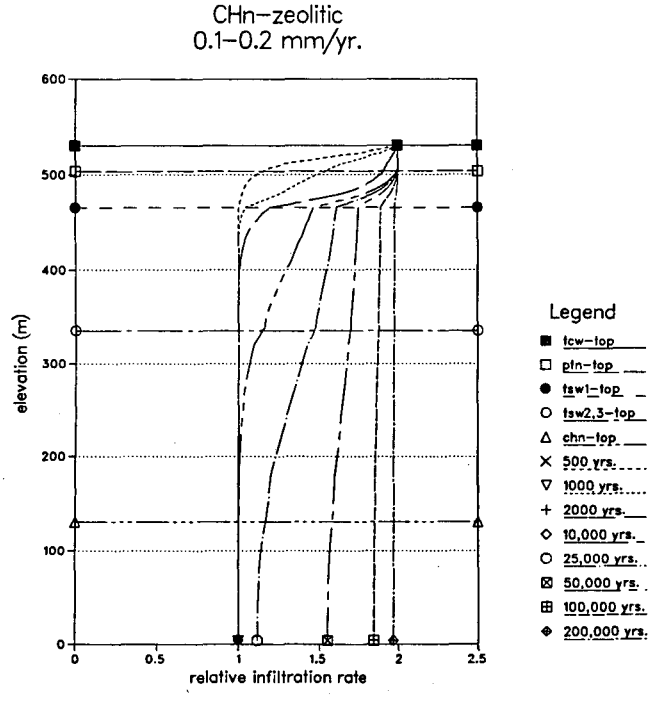

Figure 5. Normalized flux (calculated flux divided by half the imposed flux) versus distance above the water table at progressive times. [XBL 871-216]

present the pressure-head profile and relative-infiltration profile for one of the cases studied. The transient cases are concerned with step changes in the surface infiltration rate. For example, the infiltration flux is step changed from 0.1 mm/yr to 0.2 mm/yr at $t = 0$. The transient simulations were terminated at a prescribed time determined by the travel time for that specific case. Figures 4 and 5 present the pressure-head profile and relative-infiltration profile for one of the cases studied.

REFERENCES

Peters, R.R., Gauthier, J.H., and Dudley, A.L., 1985. The effect of percolation rate on water travel time in deep, partially saturated zones. Sandia National Laboratories Report SAND85-0854c, Albuquerque, NM, 36 p.

van Genuchten, M.Th., 1980. A closed-form equation for predicting the hydraulic conductivity of unsaturated Soils. Soil Sci. Soc. Am. J., v. 44, p. 892–898.

Computerized Data Acquisition System for Production, Injection, and Interference Tests

S.M. Benson and R.D. Solbau

A computer-based system for collecting, processing, and analyzing pressure-transient data has been developed. Primary components include downhole pressure sensors, line drivers, a microcomputer, data-storage disk, scanner, frequency counter, digital voltmeter, power supply, graphics plotter, and printer. In-field data processing and analysis greatly aid in handling the large volume of data collected during pressure-transient tests, particularly the multiwell interference tests that are so important for characterizing and assessing groundwater systems, hydrocarbon reservoirs, and geothermal reservoirs. In-field data processing provides the field engineer with the real-time information needed to make decisions regarding test parameters and duration. The system has been used on numerous occasions and has proved itself to be reliable under the harsh operating conditions that are usually encountered in the field.

Production, injection, and interference tests require collecting and processing large volumes of data. Typically, little, if any, of the test data are processed during the test. Only after returning from the field, and after considerable preparation, is it possible to begin assessment and analysis of the data. The lack of real-time access to the bulk of the data makes it impossible to judge the quality of the data and make informed decisions regarding the test parameters and test duration while there is still an opportunity to make changes in the instrumentation or test design. In-field data processing, display, and analysis greatly enhance the control the field engineer has over the quality of the test.

During a well test several types of data from various physical locations must be collected. At a minimum these include wellbore pressures, flow rates (perhaps both steam and water), temperatures, and barometric pressure. Also sometimes required are pressures, temperatures, and flow rates at various points in the piping system, as well as in-line monitoring of fluid properties or composition. Collecting data from all of these sources is time-consuming and subject to human error when each type of data is collected and recorded individually.

For pressure-transient analysis, the most detrimental errors result from collecting data with more than one time reference (clock). Since pressure-transient analysis is very sensitive to time-measurement errors, especially during the time periods near flow-rate changes, errors as small as several minutes may result in a large degree of uncertainty in the data interpretation. This uncertainty can be eliminated by collecting all of the data with a single time reference. Computerized data acquisition makes it possible to do just that, thereby reducing

both the labor requirements and measurement errors associated with well testing.

Additional benefits from using a computer-based data-acquisition system include increased measurement rates, improved measurement accuracy and resolution, real-time barometric and earth-tide corrections for pressure measurements, minimized time and effort for data handling, and enhanced capabilities for applying some of the more novel well-testing techniques, such as pulse testing. At the present time the system can measure (1) downhole pressures of up to 2×10^7 Pa at temperatures up to 125°C, (2) the pressure differential across an orifice plate (for measuring flow rates), (3) the surface pressure of a gas-filled capillary tube (for making downhole pressure measurements in high-temperature geothermal wells), and (4) the barometric pressure. In the high-speed mode, up to 100 readings per second can be obtained, with a pressure resolution of 10 Pa out of 2.5×10^6 Pa.

HARDWARE

The entire data-acquisition system is housed in a large delivery-type van equipped with a generator, air conditioning, back-up battery bank, and instrument racks. A schematic diagram of the system, with all of the principal components, is shown in Fig. 1. A microcomputer performs the central role of interacting with the operator, preparing the instruments for measurement, controlling the flow of data, interfacing the various components of the system, and tracking the test status. The system is currently configured for purely digital data acquisition because the pressure sensors are piezoelectric transducers with a digital output. However, devices with analog output signals are easily incorporated into the system with the addition of a digital voltmeter.

SOFTWARE

A schematic diagram of the program's structure and capabilities is shown in Fig. 2. The code is written so that data acquisition (measurement, display, storage, and printing) is the primary task of the computer. However, at the touch of a button, the program changes context and can perform the following tasks: graphing previously stored data; copying data from the hard disk to a 3.5-inch microfloppy disk; printing previously stored data; printing test specifications (well names, instruments, calibration information, data files, etc.); reinitializing test specifications (adding instruments and wells, changing data files, etc.); and halting operation of the logging program.

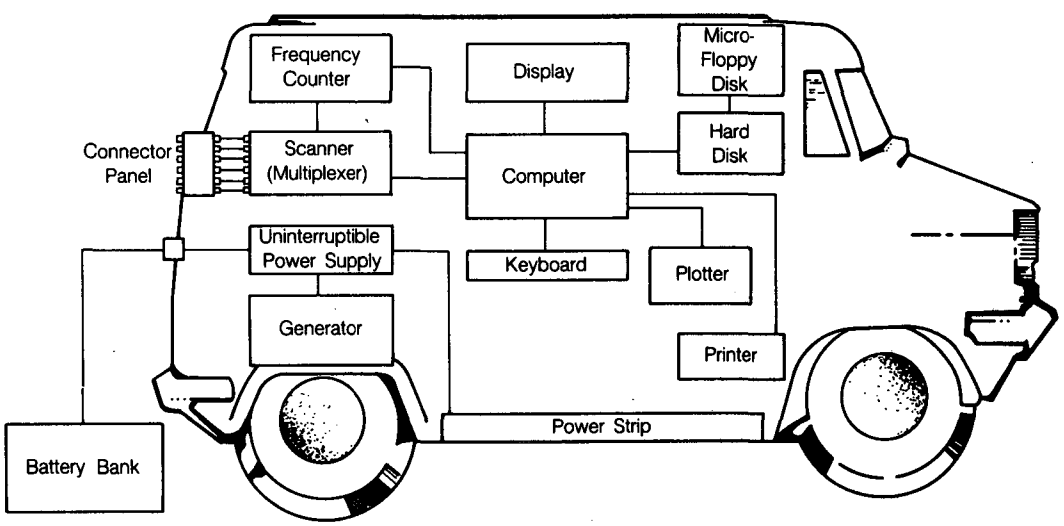

Figure 1. Schematic diagram of the data-acquisition van, showing the principal components of the data-acquisition system. [XBL 865-10795]

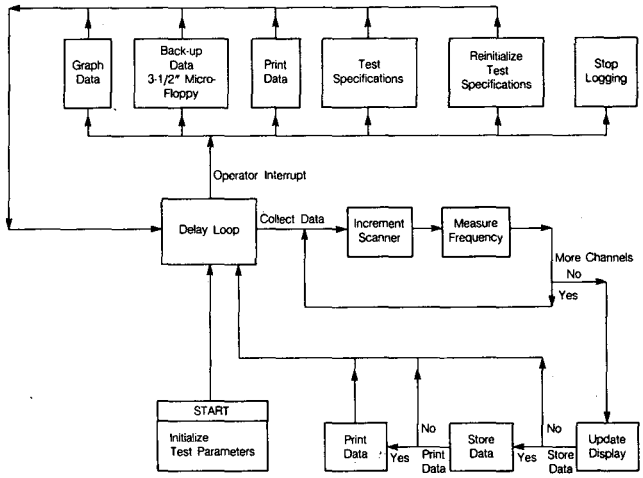

Figure 2. Flow chart for the data-acquisition software. [XBL 865-10804]

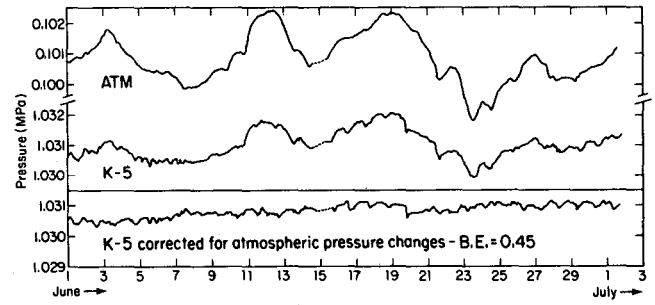

Figure 3. Atmospheric pressure, well data, and corrected pressure data from an interference test well in southern Sweden. [XBL 848-9861]

APPLICATIONS

Barometric Pressure Corrections

Atmospheric pressure changes strongly influence measurements of water level and reservoir pressure. In areas where frequent and large atmospheric pressure changes occur, measured water levels and reservoir pressures must be corrected to remove this influence from the data before it is used to calculate the reservoir properties. The data shown in Fig. 3, collected during an interference test in a deep sandstone aquifer in southern Sweden, provides an excellent example of the need to make atmospheric corrections on a real-time basis. The top curve in the figure is the atmospheric pressure, the middle curve shows the raw data from the well, and the bottom curve shows the corrected data. Pressure fluctuations corresponding to 20 cm of water-level change (0.002 MPa) are measured in the observation well, whereas the corrected data show fluctuations of about 1 to 2 cm. These 1- to 2-cm fluctuations are the result of earth-tide effects and are within the tolerable noise range for the interference test. On the other hand, the large fluctuations in the uncorrected data mask the fact that the well did not respond to pumping during the interference test.

Interference Test

Interference tests are one of the most powerful techniques for evaluating the hydrologic properties of heterogeneous aquifers. The wells shown in Fig. 4 were drilled specifically for the purpose of measuring the average horizontal permeability, vertical permeability, and anisotropy of the sands, silts, and clays of a near-surface aquifer in the Central Valley of California. Each of the wells I-1 to I-9 was instrumented (see Fig. 4) with a Paroscientific Digiquartz pressure transducer (some wells with 45-psia range transducers and some with 400-psia units). Inflatable packers were placed above the transducers in order to minimize wellbore-storage effects in the observation wells and isolate the effects of barometric-pressure fluctuations on the aquifer pressure (see Fig. 5).

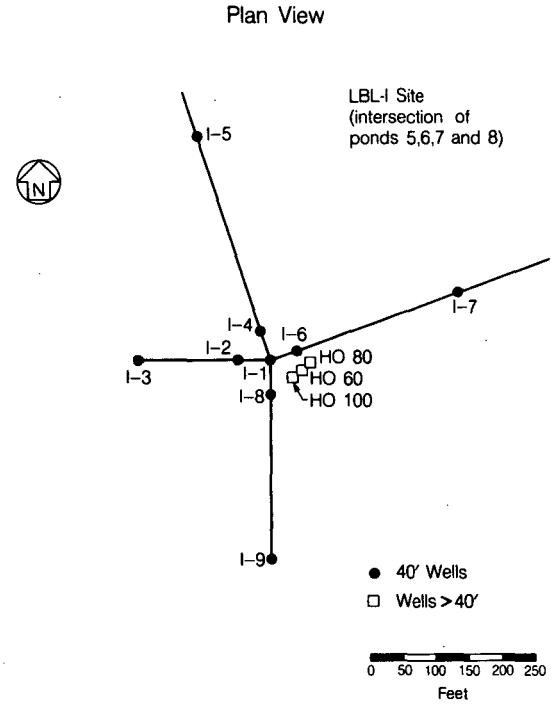

Figure 4. Array of wells for an interference test in the Central Valley, California. [XBL 863-19039]

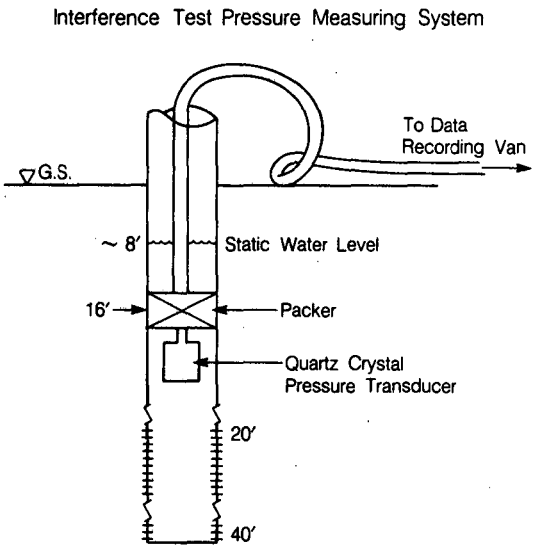

Figure 5. Schematic diagram of the setup for monitoring observation wells, showing the location of the packer, water level, slotted interval, and instrument package. [XBL 863-10740]

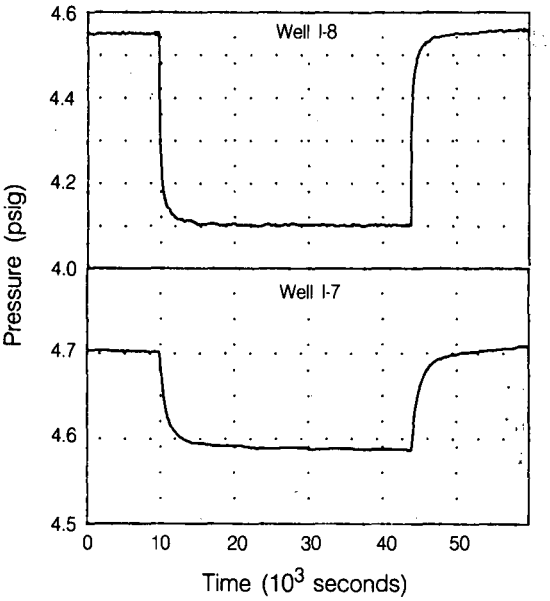

Figure 6. Pressure data with barometric corrections from observation wells I-7 and I-8. [XBL 871-9897]

The interference test was conducted over a 16-hour period, which included collecting 2 hours of background data, 10 hours of drawdown data, and 4 hours of recovery data. A total of 5000 data points were collected during this period. Without the aid of computer graphics, data processing, and storage, handling this volume of data would require weeks of hand plotting, keypunching, etc. With the aid of the computer, all data were processed and plotted during the test itself. In fact, 10 similar tests, during which over 50,000 data points were obtained, were conducted during a 1-month period.

Graphs of the pressure data (with barometric corrections) from two of the observation wells are shown in Fig. 6. Notice that well I-7, at a distance of approximately 100 m from the pumped well, has a maximum drawdown of approximately 7 cm (0.1 psi). This small drawdown would be very difficult to measure with conventional instrumentation. However, the drawdown is far greater than the 0.00025-psi resolution of the 45-psia pressure transducer; therefore, it is easily measured with the system described here.

SUMMARY

A computer-based data-acquisition system for conducting pressure-transient tests has been developed. Advantages of using such a system include (1) improving data quality by using a single time reference for all measurements, (2) improving test design and control by providing the field engineer with real-time access to the test data, (3) facilitating manipulation and processing of the large volume of data typically obtained during interference tests, (4) enhancing data quality by allowing high-speed, high-resolution pressure measurements, and (5) facilitating application of advanced well-testing techniques that require high-speed, high-resolution pressure measurements.

Groundwater Flow and Solute Transport At Kesterson Reservoir

S.M. Benson, T.K. Tokunaga, R.D. Solbau, M. Alavi, R. Long, and S.E. Halfman

From 1978 to 1986 Kesterson Reservoir, situated within the Kesterson National Wildlife Refuge, was used as a storage/disposal facility for subsurface drainage water from agricultural lands in the San Joaquin Valley, California. In 1982, shortly after the reservoir was put into full operation, elevated levels of selenium were detected in fish collected from the reservoir. In 1983, numbers of young waterfowl were found dead and deformed; investigations showed the cause to be selenium poisoning. The selenium was found to originate in the soils and shallow groundwater of the irrigated lands on the west side of the valley.

Kesterson Reservoir consists of 12 unlined storage ponds covering 5.2×10^6 m^2 (see Fig. 1). The reservoir overlies a saline aquifer that is used locally to supply water for livestock and agricultural purposes. Immediately below the reservoir the sediments consist of loam, silt, and sandy silt, with a minor amount of clay. This fine-grained surface layer impedes flow into the aquifer, but approximately half of the 10^7 m^3 of drainage water received annually at the facility has seeped into the underlying aquifer. Extensive groundwater sampling and analyses have shown that most of the selenium is removed from the infiltrating water by the pond-bottom sediments, but boron, various salts, and several trace elements have entered the groundwater system (Weres et al., 1985).

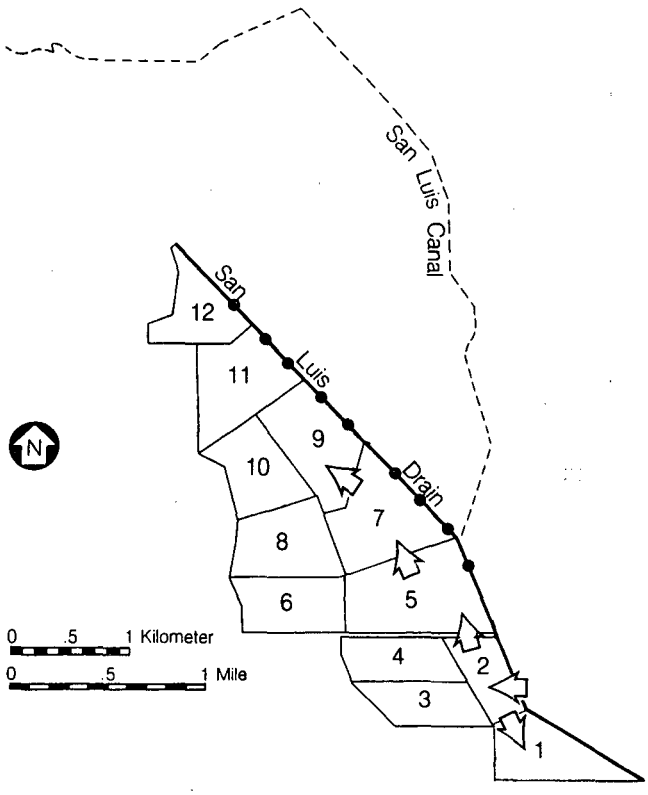

Figure 1. Map showing the configuration of Kesterson Reservoir and the location of the six study sites. [XBL 867-10887]

In 1986, in response to an order issued by the State Water Quality Control Board, influx of drainage water into the reservoir ceased, and an intensive program was initiated to assess the extent of groundwater contamination and determine the best alternative for cleaning up the reservoir. A discussion of the cleanup alternatives and an overview of the multidisciplinary research plan are given by Weres et al. (1987). To assess the feasibility of each of the cleanup alternatives, an understanding of both the past and present interactions between the reservoir and the groundwater under Kesterson Reservoir is essential. The risk of continued groundwater and surface water contamination with each of the alternatives must also be assessed. The hydrologic program focuses on developing the data base required to characterize the transport properties of the sediments underlying the aquifer, assessing the extent of groundwater contamination, predicting the rate at which dissolved chemical species travel through the groundwater system, identifying the pathways along which they migrate, and developing a strategy for minimizing the risk of present-day and future contamination of subsurface and surface waters. The specific components of the hydrologic research program are discussed below.

HYDROLOGIC SETTING

Kesterson Reservoir is situated in the midst of a seasonal wetland. Within a 124-square-mile region centered on Kesterson Reservoir, approximately 18% of the land is seasonally flooded for duck ponds. Kesterson Reservoir accounts for approximately 8% of the total seasonal wetland within this region. The average depth to the water table ranges from 0.5 m in the west to 3 m in the east. Annual fluctuations of approximately 1.5 m are caused by controlled flooding of nearby duck ponds and by winter precipitation. On a regional scale groundwater movement is

from the south and west to the northeast. On a local scale the reservoir creates a groundwater mound (see Fig. 2). After seeping through the bottom of the ponds, water flows subradially away from the reservoir, where it mixes with the native groundwater and migrates down gradient.

On a smaller scale the infiltration and solute migration are strongly influenced by local variations in the physical properties, chemical composition, and thickness of the fine-grained surface layer, as well as reservoir operations. Before the influx of drainage water was stopped, seasonal variations in the water supply, evaporation rate, and water-table elevations resulted in periodic flooding of the different ponds. This created two distinct hydrologic and geochemical regimes. Ponds in the southern part of the reservoir were flooded year round, and the underlying sediments remained fully saturated: a downward hydrologic gradient persisted throughout the year. The northern ponds were only used periodically, primarily during the winter and spring months. Under these ponds, the water table rose to the surface during the wet season and dropped below the surface in the dry season. During the summer and autumn, the hydraulic gradient was primarily upward. In the winter and spring, the gradient was downward.

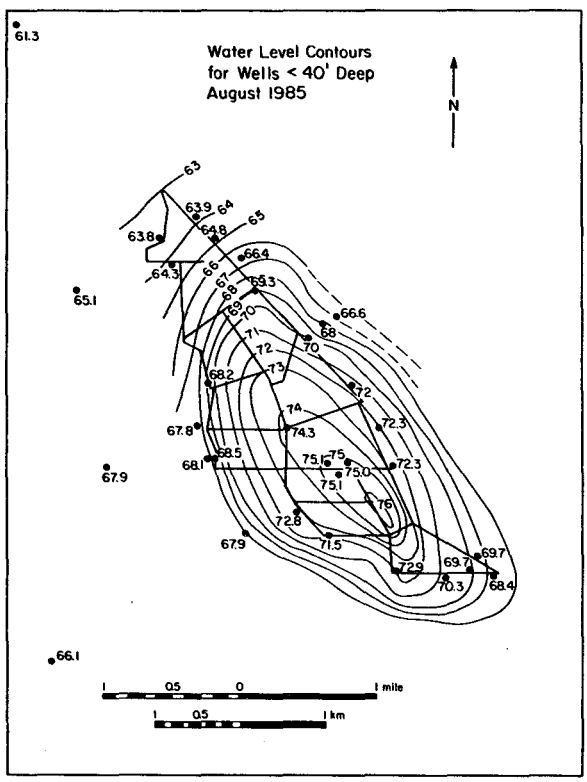

Figure 2. Water-table contours at Kesterson Reservoir. [XBL 8511-12675]

HYDROLOGIC PROPERTIES OF THE UNDERLYING AQUIFER

Six reservoir sites have been chosen for intensive investigation, each within a different hydrologic/geochemical/ecological regime. Numerous boreholes have been drilled at each of the sites, providing information on the local geology, hydrology, and geochemistry. Investigations include geophysical logging for defining the subsurface lithology, steady-state pumping tests for evaluating permeability variations in the aquifer, chemical sampling and analysis for evaluating the lateral and vertical extent of the contaminant plume, pressure-transient pumping tests, and interference tests for measuring average vertical and horizontal permeabilities. A summary of the results of these investigations is provided below.

Correlation of lithologic and geophysical profiles indicate the presense of thick sands, interbedded by three major clay/silt layers (see Fig. 3). The average horizontal permeability of the sandy aquifer is approximately 3×10^{-11} m^2 (30 d), but steady-state tests indicate that average permeabilities may vary locally by as much as a factor of 4. The average vertical permeability of the silt/clay layers is on the order of 10^{-14} m^2 (10 md). Analyses of the chemical composition of the groundwater show that the clay/silt layers impede the vertical flux of drainage water and, where they are encountered at depth, act as local barriers to vertical migration. Boron concentrations of 10 to 20 ppm in the groundwater beneath the reservoir indicate that drainage water has migrated to an average depth of 17 m but varies from less than 6 m to over 35 m. In general, low concentrations of selenium in the groundwater ($<$ 5 ppb) confirm earlier observations that selenium is removed from the water as it infiltrates through the organic-rich layer of mud covering the bottom of the ponds.

TRACER TESTING

Although hydrologic measurements provide information that is useful for predicting the average velocity at which solutes migrate through the groundwater system, they provide little data on the variability of the sediments, which plays a major role in controlling solute transport. A review of tracer-testing techniques indicated that a multiwell tracer test, with an injection/pumping well doublet, and multiple observation wells located midway between the two active wells would provide the most information on the heterogeneity of the sediments underlying the reservoir and a direct measure of solute

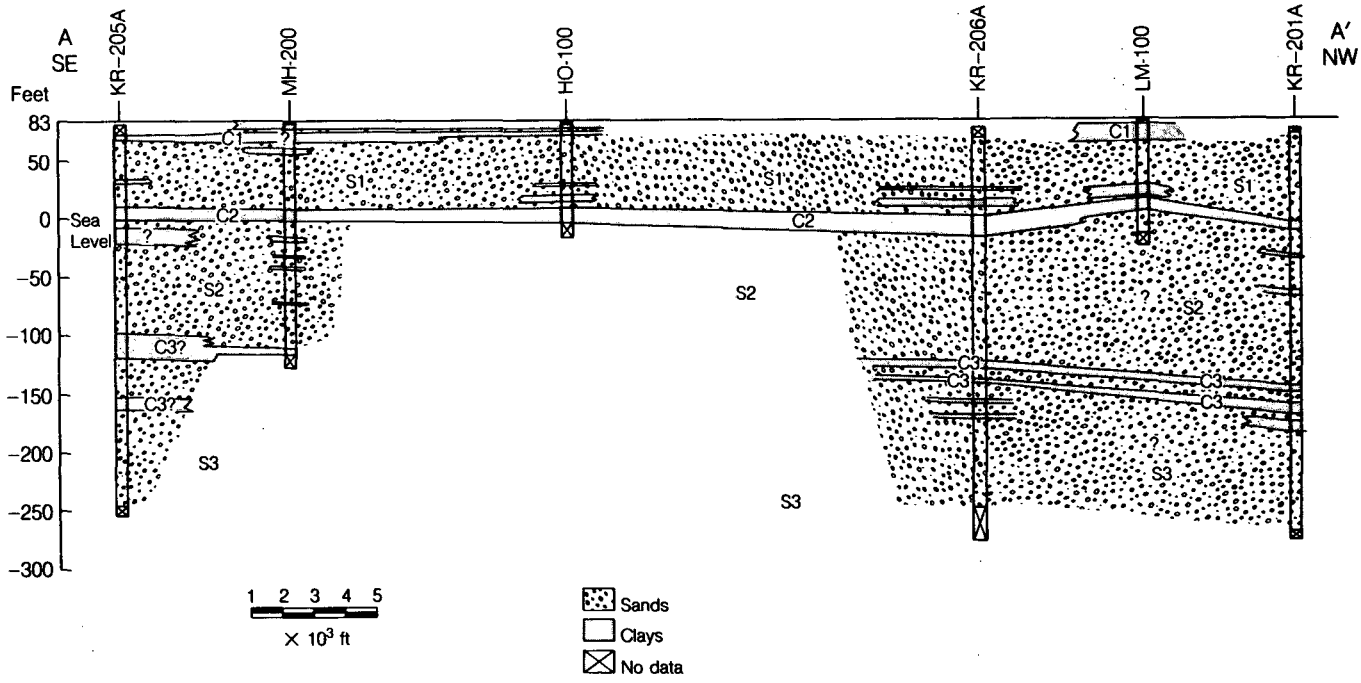

Figure 3. Geologic cross section of the sediments underlying Kesterson Reservoir. [XBL 867-10888]

migration (see Fig. 4). The test began by establishing a steady-flow field between the two wells by pumping water (4.8×10^{-3} m^3/s) from one well and injecting it into another well located 30 m away. Once the steady-flow field was established, a 1-hour slug of a 300-ppm fluorescein solution was injected into the aquifer. Pumping and injection continued for the approximately 10 days it took for the tracer to travel from the injection well to the pumping well. Fluid samples from five observation wells, located midway between the pumping and injection wells, were collected at regular intervals until the tracer slug passed by the observation wells.

The tracer recovery curve from one of the observation wells is shown in Fig. 5. The multiple-peak recovery curve indicates that fluid is flowing through several distinct lithologic strata, each of different permeability and thickness. Analysis of tracer recovery data indicates that within this 6-m section of the aquifer, there are at least 12 distinct strata. The layers range in thickness from less than 0.075 m to approximately 1 m. The hydraulic conductivity of the layers varies by a factor of 3 to 4. Data from the test indicate that hydrodynamic dispersion (due to pore-level mixing), molecular diffusion, and the

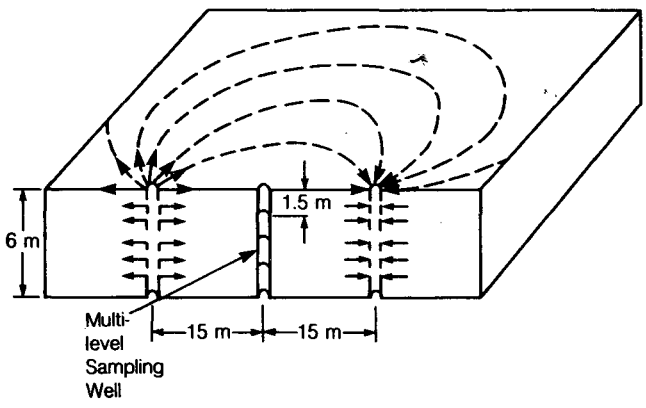

Figure 4. Schematic diagram of a two-well tracer test with a midpoint multilevel sampling well. [XBL 873-9999]

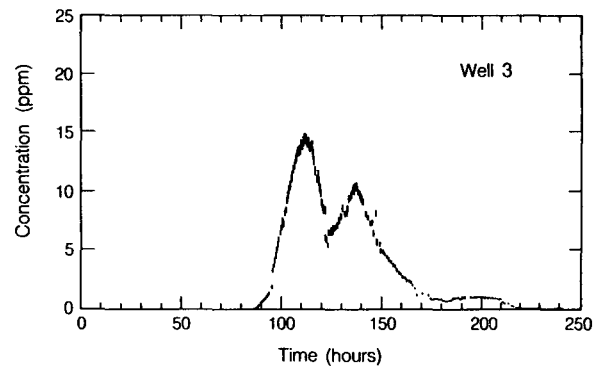

Figure 5. Tracer-recovery curve in observation well 3. [XBL 873-10000]

effects of geologic heterogeneity are all important dispersive mechanisms for chemical transport in this aquifer. Additional analysis of the tracer data will provide more detailed information on the relative importance of each of these factors and provide insight into the appropriate physical scales for modeling chemical transport in the aquifer.

WET/DRY-CYCLE MONITORING

A key concern in choosing the optimal strategy for cleaning up the reservoir is the fate of the selenium when the contaminated sediments are dried out and subsequently rewetted. When exposed to oxidizing conditions, some of the selenium may be converted from the relatively insoluble forms to the highly soluble selenate form (Weres et al., 1987). The potential for the occurrence of this phenomena and the potential adverse environmental impacts caused by it are being addressed in a field monitoring study. Pond 1, the southernmost pond, was instrumented with nine nests of tensiometers (for measuring fluid potential) and soil water samplers. Pore-water samples were collected while the pond was dry to provide data on preflooding concentrations of selenium in the pore water. In mid-October the pond was intentionally flooded with a low-selenium water supply (10 ppb). Pore-water samples were then collected at regular intervals to determine the extent to which selenium is remobilized and the rate at which selenium is transported through the sediments.

A typical response at one of the water-sampling nests is shown in Fig. 6, where the concentration of selenium is plotted as a function of depth below the surface for four different sampling times. Before flooding, the concentration of selenium ranges from 50 ppb at the surface to 3 ppb at a depth of 4 ft. Immediately after flooding, the concentration in the top 2 ft increases abruptly to 200 ppb. This is the result of dissolving the selenium at the ground surface and rapidly transporting it through the unsaturated zone. With time, the selenium concentrations decrease as the pulse of selenium-rich water migrates downward. Preliminary analysis of the data from the nine monitoring sites shows that although the selenium is quickly remobilized after flooding, a significant proportion of the selenium is reprecipitated within several weeks as the reducing conditions that favor the relatively insoluble forms of selenium become re-established.

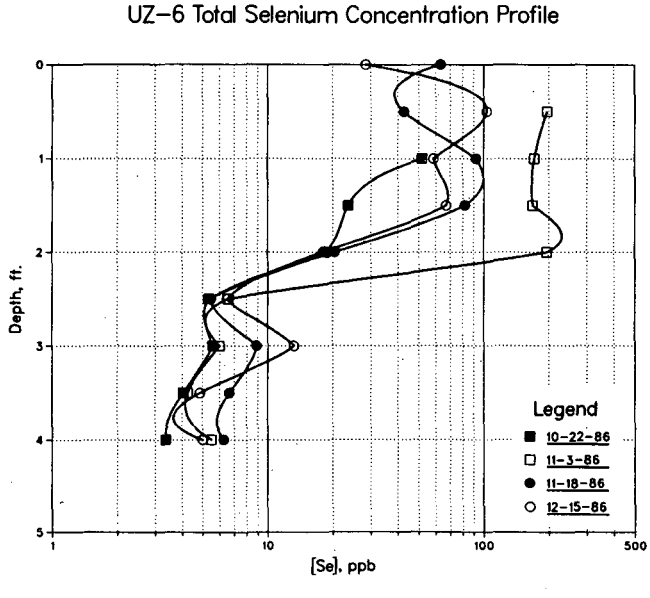

Figure 6. Pore-water concentration of total selenium and boron at site UZ-6. [XBL 873-1110]

LABORATORY STUDIES

A series of laboratory studies have been conducted in conjunction with the wet/dry-cycle field monitoring for the purpose of investigating selenium leaching under more systematic and controlled circumstances. The experiments were designed to investigate the effects of varying the leaching rate, presaturating the core with the percolating solution, and using sediment from two different depths beneath the pond bottom.

The results of one series of experiments is shown in Fig. 7. The graph includes data for two leaching rates and for both initially unsaturated and presaturated conditions. The figure shows that presaturating the sediments for a period of 1 week has little effect on the outflow concentration of selenium.

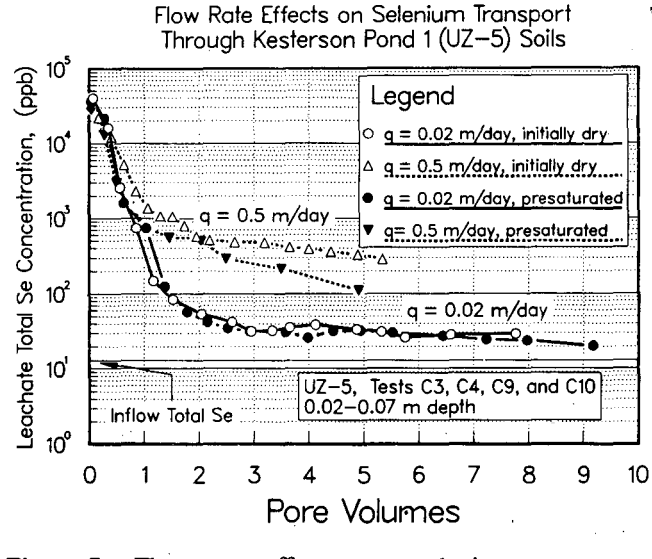

Figure 7. Flow-rate effects on selenium transport. [XBL 873-1109]

Although presaturating the sediments had the expected effect of creating reducing conditions, the reducing conditions apparently had little influence on the selenium speciation. This result remains to be explained. On the other hand, the leaching rate has a significant impact on leachate concentrations and on the total quantity of selenium that is leached from the soils. At higher flow rates, the outflow concentrations and total outflow are much higher. This suggests that there are kinetic limitations on selenium immobilization. We have not yet been able to isolate the effects of biological processes from those of nonbiological chemical processes on selenium immobilization. Additional laboratory leaching experiments are being done to address this issue further.

MODELING STUDIES

Predicting the migration of the contaminant plume (selenium- and boron-rich waters) in response to historical operation of the reservoir and to the various cleanup options requires development of a model for groundwater flow and chemical transport. At present the uncertainty about the complex chemical reactions that remove selenium from the pond water as it infiltrates through the pond-bottom sediments precludes application of simplistic chemical-transport models for predicting the migration of selenium (LBL, 1986). When both a sufficient data base and a theoretical understanding of these reactions are developed, they can be incorporated into mathematical models that predict fluxes of the various species of selenium from the ponds into the groundwater system and be used to predict where the selenium that has already entered the aquifer will migrate. In the meantime boron in the groundwater aquifer appears not to react with the sediments and serves as a natural indicator of solute transport (LBL, 1986). A large-scale highly simplified model of the reservoir has recently been used to provide a coarse calibration of the groundwater-flow model.

The numerical simulator CHAMP (chemical transport accompanying transient fluid flow in variably saturated systems) is used for these calculations (Narasimhan and Alavi, 1986). The code, which is a combination of TRUST (fluid flow in variably saturated systems) and a modified version of TRUMP (chemical transport), uses the integral finite-difference method for formulating the governing equations. CHAMP can calculate time-dependent solute and water transport in multidimensional heterogeneous systems with time-dependent boundary conditions and material properties. The chemical transport algorithm has the capability of

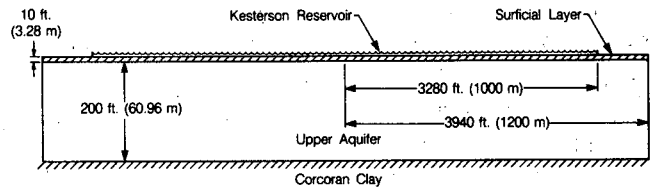

Figure 8. Schematic of the reservoir model used for the coarse-scale calibration runs. [XBL 863-10744]

including the effects of advection, molecular diffusion, hydrodynamic dispersion, adsorption, and solid diffusion.

In order to assess the vertical and horizontal extent of the plume of boron-rich water that has infiltrated from the ponds into the aquifer, a two-dimensional radially symmetric geometry is used to approximate the configuration of the ponds (see Fig. 8). The simulation predicts that during the period from 1982 to 1986, the plume migrated to an average depth of approximately 20 m below the ground surface directly underneath the reservoir (see 0.5 contour in Fig. 9). The depth of the plume decreases with increasing distance from the edge of the reservoir to a depth of approximately 6 m at the leading edge of the front. After 4 years the front has migrated approximately 120 m from the edge of the

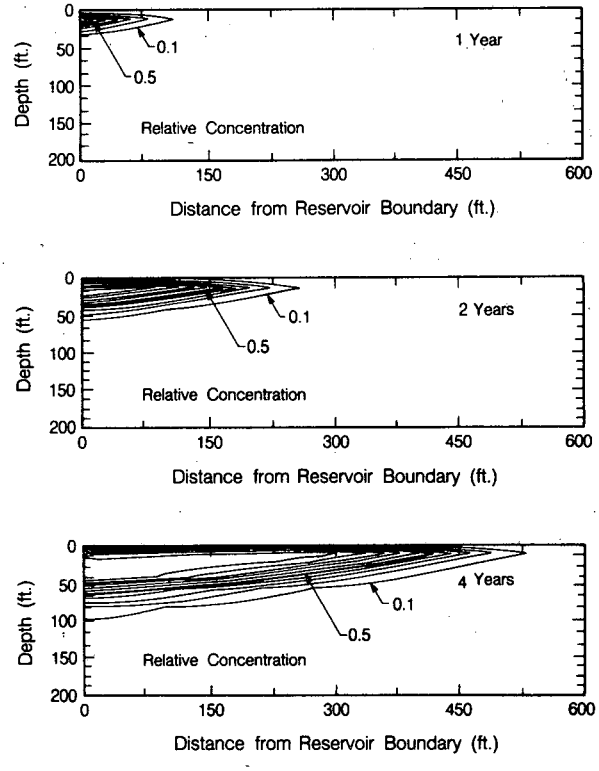

Figure 9. Migration of the plume of boron from calibration model. [XBL 863-10745]

reservoir. Although the above calculations neglect many important parameters that affect movement of the plume, they do provide a basis for comparison with the actual migration of the plume. Data from the hydrologic study sites show that with one exception, undiluted pond water has migrated to a depth of at least 13 m below the reservoir. The average depth of the plume (from the remaining five sites) is approximately 17 m. This is in reasonable agreement with the value calculated from the model (20 m). On the other hand, the large variations observed in the depth of the plume (no pond water to over 37 m), suggest that local stratigraphy and reservoir operations play an important role in controlling movement of the plume. A more accurate model that incorporates both of these factors is being developed.

REFERENCES

LBL, 1986. Hydrological, geochemical, and ecological characterization of Kesterson Reservoir. Progress Reports 1, 2, and 3 prepared for the Bureau of Reclamation. Lawrence Berkeley Laboratory Internal Documents LBID-1101, LBID-1188, and LBID-1213.

Narasimhan, T.N., and Alavi, M., 1986. A technique for handling tensorial qualities in the integral finite-difference method. *In* Earth Sciences Division Annual Report 1985. Lawrence Berkeley Laboratory Report LBL-20450, p. 111–113.

Weres, O., Benson, S.M., Bowman, H.R., Horne, A., Roth, J., Tokunaga, T.K., White, A.F., Wollenberg, H.A., and Yee, A., 1987. Selenium at Kesterson Reservoir: Hydrologic, chemical, and ecological appraisal. *In* this Annual Report.

Weres, O., White, A., Wollenberg, H., and Yee, A., 1985. Geochemistry of selenium at Kesterson Reservoir: Possible remedial measures. Earth Sciences, (Lawrence Berkeley Laboratory PUB-431), v. 8, no. 3, p. 1–8.

Plotting Program for Disc Meshes: Dimes

D. Billaux

We have developed over the past 2 years a three-dimensional fracture-mesh generator, FMG3D (Gilmour et al., 1986). This program is able to produce and analyze complex fracture meshes made of disc-shaped fractures randomly distributed in a given volume. To use it we also need a means to represent the meshes generated. Visual inspection is an incomparably more efficient way to check the output of the generation procedure than scrolling through very long numerical files. For example, checking that the program has found the right intersections between fractures is easy on a plot of both fractures and intersections but quite difficult without such a plot.

Existing software does not have the versatility needed to plot a number of fractures and perform the hiding procedures required to make the plot intelligible. Therefore, we have developed the program DIMES (DIscs MEShes). The program was designed (1) to give a reasonably accurate plot of the discs, allowing for any viewpoint; (2) to keep the computing time within manageable limits; (3) to provide enough versatility for use with any plotter; (4) to show the relative position of the fractures and the flow and generation regions; and (5) to allow a subset of the fractures to be selected in the flow region, both for reducing computing time and for seeing inside the fracture mesh without being blinded by big fractures in the foreground.

PROGRAM CHARACTERISTICS

The program is potentially able to handle data from any code that will generate circular fractures, merely by changing the input orders. The user may specify a rectangular subregion of the generation region from one point to the whole generation region; the program then plots all the fractures that occupy at least part of this subregion.

We chose the orthographic projection method, which is a projection normal to the plane of the plot, because it is very easy to implement. Once the viewpoint has been chosen, the coordinates of all points in the plot are rotated accordingly, so that the xy plane corresponds to the plane of the plot. When plotting, the z coordinate is dropped.

To give a good idea of orientation and aperture, the fractures are plotted as two parallel discs separated by a distance proportional to the aperture. Each disc is approximated by a polygon, putting more segments where the tip of the ellipse will be on the plotting plane. Only half of the lower disc polygon is generated, since the half farthest from the viewpoint would be automatically hidden by the upper disc. The number of segments in one polygon varies with the size of the fracture and its orientation relative to the plotting plane, with a maximum for the biggest fracture set by the user. The lines that represent the intersections between fractures are then added. It is necessary to keep track of the fractures that form the intersection so that a fracture disc never hides one of its own intersections. An intersection is plotted as a solid line if it is inside the flow region and as a dotted line if it is outside the flow region.

The core of this program is two nested do loops; the exterior loop governs the discs and the interior one the line segments. Any segments found to be hidden are eliminated from this loop. DIMES checks to see if a segment is hidden by the disc; if it is, then the program either deletes the old segment or calculates the coordinates of the endpoints of the new shorter segment. Creating a second new segment is necessary if the old segment is hidden only in its middle. The hiding process takes the greatest share of the computer time needed by the program, because the number of segments is high even in relatively simple sets. For example, 50 fractures divided each into two discs of 40 segments and 20 segments and having 100 intersections make up a set of about 3100 segments at the first iteration of the discs loop.

To reduce the time involved in the hiding process outlined above, the upper discs are sorted with respect to the volume they hide behind them in descending order. The lower discs, which will hide very few segments, are kept at the end. Looping over the discs in this order results in hiding more segments in the early iterations, thus saving a number of later comparisons.

Because we did not want to bind ourselves to any particular plotting device or driver, we resolved to use only very simple orders from the plotting software, namely "draw a segment" or "write a line of text," apart from the initialization and end-of-plot orders. Moreover, all the plotting orders are grouped into one subroutine, thus making the software readily adaptable to any other plotting interface. The plotting software currently in use is DISPLA, by ISSCO corporation.

From information on the size and orientation of the generation and flow regions, and given the viewpoint angles, DIMES draws the flow region into the main plot area, showing its edges only when they are not hidden behind a fracture. In addition, to help the user visualize both the viewpoint and the orientation and size of the flow region, a small "orientation box" is drawn in the lower left corner of the plot, showing the relative size and orientation of the flow region and the cube encompassing the generation region from the same viewpoint as the main plot. Recall that the generation region is created in global coordinates and that the flow region is selected inside the generation region. The flow region may be rotated with respect to the generation region. The plot created by DIMES has a viewpoint that amounts to rotating the generation region and flow region by the same amount. The coordinate axes shown in the "orientation box" pass through the lowermost edges of the generation and flow regions, respectively, toward increasing coordinates. To differentiate the x, y, and z axes one needs to know three things: first, the axes form a right-hand coordinate system. Second, because of the order of rotations used to determine the point of view, the z axis of the generation region is always vertical in the plot plane. Third, the y axis of the rotated flow region is always horizontal because of the nature of the two rotations that can be performed by FMG3D.

EXAMPLES OF DISC NETWORK PLOTS

Figure 1 shows a regular and symmetrical fracture network with the flow region totally included in all fractures. Figure 2 shows a simple random mesh

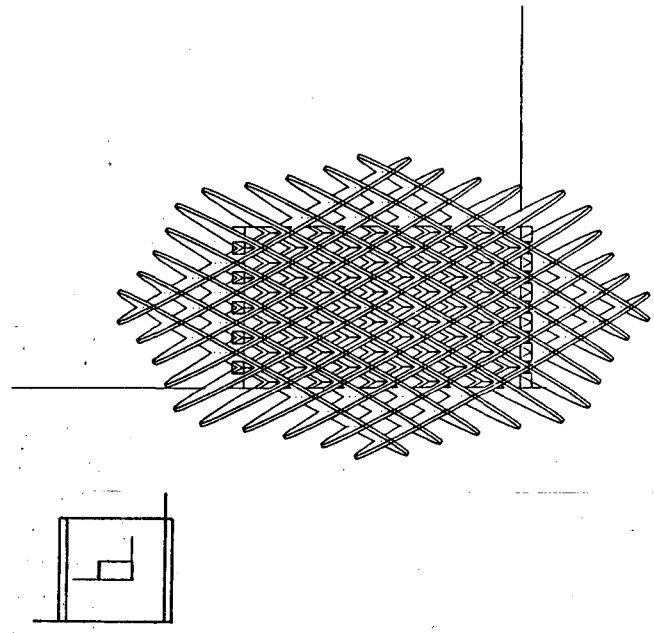

Figure 1. Regular fracture network. [XBL 871-219]

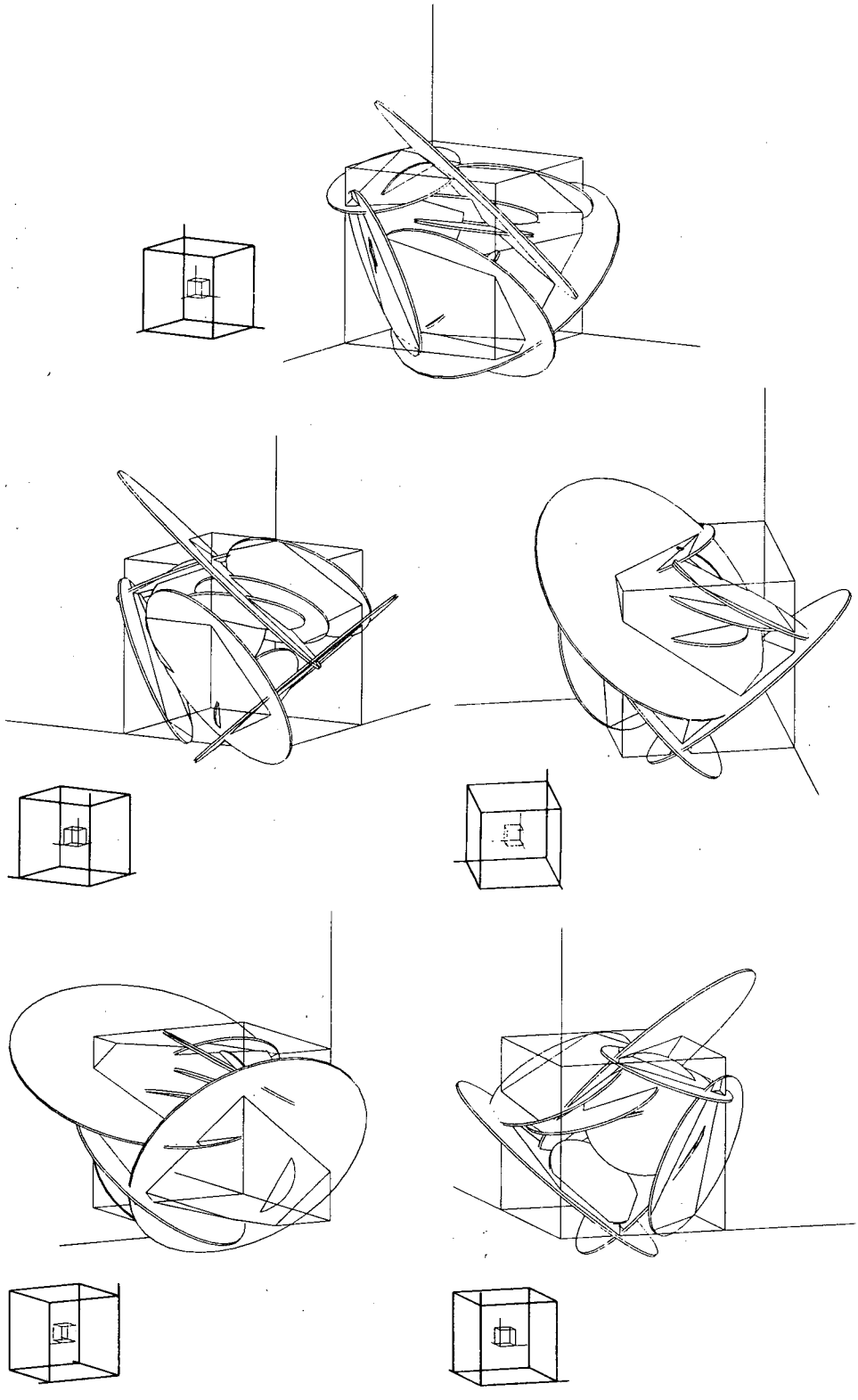

Figure 2. Simple random mesh, seen from varying points of view. [XBL 869-11039]

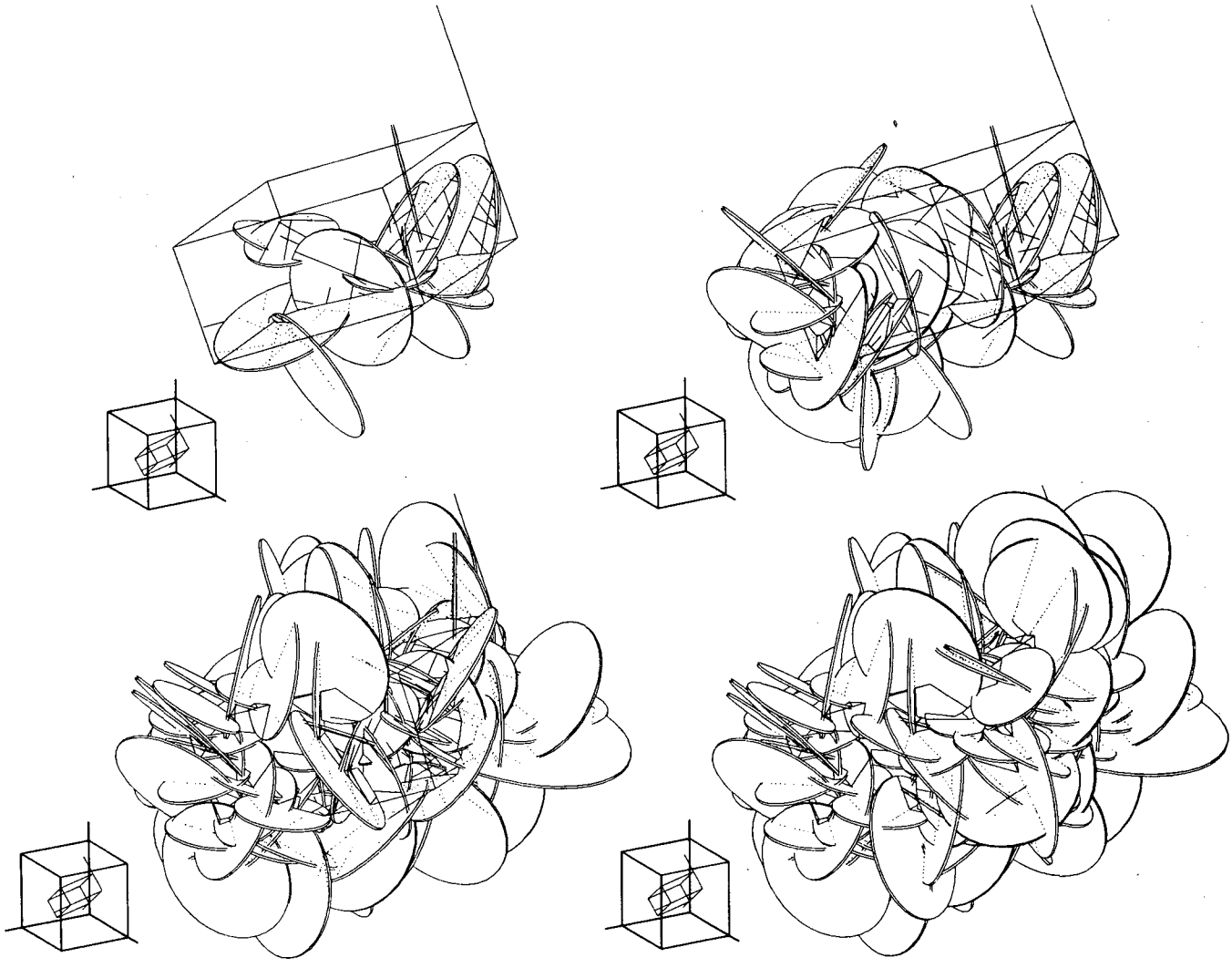

Figure 3. Random network, rotated flow region. [XBL 869-11040]

and the use of varying viewpoints to give a complete description of the mesh. Figure 3 shows how DIMES can be used for plotting a subregion instead of plotting all the fractures.

REFERENCE

Gilmour, H.M.P., Billaux, D., and Long, J.C.S., 1986. Models for calculating fluid flow in randomly generated three-dimensional networks of disc-shaped fractures: Theory and design of FMG3D, DISCEL, and DIMES. Lawrence Berkeley Laboratory Report LBL-19516.

Model Studies of the Svartsengi Geothermal Field, Iceland

G.S. Bodvarsson

In the evaluation of geothermal systems, modeling studies are necessary to develop the proper exploitation scheme for a resource. It is generally advisable to use the simplest model possible that considers the important physical processes occurring in the system (Bodvarsson et al., 1985). Complex models introduce a greater degree of freedom, so that problems of solution uniqueness may arise. On the other hand, an oversimplified model will not consider all the important processes or their coupling. The choice of a model depends on the questions to be addressed and on the field complexities that will affect answers to these questions.

The field data from the Svartsengi geothermal field in Iceland are well suited for testing exploitation models and methods. The field has been under exploitation since 1976 and has a documented production and drawdown history (Gudmundsson and Olson, 1985). Fluids from the reservoir are used to heat fresh water that is piped to nearby villages for space heating (capacity 125 MW_t); the geothermal fluids are also used for electric power production (capacity 8 MW_e; Thorhallsson, 1979). Material balance analysis of the field data has been carried out by Kjaran et al. (1979, 1980), Regalado (1981), and Gudmundsson and Olsen (1985). Here we employ a numerical model with a coarse spatial discretization for the analysis of the Svartsengi data.

THE SVARTSENGI GEOTHERMAL FIELD

The Svartsengti geothermal field is located in southwest Iceland on the Reykjanes peninsula. Eleven geothermal wells have been drilled in the area, with an average well spacing of some 200 m; the total wellfield area is approximately 0.6 km^2 (Gudmundsson and Thorhallsson, 1986). The wells have revealed the presence of a high-temperature reservoir (240°C) at depths below 600 m (Eliasson et al., 1977; Kjaran et al., 1980). The production history is shown in Figure 1. As of March 1983 30 $\times$ 10^9 kg of fluids had been extracted, with a total pressure decline in the reservoir of 104 m (8–9 bars; Vatnaskil 1983; Gudmundsson and Olsen, 1985).

Conceptual models of the Svartsengi field have been developed by Eliasson et al. (1977) and Kjaran et al. (1980). They postulate that the field is recharged by fluids originating as rainfall in a mountainous area some 20 km east of the field. The fluids percolate to depths of approximately 3 km and are heated as they flow west toward the field. The fluids ascend in the Svartsengi region because of buoyancy effects, developing a convection cell, which explains the near-isothermal conditions (240°C) in the reservoir. It is believed that a small boiling zone is present at depths between 200 and 400 m in the vicinity of the shallow wells (wells 2, 3, and 10). The presence of the two-phase zone strongly suggests that the caprock is leaky, perhaps because of faulting.

MODEL DEVELOPMENT

Analytical models of the Svartsengi field have been developed by Kjaran et al. (1980), Regalado (1981), Vatnaskil (1983), and Gudmundsson and Olsen (1985). The models by Kjaran et al. (1980), Regalado (1981), and Gudmundsson and Olsen (1985) are very similar and are based upon the pressure-diffusion equation of single-phase water. These models do not consider energy balance, the presence of the two-phase zone, or variations in rock properties in the reservoir.

The primary objectives of developing a new model of the Svartsengi field are to investigate the effects of the two-phase zone on the pressure decline and to determine if the rather restricted reservoir geometry determined by the previous models is indeed necessary to explain the field data. The basic

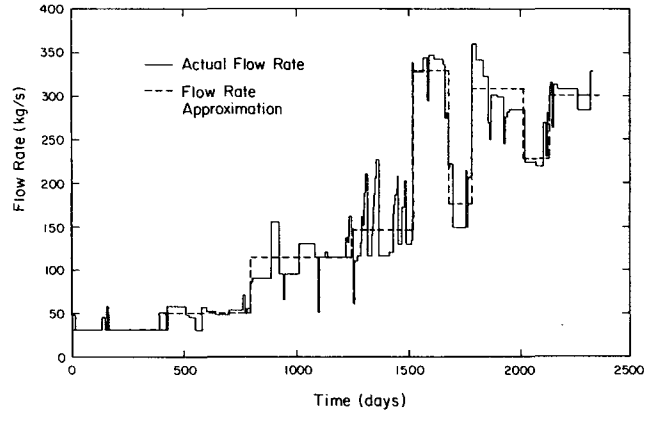

Figure 1. The total production history of the Svartsengi field during the period October 1976 to March 1983. The broken line represents average flow rates used in the numerical simulation (After Vatnaskil et al., 1983; Gudmundsson et al., 1985). [XBL 8511-12488]

model used is quasi-two-dimensional, with a 1400-m-thick reservoir of infinite radial extent. The wellfield is modeled using a single element with a surface area of 1 km^2 (radius of 564 m); radial elements outside the wellfield provide recharge. Recharge is also allowed from the overlying two-phase zone to the main reservoir cell. The two-phase zone is assumed not to be in hydrologic communication with the surrounding cooler fluids, which is in agreement with shallow pressure data. In this work the computer code MULKOM (Pruess, 1983) was used.

MODEL RESULTS

In the modeling it is assumed that the rock layer (confining layer) between the liquid reservoir and the overlying two-phase zone is permeable, so that recharge to the wellfield can occur both radially from outer regions of the reservoir and from above. The permeabilities in the confining layer and the reservoir are adjusted until a match with the observed pressure decline is obtained. All other parameters are assumed constant, with values given in Table 1.

Figure 2 shows the comparison between the calculated and observed pressure decline. The match is reasonably good at all times, with a little undershooting in the calculated pressures when the total production rate decreases (at approximately 1750 and 2200 days). These slight differences can readily be eliminated by further parameter adjustments, such as increasing the effects of the two-phase zone (increasing the permeability of the confining layer).

For the match shown in Fig. 2 the reservoir permeability and the permeability of the confining layer were 15 md. This value appears to be rather high for the confining layer, but vertical faults are common at Svartsengi (Franzson, 1983) and may create good hydraulic communication between the reservoir and the two-phase zone.

Figure 3 shows the flow patterns of steam and liquid water in the reservoir system. At the end of the simulation (2331 days) 25% of the fluids recharging the wellfield come from the two-phase zone (70 kg/s). Counterflow of steam and water has developed in the two-phase zone with about 20 kg/s of steam flowing toward the surface. Some of the steam condenses and increases the temperature in the shallow two-phase zone. At the end of the simulation the temperature at the top of the two-phase zone has increased by 5°C. There is evidence from field data that the temperature has actually increased

Table 1. Rock properties used in the simulation studies of Svartsengi.

Rock properties	Values
Rock density	2500 kg/m^3
Heat capacity	900 J/kg·°C
Porosity	10%
Thermal conductivity	2 W/m·°C
Relative permeabilities	Linear curves with S_{rl} = 0.40 and S_{rv} = 0.05

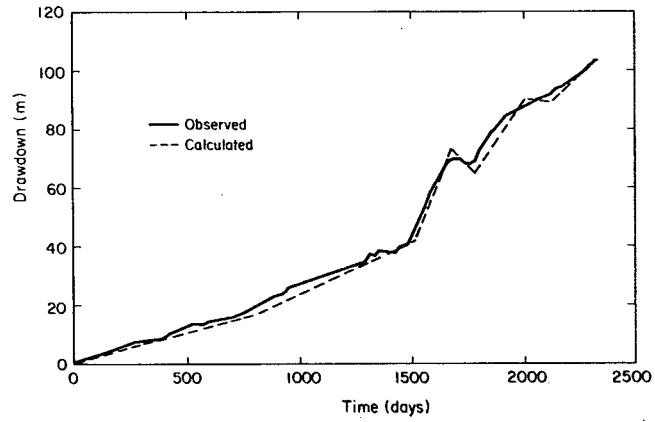

Figure 2. Comparison between calculated and observed water level decline for the radial model with an overlying two-phase zone. [XBL 8511-12497]

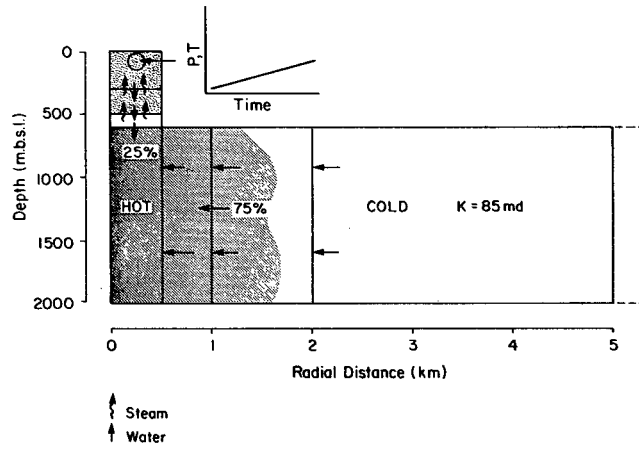

Figure 3. Steam and liquid flow patterns in the system and the location of hot and cold fluid zones. [XBL 8511-12493A]

in shallow regions of the field as a result of exploitation (Steingrimsson and Gudmundsson, 1983). Another evidence for an increasing upflow of steam due to exploitation is the fact that steaming grounds are now common at Svartsengi, whereas before exploitation steam was visible only on very cold winter days.

It is of interest to investigate reasons for the apparent permeability contrast between the inner and outer zones. One interesting possibility is that the apparent mobility difference between the inner and outer zones of the reservoir is due to temperature effects on the fluid properties rather than permeability changes. Kjaran et al. (1980) used resistivity data analyzed by Georgsson (1979) to estimate a temperature of 41°C at the reservoir depth outside the hot anomaly. the ratio of the viscosities inside and outside the hot anomaly is

$$\frac{\mu(T = 240°C)}{\mu(T = 41°C)} = \frac{1.1 \times 10^{-4}}{6.4 \times 10^{-4}} = 0.173.$$

This ratio agrees very well with the ratio of permeabilities inside and outside the high-mobility zone as determined from the modeling results:

$$\frac{k_{out}}{k_{in}} = \frac{15 \text{ md}}{85 \text{ md}} = 0.176 .$$

It is therefore possible that the permeability at Svartsengi is radially uniform, with a value of approximately 85 md, and that the mobility changes are due to cooler fluids with higher viscosity outside the 1-km-radius inner (hot) zone. The resistivity data indicate that the hot zone covers an area of 6–7 km^2, which is approximately twice the areal extent of the high-mobility region as determined by our modeling. On the other hand, periodic cooling has been observed in the field, primarily in wells located close to the edges of the wellfield. This cooling supports somewhat our radial model and the presence of cooler fluids close to the wellfield. For a hot zone with a radius of 1 km, reservoir thickness of 1.4 km, and porosity of 10%, there is a total of 370 kg of hot fluids in place. This is more than 10 times the amount produced by March 1983. Cooling by cold water flow through preferential pathways to the wellfield is certainly possible. It should be noted, however, that the wells experiencing cooling recovered fully in temperature (Steingrimsson and Gudmundsson, 1983).

REFERENCES

Bodvarsson, G.S., Pruess, K., and Lippmann, M. J., 1985. Modeling of geothermal systems. Paper SPE 11311 presented at the SPE 1985 California Regional Meeting, Bakersfield, California, March 27–29.

Eliasson, J., Arnalds, S.S., and Kjaran, S.P., 1977. Svartsengi. National Energy Authority Report OSROD-7718, Reykjavik, Iceland, 37 p. (in Icelandic).

Franzson, H., 1983. The Svartsengi high-temperature field—Subsurface geology and alteration. Geoth. Resour. Counc. Trans., v. 7, p. 141–145.

Georgsson, L.S., 1979. Svartsengi—Resistivity measurements. National Energy Authority Report OS79042/JHD, Reykjavik, Iceland, 100 p. (in Icelandic).

Gudmundsson, J.S., and Olsen, G., 1985. Water influx modeling of Svartsengi geothermal field, Iceland. Paper SPE 13615 presented at the SPE 1985 California Regional Meeting, Bakersfield, California, March 27–29, 1985.

Kjaran, S.P., Halldorsson, G.K., Thorhallson, S., and Eliasson, J., 1979. Reservoir engineering aspects of Svartsengi geothermal area. Geoth. Resour. Counc., v. 3, p. 337–339.

Kjaran, S.P., Eliasson, J., and Halldorsson, G.K., 1980. Svartsengi—Studies of geothermal activity. National Energy Authority Report OS80021/ROD10/JHD17, Reykjavik, Iceland, 98 p. (in Icelandic).

Pruess, K., 1983. Development of the general purpose simulator MULKOM. *In* Earth Sciences Division Annual Report 1982. Lawrence Berkeley Laboratory Report LBL-15500, p. 133–134.

Regalado, J.R., 1981. A study of the response to exploitation of the Svartsengi geothermal field, SW-Iceland. UNU Geothermal Training Program Report 1981-7, Reykjavik, Iceland.

Steingrimsson, B., and Gudmundsson, G., 1983. Svartsengi—Temperature and pressure in the Svartsengi reservoir. National Energy Authority Report OS-83086/SHD-17, Reykjavik, Iceland (in Icelandic).

Thorhallson, S., 1979. Combined generation of heat and electricity from geothermal brine at Svartsengi in S. W. Iceland. Geoth. Resour. Counc. Trans., v. 3, p. 773–736.

Vatnaskil, 1983. Svartsengi report. National Energy Authority Report PS-83086/JHD-17, Reykjavik, Iceland, (in Icelandic).

Reservoir Engineering Studies of The Geysers Geothermal Field, California

G.S. Bodvarsson and M. Ripperda

The Geysers geothermal field in northern California is the largest known geothermal field in the world. Development of the field for electric power production started in the 1960s, with the commencement of units 1 through 4, capable of generating approximately 80 MW_e of electricity. In the 1970s and 1980s the development at The Geysers accelerated to the extent that over 1700 MW_e are now being produced from the field. About 500 wells have been drilled, with over 300 wells feeding more than 20 power plants. Well drilling has been carried out by various private companies, including Unocal (formerly Union Oil Company of California). Most of the power plants are operated by Pacific Gas and Electric (PG&E), with several other utility companies operating one or two plants each.

The California State Lands Commission (SLC) oversees the use of State leases for geothermal development. At the request of the SLC, the Earth Sciences Division (ESD) began a research project to analyze field data from The Geysers and to construct models of the field response to exploitation. These studies are intended to help establish an understanding of the long-term generating capabilities of the various State leases. In the first year of activity the ESD developed a comprehensive data base for The Geysers, reviewed the existing literature, and analyzed some of the reservoir engineering data.

THE DATA BASE

A computerized data base for The Geysers field has been developed that utilizes a sophisticated data base management system to store and retrieve the data. A computer graphics package has been written to display the data in the most convenient form. The bulk of the data consists of production and injection histories of wells obtained from the Division of Oil and Gas. Monthly records dating back to 1968 are available for the flow rate, enthalpy, wellhead pressure, and temperature. Also incorporated into the data base are heat-flow data, directional surveys, well location data, lithologic data, well test data, and geochemical data.

A computerized base map has been developed for the geothermal area. It contains information regarding section, county, and lease lines; locations of wells and power plants; and geomorphic features, such as rivers, lakes, and topography. Figure 1 is a detailed map of the wellfield in State lease 4596.

DATA ANALYSIS

The directional surveys, generalized lithology, and steam entries for productive wells have been digitized. A graphical display program was developed that allows a cross section for any number of wells to be displayed. Figure 2 shows a generalized east-west cross section (A – A′) that includes several wells in Sulphur Bank, Happy Jack, and State lease 4596 (Ottoboni State and DX State). The figure shows some of the predominant rock types at The Geysers, such as graywacke, greenstone, chert, and argillite. For the wells shown, all of the steam entries are located within the primary reservoir formation, the Franciscan Graywacke. Most of the wells in the field contain 2–10 major steam entries; numerous smaller steam entries may be found in many of the wells. Most wells in The Geysers field are good producers, with an average production rate of about

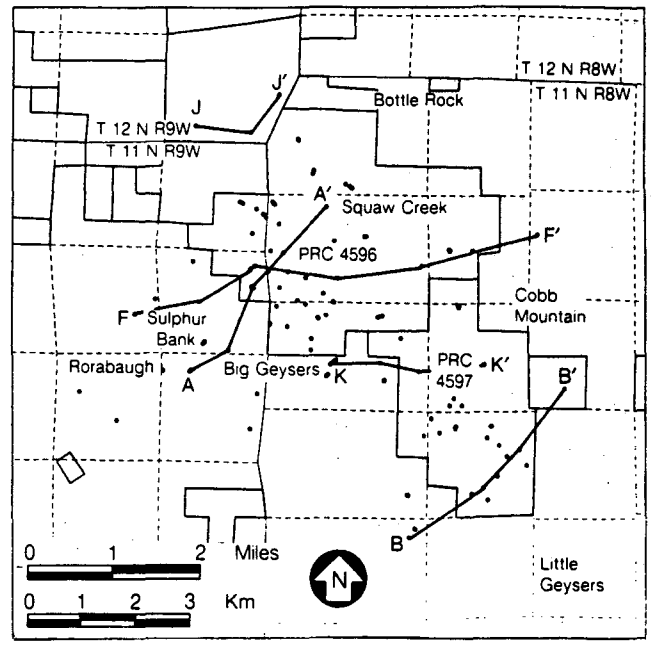

Figure 1. Map of The Geysers geothermal field, showing the surface locations of wells, with lithologic data and the locations of cross sections A – A′, B – B′, F – F′, J – J′, and K – K′. [XBL 868-10935]

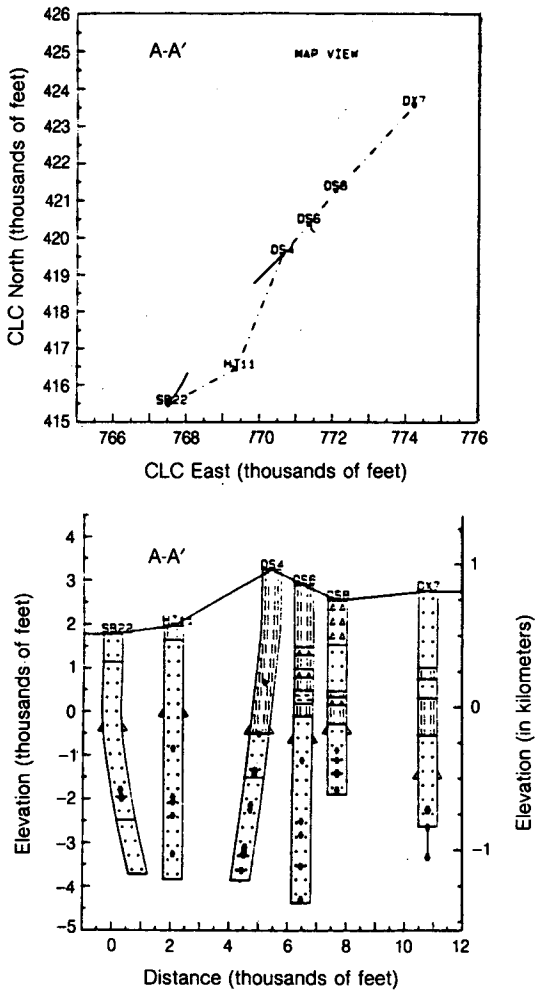

Figure 2. Map view and cross section for profile A – A', showing wells Sulphur Bank 22, Happy Jack 11, Ottoboni State 4, 6, and 8, and DX State 7. Lithologic units shown include graywacke (dots), greenstone (vertical lines), chert (triangles), and argillite (horizontal lines). Triangles on sides of columns indicate bottom of casing; stars indicate steam entries. [XBL 872-9925]

150,000 lb/h (20 kg/s). A few wells produce steam at a rate in excess of 250,000 lb/h (30 kg/s). The flow rate from the wells declines with time as pressure declines in the reservoir (Ramey, 1970; Dykstra, 1981).

The rate of the flow decline depends on many factors, such as the average well spacing, characteristics of the fracture system around the well, conditions of the well itself, and the availability of fluid reserves near the well. Budd (1972) performed model calculations to investigate the influence of well spacing on average flow-rate decline of Geysers wells. Dykstra (1981) compiled data from 18 wells and developed an empirical decline curve from the data, neglecting the effects of well spacing. He concluded that on the average the wells decline to 50% of the initial rate in about 8 years.

We have analyzed the decline of hundreds of wells and developed empirical decline curves for different well spacings and different areas of the field. The conventional "theoretical" decline curves (exponential, harmonic, and hyperbolic) were applied to the available data. Figure 3 shows a typical fit of a calculated decline curve with production data for well Ottoboni State 22. In general, we found that the hyperbolic curves best fit the available data, but the coefficient a in the hyperbolic formulation is close to unity (generally varies from 0.75–0.95), hence the decline is near harmonic. The average decline curves for various well spacings are shown in Fig. 4; also shown are the curves developed by Budd (1972) and Dykstra (1981). These curves indicate that an average well at The Geysers can be expected to decline by 50% in 8–12 years, depending upon the well spacing. The curve proposed by Dykstra is very similar to our curve for 5-acre well spacing, which is reasonable, since he primarily used data from wells located in densely drilled areas.

Our results show much less dependence on well spacing than those obtained from the theoretical calculations of Budd (1972). We believe that the reason for this is the near-uniform pressure decline over large areas within the reservoir. The reservoir permeability is high enough that pressures decline rather uniformly regardless of the well spacing. Other work carried out during the year includes analysis of heat-flow data, pressure-buildup data, and the pressure decline in the reservoir system. A detailed description of all of this work is given in Bodvarsson et al. (1987).

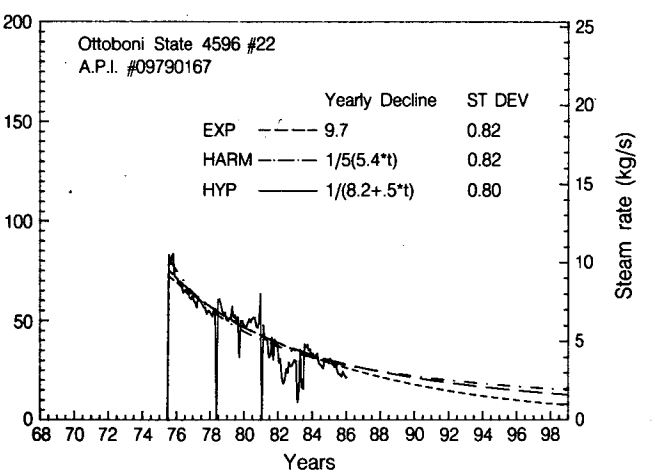

Figure 3. Flow-rate decline curves for well Ottobini State 22. [XBL 872-9926]

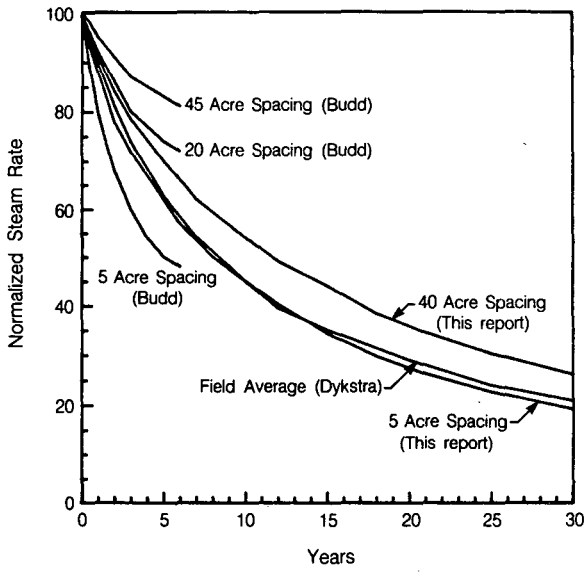

Figure 4. Comparison of ESD data with normalized flow-rate decline curves from Budd (1972) and Dykstra (1980). [XBL 868-10926]

REFERENCES

Bodvarsson, G.S., Cox, B.L., Fuller, P., Ripperda, M., Stein, D., Tulinius, H., Witherspoon, P.A., Flexser, S., Goldstein, N., Pruess, K., and Truesdell, A., 1987. A database for The Geysers geothermal field. Lawrence Berkeley Laboratory Report LBID-1257 (Vol. I).

Budd, C.F., Jr., 1972. Producing geothermal steam at The Geysers field. Paper SPE 4178 presented at the 1972 SPE Annual Meeting, Bakersfield, California, November 8–10, 1972.

Dykstra, H., 1981. Reservoir assessment. *In* A.D. Stockton, principal investigator, A Reservoir Assessment of The Geysers Field. California Division of Oil and Gas, Sacramento, California, p. 35–49.

Ramey, H.J., Jr., 1970. A reservoir engineering study of The Geysers geothermal field. Reich and Reich, Petitioners vs. Commissioner of Internal Review, 1969 Tax Court of the United States, 52, T.C. No. 74.

A Regionalized Parent-Daughter Model for Three-Dimensional Fracture Networks

J.P. Chiles, D. Billaux, and J.C.S. Long

This report describes how field data were used to model the three-dimensional fracture systems that we have developed over the past year. We recently completed a two-dimensional study of the fracture hydrology at the Fanay-Augeres mine in France (Long and Billaux, 1986). In this study we generated a network of fractures subregion by subregion in which some of the properties of each subregion were predicted through geostatistics and some were randomly varied. Mean fracture length and fracture density in each subregion were the parameters obtained through geostatistical simulation. Fracture location within the subregion, actual fracture length, aperture, and orientation were all chosen randomly. We have now designed an extension of this technique that generates three-dimensional disc-shaped fractures and allows regional fracture density variation through a simulation procedure that may be conditioned on data. Fractures are nucleated as "daughters" of a "parent," or seed, which allows the simulation of swarms of fractures. The simulation also allows for simulation of regional variation of orientation within each set of fractures.

Derivation of the model parameters from field data has required refinement in both the determination of the disc diameter distribution from the trace length distribution and in the development of parameters for regionalized density and orientation distribution with a parent-daughter process rather than a simple Poisson distribution. Discussion of these topics is followed by an outline of the generation procedure.

DETERMINATION OF DISC-DIAMETER DISTRIBUTION

To generate fractures in three dimensions from data that are essentially two-dimensional (drift-wall mapping) or one-dimensional (wellbore data), we need to derive the statistical relationships among the radii distribution, the volumetric density, the trace-length distribution, the frequency, and the areal density.

Obtaining data for the two-dimensional analysis was relatively straightforward because the vertical plane of analysis was exposed in the drift. This made it possible to obtain the areal fracture density simply by counting the fractures in the plane and estimating the trace-length distributions by direct measurement. For three-dimensional analysis we cannot see into the rock to count the fractures and determine their shape. Perhaps geophysics will help us with this problem in the future, but for now we must use statistical geometry to estimate these parameters.

To make an estimate of fracture density we assume that the fractures are randomly located in space on the scale of the subregion. If the volume is cut by a plane, then the statistical relationship between λ_A, the areal density on that plane, and λ_V, the volumetric density, is

$$\lambda_A = \lambda_V \bar{D}\, \overline{(\cos\theta)}\,, \tag{1}$$

where $\bar{D}$ is the mean fracture diameter, $\overline{(\cos\theta)}$ is a sampling orientation correction, and θ is the angle between the pole of each fracture and the plane of interest.

To determine λ_V we need to know $\bar{D}$, $\overline{\cos\theta}$, and λ_A. From the drift-wall mapping we can obtain θ, λ_A, and the distribution of trace length, l. Once we have an estimate of $\bar{D}$ we can calculate λ_V. Given below is the functional relationship between the distribution of fracture trace lengths and the distribution of fracture diameters, which was developed by Warburton (1980). In order to determine the parameters of the radii distribution from this relationship, one must assume the form of the distribution.

Let D = the diameter of a given fracture, x = the distance between the fracture center and the plane of intersection, $l = h(x)$ = the trace length of the fracture in the plane, $f(D)$ = the distribution of fracture diameters, $g(l)$ = the distribution of fracture traces, and $\bar{D}$ = the mean of $D \equiv \int_0^\infty Df(D)\,dD$. We have the relationship

$$l^2 = D^2 - 4x^2 \quad \text{for } x \leqslant \frac{D}{2}\,,$$

$$l = 0 \quad \text{for } x < \frac{D}{2}\,.$$

Warburton (1980) shows that

$$g(l) = \frac{l}{\bar{D}} \int_l^\infty \frac{f(D)}{\sqrt{D^2 - l^2}}\, dD\,. \tag{2}$$

Given the above relationship one can assume the distribution of fracture diameters, $f(D)$, and evaluate the integral to obtain the distribution of trace lengths, $g(l)$. One can then compare the computed distribution of trace lengths with that obtained from the field data. By trial and error, one can find a reasonable, but not necessarily unique, distribution for fracture diameters.

Knowing the first two moments of $g(l)$ from the corrected distribution, we can now calculate the relationship between the moments of $f(D)$ by trial and error. This information in turn will guide initial choices of $f(D)$ in the trial-and-error process. Recall that the fractures are discs and that they are cut by a random plane. Let us consider a fracture with a known diameter D. The expected values of the length $E(l\,|\,D)$ and of the square length $E(l^2\,|\,D)$ are given by

$$E(l\,|\,D) = \frac{1}{D}\int_0^D h(x)\,dx\,,$$

$$E(l\,|\,D) = \frac{1}{D}\cdot(\text{area of disc}) = \frac{\pi D}{4}\,,$$

$$E(l^2\,|\,D) = \frac{1}{D}\int_0^D h^2(x)\,dx$$

$$= \frac{1}{D}\int_0^D [D^2 - 4(\frac{D}{2} - x)^2]\,dx\,,$$

$$D(l^2\,|\,D) = \frac{2D^2}{3}\,. \tag{3}$$

In fact, the fractures have varying diameters, with a probability density $f(D)$. To find the expected value of l and l^2, we then have to integrate $E(l\,|\,D)$ and $E(l^2\,|\,D)$ over the range of possible diameters, taking into account the relative probability $D/\bar{D}$ of having a trace for a given diameter. It follows that

$$E(l) = \int_0^\infty \frac{D}{\bar{D}}\, E(l\,|\,D)\, f(D)\, dD\,,$$

$$E(l) = \frac{\pi}{4\bar{D}} \int_0^\infty D^2 f(D)\, dD \,. \tag{4}$$

Moreover,

$$E(l) = \frac{\pi}{4} \frac{E(D^2)}{E(D)} \,,$$

$$E(l^{2)} = \int_0^\infty \frac{D}{\bar{D}} E(l^2 | D) f(D)\, dD \,,$$

$$E(l^2) = \int_0^\infty \frac{2}{3\bar{D}} D^3 f(D)\, dD$$

$$= \frac{2}{3\bar{D}} \int_0^\infty D^3 f(D)\, dD \,, \tag{5}$$

$$E(l^2) = \frac{2}{3} \frac{E(D^3)}{E(D)} \,.$$

Or, if we call μ_l and σ_l the mean and standard deviation of trace length, then

$$\mu_l = \frac{\pi}{4} \frac{E(D^2)}{E(D)} \,, \tag{6}$$

and

$$\mu_l^2 + \sigma_l^2 = \frac{2}{3} \frac{E(D^3)}{E(D)} \,. \tag{7}$$

We have

$$E(D) = \mu_D \quad E(D^2) = \mu_D^2 + \sigma_D^2 \,. \tag{8}$$

If we assume the diameter distribution is lognormal with mean μ_D and standard deviation σ_D, then

$$E(D^3) = \mu_D^3 \,[1 + (\sigma_D^2/\mu_D^2)]^3 \,. \tag{9}$$

Replacing the moments of D in Eqs. (6) and (7) and arranging the equations, we have:

$$\mu_D = \mu_l \cdot \frac{128}{3\pi^3} \frac{1}{1 + (\sigma_l^2/\mu_l^2)} \,. \tag{10}$$

and

$$\sigma_D = \mu_l \cdot \frac{16}{\pi^2}$$

$$\times \sqrt{\frac{2}{3[1 + (\sigma_l/\mu_l)^2]} \left[1 - \frac{32}{3\pi^2[1 + (\sigma_l/\mu_l)^2]}\right]} \,. \tag{11}$$

A problem remains in that we do not have an infinite plane on which to observe l. Thus we cannot measure $g(l)$ very well because of the truncation of visible traces. Baecher and Lanney (1978) and Warburton (1980) have both addressed this problem, and a new approach has been developed by Chiles for parallel fractures. This approach does not require any a priori assumption on the shape of the distribution of length. The trace data are divided into three groups: fractures with both end points visible, fractures with one end point visible, and fractures with no end point visible. For each of these groups, histograms are plotted and the relationship between the true distribution and the observed one are derived.

Now one can make a trial guess at the histogram for real length and of the number of trace centers in the survey area. The program SALVE, developed by Chiles, then calculates the number of traces with no end point, one end point, and two end points in the sample area. We fit the lower end of the distribution using the results for two end points. We fit the tail knowing that the histogram for one end point is more sensitive to the middle of the distribution and the number of fractures with no end point is more sensitive to the tail.

REGIONALIZED THREE-DIMENSIONAL PARENT-DAUGHTER MODEL

We often observe that fractures occur in swarms or zones. The statistical description of this type of pattern is called a "parent- daughter" model. In this model the fracture swarms, or daughters, are nucleated around seeds, or parents. The location of the parents may be purely random, i.e., a Poisson process, or there may be a regional variation in the density of the parents. Once the parents have been determined, the daughters are found some distance

from the parents; this distance may have a normal distribution. Thus implementation of the model requires that we know the distribution of the density of the parents, the distribution of the number of daughters per parent, and the distribution of the daughters around the parents.

There are two major difficulties in obtaining these distributions from field data such as that available at Fanay-Augeres. The first problem is that it is not necessarily clear to which parent a fracture daughter belongs. This is further complicated by regional changes in the density of fractures. The second problem is that the parents and daughters are distributed in three-dimensional space but we can only observe traces. The centers of the traces are not the same as the centers of the fractures, and the parent is a point that does not necessarily lie in the plane of observation. The first problem requires that we propose a parent-daughter model and see how well it fits. A logical way to do this, which includes regional variation in density, was proposed by Deverly (1986). An approach to the second problem has been worked out at Lawrence Berkeley Laboratory by J.P. Chiles. Details are complex and therefore not given here.

These results have been incorporated in the program SALVE. To use this program we estimate the density of parents, the mean number of daughters, the dispersion of daughters, the distribution of disc size, and the variogram of the density of parents. Given these and the size of the support sample (i.e., the subregion volume over which density is measured), the program calculates the variogram of the fracture density. This variogram can then be compared with the variogram derived from the field data. We can then change the estimates until a good fit to the variogram is found.

When a good fit is found, we have obtained an estimate of the parameters for the parent-daughter model; this estimate can be used to simulate the density of parents in each subregion. This simulation and the other parent-daughter parameters are used to generate realizations of the fracture system, as described in the previous section.

ORIENTATION

Within a given set there may be a large dispersion in orientation. Locally, however, especially within a swarm, the orientation distribution may be quite narrow. Thus orientation has spatial structure. To account for this we can construct variograms for orientation. These variograms typically will have a nugget that represents the local variation of orientation. If this nugget is subtracted from the variogram, the result can be used in a simulation to predict the mean orientation on a grid throughout the region. When a particular fracture is nucleated by the process described below, the orientation can be found by interpolating the mean orientation from the nearest-neighbor grid points and adding to that a random component dictated by the nugget of the variogram.

GENERATION SCHEME

The following steps are used to create a realization of the fracture system once an acceptable parent-daughter model has been obtained: (1) Define subregions on the same scale as the sample support. (2) For each subregion, read the strength of the parent Poisson process from the simulation. (3) From this Poisson process, pick the number of parents to be generated in the subregion. (4) For each parent, pick random values of x,y,z in the subregion. (5) Pick the number of fracture daughters from the distribution determined above. (6) Pick the location of the fracture centers distributed around the parent. This may be an anisotropic distribution. (7) Pick the orientation in two steps. First, pick the continuous part from the simulation described above. Then add a random component as determined by the nugget of the orientation variogram. (8) Pick the fracture length and aperture from the global distributions.

REFERENCES

Baecher, G.B., and Lanney, N.A., 1978. Trace length biases in joint surveys. *In* Proceedings, 19th U.S. Symposium on Rock Mechanics, AIME, p. 56–65.

Long, J.C.S., and Billaux, D., 1986. From field data to fracture network modeling—An example incorporating spatial structure. Water Resour. Res., in press.

Warburton, P.M., 1980. A stereological interpretation of joint trace data. Int J. Rock Mech. Min. Sci. Geomech. Abstr., v. 17, p. 181–190.

Two-Phase Effects on Pressure-Transient Data

B.L. Cox and G.S. Bodvarsson

Few methods are now available for analyzing pressure-transient data from two-phase reservoirs. The presence of two-phase zones in geothermal reservoirs introduces several complications that can greatly influence the pressure transients. First, the mobility of two-phase mixtures can differ significantly from that of single-phase fluids. Second, the compressibility of two-phase mixtures is orders of magnitude higher than for single-phase liquid and vapor (Grant and Sorey, 1979). Third, large density differences between vapor and liquid water can give rise to counterflow of vapor and liquid (Martin et al., 1976), with vapor moving upward and liquid percolating downward. Associated with the counterflow is strong heat transport resulting from the large differences in the enthalpy of vapor and liquid water.

We have performed numerical simulations to study the effects of two-phase zones on pressure transients and will show the results obtained for two different reservoir systems. The first is a single-phase liquid reservoir having an isolated two-phase zone. This problem was studied previously by Sageev and Horne (1983a,b) and Sageev (1985), who used a constant-pressure approximation for the two-phase zone because of the high compressibility of two-phase fluids relative to single-phase liquid water. We compare the pressure transients resulting from numerical simulations with type curves based upon the constant-pressure approximation to test the validity of this approximation. The second system is a single well producing from a reservoir that is two phase throughout. We also examine the pressure-transient behavior from observation wells with feed zones at different depths in the reservoir as well as the overall fluid-flow patterns.

APPROACH

Both cases were modeled as porous-medium reservoirs, with a thickness of 500 m, a porosity of 0.05, and a permeability of 5 md. These two cases are illustrated in Fig. 1. Linear relative permeabilities with immobile liquid saturation of 0.40 and immobile vapor saturation of 0.05 were used. The numerical code MULKOM (Pruess, 1983) was used to simulate the two cases.

For the first case (Fig. 1, top) the two-phase zone is modeled as a rectangular subregion, with size variations of 100 and 1500 m^2. The two-dimensional single-layer grid was calibrated by running cases in which the two-phase zone was modeled as a constant-pressure zone, and the results matched well those of Sageev and Horne (1983a,b). To simulate the actual two-phase zone, a uniform initial pressure of 100 bars was assigned to all the elements in the grid. An initial temperature of 250°C was assigned to the single-phase region, and the temperature of the two-phase region corresponding to 100 bar pressure was 310°C. We investigated the heat-conduction effects that would result from the large temperature gradient across the boundary between single-phase and two-phase regions and found that conduction had insignificant effects on the pressure transients within the time frame studied (3 years).

For the second case (Fig. 1, bottom), a single well penetrates a two-phase reservoir; production from the well is assumed to be either at the top or bottom of the reservoir. A 10-layer radial grid is

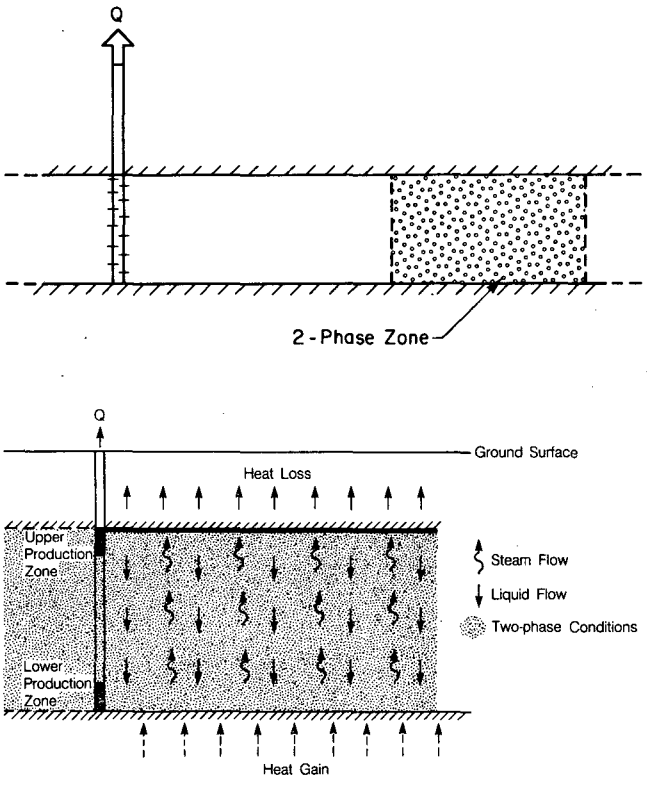

Figure 1. Problems considered. **(Top)** Isolated two-phase zone in a single-phase liquid reservoir. **(Bottom)** Stable two-phase reservoir achieved by heat flow through the reservoir. [Top, XBL 861-10511A; bottom, XBL 866-10846]

used, each layer being 50 m thick, and a production interval of 50 m is assumed. Initially, the system is entirely two phase with a nearly uniform vapor saturation (S_v = 0.05) achieved by maintaining an appropriate heat flow through the system (Martin et al., 1976). Constant heat flux is applied at the bottom, and the energy is transferred to the top of the reservoir by liquid-vapor counterflow. A constant heat sink of 0.4 W/m^2 is specified at the top of the reservoir, representing conductive heat losses. Initial pressure is practically hydrostatic with depth, and the initial temperatures vary from 245°C at the top to 287°C at the bottom.

LOCALIZED TWO-PHASE ZONE

The pressure transients resulting from the case of a well producing in a liquid reservoir with a localized two-phase zone are summarized in Fig. 2. The simulations were carried out for a period of 3 years, assuming a constant production rate of 25 kg/s. The pressure transients differ significantly from those obtained when a constant-pressure solution is used, because of the higher kinematic viscosity (and therefore lower mobility) of two-phase fluids as compared to the single-phase fluids. For the case with a larger two-phase zone, the pressure transients are similar to those of a constant-pressure approximation for about 2 months. However, at later times the relatively low fluid mobility in the two-phase zone causes much more rapid pressure changes, in some cases even resulting in a steeper slope than that given by the line-source (Theis) solution. The time of deviation from the line-source solution could be used to estimate distance between the producing well and the two-phase zones, and data from several observation wells could be used to estimate the size of the two-phase zone. Detailed description of this work is given by Cox and Bodvarsson (1986).

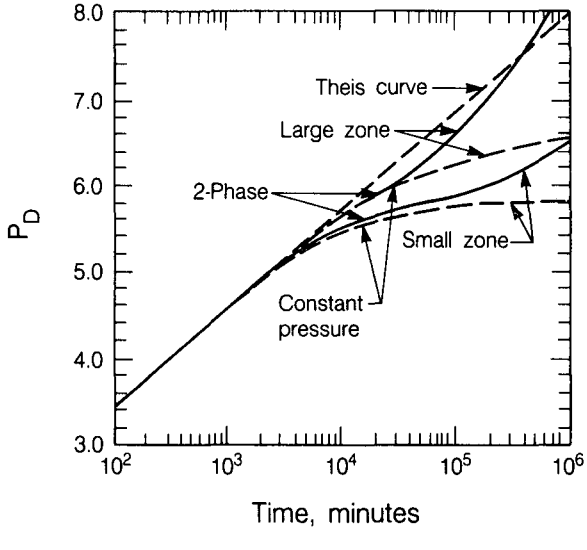

Figure 2. Computed pressure transients from a well producing in a single-phase liquid reservoir with both small and large two-phase zones and constant-pressure zones. [XBL 872-9927]

LOCALIZED FEED ZONES IN TWO-PHASE RESERVOIRS

The fluid flow patterns and reservoir depletion resulting from production from deep feed zones in two-phase reservoirs are shown in Fig. 3. The pressure declines observed for this model are near linear at early time, and then stabilize, as fluids from above recharge the producing layer. Vertical flow is dominant, and the later time pressure-transient data are mostly affected by the vertical liquid flow and the expansion of a vapor-dominated zone at the top of the system.

This vapor-dominated zone will practically remain at a constant pressure because the nearly hydrostatic pressure gradient does not allow downward flow of steam to the production zone. A subcooled liquid zone can be found in the middle of the reservoir; this single-phase liquid zone evolves by downward percolation of cooler (and denser) liquid water from the two-phase fluid above.

Pressure transients recorded at an observation well in response to deep fluid production from a two-phase well will differ markedly, depending upon the distance to the observation point and its depth. Pressure transients for deep observation points are influenced by the expanding constant-pressure vapor zone and hence resemble those of a system with a constant-pressure boundary. On the other hand, near the top of the system, pressures may actually

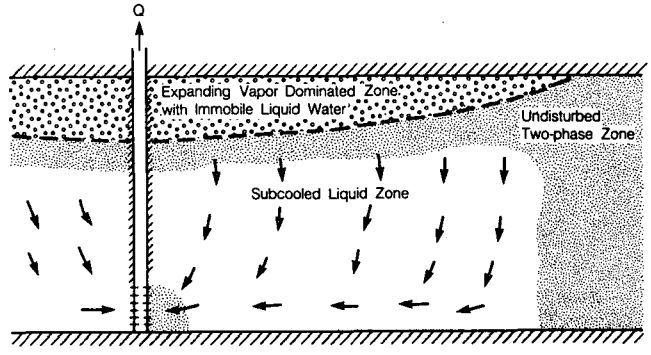

Figure 3. Schematic model of flow patterns and depletion mechanisms for a well with a deep feed zone. [XBL 866-10863]

increase as a result of the condensation of upward-flowing steam. Hence, for two-phase systems with significant vertical permeability, the depth of the observation point must be considered in the analysis of the data. It is possible that the counterflow of steam and liquid in two-phase systems is the reason for the dilemma that the permeabilities calculated from interference tests are higher by as much as an order of magnitude than individual well tests.

The pressure decline for production from a shallow feed zone is considerably higher than that of production from a deep feed zone. The primary cause of this is gravity effects, which enhance recharge to a well with a deep feed zone but oppose upward recharge of liquid water in the case of shallow production. Eventually, the gravity effects are overcome, and liquid water is recharged from below, reducing the enthalpy of the produced fluids. This stabilizes the pressure transients. More detailed descriptions of the effects of localized feed zones on pressure transients are given by Bodvarsson and Cox (1986).

CONCLUSIONS

1. For single-phase liquid reservoirs with an isolated two-phase zone, the constant-pressure approximation generally appears not to be valid. The size of a two-phase zone and the distance to it may be approximated by pressure-transient data from two or more observation wells.

2. Production from deep feed zones in two-phase reservoirs gives rise to an efficient gravity drainage mechanism that causes only gradual long-term pressure changes at the well, because of an expanding steam zone of nearly constant pressure.

3. Production from deep feed zones results in the recharge of cooler fluids from shallow regions, and a subcooled liquid-dominated zone develops in the middle of the reservoir system.

4. Production from shallow feeds results in considerably higher pressure drops than those from deeper zones because of gravity effects.

REFERENCES

Bodvarsson, G.S., and Cox, B.L., 1986. Numerical studies of gravity effects in two-phase reservoirs. Geoth. Resour. Counc. Trans., v. 10, p. 429–436.

Cox, B.L., and Bodvarsson, G.S., 1986. Preliminary studies of two-phase effects on pressure transient data. *In* Proceedings, Eleventh Workshop, Geothermal Reservoir Engineering, Stanford, California, January 21–23. Stanford Geothermal Program Report SGP-TR-84, p. 7–14.

Grant, M.A., and Sorey, M.L., 1979. The compressibility and hydraulic diffusivity of a water-steam flow. Water Resour. Res., v. 15, no. 3, p. 684–686.

Martin, J.C., Wegner, R.E., and Kelsey, F.J., 1976. One dimensional convective and conductive geothermal heat flow. *In* Proceedings, Second Workshop, Geothermal Reservoir Engineering, Stanford, California, December 1–3, 1976. Stanford Geothermal Program Report SGP-TR-20, p. 251–262.

Pruess, K., 1983. Development of the general purpose simulator MULKOM. *In* Earth Sciences Division Annual Report 1982. Lawrence Berkeley Laboratory Report LBL-15500, p. 133–134.

Sageev, A., 1985. Interference testing near a steam cap. Geoth. Resour. Counc. Trans., v. 9, part II, p. 569–572.

Sageev, A., and Horne, R.N., 1983a. Drawdown pressure transient analysis of a well near a steam cap. Geoth. Resour. Counc. Trans., v. 7, p. 473–476.

Sageev, A., and Horne, N.H., 1983b. Pressure transient analysis in a reservoir with a compressible or impermeable circular subregion: Gas cap or EOR-induced. Paper SPE 12076 presented at the 1983 SPE Annual Fall Meeting, San Francisco, California, October 5–8, 1983.

Heat-Pipe Effects in Nuclear Waste Isolation

C. Doughty and K. Pruess

The term "heat pipe" is used to describe a variety of man-made or natural systems in which a very efficient heat transfer with small temperature drop results from multiphase convection. The basic ingredients of a heat pipe are (1) a volatile fluid and (2) a mechanism by which liquid and gas phases can flow in opposite directions, usually capillary action in a porous material (see Fig. 1). If heat is injected into such a system, vaporization and pressurization of the gas phase take place, causing gas-phase flow away from the heat source. The gas condenses in cooler regions away from the heat source, depositing its latent heat of vaporization there. This sets up a saturation profile, with liquid-phase saturations increasing away from the heat source. In engineered heat-pipe systems incorporating porous media, or in drying processes accompanied by heat-pipe effects, backflow of the liquid phase toward the heat source is driven by capillary forces. The heat-transfer mechanism can be so efficient that effective heat conductivity (ratio of heat flux to temperature gradient) can exceed that of the best metallic heat conductors by factors of several thousand or more.

Heat pipes occur naturally on a large scale (kilometers) in systems known as vapor-dominated geothermal reservoirs. In these systems a deep heat source of magmatic origin vaporizes water present in fractured porous rocks. The vapor rises in the fractures and condenses on the cooler rock surfaces at shallower depths. The downflow of liquid condensate toward the heat source is caused simply by gravity. Effective heat conductivity in these systems can be on the order of several hundred W/m°·C, whereas heat conductivity of rocks is typically in the range of 1–3 W/m°·C.

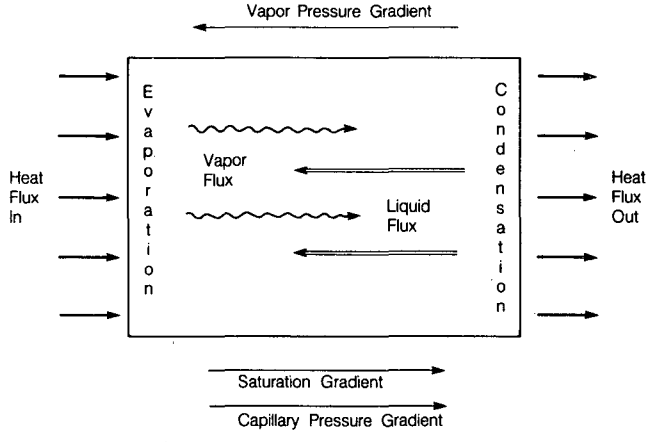

Figure 1. Schematic diagram of a porous heat pipe (after Jennings, 1984). [XBL 8510-12376]

In the context of nuclear waste isolation, heat-pipe systems may evolve in the thermal regime near the waste packages. They may have very substantial effects on important aspects of repository performance, including peak temperatures, salinity, and gas content of the fluids near the waste packages and migration of chemical species.

FLUID AND HEAT TRANSFER IN HEAT PIPES

In the simplest case the equation governing the steady state of a heat pipe can be written as

$$\mathbf{F}_l + \mathbf{F}_v = 0 , \tag{1}$$

expressing the fact that the mass fluxes of liquid and vapor phase are equal in magnitude and opposite in direction (balanced counterflow). The convective heat flux associated with the mass fluxes as given in Eq. (1) is

$$\mathbf{G} = \mathbf{F}_v h_v + \mathbf{F}_l h_l = \mathbf{F}_v h_{vl} , \tag{2}$$

where $h_{vl} = h_v - h_l$ is the vaporization enthalpy (latent heat) of the volatile fluid in the heat pipe. In the context of nuclear waste isolation the fluid is primarily water, but noncondensible gases and dissolvable solids may also be present and impact on heat transfer. The convective heat transport may be quite large, and it occurs at nearly constant temperature, creating the large value of effective heat conductivity typical of heat-pipe phenomena.

Several heat-pipe-related problems of current interest are outlined below.

1. The presence of a noncondensible gas such as air in a heat pipe diminishes the flow of water vapor, thus limiting convective heat transfer and effectively shortening the length of the heat pipe.

2. In order to obtain good heat-transfer characteristics, the permeability of the heat pipe must be high enough to allow ample vapor flow, but pore sizes must be small enough to produce strong capillary pressures (inversely proportional to pore size) to

drive the liquid counterflow. These two requirements are conveniently met by heterogeneous media. In particular, fractured porous media provide both high-permeability pathways for the vapor flow (the fractures) and a porous wick (the matrix blocks) for the liquid counterflow.

3. Mineral redistribution due to solubility variation with temperature and the precipitation or dissolution associated with phase change may significantly alter the properties of the rock, gas, and liquid throughout the heat-pipe region, thus modifying the vapor and liquid flow pattern.

ISSUES IN NUCLEAR WASTE ISOLATION

The heat generated by a nuclear waste repository provides a potential energy source for a heat pipe, and saturated or partially saturated, possibly fractured rock surrounding the repository may be an appropriate heat-pipe medium. Whether a heat pipe is likely to develop for given repository conditions is of major importance in predicting the overall behavior of the repository. The wick limit and critical dry-out flux, obtained from analytical solutions to simplified heat-pipe problems (Doughty and Pruess, 1985), can give a general indication of the likelihood of heat-pipe development in a specific repository environment, but for detailed predictions mathematical models that can represent fluid and formation properties in more realistic detail are needed.

Studies of vapor-dominated geothermal reservoirs (Pruess, 1985) indicate that several geological conditions are necessary for the existence of a heat pipe. If the heat-pipe region lies below the water table, it must be sealed laterally to prevent the inflow of liquid water from surrounding higher-pressure regions. The presence of fractures is necessary to provide high-permeability paths for vapor flow. If the matrix permeability is too low to allow liquid flow through the matrix sufficient to balance vapor flow, then the liquid in the fractures must be mobile, requiring that liquid saturation in the matrix be high enough (and capillary forces correspondingly low enough) to allow sufficient liquid to remain in the fractures to be mobile.

We do not expect heat-pipe effects to play a role in nuclear-waste repositories in saturated rock. Studies by Pruess and Bodvarsson (1982) for the Basalt Waste Isolation Project have indicated that boiling conditions with two-phase flow are confined to the immediate vicinity (a few centimeters) of the waste-package emplacement hole. No heat-pipe mechanism was observed in this study because of the absence of a force for driving vapor away from the heat source. Ambient pore pressure was high (130 bars), so that flow of both liquid and vapor phases was toward the low-pressure region around the canisters (assumed to have been emplaced in an open hole, at P = 1 bar). It appears that, generally speaking, ambient pore pressures in repository host formations below the water table will exceed the maximum vapor pressures expected near the waste packages. Therefore, zones with boiling conditions will be of very limited extent, if they form at all. Furthermore, before resaturation, vapor will tend to flow toward the pressure sinks at the waste packages rather than away from them, precluding development of a two-phase counterflow pattern.

The situation is entirely different for a waste repository in partially saturated rock, where ambient pore pressure is near one bar. Under these conditions, heat-pipe development is quite probable and has been observed in a number of studies (e.g., Pruess et al., 1984).

The primary benefit of having of a heat-pipe region around a repository is the transfer of a great amount of heat away from the vicinity of the repository without a large temperature increase. The temperature of a heat pipe remains near the saturation temperature for the prevailing pressure. For a repository in a partially saturated formation with "sufficient" gas-phase permeability, this condition is atmospheric pressure and 100°C. A low maximum temperature, as well as a small temperature gradient, helps maintain the integrity of the rock surrounding the waste canister by minimizing thermal expansion effects. In general, canister corrosion proceeds more slowly at lower temperature. Additionally, some relevant material properties and thermodynamic data are poorly known for the high temperatures that may develop around a repository with conduction-dominated heat transfer, but they are well known at lower temperatures, allowing more accurate predictions of repository behavior. The concentration of air and liquid water at the cold end of the heat pipe, away from the canisters, lessens the likelihood of corrosion. The liquid flow toward the canister further inhibits outward transport of liquid-dissolved wastes (e.g., actinides), although the gas phase may transport droplets of liquid as an aerosol and volatile components of the waste (e.g., ^{14}C, ^{3}H, ^{85}Kr, ^{129}I) away from the repository.

If a dry-steam zone develops at the hot end of the heat pipe, it is accompanied by a large temperature increase as conduction becomes the dominant mode of heat transfer. The absence of liquid water changes the chemical environment of the waste packages. In particular, corrosion of canisters is greatly lessened.

Mineral redistribution can play a major role in the development of a heat pipe around a repository. Evaporation at the hot end of the heat pipe causes precipitation of dissolved minerals, whereas condensation at the cold end causes dissolution of minerals. The temperature, salinity, and pH dependences of mineral solubility may reinforce or counteract this process.

Extensive dissolution of rock minerals may threaten the structural integrity of the rock. Extensive precipitation may also be hazardous, decreasing permeability to the point where steam cannot flow away from the repository, leading to pressure increases and possible fracturing of the rock. Precipitation adjacent to the canisters may inhibit corrosion. The effect of precipitation on porosity is straightforward given the mass and density of the precipitate, but the relationship between porosity and permeability is complex (Verma and Pruess, 1985). Experimental results on granite (Vaughan, 1985) show that for a porosity decrease of 8%, permeability decreases 96%, whereas uniform deposition of silica predicts a decrease of only 26%. Furthermore, not only are the equilibrium solubilities of minerals necessary for an understanding of heat-pipe behavior, but reaction kinetics may also be important. Thus the net effect of mineral redistribution is difficult to anticipate without detailed modeling studies.

Knowledge of a number of relevant physical and chemical properties of fractured rocks is far from complete. Laboratory experiments have been done to determine relative permeability and capillary-pressure variations with liquid saturation and the kinetics of silica dissolution and precipitation, but the extrapolation from laboratory experiments involving small-scale samples to field settings is definitely nontrivial.

REFERENCES

Doughty, C., and Pruess, K., 1985. Heat pipe effects in nuclear waste isolation: A review. Lawrence Berkeley Laboratory Report LBL-20738.

Jennings, J.D., 1984. The heat pipe effect in a dual-permeability porous system (M.S. thesis). University of California, Berkeley.

Pruess, K., 1985. A quantitative model of vapor dominated geothermal reservoirs as heat pipes in fractured porous rock. *In* Geoth. Res. Council Trans., v. 9, part II, p. 353–361.

Pruess, K. and Bodvarsson, G., 1982. Hydrothermal conditions and resaturation times in underground openings for a nuclear waste repository in the Umtanum flow at the Basalt Waste Isolation Project. Lawrence Berkeley Laboratory Report LBL-18451.

Pruess, K., Tsang, Y.W., and Wang, J.S.Y., 1984. Numerical studies of fluid and heat flow near high-level nuclear waste packages emplaced in partially saturated fractured tuff. Lawrence Berkeley Laboratory Report LBL-18552.

Vaughan, P.J., 1985. Analysis of permeability reduction during flow of heated, aqueous fluid through Westerly Granite. *In* C.F. Tsang (ed.), Coupled Processes Associated with Nuclear Waste Repositories. Academic Press, Orlando, Florida, p. 529–539.

Verma, A. and Pruess, K., 1985. The effects of silica redistribution on the performance of high-level nuclear waste repositories. *In* C.F. Tsang (ed.), Coupled Processes Associated with Nuclear Waste Repositories. Academic Press, Orlando, Florida, p. 541–563.

Numerical Modeling of a Porous Heat Pipe: Comparison with a Semianalytical Solution

C. Doughty and K. Pruess

Calculations made with the numerical simulator TOUGH have been compared with a semianalytical solution for the steady-state behavior of a one-dimensional porous heat pipe. (See previous article for a general description of heat pipes.) The semi-analytical solution (Udell and Fitch, 1985) considers the flow of heat, air, water vapor, and liquid water (the wetting phase) through a homogeneous porous medium. The left boundary of the porous medium ($x = 0$) is held at constant-temperature, constant-

pressure, liquid-saturated conditions. The right boundary conditions are specified as no mass flux and a heat flux of magnitude q into the porous medium. Fluid flow is governed by Darcy's law modified for two-phase conditions; capillary forces are considered important; and air flow is due to convection and Fickian diffusion. Kelvin's equation for vapor-pressure lowering and the Clausius-Clapeyron equation are used to calculate saturation conditions.

The following assumptions are made.

1. The variations in gas and liquid densities, ρ_g and ρ_l, due to changes in pressure, temperature, or composition are negligible.
2. Interfacial tension, σ, gas and liquid viscosities, ν_g and ν_l, and water heat of vaporization, h_{vl}, are constant.
3. The porous medium is homogeneous and incompressible.
4. The density of the gaseous phase is negligible compared with the liquid density.
5. Capillary pressure, P_c, gas and liquid relative permeabilities, k_{rg} and k_{rl}, effective thermal conductivity, K, and effective molecular diffusivity, D_{eff}, can be expressed as single-valued functions of the wetting-phase saturation. (Functional dependences are given in Table 1.)

Tables 2 and 3 list the material properties and boundary conditions, respectively, used in the semianalytical solution.

The numerical simulator TOUGH (Pruess, 1986) accounts for all the physical processes considered in the semianalytical formulation with the exception of vapor-pressure lowering, which has a negligible effect on the present problem. TOUGH calculates interfacial tension and liquid and vapor viscosity as a function of temperature and calculates liquid and vapor density as a function of temperature, pressure, and composition. Saturation conditions are calculated from steam-table equations.

Table 2. Material properties.

K_0	= 0.582 W/m·K	S_{lr}	= 0.15
K_1	= 1.130 W/m·K	σ	= 0.05878 N/m
ρ_g	= 0.960 kg/m^3	D	= 26.0×10^{-6} m^2/s
ρ_l	= 958.4 kg/m^3	τ	= 0.5
ν_g	= 21.0×10^{-6} m^2/s	ϕ	= 0.4
ν_l	= 0.3066×10^{-6} m^2/s	k	= 10^{-12} m^2
h_{vl}	= 2.257×10^6 J/kg		

Table 1. Functional dependences of material properties on saturation.

Capillary pressure

$$P_c = -\sigma\left(\frac{\phi}{k}\right)^{1/2}\left[\,1.417(1-S) - 2.12(1-S)^2 + 1.263(1-S)^3\,\right],$$

where σ is interfacial tension, ϕ is porosity, k is intrinsic permeability, $S = (S_l - S_{lr})/(1 - S_{lr})$, and S_{lr} is irreducible liquid saturation.

Relative permeabilities

$$k_{rg} = (1-S)^3, \quad k_{rl} = S^3.$$

Effective thermal conductivity

$$K = K_0 + \sqrt{S_l}(K_1 - K_0),$$

where K_0 and K_1 are thermal conductivities of dry and fully saturated porous media, respectively.

Effective molecular diffusivity

$$D_{eff} = \phi(1 - S_l)\tau D,$$

where D is molecular diffusivity and τ is the medium tortuosity factor.

Table 3. Boundary conditions.

At $x = 0$	$S_l = 1$ $(P_c = 0)$
	$P_g = 1.01$ bar
	$T = 70°C$
At $x = 2.25$ m	$q = 100$ W/m^2

The calculational mesh consists of 90 nodes with a length of 2.5 cm each and a cross-sectional area of 1 m^2. Adjacent to the first node is a boundary node with a volume of 10^{30} m^3 that maintains the constant boundary conditions for $x = 0$. The last node ($x = 2.25$ m) contains a 100-W heat source. The initial conditions specified for each node are $T = 70°C$, $P = 1.01$ bar, $S_g = 0.5$. The air-mole fraction is then calculated internally to be $Y = 0.698$. For the boundary node the capillary pressure is set to zero, so that although $S_g = 0.5$, the node behaves as though it were liquid saturated.

The calculation begins with a time step of 1 s. The time step is allowed to double whenever convergence is achieved within four iterations. The time step grows steadily until 0.5 days (51 cycles), when it is about 0.1 day long, then increases much more slowly. Steady state is reached after about 79 days and a total of 280 cycles. The final time step is 3 days long. The calculation requires about 10 min of computer time on a Cray X-MP. Figure 1 shows the TOUGH-generated profiles of temperature T, pressure P, saturation S, and air mole fraction Y as they evolve from the uniform initial conditions to steady state. The final frame also shows the semianalytical solution. The saturation shown is scaled liquid saturation, given by $S = (S - S_{lr})/(1 - S_{lr})$, where S_{lr} is the irreducible liquid saturation.

The agreement between the TOUGH-calculated steady state and the semianalytical solution is quite good. Mesh variations have shown that the calculation is somewhat sensitive to mesh spacing, especially in the region where $S_l \to 0$. The present mesh spacing represents a compromise between accuracy and economy. The finest mesh used (each node 1 cm long) yields saturation and pressure curves about 20% closer to the semianalytical curves, with the temperature and air-mole-fraction curves unchanged. For a finer mesh the calculation is more expensive for two reasons: the greater number of nodes requires that more calculations be done for each cycle, and the time step stabilizes at a smaller value, so it takes more cycles to reach steady state.

In order to examine the discrepancies between the semianalytical and numerical solutions, modifications were made to TOUGH to duplicate the material properties of the semianalytical solution as nearly as possible. The following features were implemented.

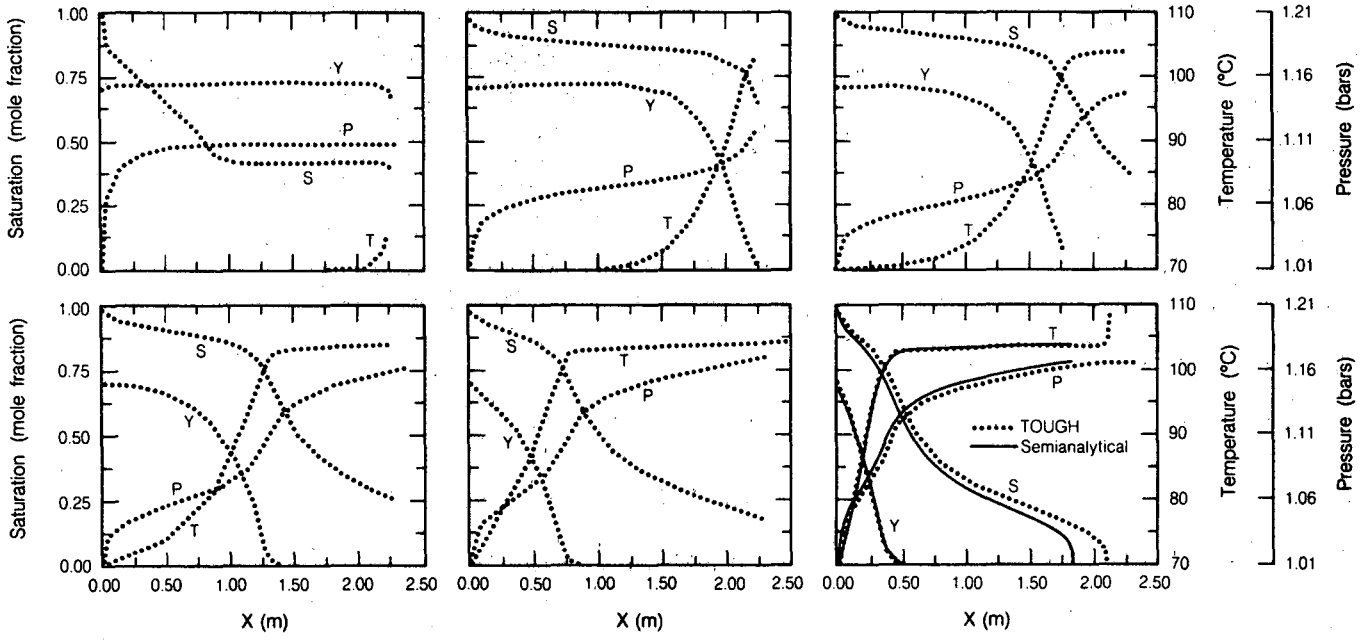

Figure 1. Temperature, pressure, scaled liquid saturation, and air-mole-fraction profiles calculated with TOUGH during heat-pipe development and with the steady-state semianalytical solution. [XBL 871-9895]

1. A constant value (from Table 2) is used for interfacial tension, liquid and vapor density and viscosity, and heat of vaporization.

2. Saturation conditions are calculated from the Clausius-Clapeyron equation.

3. Binary diffusion is calculated from mole-fraction gradient rather than mass-fraction gradient.

4. Composition of air is taken to be pure nitrogen rather than 80% nitrogen and 20% oxygen.

The resulting steady-state temperature, pressure, saturation, and air-mole-fraction profiles are shown in Fig. 2, along with the semianalytical solutions for comparison. The agreement is excellent. The similarity between the TOUGH results shown in Figs. 1 and 2 indicates that the approximations made for the semianalytical solution have a modest effect on the overall behavior of the system.

The present problem incorporates a number of physical effects that are relevant to problems in nuclear waste isolation, unsaturated-zone thermal-energy storage, and vapor-dominated geothermal reservoirs. The ability of TOUGH to match the semianalytical solution, therefore, provides a valuable verification of the code.

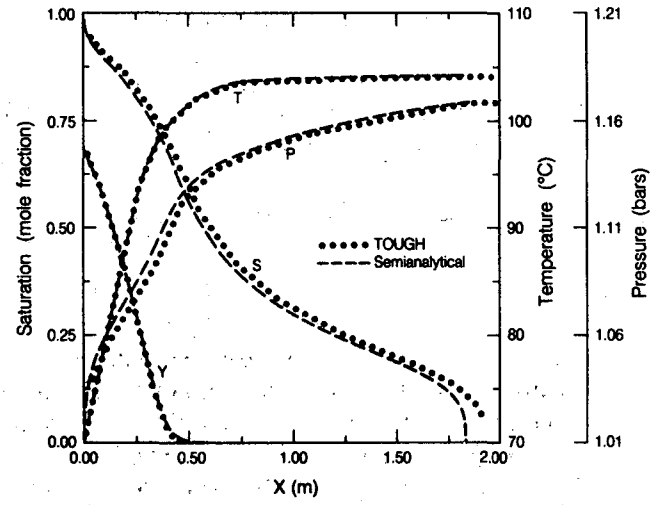

Figure 2. Steady-state conditions calculated with the semianalytical solution and with a modified version of TOUGH, which uses the same approximations as the semianalytical solution. [XBL 871-9891]

REFERENCES

Pruess, K., 1986. TOUGH user's guide. Lawrence Berkeley Laboratory Report LBL-20700.

Udell, K.S., and Fitch, J.S., 1985. Heat and mass transfer in capillary porous media considering evaporation, condensation, and noncondensible gas effects. *In* Heat Transfer in Porous Media and Particulate Flows (HTD Vol. 46), Proceedings, 23rd ASME/AIChE National Heat Transfer Conference, Denver, Colorado, August 4–7, 1985.

Fluid Recovery from Gas-Rich Reservoirs

S.W. Gaulke, G.S. Bodvarsson, and K. Pruess

Many geothermal reservoirs contain large amounts of noncondensible gases. The concentration of gases typically ranges from 0.1 to 9% by mass at separator conditions (Bjornsson and Bodvarsson, 1986); however, higher concentrations are found. Carbon dioxide (CO_2) generally accounts for more than 90% of the noncondensible gases present (Michels, 1969). It has been shown that significant amounts of CO_2 can greatly affect the behavior of a reservoir during exploitation (Grant, 1977). The main effect of the gas is to alter the boiling curve for water. Little CO_2 can be dissolved in the liquid phase, so that most of the CO_2 resides in the gas phase. The total pressure of the gas phase is basically the sum of the partial pressures of the water vapor and CO_2 gas, and this causes the saturation temperature for H_2O–CO_2 mixtures to be lower than that for pure water. The amount of saturation temperature lowering is directly related to the partial pressure of CO_2; the higher the partial pressure of CO_2, the lower the saturation temperature. If the partial pressure of CO_2 is kept constant, an increase in the mass fraction of CO_2 must be accompanied by an expansion of the vapor phase to accommodate the excess CO_2 not dissolvable in the liquid phase (O'Sullivan et al., 1985).

Most investigations of the effects of noncondensible gases on well and field behavior during exploi-

tation have been based on the assumption that the reservoir behaves as a porous medium. Various studies have shown that individual-well and overall-field behaviors for a fractured porous medium differ significantly from that for a purely porous medium (Pruess and Narasimhan, 1982a; Bodvarsson and Witherspoon, 1986).

Bodvarsson and Gaulke (1986) investigated CO_2 transients in fractured rocks and found that, in order to satisfy necessary equilibrium conditions for H_2O-CO_2 mixtures, backflow from the fractures to the matrix blocks at later time must be possible. In this article we extend this work to including the effects of binary diffusion and derive an approximate analytical expression for the amount of backflow. Furthermore, we discuss the effects of chemical buffers on the results.

The simulations were conducted using the numerical simulator MULKOM (Pruess, 1983) and an equation of state for H_2O–CO_2 mixtures developed by O'Sullivan et al. (1985). The effects of capillarity have been neglected.

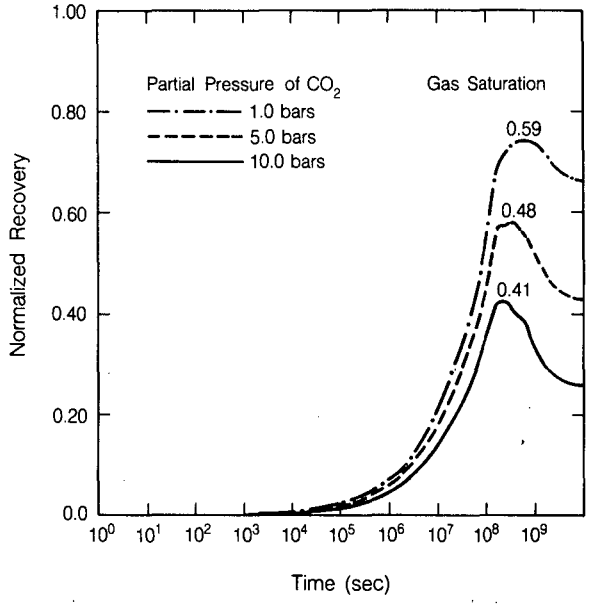

Figure 1. Effect of gas saturation in the fracture on backflow of fluid to the matrix. [XBL 869-12104]

THE EFFECTS OF THE INITIAL PARTIAL PRESSURE OF GASES ON FLUID RECOVERY

A simple model that includes a single logarithmically discretized matrix element (100 m^3) with time-independent boundary conditions was used to investigate fracture-matrix interaction in H_2O–CO_2 systems. Models used in this study are based on the MINC (multiple-interacting-continua) method (Pruess and Narasimhan, 1982b). The fracture element is assumed to be near a producing well, so that the thermodynamic state of the fracture remains constant with time. The fracture conditions were defined by determining the steady-state conditions within an infinite reservoir under exploitation. This approximation neglects the early-time transients of pressure and gas saturation in the fracture; however, these are not very important in our analysis. The pressure in the fracture was 40 or 70 bars, corresponding to a constant bottomhole production, and the matrix is initially at 90 bars. Note that for the following cases the total initial pressure is always kept the same, so that when different initial partial pressures of CO_2 are used, the initial temperature will be different. Other reservoir parameters used are typical of high-temperature geothermal systems.

Figure 1 illustrates the effects of CO_2 partial pressure on the mass recovery normalized by the fully saturated mass in the matrix. This figure shows an inverse relationship between initial partial pressure of CO_2 and the amount of fluid that can be recovered from the matrix; the higher the initial partial pressure, the lower the recovery from the matrix. This relationship is due to the effects of CO_2 on the boiling curve of water; a decrease in the partial pressure of CO_2 will cause a decrease in the total pressure without affecting the stable temperature of the system. A large pressure drop can occur without a significant amount of boiling in the system, thereby reducing the amount of fluids produced from the matrix. This phenomenon can result in an initial pressure drop of tens of bars (Atkinson et al., 1980; O'Sullivan et al., 1985), which will dramatically reduce the amount of recoverable reserves in liquid-dominated geothermal systems containing large amounts of gas.

THE MASS AND HEAT TRANSFER BETWEEN FRACTURES AND MATRIX

In order to achieve complete thermodynamic equilibrium between the fracture fluids and those in the adjacent matrix, there must be equality in the pressure, temperature, and partial pressures of the noncondensible gases that are present (Bodvarsson and Gaulke, 1986). Most geothermal systems are considered to be in approximate thermal and hydrologic equilibrium before exploitation. During exploitation, the fluid pressure in the fracture near the well will stabilize rapidly at the production level, creating

a large pressure gradient between the fracture and the matrix. Figure 2 schematically shows the results of changes in pressure, temperature, gas saturation, and CO_2 partial pressure with time for a typical matrix block. Two cases are represented in Fig. 2: the solid line represents the case when chemical reactions involving CO_2 may be neglected, and the dotted lines represent results when chemical buffers are included. The chemical buffers in the latter case are assumed to provide CO_2 to the matrix by rock-fluid reactions at a rate necessary to preclude recharge of CO_2 from the fracture fluids. Initially, the large pressure gradient drives fluid to the fracture from the matrix. This results in declining pressures, boiling, and an increasing gas saturation. Carbon dioxide flows into the fracture with the gas phase, and, since little CO_2 is produced by boiling because of its low liquid solubility, the partial pressure of CO_2 in the matrix drops drastically. Eventually, the pressure in the matrix becomes the same as that in the fracture, but a temperature gradient still exists because of the imbalance in the partial pressures of CO_2. The equilibration of CO_2 partial pressures between the fracture fluids and matrix fluids may be accomplished in two ways, either by chemical reactions in the matrix that produce CO_2 or by flow of gas-rich fluids from the fracture into the matrix (backflow). If CO_2 is produced by rock-fluid reactions in the matrix as the temperature equilibrates as a result of conduction, the saturation will stabilize because the production of CO_2 by reactions will maintain a total pressure in the matrix equal to that of the fracture. However, if the rate of CO_2 production by rock-fluid reactions in the matrix is low compared to the rate of heat transfer to the fracture fluid, the temperature drop in the matrix will cause the total pressure in the matrix to dip below that in the fractures, since two-phase conditions prevail in the matrix. The pressure imbalance is due to the excess CO_2 in the fractures, which increases the total pressure there without affecting the stable temperature. This in turn will drive gas-rich fluid from the fracture to the matrix until the two continua achieve total equilibrium. Fluid recharge to the matrix from the fractures causes a declining gas saturation there, as shown in Fig. 2.

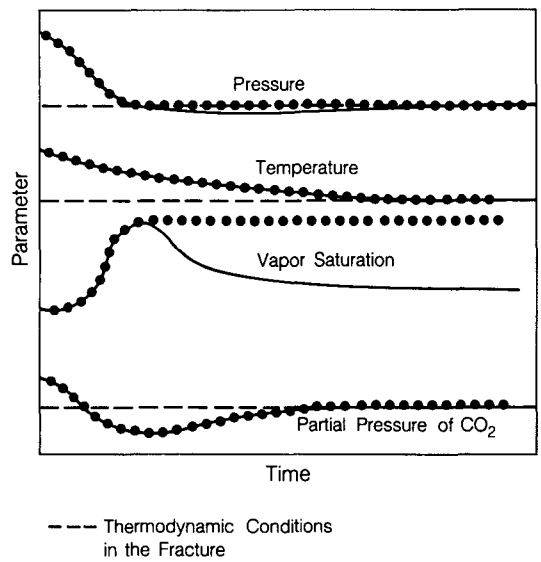

Figure 2. Schematic results of changes in pressure, gas saturation, temperature, and CO_2 partial pressure with time for cases with and without chemical buffers in the matrix. [XBL 866-10865]

An analytical expression has been derived for estimating the amount of backflow that will occur independent of the saturation. The amount of backflow per unit pore volume is given by

$$\frac{M}{\phi V} = \frac{\rho_{CO_2} S_g + \rho_l X_l^{CO_2}(1 - S_g)}{\frac{k_{rl}}{\mu_l}\rho_l \nu_t X_l^{CO_2} + \frac{k_{gl}}{\mu_g}\rho_g \nu_t X_g^{CO_2}}, \qquad (1)$$

where M is the total mass, ϕ is the porosity, V is the volume where backflow occurs, ρ_{CO_2} is the density of CO_2, S_g is the gas saturation, ρ is the density, X^{CO_2} is the mass fraction of CO_2, k_r is the relative permeability, μ is the viscosity, ν_t is the total kinematic mobility, and l and g refer to the liquid or gas phase, respectively. This expression defines the total amount of fluid per unit pore volume that must be supplied to the matrix to equilibrate the partial pressure of the matrix with that of the fracture. Using the final saturation in the matrix, the numerator gives the total amount of CO_2 required to balance the partial pressures in the matrix with that in the fracture on the assumption that there is no CO_2 in the matrix when backflow begins. This approximation appears reasonable, since complete degassing of the matrix block during pressure equilibration occurs in most cases. The final gas saturation of the matrix is what primarily determines how much CO_2 is necessary to equilibrate the fracture and matrix partial pressures given a liquid-vapor distribution determined by Henry's law. The denominator defines the fraction of each phase that is mobile, thereby designating the relative amounts of each phase flowing into the matrix. Figure 1 also shows the normalized recovery from the matrix of our two-continua model versus time independent of the flowing saturation in

the fracture. The matrix has 20% initial saturation, and other conditions are as listed before. A decrease in the recovery in the matrix at late times is indicative of backflow of fluid from the fracture to the matrix. The amount of backflow is inversely related to the flowing gas saturation in the fractures; a high gas saturation in the fracture indicates high gas-phase mobility. Therefore, little fluid mass is required to equilibrate the CO_2 partial pressures because of the high CO_2 concentration in the vapor phase. However, if the gas saturation is low, liquid mobility is high, and a large amount of fluid backflow to the matrix is required to equilibrate the CO_2 partial pressures. Gas saturation and mass fraction of CO_2 scale linearly for a given partial pressure. This indicates that the amount of backflow that will occur can be estimated by measuring the mass fraction of CO_2 at the surface. Figure 3 shows the amount of backflow per unit pore volume independent of matrix-gas saturation and the flowing mass fraction of CO_2. This figure neglects molecular diffusion; however, molecular diffusion had little effect on the numerical results. These plots assume Corey curves for relative permeabilities and no chemical reactions producing CO_2. Since the amount of backflow is primarily dependent on the flowing mass fraction of CO_2, Fig. 3 indicates that the backflow is very substantial for low-enthalpy wells but is insignificant for wells that predominantly produce steam.

Figure 4 shows the normalized recovery versus the initial pressure gradient for various initial partial pressures of CO_2. Two curves are included for each partial pressure; the upper curve indicates recovery before backflow, and the second includes the effects of backflow. This figure confirms that the initial partial pressure of CO_2 has large effects on recovery.

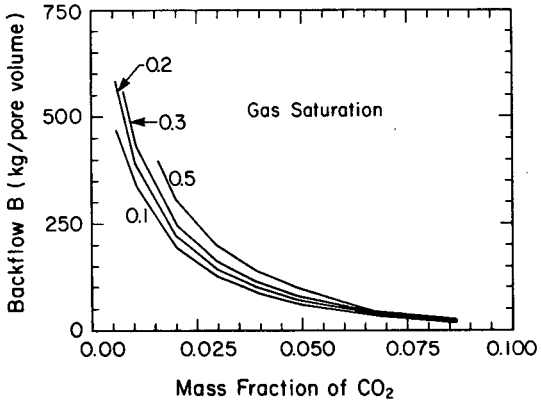

Figure 3. Effect of total flowing mass fraction of CO_2 on the amount of backflow per unit pore volume for various final matrix gas saturations. [XBL 864-10749]

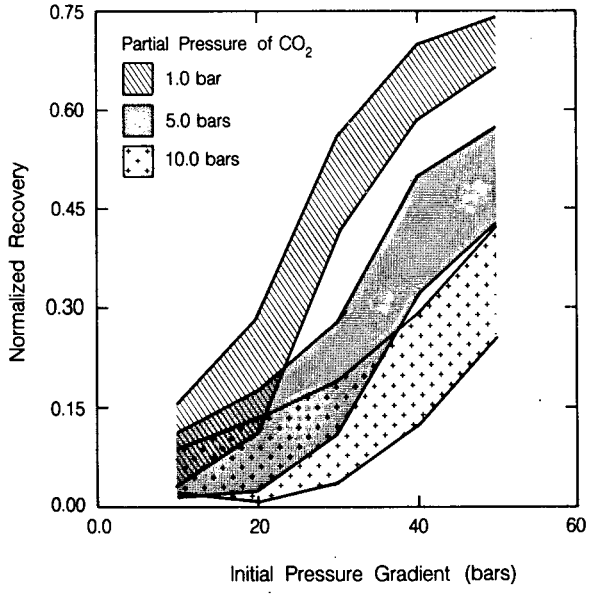

Figure 4. Effect of initial pressure gradient on intermittent recovery and recovery after backflow. Recovery is normalized by the mass necessary to fully saturate the matrix for various initial partial pressures of CO_2. [XBL 873-866]

This figure also shows that the amount of fluid required to equilibrate partial pressures between the fracture and the matrix is practically independent of the initial pressure gradient. Since the partial pressure of CO_2 rapidly decreases, because CO_2 flows out with the gas phase and boiling produces little CO_2, the matrix becomes depleted of CO_2 even for small initial pressure gradients.

Figure 5 shows the normalized recovery versus the initial gas saturation for various initial partial pressures. This figure shows that the recovery is strongly influenced by the initial partial pressure, as previously indicated. Moreover, the effects of backflow are indicated by the deviation of the curves from the ideal recovery slope, shown as a broken line at low gas saturations. Since initial gas saturations are indicative of the flowing gas saturations, it is known that the mobility of the gas-poor liquid phase will be higher at low saturations. Therefore, backflow will be greater at low gas saturations, as shown in Fig. 3.

It is of interest to determine which factors control the rate of backflow and over what time period it occurs. This is very important if chemical buffers involving CO_2 are present, as it is necessary that there be ways to compare the kinetic rates of reactions that supply CO_2 with the rate of backflow. The primary factors controlling the rate of the backflow are the geochemical, thermal, and hydrologic param-

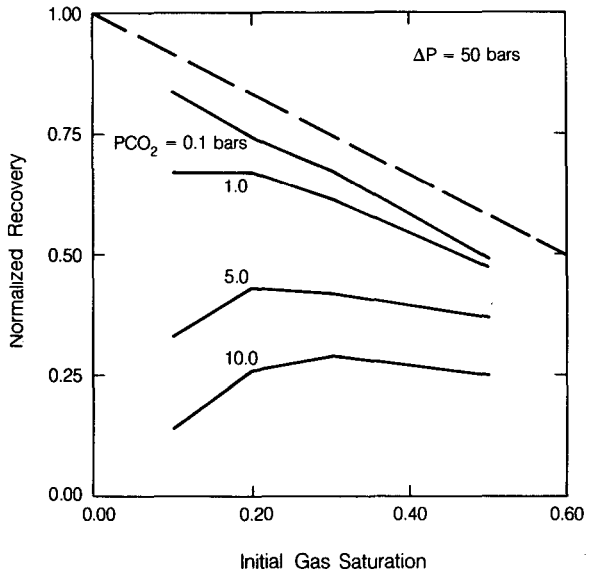

Figure 5. Effect of initial gas saturation on recovery normalized by the mass necessary to fully saturate the matrix for various initial partial pressures of CO_2. [XBL 869-12103]

eters of the matrix blocks. Since backflow occurs during the time when the temperatures in the fractures and matrix are equilibrating, the thermal parameters, especially the thermal conductivity, are important. The hydrological parameters of the matrix are also important, especially the absolute and relative permeabilities. However, the fracture spacing is probably the single most significant parameter controlling the rate of backflow. The fracture spacing (D) strongly affects both the conductive heat transfer and the rate of fluid flow, because the surface area (per unit surface area) between the matrix and the fractures is proportional to D^2. Thus one would expect that for reservoirs with relatively small average fracture spacing, the time period necessary for backflow to occur would be small.

Conclusions

Numerical simulation techniques are used to investigate the effects of CO_2 on matrix depletion and fluid recovery from fractured geothermal reservoirs. The main conclusions are:

1. Degassing of liquid-dominated geothermal reservoirs due to the effects of CO_2 on the boiling curve of water can substantially reduce fluid recovery from liquid-dominated systems.

2. Thermodynamic equilibrium including the partial pressures of CO_2 must be considered to understand fracture-matrix interaction in a producing reservoir.

3. Carbon dioxide equilibration between the fracture and matrix can occur mechanically by backflow of gas-rich fluids or chemically by rock-fluid reactions.

4. The backflow can be very substantial for low-enthalpy two-phase systems. It will not be very significant in vapor-dominated systems.

REFERENCES

Atkinson, P.G., Celati, R., Corsi, R., and Kucak, F., 1980. Behavior of the Bagnore steam/CO_2 geothermal Reservoir, Italy. Soc. Pet. Eng. J., v. 20, p. 228–238.

Bjornsson, G., and Bodvarsson, G.S., 1986. A limited survey of geothermal reservoir properties. Lawrence Berkeley Laboratory Report, in preparation.

Bodvarsson, G.S., and Gaulke, S.W., 1986. Effects of noncondensible gases on fluid recovery in fractured geothermal reservoirs. Res. Eng. J. Soc. Pet. Eng., in press.

Bodvarsson, G.S., and Witherspoon, P.A., 1986. Flow rate decline of steam wells in fractured geothermal reservoirs. *In* Proceedings, Tenth Workshop on Geothermal Reservoir Engineering. Stanford Geothermal Program Report SGP-TR-84, p. 105–112.

Grant, M.A., 1977. Broadlands — A gas dominated geothermal field. Geothermics, v. 6, p. 9–29

Michels, D.E., 1969. CO_2 and carbonate chemistry applied to geothermal engineering. Lawrence Berkeley Laboratory Report LBL-11509.

O'Sullivan, M.J., Bodvarsson, G.S., Pruess, K., and Blakeley, M.R., 1985. Fluid and heat flow in gas-rich geothermal reservoirs. Soc. Pet. Eng. J., v. 25, p. 215–226

Pruess, K., 1983. Development of the general purpose simulator MULKOM. *In* Earth Sciences Division Annual Report 1982. Lawrence Berkeley Laboratory Report 15500, p. 133–134.

Pruess, K., 1983. GMINC — A mesh generator for flow simulations in fractured reservoirs. Lawrence Berkeley Laboratory Report LBL-15227.

Pruess, K., and Narasimhan, T.N., 1982a. On fluid reserves and the production of superheated steam from fractured, vapor-dominated geothermal reservoirs. J. Geophys. Res., v. 87, no. B11, p. 9329–9339.

Pruess, K., and Narasimhan, T.N., 1982b. A practical method for modeling fluid and heat flow in fractured porous media. Paper SPE 20509 presented at the 1982 Annual Meeting, New Orleans, February 1–3, 1982.

Quantitative Model of the Cerro Prieto Geothermal Field, Mexico

S.E. Halfman, M.J. Lippmann, and G.S. Bodvarsson

A three-dimensional computational model of the Cerro Prieto geothermal field, Mexico, is under development. It is based on an updated version of LBL's updated hydrogeologic model of this field (Halfman et al., 1986). It takes into account major faults and their effects on fluid and heat flow in the system. The multiphase, multicomponent simulator MULKOM (Pruess, 1983) is used to compute the heat and mass flow in the system.

COMPUTATIONAL MESH

The three-dimensional mesh used in this study was designed on the basis of the geologic characteristics of the field (Fig. 1). One side of the model is oriented in a NW–SE direction along the approximate strike of normal Fault L; the SW–NE side is parallel to another normal fault, Fault H. Both faults are important features in the hydrogeologic model of Cerro Prieto (Halfman et al., 1984). In plan view, the modeled region extends over an area of 8600 m SW–NE by 9000 m (NW–SE). The thickness of the model varies, considering depths between 800 and 4000 m. The mesh consists of 242 elements: 146 internal elements and 96 boundary blocks.

Figure 2 shows the computational mesh for a SW–NE cross section in the NW upthrown block. The elements are designed to reproduce schematically the geology and characteristics of the various layers constituting the system. Of special importance are the α, β, and γ reservoirs. Most of the upper and lateral boundaries are assumed impermeable. The recharge of hot fluids is modeled by injection into the mesh elements representing the deep γ reservoir. The discharge of the fluids is through boundary elements located along the western margin of the grid, at 800 m depth. The rocks below the β reservoir are assumed to be of low permeability, except for the sandy γ reservoir. Similar assumptions are made for the corresponding downthrown SE block.

RESULTS

The material properties that resulted in the best match to the observed temperatures and pressures (Fig. 2) show that the shaly layers (hatched zones) have permeabilities between 0.005 and 1 md; the sandy layers (white zones, excluding Fault L and Fault H), between 1 and 100 md; and the fault zones, approximately 50 md. In the three reservoirs (α, β, and γ), the horizontal permeability is 100 md, and the vertical permeability ranges between 1 and 10 md. These values agree reasonably well with the results of well tests and with permeabilities used in earlier simulations of the field (Lippmann and Bodvarsson, 1983; Ayuso, 1984). A thermal conductivity of 2.0 W/m·°C is used for most zones. A constant rock density of 2650 kg/m^3 is assumed for all materials.

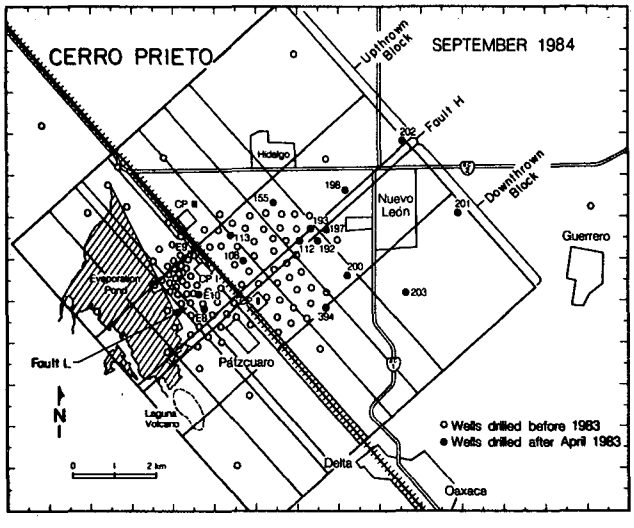

Figure 1. Plan view of the computational mesh used in this study. [XBL 849-9922A]

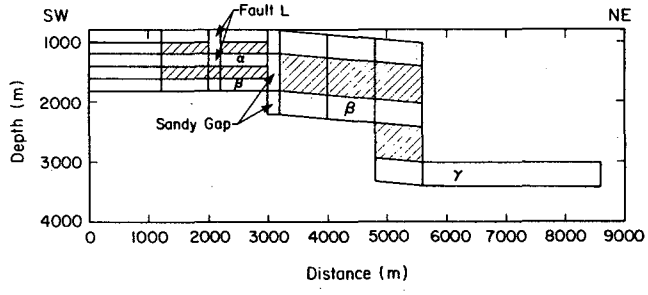

Figure 2. Cross section through the SW-NE row of elements just north of Fault H. Grid elements are shown; hatched zones represent layers of lower permeability. [XBL 861-10527]

Natural-State Model

The natural-state model describes the heat and fluid flows and the distribution of pressures, temperatures, and steam saturations in the Cerro Prieto system before commercial fluid production was initiated in 1973. The total rate of hot-water (1512 kJ/kg) recharge along the eastern side of the model is 100 kg/s. Figure 3 shows the observed and calculated isotherms, respectively, for the SW-NE cross section shown in Fig. 2. In the eastern portion of the field, there is a good temperature match. The temperatures along the western region might have matched better if the observed cold-water recharge between 1200 and 1400 m depth (Lippmann and Bodvarsson, 1983) had been considered in our calculated study. This recharge will be taken into account in the future. The calculated pressures were a bit lower than observed values (Ayuso, 1984) and calculated values from Lippmann and Bodvarsson's (1983) study. Again, with the addition of cold-water recharge, the pressures should increase.

On the basis of the hydrogeologic model developed by Halfman et al. (1986), it was concluded that the general geothermal fluid-flow pattern at Cerro Prieto is from large depths in the east to shallower depths in the west and that some of the hot fluids escape to the surface along the western margin of the field. Our three-dimensional model essentially shows the same flow pattern. Figure 4 shows the

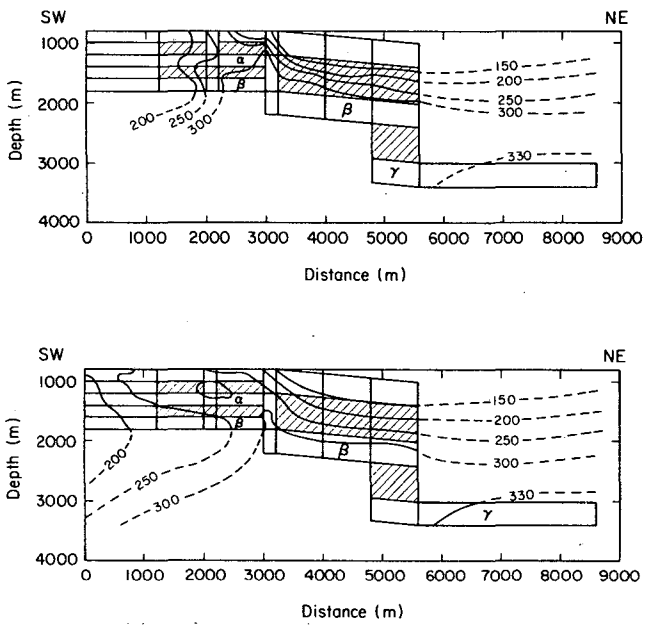

Figure 3. Cross section given in Fig. 2, showing observed temperature distribution (°C) (**top**) and calculated temperature distribution (°C) (**bottom**). [top, XBL 861-10529; bottom, XBL 861-10530]

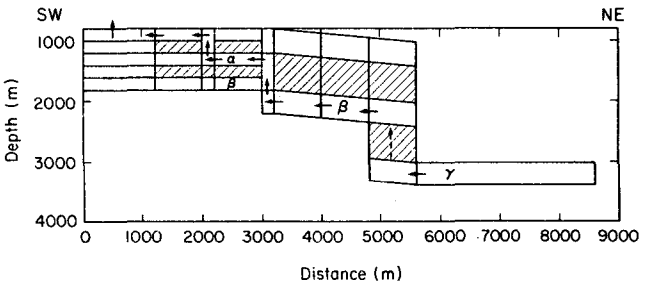

Figure 4. Generalized fluid-flow pattern for the cross section shown in Fig. 2. The broken arrows between the β and γ reservoirs indicate vertical flow in the fault zone (located to the southeast). [XBL 861-10528]

fluid flowing from the γ reservoir, up a fault (Fault H), into and westward through the β reservoir, up a sandy gap to the α reservoir, up Fault L, and westward through a permeable zone and then finally escaping upward toward the surface.

Production Model

As part of the validation of our three-dimensional model of Cerro Prieto, the exploitation of the α reservoir from 1973 to the end of 1979 was simulated. At this stage, we assumed yearly constant production rates.

For the period considered, the flow rates were 345, 590, 603, 695, 751, and 716 kg/s. Figure 5 shows that the agreement between computed and observed α-reservoir pressures is quite reasonable. This is very encouraging, since it indicates that the physical parameters assumed for the model, especially for the α reservoir, are generally correct. As we refine the natural-state model of the field, we expect to obtain a better match with the pressures reported by Bermejo et al. (1979).

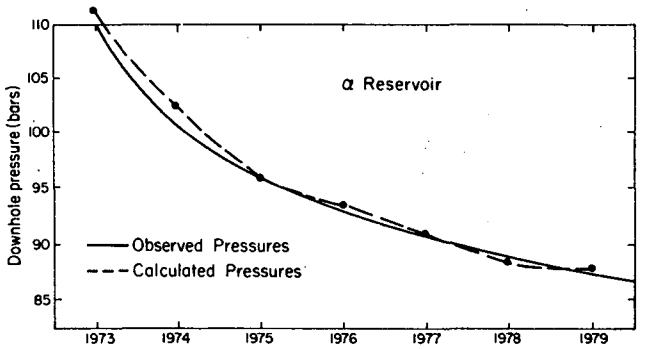

Figure 5. Comparisons of observed (Bermejo et al., 1979) and calculated pressure changes (in bars) in the α reservoir. [XBL 863-10692]

We expect to improve the agreement between observed and computed data by refining our three-dimensional model and by including in the calculation cold-water recharge along the edges of the field. These future improvements of the model will allow its use for predicting the behavior of Cerro Prieto as fluid production is expanded to the eastern areas and to deeper reservoirs.

REFERENCES

Ayuso, M.A., 1984. Gerencia de proyectos geotermoeléctricos. Commisión Federal de Electricidad Internal Report 1384–027 and –028, Departamento de Evaluación y Yacimientos, 15 p.

Bermejo M., F.J., Navarro O., F.X., Castillo B., F., Esquer, C.A., and Cortez A., C., 1979. Pressure variations at the Cerro Prieto reservoir during production. *In* Proceedings, Second Symposium on the Cerro Prieto Geothermal Field, Baja California, Mexico, October 17–19, 1979. Comisión Federal de Electricidad, Mexicali, Mexico, p. 473–493.

Halfman, S.E., Lippmann, M.J., Zelwer, R., and Howard, J.H., 1984. Geologic interpretation of geothermal fluid movement in Cerro Prieto field, Baja California, Mexico. Am. Assoc. Pet. Geol., v. 68, no. 1, p. 18–30.

Halfman, S.E., Manõñ, A., and Lippmann, M.J., 1986. Update of the hydrogeologic model of the Cerro Prieto field based on recent well data. Geoth. Resour. Counc., Trans., v. 10, p. 369–375.

Lippmann, M.J., and Bodvarsson, G.S., 1983. Numerical studies of the heat and mass transport in the Cerro Prieto geothermal field, Mexico. Water Resour. Res., v. 19, no. 3, p. 753–767.

Pruess, K., 1983. Development of the general purpose simulator MULKOM. *In* Earth Sciences Division Annual Report 1982. Lawrence Berkeley Laboratory Report LBL-15500, p. 133–134.

Update of the Hydrogeologic Model of the Cerro Prieto Geothermal Field, Mexico

S.E. Halfman, A. Mañón, and M.J. Lippmann*

The hydrogeologic model of the Cerro Prieto geothermal field in Baja California, Mexico, has been updated and modified on the basis of geologic and reservoir engineering data from 21 newly completed wells (Fig. 1). Previously, only two reservoirs had been discovered: the shallow α reservoir and the deeper β reservoir. Recently, three deep wells drilled east of the main wellfield (M-201, M-202, and M-203) penetrated a third geothermal reservoir (called the γ reservoir) below the sandstones corresponding to the β reservoir in the main part of the field. The new well data delimit the β reservoir, confirm the important role of Fault H in controlling the flow of geothermal fluids, and enable us to refine the hydrogeologic model of the field.

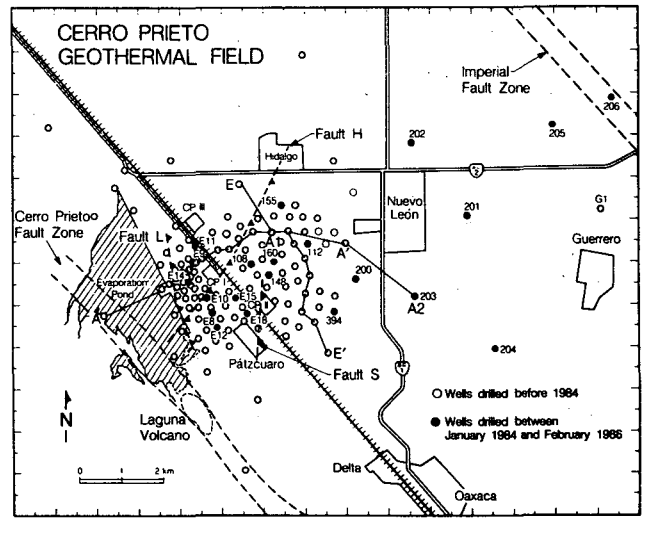

Figure 1. Location of new wells (drilled between January 1984 and February 1986), principal faults, and cross sections A–A′, A1–A2, and E–E′. The faults are projected to the surface. [XBL 864-10775]

*Comisión Federal de Electricidad, Mexicali, Baja California, Mexico.

ORIGINAL HYDROGEOLOGIC MODEL

In the original model (Halfman et al., 1984), the deepest identified geothermal aquifer (β reservoir) is in Sand Unit Z, at a depth of about 2650 m in well NL-1 (located at the eastern edge of cross section A–A′ in Fig. 2). The shallower α reservoir is associated with a sandy-shale group within Sand Unit O and is restricted to the western part of the system, west of the railroad tracks shown in Fig. 1.

The model showed that the subsurface movement of hot fluids in Cerro Prieto is controlled by stratigraphic and structural features. The permeable sandstones (especially Sand Unit Z) and faults are the conduits, and the discontinuous densified shales (particularly Shale Unit O) form the local cap rocks. According to the natural-state model, the geothermal fluids originate in a deep reservoir in the downthrown portion of Sand Unit Z (Fig. 2) and then flow upward along Fault H, westward through Sand Unit Z (from M-191 to M-123), up into the sandy gap (in the vicinity of M-10A), westward through the sandy-shale group in Shale Unit O (between M-14 and M-25), up Fault L, and westward through a shallower sandstone between M-29 and M-9. Finally, the geothermal fluids either mix with cold ground waters or discharge at the surface as mudpots, fumaroles, and hot springs.

UPDATED HYDROGEOLOGIC MODEL

Our updated hydrogeologic model of the Cerro Prieto circulation system assumes that geothermal fluids ascend from depths greater than the deepest well drilled to this date (>4400 m). Truesdell et al. (1981, 1984) suggest that the geothermal fluids are Colorado River water that has circulated deeply (below 2500 m) and mixed with a hypersaline, oceanic brine (Fig. 3). As the fluids ascend, they mix with more Colorado River water. The heat source is thought to be related to a thinner crust and the intrusion of igneous dikes into the sediments filling the pull-apart basin associated with the Cerro Prieto field (Elders et al., 1984; Goldstein et al., 1984).

Based on the new and old well data, we suggest that the geothermal fluids rise from depth along Fault H (Fig. 4), a major normal fault in the pull-apart basin. Most of the hot fluids flow into the upthrown portion of the β reservoir (upthrown Sand Unit Z) and continue to move westward and upward, as explained in the original hydrogeologic model. Lesser amounts seem to leak into the γ reservoir (Sand Unit K) and the downthrown portion of the β reservoir (downthrown Sand Unit Z).

The general flow pattern for the geothermal fluids described by the 1984 hydrogeologic model is still valid. The three geothermal reservoirs identified to date in Cerro Prieto have different properties and are restricted to different areas of the field. The α reservoir, originally at temperatures of 260 to 310°C, is located in the western part of the field, between approximately 1000 and 1500 m depth, in the upthrown block of Fault H (in the sandy-shale group of Shale Unit O). This aquifer does not extend to the upthrown section east of the railroad tracks because of the disappearance of permeable layers within Shale Unit O. In addition, mineral precipitation, caused by the inflow of cooler groundwater from shallower aquifers, has significantly reduced the permeability of the rocks. In the downthrown block of Fault H, a small quantity of geothermal fluid enters a few permeable layers within and above Shale Unit O. However, the geothermal fluids do not migrate far from the fault (as evidenced by wells E-15, E-51, and M-90, for example), possibly because of a lack of hydraulic gradient (in the southern area of the field there are no continuous permeable conduits allowing discharge of geothermal fluids to the surface).

The hotter and deeper β reservoir (320 to 340°C, below 1500 m) is present in both blocks of Fault H (in Sand Unit Z). Because of the general east-to-west direction of geothermal fluid flow, the extension of this reservoir toward the northwest and southeast is limited. The hot fluids rise through Fault H into this aquifer, move mainly toward the west, and eventually discharge at the surface along the western margin of the field.

Little is known about the γ reservoir. Although it is deeper, it seems to have temperatures similar to those of the β reservoir. We believe that the γ reservoir fluids are below the boiling-point-to-depth curve and are less likely to boil as a result of exploitation. Eventually, the characteristics of the γ aquifer will have to be determined by testing the deep wells of the M-200 series.

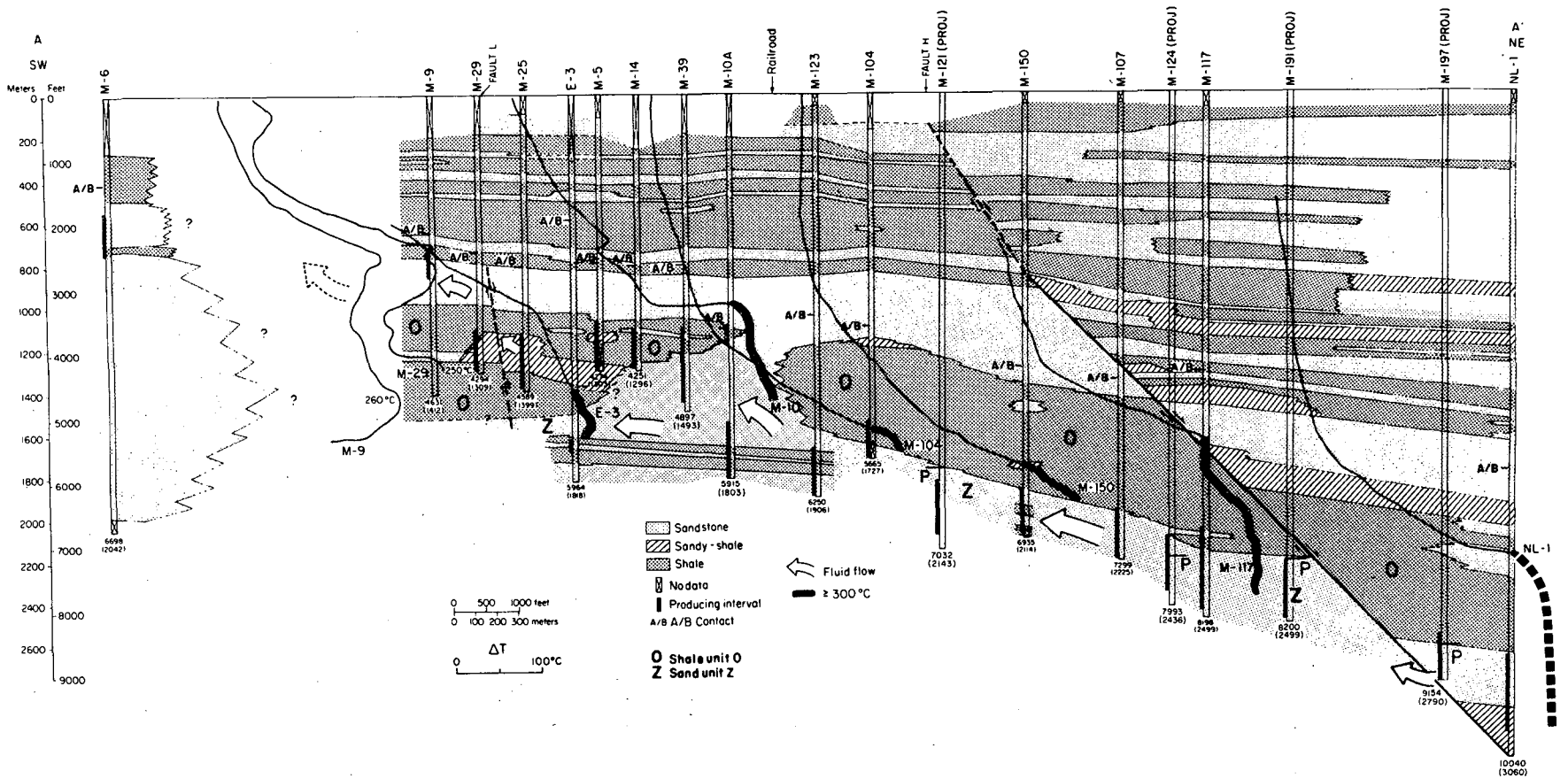

Figure 2. Lithofacies cross section A–A′ showing well locations, lithofacies groups, faults, temperature profiles, producing intervals, Shale Unit O, Sand Unit Z, and arrows indication direction of geothermal fluid flow according to the hydrogeologic model of Halfman et al. (1984). On the temperature profiles, the points corresponding to 300°C are located below the respective wells. The parts of the temperature profiles shown by heavy lines indicate temperatures of 300°C or greater. [XBL 828-10945C]

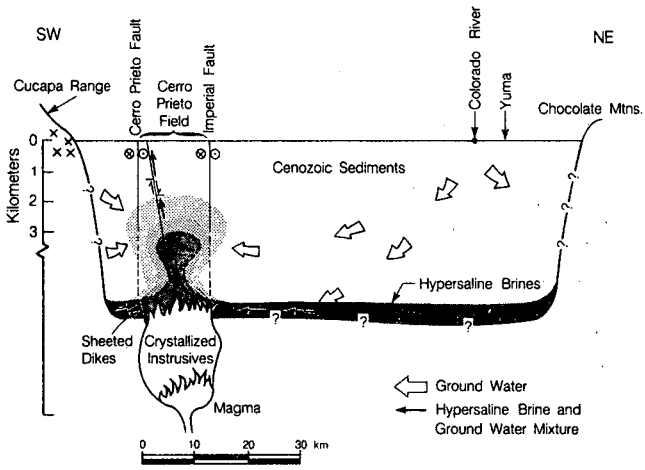

Figure 3. Schematic diagram of the geology and fluid flow across the Mexicali Valley. [XBL 865-10823]

REFERENCES

Elders, W.A., Bird, D.K., Williams, A.E., and Schiffman, P., 1984. Hydrothermal flow regime and magmatic heat source of the Cerro Prieto geothermal system, Baja California, Mexico. Geothermics, v. 13, p. 27–47.

Goldstein, N.E., Wilt, M.J., and Corrigan, D.J., 1984. Analysis of the Nuevo Léon magnetic anomaly and its possible relation to the Cerro Prieto magmatic-hydrothermal system. Geothermics, v. 13, p. 3–11.

Halfman, S.E., Lippmann, M.J., Zelwer, R., and Howard, J.H., 1984. A geologic interpretation of geothermal fluid movement in Cerro Prieto field, Baja California, Mexico. Am. Assoc. Pet. Geol. Bull., v. 68, no. 1, p. 18–30.

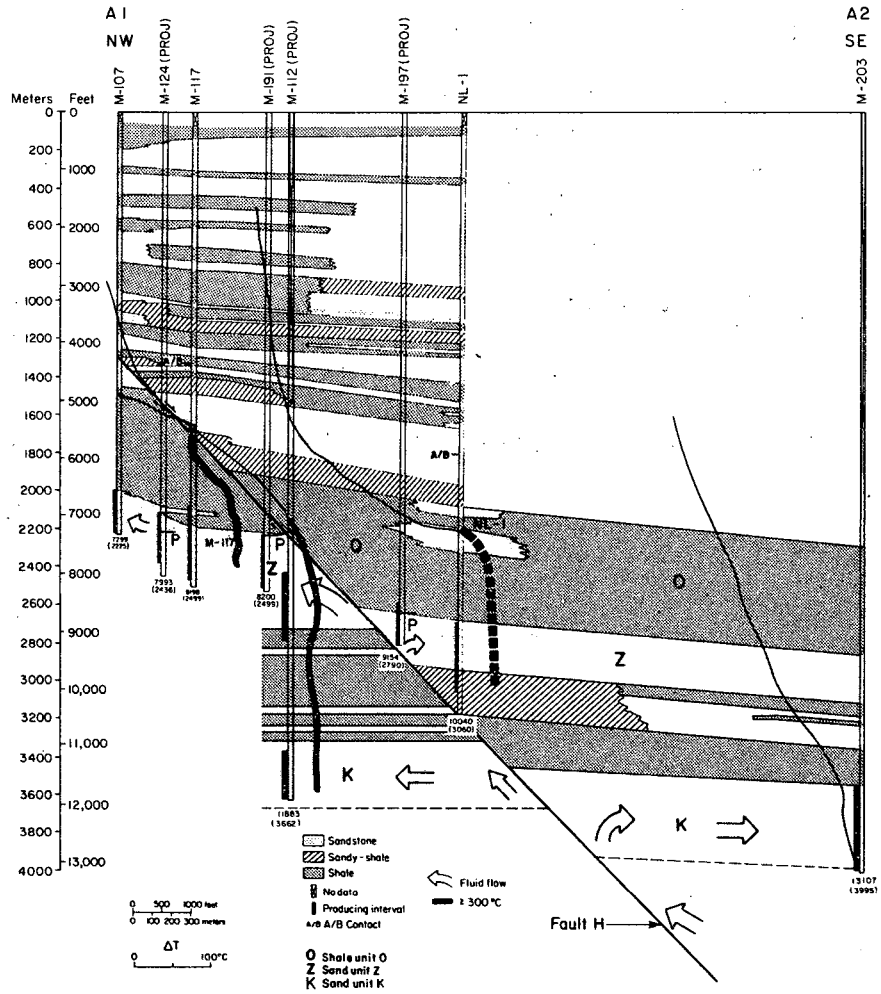

Figure 4. Lithofacies cross section A1–A2, showing the updated geothermal fluid-flow pattern. [XBL 864-10773]

Truesdell, A.H., Nehring, N.L., Thompson, J.M., Janik, C.J., and Coplen, T.B., 1984. A review of progress in understanding the fluid geochemistry of the Cerro Prieto geothermal system. Geothermics, v. 13, no. 1/2, p. 65–74.

Truesdell, A.H., Thompson, J.M., Coplen, T.B., Nehring, N.L., and Janik, C.J., 1981. The origin of the Cerro Prieto geothermal brine. Geothermics, v. 10, no. 3/4, pp. 225–238.

Estimating the Vertical Distribution of Gasoline in the Subsurface

H.-Y. Holman and I. Javandel

The extent of subsurface gasoline contamination is generally delimited by direct measurement of the free gasoline in monitoring wells. The elevation of the free-gasoline surface in a well is traditionally presumed to be the elevation of the gasoline surface within a contaminated porous medium. This interpretation can be deceiving, because it is based on hydrostatic considerations alone. More correctly, the pressure head of gasoline as a dispersed phase in a porous medium is controlled by both gravitational and capillary forces. For this reason, we have developed an approximate method—derived on the basis of information in van Dam (1967)—for estimating the distribution of gasoline saturation in the subsurface environment.

THEORY

This technique is based on the relationship between the gasoline saturation and the potential energy level of gasoline in a porous medium. Consider the three-phase system gasoline-water-air in a porous unconfined aquifer. Assume that all components are immiscible and nonreactive. Let Φ_o be the potential energy per unit mass of gasoline within a porous medium. It represents the work required to transport a unit mass of gasoline from the standard state, i.e, water table ($z = 0$) and atmospheric pressure ($p = 0$), to any position in either a water-unsaturated or water-saturated porous medium. The potential energy per unit mass of gasoline at a given point is then given by (Hubbert, 1953)

$$\Phi_o = gz + \frac{p_e}{\rho_o} + \frac{p_c}{\rho_o}, \qquad (1)$$

where g is the acceleration of gravity, z is the elevation with respect to the water table, p_e is the pressure of the environmental fluid that now occupies the region of the porous medium, ρ_o is the density of gasoline, and p_c is the capillary pressure at the interface between gasoline and the environmental fluid.

Assume that (1) the porous medium is homogeneous and isotropic, (2) the water saturation in the unsaturated zone is the irreducible saturation, and (3) the gasoline displaces air in the unsaturated zone and water in the saturated zone. The gasoline potential above the water table in the residual-water zone may then be given as (van Dam, 1967)

$$(\Phi_o)_o^a = gz - \frac{p_c(S_o)_o^a}{\rho_o}, \qquad (2)$$

where S_o is the gasoline saturation and $p_c(S_o)_o^a$ is the capillary-pressure saturation function in a gasoline-air two-phase system that must be determined empirically for each porous medium.

In the water-saturated zone the gasoline potential energy becomes

$$(\Phi_o)_w^o = -\frac{\rho_w - \rho_o}{\rho_o} gz + \frac{p_c(S_o)_w^o}{\rho_o}, \qquad (3)$$

where ρ_w is the density of water.

However, within the original air-water capillary zone immediately above the water table, gasoline displaces both air and water. Consequently, Eqs. (2) and (3) cannot be used directly to calculate the gasoline potential in this zone. A graphic extrapolation technique described by van Dam (1967) may be used to estimate Φ_o within this zone if $(\Phi_o)_o^a$, $(\Phi_o)_w^o$, and the average gasoline capillary rise above the water table are known. The average gasoline capillary rise is given by (Leverett, 1941)

$$(\bar{h}_c)_o^a = \frac{\beta_o^a \sigma_o^a}{\Delta\rho\, g} \sqrt{\frac{\phi}{k}}, \qquad (4)$$

where β_o^a and σ_o^a are the wettability and the surface tension in a gasoline-air two-phase system, ϕ is the porosity, and k is the permeability of the porous medium.

REQUIRED DATA

The following data are necessary to utilize this method: properties of the porous medium, such as porosity and permeability; physical properties of the fluids, such as density, surface tension, and wettability; empirical relationship between capillary pressure and the gasoline saturation within the concerned medium, the second mobile fluid being either air or water (such relationships could be obtained through laboratory experiments, such as the one described by Marle, 1972); and thickness of the free-gasoline lens measured in the monitoring wells.

PROCEDURE

The method includes the following procedures:

1. Use Eqs. (2) and (3) and the relationship between capillary pressure and the gasoline saturation to calculate the gasoline potential. Potentials will be calculated in that part of the vadose zone where water content is equivalent to the residual amount and below the water table for various distributions of gasoline-water-air saturation as a function of elevation.
2. Plot the computed potentials versus elevation for various gasoline-water-air saturations to produce a diagram like that in Fig. 1. In this figure the water saturation above the water table is assumed to be 20%, which is its irreducible saturation. Below the water table, the medium is supposed to be saturated only with water and gasoline.
3. Compute the average gasoline capillary rise above the water table from Eq. (4).
4. Modify Fig. 1 for the capillary zone above the water table, where the original water saturation is larger than the immobile (irreducible) level. Figure 2 shows the distribution of gasoline potential throughout a hypothetical site with an unconfined aquifer after the modification. For any potential energy level, the broken lines represent the elevation of the free-gasoline above and below the water table. Therefore, the distance between the two broken lines represents the thickness of the free-gasoline measured in a monitoring well under equilibrium conditions.
5. Drill monitoring wells that penetrate the entire thickness of the contaminated zone under investigation.

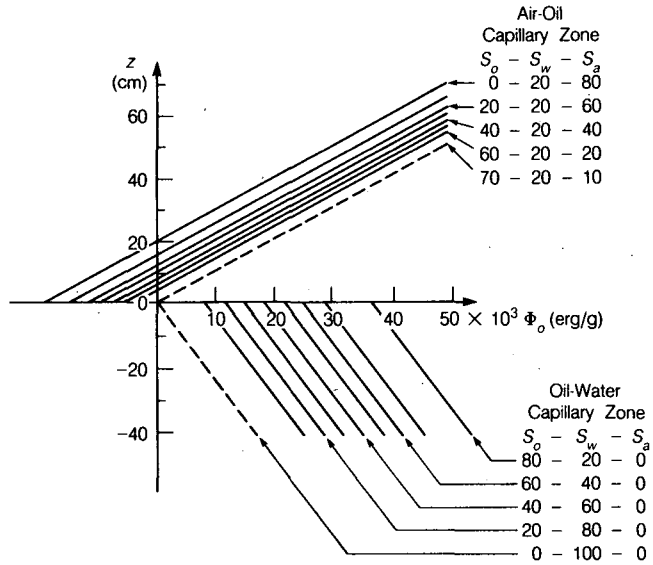

Figure 1. Preliminary distribution of gasoline potential in a hypothetical subsurface environment. Symbols S_o, S_w, and S_a represent the saturations of oil, water, and air in the porous medium (data from van Dam, 1967). [XBL 871-9893]

6. Measure the thickness of the free-gasoline in each monitoring well.
7. Locate the corresponding gasoline potential in Fig. 2 and draw a vertical line. Intersections of this line with equal saturation lines in Fig. 2 give the values of gasoline saturation at various elevations above and below the water table at the position of the monitoring well.

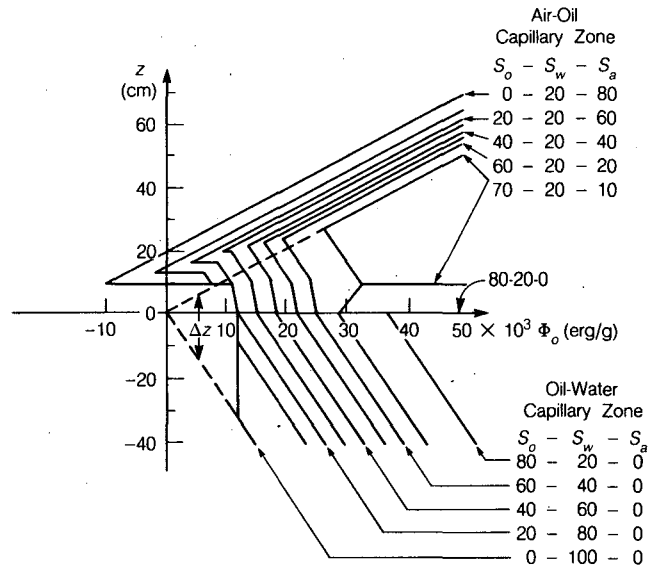

Figure 2. Final distribution of gasoline potential in a hypothetical subsurface environment. Symbols S_o, S_w, and S_a represent the saturations of oil, water, and air in the porous medium (data from van Dam, 1967). [XBL 871-9894]

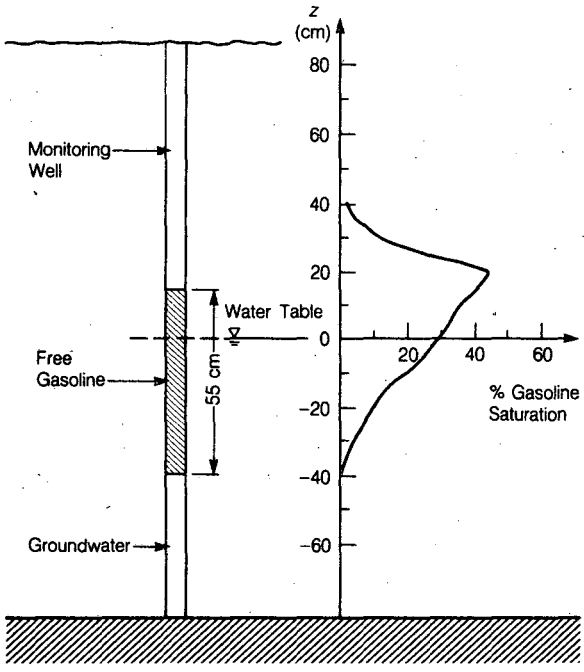

Figure 3. Gasoline saturation distribution profile. [XBL 873-9967]

Figure 3 shows the profile of subsurface gasoline saturation when the measured thickness of free gasoline in the monitoring well is 55 cm. Notice the amount of error one can have if one assumes the top of the free gasoline in a well to be the upper boundary of the gasoline lens within a porous medium.

REFERENCES

Hubbert, M.K., 1953. Entrapment of petroleum under hydrodynamic conditions. Bull. Am. Assoc. Pet. Geol., v. 37, p. 1954–2026.

Leverett, M.C., 1941. Capillary behavior in porous solids. Trans. Am. Inst. Min. Eng., v. 142, p. 152–169.

Marle, C., 1972. Les ecoulements polyphasiques en milieu poreux. *In* Cours de Production IFP (4th ed). Technip, Paris, France, 300 p.

van Dam, J., 1967. The migration of hydrocarbons in a water-bearing stratum. *In* P. Hepple (ed.), Joint Problems of the Oil and Water Industries. Institute of Petroleum, London, p. 55–96.

Aquifer Restoration: Legal Issues

I. Javandel and C.F. Tsang

A major environmental concern in the United States today is the proper disposal of large quantities of contaminated liquid wastes. A 1977 survey indicated that over 17 million waste-disposal facilities in the United States are discharging at least 6.5 billion m^3 of liquid waste into the ground each year (EPA, 1977). Of this total, 3.5 billion m^3 comes from nondomestic facilities. Much of this discharge—combined with leakage from underground tanks containg hazardous substances (raw or refined) such as organic solvents and gasoline—is contaminating groundwater aquifers throughout the country. As of October 1986, the EPA has inventoried more than 25,000 uncontrolled hazardous waste sites. The groundwater beneath many of these sites is contaminated or is threatened with contamination by various chemicals.

According to the Comprehensive Environmental Response, Compensation, and Liability Act of 1980 (CERCLA, 1980),[1] the EPA has the primary responsibility for managing remedial actions at these sites. The procedure for undertaking the removal of hazardous waste and remedial action for the contaminated aquifers is provided by the National Contingency Plan (NCP) (EPA, 1983). An important issue that has not been clearly addressed in the NCP is the extent to which the contaminated aquifers should be cleaned up.

The objective of this work was to study the key issues relevant to aquifer cleanup and introduce a procedure to assist the decision makers in determining the appropriate extent of cleanup activities. Details of this study are available elsewhere (Javandel et al., 1985). This article and the following one briefly discuss legal and health issues, respectively, in aquifer restoration.

The Superfund Act of 1980 (CERCLA) is the main legislation concerning detection and correction

[1]Readers should note that this article refers to work that was finished in 1985. Therefore the contents of the Superfund Act as amended in 1986 are not discussed here.

of groundwater contamination. Therefore, we examine pertinent sections of this Act, together with relevant portions of the NCP. Health is one of the major issues in determining the appropriate extent of cleanup and thus is discussed to the extent necessary to put the subject in perspective.

In the late 1970s public concern about contamination of groundwater, which is the source of drinking water for more than 50% of the U.S. population, led to passage of the CERCLA.

Section 104(a)(1) of the CERCLA authorizes the EPA to take action on any groundwater aquifer in the U.S. that is contaminated by the release of hazardous substances, whether the aquifer is in current use or not. Section 104(c)(2) of the CERCLA requires that the EPA consult with the affected state or states before determining any appropriate remedial action to be taken pursuant to the authority granted under subsection (a) of this section, as discussed above. Section 104(c)(3) of the CERCLA states that the EPA shall not provide any remedial actions pursuant to this section unless the state in which the release occurs first enters into a contract or cooperative agreement with the EPA providing that (1) the state will assume responsibility for all future maintenance of the removal and remedial actions; (2) the state will ensure the availability of a hazardous waste disposal facility acceptable to EPA; and (3) the state will pay or assure payment of (a) 10% of the costs of the remedial action, including all future maintenance, or (b) at least 50% of the cost at a facility that was owned at the time of any disposal of hazardous substances therein by the state or a political subdivision thereof.

Note that because of the requirements of Sections (104)(c)(2) and (3), the EPA cannot undertake any appropriate remedial actions without the close cooperation of the affected state. However, Section 106(a) of the Act gives full authority to the EPA to protect the public health and welfare and the environment if either is in imminent and substantial danger.

In regard to the extent of remedial actions, Section 104.(c)(4) requires that the EPA select appropriate remedial actions that are, to the extent practical, in accordance with the NCP and provide a cost-effective response while maintaining a balance between (1) the need for protecting the public health and welfare and the environment at the facility under consideration and (2) the availability of funds established by this Act for use at other sites.

Section 105 of CERCLA requires that within 180 days after the enactment of the CERCLA, the EPA should revise and republish the NCP for the removal of oil and hazardous substances. This section requires that the revised form of the NCP include a section called "national hazardous substance response plan" for the purpose of establishing procedures and standards for responding to releases of hazardous substances. Among other things, the national hazardous substance response plan was to include:

1. Methods for evaluating (including analyses of relative cost) and remedying any release or threats of release from facilities that pose a substantial danger to the public health or the environment.
2. Methods and criteria for determining the appropriate extent of removal, remedy, and other measures authorized by CERCLA.
3. Means of ensuring that remedial action measures be cost effective over the period of potential exposure to the hazardous substances from such facilities.

On July 16, 1982, the EPA published the NCP, which was later amended on September 8, 1983. Subpart F of the NCP addresses the subject of "Hazardous Substance Response." Under this heading seven phases of action are planned. In phase IV of this subpart, methods for establishing priorities of various sites and a hazard-ranking system are discussed for Superfund-financed responses. Procedures for preparation of the National Priorities List (NPL) are also discussed in this phase. Phase V identifies the sites that are not on the NPL but should be considered for remedial action because of a substantial risk to the public and the environment.

Phase VI addresses remedial actions at the sites on the NPL as well as those superfund-financed cases undertaken by the states and privately financed remedial actions undertaken by parties responsible for the release. It is recommended that those persons responsible for the release carry out the cleanup operation in a manner that effectively mitigates and minimizes damage to, and provides adequate protection of, the public health and the environment. The lead agency shall evaluate the adequacy of cleanup proposals submitted by responsible parties or determine the level of cleanup to be sought through enforcement efforts by consideration of the factors discussed in paragraphs (e) through (j). The adequacy of cleanup operations or the level of cleanup to be sought, which was left for the EPA to determine, are given in Section 300.68(e) through (j) of the NCP, which are discussed below.

In part (e) factors that should be used to determine the type(s) of remedial action are addressed.

Part (f) requires that the lead agency or the party responsible for carrying out a remedial investigation determine the nature and extent of the problem caused by the release. The results of such investigations should be used to determine the need for, and proposed extent of, remedial action. Once the type of response, such as source control or offsite remedial action or both, is determined, part (g) requires that a limited number of alternative actions be developed. Part (h) requires the initial screening of alternatives developed under part (g). Part (i) requires detailed evaluation of the remaining alternatives. Here one has to prepare a detailed cost estimate assessing each alternative in terms of the extent to which it is expected to mitigate and minimize damage and specifying each alternative. Finally, part (j) states that "The appropriate extent of remedy shall be determined by the lead agency's selection of the remedial alternative which the agency determines is cost effective (i.e., the lowest cost alternative that is technologically feasible and reliable and which effectively mitigates and minimizes damage to and provides adequate protection of public health, welfare, or the environment)."

UNRESOLVED ISSUE

As was discussed earlier, Section 105 of CERCLA gives the EPA the responsibility for deciding the extent of remedial action and publishing it in the NCP. Phase VI of subpart F of the NCP is the section that discusses this important subject. However, as noted before, the language used in this section includes such phrases as "minimizing damage" or "providing adequate protection of the public health." Parts (e) through (j) of this phase establish a procedure for selecting the remedial action. According to part (j), the extent of remedial action deemed appropriate is selected on the basis of cost effectiveness. This means that the alternative selected is expected to have minimum cost and to have the following goals:

1. To mitigate and minimize damage to public health, welfare, or the environment.
2. To provide adequate protection of public health, welfare, or the environment.

Obviously, the above goals are qualitative. Strictly speaking, minimizing damage to the environment in the case of aquifer cleanup means that the cleanup operation should continue until no hazardous agent can be detected in the aquifer. However, it is impossible to determine what minimum level of contamination in drinking water would be indicated by the phrase "adequate protection of the public." In short, the issue of the extent of cleanup of a contaminated aquifer is not properly addressed in the NCP.

REFERENCES

CERCLA, 1980. Comprehensive Environmental Response, Compensation, and Liability Act of 1980. Public Law 96–510. The Bureau of National Affairs, Inc. S-632,71-0701-0716.

Javandel, I., Tsang, C.F., and Haimes, Y.Y., 1985. Practical guide to aquifer restoration: Issues, methodologies, and cost effectiveness. Lawrence Berkeley Laboratory Report LBL-20504, p. 348.

EPA, 1977. Waste disposal practices and their effects on groundwater. The Report to Congress, Washington, D.C., p. 512

EPA, 1983. National oil and hazardous substances pollution contingency plan under the Comprehensive Environmental Response, Compensation, and Liability Act of 1980. 40CFR300. Amended by 48 FR 40669, September 1983. The Bureau of National Affairs, Inc. S-672,101:1001–1043.

Aquifer Restoration: Health Issues

I. Javandel and C.F. Tsang

A major objective of most environmental legislation has been to protect human health. When considering aquifer cleanup, therefore, the most important concern is to determine the extent to which the aquifer must be cleaned to ensure that it does not threaten public health. It is assumed that the aquifer water will be consumed without further treatment for removal of contaminants. Thus it becomes necessary to know the maximum concentration of a contaminant that will not adversely affect public health.

To resolve this problem the U.S. Congress asked the EPA to contract the National Academy of Science (NAS) to assess the potential health effects of contaminants in drinking water and to provide the EPA with recommended maximum contaminant levels (RMCL). The results of the NAS studies were published in a report entitled "Drinking Water and Health" (NAS, 1977). However, the report did not contain specific RMCLs.

The fact is that our knowledge of the adverse effects of many commonly used chemicals is quite limited. According to another report issued in March 1984 by the NAS, only 10% of the pesticides now in use have sufficient health and safety data for a complete assessment, and only 36% have been studied in sufficient depth to yield even minimal toxicity data (Meyerhoff and Mott, 1984).

Hazardous chemical compounds in groundwater may be divided into two groups: carcinogens and noncarcinogens. The following discussion focuses primarily on carcinogens, which are the more controversial. The proposed guidelines published by the EPA (1984a) set the framework for risk assessments of human exposure to chemical compounds. According to these guidelines risk assessment includes one or all of the following components: hazard identification, dose-response assessment, exposure assessment, and risk characterization. The first two components are the most critical issues and are discussed briefly below.

HAZARD IDENTIFICATION

There are four general methods for identifying the adverse effects of a particular chemical: human studies, animal studies, short-term studies, and comparison of molecular structure (National Research Council, 1983). Human studies, generally referred to as epidemiologic studies, attempt to compare two populations, one of which has been exposed to a particular chemical. Well-conducted epidemiologic studies provide some of the most convincing evidence about human risk (National Research Council, 1983). Two major types of problem are associated with epidemiologic studies.

1. Existing data may be difficult to interpret or apply. Typically, only a small number of people are exposed to a toxic environment, and exposures are to mixed and multiple potentially toxic agents. Furthermore, the latent period between exposure to a carcinogen and clinical confirmation of the disease is often very long. Therefore, establishing a definitive cause and effect relationship for a specific agent is difficult.

2. Epidemiologic studies are limited to a few chemicals only, and no data are available for most of the chemicals found in groundwater. Legally, socially, and medically it is not acceptable to expose humans intentionally to possibly hazardous chemicals to determine whether they will have adverse effects.

Animal-bioassay studies are the source of most available data in hazard identification. These studies are generally performed on controlled groups of animals. In current testing practice, one group of animals is given the highest tolerable dose, a second group is exposed to half that dose, and the third group is not exposed at all (National Research Council, 1983). After a certain length of time, the responses of the three groups to the chemical are compared to reveal any adverse effects of the agent on this particular type of animal. The results obtained from animal studies are generally used to infer the effects of the chemical in humans. Listed below are some of the uncertainties in using results of animal studies to determine adverse effects in humans.

1. For any one study the genetic pool of animals is usually very similar because the animals are inbred; this is not true for the human population.
2. Some chemicals known to be carcinogens in humans may not show the same effect in animals. For example, benzene has been shown to induce leukemia in humans, whereas there is no readily reproducible model for bezene-induced leukemia in animals (EPA, 1984b).
3. Although the basic biological processes of molecular, cellular, and organ function are similar from one mammalian species to another, there are marked differences between the standard rodent model and humans (Somers and Krewski, 1983). For example, mice are known to metabolize chemicals more rapidly than man. Generally speaking, a larger animal will have a lower metabolic rate and slower distribution of chemicals throughout its system (Kim and Stone, 1981). Kim and Stone (1981) conclude from their studies that "Facts tend to indicate that a substance may be less toxic in smaller animals than in man."

In spite of uncertainties associated with the interpretation of some animal tests, they have, in general, proved to be reliable indicators of carcinogenic properties and will continue to play a pivotal role in efforts to identify carcinogens (National Research Council, 1983).

Available experimental data seem to suggest that most chemical carcinogens are mutagens and vice versa (National Research Council, 1983). Therefore, once a chemical is proved to be a mutagen, it is also likely to be regarded as a carcinogen. Furthermore, studies show that the formation of a DNA adduct is a crucial step in the development of carcinogenesis and mutagenesis. This has been shown to be true in the cells of laboratory animals and in cultured human cells. The presence of specific DNA adducts in cells provides indisputable evidence that the individual from whom the cells came has been exposed to a carcinogenic chemical (Maugh, 1984). These biological studies to detect adducts in human cells are valuable because they take into account desorption by all routes. Therefore, they can be used as a basis for estimating risk from multiple chemicals.

In general, this type of study takes much less time and is less expensive than a mammalian carcinogenicity study. However, there are some uncertainties that should be resolved. One of these uncertainties is that most DNA adducts are repaired relatively fast, and it is believed that the formation of a DNA adduct is only a necessary, but not a sufficient, step for carcinogenesis. After the formation of a DNA adduct, further steps are required to generate a tumor. Exposure to other chemicals called promoters could then lead to the development of a tumor. When a DNA adduct is detected, one can infer that the individual has been exposed to a carcinogenic chemical and that the risk of cancer is increased but of unknown magnitude.

Comparing the molecular structure and physical properties of a chemical with those of known carcinogens may provide some evidence of potential carcinogenicity. This type of study can determine the priority of chemicals for further investigation.

DOSE-RESPONSE ASSESSMENT

In most cases quantitative risk assessment is carried out on the basis of animal data. These data are generally based on exposures to very high doses. The exposure of humans to these chemicals in general is on a far lower level than that for which data are available from animal experiments. Furthermore, to date, it has not been possible to demonstrate experimentally a threshold of the effect for carcinogens (EPA, 1984c). In other words, because there is no recognized "safe" concentration for a human carcinogen, the recommended concentration of these agents in water for maximum protection of human health is zero (EPA, 1980a,b,c). However, zero level may not be attainable at the present time.

Therefore, the high-dose animal data are extrapolated to estimate the excess cancer risk in humans at low dose levels. Essentially, this can be done by fitting a mathematical model to animal dose-response data and using the model to predict risks at lower doses corresponding to those experienced by humans (National Research Council, 1983). One of the problems inherent in low-dose extrapolation is that a number of models fit the high-dose experimental data, and it is impossible to judge which one of them would yield the correct answer at low doses. As a result, the dose-response curves derived from different models may be completely different at low-dose values. Thus, in addition to a simple curve-fitting procedure, one has to incorporate extra biological information. Even so, models using different assumptions may lead to risk estimates ranging over several orders of magnitude.

Using the multistage model, EPA's Carcinogen Assessment Group estimated the upper-bound excess cancer risk rate at a specific exposure level for a 70-kg adult who consumes 2 liters of drinking water per day every day over a 70-year lifespan.

UNCERTAINTIES

The following are some of the areas in quantitative risk estimation that are not quite clear and ought to be kept in mind when the quantitative results are used for risk management.

1. The mechanisms by which carcinogens cause the formation of a specific adduct on the DNA and the subsequent development of malignant tumors are not yet known.
2. The parameter of time is not generally accounted for in dose-response analyses. Extrapolations are generally made from short-term high-dose experiments to long-term exposures to low levels of carcinogens in groundwater. Experiments have shown that exposure of a group of Stain A mice to 30 doses of 1.6 ml/kg of body weight in 30 days did not cause any hepatomas to develop. On the other hand, application of 30 doses of 0.1 ml/kg of body weight over 90 days did cause a significant number of hepatomas to develop in another group of the same mice (International Agency for Research on Cancer, 1979). In other words, at 3 times the period, just 1/16 the dose resulted in a positive response.
3. It is not uncommon for several carcinogenic agents to be present in contaminated aquifers. However, most of the experiments are carried out for single compounds. This tends to ignore the synergistic effect between different compounds.

4. The validity of data transformation from laboratory animals to humans is questionable.

5. The shape of the dose-response relationship at low doses is a matter of great concern. As mentioned above, selection of different shapes may lead to risk estimates that differ by several orders of magnitude.

REFERENCES

EPA, 1980a. Ambient water quality criteria for trichloroethylene. Environmental Protection Agency Report 440/5-80-077.

EPA, 1980b. Ambient water quality criteria for tetrachloroethylene. Environmental Protection Agency Report 440/5-80-073.

EPA, 1980c. Ambient water quality criteria for chlorinated ethanes. Environmental Protection Agency Report 440/5-80-029.

EPA, 1984a. Proposed guidelines for carcinogenic risk assessment; request for comments. Federal Register, v. 49, no. 227, p. 46294–46301.

EPA, 1984b. Draft criteria document for benzene. Office of Drinking water.

EPA, 1984c. National primary water regulations; volatile synthetic organic chemicals; proposed rulemaking. Federal Register, v. 49, no. 114, p. 24330–24355.

IARC, 1979. Some halogenated hydrocarbons. *In* IARC Monographs, Vol. 20, p. 378–381.

Kim, N.K., and Stone, D.W., 1981. Organic chemicals and drinking water. New York State Dept. of Health, p. 104.

Maugh, T.H., 1984. Tracking exposure to toxic substances. Science, v. 226, p. 1183–1184.

Meyerhoff, A., and Mott, L., 1984. Pesticide residues swallowing the government's line. Sierra, p. 21–27, July/August.

NAS, 1977. Drinking Water and Health (Vol. 1). National Academy of Sciences.

National Research Council, 1983. Risk Assessment in the Federal Government: Managing the Process. National Academy Press, Washington, D.C.

Somers, E., and Krewski, D., 1983. Risk from environmental chemicals. *In* J.T. Rogers and D.V. Bates (eds.), Proceedings, Symposium on the Assessment and Perception of Risk to Human Health in Canada, October 18–19, 1982, p. 43–51.

A New Advection-Dispersion Code for Calculating Transport in Fracture Networks

K. Karasaki

A new advection-dispersion code was developed to study the flow and transport phenomena in fracture networks. The code incorporates the Lagrangian and Eulerian scheme with adaptive gridding. A preliminary study shows that the code is virtually free of numerical dispersion even with extremely large Peclet numbers, and it is not restrained by the Courant condition. The code is designed to simulate field tracer tests such as drift and pumpback and two-well circulation tests.

The transport mechanism in fracture networks is twofold, i.e., transport within an individual fracture and transport due to network geometry. Robinson (1984), Endo (1984), and Long and Shimo (1986) studied transport properties of fracture networks extensively. Since they were mainly concerned with the dispersion mechanism due to network geometries, Robinson (1984) and Long and Shimo (1986) neglected diffusion and dispersion within fractures in their numerical model. Endo (1984) accounted for the dispersion effect within fractures by assuming a Poiseuille velocity profile. Miller (1983) incorporated the random-walk method introduced by Ahlstrom et al. (1977) to simulate diffusion in fractures in his dual-porosity reservoir simulator. He also assumed a Poiseuille velocity profile to account for dispersion within fractures.

Past works have either neglected diffusion and dispersion effects within fractures or assumed that fractures can be represented by pairs of parallel plates with smooth walls. However, fractures generally have contact areas and asperities (Tsang and

Witherspoon, 1982; Pyrak et al., 1986). Because of these irregularities, the velocity profile may not be that of Poiseuille, and there may exist preferred fluid paths or channels in fractures. Therefore, in a two-dimensional model of fracture networks, where fractures are represented by line segments, transport phenomena within fractures may be better approximated by those occurring in a one-dimensional porous medium than those occurring between parallel plates. Here it is assumed that the governing equation for advection and dispersion in a fracture can be written as

$$\frac{\partial C}{\partial t} = D^* \cdot \frac{\partial^2 C}{\partial x^2} - u \cdot \frac{\partial C}{\partial x} \quad ,$$

where C is the chemical concentration, D^* is the dispersion coefficient, and u is the fluid velocity; D^* is a lumped parameter that accouts for molecular diffusion and mechanical dispersion due to a velocity distribution and channeling within a fracture. In the present model, D^* is assumed to be a constant, although the part of dispersion caused by a velocity distribution is probably a function of local velocity.

The advection-dispersion equation shown above is very difficult to solve numerically, especially when the Peclet number, $u\Delta x/D^*$, where Δx is the element length, is large. Large Peclet numbers make the advection-dispersion equation hyperbolic. Conversely, small Peclet numbers result in a parabolic equation. When transport is modeled in fracture networks, the Peclet number is expected to vary over a wide range of magnitude because of the heterogeneous nature of fracture networks, especially when modeling tracer tests with the forced flow field, such as pumpback and two-well circulation tests. Classical numerical treatment of the advection-dispersion equation inevitably introduces either an artificial (numerical) dispersion or oscillation. Many works have been devoted to the subject of avoiding these numerical difficulties (Miller and Miller, 1981; Neuman, 1981, 1983; Cheng et al., 1984; Lai, 1985). One of the promising methods proposed in the literature is a mixed Eulerian-Lagrangian method. Neuman (1983) included an adaptive scheme in his previous work and improved the accuracy of the model. This method selectively introduces forward-moving particles around sharp fronts. However, the method still suffers from some numerical dispersion when the advected front is projected back to the fixed-finite-element grid. The proposed model in the present study is a mixed Lagrangian-Eulerian scheme with adaptive gridding. The model avoids the numerical dispersion by creating new Eulerian grid points instead of interpolating the advected profile back to the fixed Eulerian grid.

The code first solves the flow field using a simple Galerkin finite-element method. The flow can be either steady state or transient, where the time derivative is treated in a usual finite-difference manner. From the pressure distribution at a given time the velocity distribution in the fracture network is calculated. Since linear shape functions are used to solve the flow field, the velocity is assumed to be uniform within a given element. The advection-dispersion equation for mass concentration is then solved by decoupling the equation into two stages. In this way it is possible to solve the advection term independently of the diffusion term and minimize the numerical dispersion. First, the advection equation is solved by using the method of characteristics. The concentration profile at the end of the calculation in the previous time step is, in effect, the initial-value distribution for the new advection problem. This profile is advected explicitly in the Lagrangian manner according to the velocity in each element. It has been found that the mapping back from the Lagrangian grid to the Eulerian grid is the primary cause of the numerical dispersion in this operator-splitting scheme. This is because the location of the front seldom matches the nodal points in the fixed Eulerian grid, thereby necessitating the use of some interpolation scheme, which disperses the sharpness of the front. In the present model, the advected front is placed on the Eulerian grid, and new nodal points generated to preserve the exact shape of the front. At every time step the element catalog is revised and the nodal points renumbered to keep the bandwidth minimized. Because it is necessary to preserve the geometry of the fracture network itself, the original nodal points must be kept intact. The method of single-step backward particle tracking or reverse streak lines is used to obtain the concentration values for these fixed nodal points. This leaves room for some numerical dispersion to be introduced because an interpolation scheme is used to obtain the values. However, in the present model the amount of numerical dispersion is much less compared with the code that uses the method of reverse streak lines alone. The new concentration profile at the end of the advection stage is now the initial value for the dispersion calculation in the second stage. The dispersion is treated in the usual finite-element manner. Currently, linear shape functions are used to approximate the concentration profile in an element.

As a preliminary study, the model was compared with the analytical solution of an advection-

dispersion problem in a semi-infinite rod. The initial concentration is zero everywhere, and for $t>0$ the inlet concentration $C(0,t)$ is raised to unity and kept constant. The analytical solution is given by Carslaw and Jaeger (1959) and can be written as

$$C(x,t) = \frac{1}{2}\left\{ erfc\left(\frac{x-ut}{\sqrt{4D^*t}}\right) + \exp\left(\frac{ux}{D^*}\right) erfc\left(\frac{x+ut}{\sqrt{4D^*t}}\right)\right\}.$$

As can be seen in Fig. 1, the model compares quite favorably with the analytical solution for a wide range of Peclet numbers. It is even capable of accurately calculating a pure advection problem.

It is usually very difficult to satisfy the Courant-Friedrichs-Lewy condition, $|\sigma| = |u\Delta t/\Delta x| \leq 1$, because of the nature of the random fracture network; i.e., there sometimes exists a very small element that requires a very small time step, Δt, to keep the Courant number (σ) below unity. However, the present model does not seem to be restricted by the Courant condition. In the example shown in Fig. 1, the courant number larger than 1.

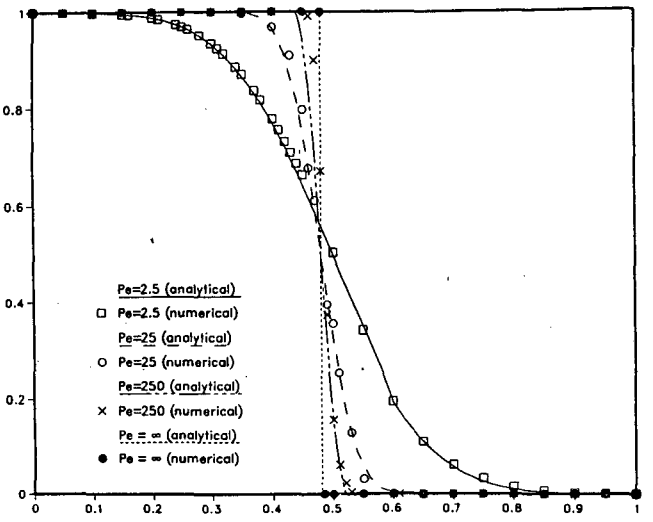

Figure 1. Comparison of numerical solutions and analytical solutions for various Peclet numbers. [XBL 871-217]

REFERENCES

Ahlstrom, S.W., Foote, H.P., Arnett, R.C., Cole, C.R., and Serne, R.J., 1977. Multicomponent mass transport model: Theory and numerical implementation (discrete-parcel-random-walk version). Battelle Northwest Laboratory Report BNWL-2127.

Carslaw, H.S., and Jaeger, J.C., 1959. Conduction of Heat in Solids. Clarendon Press, Oxford.

Cheng, R.T., Casulli, V., and Milford, S.N., 1984. Eulerian-Lagrangian solution of the convection-dispersion equation in natural coordinates. Water Resour. Res., v. 20, no. 7, p. 944–952.

Endo, H.K., 1984. Mechanical transport in two-dimensional networks of fractures (Ph.D. thesis). Lawrence Berkeley Laboratory Report LBL-21171.

Lai, C-H., 1985. Mathematical models of thermal and chemical transport in geologic media (Ph.D. thesis). Lawrence Berkeley Laboratory Report LBL-21171.

Long, J.C.S., and Shimo, M., 1986. The control of fracture aperture on transport properties of fracture network. *In* Earth Sciences Division Annual Report 1985. Lawrence Berkeley Laboratory Report LBL-20450, p. 107–110.

Miller, J.D., 1983. A fundamental approach to the simulation of flow and transport in fractured media. *In* Proceedings, Ninth Workshop on Geothermal Reservoir Engineering. Stanford Geothermal Program Report SGP-TR-74, p. 373–379.

Miller, K., and Miller, R., 1981. Moving finite elements. SIAM J. Num. Anal., v. 18, no. 6, p. 1019–1032.

Neuman, S.P., 1981. An Eulerian Lagrangian numerical scheme for the dispersion-convection equation using conjugate space-time grids. J. Comput. Phys., v. 41, 270–294.

Neuman, S.P., 1983. Computer prediction of subsurface radionuclide transport—An adaptive numerical method. U.S. Nuclear Regulatory Commission Report NUREG/CR-3076.

Pyrak, L.J., Myer, L.R., and Cook, N.G.W., 1986. Determination of fracture void geometry and contact area as a function of applied load. *In* Earth Sciences Division Annual Report 1985. Lawrence Berkeley Laboratory Report LBL-20450, p. 16–17.

Robinson, P.C., 1984. Connectivity, flow and transport in network models of fractured media (Ph.D. thesis). Oxford University.

Tsang, Y.W., and Witherspoon, P.A., 1981. Hydromechanical behavior of a deformable rock fracture subject to normal stress. J. Geophys. Res., v. 86(B10), p. 9287–9298.

The Creation of Hypothetical Fracture Networks from Borehole Data

J.C.S. Long, K. Karasaki, and D. Billaux

This paper describes how the results of numerical studies of fracture systems can be used to develop a series of hypothetical networks that behave like the fracture systems observed in well tests. The general concept is that we generate networks that are constrained to have the same geometric properties as those observed in the field. We then sequentially vary the other fracture properties such that we obtain a series of networks that have the same hydrologic properties observed in the well tests. An example application of this technique to actual field data collected from deep boreholes is shown.

Two numerical studies form the basis for this approach. The first is described in Long and Witherspoon (1985). They studied two-dimensional networks with fractures of constant aperture and length. All of these networks would look the same from the borehole because the orientation distribution of the fractures and the fracture frequency (the number of fractures observed per unit length of line sample), λ_L, were the same in each sample. In order to maintain the frequency, the density (number of fractures per unit area), λ_A, was increased at the expense of the fracture length according to the relationship

$$\frac{\lambda_l}{\overline{\cos\theta}} = \lambda_A l,$$

where $\overline{\cos\theta}$ is a correction factor for orientation and l is the fracture length. The results of the study show that, for small values of fracture length and large values of fracture density, the permeability is zero because the fractures are not connected. As fracture length increases and the fracture density decreases, the network reaches a critical point where it begins to conduct, and the permeability increases.

A second numerical study looked at transport in random fracture networks (Long and Shimo, 1987). In this study the pattern of fractures in a two-dimensional network was fixed. It was assumed that the permeability is proportional to the aperture cubed, b^3, and the porosity is proportional to b. Then the apertures to the fractures were assigned in various ways, but in all cases the mean value of b cubed, $E(b^3)$, is constant. Two factors were allowed to vary; these were the coefficient of variation of the hydraulic aperture ($\nu_b = \sigma_b/\mu_b$) and the correlation between fracture length and aperture, C. If the correlation between aperture and length is near unity, the long fractures get the larger apertures. The bulk average permeability of each network and the breakthrough curves under continuous injection were calculated.

The results show that permeability and velocity decrease as the coefficient of variation of aperture increases. The reason is that heterogeneity in conductivity in the network causes the larger conductors to have their flow restricted by smaller fractures that feed them. Permeability and velocity increase as the correlation between length and aperture approaches unity. In the cases Long and Shimo studied, dispersivity length increases slightly as the coefficient of variation of aperture increases or the coefficient of correlation decreases, and it becomes increasingly difficult to find a unique fit based on the Fickian model. Correlation between length and aperture has an effect opposite that of the coefficient of variation.

These results suggest a methodology for the hydrologic evaluation of homogeneously fractured rocks. One can develop a series of statistical parameter sets for the fracture networks that explain the measured permeability of the system conditioned by the observed fracture frequency, orientation distribution, and any other available data. Then from the breakthrough curve of a tracer test, velocity and dispersivity can be obtained. By comparing the tran-

sport behavior of the various fracture networks in numerical models (each defined by a different parameter set) to the field results, we may be able to exclude many possibilities. This approach is attractive for sites for which data are limited to surface and borehole investigations.

In this approach, one first develops a conceptual model for the fracture network. In the present example, we used the two-dimensional model proposed by Baecher et al. (1977), where fractures are lines randomly located in space. This is rarely a good assumption. In general, these techniques should be extended to three dimensions for accuracy. However, in the case where fractures are expected to be stratabound and subparallel, as in the present example, a two-dimensional network may be appropriate.

Now, from the drilled, logged, and well-tested boreholes we have the following information: fracture frequency, λ_l, fracture orientation distribution, and values of permeability, K_m, estimated from pump tests. In the present field example, the fracture data were obtained using a borehole seisviewer. As explained above, we use the statistical relationship between λ_l, the mean fracture length, $\overline{l}$, the number of fractures per unit area, λ_A, and the orientation distribution of the fractures relative to the well. In this case, the fractures are stratabound in subhorizontal strata, the fractures are subvertical, and the well is vertical. Thus the expression relating the length and density of traces in the horizontal plane of analysis to the frequency in the borehole is

$$\frac{\lambda_l}{\cot\theta} = \lambda_A \overline{l}.$$

Given λ_l and the distribution of strike and dip, a variety of numerical models of fracture systems have been constructed by assuming the fracture length and calculating λ_A from Eq. 1. An example plot of such models is shown in Fig. 1. We are in the process of constructing a series of such fracture meshes that will be used for modeling field tracer tests. We can then calculate the permeability versus $\overline{l}$ for the value of λ_l observed in the borehole and various arbitrary values of b^3. This procedure is explained in Long and Witherspoon (1985). A cartoon of such plots is shown in Fig. 2A. Knowing K_m from the well-test results then allows us to choose pairs of $\overline{l}$, λ_A, and b^3 that match the observed values of K_m, orientation distribution, and fracture frequency.

The next step is to find networks with variable aperture that also can explain these observations. For each set of $\overline{l}$, λ_A, and $E(b^3)$, from Fig. 2A, we can perform parameter studies to prepare a plot like

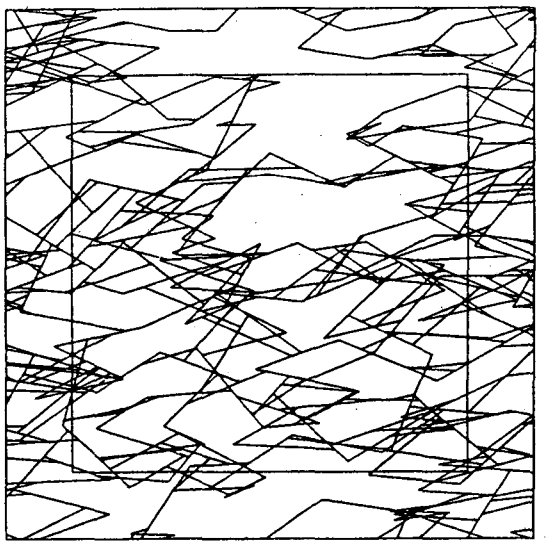

Figure 1. Fracture network model created by using borehole logs. [XBL 871-218]

that shown in Fig. 2B. This figure shows that a constant value of K_m can be maintained by increasing $E(b^3)$ when ν_b is increased.

At this point in our example we have identified four possible network parameter sets with constant apertures that explain the data, and for each of these four we have identified three more parameter sets with variable aperture that also explain the data. Sixteen parameter sets have been found. This number can always be made larger by generating intermediate curves, if necessary, for matching data. However, our ultimate goal is to narrow the possibilities as much as possible. To that end we might look for independent information about the length and apertures of the fractures. This could come from well-test analysis, as suggested by Karasaki (1986), or geologic investigations. If we can determine, for instance, that the fractures are more likely 10 m than 100 m or that $E(b^3)$ is closer to 10^{-20} than 10^{-10} m, then we might be able to ignore some of the points on Fig. 2A, and each of these would eliminate three more points on 2B from consideration.

So far we have ignored the distribution of fracture lengths. It seems that the connectivity of fracture systems depends much more strongly on the mean fracture length than it does on the standard deviation of fracture length (Long, 1987). So up to this point it is probably correct to ignore the standard deviation of length. However, if we wish to include a correlation between length and aperture, we must allow length to be variable. We have not studied the effect of the standard deviation of length

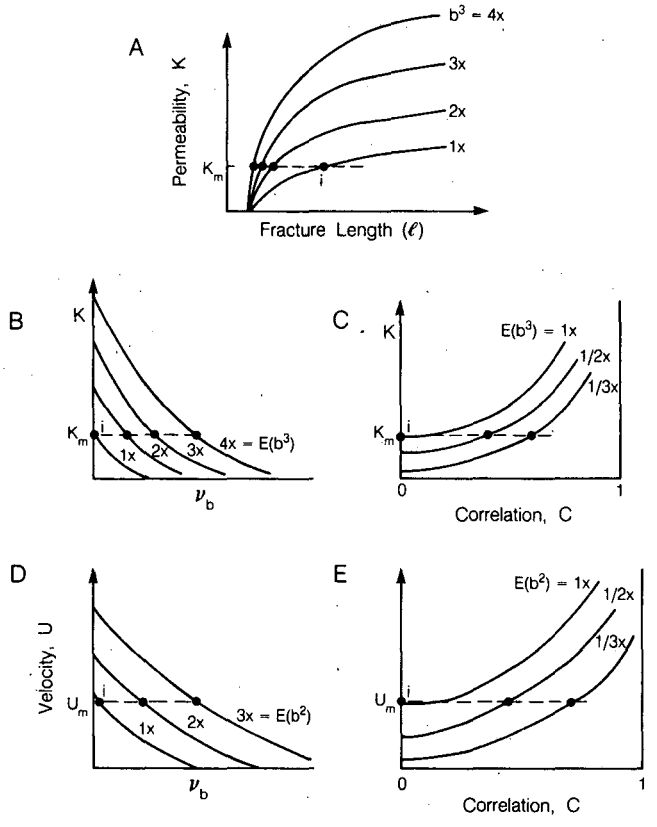

Figure 2. Parametric relationships between: (**A**) K and b^3 as a function of l for constant-aperture fractions and given values of λ_l and orientation distribution, $f(\theta)$; (**B**) K and E (b^3) as a function of ν_b given values of $\lambda_l f(\theta)$ and l; (**C**) K and E (b^3) as a function of C given values of $\lambda_l f(\theta)$, l, and ν_b; (**D**) U and $E(b^2)$ as a function of the ν_b for given values of $\lambda_l f(\theta)$ and l; (**E**) U and $E(b^2)$ as a function of C for given values of $\lambda_l f(\theta)$,l, and ν_b. [XBL 867-10896]

on transport parameters when the length is correlated to aperture. This may be important, but for now we will assume it is minor and pick an arbitrary, but realistic, value for the coefficient of variation for length, ν_l, say 1.0. We continue in the same pattern, and for each point on Fig. 2B we construct the curves shown on Fig. 2C. These curves tell us how to decrease $E(b^3)$ in order to maintain the same permeability when there is correlation between length and aperture. If we choose three curves on this plot we now have a total of 48 parameter sets to explain the data so far.

We now perform a tracer test in the boreholes. We obtain breakthrough curves, and from these we obtain mean pore velocity, U, and dispersion length, L_d. We then model the tracer tests in fracture networks in order to produce curves 2D and 2E for mean pore velocity instead of permeability. We look at mean pore velocity because it appears to be more sensitive to changes in network parameters than dispersion length. The curves generated in this manner will be similar to 2B and 2C, except that we plot the curves for constant values of $E(b^2)$ because velocity is related to b^2, and permeability is related to b^3. Given $E(b^2)$ and ν_b, we can calculate $E(b^3)$. Thus we should find a different set of values of ν_b, $E(b^3)$, and C that explain the mean pore velocity. Sets of ν_b, $E(b^3)$, and C that explain both the permeability and the pore velocity can now be identified. With luck, this will be a small, but nonzero, subset of the original 48 sets.

Another attempt at refining our estimate of the fracture network parameters can be made by comparing the breakthrough curve from the field test with the breakthrough curves generated by the model results. High values of ν_b and low values of C result in flat breakthrough curves and large deviations from Fickian behavior. Small values of ν_b and large values of C result in steep breakthrough curves and small deviations from Fickian behavior. This information should give more confidence in some sets of parameters than others. Similar refinements to the estimate could be found by modeling other field tests, such as resistivity measurements or cross-hole tests, or by using other geologic information about the rock mass.

If we are able to reduce the probable fracture parameters to a small number, we can use these parameters to predict the behavior of the fractured rock mass under various conditions, which is an important component of both reservoir engineering and waste storage problems.

REFERENCES

Baecher, G.B., Lanney, N.A., and Einstein, H.H., 1977. Statistical descriptions of rock properties and sampling. *In* Proceedings, 18th U.S. Symposium on Rock Mechanics, p. 5C1-1–5C1-8.

Karasaki, K., 1986. Well test analysis in fractured media (Ph.D. thesis). University of California, Berkeley, 239 p.

Long, J.C.S., and Witherspoon, P.A., 1985. The relationship of the degree of interconnection to permeability in fracture networks. J. Geophys. Res., v. 90, B4, 3087–3098.

Long, J.C.S., 1987. Permeability of homogeneous fracture systems, in preparation.

Long, J.C.S., and Shimo, M., 1987. The control of fracture aperture on transport properties of fracture networks. To be published by Water Resour. Res.

Injection and Falloff-Test Analysis to Estimate Properties of Unsaturated Fractures

S. Mishra, G.S. Bodvarsson, and M.P. Attanayake

Hydraulic properties of fractures, such as conductivity and aperture, are usually measured in an indirect manner. A common approach involves injecting gas into a packed-off section of a borehole that intersects the fracture(s) of interest. Gas is injected at a series of rates, and the stabilized pressure that corresponds to each rate is then measured. Permeability (or equivalently, conductivity) is calculated from the appropriate steady-state form of a solution of the pressure-diffusion equation. Such a solution typically relates mass rate q_m to the pressure drop between the injection borehole and some observation point expressed as Δp^2 through a constant of proportionality that includes the conductivity (e.g., Montazer, 1982; Trautz, 1984).

We have explored the alternative approach of using unsteady-state pressure data from injection and falloff tests. This method involves injecting a fluid into a formation for a period of time and then shutting the borehole to allow pressure to fall off. Graphic analysis of transient pressure-time data yields formation permeability, distance to linear barriers (such as lateral fracture boundaries), and formation pressure at initial conditions (e.g., Earlhougher, 1977).

INTERPRETATION MODEL

The system of interest contains a plane natural fracture with constant width and aperture, bounded above and below by an impermeable matrix and intersected by a cylindrical borehole (Fig. 1). Initially, the fracture is unsaturated; i.e., it contains a two-phase mixture of water and air. When a fluid is injected into the fracture, it is assumed that the in situ fluids are displaced in a piston-like manner and that a sharp moving front develops in the system, which creates a mobility contrast between the inner (invaded) and the outer (uninvaded) zones. The front is assumed to move at a constant areal velocity during injection and to be stationary during the falloff period. The analytical model developed in this study is for the case of a horizontal fracture; effects of fracture inclination are studied numerically.

At early times, before either the pressure or the saturation front has reached the lateral boundaries of the fracture, flow will be radial. Once the effects of the lateral boundaries have been felt, the flow regime

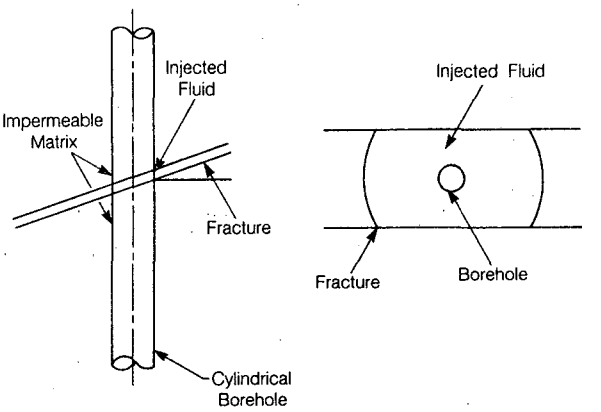

Figure 1. Schematic diagram of the physical system. **(Left)** Cross-sectional view. **(Right)** Plan view. [XBL 869-11002]

will gradually change from radial to linear. At late times the borehole will behave like a plane source, and both pressure and saturation fronts will move in a linear fashion. This suggests that an early-time radial flow solution and a late-time linear flow solution may be superimposed to describe the flow behavior approximately. Our interpretation model, based on this rationale, is described in detail elsewhere (Mishra et al., 1986). Here we briefly review the suggested procedure for analyzing data from injection-falloff tests.

A graph of injection pressure squared, p_{wf}^2, versus the log of the injection time, t, should yield a straight line with slope inversely proportional to the permeability-thickness of the inner zone, k_1h. The same slope is also obtained when the square of the early-falloff pressure, p_{ws}^2, is plotted against the log of the time ratio $(t_P + \Delta t)/\Delta t$. The hydraulic aperture is estimated from the permeability-thickness product by using the cubic law (e.g., Trautz, 1984). The volumetric aperture can be calculated from the time at which the early-time falloff data deviate from the semilog straight line. When the middle-time falloff pressure data are graphed in terms of p_{ws}^2 versus $\log (t_P + \Delta t)/\Delta t$, the resulting semilog slope is inversely proportional to the permeability-thickness of the outer zone, k_2h. The late-time falloff pressure data will also result in a straight line when p_{ws}^2 is plotted against the time group $(\sqrt{t_P + \Delta t} - \sqrt{\Delta t})$.

The slope in this case is inversely proportional to the fracture width b.

DISCUSSION

Our model has been validated by interpreting simulated falloff-test data for air and water injection, the results of which are in good agreement with simulator input values. Figures 2 to 4 show the pressure data from injection, early-falloff, and late-falloff periods for air injection. Typically, air injection results in a near-unity mobility-ratio displacement, and a sharp moving front does not develop. Consequently, it may be difficult to estimate the volumetric aperture from pressure data alone. However, air injection leaves the fracture practically undisturbed (unlike water injection) and may be more attractive if the fractured system is a potential hazardous waste disposal site. Parameters that can then be estimated from unsteady-state injection-falloff tests are fracture conductivity, hydraulic aperture, and fracture width.

We have investigated the effects of fracture inclination and gravity numerically using TOUGH (Pruess, 1985) and have found that these effects are negligible for air as well as for water injection. This happens primarily because of large pressure gradients (induced even at small rates because of the small fracture apertures), which tend to dominate gravitational forces. This facilitates the use of equations that were derived for horizontal fracture systems in the analysis of data from inclined fractures.

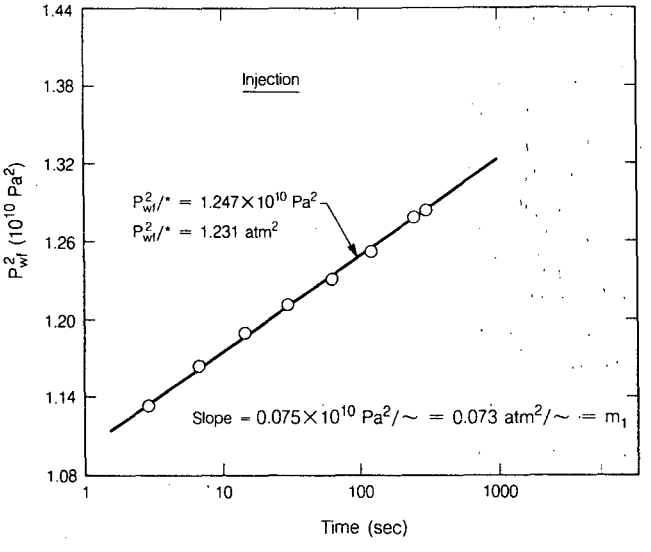

Figure 2. Semilog graph of pressure response for air-injection test. [XBL 869-11007]

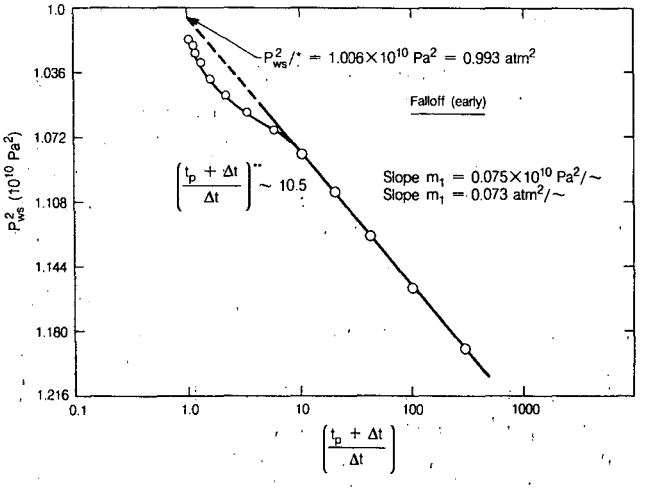

Figure 3. Horner graph of early-time falloff-pressure data; air injection. [XBL 869-11008]

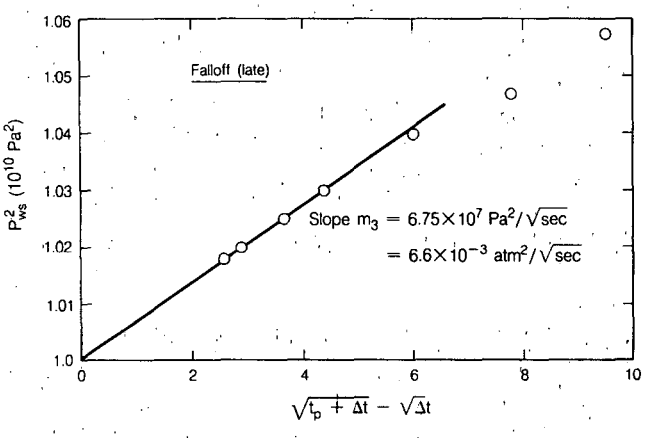

Figure 4. Square-root-of-time graph for late-time falloff-pressure data; air injection. [XBL 869-11009]

REFERENCES

Earlhougher, R.C., Jr., 1977. Advances in Well Test Analysis. Monograph 5, Society of Petroleum Engineers, Dallas.

Mishra, S., Bodvarsson, G.S., and Attanayake, M.P., 1986. Estimating properties of unsaturated fractured formations from injection and falloff tests. Lawrence Berkeley Laboratory Report LBL-22102, in preparation.

Montazer, P.M., 1982. Permeability of unsaturated, fractured metamorphic rocks near an underground opening (Ph.D. thesis). Colorado School of Mines, Golden, Colorado.

Pruess, K., 1985. TOUGH users guide. Lawrence Berkeley Laboratory Report LBL-20700.

Trautz, R.C., 1984. Rock fracture aperture and gas conductivity measurements in-situ (Masters thesis). University of Arizona, 352 p.

Simulation of Flow on the Face of a Large-Aperture Fault

K. Muralidhar and G.S. Bodvarsson

The unsaturated zone at Yucca Mountain, Nevada, is being investigated as a possible site for the disposal of nuclear waste. The zone is approximately 600 m thick and contains various lithologic units, as described by Montazer and Wilson (1984). Some of these units are densely fractured with low matrix permeability, whereas other units have sparse fractures and high matrix permeability. It is believed that water flows naturally through the unsaturated zone at a rate of 0.1–1 mm/yr (Montazer and Wilson, 1984). In addition to the strata-bound small-scale fractures at Yucca Mountain, there are large-scale faults that extend from the surface, through the repository unit, and perhaps all the way to the water table. Montazer and Wilson (1984) hypothesized that some of the water infiltrating at the surface is diverted laterally to these major conduits because of their high permeability and the dip of the various lithologic units. Rulon et al. (1985) have developed a coarse two-dimensional model of the site, and they conclude that the lateral-flow component could be very significant.

In light of these results, it is very important to learn whether such large-scale faults are present in the repository block itself in Yucca Mountain. One possibility is the Ghost Dance Fault, which can be traced at the surface and is believed to extend at least through the repository unit and perhaps all the way to the water table. It is not known at present how permeable the fault is or whether significant amounts of water can flow down it, but it is recognized that this feature deserves extensive field and model studies so that the flow regime in and around it will be understood.

It is believed that the large-scale faults and fractures in the area consist of a number of fractures forming a rubble zone. The fracture aperture in this zone is small, and conventional capillary theories should be applicable. However, some parts of the fault may contain large-aperture openings, causing the gas-liquid interface to have a smaller curvature and, consequently, small forces of surface tension. In this case the capillary model is not applicable; instead, one requires a model involving liquid flow down the walls of the fractures and around various obstacles. However, the usual momentum equations (e.g., Darcy's law) may not be valid for liquid flow. The objective of this work is to investigate the flow of liquid down a fault and the effects of obstacles placed in the flow path.

Two flow models have been considered. The first of these utilizes Darcy's law for the description of the flow path, and the variation in geometry is incorporated into a suitable permeability distribution. The second of these uses the direct solution of Navier-Stokes equations in a complex flow region. Both models are solved numerically. The two models have been compared for their prediction of permeability. The flow is taken to be incompressible, two dimensional, and uniform across the aperture of the fault.

CONTINUUM SOLUTION OF FLOW OVER A FRACTURE PLANE

As a preliminary step, flow in a fault is modeled by Darcy's law. The asperities (to be referred to as obstacles henceforth) are represented as regions of very low permeability. Their exact values are chosen by a limiting procedure that makes the equivalent permeability take on an asymptotic value. A stream-function/pressure formulation is used, which is numerically solved by a controlled-volume finite-difference scheme, with harmonic averaging of permeability at nodes on the obstacle-matrix interface. Matrix inversion is accomplished by a Gauss-Seidel iterative procedure.

SOLUTION OF NAVIER-STOKES EQUATIONS OVER A FRACTURE PLANE

The equations governing incompressible fluid flow in a two-dimensional region containing obstacles are

$$\partial \mathbf{u}/\partial t + \mathbf{u} \cdot \nabla \mathbf{u} = -\nabla p/\rho + \nu \nabla^2 u, \quad (1)$$

$$\nabla \cdot \mathbf{u} = 0, \quad (2)$$

where $\mathbf{u}$ is the velocity vector, p is pressure, $\nabla = (\partial/\partial x, \partial/\partial y)$, and ρ and ν are, respectively, the fluid densities and kinematic viscosity. These equations are solved by a Galerkin finite-element method subject to no-slip conditions on the solid boundaries, prescribed flow at the fracture inlet, and zero trac-

tion at the fracture exit. No special pressure treatment is employed, and Eqs. (1) and (2) are solved simultaneously to extract a pressure and velocity field. Triangular isoparametric elements have been used, with velocity being interpolated at six nodes and pressure at three nodes. All integration formulas are evaluated by a Gaussian quadrature. A streamline-upwind scheme has been implemented to treat the nonlinear terms, especially at high flow rates. The time derivative is finite-differenced by a fully implicit procedure. A Newton-Raphson scheme has been used to iterate on the nonlinear matrix equation.

SOFTWARE DEVELOPMENT

Each of the computer programs developed is general enough to handle any domain size, grid refinement, and number of obstacles. Grid generation is accomplished by solving a Laplace equation in the flow region occupied by the obstacles. This allows the circular obstacles to be mapped as square ones, which facilitates the numbering of nodes. All matrix manipulations are contained within the bandwidth and directly assembled into a column vector, as required by the matrix inverter. The inversion programs used here permit zeroes on the diagonals, as well as lack of symmetry. For the nonlinear problem, iteration continues until a convergence criterion of 0.01% is met.

PRELIMINARY RESULTS

Figure 1 shows the flow pattern calculated using the Darcy flow model for a region containing eight obstacles. These obstacles occupy 45% of the flow region, and the equivalent value of permeability relative to the case of no obstacles is 0.7. Figure 2 shows the flow pattern in a region containing eight obstacles, with a contact area of 18% computed using the Stokes equations. The equivalent permeability, relative to the case of no obstacles, is 0.022, a value much smaller than what would have been predicted by Darcy's law. This value includes the influence of the top and bottom walls, on which the no-slip conditions of flow are applied. This cannot be included in the Darcy formulation. Further studies show that along with its magnitude, the distribution of contact area is also a significant factor in determining permeability of the fault zone. As flow rate is increased (as measured by Reynolds number), inertial effects become important, leading to the formation of additional patterns in the flow field. The permeability is then expected to be a function of the flow rate itself. Figure 3 shows the flow past a single obstruction; the

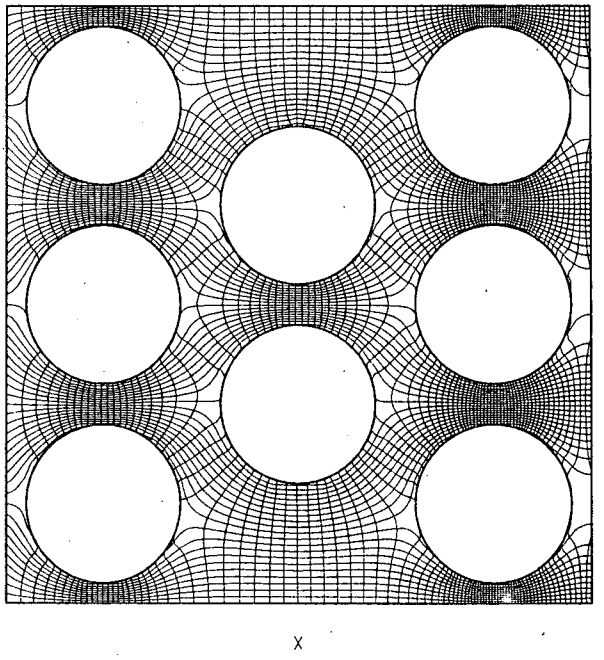

Figure 1. Pressure distribution and streamline pattern in a region of variable permeability. Permeability ratio = 1 $\times$ 10^{-5}, region size = 6 $\times$ 6, obstacle radius = 0.8. [XBL 8610-4053]

small recirculation pattern visible beyond the obstacle is a direct consequence of including inertial terms in the flow equations. Table 1 shows the influence of flow rate on permeability as the Reynolds number is increased.

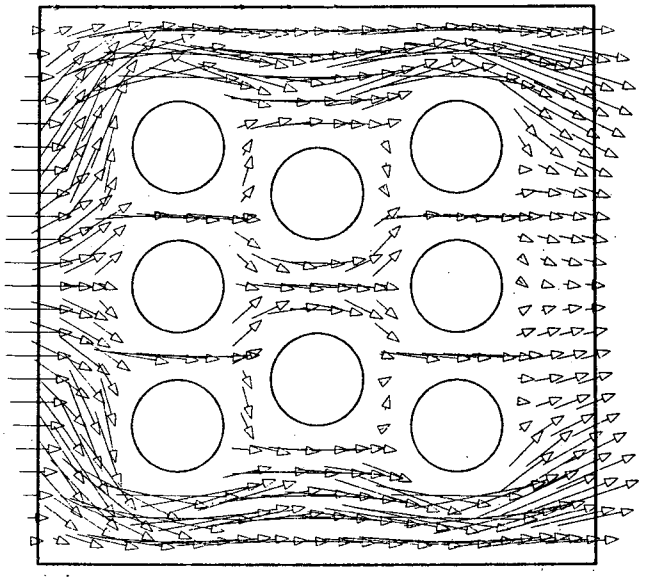

Figure 2. Stokes flow past several obstacles. Obstacle radius = 0.5, region size = 6 $\times$ 6, Reynolds number = 1, equivalent permeability = 0.0218. [XBL 8610-4044]

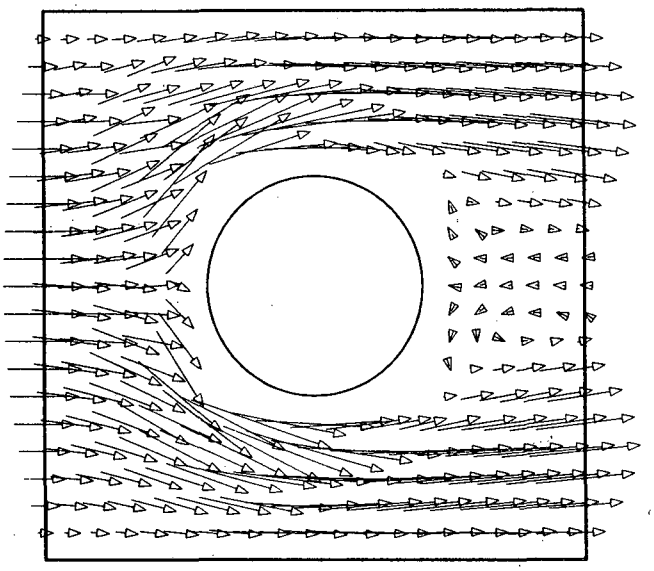

Figure 3. Velocity-vector plot for flow around a single obstacle. Region size = 5, obstacle radius = 1, Reynolds number = 25, equivalent permeability = 0.049. [XBL 871-317]

Table 1. Effect of Reynolds number on equivalent permeability

Re	K_{eq}
0.5	0.1545
1	0.1542
2	0.1521
5	0.1384
7	0.1312
10	0.1244

DISCUSSION

The model using Navier-Stokes equations is being extended to cover other phenomena of interest, such as matrix diffusion and capillarity. In its present form, however, it is best applied to the study of fully saturated flow in a fracture with prescribed boundary shape, permeability as a function of saturation (i.e., the contact area), the effect of distribution of obstacles on permeability for a constant obstacle area, the effect of geometric scaling for a fixed ratio of obstacle area to flow region (i.e., effect of Reynolds number), and individual versus group representation of asperities.

REFERENCES

Montazer, P., and Wilson, W.E., 1984. Conceptual hydrologic model of flow in the unsaturated zone, Yucca Mountain, Nevada. U.S. Geol. Survey, Water Resources Investigations Report 84-4345.

Rulon, J., Bodvarsson, G.S., and Montazer, P., 1985. Preliminary numerical simulations of groundwater flow in the unsaturated zone, Yucca Mountain, Nevada. Lawrence Berkeley Laboratory Report LBL-20553.

A Scheme for Calculating Flow in Fracture Channels Using Numerical Grid Generation in Three-Dimensional Domains of Complex Shape

K. Muralidhar and J.C.S. Long

The science of fracture hydrology is a relatively new field. It is a separate endeavor from classical porous-media groundwater hydrology, because analysis techniques developed for porous media do not work well for fractured rock. Basic research is needed to understand how the features of individual fractures control flow in the rock.

Fractures in general have rough walls, and these walls are held apart through the contact of asperities on the surfaces. The contact area is irregular, as is the aperture of the fracture. Thus from the point of view of fluid mechanics, a fracture is an irregular three-dimensional channel with obstacles of irregular size and spacing.

Characterizing the geometry of such a channel is a problem in itself. Research has been initiated to quantify the geometry through the use of several laboratory and analytical techniques. Casts of the

fracture can be made by injecting a low-melting-point metal into the fracture. The fracture can then be taken apart and both sides photographed. In such a photo the contact area shows up as the color of the rock, and the open area shows up as the color of the metal. Both photographs and profile data can be used in a conditional geostatistical simulation that will provide an estimate of the aperture as a function of location in the fracture plane. Once the geometry is defined, one proceeds to analyze fluid flow through the channel. Analysis of flow through such a channel is the subject of this article.

In general, the problem of fluid flow in an irregular geometry can be solved only if a numerical approach is adopted. Further, any such scheme must have a definite capability to handle boundary shapes that do not coincide with coordinate lines. In the work described here, a three-dimensional grid-generation procedure has been used to map the interior of a complex region onto the interior of a rectangular parallelipiped. The central idea involves the pointwise determination of a natural coordinate system, with respect to which the boundaries of the fracture represent constant-coordinate surfaces. The flow computation is performed in the newly defined region, and an inverse-transformation rule extracts values of flow velocities and pressure in the geometry of interest. The implications of using this procedure are listed below:

1. Boundary conditions of flow can be imposed exactly (without requiring the use of interpolation) on an irregular surface.
2. The grid lines in the transformed region are evenly spaced, thus making finite-difference rules algebraically simple.
3. The procedure used to generate a grid allows the specification of a predetermined amount of orthogonality of the mesh lines. This is important in the control of truncation error in flow calculation. The method can be easily extended to include other mesh properties, such as concentration of nodes near a region of severe velocity gradients.
4. Since the flow is dynamically invariant to mapping of geometries, the mathematical model of flow must be modified when it is solved in the regularly shaped domain in order to account for the change in the measurement of distance. This is accomplished by viewing the whole process of transformation as one of change of coordinates. In general, the new model has a more complicated form than the expression in Cartesian coordinates. For this reason it is possible to interpret the approach taken here as a change from irregular, complex geometry and simple equations to regular geometry and expanded equations.

GRID GENERATION

The actual differential equations chosen to define the mapping function depend ultimately on the physical problem prevailing in the flow domain. This study is restricted to low-Reynolds-number steady flow in rock fractures, and the respective equations and boundary conditions are known to form an elliptical problem. The grid generated from such a system of equations has built-in smoothing properties, as is observed in related diffusion-dominated problems. Little modification is required to extend this to time-dependent cases. The ellipticity of the physical problem permits the use of a variational principle for defining the grid. The advantage of using such minimization rules is that mesh quality can be imposed as a constraint on the problem, and the desired grid pattern can be generated in a systematic way. Only one such constraint—orthogonality—has been used in this study. Other techniques of grid generation, which are problem dependent, have been described in Thompson (1982). The use of grid generation in the solution of problems in fluid mechanics has been described in Hauser and Taylor (1986).

The integral statement provided by the variational principle (Brackbill and Saltzmann, 1982), and applicable over a finite region, can be converted to a system of differential equations applicable pointwise from the appropriate Euler-Lagrange equations of the problem. These are subsequently solved by finite differences. The boundary conditions correspond to (1) imposing the shape of the fracture and (2) requiring the intersecting grid lines be orthogonal to the boundary. These constitute the Dirichlet-Neumann conditions, which, along with the governing differential equations, guarantee a unique solution to the grid-generation problem.

CALCULATION OF FLUID FLOW

The primary thrust of this work is to replace Darcy's law of fluid motion as a constitutive relationship by the complete momentum equations of flow based on Newton's second law. These are the Navier-Stokes equations; along with the equation of continuity, they determine every state of flow, whether laminar or turbulent, for a wide class of fluids, including air and water. The flow is taken to be steady and incompressible. The two primary difficulties in solving this system of equations are encountered in (1) the treatment of nonlinear

acceleration terms and (2) the treatment of incompressibility. The problem of nonlinearity has been circumvented within the framework of finite differences by the use of a hybrid scheme. This employs central differencing of all first-order derivatives (unless the local Paclet number exceeds a certain value based on one-dimensional considerations). Otherwise, an upwind approximation is employed. Any false diffusion generated by upwinding is expected to be insignificant, since the flow has reached steady state and the Reynolds number of flow is small. The incompressibility constraint is handled by replacing it with the Poisson equation of pressure. This has the advantages that pressure values can be directly imposed as boundary conditions and that pressure is identified as a basic variable of the problem. Further discussion of these issues can be found in Muralidhar and Long (1986). For the fracture surfaces the momentum equations are replaced by the no-slip condition for velocity, and they are used simultaneously to approximate wall-pressure gradients. The generalized form of the Navier-Stokes equations in a nonorthogonal coordinate system is derived by applying the chain-rule relationship to the Cartesian form.

The numerical solution of both the grid-generation equations and the flow equations is carried out by finite differences. The reduced algebraic problem is solved by a pointwise iterative scheme, which does not require the formation of large matrices. For convergence, this requires the use of a diagonally dominant system of equations, which imposes certain restrictions on the difference approximations of the equations and boundary conditions. The use of a hybrid scheme for the acceleration terms is one of the most significant of them.

RESULTS

The grid-generation equations have been programmed for both two- and three-dimensional geometries and tested for a variety of problems. The special formulation for the flow field (involving a pressure equation) has been programmed in both two and three dimensions in Cartesian coordinates. This has been extended to cover flow in complex two-dimensional geometries. Work on the full three-dimensional geometry in generalized coordinates is in progress.

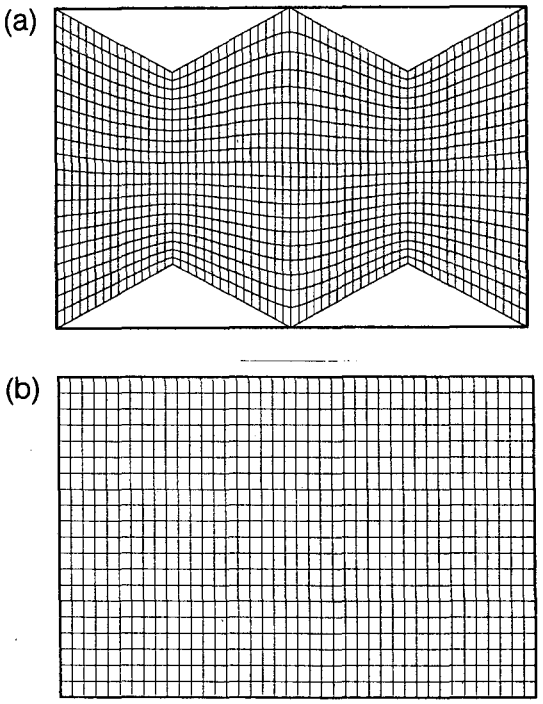

Figure 1. Grid generation in a wavy channel with constriction. **(a)** Physical region. **(b)** Transformed region. Aperture = 2, length = 6. [XBL 8610-3691]

Figure 1 shows grid generation in a wavy channel. The rectangular region is the transformed plane in which computation of fluid flow is carried out. Figure 2 shows grid generation in a region with a circular obstacle. The transformed plane views the obstacle as a square constructed from the grid lines. This greatly simplifies the application of boundary conditions on its surface. Figure 3 shows the flow pattern in a three-dimensional rectangular duct with a square obstacle. The roll pattern beyond this object is a consequence of solving the full-flow equations including nonlinearity. It is this flow behavior that is expected to lead to departure from Darcy's law.

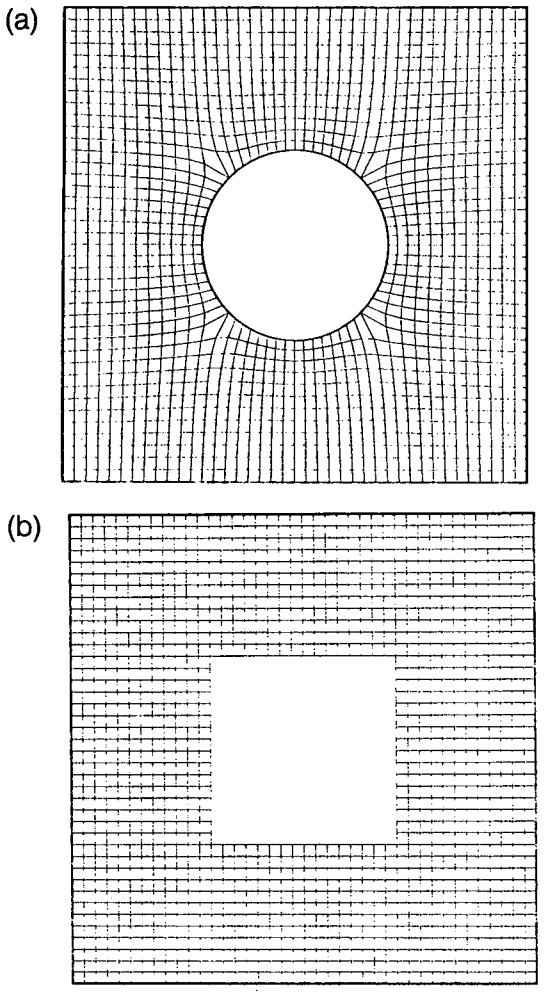

Figure 2. Grid generation in a square region with a circular contact area. (**a**) Physical region. (**b**). Transformed region. Region size = 6, obstacle diameter = 2. [XBL 8610-3696]

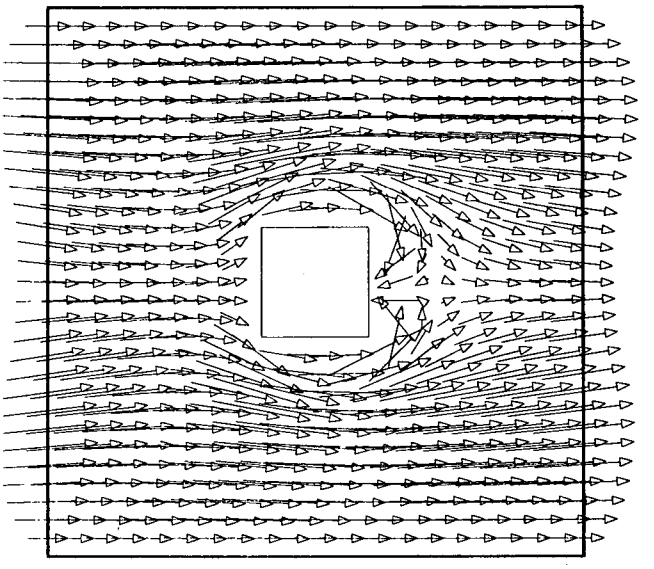

Figure 3. Velocity-vector plot in a three-dimensional duct with an obstacle. Reynolds number = 25. [XBL 8610-3686]

REFERENCES

Brackbill, M.V., and Saltzmann, J.S., 1982. Adaptive zoning for singular problems in two dimensions. J. Comp. Phys., v. 46, p. 342–368.

Hauser, J., and Taylor, C. (eds.), 1986. Numerical Grid Generation in Computational Fluid Mechanics. Pineridge Press, Swansea, U.K.

Thompson, J.F., Ed., 1982. Numerical Grid Generation. Elsevier, New York.

Unsaturated-Zone Thermal Energy Storage: Design Considerations for Warm Climatic Zones

A. Nir, C. Doughty, and C.F. Tsang*

Seasonal heat storage is considered to be an essential element in the utilization of alternative energies with low-temperature heat supplies, as it helps in solving some of the inherent problems arising from the stochastic nature of the supply-demand pattern. Present-day alternative heat sources include solar energy, natural thermal waters, and industrial waste heat. A prospective future source of heat lies in the use of large-scale electrical energy storage in batteries, fuel cells, and compressed air.

Significant advances have been reported, demonstrating the feasibility of the operation of seasonal heat storage in various soil formations—by far the

*Also at Institute of Desert Research, Ben-Gurion University of the Negev, Israel.

least expensive and most widely available storage medium. However, these applications refer mainly to cold or moderate climatic zones, whereas only limited progress on the application of this concept is reported for warm climatic zones. Although seasonal heat storage in warm climatic zones may be expected to benefit from lower heat losses to the environment and higher solar inputs, the lower specific demand for domestic heat and shorter heating periods make the need for heat storage seem less urgent and the investment less attractive. Cursory analysis indicates that this is not necessarily the right conclusion. These zones, which include the southwest United States, parts of Australia, and the Mediterranean countries, are subject to intensive growth in population and in industrial and agricultural development. They should be expected to develop and benefit from suitable methods of heat storage.

DESIGN CONSIDERATIONS

Principles of Design

Generally, the storage method adopted depends on the local availability of storage media, on environmental conditions, on operating temperatures at heat source and at site of use, and on the type of back-up system required. For example, the storage temperature, which can be above, below the ambient temperature, is determined by environmental conditions and source temperatures. Storage temperature in turn influences the physical design of the storage system and the operational procedure of heat supply and extraction. Another classification is made with regard to the source of stored energy: active replacement, passive replacement, or recharge from a semi-infinite reservoir (earth). Again, each option requires a different technical approach in order to optimize its potential.

Choice of Storage Media

There are a number of proposed storage media, and several have been analyzed theoretically or tested experimentally. For warm climatic zones, however, unsaturated-zone soil appears likely to be the only available storage medium. Artificial or excavated storage is excluded for seasonal storage on technological and economic grounds. Rock formations are rare and likely to be too expensive for storage installation. Aquifers are likely to be used or destined for use as sources of water supply, which makes them incompatible with heat storage use. Aquifers with poor water quality, unusable for water supply, are available in more arid zones but tend to be found at greater depth, thus increasing installation and operation costs.

Climatic Considerations

Climate determines the length of the charge and demand periods, typically 8 months (for solar input) and 4 months, respectively. If cold storage is planned the cooling demand may last 5–7 months. The insolation intensity and high ambient temperatures allow high collection temperatures with simple solar collector design and cost. In some cases solar input is available during the demand period, typically 20–25% of the yearly total. Heat losses that occur during storage and during transport between storage and users are low because of the high ambient soil and air temperatures and the high thermal resistance of dry surface soil. Average ambient temperatures for ground surface, deep soil, and groundwaters are 17–19°C, compared with 4–8°C for cold zones and 10–13°C for intermediate climatic zones. In the more arid areas rainfall tends to be limited to winter months, with little ground infiltration, eliminating a common cause of convective heat loss in rainy areas.

Consideration of Soil Properties

An estimate of thermal, hydraulic, and geochemical properties of the soil in the storage area and its environment is required for the planning stage of the storage system. This estimate can be deduced from published data, accumulated experience with local soils, or in situ tests. However, detailed local tests are expensive and time consuming and may still leave many unexplored details within the storage area. We propose instead to estimate the expected values of soil properties and their variability, then design a system robust enough to allow effective operation for the range of possible values.

Temperature- and moisture-dependent values of thermal and hydraulic properties for common soil types have been widely studied (e.g., Sepaskah and Boersma, 1979; Childs and Malstaff, 1982). A high correlation between thermal conductivity and both quartz content and dry density has been noted. Unfortunately, the common classification of soil types by grain size does not lead to consistent values of thermal conductivity; results differ by as much as 30% for various soils with similar grain size. Up to 70°C thermal conductivity is a monotonic function of temperature, with a broad plateau above ~ 20% water content. Because heat capacity is an extensive property of the medium, it can be readily evaluated

from known basic data. It is strongly dependent on the variable water content, but weakly dependent on temperature, within the range of conditions found in the storage system. Matric potential has been widely studied for various soil types, primarily in the agricultural domain. Soils with high clay content are subject to chemical and structural changes at high temperatures and high temperature gradients. Drying and chemical modification are expected at the heat-exchanger surface.

The cumulative experience and theoretical analysis seem to indicate that at a water content of more than ~ 15% and temperatures below ~ 70°C, there is a high probability of stable heat transfer with only limited moisture transfer. The heat-transfer process can then be described by a heat-transfer equation that is not coupled to the moisture-transfer equation, although it is still nonlinear and depends on local moisture content. This uncoupling allows the application of numerical methods with reasonable effort, whereas the application of the fully coupled equations in two or three dimensions with variable boundary conditions is beyond the capabilities of the available computational methods.

Spatial Variabililty of Soil Properties

Thermal and hydraulic properties of soils may vary significantly over the storage area. Vertical variability is relatively easy to determine from existing wells or test logs. Thermal logs are not commonly available but are easily performed in test logs. The thermal profile reflects the thermal properties of stratified soils through the attenuation of surface temperature amplitudes and the phase shift. The storage area may also have large horizontal variability, even in areas of generally horizontal stratification. Variations can be determined with reasonable effort using the recently developed methods of computerized geophysical tomography and the application of ground-penetrating radar to map natural soil and rock conditions in the unsaturated zone. The commonly found variability of soil composition is not expected to have significant effects on heat storage and transfer. Rock outcrops, however, may increase drilling expenses.

Siting Considerations

The main factors affecting site selection are: (1) soil properties; (2) hydrogeologic conditions; (3) distance to source and users of heat (or cold); and (4) economics of excavation, installation, and operation of the storage site. Soil properties are discussed above. The relevant hydrogeologic condition is the distance to areas of saturated water transport. The proximity of aquifers or of seasonal interflow and infiltration increases the heat losses of the storage system to the environment. Distances to source and users are minimized in order to reduce heat losses in transit, circulation energy, and investment in piping. The warm climatic zones benefit by having lower heat losses in transit. Heat pipes buried in dry surface soil during the summer charge period have lower conductive losses because of the higher thermal resistance and higher ambient temperatures. Protection against freezing is unnecessary in most cases.

Vertical siting has two opposing constraints: shallow sites have high conductive heat losses to the surface, and deeper sites are more expensive to construct and have a shorter distance to the saturated zone—a virtual sink for conductive heat flow. As site depth increases, the heat flux to the surface is delayed with respect to the charging period as well as diminished. With a suitable delay a surface heat flux can be transformed from a loss to a usable output. A specific siting option that offers several operational and economic advantages is a greenhouse overlying the storage area, thus offering both protection from direct infiltration and lower heat losses. An added feature of this design is direct root-zone heating, which benefits certain plants more than conventional space heating. This siting option is readily available for agricultural applications but is not suitable for retrofitting existing structures; it is best installed in advance of construction as underfloor heating.

PROPOSED DESIGN

On the basis of the above considerations, a design for an unsaturated-zone thermal-energy-storage system has been proposed. A square array of vertical helical storage ducts is emplaced in unsaturated-zone soil initially at a temperature of 24°C. The top of each helix is 4 m below the ground surface, and its length is 12 m. The helix has a diameter of 1 m, and the spacing between adjacent ducts is 6 m. Between 0.5 and 1 m below the ground surface there is a shallow charge zone consisting of horizontal ducts. During summer water warmed by solar collectors to 65°C is pumped into the bottom of the vertical helix and cools as it flows to the top, depositing heat in the surrounding soil. During winter cool water at 20°C is pumped into the top of the helix and warms as it flows to the bottom, extracting heat from the soil. The shallow heat-storage zone is used during winter to provide short-term storage between daily peak periods of energy

supply (daytime) and demand (nighttime). Heat is transferred by diffusion from the soil to the ground surface and then into the overlying air.

The numerical code PT (Bodvarsson, 1982) has been used to study how the proposed design can be expected to behave in typical energy supply and demand situations. On the basis of the soil property considerations given above, it can be assumed that heat transfer will be accompanied by limited moisture transfer in the unsaturated-zone soil. Therefore, no fluid flow is considered to take place in the soil, heat transfer there being purely by conduction. Uniform temperature- and saturation-independent thermal properties for a medium consisting of 60% soil, 20% water, and 20% air are used. Heat transfer in the duct is by convection and conduction.

From symmetry considerations, a duct in the interior of the array can be represented by an isolated duct enclosed in a square insulated boundary. For modeling purposes the square boundary is approximated by a circular boundary, and the helix is approximated by a cylindrical conduit, yielding an axisymmetric model. A discretized mesh composed of 500 nodes is used for the calculation. The mesh extends vertically from the ground surface to a depth of 50 m and radially from 0 to 3 m. The mesh spacing is finest close to the duct ($-16 < z < -4$, $r =$ 0.5 m). The contribution of ducts on the edge of the array is studied by modeling a single duct surrounded by a radially infinite storage medium. The initial values for soil thermal properties adopted for this model are intermediate with respect to the published values, and the calculations include sensitivity tests to parameter variations. Detailed results of the calculations may be found in Doughty et al. (1983) and Nir et al. (1986).

POTENTIAL APPLICATIONS

Residential and Industrial Space Heat Supply

The application of seasonal heat storage for residential and industrial space heating has been widely discussed, experimentally tested, and proven to be technologically sound and even economically competitive in several locations in the colder climatic zones. Most factors specific to the warm climatic zones favor such applications: lower heat losses in storage and transport, readily available storage areas, shorter heating periods, higher inputs (for solar source), possibility of direct use, and higher coefficient of performance with the use of heat pumps. The proposed design favors application to housing areas or industrial structures requiring a storage system with over 2000 m^2 of surface area ($\sim$ 30,000 m^3 volume), with $\sim$ 1000 GJ of energy stored per cycle. Application to single homes, however, is not efficient.

Agricultural Uses

Agricultural uses were considered initially to be the preferred candidates for seasonal heat-storage applications in warm climatic zones. Several designs have been offered for greenhouse space heating with an associated or independent root-zone heating (Nir et al., 1986). In many warm climatic zones, intensive winter-crop cultivation is a major component of the overall agricultural production. Winter productivity is shown to be significantly enhanced by additional heat in protected and semiprotected environments. Therefore, the availability of the inexpensive, widely distributed, and reliable heat supply at relatively low temperatures offered by the seasonal storage of solar energy is of great interest.

Effects on Resource Development

The feasibility of seasonal heat storage may have a significant influence on the development of alternative energy resources. Because of the relatively short heating season, the mismatch between supply and demand of heat is greater in warm climatic zones than in the colder zones. Therefore, many potential resources, such as solar, low-temperature geothermal, and industrial waste heat, may not justify development without seasonal storage to allow year-round operation of the facilities and reduction in peak heat-transport demand and the associated investment in transport facilities.

REFERENCES

Bodvarsson, G.S., 1982. Mathematical modeling of the behavior of geothermal systems under exploitation. Lawrence Berkeley Laboratory Report LBL-13937.

Childs, S.W., and Malstaff, G., 1982. Final Report: Heat and mass transfer in porous media. Pacific Northwest Laboratory Report PNL-4036.

Doughty, C., Nir, A., Tsang, C.-F., and Bodvarsson, G., 1983. Heat storage in unsaturated soils: Initial theoretical analysis of storage design and operational methods. *In* Proceedings, International Conference on Subsurface Heat Storage in Theory and Practice, Swedish Council for Building Research, Stockholm, June 6–8, 1983, p. 518.

Nir, A., Doughty, C., and Tsang, C.-F., 1986. Seasonal heat storage in unsaturated soils: Example of design study. *In* Proceedings, 21st Intersociety Energy Conversion Engineering Conference, San Diego, August 25–29, 1986, p. 669.

Sepaskah, A.R., and Boersma, L.L., 1979. Thermal conductivity of soils as a function of temperature and water content. Soil Sci. Soc. Am. J., v. 43, p. 439–444.

Development of the Nonisothermal Nonequilibrium Reactive Transport Code CHMTRNS

J. Noorishad and C.L. Carnahan

Almost all reactive-solute transport codes incorporate the assumption of local chemical equilibrium. The lack of kinetic constraints on chemical reactions can be a serious deficiency in applications to certain chemical systems. For example, comparison of results of theoretical computer simulations, assuming chemical equilibrium with observed fluid compositions and mineral assemblages of geothermal systems, can reveal dissimilarities that are indicative of kinetic hindrance of certain reactions in the real systems. A demonstration of the utility of such comparisons has been given by Vallete-Silver et al. (1981). In spite of this fundamental weakness, the practice of equilibrium modeling continues for the following reasons:

1. It has so far been possible to simulate many systems of interest with the simple equilibrium approach. Thus there has been little incentive to incorporate chemical kinetics into reactive-chemical transport codes.
2. The rate constants required for kinetic models have been available only in rare cases.

However, studies of geochemical reaction kinetics are beginning to appear in the literature (Aagaard and Helgesson, 1982; Reddy et al., 1982).

According to Pearson (1983), "Most of the geochemical mass transfer models which could be chosen for coupling with flow models do not have the capability to consider rate control on reactions they simulate. Notable exceptions to this statement are the reaction path codes developed by Helgesson and his colleagues and the EQ6 code of Wolery (1979). Given sufficient rate data these codes could provide rate controlled reaction descriptions if coupled to flow codes."

The limits of the local chemical equilibrium assumption have been explored to some degree by certain investigators, such as Palciauskas and Domenico (1976) and James and Rubin (1979). However, further work is needed before the limits of validity of the equilibrium assumption can be established on a firm basis.

For many problems the slowness of reaction rates clearly calls for kinetic calculations. In these cases, computer codes with the ability to simulate chemical reaction kinetics are the only means to achieve realistic modeling of time-dependent phenomena, such as naturally occurring dissolution of carbonate rocks. The existence of laboratory kinetic data in the form of reaction-rate mechanisms and coefficients offers an opportunity to proceed with work like that summarized here. In this article we describe our nonisothermal nonequilibrium reactive-chemical transport code CHMTRNS. This code, which is based on the equilibrium chemical-transport code CHEMTRN (Miller and Benson, 1983), can simulate kinetic dissolution/precipitation of calcite and silica as well as nonreversible dissolution of glass. Thermodynamic parameters are temperature dependent, and by virtue of a companion heat-transport simulator, the effects of transient temperature conditions can be considered. Oxidation and reduction capability is also an option in this code, and carbon fractionation during transport processes has been included. The performance of the code CHMTRNS is demonstrated in a number of simulations.

Description of the Code CHMTRNS

Partial differential equations of reactive dispersive convection transport are modified to include a

source term. This term represents the rate phenomena that directly affect an aqueous species. Ordinary differential equations are replaced by mass action equations for the appropriate chemical component that evolves according to a kinetic rule. To account for stable-carbon-isotope fractionation during reactive transport, we add a dispersive-convective equation of transport for a carbon-13 solution parameter to the list of the differential equations. This parameter represents the product of the mass of aqueous species (m_C) and the solution shift ($\delta^{13}C$). Depending on whether precipitation or dissolution occurs, the transport equation varies with respect to the contribution it receives from the solid carbonate species. Moreover, to consider reduction and oxidation, an additional mass-action equation representing redox complements the set of algebraic equations. In this treatment redox occurs as a result of electron transfer.

For solution purposes the set of differential-algebraic equations is first approximated in a one-dimensional discretized space-and-time domain using the implicit finite-difference scheme with an upstreaming option. Algorithms for various boundary conditions are developed using Crank's method. Because of the strong nonlinearity of this set of numerically created algebraic equations, the Newton-Raphson scheme provides the final solution algorithm, along the same lines used in CHEMTRN. However, here, the numerical method of Jacobian evaluation avoids repetitive calculation of the spatial component of the Jacobian elements in this iterative solution scheme. Furthermore, the modified algorithms for equilibrium dissolution and precipitation of solids provide a final solution upon convergence, thus eliminating the need for a re-equilibration procedure.

Because of the significance of the role of temperature in some geochemical processes, heat-transport analysis capability is also included in CHMTRNS. Accordingly, proper algorithms for temperature dependencies of chemical reaction constants have been implemented.

Applications

A number of reported kinetic experiments and calculations have been simulated. For example, the batch experiment for silica-water reactions (Rimstidt and Barnes, 1980) and the glass dissolution calculations (Claassen and White, 1979) have been modeled satisfactorily. The results are shown in Figs. 1 and 2. The parameters for the above simulations were obtained from the cited literature. Several isothermal and nonisothermal kinetic transport problems have been solved and will be discussed in a future publication. Finally, a hypothetical simulation aimed at investigation of groundwater evolution processes has been solved and is reported the next article.

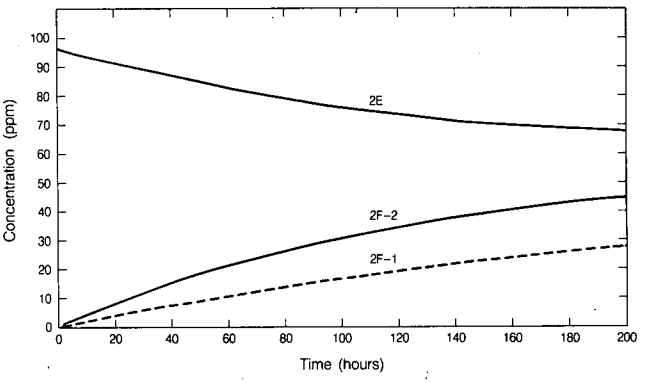

Figure 1. Variation of silica concentration versus time in undersaturated and oversaturated silica solution. [XBL 8610-12648]

CONCLUSION

A nonequilibrium nonisothermal reactive-transport code (CHMTRNS) has been developed, with options for redox and stable-carbon-isotope

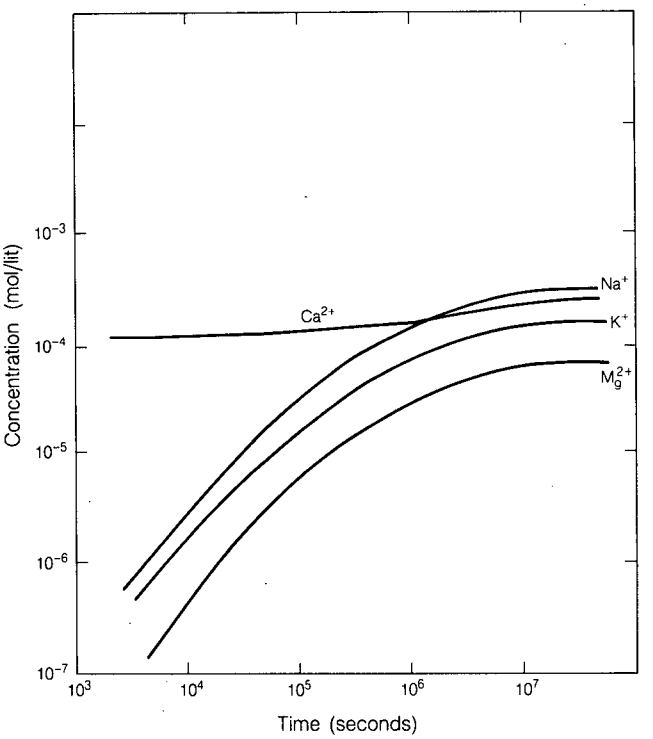

Figure 2. Breakthrough of Mg^{2+}, Na^+, Ca^{2+}, and K^+ near the inflow boundary. [XBL 8610-12657]

fractionation options. The code is based on the thoroughly revised algorithm of the CHEMTRN code. CHMTRNS has been verified against experiments and other existing codes. Silica-water reaction and glass dissolution have been simulated. Future reports will describe solutions to a number of other problems.

REFERENCES

Aagaard, P., and Helgesson, H.C., 1982. Thermodynamic and kinetic constraints on reaction rates among minerals and aqueous solution. I. Theoretical considerations. Am. J. Sci., v. 282, p. 237–285.

Claassen, H.C., and White, A.F., 1979. Application of geochemical kinetic data to groundwater systems. *In* E.A. Jenne (ed.), Chemical Modeling in Aqueous Systems. Amerian Chemical Society Symposium Series No. 93, p. 771–793.

James, R.V., and Rubin, J., 1979. Applicability of local equilibrium assumption to transport through soils affected by ion exchange. *In* E.A. Jenne, (ed.), Chemical Modeling in Aqueous Systems. American Chemical Society Symposium Series No. 93, p. 225–235.

Miller, C.W., and Benson, L.V., 1983. Simulation of solute transport in a chemically reactive heterogeneous system: Model development and application. Water Resour. Res., v. 19, p. 381–391.

Palciauskas, V.V., and Domenico, P.A., 1976. Solution chemistry, mass transfer, and the approach to chemical equilibrium in porous carbonate rocks and sediments. Geol. Soc. Am. Bull., v. 87, p. 207–214.

Pearson, F.J., 1983. Linking flow and geochemical models: Status and problems of developing a fully-coupled model. *In* N.A. Chapman and F.P. Sargent (eds.), Proceedings, AECL/CEC (EURATOM) Workshop on the Geochemistry of High Level Waste Disposal in Granitic Rocks, Oxfordshire, England, September 12–16, 1983, p. 63–83.

Reddy, M.M., Plummer, L.N., and Busenberg, E., 1982. Crystal growth of calcite from calcium bicarbonate solutions at constant PO_2 and 25°C: A test of a calcite dissolution model. Geochim. Cosmochim. Acta, v. 45, p. 1281–1289.

Rimstidt, J.D., and Barnes, H.H., 1980. The kinetics of silica-water reactions. Geochim. Cosmochim. Acta, v. 44, p. 1683–1699.

Vallete-Silver, J.N., Thompson, J.M., and Ball, J.W., 1981. Relationship between water chemistry and sediment mineralogy in the Cerro Prieto geothermal field: A preliminary report. *In* Proceedings, Third Symposium on the Cerro Prieto Geothermal Field, Baja California, Mexico, March 24–26, 1981. Lawrence Berkeley Laboratory Report LBL-11967, p. 263.

Wolery, T.J., 1979. Calculation of chemical equilibrium between aqueous solution and minerals: The EQ3/EQ6 software package. Lawrence Livermore Laboratory Report UCRL-52658, 41 p.

Simulation of ^{13}C Fractionation during Nonequilibrium Reactive Solute Transport in Geologic Systems

*J. Noorishad, C.L. Carnahan, and L.V. Benson**

Major issues regarding the evolution of groundwater are the composition of recharge waters; the travel times to, from, and within aquifers; and the chemical processes that occur during transport. Traditionally, such studies have been limited to direct age determination of aquifer waters based on the assumption that carbons of various origins are mixed. In this approach the ^{13}C content of the water sample is defined as (Pearson and Hanshaw, 1970)

$$^{13}\delta_{sol_{sm}} = \frac{\sum {}^{13}\delta_{solj}\, m_{cj}}{\sum m_{cj}}, \qquad (1)$$

and the activity of ^{14}C is similarly

$$A_{sm}(^{14}C) = \frac{\sum m_{cj} A_j^0 e^{\lambda t_j}}{\sum m_{cj}}, \qquad (2)$$

*U.S. Geological Survey, Denver, Colorado.

where m_{cj} denotes the stable carbon isotope from source j dissolved in water and A^0 can be taken as almost 100% modern ^{14}C. For only two sources of carbon, one belonging to the recharge waters and the other to that of a heavy stable isotope rock, Eq. (1) becomes

$$\delta^{13}C_{sm} = \frac{^{13}\delta_{sol_a} m_{Ca} + \delta_{sol_s} m_{C_s}}{m_{Ca} + m_{C_s}},$$

where the subscripts a and s refer to the recharge water (air) and dead carbon. After simple manipulations of the above relationship, we get

$$\frac{m_{Ca}}{m_{Ca} + m_{C_s}} = \frac{^{13}\delta_{sol_{sm}} - ^{13}\delta_s}{^{13}\delta_{sol_a} - \delta_s}. \quad (3)$$

Equation (2), therefore, changes to

$$A_{sm}(^{14}C) = \frac{m_{Ca} A_0 e^{-\lambda t}}{m_{Ca} + m_{C_s}}. \quad (4)$$

Assuming reasonable values for the parameters in Eq. (3) makes it possible to obtain a correct age for the waters. However, as we mentioned earlier, derivations like that given above are based on simple batch-mixing assumptions, whereas the evolution of groundwater may have involved complex nonequilibrium chemical processes during transport through the subsurface. CHMTRNS can serve as a basis for testing the validity of total and simple dilution assumption for specific problems. Moreover, it can be employed for general investigation of groundwater evolution processes. Examples of such attempts are described below.

GENERIC SIMULATIONS

We have investigated the ^{13}C fractionation of soil recharge waters as they percolate through heavy carbonate rocks. Deines et al. (1974) report that for most soil waters, $\delta^{13}C \approx -25\%$, P_{CO_2} ranges from $10^{-0.5}$ to $10^{-3.5}$ atm, pH ranges from 4.0 to 3.70, and ^{14}C = 100% modern. Thus a typical water of this nature entering marine carbonate rocks that have $\delta^{13}C = 0\%$ and $^{14}C = 0\%$ will tend to have $\delta^{13}C \approx -12.5\%$ and $^{14}C = 50\%$ modern after equilibrium has been reached in the dissolution reaction

$$CO_2 + H_2O + CaCO_3 \rightarrow Ca^{2+} + 2HCO_3^-. \quad (5)$$

The reason is evident from the mass balance of Eq. (5). However, if this reaction does not go to 100% saturation—whether from kinetic effects, reactive transport effects, or paucity of solid carbon in the flow path—the dilution by the dead carbon from the rocks would be between −25% and −12.5%. Some of the above conditions are simulated in three hypothetical cases we have solved. Before discussing these results, we draw attention to the fact that for all cases initial equilibrium calculations were based on CO_2 dissolution in water with pH = 5 to obtain the recharge water composition. For initial conditions in the carbonate rock, we assumed the composition of pure water at equilibrium with the rock. The flow path is a one-dimensional discretized space. The three runs simulate batch kinetic calcite dissolution, transport equilibrium dissolution, and transport kinetic dissolution of calcite. The results are shown in Fig. 1. Although the first two simulations reduce the soil-water dilution to 50% and reduce $^{13}\delta$ to 13%, the kinetic transport is only about 30% effective, even after a year.

SCOPING MODEL FOR YUCCA MOUNTAIN (NEVADA) GROUNDWATER

Here we consider the role and the effects of kinetic dissolution during transport at a particular site. In this first-order study of the Yucca Mountain groundwater evolution process, we used the typical

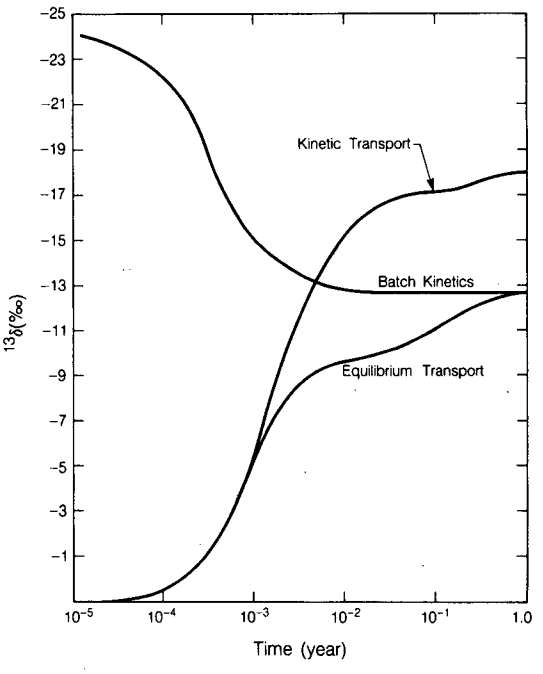

Figure 1. Time variation of $^{13}\delta_{sol}$ as a result of dilution of the carbonate species by marine calcium carbonate in various scenarios. [XBL 8610-12649]

composition of surface waters of the Busted Butte site (Fig. 2), shown in Table 1, for the recharge water. In this simulation a constant flux of the solute was input at the boundary of a one-dimensional column of carbonate rocks saturated with pure water. We allowed reversible kinetic dissolution of calcite and silica and nonreversible kinetic dissolution of glass. Because this was a scoping study, we excluded other complex reactions that might be of relevance and made numerous simplifications. To reduce simulation time, the percolation velocity is increased from the actual order of cm/yr to m/yr, and the flow path is reduced to a 10-m distance geometrically discretized into 20 segments. The latter assumption poses no drawback because we consider the events that are not affected by the exit-boundary effects during the observation time. That is, we only analyze near-entrance events that stabilize before the far boundary senses any change. The results of this simulation are not very dramatic because of the very low dissolution capability of the water. Therefore, expectedly, a front with the composition of the flux water swept through the column. No appreciable change of $\delta^{13}C$ was observed because so little dilution took place. The results of this simulation are depicted in Figs. 3 to 7. Figure 3 shows the small pH variations. Figure 4 shows the advance of the $\theta(-\theta = {}^{13}\delta_s - {}^{13}\delta_{sol})$ front; Fig. 5 shows the very sharp front of $\delta^{13}C \approx -16\%$ that develops at around 100 days into the simulation. At the end of the 1-year simulation, $\delta^{13}C$ in the upstream part of the flow path approaches the quantity for the recharge water, as shown in Fig. 6. Figure 7 shows the variation of the carbonate species for a point near the entrance as a function of time.

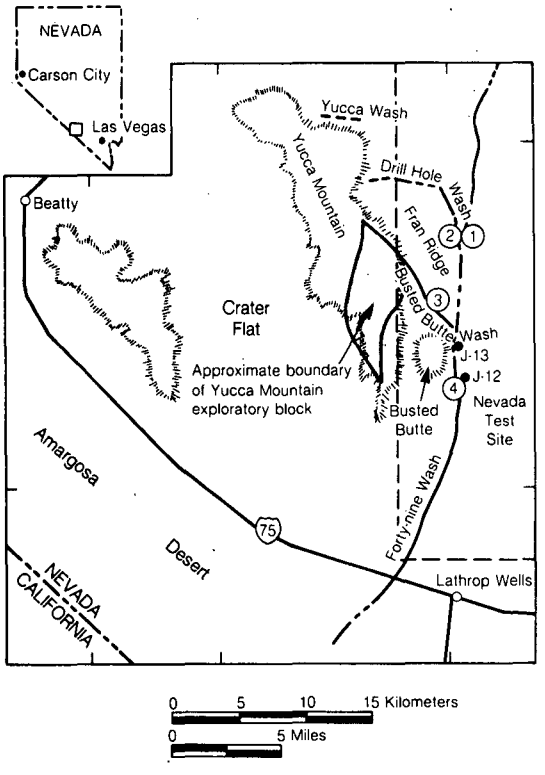

Figure 2. Location of sampling sites near Yucca Mountain. [XBL 8610-12663]

CONCLUSION

Using the nonequilibrium reactive chemical transport code CHMTRNS, we investigated the fractionation of carbon-13 during transport. In our first case, we studied the generic fractionation of ^{13}C of the recharge waters as they percolated into carbonate rocks. We verified that the increase in the $\delta^{13}C$ shift from the $-24‰$ level in soil waters is dependent upon processes that are involved in transport. In a second study, we attempted to analyze the evolution of groundwaters of the Yucca Mountain basin in Nevada. The high pH of the surface waters in this region does not allow an appreciable change in the $\delta^{13}C$ during transport, the main reason being the lack of major dissolution of the heavy carbonate rock in the transport process. The results of this simulation, in spite of the very rough approximation of real processes, point to the need for more complex conceptualization than we used. However, the code CHMTRNS provides the capability needed for more realistic modeling in such investigations.

REFERENCES

Deines, P., Langmuir, D., and Harmon, R.S., 1974. Stable carbon isotope ratios and existence of a gas phase in the evolution of carbonate ground waters. Geochim. Cosmochim. Acta, v. 38, p. 1147–1164.

Pearson, J.F., and Hanshaw, B.B., 1970. Sources of dissolved carbonate species in groundwater and their effects on carbon-14 dating. *In* Proceedings, Isotope Hydrology 1970. International Atomic Energy Agency, Vienna, p. 271–286.

Table 1. Chemical analysis from Fortymile Wash surface water samples.

Station	Date	Time	Na (mg/c)	Ca (mg/c)	Mg	K	HCO_3 field	HCO_3 lab	SO_4	Cl	SiO_2	Li (μg/L)	Sr (μg/L)	F	Dissolved solids	pH field	pH lab	SC field	SC lab	δD	δO^{18}	C^{14} (y.b.p.)	$^{13}C/^{12}C$
1	7/22/84	1925	9.0	27	3.6	8.9	110	83	11	4.5	26		120	0.2	140	7.6	7.2	198	212	—	—	—	—
2	7/24/84	2005	8.1	24	3.3	7.8	106	125.6	10	3.7	25	6	100	0.2	145	7.3	7.4	182	201	−89	−12.3		
3	8/14/84	1505	4.1	8.1	0.90	5.6	—	43.9	6.2	1.3	8.7	6	34	—	57	8.4	7.5	70	198	−60	−9.0	—	—
4	3/15/84	2230	8.2	21	2.9	9.1	—	91.5	10 0.69	1.4 0.316	24	7	100	0.2 0.038	122	8.0	7.4	170	259	−96	−13.7	0	−13.8
5	8/14/84	1510	8.6	9.5	1.3	7.4	—	51.2	12	2.2	20	14	66	0.3	92	8.3	7.8	100	218	−57.3	−8.9	—	−12.7
6	7/19/85	1900	11	19	2.6	10	—	103.7	10	3.2	26	14	120	0.3	134	—	7.9	—	193	—	—	—	—
7	8/14/84	1530	7.0	12	1.8	8.1	—	57.5	7.9	1.7	23	17	86	0.3	100	8.3	7.8	120	217	−69.5	−10.1	+846	−16.1
8	8/15/84	0230	6.9	9.8	1.5	5.8	—	52.4	4.9 0.69	1.2 0.?16	16	14	67	0.2 0.038	73	8.3	8.0	90	184	−70.5	−10.5	—	−17.4
9	8/14/84	1600	2.4	6.7	0.7	6.3	—	31.7	6.3	2.0	4.5	5	31	—	45	8.2	7.0	59	100	−64.5	−9.5	—	−16.1

Stations 1 to 4, Fortymile Wash above Drill Hole Wash; 5 and 6, Drill Hole Wash; 7 and 8, Busted Butte; 9, Fortymile Wash near well J-12.

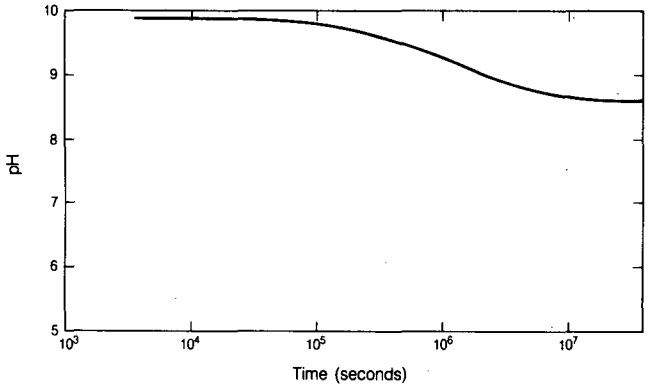

Figure 3. Variation in pH versus time. [XBL 8610-12645]

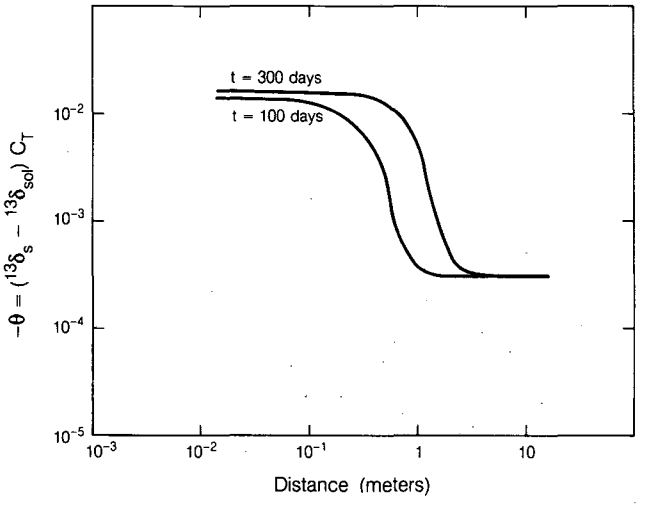

Figure 4. Profile of $-\theta$ along the flow path at different times; $^{13}\delta_s$, $^{13}\delta_{sol}$, and m_T describe $^{13}\delta$ of rocks, $^{13}\delta$ of the infiltrating water, and the total carbonate concentration of the solute. [XBL 8610-12641]

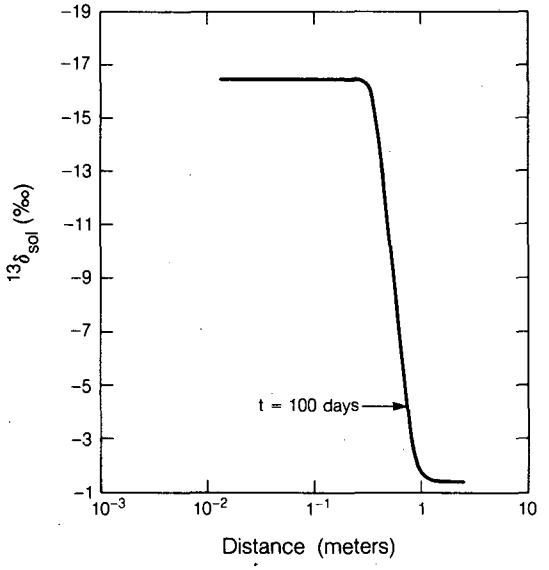

Figure 5. Profile of $^{13}\delta_{sol}$ along the flow path for 100 days. [XBL 8610-12646]

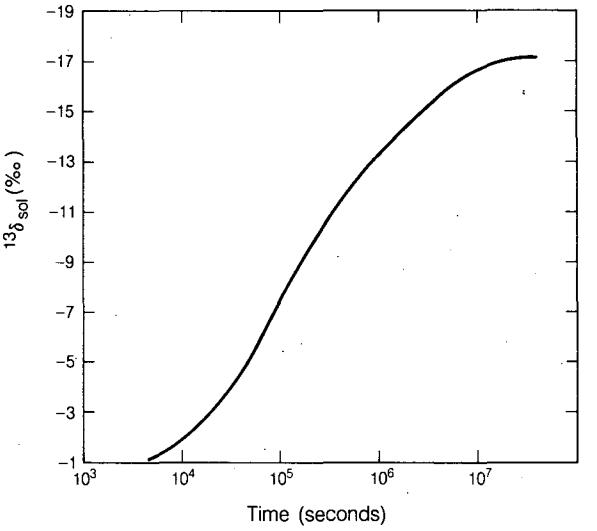

Figure 6. Breakthrough of the solution shift in the percolating water. [XBL 8610-12647]

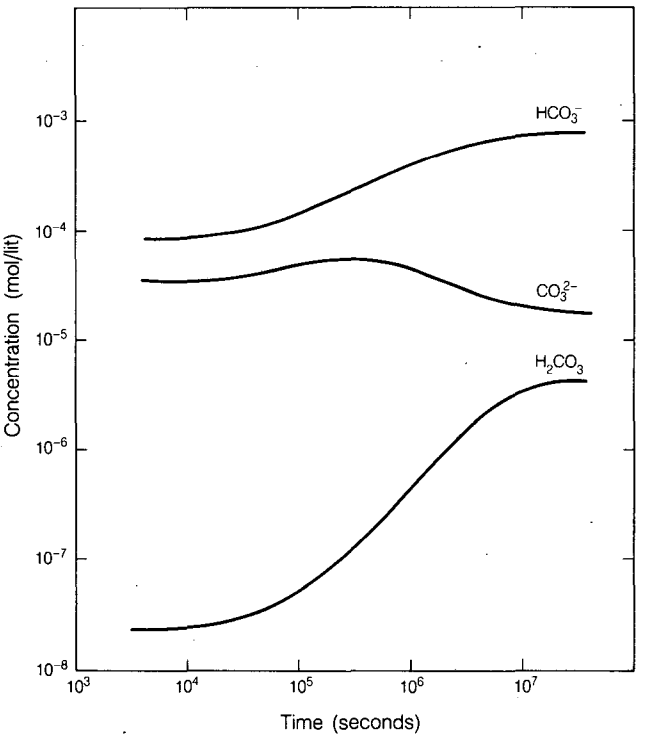

Figure 7. Breakthrough of the aqueous carbonate species near the inflow boundary. [XBL 8610-12655]

Conceptual Model of the Klamath Falls, Oregon, Geothermal Area

R.H. Prucha, S.M. Benson, and P.A. Witherspoon

The Klamath Falls KGRA (Known Geothermal Resource Area), located in south-central Oregon, is a low- to moderate-temperature resource. The approximately 2-square-mile shallow thermal anomaly is associated with the large normal fault shown in Fig. 1 (Sammel et al., 1984). Over 500 wells have been drilled in the area, ranging in depth from 90 to 1900 ft. Most temperatures encountered in these wells range from 70 to 120°C. The geothermal resource has been used for space heating for some 70 years; special uses include heating greenhouses and swimming pools, snow melting, and milk pasteurization.

Over the last 50 years significant amounts of data have been obtained from the Klamath Falls geothermal resource. To date, the complexity of the system has stymied researchers, leading to the development of only very generalized hydrogeologic and geothermal models of the area. Recently, the large quantity of available temperature data has been re-evaluated, revealing new information on subsurface heat flow and locations of faults in the system. These inferences are supported by borehole, geochemical, geophysical, and hydrologic data. A re-evaluation of all available data has led to the development of a detailed conceptual model for the Klamath Falls geothermal resource.

GEOLOGY

The Klamath Falls geothermal area, east of the Cascade Range and north of the Medicine Lake Highlands, California, is situated in a horst-and-graben structure typical of the Basin and Range province. The Klamath graben complex extends some 80 km, from Lower Klamath Lake to as far north as Crater Lake, trending approximately N40W. Faulting in the area is believed to have commenced during the late Pliocene and continued well into the Pleistocene. Large, steeply dipping normal faults with vertical throws up to 1600 ft flank either side of the graben complex and trend N25-35W. On the western shore of Upper Klamath Lake the large fault blocks dip toward the southwest, whereas on the eastern shore they dip to the northeast, suggesting that the axis of the graben complex passes through the lake. The two types of faulting in the immediate region are northwest-trending normal faults and northeast-trending strike-slip cross faults.

The geology of the area has been mapped and described by Peterson and McIntyre (1970). Four

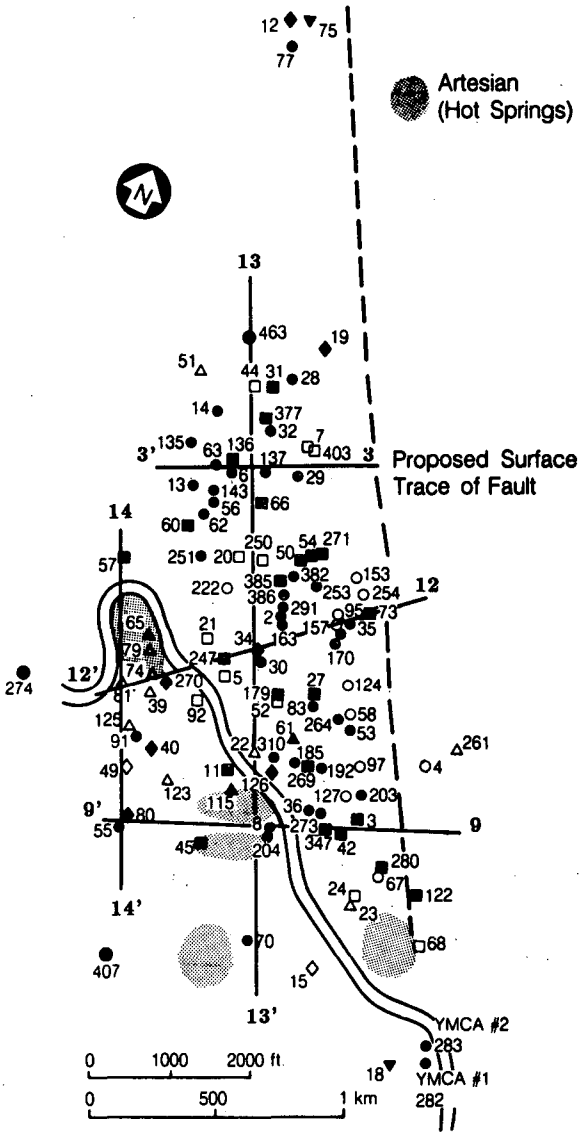

Figure 1. Wells supplying temperature data. Line drawn across the wells indicate the location of temperature profile cross sections. [XBL 8612-12853]

dominant rock units have been identified in the immediate Klamath Falls area by outcrops and borehole data (Newcomb, 1958). These rock units are, from earliest to most recent, a Pliocene basement basalt, the thick Pliocene Yonna Formation, a Pleistocene andesitic-basaltic flow sequence, and Quaternary alluvium.

The Pliocene Yonna Formation, a sequence of lacustrine and fluvial tuffaceous siltstone, sandstone,

ashy diatomite, basaltic tuff and breccia, and a few thin basalt flows, uncomformably overlies the basement rock (Newcomb, 1958). This formation is primarily subaqueous in origin, as evidenced by the brecciated and altered basalt flows, deposited during a period when swamps and lakes covered the region. Explosive and quiescent episodes of volcanism were nearly contemporaneous with the deposition of the Yonna Formation, as is suggested by the maars, tuff rings, and welded tuffs. The Yonna Formation is estimated by Newcomb (1958) to be approximately 1000 ft thick.

Nearby volcanic activity has been dated by both paleontological data and potassium/argon (K/Ar) methods. K/Ar methods have indicated volcanic activity as recent as 1.9 m.y.b.p. and up to 4 to 5 m.y.b.p., for rocks on the KGRA periphery.

GEOTHERMAL AQUIFER

Numerous well tests have been conducted within the Klamath Falls KGRA. From these tests, the hydrological parameters of the reservoir (kH/μ and $\phi c_t H$) and the nature of the geothermal aquifer have been investigated. Results show the aquifer to be highly permeable. In general, the data are indicative of a naturally fractured system, with high-permeability fractures and relatively low permeability matrix blocks (Sammel et al., 1984). Several localized heterogeneities have also been detected in the reservoir, including a high-permeability region centered in the Old Fort Road area and a semipermeable fault near the Oregon Institute of Technology (OIT) (Benson and Lai, 1986; Nork, Inc., 1986). Unexpectedly, the faults and fractures in the KGRA behaved neither as classical constant-potential boundaries nor as no-flow boundaries.

On the basis of logs from a well drilled at the OIT campus, Sammel (1980) concluded that the rocks that make up the geothermal aquifer are believed to extend to at least 2000 ft. Water in the aquifer flows preferentially through strata consisting of volcanic breccia (cinders, broken lava, porous lava, etc.), jointed and fractured vesicular basalt flows, and fractured, indurated lacustrine sediments. These strata range in thickness from one to a few feet and have high vertical and areal variability. The permeable strata are interspersed with layers of lacustrine and tuffaceous sediments and diatomite ranging from 30 to 150 ft in thickness.

Fluid flows from the fault zone toward the southwest, following the general surface topography, as indicated by static water-level maps drawn by Lund (1978) and Sammel et al. (1984).

GEOCHEMISTRY

Geochemical data contribute valuable information regarding maximum reservoir temperatures, mixing of thermal waters, fluid residence times, and possible sources of recharge. Janik et al. (1985) used tritium data to determine the cold-water residence time in the aquifer to be at least 30 years and that of the thermal waters to be at least 60 years. From tritium and deuterium data they were also able to conclude that the cold-water recharge probably does not originate from the modern Klamath Lake (Sammel, 1980). The tritium data also lead Janik et al. (1985) to suspect two cold-water sources—a very shallow one containing tritium and a deeper one that is tritium free. Geothermometry and mixing models indicate a maximum source-water temperature of 190°C.

TEMPERATURE DISTRIBUTION

Temperature data are very important to the understanding of a hydrothermal system. The temperature data used in this study were obtained primarily from driller's logs. Temperatures in most cases were measured using a maximum-reading thermometer or a simple thermistor apparatus. According to Sass and Sammel (1976), temperature profiles typical of this type of hydrothermal system are classified into four distinct types: (1) near-isothermal temperature profiles, indicating hydrologic recharge; (2) quasiconductive temperature profiles; (3) convex-upward profiles with elevated temperatures, indicating areas of discharge; and (4) temperature profiles exhibiting varied types of curvature, implying a combination of upward and downward flow. As shown in Fig. 2, profiles from Klamath Falls exhibit all four types of characteristics; however, most temperature profiles show a combination of conductive and convective heat flow.

To allow closer examination of the temperature data, cross sections were constructed approximately parallel and perpendicular to the proposed surface trace of the main normal fault associated with the geothermal system. Twenty such cross sections were constructed for the geothermal area; five are shown in Figs. 3 and 4, and their locations are shown in Fig. 1. Since relatively few temperature data are available east of the normal fault, no cross sections or horizontal contour maps were constructed for that area.

Figure 3 shows two cross sections parallel to the main normal fault; Fig. 4 shows three cross sections perpendicular or oblique to the fault. Both sets of cross sections show thermal features that can only be

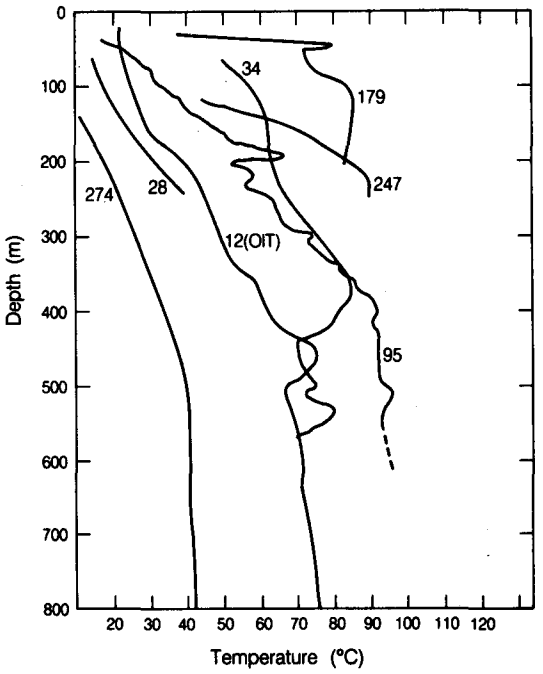

Figure 2. Various temperature profiles from the Klamath Falls geothermal resource. [XBL 8612-12852]

explained by complex convective heat-transfer mechanisms. Cross section 13, which is parallel to the fault, shows temperatures at both ends of the anomaly decreasing rapidly. We propose that northeast-trending cross faults limit the northern and southern extension of the resource and that the region between wells 31 and 9 is the primary zone of hot-water recharge.

In cross sections 3, 12, and 9, perpendicular to the normal fault, a higher thermal gradient zone is seen on the right (northeast) side, most likely indicating the location of the main normal fault. This helps to confirm the existence and define the location of this normal fault, as suggested in previous reports.

Both sets of cross sections show the locations of very high, near-surface thermal gradients. When the cross sections are aligned, these thermal anomalies fall along lineaments, which are interpreted in this report as faults (see Fig. 5). Several three-dimensional models were constructed to delineate these fault lineaments in more detail. Cross sections 3, 12, and 9 in Fig. 5 suggest the existence of a subsidiary normal fault (Fault 1b) parallel to the main

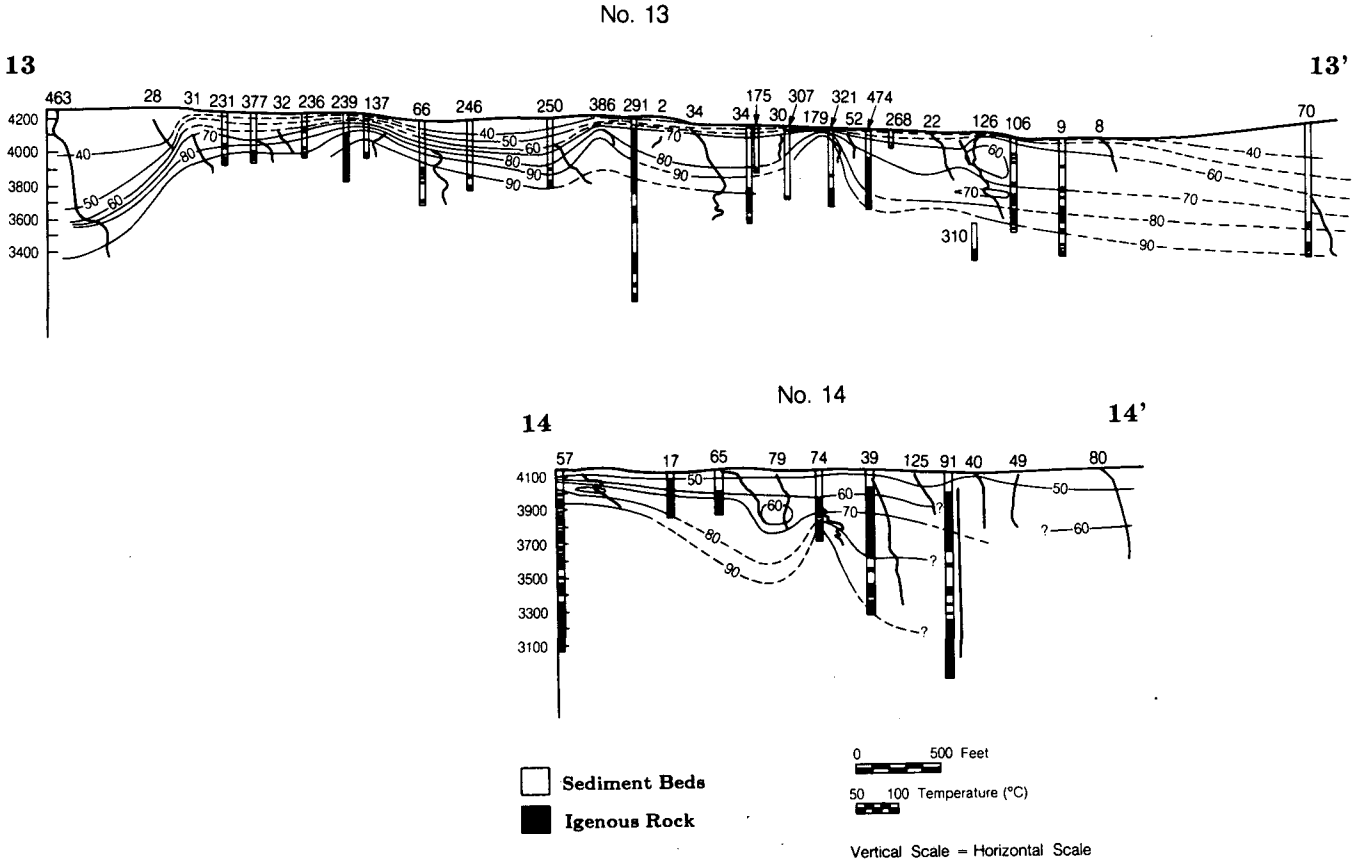

Figure 3. Cross-sectional temperature profiles drawn parallel to the main normal fault. Well numbers appear above the isotherms. [XBL 8610-12708]

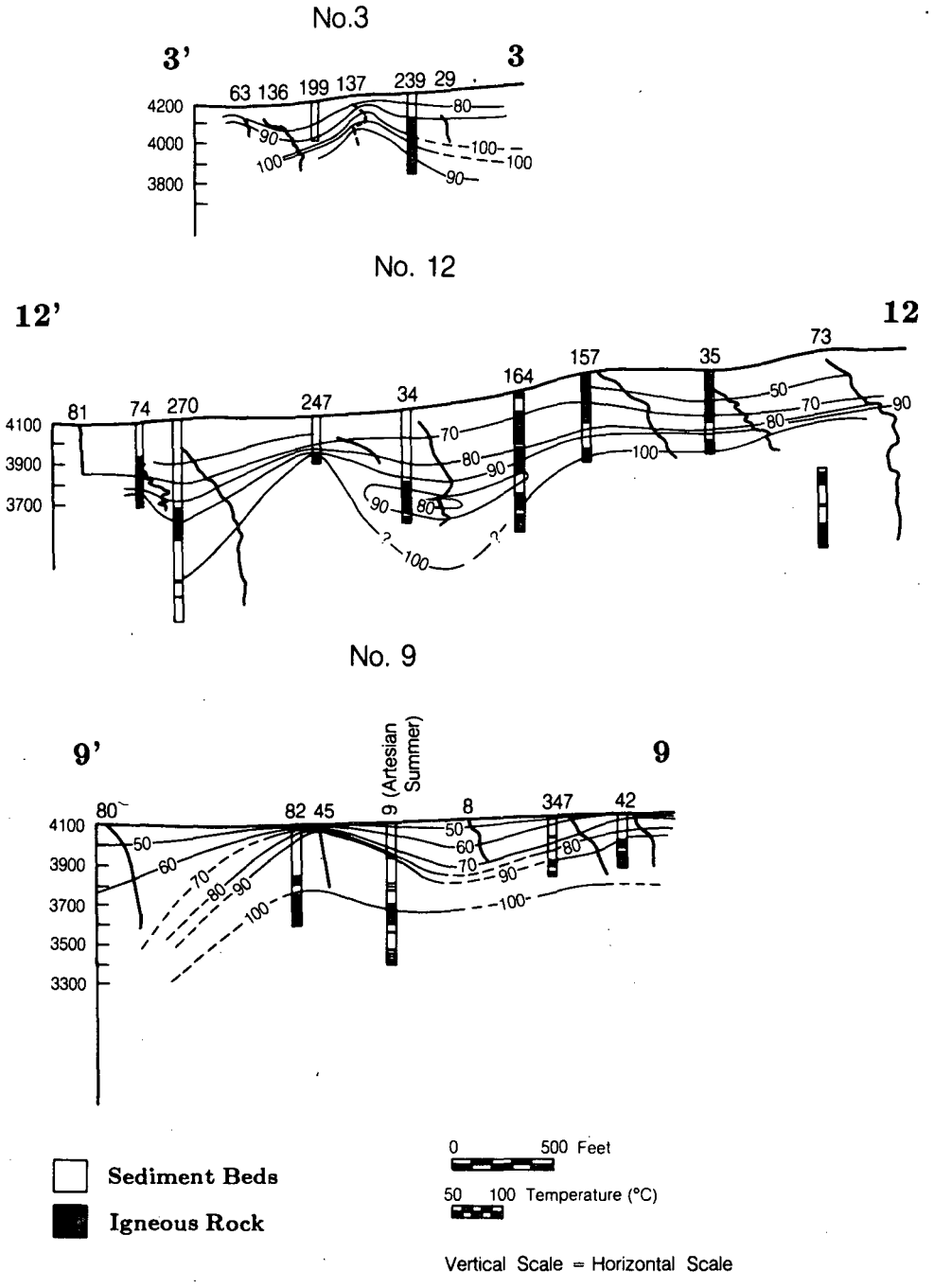

Figure 4. Cross-sectional temperature profiles drawn perpendicular to the main normal fault. Well numbers appear above the isotherms [XBL 8610-12711A]

normal fault (Fault 1a) intersecting wells 45, 247, and 137. The north-south extent of the subsidiary normal fault cannot be determined from the available data. The locations of the right-lateral strike-slip cross faults shown in Fig. 6 are also inferred from cross sections 13 and 14 (Fig. 3).

FAULT LOCATIONS

To confirm the existence of the faults shown in Fig. 5, hydrologic and lithologic data and high-altitude infrared photographs were analyzed. Faults 1a, 2, 3, 4, 8, and 9 were easily identified from the high-altitude photographs because of their clearly

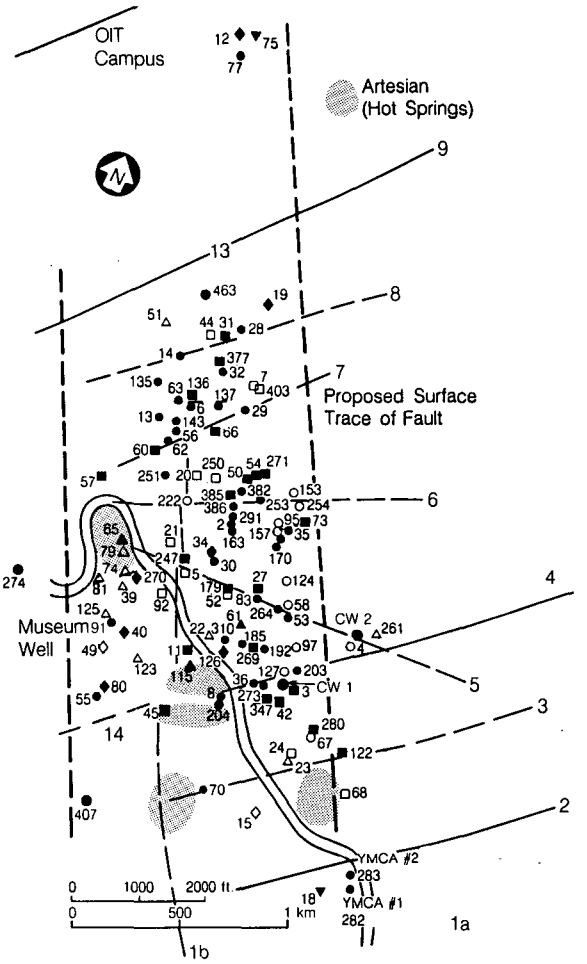

Figure 5. Fault locations inferred from the temperature-profile cross sections and temperature-contour maps. [XBL 871-9801]

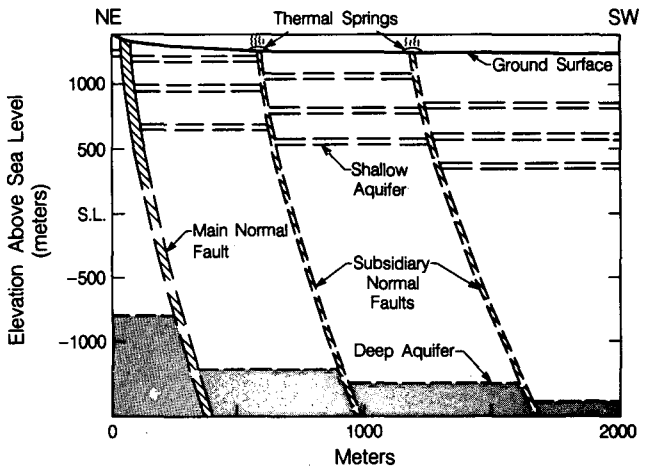

Figure 6. Conceptual model for the Klamath Falls geothermal system. [XBL 873-10023]

visible surface traces. Faults 5, 6, and 7 were less pronounced because their traces tend to be localized, and fault 1b could not be detected. The exact locations of Faults 2, 3, and 9 were more easily recognized using areal photographs, as their traces were found to extend well into the region east of the main normal fault (Fault 1a). All of the faults in Fig. 5 conform to the regional fault pattern, one set trending northwest and the other northeast.

Lithologic data were re-examined with the intention of confirming the existence of the newly proposed faults; however, this proved more difficult than anticipated. Poor lithologic correlations were found between nearby wells, both within the fault blocks and across their boundaries. This is partly due to the poor quality of the driller's logs and the complexity of the sedimentation and erosion processes. However, the system most likely experienced faulting concurrently with erosion and deposition of sediments, resulting in the highly complex subsurface geologic structure.

Well-test data are also consistent with a highly faulted system. The geothermal reservoir appears to have a high degree of transmissivity and connectivity between wells, implying a highly fractured and faulted medium. The results of the many well tests conducted in the area can be interpreted within the framework of a fault- and fracture-dominated hydrologic regime. The normal faults, cross faults, and contacts between lithologic layers act as high-permeability conduits. Low-permeability strata within the fault blocks provide a large storage volume for the thermal fluids. The double-porosity behavior reflected by the well-test data support this interpretation (Benson and Lai, 1986). Well-test data also suggest the presence of an approximately cylindrical region with a permeability 7.5 times higher than the rest of the reservoir. This region coincides with the proposed intersection of Faults 1a, 4, and 5. Local regions with higher permeability are expected at each intersection of two or more faults. Although data to support this hypothesis at Klamath Falls are not yet available, the locations of once-active artesian hot springs generally coincide with the intersection of the strike-slip and normal faults (see Fig. 5). This suggests that higher-permeability regions are associated with the intersections of two or more faults throughout the KGRA.

CONCEPTUAL MODEL

Figure 6 represents a simplified conceptual model of the Klamath Falls geothermal area. The reservoir consists of a shallow and a deep aquifer. Actually, the aquifer consists of a zone of three

permeable layers. The deep aquifer is inferred from geochemical data, although it has not been penetrated by wells. The two aquifers are connected through the main normal fault and possibly by the two subsidiary normal faults. Although upflow occurs along fault planes, we propose that the most permeable zones occur at the intersections of the normal and cross faults, as described in the previous section.

The dominant normal fault and two subsidiary normal faults indicate downthrows toward the southwest. This displacement might explain the successively lower temperatures encountered at greater distances from the main normal fault.

Hot-water recharge is derived from two possible sources. Thermal waters may flow into the geothermal system from the upthrown block (mountainous region to the east of the main normal fault), or hot water may be recharged from the west, indicating a possible connection to a deep aquifer within the Klamath Falls graben.

At shallow depths thermal waters spread laterally through permeable strata and mix with colder regional groundwater. Mixing also occurs along the faults. As the thermal water flows toward the southwest, temperatures are cooled to regional groundwater temperatures.

Additional deep drilling is needed to further characterize the source recharging the Klamath Falls geothermal system. Further work is still needed to identify and describe the actual fault systems in the area and determine the role of the various faults in the development and dynamics of the geothermal reservoir.

ACKNOWLEDGEMENTS

The authors are indebted to Kent Colahan of the City of Klamath Falls and to Gene Culver and Paul Lineau of the Oregon Institute of Technology for supplying crucial data needed for this report.

REFERENCES

Benson, S.M., and Lai, C.H., 1986. Analysis of interference data in a highly heterogeneous and naturally fractured geothermal reservoir. Formation Evaluation, June 1986, p. 236–248.

Janik, C.J., Truesdell, A.H., Sammel, E.A., and White, A.F., 1985. Chemistry of low-temperature geothermal waters at Klamath Falls, Oregon. Geoth. Resour. Counc. Trans., v. 9, p. 325–331.

Lund, J.W. (principal investigator), 1978. Geothermal hydrology and geochemistry of Klamath Falls: Oregon, urban area, Klamath Falls. Oregon Institute of Technology, Geo-Heat Utilization Center, Final report to the U.S. Geological Survey (Grant 14-08-0001-G-291), 123 p.

Moore, B.N., 1937. Nonmetallic mineral resources of eastern Oregon. U.S. Geol. Survey Bull. 875, 180 p.

Newcomb, R.C., 1958. Yonna Formation of the Klamath River Basin, Oregon. Northwest Sci., v. 32, no. 2, p. 41-48.

Nork, 1985. Hydrologic assessment of the geothermal aquifer, Klamath Falls, Oregon. Report prepared by W.E. Nork, Inc., for City of Klamath Falls, 73 p.

Nork, 1986. College Industrial Park Well No. 1 aquifer stress test results. Prepared by W.E. Nork, Inc., for Oregon Institute of Technology, 34 p.

Peterson, N.V., and McIntrye, J.R., 1970. The reconnaissance geology and mineral resources of eastern Klamath County and western Lake County, Oregon. Portland, Oregon, Department of Geology and Mineral Industries Bulletin 66, 70 p.

Sammel, E.A., 1980. Hydrogeologic appraisal of the Klamath Falls geothermal area, Oregon. U.S. Geol. Survey Profs. Paper 1044-G, 45 p.

Sammel, E.A., Truesdell, A.H., Janik, C.J., Gudmundsson, J.S., Benson, S.M., Solbau, R.D., and Lai, C.H., 1984. Analysis and interpretation of data obtained in tests of the geothermal aquifer at Klamath Falls, Oregon. U.S. Geol. Survey Water Resources Investigations Report 84-4216.

Sass, J.H., and Sammel, E.A., 1976. Heat flow data and their relation to observed geothermal phenomena near Klamath Falls, Oregon. J. Geophys. Res., v. 81, no. 26, p. 4863–4868.

Modeling Studies of Cold-Water Injection into Superheated Vapor Zones

K. Pruess, C. Calore, and R. Celati

Reinjection experiments in the strongly fluid depleted reservoir of Larderello have revealed the possibility of increasing production rates and overall heat extraction by injection into high-permeability low-pressure zones of the reservoir (Giovannoni et al., 1981; Cappetti et al., 1982; Bertrami et al., 1985). A large fraction (over 80%) of the injected water was recovered as steam in the most favorable area, and despite the short distance between injection and production wells (the minimum distance being about 150 m), no significant temperature change has been observed in the production wells, after 3 years of injection at rates ranging from 10 to 50 kg/s (Bertrami et al., 1985).

The physical processes involved in cold-water injection into a "superheated" fractured reservoir are not yet fully understood. Using the geothermal reservoir simulator MULKOM (Pruess, 1983), we have performed numerical experiments on simple one- and two-dimensional porous and fractured reservoir models to study heat extraction, vapor generation, the migration of injected water, and thermodynamic conditions in the boiling zone (Calore et al., 1986).

ONE-DIMENSIONAL MODELS

Cold-water injection into porous and fractured media was studied in linear and radial flow geometry. Formation parameters and conditions were chosen as representative of the strongly depleted zones of the Larderello field. Figure 1 shows a typical example of simulated temperature-and-saturation profiles after an extended injection period. In this example the reservoir is in single-phase (vapor) conditions at an original temperature of $T = 240°C$ for distances ≥ 85 m from the injection well. Closer to the well there is a very broad two-phase zone in which water saturation varies from 0 to 1. This zone is very nearly isothermal, with a temperature lower than the original reservoir temperature. Surrounding the injection well is a single-phase liquid plume in which temperatures decline gradually to the injection temperature (30°C). The temperature in the two-phase zone is lower than the original reservoir temperature because of heat transfer from the rock to the fluid, causing vaporization of part of the injected water. The rate of heat transfer is proportional to the temperature difference between fluid in the fractures and the adjacent rock. It is largest at the outer boundary of the two-phase zone.

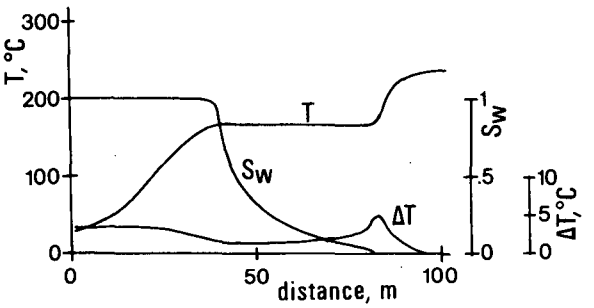

Figure 1. One-dimensional radial fractured porous-medium model (injection rate = 2.78 kg/s, $k = 5 \times 10^{-13}$ m^2). Curves show the variation with radial distance of temperature and liquid saturation in the fractures and the temperature difference between the outermost matrix elements and fractures. [XBL 861-128]

The rather diffuse phase and thermal fronts observed when injecting into a fractured medium arise from the finite-rate heat transfer between rocks and fluid. In an idealized porous-medium model local thermodynamic equilibrium between rock and fluid is instantaneous, giving rise to sharp fronts.

From an inspection of simulation results and the governing mass- and energy-balance equations, simple relationships were derived between the important problem parameters (permeability, injection rate, temperature of boiling front, fraction of injected liquid vaporized; see Calore et al., 1986).

TWO-DIMENSIONAL MODELS

The one-dimensional simulations give some interesting insight into fluid and heat flow processes near an injection well. However, for a realistic evaluation of field conditions it will be necessary to include gravity effects. To this end a two-dimensional axisymmetric flow system was investigated, as schematically depicted in Fig. 2. Injection was studied at different rates and for different values of formation permeabilities and porosities believed applicable for conditions at the Larderello field. In all cases it was observed that injection plumes move

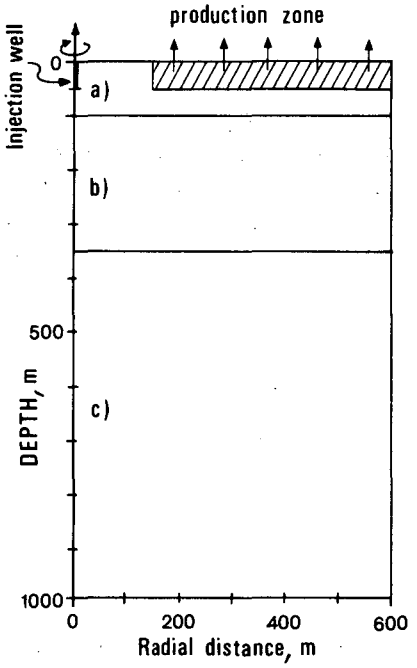

Figure 2. Two-dimensional radial porous-medium model. [XBL 861-130]

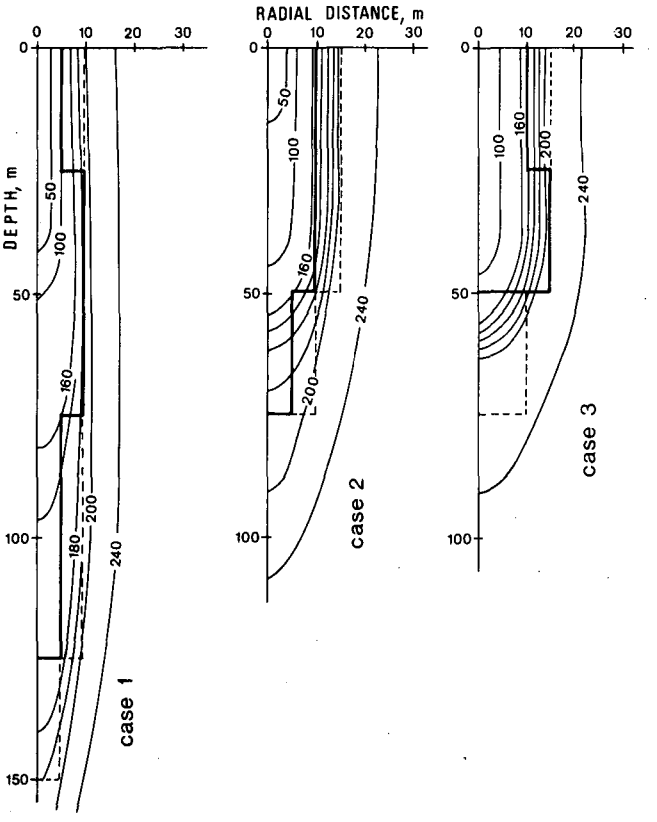

Figure 3. Two-dimensional radial isotropic porous-medium model. Shape of the injection plume and isotherms for different injection rates. In all three cases the liquid volume (including the liquid in the two-phase elements) is about 2800 m^3. Solid lines show limit of liquid-saturated region. Broken lines show limit of two-phase region. [XBL 861-135]

primarily downward rather than outward (Fig. 3). Most of the plume is in single-phase liquid conditions, with boiling restricted to the outer "skin" of the plume. A complex interplay of boiling and condensation processes, with liquid-vapor counterflow akin to a heat pipe (Pruess, 1985), tends to limit temperature variations over the surface of the plume and serves as an efficient mechanism for heat extraction from deeper regions.

CONCLUSIONS

Cold-water injection into depleted geothermal reservoirs gives rise to complex patterns of fluid and heat flow. The occurrence of thermal and phase fronts make these processes difficult to simulate numerically. With careful attention to space- and time-discretization errors, it is possible to obtain reliable results. Our studies indicate that a number of fluid-flow and heat-transfer processes combine to make cold-water injection into depleted vapor zones an efficient heat-extraction process.

ACKNOWLEDGEMENT

In addition to the Department of Energy funding, this work was supported by the Progetto Strategico Valorizzazione Materie Prime Minerali, CNR, Italy.

REFERENCES

Bertrami, R., Calore, C., Cappetti, G., Celati, R., D'Amore, F., 1985. A three year recharge test by reinjection in the general area of Larderello field: Analysis of production data. *In* Proceedings, 1985 International Symposium on Geothermal Energy, Kailua-Kona, Hawaii, August 26–30, 1985, v. 9, pt. 2, p. 293–298.

Calore, C., Pruess, K., and Celati, R., 1986. Modeling studies of cold water injection into fluid-depleted, vapor-dominated geothermal reservoirs. Lawrence Berkeley Laboratory Report LBL-21252.

Cappetti, G., Giovannoni, A., Ruffilli, C., Calore, C., Celati, R., 1982. Reinjection in the Larderello geothermal field. *In* Proceedings, International Conference on Geothermal Energy, Firenze, Italy. BHRA Fluid Engineering, Cranfield, Bedford (England), p. 395–408.

Giovannoni, A., Allegrini, R., Cappetti, G., Celati, R., 1981. First results of a reinjection experiment at Larderello. *In* Proceedings, Seventh Workshop, Geothermal Reservoir Engineering, Stanford, California, December 15–17, 1981. Stanford Geothermal Program Report SGP-TR-55, p. 77–84.

Pruess, K., 1983. Development of the general purpose simulator MULKOM. *In* Earth Sciences Division Annual Report 1982. Lawrence Berkeley Laboratory Report LBL-15500, p. 133–134.

Pruess, K., 1985. A quantitative model of vapor-dominated geothermal reservoirs as heat pipes in fractured porous rock. Geoth. Resour. Counc. Trans., v. 9, pt. II, p. 353–361.

On the Interpretation of Vapor Fractions and Their Temporal Variation in the Larderello Geothermal Field

K. Pruess and F. D'Amore

From the viewpoint of reserve estimation and reservoir engineering analysis, one of the most important parameters of a vapor-dominated reservoir is in-place vapor saturation. Unfortunately, there is no direct method available by which this parameter could be measured in the field. The pioneering work of Giggenbach (1980) and D'Amore and Celati (1983) has for the first time opened up a possibility of inferring in-place phase composition of produced geofluids on the basis of the concentrations of noncondensible gases in well discharges. Giggenbach assumed that certain chemical species (e.g., water, methane, carbon dioxide, and hydrogen) are in chemical equilibrium in the gas phase in a geothermal reservoir, so that their concentrations obey the law of mass action. Depending upon their solubilities, these species then would be present in different concentrations in the liquid phase. Provided that equilibrium constants and solubilities are known, it is then possible to use the total concentration of the various species in the sample to back calculate the mass fraction y of a sample of geofluid that originated as gas phase in the reservoir.

APPLICABILITY OF APPROXIMATION

A number of assumptions and approximations are implicit in accepting a vapor fraction y computed from the methods of Giggenbach and D'Amore and Celati as representative of the phase composition of the source fluid. The most important conditions are these:

1. The discharge sample should be obtained from a single fluid source that consists of a two-phase mixture of liquid and vapor.

2. The fluid source should be in thermodynamic and chemical equilibrium.

3. The chemical reactions considered should be in equilibrium in the gas phase.

4. A "small" two-phase sample of discharge fluid should be taken such that there is negligible change in chemical or phase composition in the source.

5. The sample should be transferred to the wellhead without any mass gain or loss.

6. There should be no re-equilibration of species during transport from the source to the wellhead (i.e., the species mole fractions $x_{d,i}$ present in a parcel of fluid maintain their values from the original source).

In actual field applications the conditions stated above will usually be violated to some extent. The source of the fluid is a large volume of porous rock in which substantial spatial variations in temperature, pressure, vapor saturation, and chemical composition of fluids may be present. Fluids sampled at the wellhead represent a spatial and temporal average over different source conditions, which vary continuously throughout the drainage volume of the well. The two requirements that reservoir fluids be in chemical equilibrium locally but not re-equilibrate as they flow toward the well will in general not be compatible. If reaction kinetics are "slow," then these requirements may be compatible as long as the natural state of the reservoir, and the chemical compositions of fluids in that state, are not significantly disturbed by exploitation. However, as fluids are being produced, the chemical composition of liquid and vapor phases in situ will change because of production-induced boiling and quite likely also

from release of gaseous species from minerals. If reaction kinetics were fast enough to permit re-equilibration of gaseous species in situ, then one should also expect at least partial re-equilibration to occur along the flow path toward the well. If reaction kinetics were really "fast," then all gas reactions would be in local equilibrium everywhere, and one would obtain $y = 1$ for Larderello wells, because in the vicinity of well feeds single-phase vapor conditions prevail in the reservoir. That the observed y values at Larderello are considerably smaller than 1 (typically $y = 0.3$) clearly shows that gaseous species re-equilibrate only partially, or not at all, in the single-phase vapor regions. This suggests that kinetics are "slow" and that re-equilibration in response to exploitation-induced chemical composition changes should also be expected to be partial at most. Conditions may be closer to equilibrium in reservoir regions where fluid-flow velocities and phase-change rates are smaller, i.e., at larger distances from wells.

A more detailed analysis shows that under the most favorable conditions, vapor fraction y can provide an estimate of flowing steam quality. Conclusions regarding in-place vapor saturation can only be made if relative permeabilities are known. In practical cases, however, additional uncertainties arise from rock-fluid interactions and finite-rate kinetics. Therefore, we consider it more appropriate to interpret observed vapor fractions as a qualitative indicator of reservoir conditions and changes rather than as a quantitative measure.

VAPOR FRACTION TRENDS IN LARDERELLO

Following D'Amore et al. (1982), vapor fractions y were calculated for a number of Larderello wells on the basis of the concentrations of H_2S, H_2, CH_4, and CO_2. As an example, Fig. 1 shows temporal trends of discharges for well FAB over a 40-year period. Comparison of data from several wells reveals the following trends:

1. Flow initially decreases rather rapidly during the early years of production and then stabilizes at values between 5 and 70 t/h, showing a very slow decrease from then on.
2. Although the HCl content varies greatly from one well to another, depending on the position of the well within the field, it tends to increase strongly whenever the flow rate starts to stabilize.
3. The gas/steam ratios tend to increase to a maximum value that is usually quite close to the point at which the flow rates stop decreasing, and then they stabilize. During the final stage, coinciding with the maximum observed HCl values, the gas/steam ratio tends to decrease.
4. H_3BO_3 generally decreases until it levels out at the same time as the flow rates begin to stabilize.
5. The calculated y values usually increase until flow rate stabilizes and the gas/steam ratio reaches its maximum. In many cases they tend to decrease with an increase in HCl or a decrease in the gas/steam ratio.

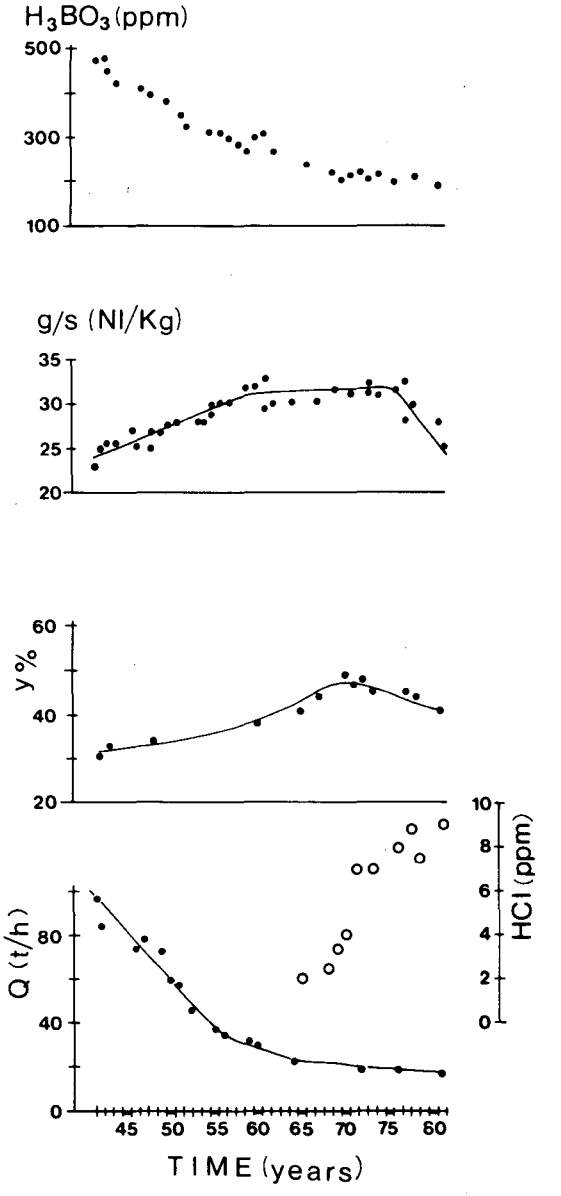

Figure 1. Temporal evolution for well FAB of flow rate Q in t/h, together with HCl in ppm, vapor fraction y, gas/steam ratio in Nl/kg (liters of gas at standard conditions per kg of steam), and H_3BO_3 in ppm. [XBL 854-2209]

6. Wellhead temperature generally increases rapidly from less than 200°C to stabilize eventually around 230–260°C. This temperature increase usually coincides with the maximum decrease in flow rate. At times the temperatures also tend to decrease during the last stages of production, when the HCl contents are highest. These temporal trends can be explained by the "multiple-source" model of D'Amore and Truesdell (1979). According to this model, early discharges have large contributions from a condensate layer at the top of the reservoir. At intermediate times, most of the fluids originate from the main vapor-dominated reservoir, whereas at late times there are increasing contributions from a deep layer of brine. The observed trends in vapor fraction y are consistent with a model in which the early and late production originates from regions with larger liquid saturation. Our quantitative analysis indicates, however, that observed vapor fractions in Larderello are significantly affected (enhanced) by release of CO_2 from minerals and/or partial re-equilibration of gaseous species in single-phase vapor regions.

ACKNOWLEDGEMENT

One of us (K.P.) would like to acknowledge the hospitality and support extended by the Istituto Internazionale per Le Ricerche Geotermiche, Pisa, Italy, without which this work would not have been possible.

REFERENCES

D'Amore, F., and Celati, R., 1983. Methodology for calculating steam quality in geothermal reservoirs. Geothermics, v. 12, no. 2/3, p. 129–149.

D'Amore, F., and Truesdell, A.H., 1979. Models for steam chemistry at Larderello and The Geysers. *In* Proceedings, Fifth Workshop, Geothermal Reservoir Engineering, Stanford, California, December 12–14, 1979. Stanford Geothermal Program Report SGP-TR-40, p. 283–297.

D'Amore, F., Celati, R., and Calore, C., 1982. Fluid geochemistry applications in reservoir engineering (vapor-dominated systems). *In* Proceedings, Eighth Workshop, Geothermal Reservoir Engineering, Stanford, California, December 14–16, 1982. Stanford Geothermal Program Report SGP-TR-60, p. 295–308.

Giggenbach, W.F., 1980. Geothermal gas equilibria. Geochim. Cosmochim. Acta, v. 44, p. 2021–2032.

Thermohydrologic Conditions and Silica Redistribution Near High-Level Nuclear Wastes Emplaced in Saturated Geologic Formations

K. Pruess and A. Verma

Evaluation of the thermohydrologic conditions near high-level nuclear waste packages is needed for the design of the waste canister and for overall repository design and performance assessment. Most available studies in this area have assumed that the hydrologic properties of the host rock are not changed in response to the thermal, mechanical, or chemical effects of waste emplacement. However, the ramifications of this simplifying assumption have not been substantiated. In fact, numerous processes have been identified that couple thermal, hydrologic, chemical, and mechanical effects (Panel Report, 1984).

We have studied dissolution and precipitation of silica in thermally driven flow systems. In the context of nuclear waste isolation, it is not the redistribution of silica itself that is of concern but its potential impact on the transport of heat, fluid, and chemical constituents. Dramatic effects of silica redistribution on rock porosity and permeability have been observed in laboratory experiments (Morrow et al., 1981; Moore et al., 1981; Keith et al., 1983; Vaughan, 1985).

In our study we have considered a room-scale problem (which was previously considered, without including silica redistribution effects, by Pruess and Bodvarsson, 1982) and a repository-scale problem. Using numerical simulation, we have compared predictions of thermohydrologic conditions with and without inclusion of silica redistribution effects.

MODELING APPROACH

The simulations performed in this study were carried out with the numerical code MULKOM (Pruess, 1983). The version of MULKOM used here accounts for water in liquid and vapor form and for both dissolved and solid silica, the latter being represented as quartz polymorph. All phases and the rock formations are assumed to be in local thermal equilibrium. The code has the capability to handle finite rates of quartz dissolution and precipitation (i.e., kinetics), but in the present work we have assumed that dissolved silica concentrations correspond to equilibrium quartz solubilities, as given by Fournier and Potter (1982). A local equilibrium model was chosen because it will provide a conservative (upper) limit on material dissolved or precipitated and because several of the parameters controlling kinetic rates are not known for the conditions near high-level waste repositories.

The porosity changes caused by silica redistribution can be easily related to dissolved mass, but the associated permeability change is a much more complex problem. A review of the literature on porosity-permeability relationships showed that a considerable variety of parametrizations have been used by various workers. It appears that the specific form of porosity-permeability relationship applicable to a given permeable medium is a material property depending upon pore-size distribution and the correlation between pores of different size and shape. In addition we suggest that permeability change is not a unique function of porosity change but in fact depends on the mechanism by which porosity change is brought about. For example, application of mechanical stress will affect the large pores more strongly than the smaller ones, whereas numerical precipitation will cause reductions in pore volume that depend less on the pore size. Because the permeability of a porous medium is controlled primarily by the smaller pores, a given decrease in porosity will therefore cause a larger permeability change when it is brought about by mineral precipitation than by application of mechanical stress.

Much of the work on porosity and permeability change has been based on models of permeable media in which all flow channels (tubes or fractures) have uniform cross section (Fig. 1a and b; Keith et al., 1983; Braithwaite and Nimick, 1984; Vaughan, 1985; Lichtner, 1985). These models neglect what we consider an essential feature of "real" permeable media, namely, that the cross section of a flow channel will in general be highly variable along the channel axis. In this work we have considered "series models" of permeable media (see Fig. 1c,d), which

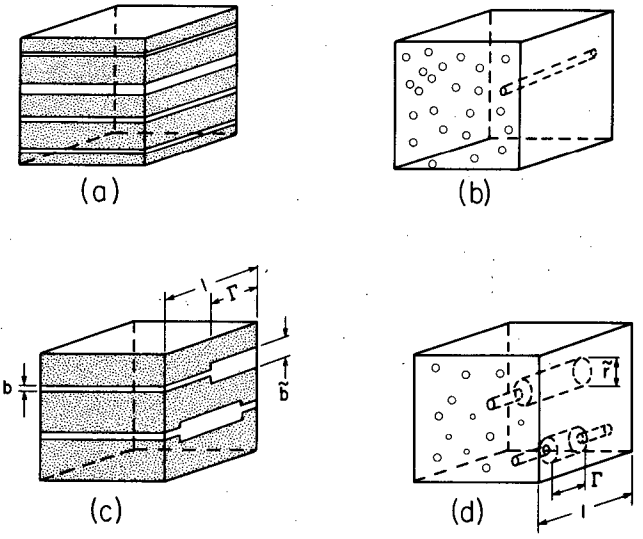

Figure 1. Idealized models of permeable media. **(a)** and **(b)** straight capillaric models. **(c)** and **(d)** "Series" models. [XBL 859-10773]

can represent constrictions in flow channels. Such models predict a very strong dependence of permeability on porosity (Fig. 2) and can explain the very strong permeability changes observed in some laboratory experiments for rather modest porosity reductions (Vaughan, 1985).

RESULTS

We have studied thermohydrologic conditions and silica redistribution effects for a room-scale model and a regional-scale model, both in a

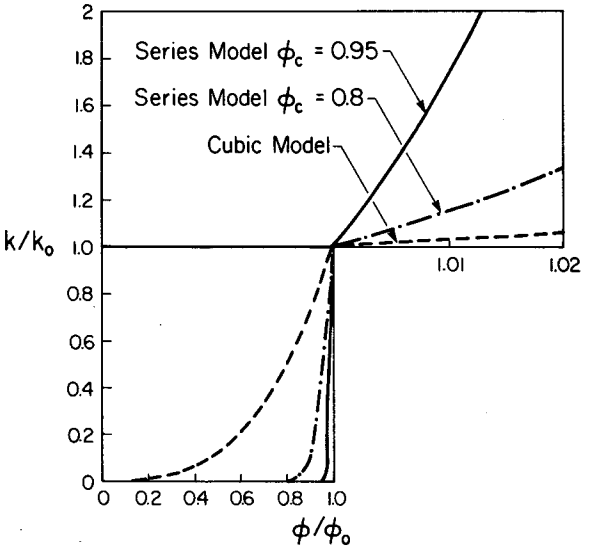

Figure 2. Porosity-permeability relationships for three models considered in this study. [XBL 859-10761]

saturated medium with properties representative of the BWIP site. The room-scale model is the same as the one previously studied, without allowance for silica redistribution, by Pruess and Bodvarsson (1982).

Figure 3 shows a sketch of the simplified geometry modeled in the room-scale problem. Detailed specifications for this, as well as for the regional-scale problem, are given in a report by Verma and Pruess (1986). As an example of results obtained, Fig. 4 shows the time dependence of fluid flow into the canister hole (normalized per canister). It is seen that silica redistribution effects enhance maximum fluid-flow rates by up to 20% in comparison to the reference case. This occurs from leaching of quartz as formation waters flow toward the canister hole in the direction of the temperature gradient. The increased flow causes some additional cooling, reducing rock temperatures by a small amount ($\leq$ 10°C). The effects of silica redistribution on thermohydrologic conditions are even smaller for the regional-scale problem, where temperature gradients are smaller.

CONCLUSIONS

Our modeling studies, although somewhat schematic in nature, indicate that silica redistribution effects near high-level wastes emplaced in saturated formations are small. Thermohydrologic conditions can be adequately predicted without taking such effects into account. However, conditions may be quite different in partially saturated media, where persistent heat-pipe conditions could conceivably cause large effects (Pruess and Wang, 1984).

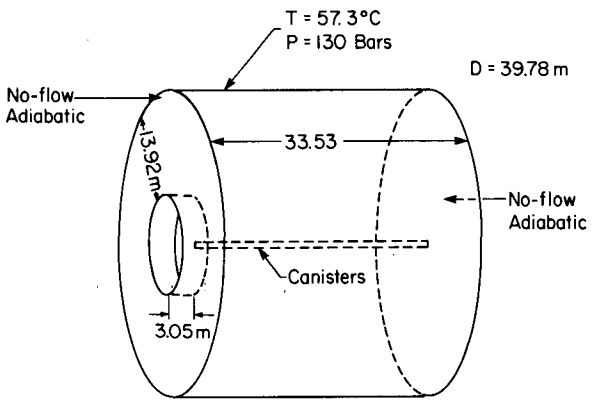

Figure 3. Axisymmetric representation of the room-scale problem. [XBL 859-10771]

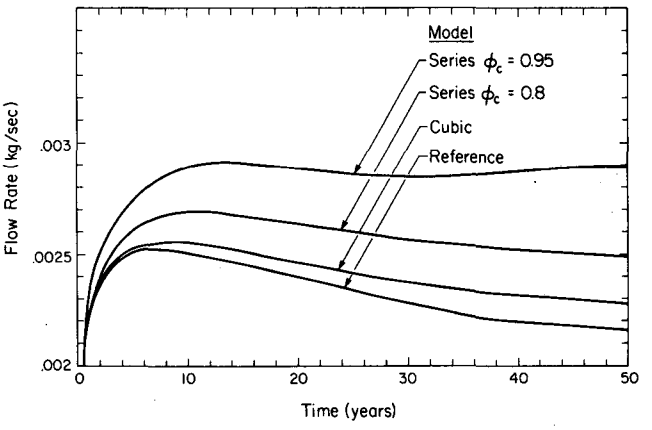

Figure 4. History of fluid-flow rates into the canister holes and storage room for room-scale problem. [XBL 859-10765]

REFERENCES

Braithwaite, J.W., and Nimick, F.B., 1984. Effect of host-rock dissolution and precipitation on permeability in a nuclear waste repository in tuff. Sandia National Laboratories Report SAND84-0192.

Fournier, R.O., and Potter, R.W., 1982. An equation correlating the solubility of quartz in water from 25°C to 900°C at pressures up to 10,000 bars. Geochim. Cosmochim. Acta, v. 56, p. 1969–1973.

Keith, L.A., Delaney, P.T., and Moore, D.E., 1983. Permeability reduction due to precipitation of quartz under nonisothermal conditions. *In* Proceedings, Ninth Workshop, Geothermal Reservoir Engineering, Stanford, California, December 13–15, 1983. Stanford Geothermal Program Report SGP-TR-74, p. 239–246.

Lichtner, P.C., 1985. Continuum model for simultaneous chemical reactions and mass transport in hydrothermal systems. Geochim. Cosmochim. Acta, v. 49, no. 3, p. 779–800.

Moore, D.E., Morrow, C.A., and Byerlee, J.D., 1981. SiO_2 precipitation accompanying fluid flow through granite held in a temperature gradient. *In* Proceedings, Seventh Workshop, Geothermal Reservoir Engineering, Stanford, California, December 15–17, 1981. Stanford Geothermal Program Report SGP-TR-55, p. 127–132.

Morrow, C., Lockner, D., Moore, D., and Byerlee, J., 1981. Permeability of granite in a temperature gradient. J. Geophys. Res., v. 86, no. 84, p. 3002–3008.

Panel Report, 1984. Panel report on coupled thermo-mechanical-hydro-chemical processes associated with a nuclear waste repository. Lawrence Berkeley Laboratory Report LBL-18250.

Pruess, K., 1983. Development of the general purpose simulator MULKOM. *In* Earth Sciences Division Annual Report, 1982. Lawrence Berkeley Laboratory Report LBL-15500, p. 133–134.

Pruess, K., and Bodvarsson, G.S., 1982. Hydrothermal conditions and resaturation times in underground openings for a nuclear waste repository in the Umtanum flow at the Basalt Waste Isolation Project. Lawrence Berkeley Laboratory Report LBL-18451.

Pruess, K., and Wang, J.S.Y., 1984. TOUGH—A numerical model for nonisothermal unsaturated flow to study waste canister heating effects. *In* G.L. McVay (ed.), Scientific Basis for Nuclear Waste Management, Materials Research Society Symposia Proceedings (Vol. 26). Elsevier, New York, p. 1031–1038.

Vaughan, P.J., 1985. Analysis of permeability reduction during flow of heated, aqueous fluid though westerly granite. *In* C.F. Tsang (ed.), Coupled Processes Associated with Nuclear Waste Repositories. Academic Press, Orlando, Florida, p. 529–539.

Verma, A., and Pruess, K., 1986. Thermohydrological conditions and silica redistribution near high-level nuclear wastes emplaced in saturated geological formations. Lawrence Berkeley Laboratory Report LBL-21613 (submitted to J. Geophys. Res).

Description of a High-Temperature Downhole Fluid Sampler

R.D. Solbau, O. Weres, L. Hansen, and B. Dudak

Downhole fluid samplers have been used for years with limited success in high-temperature geothermal wells. This article discusses the development and operating principles of a high-temperature downhole fluid sampler, reliable at obtaining unflashed samples at temperatures of up to 350°C. The sampler was used successfully for recovering a brine sample from a depth of 10,200 ft in the Salton Sea Scientific Drilling Project well.

Under a contract sponsored by the Gas Research Institute (GRI), engineers and researchers at the Lawrence Berkeley Laboratory designed and fabricated a downhole fluid sampler (Fig. 1). The sampler was originally intended to operate in geopressured gas wells, where corrosive fluids may be encountered. The sampler is constructed of MP35N alloy, which is chemically inert to wellbore fluid. It was initially designed for a maximum operating temperature of 230°C and pressures of up to 20,000 psi (Michel et al., 1982; Weres et al., 1984a). Recent modifications have extended the temperature rating to 350°C (Table 1 lists the specifications for the upgraded sampler).

OPERATING PRINCIPLE

The sampler's many parts (Fig. 2) give it the appearance of being very complex, but in reality the electrical and mechanical functions of the sampler mechanism are straightforward and very reliable. The sampler is of the flow-through type; that is, while the instrument is lowered down the wellbore, the upper and lower valves are in the open position (Fig. 1). When the valves are open, brine is free to enter at the bottom end and exit at the top of the sample chamber. By comparison, conventional samplers are typically lowered into the well with the sample chamber closed. At the desired sampling depth, a port is opened, causing the wellbore fluid to rush into the chamber. The flow-through sampler has several advantages in that (1) the sample is not altered due to decompression (possible boiling) as it enters the sample chamber; (2) precipitation of carbonate and sulfide minerals, due to boiling, does not occur; (3) gases do not come out of solution and escape or concentrate during the sampling procedure; (4) the sample will not be contaminated by mixing

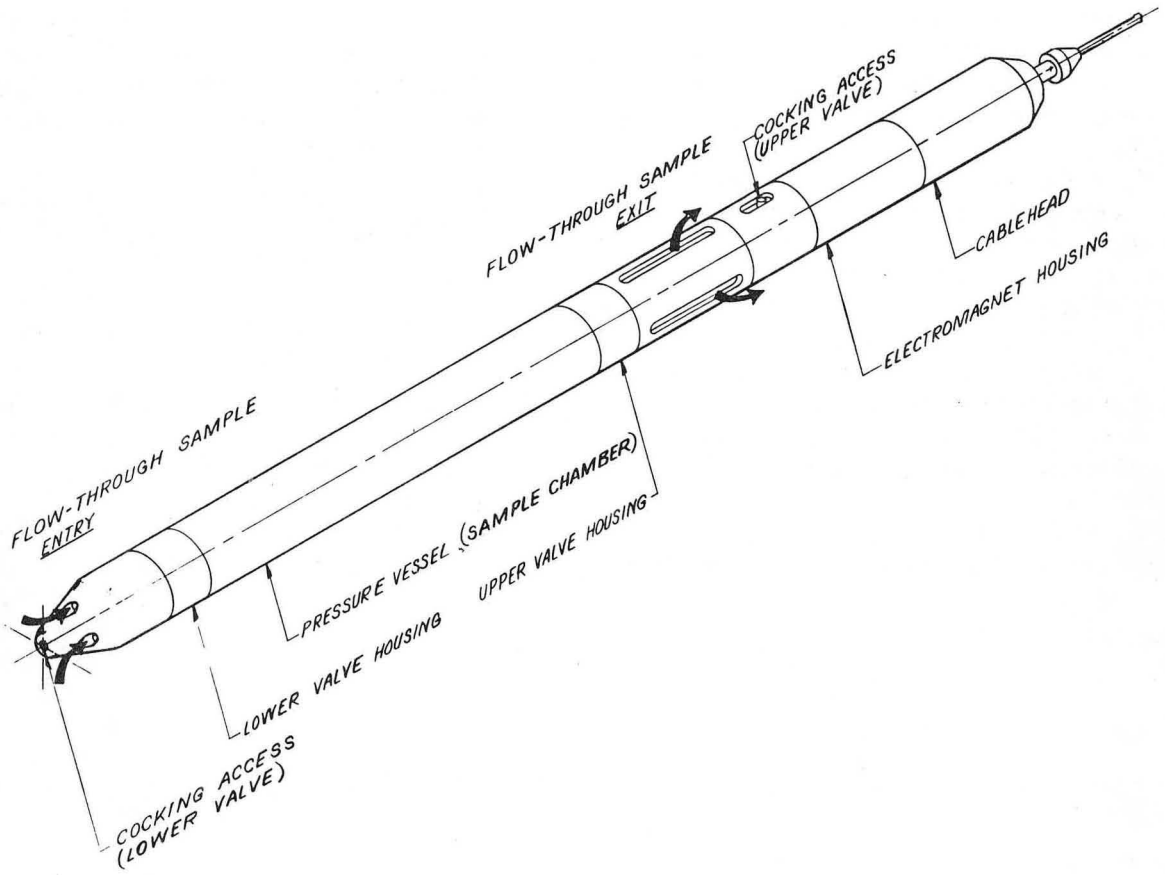

Figure 1. The sampler with its major components and the fluid flow path during sampling. [XBL 869-3547]

with air inside the sample chamber; (5) valves need be closed only during sampling.

The unique mechanism for holding the sampler valves open until closure is required consists of two primary components: an electromagnet assembly and a lock-ball arrangement. When the magnet is energized, the lock-balls hold the valves open. After the current is removed from the magnet, the lock-balls disengage and the valves close.

Table 1. Sampler specifications.

Sampler type:	Downhole flow-through
Length:	120 in (incl. cablehead)
Diameter:	2.25 in
Weight:	112 lb
Sample volume:	1000 ml
Material:	MP35N alloy (all parts in contact with well fluid)
Sampler pressure: (internal)	20,000 psi (pending hydrostatic proof test at 350°C)
Temperature limit:	350°C
Power requirement:	40 ma dc

HIGH-TEMPERATURE MODIFICATIONS

The maximum operating temperature of the sampler is dictated by its nonmetallic parts: the seals on the pressure chamber, the insulation and housing of the magnet coil, the insulating oil that protects mechanical and electrical components, and the grease used as an antiseize compound on mating sampler parts. To ensure that the sampler will operate reliably at 350°C, which is well above its design temperature of 230°C, the following modifications were made. First, the original epoxy-impregnated magnet coil was replaced. The new coil is fabricated from ceramic and wound with Kapton-insulated magnet wire. Second, since the magnet loses much of its holding power as temperature increases, the strength of the armature spring was reduced. This helps eliminate premature valve closure during a sampling run. Experience has shown

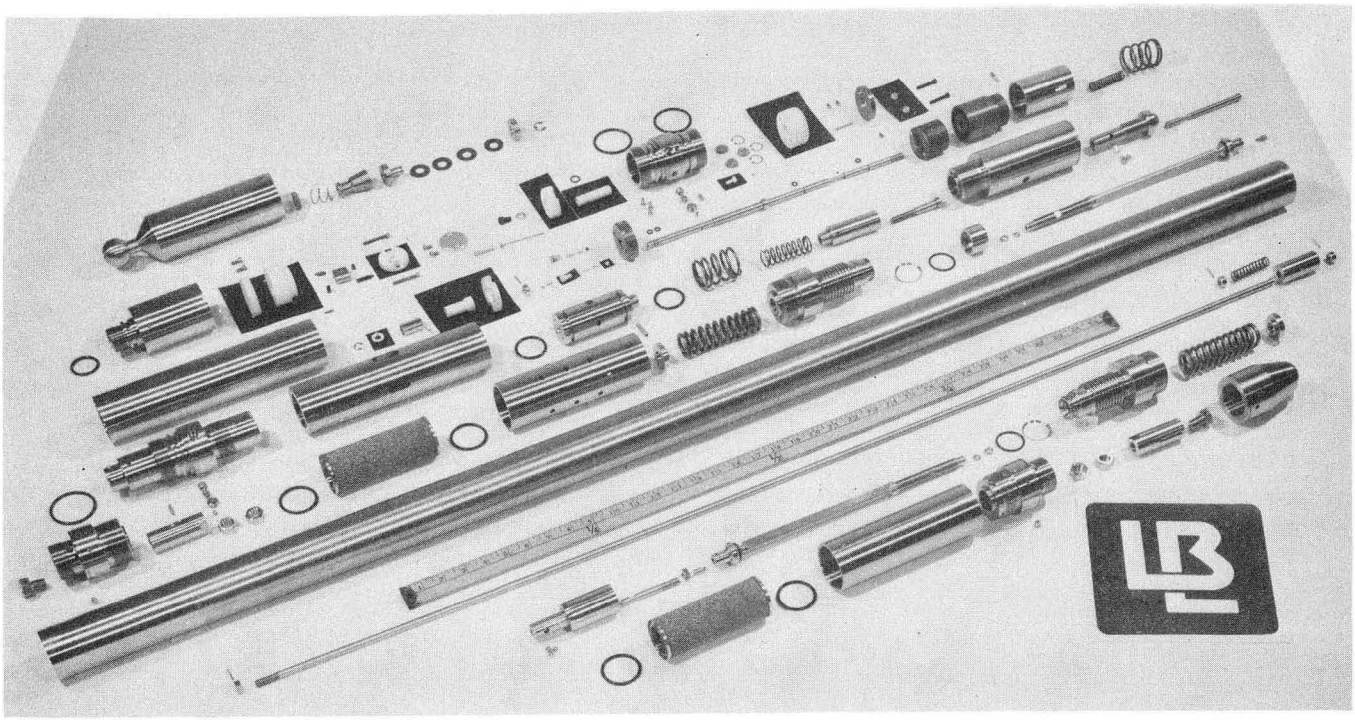

Figure 2. The disassembled sampler. [CBB 812-1494]

that Viton seals perform adequately if the duration of a sampling run is kept at two hours or less. If, however, the sampler is to be exposed to high temperatures for longer times, some other type of seal will be required.

OPERATING PROCEDURE

A specially designed cablehead is used to attach the fully assembled sampler to a high-temperature single-conductor logging cable. The interior of the magnet housing and the cablehead assembly are filled with a high-temperature insulating oil to protect the delicate mechanical and electrical components from the adverse effect of wellbore fluid. Even though these parts are in pressure equilibrium with the wellbore fluid during a sampling run, the high density of the injected oil prevents the wellbore fluid from entering near the top of the cablehead. This technique also eliminates the need for differential pressure seals, except as required for sealing the sample chamber.

Before lowering the sampler into a well, the upper and lower sampler valves are opened with the help of cocking tools and held in that position by supplying the required current through the conductor of the logging cable. The sampler is then lowered into the wellbore. After the appropriate sampling depth is reached, the sampler is "parked" there for several minutes. This ensures that the upward flow of the producing well flushes the inside of the sample chamber with brine from the sampling depth.

The sampler valves are closed by decreasing the current supply to the electromagnet. A sudden drop in the current readout at the surface indicates that the valves have closed. Since the movement of the valves from their open to their closed position is very slight, there are no adverse effects on the fluid trapped inside the sample chamber. As the sampler is brought up the well, the valves seat even better than during the initial closure, since they were designed to take advantage of the increasing pressure differential between the sample chamber and the wellbore fluid.

After retrieval of the sampler from the well, piercing valves are attached to rupture disks located in the sampler's valve bodies. A custom-designed sample-extraction system (Weres et al., 1984b) may be used to remove the brine and gas from the sampler without exposing them to air.

SUMMARY

A flow-through downhole fluid sampler capable of collecting samples at temperatures of up to 350°C has been developed at Lawrence Berkeley Laboratory

under the joint sponsorship of the Gas Research Institute and the U.S. Department of Energy. The capability of the sampler to operate under the harsh downhole conditions typical of the geothermal systems in the Imperial Valley, California, was demonstrated when the sampler was used successfully to collect a sample of brine from the bottom of the Salton Sea Scientific Drilling Project well.

The reliability of the sampler results from the simplicity of the operating concept. The need for sophisticated downhole electronics is eliminated by relying primarily on a mechanical mechanism for closing the valves of the sample chamber. The electromagnet, which is used to keep the valves open while the sampler is lowered into the borehole, need only be de-energized to initiate valve closure. The 40-mA current required to maintain a magnetic field sufficient to keep the valves open can be supplied from the surface through an electric cable or with a dewared downhole battery pack.

REFERENCES

Michel, M. (ed.), Dudak, B., Galbraith, R., Hansen, L., Sverjensky, D., and Weres, O., 1982. Fluid sampling and chemical modeling of geopressured brines containing methane: Final report (March 1980 to February 1981). Lawrence Berkeley Laboratory Report LBL-12832 (GRI-76/0018).

Weres, O., Michel, M., and Harnden, W., 1984a. Downhole sampling of geopressured wells: Final report for 1982–1984. Lawrence Berkeley Laboratory Report LBL-16518 (GRI-83/0028).

Weres, O., Harnden, W., Biocca, A., and Solbau, R., 1984b. Operating instructions for the LBL/GRI downhole sampler and sample extraction system. Lawrence Berkeley Laboratory Report LBL-18102.

Laboratory Permeability Errors from Annular Wall Flow

T.K. Tokunaga

In laboratory measurements of the saturated hydraulic conductivity, K_s, it is generally assumed that fluid flow occurs exclusively within the sample core. Fluid flow within the annulus bounded by the lateral surface of the core sample and the inner surface of the permeameter tube is generally assumed to be insignificant. In measurements of low-permeability materials and media subject to bulk volume changes, permeameter fluid flow within gaps between sample walls and permeameter walls can become substantial, leading to erroneously large estimates of K_s. This effect was noted in a work by McNeal and Reeve (1964), which presents a method for separating central-core flow from wall effects. Significantly larger flux densities due to wall effects were measured in that study. The wall-flow errors given here are estimates based on the simplifying assumption that the flow occurs within a smooth annular gap. Annular-flow errors are expressed in terms of a ratio of gap flow to core flow.

LAMINAR FLOW WITHIN AN ANNULUS

Flow between a core sample and the permeameter wall will be described by annular flow along the z direction between two concentric cylinders of length L as shown in Fig. 1. Although it is recognized that this configuration is not likely in actual laboratory permeameters, it is quite likely that gaps spanning varying fractions of the full annular region often occur. The inner cylinder wall of radius R_1 corresponds to the lateral surface of the core. The outer cylinder wall of radius R_2 corresponds to the inner surface of the permeameter tube. The ratio (R_1/R_2) is designated C. The gap width δ is equal to $R_2 - R_1$. The surface at R_1 is idealized as a constant-velocity boundary, with the fluid velocity $v_z(R_1)$ matched to the Darcy velocity within the core. The surface at R_2 is treated as a no-slip boundary. End effects at $z = 0$ and $z = L$ are assumed to have negligible influences on the annulus-velocity profile. The driving force for flow through the annulus is the hydraulic-head gradient, ∇H.

The solution to steady laminar flow in this system is obtainable through a shell momentum balance in a manner closely following a nearly identical problem described by Bird et al. (1960). The only difference between these problems is in the treatment of the boundary at R_1, where Bird and co-workers set

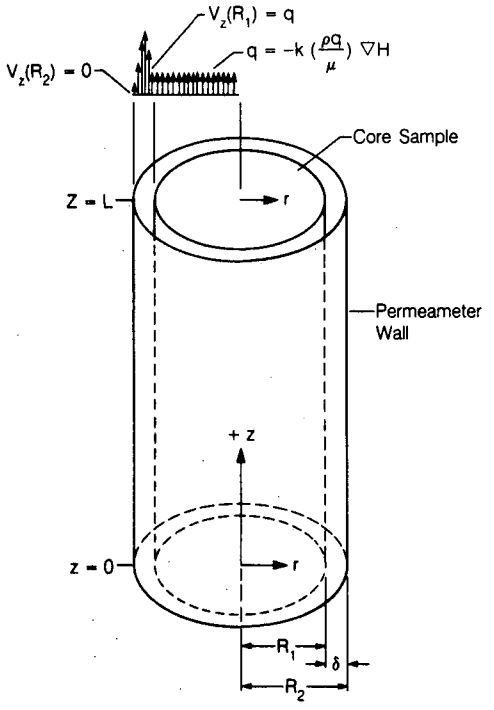

Figure 1. Permeameter and core with an annular gap. [XBL 8611-12737]

$v(R_1) = 0$. In cylindrical coordinates, the differential equation to be solved is

$$\frac{d}{dr}\left(r\mu\frac{dv_z}{dr}\right) = \rho g r\frac{dH}{dz}, \tag{1}$$

where μ is the fluid viscosity, ρ is the fluid density, g is the acceleration of gravity, and H is the hydraulic head. The boundary conditions are

$$v_z(R_1) = -k\frac{\rho g}{\mu}\frac{dH}{dz}, \tag{2a}$$

$$v_z(R_2) = 0, \tag{2b}$$

where k is the permeability of the core. In the following developments, it will be more convenient to express core flow in terms of k rather than the saturated hydraulic conductivity, $K_s = k\rho g/\mu$, since use of the former parameter permits cancellation of fluid properties. The solution to Eq. (1), subject to Eqs. (2a) and (2b), is

$$v_z(r) = -\frac{\rho g R_2^2}{4\mu}\left[1 - \left(\frac{r}{R_2}\right)^2 + \left(\frac{1 - C^2 - (4k/R_2^2)}{\ln(1/C)}\right)\ln\frac{r}{R_2}\right]\frac{dH}{dz}. \tag{3}$$

The volumetric flow rate through the annulus, Q_{gap}, is obtained upon integrating Eq. (3) over the annular cross-sectional area,

$$Q_{gap} = 2\pi\int_{R_1}^{R_2} r v_z(r)\, dr, \tag{4a}$$

resulting in

$$Q_{gap} = -\frac{\rho g \pi R_2^4}{8\mu}\left[1 - C^4 - \frac{(1 - C^2)^2}{\ln(1/C)} - \frac{4k}{R_2^2}\left(2C^2 + \frac{(C^2 - 1)}{\ln(1/C)}\right)\right]\frac{dH}{dz}. \tag{4b}$$

In the limit of $k \to 0$, Eq. (3) and (4b) become equivalent to results presented in Bird et al. (1960), as expected.

THE RELATIVE FLUX THROUGH THE ANNULUS VERSUS THE CORE

The volumetric flow through a sample of permeability k is given by Darcy's law,

$$Q_{core} = -\pi R_1^2\frac{\rho g}{\mu}k\frac{dH}{dz}. \tag{5}$$

The quantity of interest is the ratio of flow through the annular space versus the flow through the sample core. Dividing Eq. (4b) by Eq. (5) gives

$$\frac{Q_{gap}}{Q_{core}} = \frac{R_2^2}{8kC^2}\left[1 - C^4 - \frac{(1 - C^2)^2}{\ln(1/C)} + \frac{4k}{R_2^2}\left(\frac{1 - C^2}{\ln(1/C)} - 2C^2\right)\right]. \tag{6a}$$

The dependence of the gap/core flux ratio on the various system parameters is difficult to discern from Eq. (6a) because of its complexity. Even the apparently simple numerical evaluation of Eq. (6a) is susceptible to error as a result of the behavior of $1 - C^n$ and $ln(1/C)$ in the range of interest where $C \rightarrow 1$.

A clearer picture of the nature of the flux ratio can be obtained through the use of a small parameter ϵ defined by $\epsilon = (1 - C)$. From the definition of C and the gap width δ, one can see that ϵ is also equal to the ratio δ/R_2. Substituting ϵ into Eq. (6a) and expanding $\ln(1 - \epsilon)$ to at least four terms gives

$$\frac{Q_{gap}}{Q_{core}} = \frac{R_2^2}{k}\left[\frac{\frac{1}{6}\epsilon^4 + \frac{k}{R_2^2}\left(\epsilon^2 - \frac{1}{3}\epsilon^3 - \frac{1}{12}\epsilon^4\right)}{\epsilon - \frac{3}{2}\epsilon^2 + \frac{1}{3}\epsilon^3 + \frac{1}{12}\epsilon^4}\right] \tag{6b}$$

when terms higher than ϵ^4 are discarded. It is of passing interest to mention that without retaining at least four terms in the expansion of $\ln(1 - \epsilon)$, all terms in the numerator of Eq. (6b) cancel. Since ϵ is a small parameter, Eq. (6b) can be simplified to

$$\frac{Q_{gap}}{Q_{core}} \approx \frac{R_2^2}{k}\left(\frac{1}{6}\epsilon^3 + \frac{k\epsilon}{R_2^2}\right), \tag{6c}$$

which in terms of the gap width δ is

$$\frac{Q_{gap}}{Q_{core}} \approx \frac{\delta^3}{6R_2k} + \frac{\delta}{R_2}. \tag{6d}$$

COMPARISON WITH A PARALLEL-PLATE MODEL

Due to the complexity of Eqs. (4b), (6a), and (6b), it is of interest to consider a similar, though much simpler problem, for comparison with Eq. (6d). The simpler model to be considered here is that of steady laminar flow between two parallel plates, with one plate surface velocity matched to a Darcy velocity. The system is depicted in Fig. 2. Flow occurs in response to a hydraulic head gradient along the z direction in a gap of width δ and transverse length W. Fluid at the surface defined by $x = 0$ is maintained at a constant velocity equated to a Darcy velocity. Fluid at the opposite wall at $x = \delta$ obeys the no-slip condition. The velocity profile in this case is

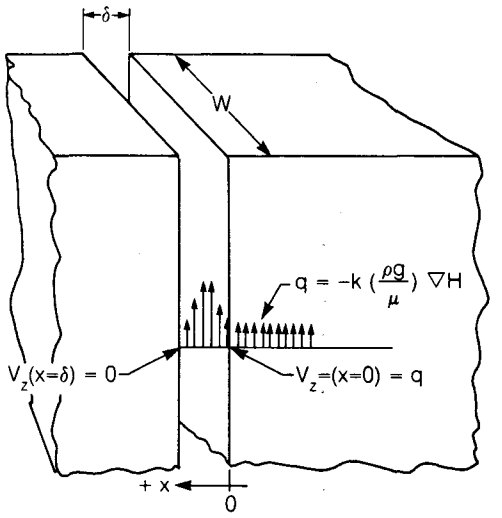

Figure 2. Flow between parallel plates with the fluid velocity at one plate boundary matched to the Darcy velocity within the plate. [XBL 8611-12736]

$$v_z(x) = -\frac{\rho g}{\mu}\left[-\frac{x^2}{2} + \left(\frac{\delta}{2} - \frac{k}{\delta}\right)x + k\right]\frac{dH}{dz}, \tag{7}$$

which when integrated over the cross-sectional area of the gap gives

$$Q_{gap} = -W\left(\frac{\delta^3}{12} + \frac{k\delta}{2}\right)\frac{\rho g}{\mu}\frac{dH}{dz}. \tag{8}$$

A comparison between Eqs. (6d) and (8) can be made by first equating the dimension W to $2\pi R_2$, the gap circumference in the annular-flow problem. With this change, dividing Eq. (8) by Eq. (5) results in the parallel-plate approximation to Eq. (6). This result is

$$\frac{Q_{gap}}{Q_{core}} = \frac{2\pi R_2\left(\frac{\delta^3}{12} + \frac{k\delta}{2}\right)}{\pi R_1^2 k}, \tag{9a}$$

which becomes

$$\frac{Q_{gap}}{Q_{core}} = \frac{\delta^3}{6R_2k} + \frac{\delta}{R_2}, \tag{9b}$$

since $R_1 \approx R_2$. The agreement between Eqs. (6d) and (9b) lends support to the approximations used in arriving at the former result.

FLOW IN FRACTURED POROUS MEDIA

The previous analysis of the parallel-plate problem is related to the processes of flow in macropores between soil aggregates as well as to flow in fractured porous rock. To elaborate on this similarity, a simple model of a parallel planar gap bounded by a porous media of permeabilities k_1 and k_2 at $x = 0$ and $x = \delta$, respectively, is considered in the following analysis. Fluid flow along the z direction is considered as before. In this case, the velocity profile is given by

$$v_z(x) = -\frac{\rho g}{\mu}\frac{dH}{dz}\left[-\frac{x^2}{2} - \left(-\frac{\delta}{2} + \frac{k_1 - k_2}{\delta}\right)x + k_1\right], \quad (10)$$

which upon integration over the gap width δ and transverse width W gives

$$Q_{gap} = -\delta W\left[\frac{\delta^2}{12} + \frac{(k_1+k_2)}{2}\right]\frac{\rho g}{\mu}\frac{dH}{dz}, \quad (11a)$$

or when $k_1 = k_2 = k$,

$$Q_{gap} = -\delta W\left[\frac{\delta^2}{12} + k\right]\frac{\rho g}{\mu}\frac{dH}{dz}. \quad (11b)$$

When either $k_1 \to 0$, or $k_2 \to 0$, Eq. (11a) becomes equivalent to Eq. (8) as expected. When $k \to 0$ at both surfaces, Eq. (11) results in the commonly used cubic flow relation with a parallel-plate fracture permeability equal to $\delta^2/12$. This permeability is also commonly used to characterize flow in fractured porous media. However, from Eq. (11), it is evident that the true fracture permeability is of the form

$$k_{frac} = \frac{\delta^2}{12} + k, \quad (12)$$

where the second term accounts for finite velocities at the fracture surfaces. The relative error introduced by omission of this second term is equal to $12k/\delta^2$. This relative error is generally small because fractures usually offer the path of least resistance to flow. It is this same phenomenon that gives rise to potentially large laboratory permeameter errors.

DISCUSSION

The inverse dependence of the ratio Q_{gap}/Q_{core} in Eq. (6d) on the permeability k is reasonable. With higher permeability materials, errors due to annular flow become less significant. On the other hand, with materials of very low permeability, annular flow becomes a very important source of experimental error. On the right-hand side of Eq. (6d), the result is dominated by the first term for reasonable values of the variables. This cubic dependence agrees with the cubic-law flow result for flow within parallel-plate gaps. The dependence of Q_{gap}/Q_{core} as a function of gap width is plotted in Fig. 3 for several values of k, with $R_2 = 36$ mm. The predicted flux ratios indicate that annular flow can contribute quite significantly to the overall flow within a permeameter, even at rather small gap widths. The curve for the moderately low-permeability core with $k = 10^{-14}$ m^2 indicates that an annular gap of only about 10 μm will lead to substantial errors in permeability measurements for such materials. Gap-flow errors at even lower permeabilities can dominate measured flows, since even micron-scale gaps will contribute significantly to the overall flow. It should be emphasized that the assumptions used in the above calculations are very idealized. It is rather unlikely that an annular gap of uniform width will be found under most experimental conditions. Nevertheless, it appears likely that gaps along fractions of sample perimeters often

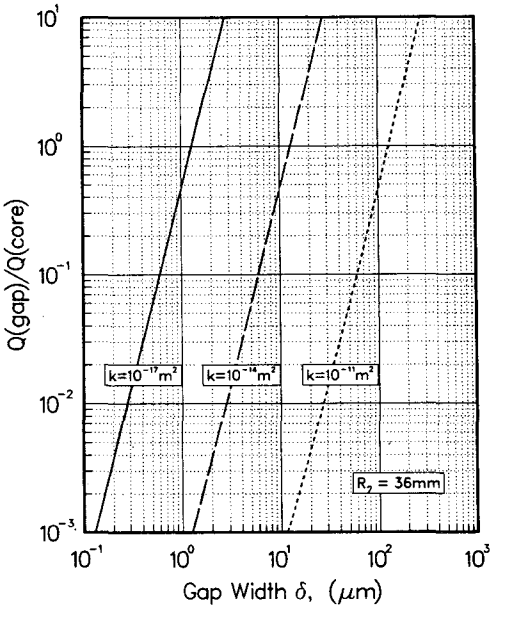

Figure 3. Dependence of annulus/core flux ratio on gap width. [XBL 871-220]

occur. The calculations presented here serve to demonstrate the potential for large measurement errors, even with these likely fractional gaps.

With the currently increasing interest in measurement of k in low-permeability soil and rock materials in association with hazardous waste disposal, annular flow in laboratory measurements becomes a potential source for very large errors. Annular-flow errors in laboratory measurements on low-permeability materials are likely for two reasons. First, because of the inverse k dependence of error effects demonstrated in Eqs. (6d) and (9), low k materials are inherently more susceptible to these errors. Second, in the case of rock samples, which lack the plasticity found in unconsolidated soils, core walls are much less capable of conforming to the surfaces of a permeameter.

CONCLUSIONS

A strong tendency for introducing wall-flow errors in laboratory permeability measurements has been demonstrated. Annular-flow errors are shown to exhibit both cubic and linear dependences on gap width. Wall flow was also shown to depend inversely on both core permeability and permeameter radius. Agreement has been demonstrated between the truncated solution for Q_{gap}/Q_{core} obtained from the annular gap model and the solution obtained by approximating the gap as an equivalent parallel-plate gap.

ACKNOWLEDGEMENT

I gratefully acknowledge Peter Persoff and T.N. Narasimhan of Lawrence Berkeley Laboratory for helpful discussion and review of this manuscript.

REFERENCES

Bird, R.B., Stewart, W.E., and Lightfoot, E.N., 1960. Transport Phenomenon. Wiley, New York.

McNeal, B.L., and Reeve, R.C., 1964. Elimination of boundary-flow errors in laboratory hydraulic conductivity measurements. Soil Sci. Soc. Am., Proc., v. 28, p. 713–714.

Measurements of the Temperature Dependence of Gas Diffusivities in Porous Media

T.K. Tokunaga

Conventional approaches used in the earth sciences to characterize the porous-media effective gas diffusivity, D_e, assume that only the gas-phase porosity, tortuosity, and ordinary gas diffusivity, D_o, are required to determine D_e (e.g., Troeh et al., 1982). These approaches predict that changes in temperature or gas pressure affect D_e solely through changes in D_o, so that the ratio D_e/D_o, known as the "diffusibility," is invariant with respect to temperature and pressure changes (for a given medium, at a fixed gas-phase porosity). For later convenience, the diffusibility, D_e/D_o, will be designated by $\tilde{D}$. More general analyses of gas diffusion in porous media demonstrate that the ratio of the gas mean free path, l_o, to the characteristic pore dimension, r_o, exerts a strong influence on the nature of the diffusion process (e.g., Pollard and Present, 1948; Evans et al., 1961; Spiegler, 1966; Tokunaga, 1985; and Clifford and Hillel, 1986). These analyses show that the Knudsen number, N_{Kn}, given by the ratio l_o/r_o, must be included in any general expression of the effective diffusivity through

$$D_e = \frac{f(\epsilon_g)D_o}{1 + N_{Kn}}, \qquad (1)$$

where $f(\epsilon_g)$ is a function of the gas porosity, ϵ_g, which accounts for the combined effects of porosity and tortuosity in impeding diffusion. Equation (1), known as the Bosanquet equation, is applicable over the full range of N_{Kn}. Because of the temperature and pressure dependencies of l_o, N_{Kn} is itself a function of these variables. It is apparent that the commonly used assumption of invariance of $\tilde{D}$ is valid in the special case where $N_{Kn} \to 0$; i.e., when the gas mean free path is much smaller than the characteristic gas pore dimension.

In a recent study (Tokunaga, 1986) the Bosanquet result was used to estimate the temperature dependence of $\tilde{D}$ within the limitations of simple

kinetic theory. As part of that work, measurements of D_e were made on several porous systems over a range of temperatures. The predicted and measured temperature dependences of $\widetilde{D}$ are summarized in that report.

TEMPERATURE DEPENDENCE OF THE DIFFUSIBILITY

For a given system of fixed gas porosity and tortuosity, the ratio of diffusibilities at two temperatures can be estimated with the use of Eq. (1), the definition of N_{Kn}, and an expression for the gas mean free path. From Eq. (1) the diffusibility at a given temperature T can be expressed as

$$\widetilde{D}(T) = \frac{r_o f(\epsilon_g)}{r_o + l_o(T)}. \tag{2}$$

The mean free path, l_o, depends not only upon T but also upon the gas species and pressure. For a given gas composition and pressure, l_o is linearly dependent on the Kelvin temperature. The ratio of $\widetilde{D}$ at two temperatures ($T_2 > T_1$) will be designated the "diffusibility ratio," represented as

$$R_{\widetilde{D}}(T_1,T_2) = \frac{\widetilde{D}(T_2)}{\widetilde{D}(T_1)} \tag{3a}$$

$$= \frac{r_o + l_o(T_1)}{r_o + l_o(T_2)}. \tag{3b}$$

Equation (3b) demonstrates that the often-assumed invariance of $\widetilde{D}(T)$ is adequate when $r_o \gg l_o$ (the continuum limit) but will generally fail as $T_2 - T_1$ becomes large.

Plots of $R_{\widetilde{D}}$ for oxygen/nitrogen diffusion in systems at various r_o are given in Fig. 1 for a reference T_1 of 0°C. This figure depicts the behavior of $\widetilde{D}$ in two limiting cases as well as under intermediate conditions. As the characteristic pore dimension r_o becomes increasingly large, the continuum limit ($l_o \ll r_o$) is reached. In this limit the mean free path of gas-molecule trajectories in porous media, l_e, is insignificantly influenced by collisions at condensed phase surfaces, resulting in D_e changes in direct proportion to D_o changes. Thus, as T is increased in the continuum limit, $\widetilde{D}$ remains constant for a given system, and $R_{\widetilde{D}}(T_1,T_2)$ therefore becomes unity. On the other hand, for systems of decreasing r_o, the Knudsen limit is approached. In this limit, $l_o \gg r_o$, so that the porous-medium effective mean free path l_e becomes equal to r_o (Tokunaga, 1985). For this case temperature

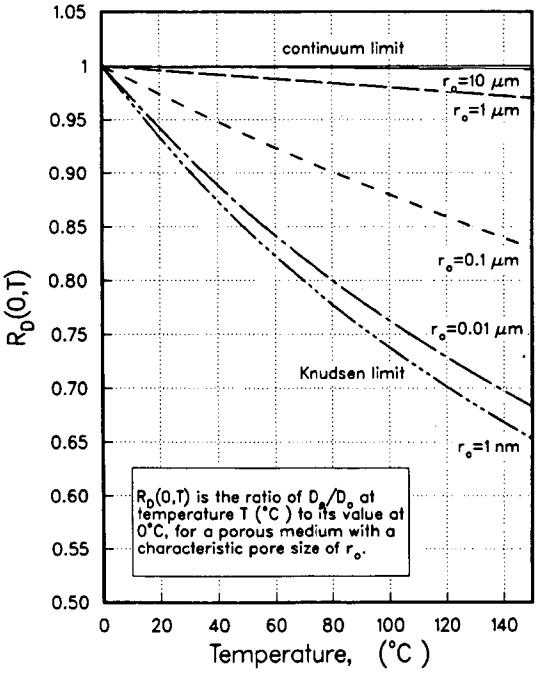

Figure 1. Decrease in D_e/D_o with temperature (oxygen-nitrogen, at 101.3 kPa). [XBL 873-999]

increases cannot contribute to lengthening of l_e. This results in less than proportional increases in D_e relative to increases in D_o as the temperature is raised, or

$$\frac{\partial \widetilde{D}}{\partial T} < 0, \tag{4a}$$

$$R_{\widetilde{D}}(T_1,T_2) \rightarrow \frac{l_o(T_1)}{l_o(T_2} < 1. \tag{4b}$$

Porous media with intermediate values of r_o (or more generally, intermediate values of N_{Kn}) are predicted by this model to exhibit moderate degrees of Knudsen diffusion arising from perturbation of the free-path distribution by pore-wall collisions.

MEASUREMENTS OF GAS DIFFUSIVITY IN POROUS MEDIA

To test the predicted temperature effects on $\widetilde{D}$ experimentally, gas diffusivity measurements were made on porous media of widely differing characteristic pore sizes at three temperatures. The porous media tested included a pack of 9.53-mm steel spheres, a sand, and a bentonite clay. Transient oxygen-nitrogen diffusion was measured in these systems using a closed-tube single-end-chamber method developed especially for this study. For this purpose

oxygen concentrations were monitored in an end-chamber in contact with an otherwise closed column containing the porous material. A polarographic-electrode method was used to measure oxygen concentrations continuously. The diffusion coefficient is obtained from the slope of the logarithm of dimensionless concentration excess versus time (Fig. 2). The experimental method was validated by demonstrating that oxygen-nitrogen D_o measured with this new design compared favorably with data previously reported by other workers. Details of the diffusion-chamber design and data analyses are provided in Tokunaga (1986).

For each system, D_e was measured at 0, 30, and 60°C. These data were then divided by the corresponding $D_o(T)$ to observe the temperature dependence of $\widetilde{D}$. Plots of $\widetilde{D}(T)$ for the three porous media are shown in Figs. 3 to 5. The plotted points represent mean values of 4–7 diffusion measurements made at a given temperature. The error bars span the range of ± one standard deviation. For the pack of steel spheres and for the sand, $R_{\widetilde{D}}$ were taken from linear regressions over the full temperature range under consideration. In the gas-diffusion experiments with the bentonite clay, numerous technical problems arose in attempting to measure D_e at 60°C, and reliable data were not obtained from these high-temperature tests. Therefore, $R_{\widetilde{D}}$ were obtained from differences in mean values of $\widetilde{D}$ at 0 and 30°C from the clay tests.

DISCUSSION

Because of scatter in the data, definitive values of $R_{\widetilde{D}}$ could not be obtained. Unfortunately, closed-tube methods (while being better than many other techniques) often are limited by uncertainties of about 3% for any single D measurement (Marrero and Mason, 1972). Nevertheless, qualitative support of the predicted behavior of $\widetilde{D}$ with T is provided by this set of experiments.

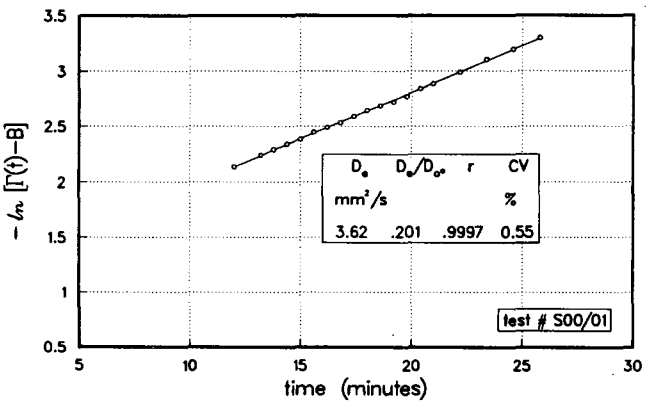

Figure 2. Gas diffusion in sand S44H at 0°C, 101.0 kPa (gas porosity = 0.381). [XBL 873-1000]

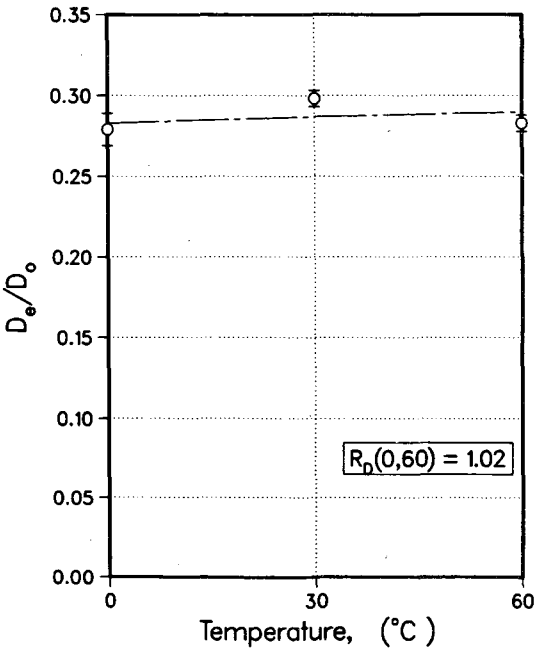

Figure 3. Gas diffusion in 9.53-mm sphere pack (porosity = 0.438). [XBL 873-1001]

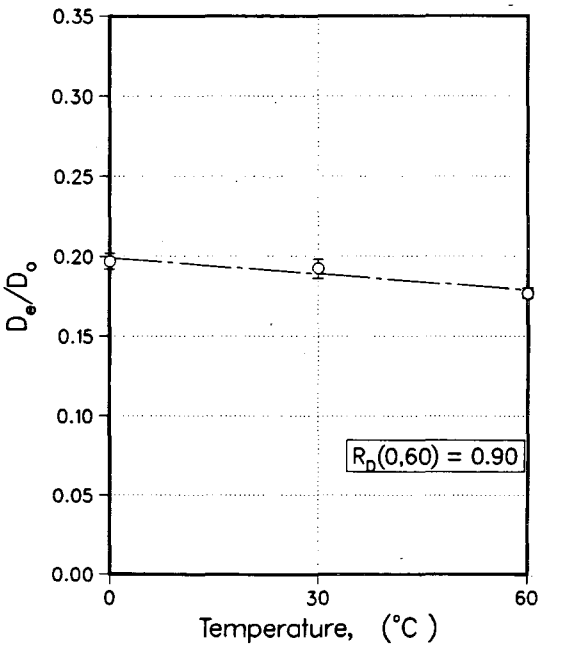

Figure 4. Gas diffusion in sand (porosity = 0.381). [XBL 873-1002]

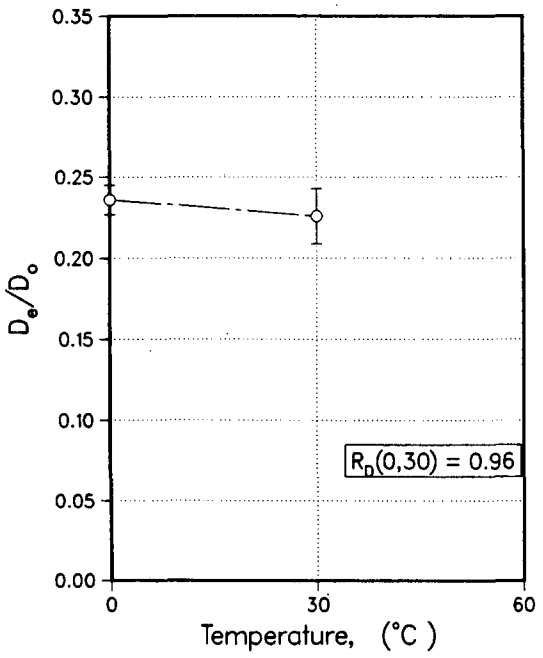

Figure 5. Gas diffusion in Volclay bentonite (gas porosity = 0.568). [XBL 873-1003]

In the case of diffusion in the pack of steel spheres, the characteristic pore dimensions are much larger than l_o, so that the continuum limit adequately describes the system. The observed lack of change in $\widetilde{D}$ with temperature ($R_{\widetilde{D}} = 1.02 \approx 1.00$) is in agreement with continuum-limit diffusion behavior. Both the sand and clay experiments demonstrated that $\widetilde{D}$ decreases measurably within the tested T range. These observations are consistent with porous systems with finer pores and some influence from wall collisions. The measured decreases in $\widetilde{D}$ for the sand were larger than expected. The $R_{\widetilde{D}}$ (0 and 60°C) of 0.90 obtained in the sand experiments implies that the system is characterized by $r_o \approx 0.07$ μm. This inference is clearly incorrect, since the sand pack is probably characterized by a much larger r_o. From the limited data obtained with the clay sample, an $R_{\widetilde{D}}$ (0 and 30°C) of 0.96 was obtained. This decrease in $\widetilde{D}$ corresponds to $r_o \approx 0.1$ μm, a reasonable result for diffusion in clay. However, scatter in the data precludes quantitative interpretation of this decrease.

Several possible improvements in experimental design could enable measurement of more definitive responses of $\widetilde{D}$ to temperature changes. A wider range of experimental temperatures would allow for wider variation of N_{Kn} and better resolution of $R_{\widetilde{D}}$. The use of a different set of gases and a different monitoring method may also improve the quality of the data. Polarographic oxygen electrodes often exhibit apparently random drift in the output signal. A steady-state experimental method, though technically more cumbersome, may yield diffusion data with higher resolution.

CONCLUSIONS

Using a free-path distribution model and the resulting Bosanquet equation, a model for predicting the temperature dependence of porous-media gas diffusivities has been developed. This model is valid over the full range of Knudsen numbers, within the limitations of simple kinetic theory. A new laboratory method for measuring porous-media gas diffusivities has been developed, with which the temperature dependence of D_e was measured for three materials of widely contrasting characteristic pore dimensions. The measured behavior of the diffusibilities over a temperature range of 60°C qualitatively supported the present model. Experiments yielding data with higher resolution will likely require some modifications in the present method. Despite the limitations of the present data, effects of pore-wall collisions and departure from the often-assumed continuum behavior of gas diffusion in porous media were observed to be as predicted.

REFERENCES

Clifford, S.M., and Hillel, D., 1986. Knudsen diffusion: The effects of small pore size and low gas pressure on gas transport in soil. Soil Sci., v. 141, no. 4, p. 289–297.

Evans, R.B., Watson, G.M., and Mason, E.A., 1961. Gaseous diffusion in porous media at uniform pressure. J. Chem. Phys., v. 35, no. 6, p. 2076–2083.

Marrero, T.R., and Mason, E.A., 1972. Gaseous diffusion coefficients. J. Chem. Phys. Ref. Data, v. 1, p. 3–118.

Pollard, W.D., and Present, R.D., 1948. On gaseous self-diffusion in long capillary tubes. Phys. Rev., v. 73, no. 3, p. 762–774.

Spiegler, K.S., 1966. Diffusion of gases across porous media. Ind. Eng. Chem. Fundam., v. 5, p. 529–532.

Tokunaga, T.K., 1985. Porous media gas diffusivity from a free path distribution model. J. Chem. Phys., v. 82, no. 11, p. 5298–5299.

Tokunaga, T.K., 1986. The temperature dependence of gas diffusivities in porous media (Ph.D. thesis). University of California, Berkeley.

Troeh, F.R., Jabro, J.D., and Kirkham, D., 1982. Gas diffusion equations for porous materials. Geoderma, v. 27, p. 239–253.

The Influence of Entrapped Gas on Transient Groundwater Storage

T.K. Tokunaga and T.N. Narasimhan

Analysis of transient subsurface water flow generally includes the assumption of full water saturation in regions below the water table. This assumption arises from the belief that equilibrium-water characteristic relations (saturation, S_w, versus pressure head, ψ) are applicable in transient groundwater flow. Specifically, equilibrium water characteristic relations usually require full water saturation for regions below a water table, where the water pressure is above atmospheric. However, it is commonly observed that air becomes entrapped as a porous medium takes up water. For positive pressure heads this entrapped air is a transient, nonequilibrium phenomenon (Peck, 1969). Although air entrapped below a water table is in disequilibrium, it can reduce water saturation to as low as about 0.5 (Adam et al., 1969). Fayer and Hillel (1986) demonstrated the need to incorporate air encapsulation effects in modeling the response of a shallow water table to infiltration. In their study the water table rose 2 to 5 times higher than predicted with the assumption of full water saturation below the water table. Thus the assumption of full water saturation in regions with pressure head $\psi \geq 0$ can be a significant source of error in the study of transient groundwater flow, especially in the vicinity of a fluctuating water table. Entrapped gas affects transient fluid flow in three ways. The most obvious effect of entrapped gas on groundwater flow is that of reducing the degree of water saturation below the generally assumed value of $S_w = 1$. This in turn results in a second effect of reducing the hydraulic conductivity, K. The use of the saturated hydraulic conductivity, K_s, in regions below the water table containing entrapped air may lead to substantial overestimations of flow because of the strong S_w dependence of $K(S_w)$. The third effect of entrapped gas on transient groundwater flow results in modifications of the pressure response of water storage. The effect of entrapped gas on transient water storage below the water table is the main focus of this article.

THEORY

The mass of water, M_w, contained in a unit bulk volume, V_b, of a porous medium is expressible as

$$\frac{M_w}{V_b} = nS_w\rho_w, \tag{1}$$

where n is the porosity, S_w is the water saturation, and ρ_w is the density of water. The pressure dependence of M_w/V_b at constant total stress may be expressed as (Narasimhan and Witherspoon, 1977)

$$\frac{1}{V_b}\frac{dM_w}{dP_w} = S_w\rho_w\left(\frac{dn}{dP_w}\right) + n\rho_w\left(\frac{dS_w}{dP_w}\right) + nS_w\left(\frac{d\rho_w}{dP_w}\right), \tag{2}$$

where P_w is the water pressure. Although we reference the pressure head ψ relative to local atmospheric pressure, in this work pressure P will refer to absolute pressure except where otherwise specified. The quantity defined by the equation is referred to as the specific fluid mass capacity, m_c^*. The first term on the right side of Eq. (2) expresses the impact of matrix compressibility on m_c^*. The second term accounts for water-saturation/desaturation responses. The third term accounts for the compressibility of water. In shallow groundwater systems matrix compressibility influences m_c^* much more than the compressibility of water. Because it is commonly assumed that ground below the water table is fully saturated, most analyses of transient groundwater flow attribute changes in local water storage primarily to deformation of the solid matrix and secondarily to the compressibility of water.

When air is entrapped by liquid water, its pressure, P_g, is generally equal neither to P_w nor to the local atmospheric pressure P_o. In this situation m_c^* cannot be related to the water characteristic relation, $S_w(\psi)$ or $S_w(P_w)$, because the entrapped air becomes isolated from the atmosphere. Thus the saturation-desaturation term in Eq. (2) cannot be obtained from the slope of the water characteristic relation, regardless of the value of P_w. Furthermore, for the case of air entrapped below the water table, $P_w > P_o$. In this range of P_w the equilibrium water characteristic relations require $S_w = 1$, and the slope of $S_w(P_w)$ vanishes. These conditions are clearly inapplicable in describing regions below the water table that contain entrapped air.

The impact of entrapped air on m_c^* for regions below the water table can be qualitatively evaluated through analysis of processes governing saturation

changes. Since dS_w/dP_w is generally associated with processes in the vadose zone, we will use dS_w/dP_{w+} to denote saturation changes below the water table. Our analysis will focus on the effects of air-phase volume changes on dS_w/dP_{w+}. Since S_w can be expressed as

$$S_w = 1 - \frac{V_g}{V_v}, \tag{3}$$

where V_g is the entrapped-gas volume and V_v is the void volume, we have

$$\frac{dS_w}{dP_{w+}} = -\frac{1}{V_v}\frac{dV_g}{dP_{w+}}. \tag{4}$$

Thus the problem of estimating saturation changes below a water table now becomes one of estimating gas volume changes with P_{w+} changes. The behavior of V_g requires knowing the pressure of the entrapped gas phase. Within entrapped air bubbles the pressure of the gas phase can be approximated by the Laplace-Young equation

$$P_g \approx P_{w+} + \frac{2\gamma_{wa}}{r}, \tag{5}$$

where γ_{wa} is the water-air surface tension and r is the average radius of curvature of entrapped air bubbles. A nominal range of P_g can now be obtained for a restricted range of bubble sizes. Just below a water table, $P_{w+} \approx 10^5$ Pa. For $\gamma_{wa} \approx 7\times10^{-2}$ N·m^{-1} and $r \geq 10^{-5}$ m, we have $P_{w+} \leq P_g \leq 1.1P_{w+}$ in systems with hydrophilic solids. Even without making assumptions regarding the wettability of solid surfaces, we still have

$$P_g \approx P_{w+} \tag{6}$$

to within about 10% for $r \geq 10^{-5}$ m. For $r < 10^{-5}$ m, the above relation deteriorates rapidly. Combining Eqs. (4) and (6) gives

$$\frac{dS_w}{dP_{w+}} \approx -\frac{1}{V_v}\frac{dV_g}{dP_g}. \tag{7}$$

From Bovle's law,

$$\frac{dV_g}{dP_g} = -\frac{V_g}{P_g}, \tag{8}$$

which, with Eqs. (3),, (6), and (7), results in

$$\frac{dS_w}{dP_{w+}} \approx \frac{1}{P_w}(1 - S_w). \tag{9}$$

Thus the contribution to m_c^* due to the change in entrapped-gas volume is given approximately by $n\rho_w(1 - S_w)/P_w$.

It is of interest now to compare the first term on the right side of Eq. (2), which represents the matrix compressibility contribution to m_c^*, with the above approximation for entrapped-air effects on m_c^*. We designate the ratio of air-compressibility effects to matrix-compressibility effects (per bulk volume) as R, defined through

$$R = \frac{n\dfrac{dS_w}{dP_{w+}}}{S_w\dfrac{dn}{dP_w}}. \tag{10}$$

From Terzaghi's relation for the effective stress, $\sigma' = \sigma - P_w^{gage}$, and $dP_w = dP_w^{gage}$,

$$\frac{dn}{dP_w} = -\frac{dn}{d\sigma'} = m_v, \tag{11}$$

where m_v is the coefficient of volume change. Combining Eqs. (9), (10), and (11) gives the ratio of air-compressibility to matrix-compressibility effects per bulk volume as

$$R \approx \frac{n(1 - S_w)}{P_w S_w m_v}. \tag{12}$$

SAMPLE CALCULATIONS OF R

Evaluation of R as expressed in Eq. (12) will yield information on the relative importance of entrapped air on m_c^*. To limit the number of variables for consideration, we will evaluate the effects of varying S_w and m_v on R while using set values of n and P_w. A value of 0.35 will be used for n. A reasonable value for P_w within a short distance below the water table is 1.06×10^5 Pa. This would be the pressure of water at about 0.5 m below the water table when the vertical hydraulic head gradient is minimal. To cover a reasonable range of compressibilities, we selected three values of m_v from Table 2.5 of Freeze and Cherry (1979). These three values are 10^{-9}, 10^{-8}, and 10^{-7} Pa^{-1}. The variation of R with S_w was then calculated for these three m_v. The results are plotted in Fig. 1.

DISCUSSION

From the results presented in Fig. 1, the significance of changes in the volume of trapped air on groundwater storage becomes evident. For most of

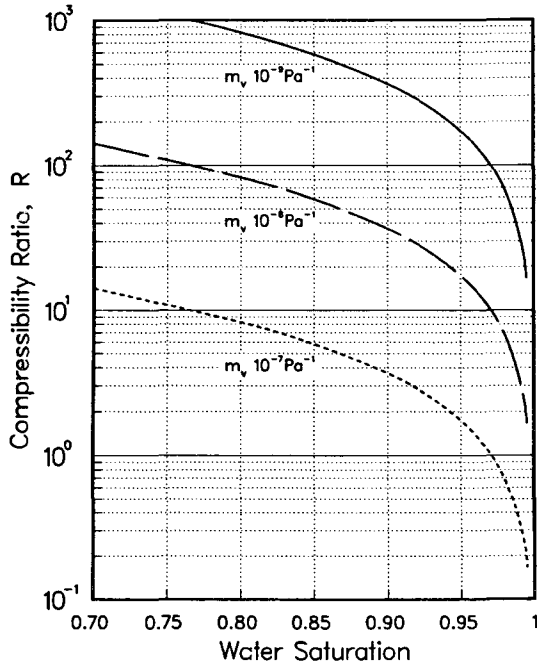

Figure 1. The ratio of air-compressibility effects to matrix-compressibility effects on groundwater storage. [XBL 871-221]

the saturation range for all three cases considered, this effect overshadows that of matrix compressibility. It must be emphasized that air entrapped below the water table is unstable and will dissipate with time. Nevertheless, the problem of incomplete water saturation is relevant in situations where a water table is rising relatively rapidly.

A problem that arises from this analysis is how to account for this effect in a physically based model. Because of the transient, nonequilibrium nature of entrapped air, equilibrium relations such as the water-characteristic relation appear irrelevant in modeling transient groundwater flow under this condition. The problem is not how to estimate the effects of changes in air volume on m_c^*. The problem is how to predict the amount of entrapped air present under various conditions and at various times. The previously mentioned work of Fayer and Hillel (1986) includes an empirically based method for predicting entrapped-air volumes for a particular set of experiments. Further work is necessary before a more general predictive model can be deduced.

CONCLUSION

From the results of this analysis, it becomes clear that the effect of entrapped-air compressibility can be quite significant in influencing water content changes below the water table. In fact, this effect will probably often overshadow the matrix-compressibility effect, to which water storage changes are commonly solely attributed. This domination of water-storage changes by entrapped-air-volume changes persists even at saturations in the range of 0.95 through 0.995 for the cases with m_v equal to 10^{-9} and 10^{-8} Pa^{-1}. It is a common laboratory experience that full water saturation of samples is difficult to achieve without the use of high pressures, long saturation times, or pretreatment with CO_2 gas. Thus, in light of observed difficulties in fully water-saturating porous media and the substantial values of R obtained from this rough analysis, it appears that the effects of changes in entrapped-air volume must be accounted for in models that seek to describe transient groundwater flow in the vicinity of a water table.

It has been noted that the more difficult problem associated with the entrapped-air phenomenon is that of predicting the volume of entrapped air to be found in a given bulk volume and its time dependence. Further analysis of this problem appears warranted in view of the apparent importance of this effect.

The effect of entrapped air on m_c^* appears amenable to laboratory studies. In a controlled setting, saturation, pressure, and compressibility can all be monitored simultaneously. Through such studies the actual importance of transient entrapped gas on groundwater storage can be evaluated.

REFERENCES

Adam, K.M., Bloomsburg, G.L., and Corey, A.T., 1969. Diffusion of trapped gas from porous media. Water Resour. Res., v. 5, no. 4, p. 840–849.

Fayer, M.J., and Hillel, D., 1986. Air encapsulation: II. Profile water storage and shallow water table fluctuations. Soil Sci. Soc. Am. J., v. 50, no. 3, p. 572–577.

Narasimhan, T.N., and Witherspoon, P.A., 1977. Numerical model for saturated-unsaturated flow in deformable porous media, 1, Theory. Water Resour. Res., v. 13, no. 3, p. 657–666.

Peck, A.J., 1969. Entrapment, stability, and persistence of air bubbles in soil water. Aust. J. Soil Res., v. 7, p. 79–90.

The Lack of Immediate Effects from the 1979–1980 Large Earthquakes on the Cerro Prieto Alpha Reservoir

A.H. Truesdell and M.J. Lippmann*

During 1979–1980 two large earthquakes of local magnitude (M_L) greater than 6.0 occurred near the Cerro Prieto, Mexico, geothermal field. These earthquakes along the Imperial and Cerro Prieto strike-slip faults (Fig. 1), which bound the pull-apart basin in which the field is located, suggest that a spreading event occurred at that time. The crustal spreading is partly accommodated by sedimentation from the Colorado River and partly by the intrusion of mantle material. The intrusions carry heat toward the surface, and this heat is undoubtedly responsible for the formation of the geothermal system. If, somehow, this thermal energy were immediately available to reheat a geothermal system that has been cooled by heavy exploitation, we would have, at least in part, a renewable energy source. This is unlikely, despite the arguments of Valette-Silver et al. (1985), who suggest that there was a 10°C average temperature increase over the whole Cerro Prieto alpha reservoir as a direct result of the 1979–1980 Imperial and Victoria earthquakes.

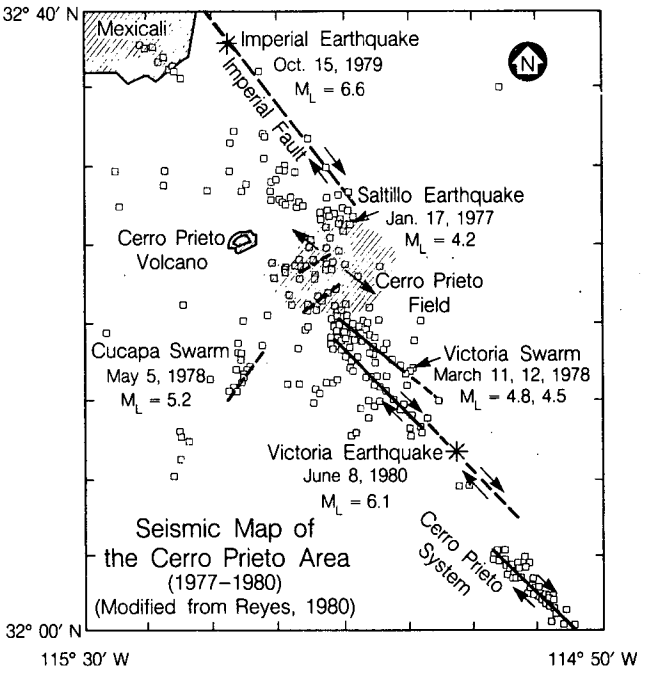

Figure 1. Seismicity of the Cerro Prieto area (modified from Reyes, 1980). [XBL 865-10806]

CHANGES AT CERRO PRIETO

The Cerro Prieto alpha reservoir fluid was originally 260–310°C, with proportional chloride concentrations between 6000 and 10,000 mg/kg (Grant et al., 1984). This reservoir is in the western part of the field and is partially fed by fluids from a deeper reservoir (beta) with higher temperatures and chloride contents (from 320 to 340°C, and from 9000 to 12,000 mg/kg, respectively). On the basis of the results of the two-dimensional natural-state modeling study of Cerro Prieto by Lippmann and Bodvarsson (1983), and assuming a 3-km north-south dimension for the alpha aquifer, this deep recharge would amount to about 100 tonnes/h.

This hot-water influx does not change significantly in response to exploitation. It seems to be limited by the presence of a two-phase zone in the permeable gap connecting the alpha and beta reservoirs (Fig. 2, modified from Halfman et al., 1984, 1986). The associated fluid mobility decrease due to relative permeability effects restricts the mass recharge from the deeper (eastern) parts of the geothermal system. Lippmann and Bodvarsson (1983) estimated that only 3% of the fluids produced between 1973 and 1978 came from the beta reservoir. The alpha reservoir is also recharged from the side (west) and above with cold water that enters in response to lower pressures due to exploitation. This influx of cold water produces a cold sweep that has resulted in a steady decrease in reservoir fluid temperature and chloride content, with temperature decline retarded by heat conduction from reservoir rocks (Grant et al., 1984; Grant and O'Sullivan, 1982).

The connections of deep hot water and shallow cold water to the alpha reservoir near the wells can be investigated using fluid chemistry. If the 1979–1980 dilation opened deep fractures, then higher-temperature, higher-chloride fluid might move upward, causing increases in temperature and salinity; if shallow fractures were opened, there might be cooling and dilution. Fortunately, since the earliest tests of Cerro Prieto wells, the Comisión Federal de Electricidad (CFE) has performed a monthly or bimonthly chemical analysis of brine samples after steam separation and made monthly measurements

*U.S. Geological Survey, Menlo Park, California.

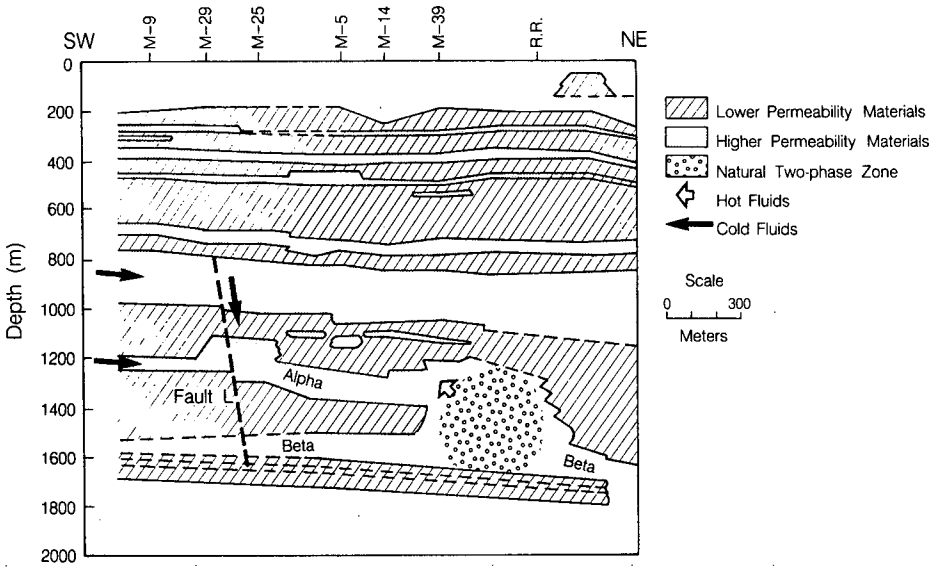

Figure 2. Postulated fluid recharge pattern in the Cerro Prieto alpha reservoir resulting from its exploitation (geology based on Halfman et al., 1984 and 1986). [XBL 865-10812]

of fluid flows and enthalpy. These data may be used to calculate reservoir temperatures and reservoir fluid chloride concentrations. Valette-Silver et al. (1985) used Na/K geothermometer temperatures processed by means of a "matched filter" to "enhance" the evidence for a thermal event and concluded that some well temperatures had risen by as much as 30°C, with an average for the whole field of 10°C.

RESULTS

Our analysis of physical and chemical data (Truesdell and Lippmann, 1986) has shown that the alpha aquifer temperature and chloride content were either unchanged or showed increased declines before, during, and after the period of the 1979–1980 earthquakes. This strongly suggests that the fluid-recharge regime in the alpha reservoir has not significantly been affected by this seismicity and the probable, related crustal spreading. The relations of the Cerro Prieto alpha reservoir to the deeper, higher-temperature beta reservoir and to cold-water aquifers indicate that there are two connections to cooler water, one in permeable sandstones to the west of the alpha reservoir and the other along a fault (Fault L, Figs. 2 and 3) connecting this reservoir to an overlying groundwater aquifer. It was through the leaky upper connection that cooler, less saline influx

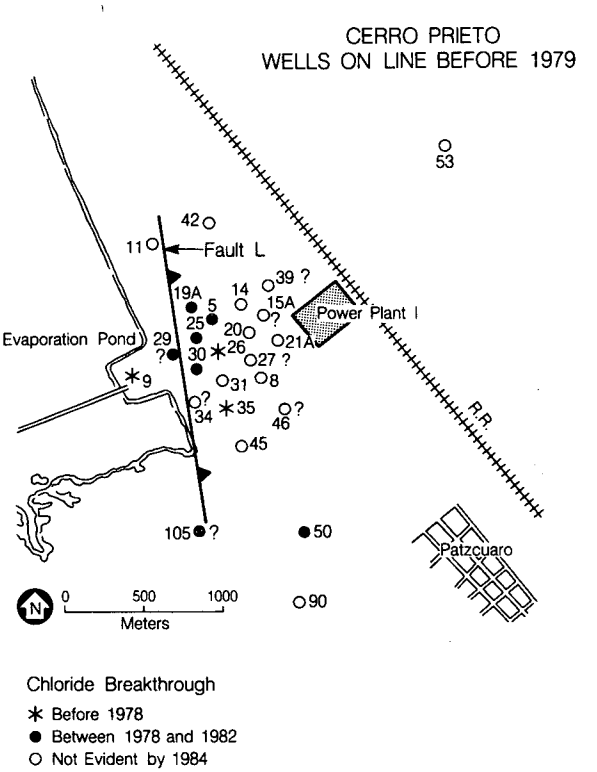

Figure 3. Chloride breakthrough in Cerro Prieto wells that were on line before 1979. The location of Fault L is based on Halfman et al. (1984). [XBL 865-10813]

occurred soon after production started in 1973. This flow was favored by both gravity and the reduced pressure in the exploited aquifer. The temperature of this recharge water is unknown because no wells have been drilled to exploit this aquifer; however, the salinity is probably about half that of the alpha brine. This is based on the salinity-temperature relationship in wells producing from the alpha reservoir and on the minimum salinity of wells strongly affected by cooler influx. The connection to the deeper beta reservoir is through a permeable zone on the eastern side of the alpha reservoir, where boiling and a higher steam saturation diminish fluid recharge (Fig. 2).

This study indicates that there were no observable effects on the alpha reservoir at Cerro Prieto from the two large 1979–1980 earthquakes that occurred in the area. The mass influx into this reservoir did not change, and there was no increase in the temperature or amount of recharge. The aquifer continued to be invaded by cooler waters moving horizontally from the west and vertically downward through Fault L. Furthermore, a simple calculation shows that the large influx of hot water needed to raise the temperature of the reservoir by even 10°C would have been easily detected in the field. Assuming conservative values—that is, (1) a temperature rise of 10°C (from 290 to 300°C); (2) a 1.2-km^3, 0.2-porosity alpha reservoir; and (3) a constant 340°C water influx during a 1-year period—one finds that the required hot-water influx would be about 20,000 tonnes/h. That amount of recharge is almost 5 times larger than the average fluid withdrawal rate at Cerro Prieto during the 1979–1980 period. This enormous influx would have significantly increased the alpha reservoir pressure, as well as the wellhead pressure and well-production rates. In addition, it would probably have raised groundwater levels and greatly increased hot spring flows. None of this was reported by CFE. If higher-temperature fluids were injected, the required mass would be smaller, but the pressure increase would still be large and easily detectable. This would be similar to events observed at Krafla, Iceland (Stefánsson, 1981).

Although the 1979–1980 earthquakes probably indicated a spreading event, possibly associated with the intrusion of some magma at great depth under the field, this event did not measurably affect the temperature or chemistry of the reservoir fluid. The existence of the Cerro Prieto field is undoubtedly due in part to the frequent occurrence of such spreading events and to the incremental heating by igneous intrusions of deep fluid that slowly convects upward through the system. Significant changes in a geothermal system of such ponderous size cannot happen quickly, and the resultant heating and cooling must occur slowly.

REFERENCES

Grant, M.A., and O'Sullivan, M.J., 1982. The old field at Cerro Prieto considered as a leaky aquifer. *In* Proceedings, Fourth Symposium on the Cerro Prieto Geothermal Field, Baja California, Mexico. Comisión Federal de Electricidad, Mexicali, Mexico, v. 1, p. 423–432.

Grant, M.A., Truesdell, A.H., and Mañón, A., 1984. Production induced boiling and cold water entry in the Cerro Prieto geothermal reservoir indicated by chemical and physical measurements. Geothermics, v. 13, no. 1/2, p. 117–140.

Halfman, S.E., Lippmann, M.J., Zelwer, R., and Howard, J.H., 1984. Geological interpretation of geothermal fluid movement in Cerro Prieto field, Baja California, Mexico. Am. Assoc. Pet. Geol. Bull., v. 68, no. 1, p. 18–30.

Halfman, S.E., Mañón, A., and Lippmann, M.J., 1986. Update of the hydrogeologic model of the Cerro Prieto field based on recent well data. Geoth. Resour. Counc. Trans., v. 10, p. 369–375.

Lippmann, M.J., and Bodvarsson, G.S., 1983. Numerical studies of the heat and mass transport in the Cerro Prieto geothermal field, Mexico. Water Resour. Res., v. 19, no. 3, p. 753–767.

Reyes, C.A., 1980. Reporte preliminar del sismo "Victoria" Baja California Norte, del 9 de junio de 1980 (M_L=6.7). Centro de Investigación Científica y de Educación Superior de Ensenada, Departamento de Geofísica, Report GEO 80-02, 13 p.

Stefánsson, V., 1981. The Krafla geothermal field, northeast Iceland. *In* L. Rybach and L.J.P. Muffler (eds.), Geothermal Systems. Wiley, New York, p. 273–294.

Truesdell, A.H., and Lippmann, M.J., 1986. The lack of immediate effects from the 1979–1980 Imperial and Victoria earthquakes on the exploited Cerro Prieto geothermal reservoir. Geoth. Resour. Counc. Trans., v. 10, p. 405–411.

Valette-Silver, N.J., Silver, P.G., and Márquez, M.R., 1985. The effect of a tectonic disturbance on the Cerro Prieto geothermal field (B.C., Mexico). Geoth. Resour. Counc. Trans., v. 9, no. 1, p. 515–520.

Comments on Model Validation

C.F. Tsang

The use of numerical models to predict the performance of a nuclear waste repository or a groundwater contamination cleanup operation has created much concern over whether those models have been properly validated. Several international projects—for example, INTRACOIN, HYDROCOIN, and INTRAVAL—have been established mainly because of this concern. A number of definitions for the term "validation" have been suggested. We believe that the best definition is the one adopted by the International Atomic Energy Agency, which states that "A conceptual model and the computer code derived from it are validated, when it is confirmed that the conceptual model and the computer code provide a good representation of the actual processes occurring in the real system. Validation is thus carried out by comparison of calculations with field observations and experimental measurements" (IAEA-TECDOC-264, 1982).

Thus, in considering model validation, it is useful to note a few important factors inherent in the problem of modeling physical and chemical processes in geologic formations. First of all, the model is no more than a conceptual picture of what the modeler constructs for the system, together with the corresponding mathematical equations and numerical solutions of these equations. The results depend strongly on how the inputs are designed and how they are used. Since the conceptual picture can never be as detailed as the real system because of the lack of information and computer capability, the model is necessarily a simplification of reality. It is a good representation of the real system if the model is adequate to yield results for specific observables of interest with the required accuracy and within a specified range of conditions. Thus, before embarking on a modeling exercise, we need to determine

1. The observables of interest.
2. The accuracy required for the prediction of those observables.
3. The range of conditions for which the model is validated.

For example, the observables of interest could be either the point tracer concentration at a given time or the integrated tracer output concentration over a spatial region and a period of a few thousand years. The former depends on knowing fine details of the system of fractures and channels in the geologic medium; we suspect no currently available model is able to give the correct predictions except under very special conditions. The latter, however, may be computed by a number of relatively simple equivalent-porous-medium or statistical models.

It is important to establish the range of applicability of "validated" models. We do not believe that a model can be developed that is valid for all situations. Defining the applicability ranges can perhaps help to avoid applications of the models to conditions for which they have not been validated.

In model processes in geologic media, it is useful to differentiate between processes and model structures. Processes are physical and chemical phenomena, such as buoyancy flow, colloidal transport, and dissolution and precipitation. Model structures represent geologic and geometric characteristics of the medium, such as faults, layering, and heterogeneity. Processes can probably be studied in the laboratory and described by mathematical equations, whereas model structures are site- and scale-dependent and are part of the input data to the model. For a successful modeling study, one needs both the proper process identification (PI) and the proper model-structure identification (MSI). A failure to match modeling results with field data could be due to errors in PI or MSI; the two are approached quite differently. In practice, of course, there are often cases where processes and model structure are intimately correlated.

Figure 1 illustrates the discussions above. Ideally there should be an element in the model that can be used to suggest what further measurements are needed to improve the confidence level of the predictions. These further measurements are shown in the figure as network design (ND), which is the design of a network of measurement points and schedules to improve the model inputs. The procedure can be repeated or iterated (line connecting ND to Input in the figure) until one of the two outcomes is reached:

1. Sufficient measurements of input data are made to ensure that the model will yield predictions with reasonable confidence. The model results are then either used as final predictions or compared with field results for validation purposes.
2. It is not possible to arrive at predictions with reasonable confidence and accuracy, because the required measurements of input data are too detailed

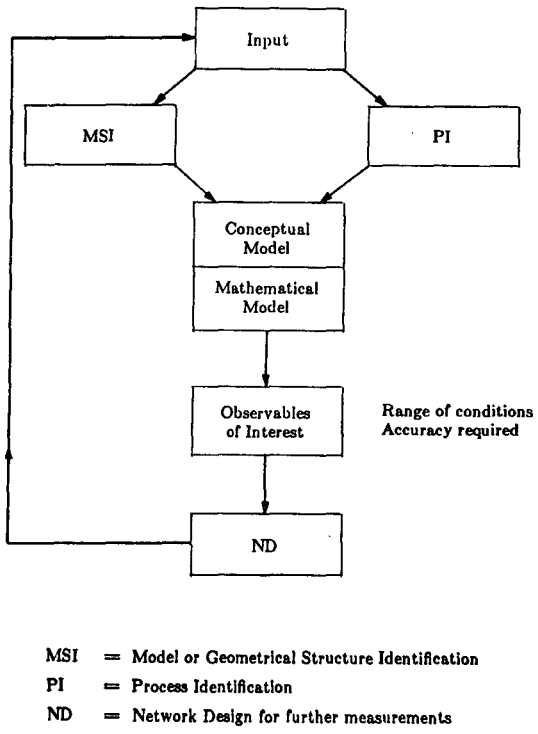

Figure 1. A modeling procedure for validation. [XBL 871-222].

and hence would be too expensive or would require an excessively long measurement period.

The list below summarizes the validation procedure.

1. Input data collection; field measurement design.
2. Construction of conceptual model (MSI).
3. Identification of appropriate processes (PI).
4. Application of computer codes.
5. Study of prediction results; determine need for new input-data measurement.
6. Collection of further field data; field measurement design (ND).
7. Repeat 1–6.

The increasing dependence of decision making on model predictions has made model validation a crucial matter. It is worthwhile for us to consider carefully what constitutes a proper validation and determine the limits and ranges of application of a validated model. This article represents a step in this direction.

Large-Scale Convection near a High-Level Waste Repository in Partially Saturated Fractured Tuff

Y.W. Tsang and K. Pruess

The tuff formation at the Nevada Test Site is one of the candidate media currently under consideration for a high-level nuclear waste repository. The potential repository horizon is located above the water table in partially saturated welded tuff. Though the matrix permeability of the tuff formation is extremely low, on the order of microdarcies, it is intensely fractured at the potential repository horizon, and the fracture permeability is several orders of magnitude higher than the matrix permeability.

Following the emplacement of waste in the repository, the heat generated by the waste provides a driving force for large-scale fluid movement. In a fully saturated medium, where liquid is the sole phase present at ambient conditions, the lower density of the heated liquid in the vicinity of the repository gives rise to a buoyancy pressure gradient that drives the warm liquid upward toward the surfaces. In the partially saturated tuff, we expect a similar thermally induced buoyancy flow for the gas phase.

GAS AND LIQUID VELOCITIES OF BUOYANCY-DRIVEN FLOW

Simple considerations of fluid viscosity and density indicate that the buoyancy velocity of Darcy flow for gas and liquid phases would be of the same order of magnitude if permeability of gas and liquid phases were identical. In fact, in a fractured porous medium, where the fracture permeability may be orders of magnitude larger than the rock matrix permeability, the permeability to the gas and liquid phases may also differ greatly if the medium is partially saturated. Pruess et al. (1985) have performed

modeling studies on the simultaneous transport of heat, liquid water, vapor, and air in partially saturated fractured porous tuff. The thermohydrologic behavior observed in those simulations shows that the strong capillary suction keeps the mobile liquid phase in the very tight matrix rock, whereas the fractures, with their larger apertures, are drained of liquid. Therefore, the permeability to the gas phase takes on the value for the fractures, which is several orders of magnitude larger than the matrix permeability, the appropriate choice for flow in the liquid phase. Because different permeabilities apply to the different phases, the Darcy velocities for buoyancy flow of those phases will scale in accord with the respective permeabilities.

The quantity relevant to contaminant transport in a porous fractured medium is not the Darcy velocity but the pore velocity, which is the Darcy velocity divided by the medium porosity. Using some representative values of permeabilities and porosities for the matrix and the fractures, we estimated the pore velocities of the buoyancy flow to be about 0.1 mm/y for the liquid phase and 22 m/y for the gas phase.

NUMERICAL SIMULATIONS

Having estimated the magnitude of the buoyancy flow, numerical simulations were carried out (Tsang and Pruess, 1986) to investigate the possible large-scale convection phenomena near a waste repository. An "effective continuum" approximation (Pruess et al. 1985) was employed to represent the hydrologic properties of the fractured porous medium. The geology at Yucca Mountain consists of alternating layers of welded and nonwelded tuff units, each unit with different formation and hydrologic characteristics (Peters et al., 1984). As the study was an initial exploration of possible large-scale gas and liquid movements in a partially saturated environment, we chose a highly simplified stratigraphic description, assuming constant hydrologic parameters throughout. These parameters were chosen to be representative (Langkopf et al., 1985) of the potential repository host rock (the Topopah Spring welded unit). Figure 1 shows schematically the modeled region with cylindrical symmetry and with symmetry axis passing through the center of the repository. The repository is modeled as a uniform heat source in the shape of a circular disk 1500 m in radius and 5 m in thickness. The thermal output of the repository is assumed to be 57 KW/acre (14 W/m^2) initially at emplacement and to follow the time-decay function as specified for an 8-year-old spent fuel waste package. A liquid infiltration of 0.1 mm/y is

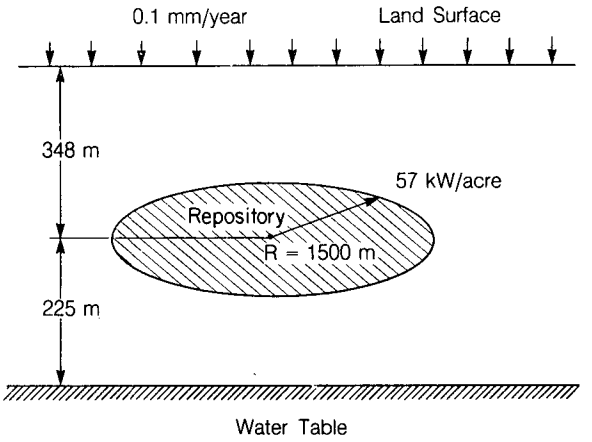

Figure 1. Schematic diagram of the modeled region. [XBL 863-10715]

included in the simulation to give a liquid saturation of about 87% at the repository horizon prior to waste emplacement. The ground surface serves as an infiltration boundary to the liquid phase and as a constant-pressure boundary to the gas phase. For this initial scoping study we assume that the entire repository is loaded instantaneously.

The liquid and gas fluxes at 100 years after emplacement are shown in Figs. 2 and 3, respectively. We note that the liquid fluxes are essentially downward and that their magnitude is on the order of the imposed infiltration rate of 0.1 mm/y. With the matrix porosity of 0.11 chosen in the simulation, the imposed infiltration corresponds to a pore velocity of about 1 mm/y, which is about one order of magnitude larger than the rough estimate given earlier for the liquid pore velocity due to buoyancy flow. Hence, in Fig. 2, any liquid buoyancy fluxes

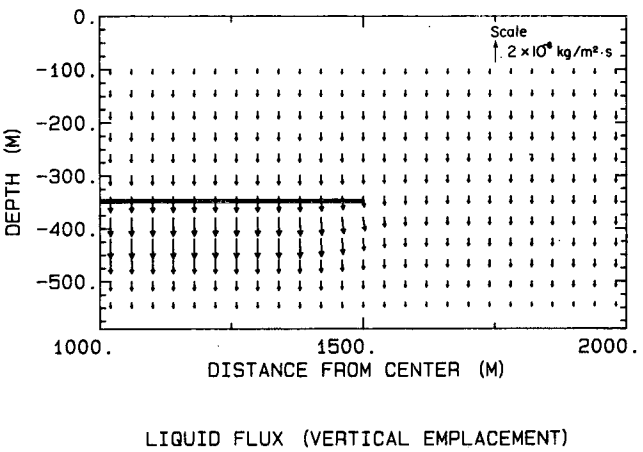

Figure 2. Liquid flux at 100 years after waste emplacement. [XBL 865-1954]

are totally masked by the imposed downward infiltration flux. The larger downward liquid fluxes near the repository are caused by condensation of vapor. The gas fluxes at 100 years after emplacement are plotted in Fig. 3, showing a striking convection pattern. Simulations were also carried out taking into account the binary diffusion of the vapor and air in the gas phase. The results demonstrate a sensitivity of gas convection to the strength of binary diffusion (Tsang and Pruess, 1986).

In Fig. 4 the gas-convection velocities along the repository center line are plotted for the numerical simulations both with and without binary diffusion. The (+) and (−) signs on the curve for the velocities with binary diffusion denote an upward velocity above the repository horizon and a downward velocity below the repository horizon. Note the huge range of values for the gas-convection velocities, particularly for the case where binary diffusion is included. Our rough estimate of buoyancy pore velocity based on air density and viscosity is consistent with the results of the numerical simulation, indicating that the dominant mechanism driving the large-scale gas movements is indeed the density change from heating.

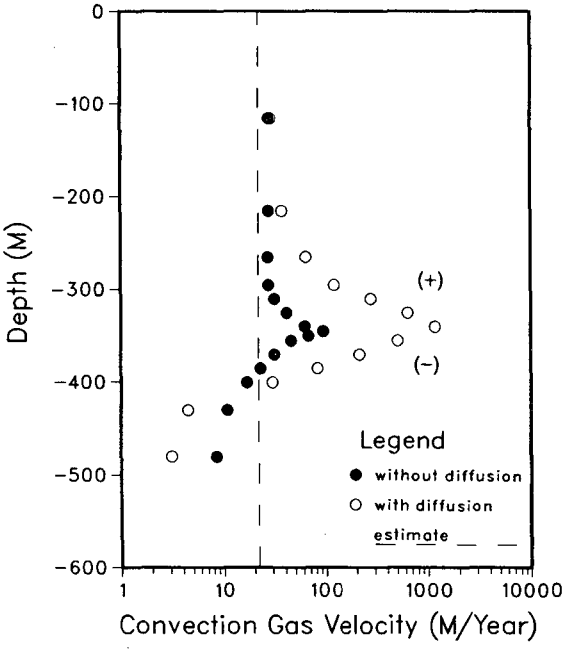

Figure 4. Gas convection velocities along the repository center line at 100 years after waste emplacement. The (+) and (−) signs denoting upward and downward velocities apply only to the curve with binary diffusion and the immediate vicinity of the repository horizon. [XBL 863-10726]

CONCLUSION

In the initial study to explore thermally induced convection near a hypothetical nuclear waste repository in a partially saturated medium, we find that large-scale convection takes place for the gas phase near the repository. Simulated flow velocities are large, ranging from 4.5 to 1174 m/y. However, these velocities depend on the values of gas permeability and fracture porosity, which have not yet been well established. We have used representative values and have not taken into account variation of parameters over the different stratigraphic layers. The large-scale gas convection may provide a useful means for nonintrusive post-closure monitoring of repository performance. The buoyant liquid flux is very small, because capillary action confines liquid to the rock matrix, whose permeability is several orders of magnitude smaller than that of the fractures.

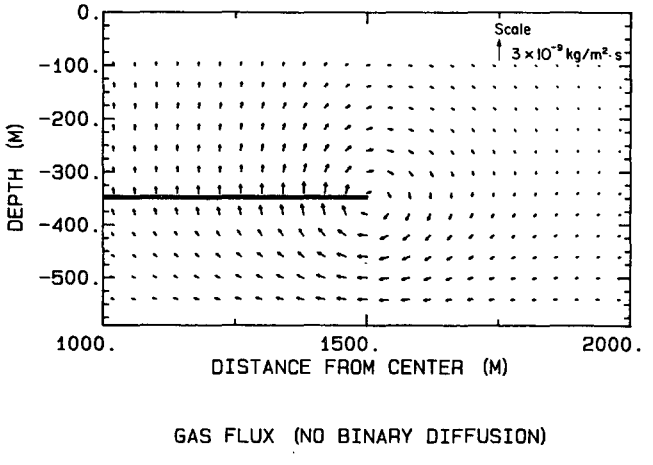

Figure 3. Gas flux at 100 years after waste emplacement, with the binary diffusion process turned off. [XBL 865-1955]

REFERENCES

Langkopf, B.S., Braithwaite, J.W., and Hayden, N.K., 1985. Memoranda (February 25, March 26, June 6, and June 20) prepared for distribution on the common near-field hydrothermal problem, Cove3. Sandia National Laboratories.

Peters, R.R., Klavetter, E.A., Hall, I.J., Blair, S.C., Heller, P.R., and Gee, G.W., 1984. Fracture and matrix hydrologic characteristics of tuffaceous materials from Yucca Mountain, Nye County, Nevada, Sandia National Laboratories Report SAND84-1471, 188 p.

Pruess, K., Tsang, Y.W., and Wang, J.S.Y., 1985. Modeling of strongly heat driven flow in par-

tially saturated fractured porous media. *In* Proceedings, IAH 17th International Congress on the Hydrogeology of Rocks of Low Permeability, University of Arizona, January 7–12, 1985, p. 486–497.

Tsang, Y.W., Pruess, K., 1986. A study of large scale convection near a high level nuclear waste repository in partially saturated fractured tuff. Lawrence Berkeley Laboratory Report LBL-21311.

Channel Model of Flow Through Fractured Media

Y.W. Tsang and C.F. Tsang

Recent concerns regarding the geologic isolation of nuclear waste and deep injection of liquid toxic waste have stimulated much interest in the study of fluid flow and solute transport through tight rocks. Flow through such low-permeability rocks predominantly occurs in interconnecting fractures.

We hypothesize that the fluid flow and solute transport through a tight rock medium is by means of a limited number of tortuous and intersecting channels. These channels vary in aperture along their lengths. Figure 1 shows schematically the channeling effect in a single fracture (top) and the parameters that define a single channel. Figure 2 shows schematically the channeling effect in a number of three-dimensional intersecting fractures. A channel is defined by the aperture density distribution $n(b)$ along its length, L. The channel width is assumed to be a constant of the same order as the correlation length, λ, since the correlation length is, by definition, the spatial range within which the apertures have similar values. The channel length does not equal the linear length between two points, but it is not expected to vary more than a factor of 2 to 3 from the actual linear length. For a given aperture density distribution and correlation length, different realizations of statistically equivalent channels may be generated (Tsang and Tsang, 1987) using geostatistical methods.

When a pressure-head difference is applied between two points, the flow paths between these two points may be represented by a number of channels, which may intersect each other at various points (Fig. 3a). Figure 3b shows two channels with one crossover. Under steady-state flow conditions, the flow through the two intersecting channels is hypothesized to be approximated by the flow through three independent, statistically equivalent nonintersecting channels. With every crossover, there is the added possibility of a different flow path.

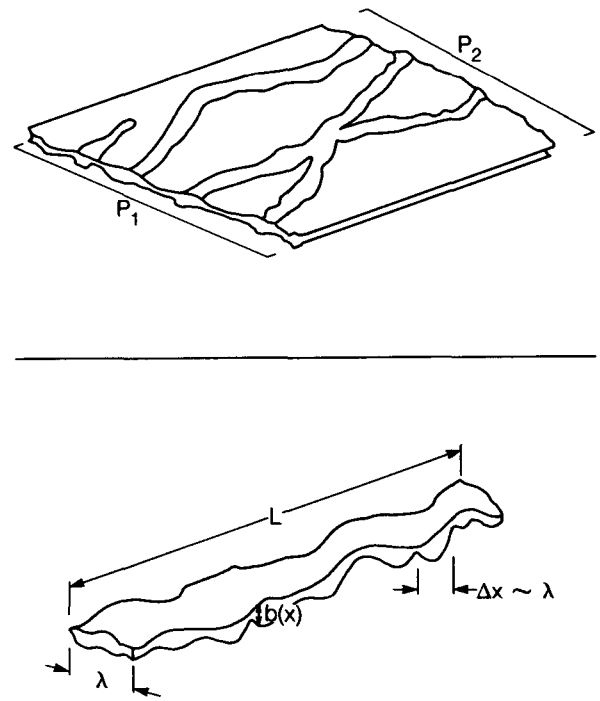

Figure 1. **(Top)** Schematic diagram of the channel representation of fluid flow in a single fracture. **(Bottom)** Schematic sketch for a single channel. [XBL 863-10710A]

In practice, the actual configuration of the channels between input and exit measurement points is not known. One is able to obtain only transient pressure- and tracer-transport concentration data. Thus, as far as the interpretation of the pressure- and tracer-transport measurements are concerned, the system of M independent, statistically equivalent channels, as shown schematically in Fig. 3c, may be an adequate and approximate representation of the realistic configuration shown in Fig. 3a. Tracer-

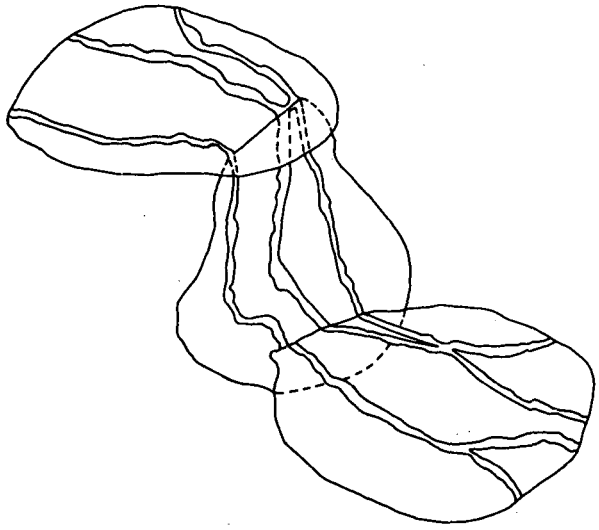

Figure 2. Schematic diagram of the channel representation of fluid flow in a multiple fractured medium. [XBL 863-10711]

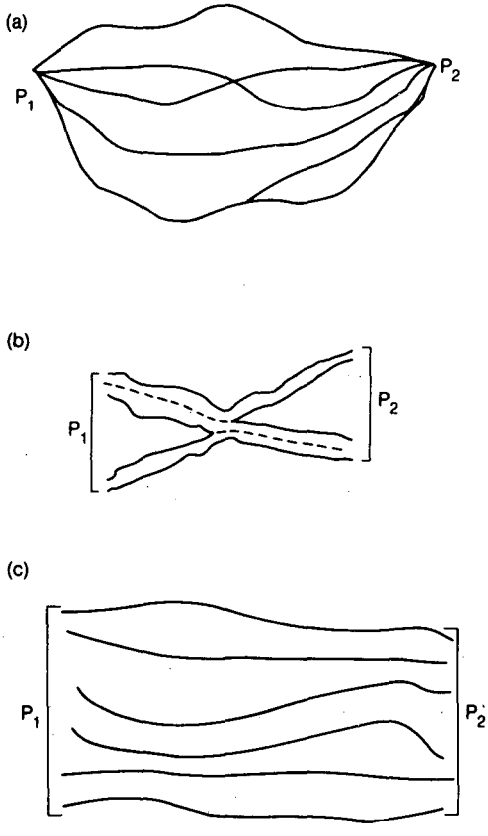

Figure 3. (**a**) A schematic diagram of fluid flow paths between two points maintained at pressures P_1 and P_2. (**b**) A diagram of two intersecting channels. (**c**) A set of independent channels, a conceptually equivalent representation of the flow paths shown in (a). [XBL 863-10712A]

concentration breakthrough curves may be calculated for transport through a system of M independent channels, as shown in Fig. 3c.

For a step-function input of tracer, Fig. 4 shows the tracer-concentration breakthrough curves as a function of time for $M = 32$ and 8, respectively. The concentration curves show a steep initial rise followed by a "stair-step" structure that is due to the finite delay that precedes breakthrough of the solute carried in the next channel. The early arrivals correspond to flow in fast channels, those with few very small aperture constrictions. The steep rise therefore indicates that a large proportion of the total flow is in fast channels. Figure 5 shows the breakthrough curves from laboratory experiments (Moreno et al., 1985) performed on a single fracture in an 18.5-cm core. Careful examination of Figs. 4 and 5 indicates that the prominent features in the theoretical curves based on the channel model (Fig. 4) are also evident in Fig. 5. These features (such as the steep rise in tracer returns and the stair-step structures) are not found in the conventional advection-dispersion curves.

When normal stress across a fracture is increased, the reduction in channel apertures affects the tracer-breakthrough curves. One may start with the experimental breakthrough data, such as that in Fig. 5, and interpret them in terms of our conceptual channel model. Assuming that all the apertures in a fracture are reduced by the linear displacement of the single fracture under stress, one can derive a new tracer breakthrough curve (Tsang and Tsang, 1987). Sample calculations indicate that even a small change in the mean fracture aperture (6% reduction) produces a large change in the breakthrough curve. The reason is that the small change affects significantly the constricted part of the channels, which control the flow rates.

CONCLUSION

We have attempted to understand and calculate transport through fractured media in terms of flow through a system of tortuous and variable-aperture channels. In this initial study, we show that calculated tracer-breakthrough curves based on the channel model have features that correspond well to those in recent data by Moreno et al. (1985). The signature of channeling in fractures is in the stair-step structure of the breakthrough curves and their sensitivity to stress applied across the fracture. These suggested possible laboratory experiments that may be performed to investigate further the channel nature of fluid flow in fractures.

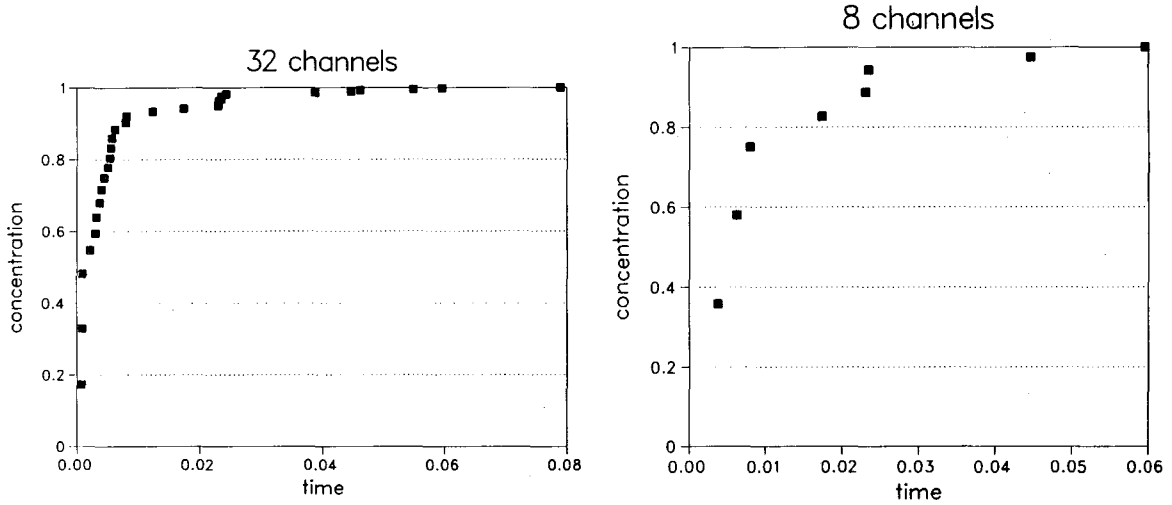

Figure 4. Theoretical tracer concentration breakthrough curves for a set of M channels with common end-point pressures P_1 and P_2. [XBL 873-9992]

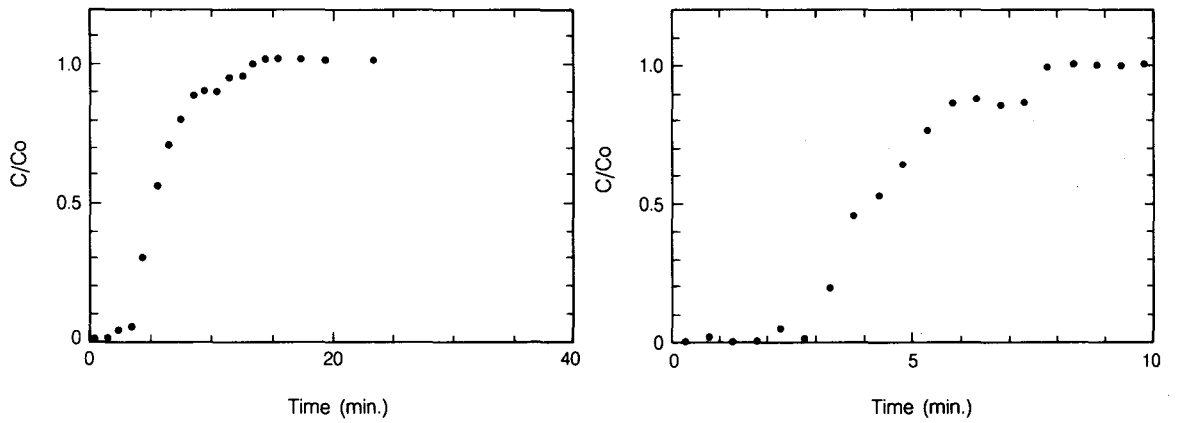

Figure 5. Tracer concentration breakthrough data from laboratory measurements on a single fracture in a granitic core 18.5 cm in height and 10 cm in diameter (Moreno et al., 1985). The two curves correspond to different runs involving different injection flow rates and different tracers (NaLS or I). [XBL 873-9993]

Validation of the conceptual channel model by experiments is crucial, since we have made a number of simplifying assumptions in our approach in order to side-step the issues of the very complicated geometry involved in the flow through a three-dimensional multifracture system. The appeal of the present approach lies in its simplicity, and our initial findings indicate that interpreting fluid flow and transport in terms of a channel model may be a promising area of research.

REFERENCES

Moreno, L., Neretnieks, I., and Eriksen, T., 1985. Analysis of some laboratory tracer runs in natural fissures. Water Resour. Res., v. 21, no. 7, p. 951–958.

Tsang, Y.W., and Tsang, C.F., 1987. Channel model of flow through fractured media. Water Resour. Res., v. 23, no. 3, p. 467–479.

Aperture Correlation of a Fractal Fracture

J.S.Y. Wang and T.N. Narasimhan

The flow and transport of fluid through a fractured medium depends sensitively on the characterization of fracture apertures. In our study we have constructed a fractal-fracture model to describe the spatial correlation of fracture aperture. A fractal fracture is defined as a rough-walled fracture whose two bounding rock surfaces are described by fractal geometry. The term "fractal" was introduced by Mandelbrot (1983) to describe a large class of irregular and fragmented patterns. The most revolutionary concept of fractal geometry is the extension of the notion of integer spatial dimension of simple geometric structures (Euclidean dimension 1 for a line, 2 for a plane, 3 for a space) to a noninteger spatial dimension characterizing the zigzag, rough, and heterogeneous structures of real media in nature. For our study of rough-walled fractures, we describe a rough surface with a fractal dimension D between 2 and 3.

Using two profilers Brown and Scholz (1985) measured the roughnesses of outcrops in the field and of core samples in the laboratory for six rock types. The profiles were analyzed by Fourier transform, and the power spectral densities were plotted versus wave numbers (spatial frequencies), k. All the power spectra of the various samples and profilers were shown to fall approximately on the same quasilinear curve in the log-log plot. A straight line in a log-log plot indicates that the power spectral density is proportional to some power of the wave number. Berry and Lewis (1980) analyzed the Weierstrass-Mandelbrot fractal function, one representation of the class of continuous and nondifferentiable fractal functions having scaling properties, and showed that the power spectrum varies as $k^{2D^p - 5}$, where D^p is the fractal dimension between 1 and 2 for a rough profile and is related to the fractal dimension D of a rough surface by $D^p = D - 1$. The log-log analyses of plots of power spectral densities versus wave numbers have been used extensively in the literature to demonstrate the fractal behavior of different geometric patterns and to determine the fractal dimensions from the log-log slopes.

To study the spatial correlation of fracture aperture, we start with a rough profile with a well-defined power spectrum of fractal dimension D^p. Two fractal surfaces with the same fractal dimension form a fractal fracture by shearing the mirror images with respect to each other over a given displacement. If the two surfaces are mirror images that match perfectly, the fracture will be closed under stress with zero aperture everywhere. A fracture can remain open if the two surfaces are displaced relative to each other so that the two surfaces no longer match. In this study we derive an analytic equation for the variogram describing the spatial correlation of the aperture of a fractal fracture. Abel transforms, Fourier analysis, angular averaging, and inverse Fourier transforms are used to relate the fractal power spectrum of profiles to the variogram of fracture aperture of a shear fracture with two rough surfaces (Wang et al., 1987). The analytic expression of the variogram is expressed in terms of a hypergeometric function. The variogram is very important in geostatistical analyses. The first step in the estimation/interpolation procedure, known as "kriging," is to evaluate the variogram.

Figure 1 illustrates the variograms $\gamma_f(r)$ for fractal fractures with different fractal dimensions. For a fractal fracture with low D close to 2, the fracture surfaces are smooth, and the aperture is nearly constant spatially. The variogram, a measure of the average aperture difference between neighboring points, is nearly zero over a range much larger than the shear displacement r_c. For a fractal fracture with higher D, the aperture variation is more pronounced and the neighboring apertures less correlated. In the case with D close to 3, the surface is rough, and the aperture at a given point in the fracture is almost completely uncorrelated with its neighboring points. For an uncorrelated aperture distribution, the autocorrelation function is zero, and the variogram is equal to the covariance of aperture distribution σ_f^2.

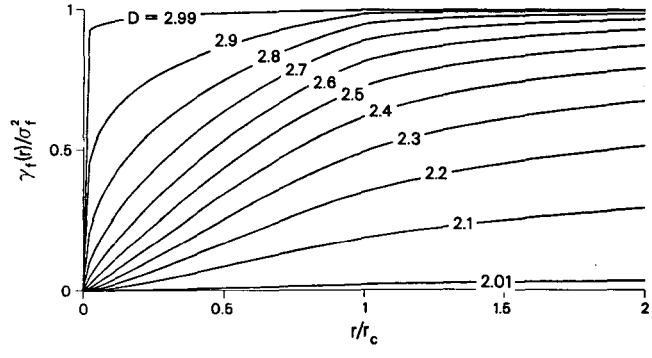

Figure 1. Variogram of fractal fracture. [XBL 871-223]

For the cases with D close to 3, the range of correlation is much shorter than the shear displacement, which generates the aperture variation.

From the analytic equation for the variogram, we also show that in the vicinity of the origin $r = 0$, the variogram is proportional to r^{6-2D}. This limiting behavior of our fractal-fracture model, which is based on integral transform analysis, agrees with the analysis of the special Weierstrass-Mandelbrot fractal function (Berry and Lewis, 1980; Burrough, 1981). The fractal dimension of a fracture can be determined by the slope of the log-log plot of the variogram versus distance in the limit $r \to 0$, as illustrated in Fig. 2. This procedure establishes a useful relationship between the notion of fractal and the notion of variogram.

For the special case with $D = 2.5$, which is referred to in the literature as the Brownian fractal, the fractal-fracture variogram is proportional to r near $r \to 0$. This is the same r dependence that is observed in the spherical model. The spherical model, also known as the Matheron model, is widely used in geostatistical analyses, especially for ore deposits, where grades become independent of each other once a range, a, is reached. The spherical model is based on geometric consideration of the volume of the intersection of two spheres of diameter a. In Fig. 3 we compare the Brownian fractal model with the spherical model. We also include in

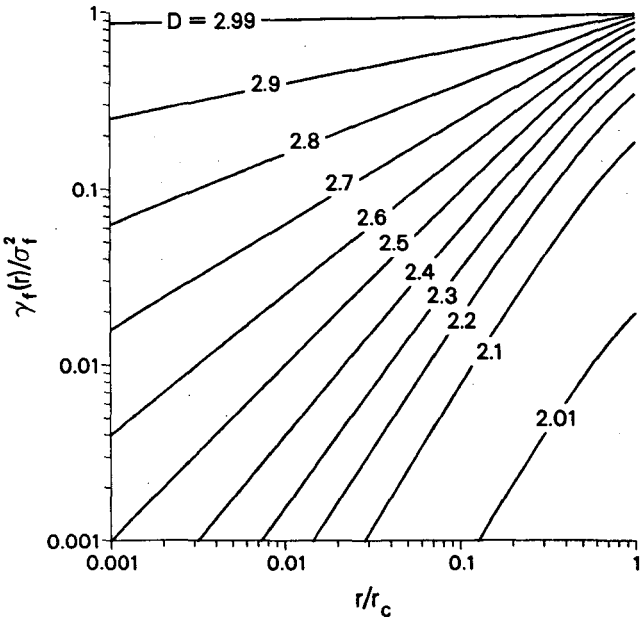

Figure 2. Log-log variogram of fractal fracture. [XBL 871-224]

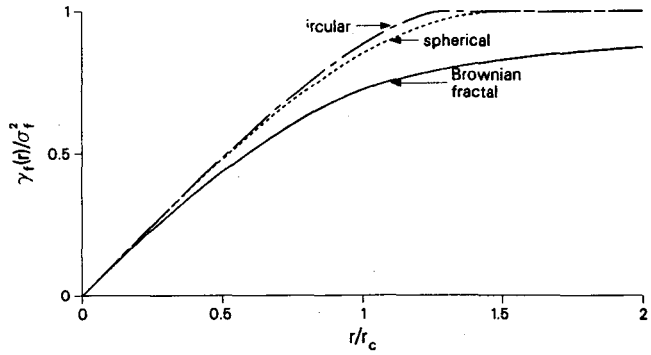

Figure 3. Variogram models. [XBL. 871-225]

Fig. 3 the result of a circular model that is constructed by analogy with the spherical model from consideration of the area of the intersection of two circles of diameter a. In Fig. 3 the ranges of the spherical model and the circular model are related to the shear displacement r_c of the Brownian fractal model, so that the leading r terms all have the same coefficient. The aperture correlation of the fractal-geometry-based Brownian model extends beyond the cutoff ranges of the Euclidean-geometry-based spherical and circular models.

The fractal-fracture model with general D between 2 and 3 is based on a physically meaningful model with two identical mirror-image rough surfaces sheared with respect to each other by a displacement r_c. The derived equation for the variogram can be used to analyze rough fracture data. The parameter D or D^p of the fractal-fracture model can be determined experimentally by log-log power spectral analyses or by log-log variogram analyses of roughness profiles. It will also be of interest to use other independent techniques to study the fractal nature of the rough surfaces directly instead of inferring it from profile measurements. For example, stereophotographic approaches can be used to analyze optical, microscopic, or scanning-electron-microscopic images of rough rock surfaces at different magnifications to probe different spatial scales. A rough rock fracture can be a good model system for understanding heterogeneous geologic media, since the "interior" of a fracture is accessible by opening it, and the exposed rock surfaces are amenable to direct measurement by both linear-profile and planar-surface studies. If the fractal nature of fracture apertures can be demonstrated, we can then proceed to use the fractal-fracture model for geostatistical analyses beyond aperture structure and use it in studies of flow and transport processes through rough fractures.

REFERENCES

Berry, M.V., and Lewis, Z.V., 1980. On the Weierstrass-Mandelbrot fractal function. Proc. Roy. Soc. London, v. A370, p. 459–484.

Brown, S.R., and Scholz, C.H., 1985. Broad bandwidth study of the topography of natural rock surfaces. J. Geophys. Res., v. 90, p. 12575–12585.

Burrough, P.A., 1981. Fractal dimensions of landscapes and other environmental data. Nature, v. 294, p. 240–242.

Mandelbrot, B.B., 1983. The Fractal Geometry of Nature. Freeman, San Francisco.

Wang, J.S.Y., Narasimhan, T.N., and Scholz, C.H., 1987. Aperture correlation of a fractal fracture. J. Geophys. Res., in press.

Development of Foam-Protected Underground Natural Gas Storage Facilities

P.A. Witherspoon, S.M. Benson, P. Persoff, K. Pruess, C.J. Radke, and Y.S. Wu

Underground storage of natural gas in aquifers has been practiced for over 40 years as a cost-effective means of meeting peak demand. The process is inefficient, however, in that much of the stored gas cannot be recovered. Reasons for poor recovery include migration of gas beyond the designated storage volume, formation of isolated gas bubbles not in communication with injection/withdrawal wells, and watering-out of withdrawal wells before all gas has been recovered. These problems result from the fact that gas has a higher mobility in porous media than the water it displaces. Historically these problems have been dealt with by injecting large amounts of "base gas," which is not expected to be recovered. Base gas currently accounts for 60% of all gas in underground storage, with the proportion being greater in specific storage facilities. Controlling the mobility of stored gas could make available much of the presently unavailable base gas and sharply reduce the base-gas requirement for future storage facilities.

Foam has been used as a mobility control agent for gas in enhanced oil recovery, and its ability to block gas flow has been demonstrated (Bernard and Holm, 1964). Figure 1 shows how a foam barrier surrounding stored gas could reduce fingering and contain the stored gas in a deeper, more compact storage bubble nearer to the injection/withdrawal well, thereby reducing the base-gas requirement. We have undertaken to investigate the feasibility of using foam to improve the efficiency of underground gas storage. During the first year of this project, laboratory experiments have resulted in developing stable, brine-compatible foamer solutions, measuring the rheological properties of foam flowing in a sandpack, and demonstrating the complete but temporary blocking of gas flow by foam in sandpacks. The first year's effort also included developing a numerical simulation capability for studying foam flow in porous media. A brief summary of each of these activities follows.

DEVELOPMENT OF STABLE FOAMER SOLUTIONS

Brines in gas storage reservoirs commonly have high salinity and hardness. A synthetic brine that simulated a typical gas storage aquifer was used in

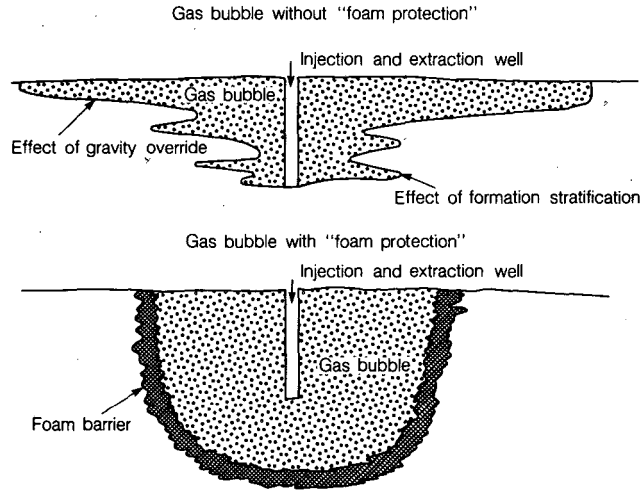

Figure 1. Improvement in gas storage resulting from use of foam to control gas mobility. [XBL 874-10557]

this work, containing 5410 mg/L Ca, 1260 mg/L Mg, 66,700 mg/L total dissolved solids, and 18,750 mg/L as $CaCO_3$ hardness. Alkylethoxysulfate surfactants (Shell Development Co. Enordet AES) were found to be compatible with this brine; sulfonate surfactants formed precipitates with the Ca ions.

Stable foams are required for gas storage applications. Foams formed by anionic surfactants such as AES can be stabilized by the addition of long-chain alcohols (Schick and Fowkes, 1957; Sharma et al., 1984). A series of foamer solutions containing various AES surfactants (1% in synthetic brine) and straight-chain alcohols (concentrations ranging from 0 to 0.8%) were evaluated for foam stability. The carbon-chain lengths of the AES molecules and the alcohols were matched as closely as possible. These commercially available materials are not single compounds but contain a range of chain lengths—e.g., C_{12} to C_{15}. Foam stability was evaluated using a Ross-Miles pour test, in which a volume of liquid is dropped from a pipette through a specified distance into a graduated cylinder. The volume of foam formed is measured initially and at intervals to determine both the foam-forming ability of the solution and the stability of the bulk foam formed in the test. This test does not duplicate the survival of foam in a porous medium but does discriminate among foamer solutions to select those that form stable lamellae (liquid films).

The results of a typical series of tests are shown in Fig. 2. Here the surfactant (designated AES 1213-6.5S) was $CH_3(CH_2)_{(11-12)}-(O-CH_2CH_2)_{6.5ave.}-OSO_3^-Na^+$, and the alcohol (Neodol 25) was $CH_3(CH_2)_{11-14}OH$. As shown in Fig. 2 addition of Neodol 25 significantly increases the stability of the foam. However, addition of Neodol 25 at concentrations greater than 0.2% mainly increases the viscosity of the solution, thereby reducing the volume of foam initially formed in the test. Similar results were obtained with other AES surfactants.

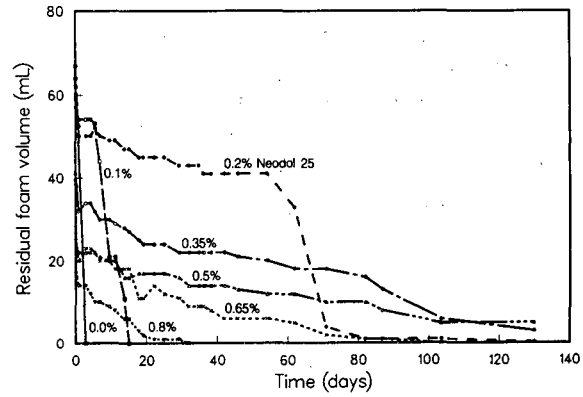

Figure 2. Increase in foam stability produced by addition of varying amounts of Neodol 25 to 1% AES 1213-6.55 in synthetic Mt. Simon brine. [XBL 871-9886]

RHEOLOGY OF FOAM FLOWING IN A SANDPACK

The rheological properties of foam in porous media are needed to design the emplacement of a foam barrier. The apparent viscosity of foam flowing in a sandpack was measured using the apparatus shown in Fig. 3. For this experiment a low-stability foam (1% Triton X-100 in distilled water) was used, because this reduced the effects of flow history and permitted repetition of measurements without excessive waiting for steady-state conditions. The sandpack was made from Ottawa flint shot 3.0 sand with a permeability of 93 d. Gas was injected at a constant pressure and liquid at a constant flow rate. The flow rates of gas and liquid were measured by timing and weighing the flow of foam exiting the sandpack into a pre-weighed graduated cylinder. Figure 4 shows the gas flow rates as a function of the liquid flow rate for a range of gas-injection pressures. The results in Fig. 4 are counterintuitive, confirming that bulk foams exhibit unusual rheological behavior. When gas was injected at constant pressure, the gas flow rate depended upon the liquid flow rate; as the liquid flow rate was increased, the gas flow rate also

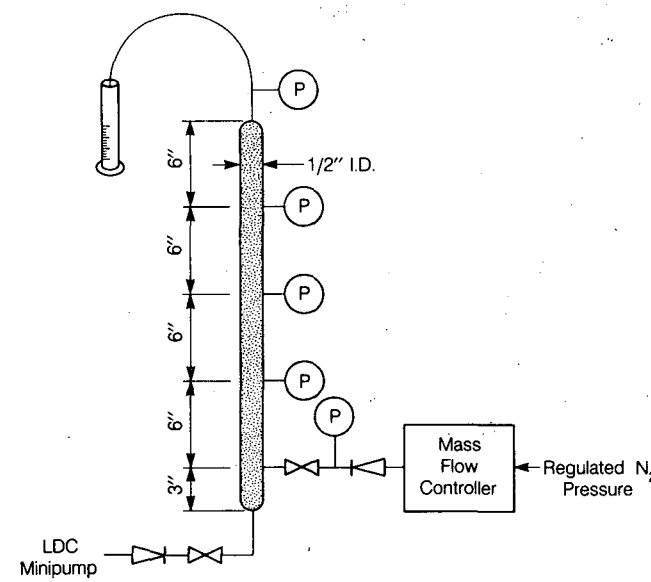

Figure 3. Apparatus for measuring rheological properties of foam flowing in a sandpack. [XBL 871-9876]

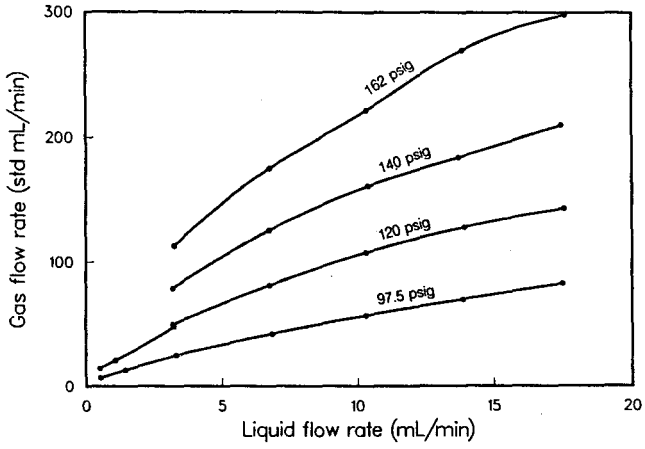

Figure 4. Foam rheology in a sandpack. Plot of gas injection rate (cm^3/min measured at 1 atmosphere) versus liquid injection rate for various values of the gas injection pressure. [XBL 873-1479]

increased. The ratio of gas to liquid flow rate was almost completely determined by the gas-injection pressure.

By evaluating the pressure distribution along the length of the sandpack, and the total volumetric flow rate, the apparent viscosity of foam can be calculated for a wide range of conditions. The results of these calculations are illustrated in Fig. 5, which demonstrates that the apparent viscosity varies with the

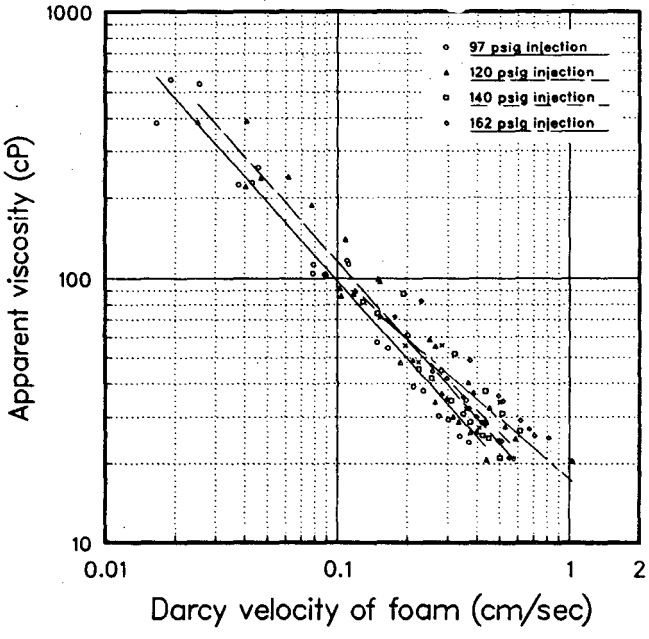

Figure 5. Foam rheology in a sandpack. Plot of calculated apparent viscosity as a function of velocity. [XBL 873-1480]

foam flow rate. This non-Newtonian flow behavior has been observed for foam both in porous media (Treinan, 1985) and in bulk foams (Fried, 1961, and many other workers since; see review by Persoff et al., 1987). Although it is convenient to use the apparent viscosity of foam for macroscopic modeling of foam flow in porous media, we do not imply that this simple description is adequate for describing flow on a pore level. We believe instead that liquid flows through small pores and that gas bubbles, separated by liquid lamellae, flow through large pores. No continuous gas phase is believed to exist. The gas bubbles and liquid continually segregate and recombine at the pore throats to form the observed foam.

BLOCKAGE OF GAS FLOW BY FOAM

The concept of using foam to control the mobility of gas injected for storage depends upon the ability of foam to block the flow of gas. We have demonstrated that gas flow can be blocked by foam in sandpacks. For these experiments a stable foamer solution consisting of 1.0% AES 1213-6.5S and 0.2% Neodol 25 in brine was used. The apparatus was similar to that shown in Fig. 3 but with only one pressure gauge at the inlet. Foam was formed by injecting gas at constant pressure and liquid at constant flow rate; after steady-state conditions were reached, the gas flow was blocked by stopping the liquid flow and rapidly reducing the gas-injection pressure from the "injection" pressure to the "holding" pressure. When this was done the bubbles in the pores expanded, causing them to become wedged in pores and unable to squeeze through pore throats under the available pressure gradient. Complete blocking of gas flow was obtained in all experiments in which the absolute holding pressure was less than 74% of the absolute injection pressure. The duration of the blocked condition was highly variable, ranging from less than 1 day to 48 days. Such variability apparently results from the difficulty of reproducing the same conditions at blocking (number and location of lamellae) and from the spontaneous rupture of the metastable lamellae, which is a random process. The permeability to gas after breakthrough was less than 1% of the intrinsic permeability of the sandpack in all cases.

NUMERICAL MODELING

The behavior and flow of foam in porous media is governed by a complex interplay of many different processes on a pore level. On a phenomenological level perhaps the most difficult aspect of foam flow

is the possibility of strong hysteretic effects: the transport properties of foam can change tremendously as a function of time, as foam quality and texture (bubble size) is altered by flow processes on different space and time scales. Many aspects of foam behavior on a pore level have been clarified in recent experimental and theoretical work, but there appears to be a long way ahead before a realistic mechanistic model for foam flow in porous media can be constructed.

Foam is a discontinuous fluid, made up of gas bubbles and thin liquid lamellae. The flow and behavior of foam in permeable media involves complex gas-liquid-solid interactions on the pore level, which are incompletely understood at the present time. In the present context we are interested in the behavior and flow of foam in porous media on a macroscopic scale. Although microscopic (pore-level) analysis can provide useful guidance, it does not offer a practical way to describe foam behavior on a field scale. We expect that much of the concepts and parameters to be employed in a macroscopic model for foam flow will have to be developed in a phenomenological way, using laboratory experiments.

The starting point of our numerical modeling efforts is the general-purpose simulator MULKOM, which was developed at LBL to model nonisothermal flow of multiphase multicomponent fluids in permeable media (Pruess, 1983). This program has been modified to simulate foam flow in a macroscopic, phenomenological manner and used to develop design parameters for the laboratory facility and to study foam injection into a storage reservoir in both one- and two-dimensional radial geometries. A more realistic version of the code that includes the non-Newtonian nature of foam is now being developed. When complete, the model will be used to investigate the performance of various schemes for using foam to improve the efficiency of underground natural gas storage projects.

CONCLUSION

This work shows that stable foams can be produced in hard brines typical of gas storage reservoirs by using a combination of AES surfactant and long-chain alcohol. Foams flowing in porous media exhibit strongly non-Newtonian rheology approximately described by a power-law relationship between apparent viscosity and foam velocity. Foams flowing in porous media can be blocked in place by reducing the gas-injection pressure and can be used in this condition to block gas flow. A phenomenological computational model for gas-foam-liquid displacement in porous media has also been developed.

REFERENCES

Bernard, G.G., and Holm, L.W., 1964. Effect of foam on permeability of porous media to gas. Soc. Pet. Eng. J., v. 4, p. 267–274, September.

Fried, A.N., 1961. The foam-drive process for increasing the recovery of oil. U.S. Department of Interior, Bureau of Mines, Report of Investigations RI-5866.

Persoff, P., Wu, Y.S., Benson, S., Radke, C., and Witherspoon, P.A., 1987. Feasibility analysis and development of foam protected underground natural gas storage: Part I. Literature survey. Lawrence Berkeley Laboratory Report LBL-23431.

Pruess, K., 1983. Development of the general purpose simulator MULKOM. *In* Earth Sciences Division Annual Report 1982. Lawrence Berkeley Laboratory Report LBL-15500, p. 133–134.

Schick, K.J., and Fowkes, F.M., 1957. Foam stabilizing additives for synthetic detergents. Interaction of additives and detergents in mixed micelles. J. Phys. Chem., v. 61, p. 1062–1068.

Sharma, M.K., Shah, D.O., and Brigham, W.E., 1984. Correlation of chain length compatibility and surface properties of mixed foaming agents with fluid displacement efficiency and effective air mobility in porous media. I&EC Fundamentals, v. 23, p. 213–220.

Treinan, R.J., Brigham, W.E., and Castanier, L.J., 1985. Apparent viscosity measurements of surfactant foam in porous media. Stanford Univ. Petroleum Research Inst. Report No. Supri TR-48, 33 p.

A Multiple-Porosity Method for Simulation of Naturally Fractured Petroleum Reservoirs

Y.S. Wu and K. Pruess

The MINC method (Multiple Interacting Continua; Pruess and Narasimhan, 1985) is used to study oil-recovery mechanisms in fractured reservoirs and to obtain insight into the behavior of water-oil flow during the imbibition process. Imbibition is regarded as a very important mechanism of oil production in waterflooding or waterconing of fractured reservoirs. For multiphase flow, pressure, viscous, gravitational, and capillary forces should all be taken into account. To understand the roles played by the four kinds of forces, we have studied the imbibition process with the MINC method, the conventional double-porosity method (Kazemi et al., 1976), and a detailed explicit discretization of matrix blocks. Comparison of the results from the three methods shows that the MINC method can give an accuracy of better than 1% at all times, whereas the double-porosity approximation with quasisteady interporosity flow can produce large errors, especially for matrix blocks with low permeability or large size.

We have also used the MINC method to match the published data of a five-spot waterflood (Thomas et al., 1980) and to study the coning behavior of a well with bottom-water drive in a fractured oil reservoir (Chen, 1983). Satisfactory results have been obtained for the two examples. In both the imbibition study of individual matrix blocks and the field-scale applications, the MINC method is found to give more reliable history matching and behavior predictions for the simulation of fractured reservoirs than the conventional double-porosity method (DPM).

In most previous analytical or numerical studies of multiphase flow in porous media, it has been taken for granted that the matrix system can be treated as a single continuum with (locally) uniform pressure and fluid-saturation distributions. It has never been established how much error will be introduced by this treatment and under what conditions the quasisteady approximation for interporosity flow is acceptable for engineering applications. Our study of the applicability of DPM is based on an analysis of the results from individual block-imbibition studies and field-scale examples with MINC and DPM. We find that DPM is often not suitable for the simulation of oil-water imbibition processes in naturally fractured reservoirs. Depending on the reservoir fluid and the rock properties, DPM may either overestimate or underestimate imbibition oil recovery from matrix blocks, especially for matrix blocks with low permeability and large size or for high oil viscosity. In some special cases, the results from MINC and DPM calculations are very close, either because of similarities in individual block responses predicted from either method or because of the compensatory effect of global flow in the fractures on individual block-imbibition response in field-scale modeling. In general, it will be difficult to determine the suitability of DPM for a given reservoir problem. We suggest that individual matrix-imbibition studies be carried out with various possible reservoir parameters, using DPM approximation as well as explicit discretization, before applying DPM to actual reservoir simulation. Comparing the results of DPM and the Explicit-Discretization Method (EDM) for individual matrix blocks may provide clues to the accuracy that can be expected from the DPM approximation in field studies. When changes in water saturation in the fractures are rapid, as may often happen in coning problems or in response to rate changes, it is usually necessary to account for the transient flow inside the matrix blocks and between matrix and fractures.

IMBIBITION OIL RECOVERY

Imbibition displacement of oil by water in relatively tight matrix blocks is a basic oil-recovery mechanism in fractured reservoirs, since most of the oil in place is present in the low-permeability matrix system and flows into the fracture system under pressure, viscous, gravitational, and capillary forces during oil production. Detailed simulations of individual matrix blocks surrounded by water and oil have been performed to study oil-recovery mechanisms and to demonstrate the validity of the MINC method. The MINC results are compared with predictions from DPM and EDM.

Comparing the oil recovery calculated by the three methods, it was found that the MINC method is accurate enough to simulate the water-oil imbibition process, whereas the DPM approach can give very large errors because it neglects transient flow in the matrix. In all cases we have studied, there is excellent agreement between the MINC and EDM results. It is interesting to note that the MINC

method requires only a modest increase in computational work in comparison with DPM because of the one-dimensional treatment of flow in the matrix, and it saves much more computer time and storage than EDM.

As can be seen in Fig. 1 (top), the results of MINC (or EDM) and DPM show a large difference in oil recovery. The reason for this difference becomes apparent from the plot of imbibition rates (flow rate of oil from matrix into fractures) versus time (Fig. 1, bottom). The imbibition rates of the two methods differ markedly at early times, because DPM underestimates the capillary gradient near the matrix block surface. In fact, in DPM the initial differences in capillary pressures between matrix and fractures are assumed to occur over a quasisteady flow distance D, which is much larger than the nodal distance we employ for the first matrix continuum in the MINC method. At later times the MINC method predicts a buildup of water saturation near the matrix block surface, which diminishes the capillary pressure gradient that drives interporosity flow, as well as oil relative permeability. This results in a steeper decline in imbibition rate than that predicted from the DPM approximation, in which all saturation changes are averaged over the entire matrix block. Therefore, at intermediate times, DPM overpredicts imbibition rates. Eventually, for very late times, the DPM imbibition rate declines below the MINC rate. This happens because, for $t \to \infty$, all approximations must converge to the same total oil recovery, which corresponds to attainment of capillary equilibrium between matrix and fractures.

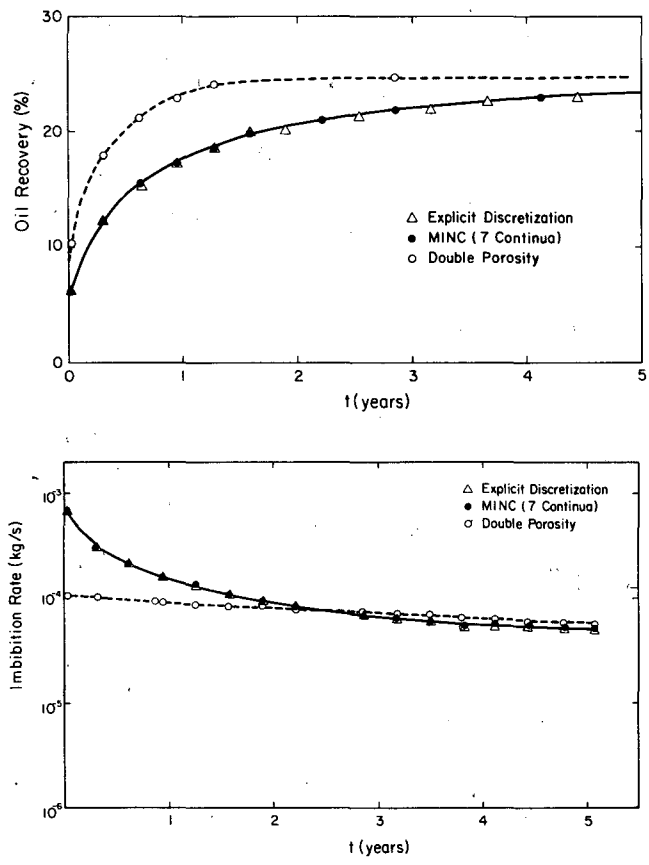

Figure 1. Imbibition recovery (**top**) and imbibition rate (**bottom**) from a cylindrical matrix block (data from Thomas et al.) [top, XBL 857-10605; bottom, XBL 856-10598]

It can be shown that, as far as interporosity flow is concerned, a change in linear matrix block size L by a factor α is equivalent to a change in block permeability k by a factor $1/\alpha^2$, provided gravity effects are small compared with capillary effects. We have verified this by comparing calculations for cylindrical and cubical matrix blocks of widely different permeability and size. This result makes it possible to plot imbibition oil recovery in terms of a dimensionless time, t_D, which is proportional to $(k/L^2)t$.

One of the most difficult problems in history matching and performance prediction of fractured reservoirs is to determine the matrix block size, because it cannot be measured directly. The parameter can usually be established only after tedious history-matching calculations. The equivalence between changes in matrix block size and permeability facilitates practical application of the MINC method to actual reservoir problems and history matching. A computational grid for a MINC model of a flow system needs to be generated only once for a given matrix-block shape; changes in matrix-block sizes can then be implemented simply by appropriate adjustments in matrix permeability.

A FIVE-SPOT EXAMPLE AND A CONING PROBLEM

To demonstrate the application of the MINC method to a field-scale problem, we present a comparison with previous calculations of Kazemi et al. (1976) and Thomas et al. (1980) for a five-spot waterflood. We have made DPM and MINC calculations for this problem using a discretization of five continua. Surprisingly, the results for the produced water-oil ratio turned out to be virtually indistinguishable from those obtained in the double-porosity approximation with shape factor $\sigma = 0.36$, even though over much of the five-spot pattern the saturation distributions are quite different in both cases. How can a transient and a quasisteady approximation for interporosity flow, which give substantially different imbibition responses for individual matrix blocks, end up yielding nearly indistinguishable

water-oil ratios in a five-spot flood? The answer is that the aggregate response of many matrix blocks in a flood problem tends to compensate for differences in individual block responses. In the present case, the double-porosity approximation gives more rapid oil recovery from an individual block over virtually the entire time period of interest. Therefore, in the double-porosity calculation, matrix blocks near the injector will take up more water and deliver more oil than predicted from the MINC method, so that blocks further downstream from the injector will "see" more oil and less water in the fractures. Therefore, those more distant blocks will give smaller imbibition rates. From this consideration it is clear that there will be a general tendency for aggregate effects of blocks to compensate for differences in individual block response. The fact that this compensation is virtually quantitative in the present case is to be considered fortuitous.

The MINC approximation was also used to match the observed coning behavior of a well in the North China oil field. The data have been previously analyzed by Chen (1983), whose basic reservoir model is axially symmetric, the symmetry axis coinciding with the well. The upper part of the reservoir is the oil zone, the middle is the transition zone, and the lower part is the water zone. Near the top of the water zone there is a thin, impervious horizontal break. The bottom water is supplied from the lowest surface on which the pressure is maintained at a constant value. The top and the lateral boundary of the reservoir are assumed to be sealed; i.e., there is no flow across those boundaries.

The results of the history matching and the behavior prediction are shown in Fig. 2, computed by MINC and DPM. Both models give a reasonable match for observed performance; differences between DPM and MINC are small in this case.

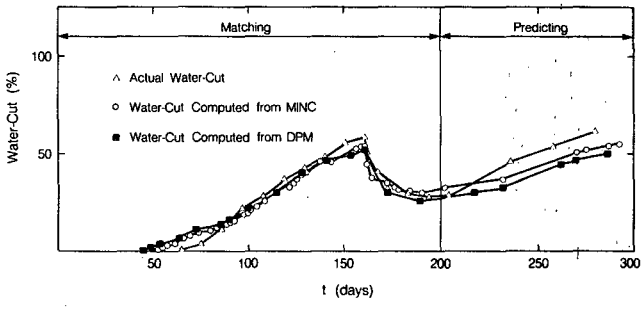

Figure 2. Chen's coning problem. [XBL 861-10503]

ON THE VALIDITY OF THE DOUBLE-POROSITY METHOD

For practical simulation applications it would be preferable to use the simpler DPM approximation whenever possible and to resort to the more complex MINC description only in cases where the accuracy of DPM is poor. The limitations of DPM can be seen best when comparing the temporal evolution of imbibition rates in individual matrix blocks with the more accurate MINC prediction. As was discussed above, one can distinguish three time periods:

1. An early period in which DPM underpredicts imbibition rate because it underpredicts the capillary gradients at the matrix block surface.
2. An intermediate period in which DPM overpredicts imbibition rate because it underestimates buildup of water saturation near the matrix block surface.
3. A late period in which DPM again underpredicts imbibition rate because in the intermediate time period the block has moved closer to eventual capillary equilibrium with the fractures than would be predicted from MINC.

The relative lengths of these time periods, and the amount by which they differ between DPM and MINC, depend upon formation and fluid properties. Generally speaking, differences tend to be larger (DPM less accurate) for small matrix permeability, large matrix-block dimensions, high matrix porosity, or high oil viscosity.

Reservoir response is in general more complicated than individual block response, because it involves a superposition of effects from many matrix blocks. Depending upon their location in the reservoir relative to the water table, and to injection and production wells, different blocks will be at different periods of the imbibition "cycle." Aggregate imbibition response of many blocks in a reservoir may be similar in DPM and MINC, even if individual block responses are rather different.

For practical reservoir simulation problems, it would be desirable to be able to evaluate the accuracy to be expected from DPM without actually going through a reservoir-wide MINC calculation as well. It may be possible to accomplish this by comparing and adjusting individual block imbibition data from MINC and DPM as a function of total recovery rather than as a function of physical time.

CONCLUSIONS

1. The conventional double-porosity method can give large errors for simulation of oil recovery from individual matrix blocks or from a reservoir by water-oil imbibition mechanisms. The errors increase rapidly with enlargement of matrix blocks or fluid viscosity and with decrease in rock permeability.

2. The method of "multiple interacting continua" (MINC) takes into account the transient flow of fluids both in the matrix system and in the fractures. Comparisons with calculations using a detailed explicit discretization of matrix blocks have shown that the MINC method gives accurate predictions for water imbibition.

3. Results of five-spot waterflood and coning simulations indicate that the aggregate response of many matrix blocks in a reservoir has a general tendency to compensate for differences in individual block response. This suggests that the double-porosity method with quasisteady approximation for interporosity flow may be applicable even in cases where its basic assumptions are poorly justified.

4. An estimation of the suitability of the double-porosity approximation for waterflooding and coning problems can be obtained by comparing quasisteady and transient imbibition predictions for individual matrix blocks.

REFERENCES

Chen, H.-Z., 1983. Numerical simulation of coning behavior of a single well in a naturally fractured reservoir. Soc. Pet. Eng. J., v. 23, p. 879–884.

Kazemi, H., Merrill, L.S., Porterfield, K.L., and Zeman, P.R., 1976. Numerical simulation of water-oil flow in naturally fractured reservoirs. Soc. Pet. Eng. J., v. 16, p. 317–326.

Pruess, K., and Narasimhan, T.N., 1985. A practical method for modeling fluid and heat flow in fractured porous media. Soc. Pet. Eng. J., v. 25, no. 1, p. 14–26.

Thomas, L.K., Dixon, T.N., and Pierson, R.G., 1980. Fractured reservoir simulation. Paper SPE 9305 presented at SPE-AIME 55th Annual Fall Meeting, Dallas, Texas, September 21–24, 1980.

GEOCHEMISTRY

Investigators in the Geochemistry group address problems that arise due to chemical reactions in the earth's crust. These problems usually involve interactions between subsurface aqueous fluids and the surrounding geologic media—both the chemical alteration of rock and soil by fluids and the chemical reactions that occur within the fluids. Many of these reactions occur during the transport of fluids; accordingly, our studies have a strong impact on the disposal of radioactive and toxic wastes. The successful containment of waste species is heavily dependent on the movement of dissolved chemical species in groundwaters. As a part of this overall study, separate investigations are conducted in areas of radiochemistry, inorganic chemistry, and surface chemistry in support of geologic transport models and codes that require such data.

Research in the Geochemistry group covers several themes related to geochemical reactions and transport. Several programs address field-oriented research, with the geochemical aspects being strongly coupled with groundwater migration. The largest one of these is that involving the agricultural drainage into the Kesterson Reservoir. This research contains large components of aqueous analytical chemistry, chemical-species modeling, and hydrochemistry. To date it has yielded considerable basic research regarding such drainage systems in general, as well as data that will help in the remediation of the selenium contamination of the site. Other research in the group is related to geochemical and chemical modeling aspects of nuclear waste repositories—specifically, how radionuclide species dissolve, react, and migrate under repository conditions.

The Geochemistry group also conducts basic research as it relates to geologic processes — processes that occur in the earth's crust and in the upper mantle. Thermodynamic studies of liquid silicate minerals are in progress, along with studies of NaCl in steam. Thermodynamically coupled processes are being modeled, along with chemical species, as a function of different experimental parameters, such as pH, temperature, and oxidation potentials. Basic research is also in progress that concerns interfacial geologic chemical reactions; these reactions address both solid-liquid and solid-gas surface reactions of geologic processes, such as petroleum-precursor reactions with rocks and minerals, carbon dioxide reactions with geologic materials, and aqueous solution chemical alteration of geologic surfaces.

Pressure-Solution Geochemistry

John A. Apps

When a fractured rock is stressed under waste repository conditions, the deformation is accommodated in part by sliding movement along the fractures. All natural fractures display a certain roughness due to the inhomogeneous nature of the rock and the crystal fabric. The roughness prevents further movement unless localized stresses build up to the level where cataclasis occurs and interstitial crystals are comminuted to form a "gouge."

If the rock is saturated with an aqueous phase and the localized stresses are below the level at which cataclasis occurs, then the asperities, or areas of contact, may change shape through mechanisms involving deformation or preferential dissolution of the minerals contained within the asperities. This leads to slow progressive movements along fractures and the redistribution and recrystallization of minerals to form characteristic "slickenside" textures. There is evidence that such a process known as pressure solution may drastically change the physical, hydrologic, and chemical properties of the rock, particularly in the near field of a nuclear waste repository, where high stress gradients are caused by excavation of the repository access tunnels and waste package wells. However, no information is readily available that permits an assessment of the significance of pressure solution, although failure to account for this process may seriously affect predicted release rates of radionuclides from breached radioactive waste containers. A satisfactory mechanistic interpretation of pressure solution has so far not been forthcoming, even through several phenomenological and theoretical studies have addressed this subject in the last decade.

The purpose of the research outlined below is (1) to review previous theoretical and experimental studies pertaining to pressure solution, (2) to develop an experimental design, which can identify the mechanism(s) and can quantitatively determine the rate of strain as a function of applied stress and temperature, (3) to apply the resulting data to quantitative models in order to predict the seismic stability of fractures subjected to stress in the pressure solution domain, and (4) to estimate the consequences of pressure solution on the porosity, permeability, strength, and rate of deformation of the rock mass in the vicinity of a waste repository. This article summarizes progress in the first two of these areas.

LITERATURE SURVEY

Rocks deform through a variety of mechanisms, depending on stress and temperature. The mechanisms have been reviewed by Rutter (1976, 1983) and McClay (1977) and include:

1. Cataclasis.
2. Dissolution and precipitation of minerals from an intergranular pore fluid (i.e., pressure solution).
3. Coble creep (interfacial-phase diffusion).
4. Nabarro-Herring creep (solid-state diffusion).
5. Intracrystalline plastic flow (e.g., dislocation creep or dislocation glide).

Pressure solution is considered by most investigators to be the dominant mechanism of rock deformation in water-saturated rocks below 500°C. Kerrich et al. (1978) have determined that pressure solution in rock grains 100–1000 μ in diameter is the most probable deformation mechanism for calcite below 300°C and for quartz below approximately 450°C. Coble creep probably participates in the pressure-solution phenomenon, but the interfacial phase-diffusion coefficient is not well known. This is a serious difficulty, as will be discussed later.

Pressure solution arises from localized stress concentrations at the points of contact of individual rock grains and leads to enhanced aqueous solubility. The increased chemical potential causes dissolved constituents to diffuse through the aqueous pore fluid to regions of lower localized stress, or voids, where precipitation occurs. Robin (1978) has conducted heuristic calculations of this mechanism with respect to quartz and shown that even supersaturation with respect to amorphous silica is possible under some circumstances, as is confirmed by de Boer et al. (1977). Experimentally observable compaction of quartz aggregates due to pressure solution has been obtained within two weeks at 290°C by Sprunt and Nur (1977) and at 340°C by de Boer et al. (1977).

A considerable divergence of opinion appears to exist regarding the actual mechanism responsible for pressure solution. Rutter (1976, 1983) and other workers (e.g., Paterson, 1973; Robin, 1978; and Green, 1980) conceive the interfacial contacts of

mineral grains to be separated by a load-bearing film of interfacial water so thin that it no longer possesses the properties of bulk water, estimated by Rutter (1983) to be about 10 Å thick. This interfacial phase, containing partially ordered water with enhanced viscosity, can resist the localized stress to the extent that it cannot be squeezed entirely from the interface. Under these conditions, the solid phase is assumed to show enhanced solubility in the interfacial phase (most minerals, including quartz, show a positive pressure-solubility coefficient), leading to dissolution at the interface and diffusion of the dissolved constituents into intergranular pores, or the voids between the asperities of a fracture. Because the interfacial phase is assumed to have properties intermediate between those of a liquid and a solid, the interfacial-diffusion coefficient is expected to lie somewhere between that in the aqueous phase ($\approx 10^{-5}$ cm^2/s at 25°C) and the diffusion coefficient in the solid at the same temperature ($\approx 10^{-25}$ cm^2/s at 25°C). The magnitude of the interfacial-diffusion coefficient is poorly known. Rutter (1976, 1983) estimates it to be about 10^{-10} cm^2/s at 25°C, whereas Elliot (1973) believes it to be about 10^{-16} cm^2/s on the basis of independent field evidence. From experimental data Rutter and Mainprice (1978) and Rutter (1983) show that the activation enthalpy, ΔH^*, lies between 8 and 10 kcal/mole, a value intermediate between that of molecular diffusion in water ($\approx$ 2–3 kcal/mole) and molecular diffusion in a solid ($\approx$ 25 kcal/mole). This has recently been substantiated by Brantley et al. (1986), who estimate about 10–17 kcal/mole.

Pressure solution depends on three transport mechanisms:

1. Surface dissolution of the mineral in the interface.
2. Diffusion of the dissolved constituents through the interfacial phase.
3. Precipitation of the mineral or secondary mineral in the voids under hydrostatic pressure.

Rutter argues that the wide temperature range over which pressure-solution phenomena are observed in nature suggests a temperature-insensitive process such as diffusion as the rate-controlling mechanism. However, it is to be expected that with falling temperature, mass transport through an aqueous phase will undergo a transition from diffusion control to surface-dissolution rate or precipitation-rate control, especially in the case of quartz.

An entirely different interpretation is advanced by Lehner and Bataille (1984), who envisage the interface between two crystals to be occupied by an aqueous phase possessing the characteristic transport properties of water, i.e., with an ionic-diffusion coefficient of $\sim$ 5 cm^2/s at 25°C and an activation energy of 2–3 kcal/mole. To account for enhanced solubility resulting from stress concentrations at the interface, a "local dissipation jump condition" is postulated in identifying the thermodynamic force during dissolution. This interpretation automatically leads to diffusion control through the interface at a much higher temperature than would be deduced by Rutter under identical conditions.

In neither of these two models is enhanced dissolution attributed to the generation of defects in the crystal lattice due to high localized stress concentrations at the points of contact of mineral grains. However, there is circumstantial information, strengthened by recent unpublished research by Meike (1986), that the primary cause of enhanced dissolution may be defect production in the crystalline solid in regions of high localized stress. Supporting evidence comes from recent studies by N.G.W. Cook (personal communication, 1986), who shows that voids or cracks in a stressed material are the locus of stress concentrations 5 to 10 times greater than the deviatoric stress. Furthermore, A. Meike (personal communication, 1986) found that defect formation in calcite crystals will occur at stresses up to 10 orders of magnitude below the yield modulus.

If pressure-solution phenomena can be attributed to a mechanistic cause of the type described, then assignment of a distinct region in applied stress-temperature space as attempted by Rutter (1976) is not strictly valid, as the same defect-producing mechanisms responsible for dislocation glide and dislocation creep, which cause deformation in high-stress high-temperature domains, are also operating at lower applied stresses and temperatures. However, under milder conditions, the dominant effect is one of enhanced aqueous solubility, rather than plastic flow. Pressure solution may still be controlled by diffusion through an interfacial fluid, but the chemical potential gradients would be substantially higher than postulated by Rutter.

EXPERIMENTAL DESIGN

The development of an experimental design to identify and quantify pressure-solution mechanisms in bulk materials is fraught with serious measurement problems. Strain rates estimated to occur in natural systems as a result of pressure solution in quartz are so small as to be unmeasurable, i.e., 10^{-12}

to 10^{-14}/s (Rutter, 1983). The practical limitation for strain measurement in the laboratory is 10^{-8} to 10^{-9}/s. At these rates, machine stiffness is critical, and temperature control must be extremely precise. Linear variable differential transformers must be employed to measure strain.

The analysis given by Rutter (1983) would suggest that the strain rate due to pressure solution in a crystal aggregate is sensitive to grain size. His analysis suggests an inverse cubic dependence. The strain rate is also accelerated by temperature, but because of the assumed impact of diffusion control through the interfacial boundary, a relatively small temperature dependence is expected. According to Rutter's model, optimum strain rates calculated to be experimentally achievable in quartz aggregates 1 to 10 μ in grain size would lie in the range of 10^{-7} to 10^{-8}/s at 300–400°C, which is close to the experimentally measurable limits. Such an approach has recently been attempted by Brantley et al. (1986) with quartz aggregates of 1–2, 3–5, and 10–30 μ grains at 400°C and 600°C, a fluid pressure of 1 kbar, and effective pressures of 0.4, 1.0, and 1.5 kbar. They interpreted their results as indicating a diffusion-controlled process responsible for compaction of the aggregate—a result not unexpected under these conditions, regardless of the model assumptions. The maximum strain rate was about 10^{-7}/s.

The disadvantage with an approach like that used by Brantley et al. (1986) is the difficulty in identifying and quantifying the actual mechanism involved in pressure solution, as only the bulk properties of the deforming crystal aggregate can be measured. However, designing an experiment that allows segregation of the mechanisms is an undeniable challenge. Three issues require clarification and quantification:

1. The effect of hydrostatic pressure on the dissolution and precipitation kinetics of mineral phases as a function temperature.
2. The effect of defect creation on the kinetics of mineral dissolution as a function of applied stress and temperature.
3. The role of interfacial-boundary diffusion and its magnitude as a function of temperature, pressure, and interfacial width.

After careful review of alternative experimental configurations, it was decided that examination of the mechanisms would be best separated into different experiments. The first experiment would measure the kinetics of dissolution under a variety of temperatures, pressures, and applied stress, essentially covering items (1) and (2), and a second experiment would deal with the role of interfacial diffusion. Quartz was chosen for examination because its thermodynamic properties have been accurately determined (Kilday and Prosen, 1973) and its solubility has been repeatedly measured as a function of temperature and pressure and is very well known. Furthermore, several studies have been made of the kinetics of quartz dissolution and precipitation in recent years that permit semiquantitative if not quantitative estimates of dissolution rates. Quartz also is a common rock-forming mineral. Other minerals might have been chosen that are more pertinent to a repository environment, e.g., halite or amorphous solids such as the glass mesostatis of basalts or vitrophyres. These may be considered at a future date.

After due consideration of alternative experimental configurations, a preliminary sample design was settled upon: a single quartz crystal fabricated into a cylinder with a slot penetrating the longitudinal axis (Fig. 1) would be enclosed in a flexible stainless steel container and be subjected to a confining pressure P_c. An aqueous fluid would be pumped through the slot at a steady rate equivalent to a pore pressure P_p that would be equal to or less than the confining pressure. Figure 2 is a schematic diagram of the complete system.

The rate of quartz dissolution would be measured as a function of P_c, P_p, temperature, and aqueous-phase composition. The anticipated experimental condition would be $P_c \leqslant 2.0$ kbars, $P_p \leqslant 2.0$

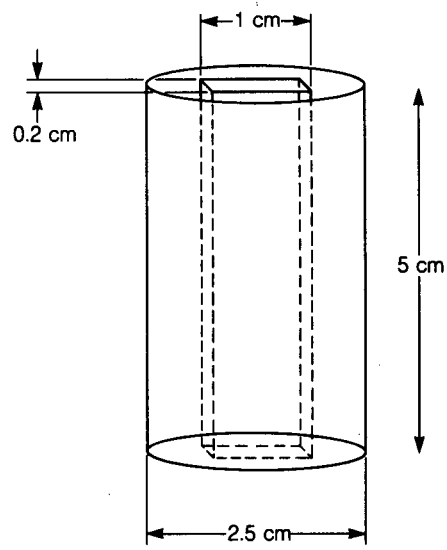

Figure 1. Schematic drawing of a single quartz crystal shaped to measure aqueous dissolution kinetics under stress. [XBL 861-12733]

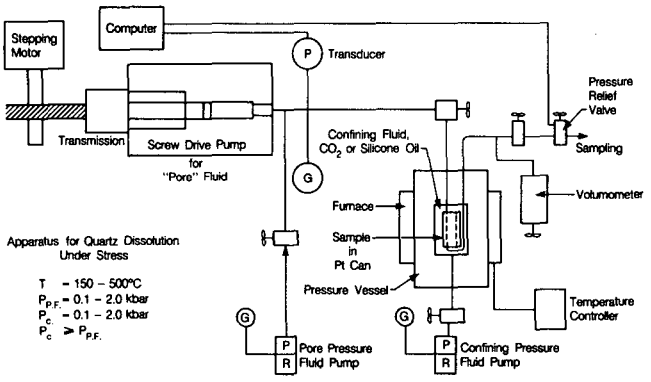

Figure 2. Schematic configuration of apparatus to measure quartz dissolution kinetics under stress. [XBL 8611-12734]

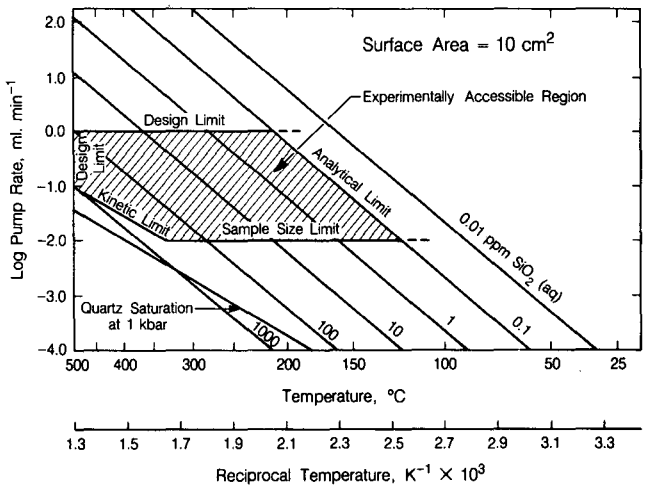

Figure 3. Experimental constraints on the measurement of quartz dissolution kinetics under stress. [XBL 8611-12732]

kbars, and T = 150–500°C. The aqueous-phase solubility would range between 0.0 and 1.0 N NaCl. These conditions are somewhat more extreme than might be encountered in a waste repository but are chosen to ensure the acquisition of experimental data in reasonable time periods.

The experiment would involve measurement of SiO_2(aq) in the effluent stream under the varying conditions of P_c, P_p, and T, with the rate of aqueous-phase flow, and the operating parameters being determined by a readily measurable concentration of silica in the effluent. Calculations using preliminary estimates of silica-dissolution kinetics (Apps et al., 1975) suggest that the range of feasible operating conditions for the base case involving hydrostatic dissolution is as illustrated in Fig. 3. However, these estimates are tentative.

By varying the operating parameters, it is hoped to model consequences of stress corrosion on quartz. When $P_c > P_p$, stress concentrations at the corners of the slot will lead to defect formation and enhanced dissolution. This will in turn accelerate dissolution by an undetermined amount and cause stress corrosion. It is possible that stress corrosion would aggravate the localized stress concentration, inducing a runaway condition. Continuous measurement of SiO_2(aq) under preset parameters would assess the significance of this process. Defect formation as a function of applied stress will be examined both on untreated samples and post-test samples using Lawrence Berkeley Laboratory's 1.5-MV high-voltage transmission electron microscope.

There remains the problem of quantifying diffusion of chemical constituents through interfacial boundaries. So far, no satisfactory experimental design has been devised that represents an improvement over refined versions of experiments already attempted (e.g., De Boer et al., 1977; Sprunt and Nur, 1977; Rutter, 1983; Brantley et al., 1986. This problem is under active consideration, and it is hoped that some resolution will be found shortly.

A major requirement of the current efforts is the quantification of quartz-dissolution kinetics. Significant discrepancies in the activation energies of precipitation are evident from a review of the literature. Because an accurate estimate of the dissolution kinetics of quartz is essential for the design of the planned experiments, a thorough review of existing information in the literature has been made. Some of the described quartz-dissolution measurements were made in alkaline and NaCl solutions at different pressures. An attempt will be made to ascertain whether available data permit an estimate of the dissolution-rate dependency on these parameters.

REFERENCES

Brantley, S.L., Crerar, D.A., and Evans, B., 1986. Rates and mechanisms of porosity reduction in quartz. Implications for fluid flow in rocks. *In* Fifth International Symposium on Water-Rock Interaction, Reykjavik, Iceland, August 8–17, 1986 Extended Abstracts, p. 79–82.

De Boer, R.B., Nagetgaal, P.J.C., and Duyvis, E.M., 1977. Pressure solution experiments on quartz sand. Geochim. Cosmochim. Acta, v. 41, p. 257–264.

Elliott, D., 1973. Diffusion flow laws in metamorphic rocks. Geol. Soc. Am. Bull., v. 84, p. 2645–2664.

Kerrich, R., Beckinsale, R.D., and Durham, J.J., 1978. The transition between deformation regimes dominated by intercrystalline diffusion and intracrystalline creep evaluated by oxygen isotope geochemistry. Tectonophysics, v. 38, p. 241–258.

Kilday, M.V., and Prosen, E.J., 1973. The enthalpy of solution of low quartz (α-quartz) in aqueous hydrofluoric acid. J. Res. Nat. Bur. Stand., Ser. A. Phys. Chem., v. 77A, p. 205–215.

Lehner, F.K., and Bataille, J., 1984. Nonequilibrium thermodynamics of pressure solution. Report No. 25, Division of Engineering, Brown University, Providence, R.I. 52 p.

McClay, K.R., 1977. Pressure solution and Coble creep in rocks and minerals: A review. J. Geol. Soc., London, v. 134, p. 57–70.

Meike, A., 1986. A study of deformation-enhanced dissolution in theory, experiment and nature, based on microstructural evidence (Ph.D. thesis). University of California, Berkeley, California, 166 p.

Paterson, M.S., 1973. Nonhydrostatic thermodynamics and its geologic applications. Rev. Geophys. Space Phys., v. 11, p. 355–389.

Robin, R., 1978. Pressure solution at grain-to-grain contacts. Geochim. Cosmochim. Acta, v. 42, p. 1383–1389.

Rutter, E.H., 1976. The kinetics of rock deformation by pressure solution. Philos. Trans. R. Soc. London, Ser. A., v. 283, p. 203–219.

Rutter, E.H., 1983. Pressure solution in nature. Theory and experiment. J. Geol. Soc., London, v. 140, p. 725–740.

Rutter, E.H., and Mainprice, D.H., 1978. The effect of water on stress relaxation of faulted and unfaulted sandstone. Pure Appl. Geophys., v. 116, p. 635–654.

Sprunt, E.S., and Nur, A. 1977. Destruction of porosity through pressure solution. Geophysics, v. 42, p. 726–741.

Thermodynamic Properties of Silicate Materials

I.S.E. Carmichael, V. Kress, R.A. Lange, and D.A. Snyder

Our program continues to concentrate on the thermochemical and physical properties of silicate melts. These data are useful both for making predictive calculations about the evolution of natural liquids (lavas) and for understanding how melt structure controls the thermodynamic properties of these liquids. Our focus this past year has been on calorimetry at extremely high temperatures and, in cooperation with the National Science Foundation, measurements of densities and compressibilities of silicate liquids.

Although these areas of research will be discussed separately in this report, they complement one another in any complete thermodynamic description of natural lavas. In predicting phase equilibria in magmas, for example, the temperature dependence of the Gibbs free energy (determined calorimetrically) must be known along with the pressure dependence (a function of volume). On a molecular level, these properties are related by similar vibrational contributions and modes of structural relaxation. Specific applications are discussed in each section.

HIGH-TEMPERATURE CALORIMETRY

Accurate thermodynamic data for minerals and their liquids are fundamental to the understanding of thermal histories and the chemical evolution of magmas. Heats of fusion of minerals are of direct use in estimating heat budgets during partial fusion of rock in the crust and mantle and for the assimilation of host rocks by hotter liquids. Chemically, these data enable calculations of solid/liquid equilibria as a function of temperature and pressure. Although such calculations have recently been attempted (Ghiorso and Carmichael, 1985), calorimetric data are still lacking for many important minerals and liquids. Virtually no calorimetric measurements exist for rock-forming minerals above 1800 K. We are rectifying this problem with the construction of an adiabatic drop calorimeter that will not only operate at temperatures up to 2700 K but will do so with an accuracy exceeding that of many measurements at much lower temperatures.

Efforts of the past year have led to the completion of this instrument. The calorimeter block is

now operational, and absolute calibration procedures have been initiated. Preparations are also underway for enthalpy measurements of alpha–Al_2O_3, an NBS calorimetric standard. We expect the system to be fully operational in early 1987.

DENSITIES OF SILICATE LIQUIDS

Recent models of the dynamics of fluids within magma chambers have suggested that small density contrasts in evolving liquids may strongly modify fractionation (e.g., McBirney et al., 1985). Similar buoyancy effects also govern the extraction of primary melts from crystal mushes (McKenzie, 1984; Richter and McKenzie, 1984). The increasing number of such models has led us to measure silicate liquid densities experimentally as a function of composition, temperature, and pressure.

In the past year we have completed a systematic measurement of densities of 23 liquids in the system K_2O–Na_2O–CaO–MgO–Al_2O_3–TiO_2–SiO_2 using the most precise technique available (the double-bob Archimedean method). This has been combined with previous measurements in our lab of the system FeO–Fe_2O_3–SiO_2 to produce a new empirical model for predicting the densities of natural magmatic liquids.

We have restricted our determinations to ternary and quaternary subsystems to facilitate interpretation of melt-structural controls of volumes. The overall precision of the data is better than 0.32% and approaches 0.08% for the least viscous liquids. Accuracy was assessed by measuring molten NaCl and comparing those values with the accepted NBS value (Janz, 1980). We agree within experimental error. All data were fitted with the model equation

$$V_{liq} = \bar{V}_i X_i, \qquad (1)$$

where $\bar{V}_i$ is the partial molar volume for component i and X_i is the mole fraction of component i. Interaction terms of the form $V_{excess} X_i X_j$ were added when significant. Fits for iron-free and iron-bearing liquids were performed separately. The results are shown in Table 1.

Previous reviews of density data of molten silicates have interpreted the data base differently (see Bottinga et al., 1982; Ghiorso and Carmichael, 1984). The controversy centers on the role of the Al_2O_3 component. Bottinga and others have suggested that a slight compositional dependence of the partial molar volume of Al_2O_3 in their fit indicates a changing structural role of the aluminum cation. The increased precision of our data set is due to the absence of interlaboratory errors and the wide range of compositions measured. It therefore serves as a more sensitive test of a possible changing role of Al. We see no evidence of any compositional dependence of the partial molar volume of Al_2O_3. This, coupled with the lack of spectroscopic evidence of such a structural change, leads us to conclude that Al does not change coordination within this compositional range.

COMPRESSIBILITY OF SILICATE LIQUIDS

In order to investigate the pressure dependence of volume, relaxed acoustic velocities have been determined for 8 melt compositions. The ultrasonic interferometry technique of Rivers and Carmichael (1987) was employed. Compositions investigated span a portion of the ternary system Na_2O–Al_2O_3–SiO_2. The compositional and thermal dependence of acoustic velocity, c, prove to be well described by simple mixing of end-member oxide components:

$$c = \left[\bar{c}_i^o + \frac{d\bar{c}_i}{dT}(T - T_o) \right] x_i, \qquad (2)$$

where in this case the bar denotes a partial derivative with respect to x_i and o denotes 1 atmosphere and 1673 K. Regressed values for $\bar{c}_i$ and $d\bar{c}_i/dT$ are in Table 2. The temperature dependence of sound velocity is very low in this system, increasing slightly with decreasing silica.

Isothermal compressibilities ($\beta \equiv (1/V)(\delta V/\delta P)_T$) have been derived for each experiment using the relation

$$\beta = \frac{V}{C^2} + \frac{TV\alpha^2}{C_p}, \qquad (3)$$

where isobaric heat capacity, C_p, volume, V, and isobaric thermal expansion, α, were previously determined in this lab (Stebbins et al., 1984; Stein et al., 1986). Values for $\bar{\beta}$ and $d\bar{\beta}/dT$ regressed from these derived quantities are presented in Table 2. The negative value for $\bar{\beta}_{Al_2O_3}$ is not unreasonable, since it represents a hypothetical component in which all aluminum is in tetrahedral coordination. Octahedrally coordinated aluminum can be expected in compositions with aluminum in excess of charge-balancing sodium (Taylor and Brown, 1979). These values will therefore not be valid in melts with Al > Na.

Though liquid of albite composition ($NaAlSi_3O_8$) is too viscous to be investigated directly, little extrapolation is required to predict an isothermal compressibility for this composition using regressed

Table 1. Empirical partial molar volumes for iron-free and iron-bearing silicate liquids. Numbers in parentheses are one standard deviation.

Iron-free liquids: K_2O–Na_2–CaO–MgO–Al_2O_3–TiO_2–SiO_2		
Oxide component	V_i (1500°C)	
SiO_2	26.86 (0.02)	
TiO_2	28.66 (0.23)	
Al_2O_3	37.55 (0.08)	
MgO	11.79 (0.06)	
CaO	16.87 (0.04)	
Na_2	29.54 (0.04)	
K_2O	47.11 (0.07)	
CaO-TiO_2	−15.24 (0.78)	(excess volume term)

Iron-bearing liquids: Li_2O–K_2O–Na_2O–CaO–MgO–FeO–Fe_2O_3–TiO_2–SiO_2				
Oxide component	V_i (1300°C)	V_i (1400°C)	V_i (1500°C)	V_i (1600°C)
SiO_2	26.92 (0.08)	26.91 (0.06)	26.90 (0.06)	26.90 (0.07)
TiO_2	27.32 (0.61)	28.20 (0.48)	29.03 (0.46)	29.87 (0.54)
Al_2O_3	36.64 (0.23)	36.93 (0.18)	37.18 (0.17)	37.44 (0.20)
Fe_2O_3	41.96 (0.38)	43.03 (0.34)	43.75 (0.36)	45.44 (0.48)
FeO	13.64 (0.09)	13.74 (0.07)	13.98 (0.07)	14.15 (0.08)
MgO	11.17 (0.17)	11.43 (0.13)	11.70 (0.13)	11.93 (0.15)
CaO	16.28 (0.12)	16.57 (0.10)	16.89 (0.09)	17.18 (0.11)
Na_2O	28.03 (0.13)	28.78 (0.10)	29.54 (0.10)	30.28 (0.12)
K_2O	44.54 (0.22)	45.79 (0.17)	47.01 (0.16)	48.18 (0.19)
Li_2O	16.20 (0.19)	16.83 (0.15)	17.38 (0.15)	17.90 (0.17)
CaO–TiO_2	−15.85 (2.22)	−16.24 (1.75)	−16.56 (1.67)	−16.86 (1.96)

values for $\bar{\beta}$. If one assumes that albite melts approximately congruently, the predicted value of 5.6×10^{-11}/Pa is too high to reconcile 1-bar volume and melting data with the high-pressure melting curve of Boettcher et al. (1982). Taken together, these data suggest a large negative value for $d\beta/dT$, with most of the structural adjustments in the liquid taking place within the first 10 kbars.

Table 2. Three-component parameters for compressibility. Numbers in parentheses are one standard deviation.

Component	$\bar{V}_i$ (km/s)	$d\bar{V}_i/dT$ (km/s)	$\bar{\beta}_{Ti}$ (10^{-11}/Pa at 1673 K)	$d\bar{\beta}_{Ti}/dT$ (10^{-11}/Pa·K)
Na_2O	2.52 (0.03)	−0.0020 (0.0002)	7.15 (0.13)	0.0107 (0.0007)
Al_2O_3	4.36 (0.08)	0.0019 (0.0005)	−3.15 (0.35	−0.0090 (0.0022)
SiO_2	2.57 (0.02)		6.82 (0.08)	

REFERENCES

Boettcher, A.L., Burnham, K.E., Windom, K.E., and Bohlen, S.R., 1982. Liquids, glasses, and the melting of silicates to high pressures. J. Geol., v. 90, p. 127–138.

Bottinga, Y., Weill, D.F., and Richet, P., 1982. Density calculations for silicate liquids. I. Revised method for aluminosilicate compositions. Geochim. Cosmochim. Acta, v. 46, p. 909–919.

Ghiorso, M.S., and Carmichael, I.S.E., 1984. Comment on "Density calculations for silicate liquids. I. Revised method for aluminosilicate compositions" by Bottinga, Weill, and Richet. Geochim. Cosmochim. Acta, v. 48, p. 401–408.

Ghiorso, M.S., and Carmichael, I.S.E., 1985. Chemical mass transfer in magmatic processes. II. Applications in equilibrium crystallization, fractionation, and assimilation. Contrib. Mineral. Petrol., v. 90, p. 121–141.

Janz, G.J., 1980. Molten salts data as reference standards for density, surface tension, viscosity and electrical conductance: KNO_3 and NaCl. J. Phys. Chem. Ref. Data, v. 9, p. 791–829.

McBirney, A.R., Baker, B.H., and Nilson, R.H., 1985. Liquid fractionation, Part I: Basic principles and experimental simulations. J. Volcanol. Geotherm. Res., v. 24, p. 1–24.

McKenzie, D.P., 1984. The generation and compaction of partially molten rock. J. Petrol., v. 25, p. 713–765.

Richter, F.M., and McKenzie, D.P., 1984. Dynamical models for melt segregation from a deformable matrix. J. Geol., v. 92, p. 729–740.

Rivers, M.L., and Carmichael, I.S.E., 1987. Ultrasonic studies of silicate liquids. J. Geophys. Res., in press.

Stebbins, J.F., Carmichael, I.S.E., and Moret, L.K., 1984. Heat capacities and entropies of silicate liquids and glasses. Contrib. Mineral. Petrol., v. 86, p. 131–148.

Stein, D.J., Stebbins, J.F., and Carmichael, I.S.E., 1986. Density of molten sodium aluminosilicates. J. Am. Ceram. Soc., v. 69, p. 396–399.

Taylor, M., and Brown, G.E., 1979. Structure of mineral glasses, II. The SiO_2–$NaAlSiO_4$ join. Geochim. Cosmochim. Acta, v. 43, p. 1467–1473.

Numerical Simulation of Transport of Multivalent Reactive Solutes under Conditions of Variable Temperature, pH, and Oxidation Potential

C.L. Carnahan

The oxidation states and consequent chemical behavior of multivalent chemical elements are determined thermodynamically by temperature, oxidation potential, and, in many cases, hydrogen ion activity of the fluid phase. Depending on its oxidation state, a given chemical element can display a significant variation in chemical behaviors, including aqueous-phase speciation and solid-phase solubility. The simulation of transport of multivalent elements under conditions of variable oxidation potential requires the ability to account for such variable chemical behavior.

The computer program THCC (Thermo-Hydro-Chemical Coupling), which accounts for variations of temperature during transport of reactive chemicals, has been described previously (Carnahan, 1986, 1987). During fiscal 1986 the capabilities of THCC were extended to account for variations of oxidation potential in space and time during a transport simulation. The new capabilities are described here, and example simulations are presented.

TREATMENT OF OXIDATION-REDUCTION REACTIONS

Oxidation-reduction reactions are treated by defining a hypothetical electron activity as a basis species subject to transport like other aqueous basis species. For multivalent elements a species in the highest oxidation state is chosen to be the basis species. Reduction to a lower oxidation state is described formally by a half-cell reaction in which the higher-valent species "reacts" with hypothetical electrons to form the lower-valent species. This pro-

cess is analogous to the one by which aqueous complexes are formed by reactions between basis species. The oxidation potentials (Eh, in volts) of initial and influent, or boundary, fluids are specified at input and are converted to equivalent electron activities within the program. Note that the electron activity is an artifice that allows treatment of reduction in the same manner as complexation; there is no implication that free electrons exist in aqueous solution.

THERMOCHEMICAL DATA

Equilibrium constants for chemical reactions must be calculated at each finite-difference node. This must be done at each new time level during simulations with evolving thermal fields, but it need be done only once at the beginning of isothermal simulations and simulations involving constant gradients of temperature. The equilibrium constants for a given reaction are calculated from the thermodynamic relation

$$\log K(T) = A + B/T + C \log T + DT, \quad (1)$$

where $K(T)$ is an equilibrium constant evaluated at absolute temperature T and the coefficients A, B, C, and D are related to the changes of standard Gibbs free energy, enthalpy, and heat capacity for the reaction. The coefficients for each reaction in a simulation are supplied as input to the program. Table 1 lists the chemical reactions and coefficients for Eq. (1) that were used in the example calculations presented here.

Table 1. Chemical reactions and coefficients for Eq. (1).

Reactions	A	B	C	D
Formation of complexes:				
$H^+ + CO_3^{2-} = HCO_3^-$	−77.11	4,593.3	29.04	5.944×10^{-4}
$2H^+ + CO_3^{2-} = H_2CO_3^0$	−40.37	5,576.6	11.33	$3.466 \times 10^{2-}$
$UO_2^{2+} + OH^- = UO_2OH^+$	83.00	−1,107.2	−32.46	$3.067 \times 10^{2-}$
$UO_2^{2+} + CO_3^{2-} + UO_2CO_3^0$	−275.3	13,160.7	7.67	-1.221×10^{-3}
$UO_2^{2+} + 2CO_3^{2-} = UO_2(CO_3)_2^{2-}$	−59.82	2,717.8	27.54	-1.091×10^{-3}
$UO_2^{2+} + 3CO_3^{2-} = UO_2(CO_3)_3^{4-}$	−393.77	20,160.4	139.90	2.087×10^{-3}
Reduction:				
$UO_2^{2+} + e^- = UO_2^+$	−356.20	13,420.1	133.24	-5.502×10^{-2}
$UO_2^{2+} + 2H_2O + OH^- + 2e^-$ $= U(OH)_5^-$	−406.50	18,088.5	152.77	-7.661×10^{-2}
Dissociation of water:				
$H_2O = H^+ + OH^-$	−76.99	−1,506.4	31.25	-3.110×10^{-2}
Dissolution of solids:				
$UO_2(c) = UO_2^{2+} + 2e^-$	644.66	−26,101.3	−243.74	1.100×10^{-1}
$SiO_{2(am)} + 2H_2O = Si(OH)_4^0$	0.338	−840.1	0.	-7.889×10^{-4}
$USiO_{4(c)} + 2H_2O$ $= UO_2^{2+} + Si(OH)_4^0 + 2e^-$	646.70	−27,639.2	−244.23	1.089×10^{-1}

EXAMPLE CALCULATIONS

The THCC program was used to simulate transport of aqueous uranium species within a porous matrix in the presence of a radial temperature distribution varying from 90°C at the inner boundary to 50°C at a distance of 10 m. Dissolved uranium is transported from two constant-concentration sources in a field of flow having a pore fluid velocity of 3×10^{-8} m/s (approximately 1 m/y), with a dispersivity of 0.05 m and a diffusion coefficient of 10^{-11} m^2/s. In all examples shown here, the fluid present in the porous matrix has an initial composition approximating that of a basalt groundwater, with pH equal to 10, Eh equal to −0.36 V at 50°C, total carbonate equal to 9×10^{-4} M, and ionic strength equal to 0.016 M, and is saturated with respect to amorphous silica. Both source fluids have 9×10^{-4} M total carbonate and ionic strength equal to 0.016 M but no silicic acid. Both source fluids are assumed in equilibrium with solid uraninite (U(IV) dioxide). One source fluid ("reduced") has Eh equal to −0.4 V at 90°C and pH equal to 10 to simulate dissolution of uraninite by a fluid in equilibrium with basalt. The other source fluid ("oxidized") has Eh equal to 0.0 V at 90°C and pH equal to 6 to simulate dissolution of uraninite by a more oxidizing fluid.

Two simulations were done with each source fluid. In one case the only solid phase allowed to precipitate reversibly is uraninite; the presence of silicic acid in the initial groundwater is ignored. In the other case both uraninite and coffinite (U(IV) silicate) are allowed to precipitate. Comparison of the two cases for each source fluid will demonstrate the effects on uranium concentration profiles of precipitation reactions during transport.

Each simulation ran to a simulated time of 10^7 s (approximately 0.3 y). Results of the calculations at this time are shown in Figs. 1 and 2. Figure 1 shows the temperature profile, constant during all simulations, and profiles of Eh resulting from transport, mixing, and chemical reactions of the two source fluids with the initial groundwater. Figure 2 shows profiles of hydroxide ion concentrations from the two source fluids, profiles of total dissolved uranium concentrations, and theoretical solubilities of uraninite and coffinite calculated for prevailing values of pH, Eh, and temperature. Solid symbols in the uranium concentration curves designate finite-difference nodes where precipitates of uraninite or coffinite exist.

Plots 1 and 2 in Fig. 2 are uranium concentration profiles for the reduced source fluid, and plot 5 is the accompanying hydroxide concentration profile. The only significant uranium species in the reduced

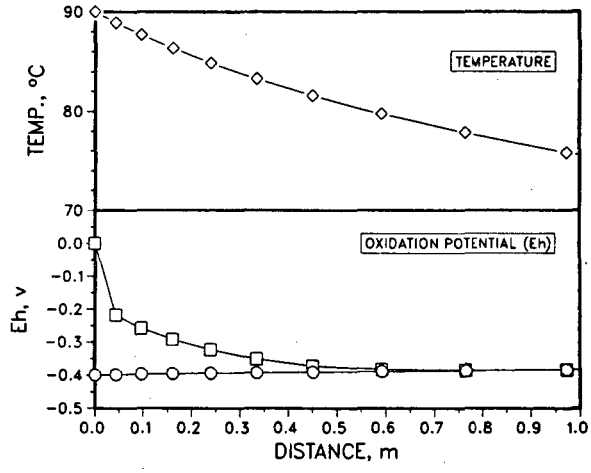

Figure 1. Temperatures and oxidation potentials at 10^7 s. [XBL 871-226]

source fluid is the U(IV) pentahydroxide complex. In simulation 1, no reaction with silicic acid is simulated, and uranium is transported without precipitation of either uraninite or coffinite. In simulation 2, dissolved uranium can react with silicic acid, and coffinite has precipitated at the first node beyond the source. The concentration of dissolved uranium has decreased by a factor of 40 at this node; thereafter, the concentration distribution follows the shape of plot 1 but is reduced in magnitude by that factor. In these two simulations neither the oxidation potential

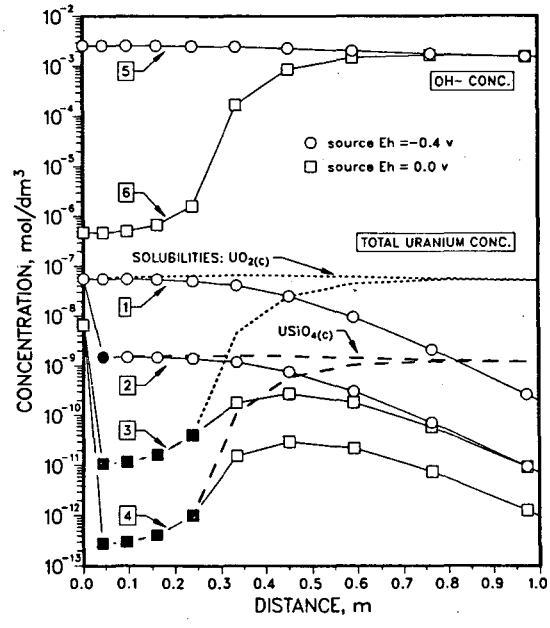

Figure 2. Total uranium concentrations, hydroxide concentrations, and solubilities of uraninite and coffinite at 10^7 s. [XBL 871-227]

nor the hydroxide concentration changes significantly between source fluids and groundwater; the reduction of uranium concentration in simulation 2 is caused only by reaction with silicic acid in the groundwater.

Plots 3 and 4 in Fig. 2 are uranium concentration profiles for the oxidized source fluid. The accompanying profile of oxidation potential is shown in Fig. 1; that of hydroxide ion is shown as plot 6 in Fig. 2. The uranium species in the oxidized source fluid are predominantly the mono- and bis-carbonato complexes of the U(VI) dioxo ("uranyl") cation, with smaller concentrations of the uranyl monohydroxide complex, the U(V) dioxo cation, and the U(IV) pentahydroxide complex. Note that the total uranium concentration in the oxidized source fluid is about an order of magnitude lower than that in the reduced source fluid. In simulation 3, in which reaction with silicic acid is not simulated, uraninite has precipitated at the first four nodes beyond the source. This is caused by the decrease of Eh at these nodes, with the result that uraninite is more stable here than it is in the source fluid. Thus at the first node beyond the source, the dissolved uranium concentration has decreased by a factor of 500. The dominant solution species at this and higher nodes is the U(IV) pentahydroxide complex. In simulation 4, reaction between silicic acid and U(IV) is allowed, and coffinite (more stable here than uraninite) precipitates at the first four nodes beyond the source, further lowering dissolved uranium concentrations by an additional factor of 50 relative to the source concentration.

In both simulations 3 and 4 at 10^7 s, a minimum in the concentration profile of dissolved uranium developed near the source. This happens because at earlier times dissolved uranium is transported into the porous matrix at concentrations such that the solubilities of neither uraninite nor coffinite are exceeded in the near-source region. Under these conditions, the concentration profile of dissolved uranium decreases monotonically with distance from the source, as in simulation 1. As time passes, high electron activities and silicic acid in the groundwater (which are displaced downstream by the advective flow from the source) diffuse upstream until one or the other solubility product is exceeded near the source, and either uraninite or coffinite precipitates. With further passage of time, activities of electrons and silicic acid continue to increase at the nodes where precipitation occurs. Consequently, uranium concentrations at these nodes is depressed by more precipitation in order to satisfy the constraints imposed by the solubility products. This process results in the interesting phenomenon that at 10^7 s dissolved uranium in the region less than 0.45 m from the source diffuses in the upstream direction toward the zone of precipitation. This effect will further reduce the outward flow of uranium from regions downstream from the zone of precipitation.

The effects of temperature variation are not obvious in Fig. 2 but are nonetheless present. For example, over the range of temperature shown in Fig. 1, the equilibrium constants for dissolution of uraninite and coffinite to form the U(IV) pentahydroxide complex change by 65% and 13%, respectively; both constants decrease with increasing temperature.

It is anticipated that the capability of THCC to treat varying oxidation potentials as well as varying temperatures will provide a means toward increased understanding of the mechanisms of migration of reactive chemicals in groundwater.

REFERENCES

Carnahan, C.L., 1986. Numerical simulation of chemically reactive solute transport under conditions of variable temperature. *In* Earth Sciences Division Annual Report 1985. Lawrence Berkeley Laboratory Report LBL-20450, p. 156–158.

Carnahan, C.L., 1987. Simulation of chemically reactive solute transport under conditions of changing temperature. *In* C.F. Tsang (ed.), Coupled Processes Associated with Nuclear Waste Repositories. Academic Press, Orlando, Florida, p. 249–257.

Mass Transfer of Soluble Species into Rock and Backfill

P.L. Chambré, C.H. Kang, C.L. Kim, W.W.-L. Lee, and T.H. Pigford

In a spent-fuel waste package placed in a geologic repository, the soluble cesium and iodine isotopes accumulated in fuel-cladding gaps, voids, and grain boundaries of spent fuel rods are expected to dissolve rapidly when groundwater penetrates the fuel rods (Stroes-Gascoyne et al., 1985; Pigford and Chambré, 1986). Even though dissolution may be rapid, the rate of release of these soluble species from the waste package will be limited by the rate of mass transfer of the dissolved species through the surrounding porous media. It is important to determine if the release of this "gap" activity will violate the performance requirements of the U.S. Nuclear Regulatory Commission (USNRC) for the engineered barrier system, especially the release-rate criterion (USNRC, 1983). Here we present the results of two mass-transfer analyses of the time-dependent release rate of species that can dissolve rapidly from the gaps and voids and more slowly from the waste matrix, as limited by molecular diffusion into the surrounding porous rock and through backfill into the rock.

In both analyses we assume that fuel cladding and a container are not present, that water contacts the interior of spent-fuel rods shortly after emplacement, and that 1% of the total inventory of cesium and iodine is rapidly dissolved in the "void water" that fills voids in the waste package. The void water is equivalent in volume to a 10-cm-thick layer of water between the waste solid and backfill or surrounding rock, and this void space is constant with time. Groundwater flow is assumed to be small enough that mass transfer through backfill and into the rock is controlled by molecular diffusion.

In the first case we consider only a waste solid exposed to the void water, with no backfill. In addition to the radionuclides dissolved instantaneously in the void water, additional amounts of those species are released to the void water by congruent dissolution from the solubility-limited waste solid matrix.

For one-dimensional planar geometry, with the void water filling a gap of width a between undissolved waste and the rock surface, Chambré (1986) has obtained the general solution for the time-dependent gap concentration of the soluble species in void water. The time-dependent void-water concentration is used in a mass balance to obtain the release rate into the rock.

To illustrate, we assume that ^{135}Cs, ^{137}Cs, and ^{129}I in the spent-fuel waste matrix dissolve congruently with matrix at a rate limited by the solubility of dissolved uranium, so that their mass-transfer rates are obtained from the equation for the time-dependent solubility-limited dissolution rate (Chambré et al., 1985). The time-dependent gap concentrations are evaluated for an assumed uranium solubility of 10^{-3} g/m^3, a conservatively high diffusion coefficient of 0.12 m^2/y that neglects rock tortuosity (Zavoshy et al., 1985), and a rock porosity of 0.01. We calculate the fractional release rates of ^{135}Cs, ^{137}Cs, and ^{129}I as a function of time after container failure, as shown in Fig. 1. Here the normalization for the fractional release rate is the initial inventory of each species in spent fuel. For ^{137}Cs the fractional release rate based on its 1000-year inventory, as specified by the USNRC, will be 10^{10}-fold greater than the fractional release rates in Fig. 1. The equivalent USNRC fractional release limit for ^{137}Cs from spent fuel is calculated to be

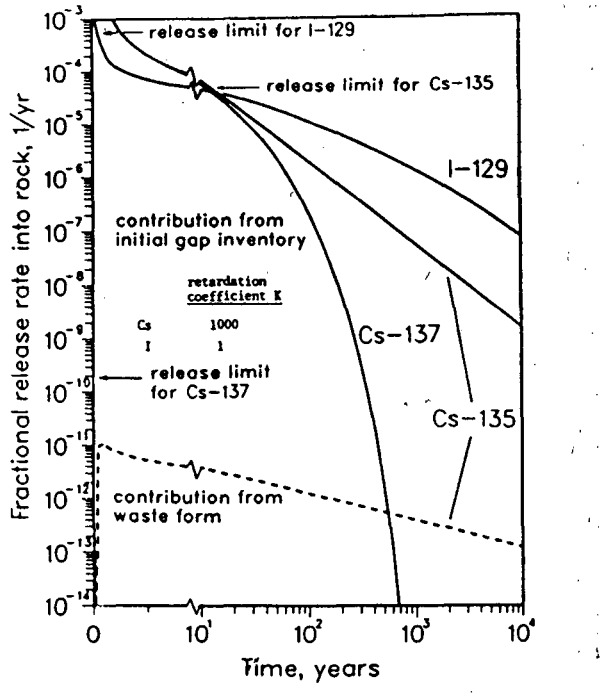

Figure 1. Fractional release rates into rock as a function of time (early container failure, 10 cm of void water, 1% of total cesium and iodine is in gap, and D = 0.12 m^2/y). [XBL 871-228]

1.8/year, on the basis of the 1000-year inventory, or 1.8×10^{-10}/year, on the basis of the initial inventory. The calculated USNRC release limits for ^{135}Cs and ^{129}I in spent fuel are 4.5×10^{-5}/year and 5.4×10^{-4}/year, respectively.

With these parameters the early contribution from the gap inventory is more than 10^7-fold greater than the contribution from the waste matrix. For early times the fractional release rates of ^{135}Cs and ^{137}Cs are almost equal, but the ^{137}Cs release rate decreases rapidly because of radioactive decay, whereas the release rate of 3×10^6-year ^{135}Cs is characteristic of a long-lived or stable species. Because of the assumed negligible sorption of iodine into the surrounding rock, the early fractional release rate of 1.7×10^7-year ^{129}I is lower than the rates of strongly sorbing cesium, but the less rapid early depletion of iodine in the void water results in a greater fractional release rate of iodine after about 20 years.

For longer-lived species of low solubility, such as ^{234}U, the void-water concentration reaches 90% of saturation within approximately 3 years, hence the early transient concentration of such low-solubility species in the void water can be neglected.

Next we consider if backfill can be of assistance in circumventing this difficulty with the release-rate criterion. We repeat the analysis used in the first case, but this time the waste package includes a layer of backfill of porosity 0.2. Here we neglect the relatively small contribution from solubility-limited congruent dissolution.

Time-dependent fractional release rates at the backfill/rock interface, normalized to initial inventories, are shown in Fig. 2 for a backfill thickness of 30 cm. Nonsorbing ^{129}I arrives at the backfill/rock interface in less than a year, with a peak release rate about 10-fold less than the equivalent fractional release rate limit calculated from the USNRC criterion. ^{135}Cs and ^{137}Cs arrive later simultaneously, but the normalized peak release rate of ^{137}Cs is less because of decay in the backfill. The peak release rate of ^{135}Cs is about 10-fold less than its release-rate limit, but the peak release rate of ^{137}Cs exceeds its limit by several orders of magnitude for hundreds of years.

Figure 3 shows the fractional release rate of ^{137}Cs, normalized to its initial inventory, as a function of time for various backfill thicknesses. Thicker backfills delay arrival at the backfill/rock interface and allow greater decay in the backfill. Backfill several times thicker than in current repository designs would be needed for compliance with the USNRC release-rate criterion, unless there can be

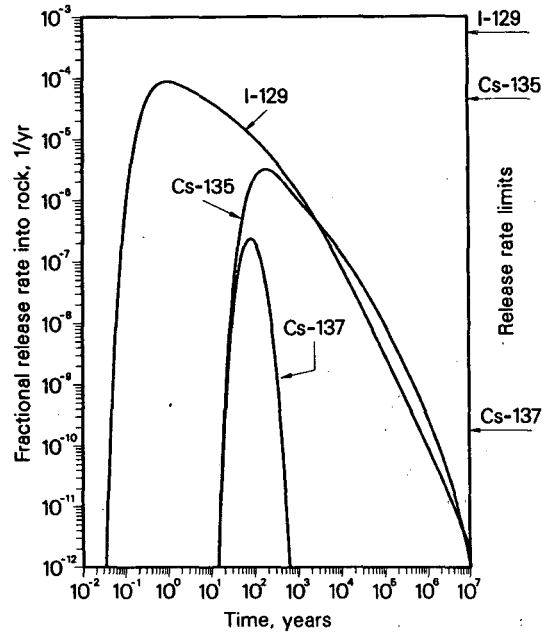

Figure 2. Fractional release rates for various nuclides through 30 cm of backfill. [XBL 871-229]

provided a reliable long-lived container with few early failures, much greater sorption in backfill, and much lower tortuosity-corrected diffusion coefficients and porosity in backfill and rock.

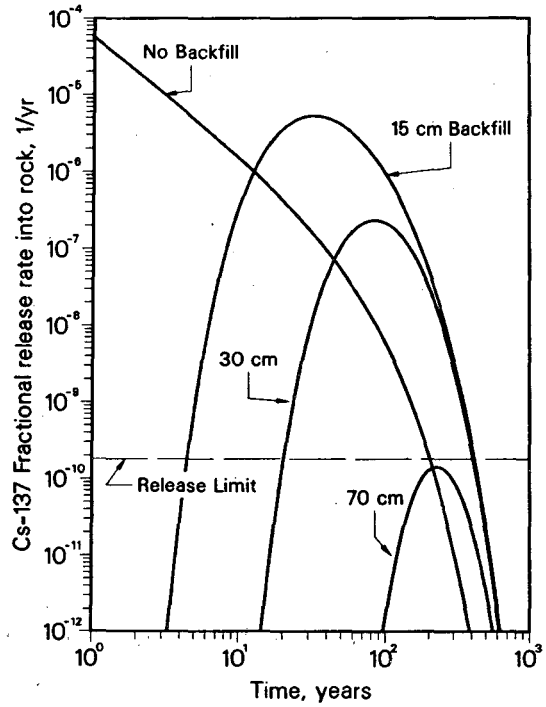

Figure 3. Cesium-173 fractional release rates as a function of backfill thickness and time. [XBL 871-230]

We have provided a theory that predicts whether the rapidly dissolved radionuclides will violate regulatory requirements and, through numerical illustrations, demonstrates the importance of considering these radionuclides in performance assessments.

REFERENCES

Chambré, P.L., 1986. Report in preparation.

Chambré, P.L., Pigford, T.H., Lee, W.W.-L., Ahn, J., Kajiwara, S., Kim, C.L., Kimura, H., Lung, H., Williams, W.J., and Zavoshy, S.J., 1985. Mass transfer and transport in a geologic environment. Lawrence Berkeley Laboratory Report LBL-19430, 193 p.

Pigford, T.H., and Chambré, P.L., 1986. Reliable predictions of waste performance in a geologic repository. *In* H.C. Burkholder (ed.), High-Level Nuclear Waste Disposal. Battelle Press, Columbus, OH, p. 163–186.

Stroes-Gascoyne, S., Johnson, L.H., Beeley, P.A., and Sellinger, D.M., 1985. Dissolution of used CANDU fuel at various temperatures and redox conditions. *In* L.O. Werme (ed.), Scientific Basis for Nuclear Waste Management IX. Materials Research Society Symposia Proceedings (Vol. 50). Elsevier, New York, p. 317–326.

USNRC, 1983. Title 10, Code of Federal Regulations, Part 60.

Zavoshy, S.J., Chambré, P.L., and Pigford, T.H., 1985. Mass transfer in a geologic environment. *In* C.M. Jantzen, J.A. Stone, and R.C. Ewing (eds.), Scientific Basis for Nuclear Waste Management VIII. Materials Research Society Symposia Proceedings (Vol. 44). Elsevier, New York, p. 311–322.

Radionuclide Transport through Penetrations in Nuclear Waste Containers

P.L. Chambré, W.W.-L. Lee, C.L. Kim, and T.H. Pigford

In this article we analyze radionuclide transport through penetrations in nuclear waste containers. Penetrations may result from corrosion or cracking and may pass through the container material or through deposits of corrosion products. The analysis deals with the resultant radionuclide transport but not with how these penetrations occur. We provide numerical illustrations for diffusive nuclide flux through these penetrations from mathematical expressions given by Chambré et al. (1986).

The U.S. Nuclear Regulatory Commission's performance objective (USNRC, 1983) for the waste package subsystem requires substantially complete containment within the waste package for 300–1000 years. Mass transfer through container holes may prevent complete containment and may also affect compliance with the release-rate requirement. Analysis of radionuclide transport through penetrations aids in the evaluation of individual barriers, such as Zircaloy cladding for spent fuel.

The mathematical expressions for time-dependent diffusion through a hole of arbitrary geometry in a thin-walled container show that such mass transport is dependent on the shape of the hole. The diffusive mass flux can be calculated for various aperture shapes, and results are given for ellipses and circles. Early-time and late-time approximations of mass transport are developed.

The calculated steady-state concentration field in the vicinity of a circular hole is shown in Fig. 1; a constant concentration of the dissolved species is assumed at the surface of the hole.

Our analytical solution for diffusion through well-separated holes shows that for small holes in a thinned container the hole-area proportionality assumed by some waste package codes in predicting release rates is not obeyed. For example, if the Zircaloy cladding of a single fuel rod contains a sufficient number of 2-mm holes so that the total hole area is about 0.3% of the container area, the rate of diffusive transport through the holes is over 40-fold greater than predicted on the basis of hole-area proportionality. This is a consequence of the large concentration gradients and large diffusive fluxes near the hole edges, and it may explain observations by Johnson et al. (1984) of large releases of cesium through apertures in Zircaloy cladding. Of course, the holes could become plugged with corrosion pro-

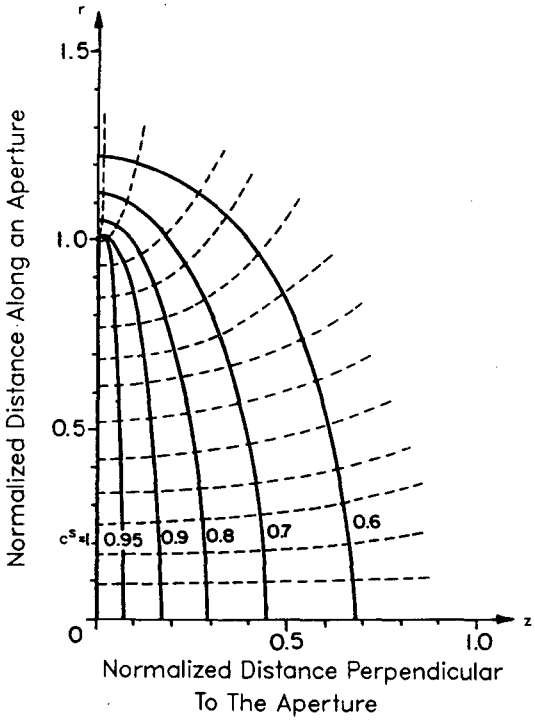

Figure 1. Surfaces of nondimensional concentrations and diffusional paths near an aperture. [XBL 871-231]

ducts, or the failure phenomena may be such that the fuel cladding is penetrated by only a few openings, so that the net release rate could be appreciably lower than that of an uncontained waste solid. Obtaining sufficient data to reliably predict the effect of partial failure of waste containers on release rates is a challenge to experiment and theory. We will not be able to predict and validate container life until a meaningful criterion for container failure is developed and until a reliable theory to predict acceptable performance toward that criterion is developed. The analysis also predicts that as the thickness of the container increases, mass flux decreases.

As a result of its fabrication history, exposure during reactor irradiation, and corrosion and mechanical stresses in the repository, Zircaloy cladding may contain many small perforations. Our results suggest that the radionuclide release rate through small holes may be significant.

In summary, this article describes an initial analysis of radionuclide transport through holes in nuclear waste containers. We plan to extend this work, and we invite experimental verification of these predictive theories.

REFERENCES

Chambré, P.L., Lee, W.W.-L., Kim, C.L., and Pigford, T.H., 1986. Steady-state and transient radionuclide transport through penetrations in nuclear waste containers. Lawrence Berkeley Laboratory Report LBL-21806.

Johnson, L.M., Stroes-Gascoyne, S., Chen, J.D., Attas, M.E., Sellinger, D.M., and Delaney, H.G., 1984. Relationship between fuel element power and the leaching of Cs-137 and I-129 from irradiated UO_2 fuel. *In* Proceedings, Topical Meeting on Fission Product Behavior and Source Term Research, Snowbird, Utah, 1984.

USNRC, 1983. Title 60, Code of Federal Regulations, Part 60.113(a).

Results from Numerical Simulations of Thermodynamically Coupled Processes

J.S. Jacobsen and C.L. Carnahan

The TIP program was developed to provide the ability to simulate heat and mass transport by thermodynamically coupled processes such as chemical osmosis, thermal diffusion, thermal osmosis, and ultrafiltration in a porous, semipermeable medium. Depending on the properties of the medium supporting the transport, the coupled processes may cause heat and mass flows in addition to those predicted by the direct processes of advection, diffusion, and heat conduction. Gradients of temperature, pressure, and solute concentration are the driving forces for heat, solute, and volume fluxes. The magnitudes of the fluxes resulting from the coupled processes are governed by the size of the gradients. The effects of

thermodynamically coupled processes have been observed in geologic materials. Examples of these have been reviewed by Carnahan (1984).

VERIFICATION OF TIP PROGRAM

The name TIP is an acronym for thermodynamics of irreversible processes, the theory used to derive the governing conservation equations. The TIP program numerically solves the system of coupled, nonlinear partial differential equations that describe a physical system in which heat and mass flows are thermodynamically coupled. The numerical method of solution and the capabilities of the code have been described by Carnahan and Remer (1986).

The program was verified by comparing the results from numerical simulations with analytical solutions of the linearized system of equations. As part of the verification process, analytical solutions were derived for one-dimensional geometry for the following cases of coupling and inner boundary conditions:

1. No thermodynamic coupling with nonzero heat, solute, and solvent boundary fluxes.
2. Chemical osmosis with nonzero solute and solvent boundary fluxes and a zero heat boundary flux.
3. Thermal osmosis with nonzero heat, solute, and solvent boundary fluxes.

Solving the linearized system of equations formulated in radial geometry is considerably more difficult. The conservation equations were transformed using the Laplace transform method, and solutions to the transformed equations were obtained for the following cases of coupling:

1. No thermodynamic coupling.
2. Chemical osmosis.
3. Thermal osmosis.
4. Combined chemical and thermal osmosis.

In all of these cases nonzero heat, solute, and solvent fluxes were imposed as boundary conditions. The solutions in the transform space were numerically inverted using an algorithm by H. Stehfest (1970) and the results compared with the numerical solutions.

For both one-dimensional and radial geometries, agreement between the analytical and numerical solutions is excellent at early simulation times. There are discrepancies at later simulation times because the magnitudes of the nonlinear terms in the conservation equations increase in comparison with the linear terms.

RESULTS

The TIP program was used to simulate heat and mass flows in the vicinity of a cylindrical heat source surrounded by a clay-like material. The set of phenomenological coefficients describing the clay material is a composite of those obtained from several sources (Carnahan, 1985). The following values were used in the simulations:

$L_{qq} = 2.6 \times 10^{2}$ W/m, coefficient of heat conduction (Fourier's law),

$L_{vq} = 3.8 \times 10^{-10}$ m^2/s, coefficient of thermal osmosis,

$L_{ss} = 6.8 \times 10^{-17}$ kg^2/m·J·s coefficient of chemical diffusion (Fick's law),

$L_{vs} = -8 \times 10^{-17}$ kg·m^2/J·s, coefficient of thermal osmosis,

$L_{vv} = 2.4 \times 10^{-16}$ m^5/J·s, coefficient of advection (Darcy's law).

Initially the temperature, pressure, and solute concentration were assigned constant values. Constant nonzero heat and solute fluxes of 10 W/m^2 and 10^{-11} kg/m^2·s, respectively, were imposed at the boundary of the heat source, and the solvent flux was set equal to zero there. All variables were held constant at their initial values at the outer boundary, which was located far from the inner boundary in order to avoid boundary effects. All of the results are shown at a simulation time of 1000 years.

Temperature

The temperature profiles (Fig. 1) for the uncoupled case and all of the coupled cases coincide, showing that the transport of heat is unaffected by thermodynamic coupling for the choice of parameters and incoming heat flux used. At a simulation time of 1000 years, the temperature near the flux boundary has increased from an initial temperature of 325 K to 337.5 K. Though the temperature is unaffected by thermodynamic coupling in the present cases, it is possible that a change in material properties, phenomenological coefficients, or incoming heat flux could result in temperature differences between the uncoupled case and coupled cases.

Pressure

Figure 2 shows the change in pressure from an initial pressure of 10^7 Pa. The pressure profiles show

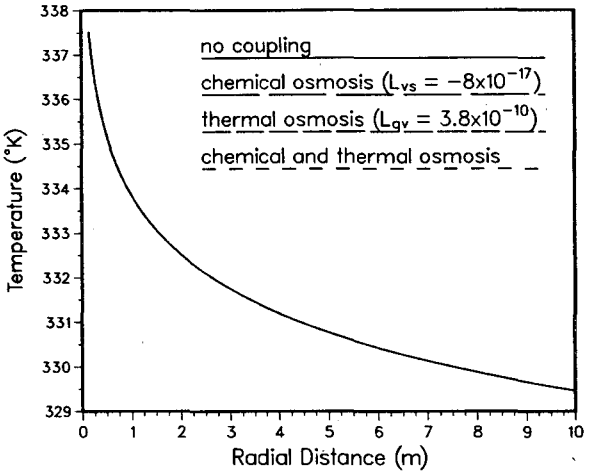

Figure 1. Temperature distribution at 1000 years with and without thermodynamic coupling. [XBL 871-233]

obvious, but small, differences between the uncoupled case and coupled cases and among the coupled cases. The differences are largest near the inner boundary, where the pressure profiles for each case are distinct. After a distance of about 2 m, the pressure profiles for the uncoupled and chemical osmosis cases coincide, and those for the thermal osmosis and combined chemical osmosis and thermal osmosis cases coincide. The difference between the two pairs of profiles continues for a distance of 100 m. Though the differences in pressure are small, they nevertheless give rise to large differences in the pressure gradients. This is important to note because the pressure gradient is the driving force for advection and ultrafiltration.

Solute Concentration

The solute profiles (Fig. 3) for the uncoupled, chemical osmosis, and combined chemical osmosis and thermal osmosis cases are distinct for the first 2 m. The profile for the thermal osmosis case coincides with the uncoupled case everywhere. After a distance of 2 m, all of the profiles converge. Near the flux boundary, the concentration for the chemical osmosis case is about 50% larger than that for the uncoupled case. The concentration for the combined chemical osmosis and thermal osmosis case is about 20% less than that of the uncoupled case. The initial concentration was 0.4 kg/m^3.

Given that the pressure gradients, and hence the advective fluxes, for the uncoupled and thermal osmosis cases are different, it is surprising that the concentration profiles for those cases are the same. However, in the conservation equation for solute for the thermal osmosis case, the larger terms involving the pressure gradient are offset by thermal osmosis terms, resulting in identical concentration profiles for the uncoupled and thermal osmosis cases.

Another important feature of the concentration profiles is the position of the profile for the combined chemical osmosis and thermal osmosis case relative to those for the other coupled cases. As noted above, the profiles for the uncoupled and thermal osmosis cases coincide, implying that the thermal osmosis processes (for the set of parameters used) do not affect solute transport. This is clearly not so when chemical osmosis processes have also been included: near the flux boundary, the concentration for the combined chemical osmosis and thermal osmosis case is only 50% of the concentration for the chemical osmosis case.

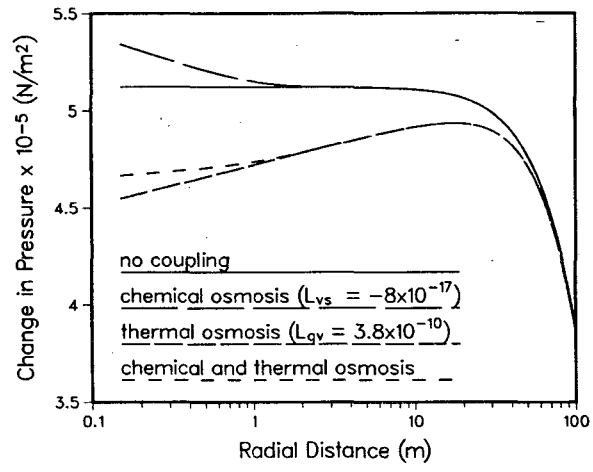

Figure 2. Change in pressure at 1000 years with and without thermodynamic coupling. [XBL 871-234]

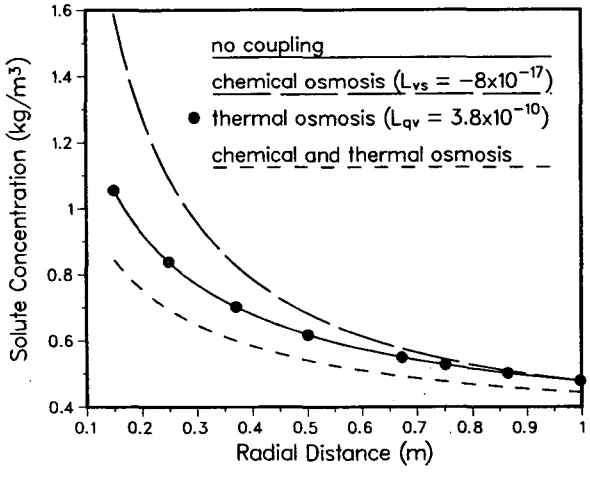

Figure 3. Solute concentration at 1000 years with and without thermodynamic coupling. [XBL 871-235]

Total Solute Flux

It is also worthwhile to examine the solute fluxes, because they provide the most direct measure of solute migration. The concentration profile shows how much solute is in the system, but the solute flux shows the rate of movement of the solute.

The total solute flux at and near the inner boundary is the same for all of the cases, because the incoming solute flux is constant (Fig. 4). After a distance of about 1 m, the total solute fluxes for the uncoupled and coupled cases differ in magnitude and shape. Solute migration is retarded in the chemical osmosis case relative to the uncoupled case and is the same as the uncoupled case when only thermal osmosis processes are considered. When both chemical osmosis and thermal osmosis processes are included, the solute migrates away from the inner boundary faster than in the uncoupled case and faster than when either coupled process is considered alone.

SUMMARY

Heat and solute transport by thermodynamically coupled processes in a clay-like material have been numerically simulated for a single set of parameters and boundary conditions. Only chemical osmosis and thermal osmosis were considered; thermal diffusion was neglected. The results of these simulations can be summarized as follows:

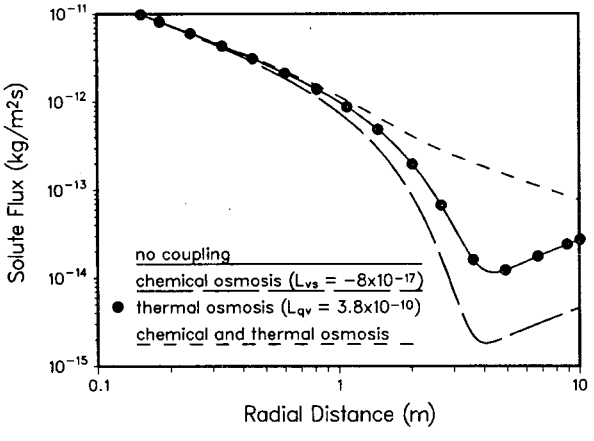

Figure 4. Total solute flux at 1000 years with and without thermodynamic coupling. [XBL 871-236]

1. Transport of heat is unaffected by thermodynamic coupling.
2. When only thermal osmosis processes are included, there is no difference in the solute concentration between the uncoupled and coupled cases.
3. When only chemical osmosis processes are included, solute migration away from the flux boundary is retarded relative to the uncoupled case, resulting in a larger solute concentration near the boundary for the coupled case.
4. When both chemical and thermal osmosis processes are included, the solute migration away from the boundary is larger than that for the uncoupled case, resulting in a smaller solute concentration near the boundary for the coupled case.

On the basis of these results, it appears that the heat-flow calculations can be decoupled from solute and volume flows and that thermal osmosis processes can be ignored if chemical osmosis processes are not being included. It is important to note, however, that the results described above depend on the properties of the medium and on the flux boundary conditions and may change in a qualitative way if different simulation parameters are used.

REFERENCES

Carnahan, C.L., 1984. Thermodynamic coupling of heat and matter flows in near-field regions of nuclear waste repositories. *In* G.L. McVay (ed.), Scientific Basis for Nuclear Waste Management VII. Materials Research Society Symposia Proceedings (Vol. 26), p. 1023–1030.

Carnahan, C.L., 1985. Thermodynamically coupled mass transport processes in a saturated clay. *In* C.M. Jantzen, J.A. Stone, and R.C. Ewing (eds.), Scientific Basis for Nuclear Waste Management VIII. Materials Research Society Symposia Proceedings (Vol. 44), p. 491–498.

Carnahan, C.L., and Remer, J.S., 1986. Numerical simulation of thermodynamically coupled processes. *In* Earth Sciences Division Annual Report 1985. Lawrence Berkeley Laboratory Report LBL-20450, p. 154–156.

Stehfest, H., 1970. Algorithm 368. Numerical inversion of Laplace transforms. ACM Comm., v. 13, p. 47–49.

Transport of Radioactive Chains through Porous Media of Limited Extent

H.C. Lung, P.L. Chambré, and T.H. Pigford

We have obtained analytic solutions (Chambré et al., 1985) and show here some numerical illustrations for the transport of radioactive decay chains of arbitrary length through porous media of finite extent, such as backfill or degraded rock near a nuclear waste package. Numerical methods have been unable to predict hydrogeologic transport of long decay chains in finite media. The analytic solutions illustrated here are exact and general.

We consider the transport problem in a finite one-dimensional domain. Transport is described through the convective-dispersion equation. Pore-water velocity in backfill is assumed to be small enough to have a negligible effect on near-field transport, and a constant diffusion coefficient is assumed for all members. To represent flow conditions at the outer edge of the finite backfill region, we used a mixed boundary condition with a constant mass-transfer coefficient h. Two of our previous analyses (Chambré et al., 1983, 1984) were used to estimate an effective value of the mass-transfer coefficient of 10^{-4} m/y for backfill in contact with low-porosity rock. The solution depends on the assumed release mode, retardation coefficients, decay constants, extent of the backfill, diffusion coefficient, mass-transfer coefficient, porosity of the backfill, and leach time.

In the first illustration, we use congruent dissolution in a band-release mode (Harada et al., 1980) for the $^{234}U \rightarrow ^{230}Th \rightarrow ^{226}Ra$ decay chain and a diffusion coefficient of 3.15×10^{-2} m^2/y, a backfill thickness of 0.3 m, a porosity of 0.3, a leach time of 10^7 years, and retardation coefficients of 120, 1500, and 300 for uranium, thorium, and radium, respectively. The initial concentrations in the backfill are zero. The boundary conditions obey the Bateman equation, with zero concentrations of the daughter nuclides at the waste-form/backfill interface initially. Figure 1 shows the concentrations of the various nuclides normalized to the initial concentration of the first nuclide in the chain at both ends of the backfill as functions of time. The solid curves represent the nuclide concentration at the inner edge of the backfill, and the broken lines represent the concentration at the outer edge. For $h = 10^{-4}$ m/y, the outer edge acts as a nearly impenetrable surface. The radium concentration at the outer edge is even higher than at the waste-form/backfill interface after 1000 years.

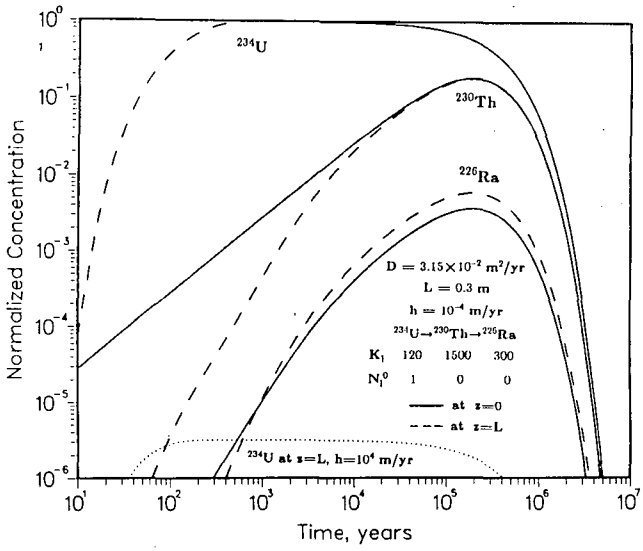

Figure 1. Normalized concentration as a function of time. [XBL 871-237]

This graph also indicates the importance of decay during diffusion in backfill. Although ^{230}Th and ^{226}Ra are initially at zero concentrations, their normalized concentrations increase significantly with time to maximum values of 1.6×10^{-1} for thorium and 3.3×10^{-3} for radium.

A much higher value of h will result if groundwater flows more rapidly outside the backfill. For $h = 10^4$ m/y, the nuclide concentrations at the outer edge drop to nearly zero, too low to be shown in Fig. 1 except for ^{234}U, which is represented by the dotted line and is about 6 orders of magnitude lower than that at the inner edge.

Figure 2 shows the mass fluxes (normalized to the initial concentration of the first member at the inner edge) at both ends of the backfill as functions of time. The solid curves represent the flux at the inner edge; the broken ones, the flux at the outer edge. For $h = 10^{-4}$ m/y, a low inner flux results from the low-porosity, low-pore-water-velocity surrounding rock, as can be seen from the broken curves compared with the flux at the outer edge at early times (< 100 years). The radium mass fluxes are so low that they cannot be read from this graph. The decay effect is even more significant for fluxes than for outer edge concentrations, since the thorium

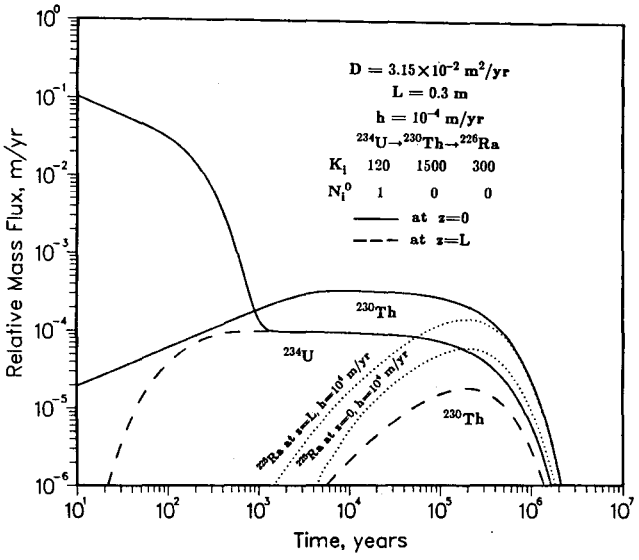

Figure 2 Relative mass fluxes as functions of time. [XBL 871-238]

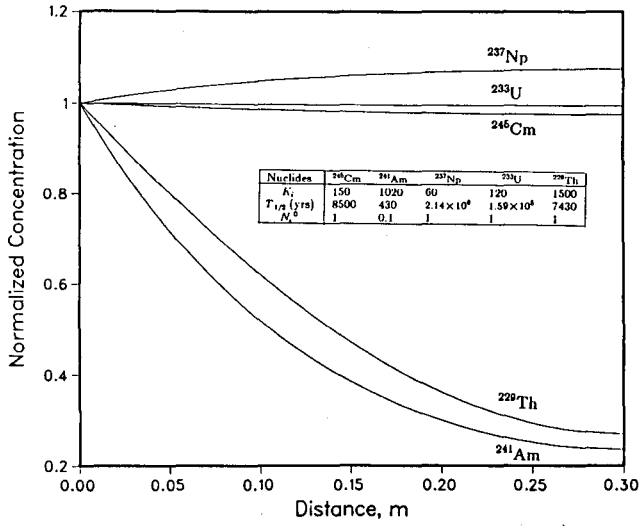

Figure 3. Distribution of a five-member decay chain in a backfill at 1000 years. [XBL 871-239]

flux at the waste-form/backfill interface is higher than that of uranium after 1000 years.

The radium mass fluxes are shown for strong water flow outside the backfill (h = 10^4 m/y). Here the radium mass flux at the outer edge is always greater than that at the inner edge except at a very early time (< 1 year). This phenomenon also occurs for smaller h. Thus the backfill can enhance the radium mass flux instead of decreasing it. We call special attention to ^{226}Ra, since the simultaneous diffusional transport of its precursors can result in radium mass fluxes greater than would be estimated by neglecting the decay precursors.

Figure 3 shows results for the ^{245}Cm→^{241}Am→^{237}Np→^{233}U→^{229}Th decay chain. The ordinate shows the normalized concentration of the radionuclides and the abscissa the extent of the backfill. The concentration of each species is normalized to the solubility of the species. The values of diffusion coefficient, backfill thickness, and porosity are the same as in Fig. 1. All members were assumed to be initially at their solubility limits at the waste-form/backfill interface, and h = 10^{-4} m/y was used. Figure 3 is a demonstration of the ability to trace the movement of a long decay chain through porous rock of finite extent for various assumed release modes at the waste source.

The examples given here show that the analysis can be applied to mass transport through porous rock of finite dimensions for a decay chain of arbitrary length.

REFERENCES

Chambré, P.L., Lung, H.C., and Pigford, T.H., 1983. Mass transport from a waste emplaced in backfill and rock. Trans. Am. Nucl. Soc., v. 44, p. 112.

Chambré, P.L., Lung, H.C., and Pigford, T.H., 1984. Time-dependent mass transfer through backfill. Trans. Am. Nucl. Soc., v. 46, p. 132.

Chambré, P.L., Pigford, T.H., Lee, W.W.-L., Ahn, J., Kajiwara, S., Kim, C.L., Kimura, H., Lung, H.C., Williams, W.J., and Zavoshy, S.J., 1985. Mass transfer and transport in a geologic environment. Lawrence Berkeley Laboratory Report LBL-19430, 193 p.

Harada, M., Chambré, P.L., Foglia, M., Higashi, K., Iwamoto, F., Leung, D., Pigford, T.H., and Ting, D., 1980. Migration of radionuclides through sorbing media: Analytical solutions—I. Lawrence Berkeley Laboratory Report LBL-10500, 233 p.

Determination of the Solubilities and Complexation of Waste Radionuclides Pertinent to Geologic Disposal at Yucca Mountain

H. Nitsche, S.C. Lee, R.C. Gatti, D.B. Tucker, and E.M. Standifer

The Nevada Nuclear Waste Storage Investigations (NNWSI) Project is studying a tuff formation at Yucca Mountain in southern Nevada to determine its suitability as a potential site for a nuclear waste repository. If the site is selected, the repository built there would have to meet overall performance regulations of the Nuclear Regulatory Commission (NRC) and the Environmental Protection Agency (EPA).

In the event of canister corrosion and the release of radionuclides from the waste package, migration of contaminated groundwater is considered to be the principal mechanism for radionuclide transport from the underground storage site to the accessible environment. The radioelements can potentially react with various chemical components of the groundwater and the host geologic medium. The formation of solution species and solubility-controlling solid phases will define the maximum concentrations and migration characteristics of radionuclides. The nature of the compounds and solution species formed will depend on the oxidation state of the radioelement, the nature and concentrations of the precipitating ions and complexing ligands, the temperature, the pH, and the redox properties of the groundwater and the surrounding geologic media. To meet the regulations and requirements of the EPA and the NRC for site characterization, it is necessary to predict the nature of the insoluble compounds and the speciation of solution complexes that will form as a result of the chemical reactions between the actinides and the groundwater ions.

SCOPE OF THE STUDY

During fiscal 1986 an extensive program was initiated at Lawrence Berkeley Laboratory to provide knowledge on the nature of compounds and solution species of waste radionuclides that form in natural waters found at or near Yucca Mountain. A general description of the overall work can be found in a document by Kerrisk (1985).

One initial task of the program is to determine the solubilities and oxidation-state distributions of neptunium, plutonium, and americium in groundwaters of the candidate repository at Yucca Mountain and in aqueous perchlorate solution of similar pH and ionic strength. In noncomplexing perchlorate solution, oxide or hydroxide formation and hydrolysis are important factors in the control of actinide solubility. In groundwater, however, the additional anions can influence the actinide solubility by the formation of new solids and the formation of new solution complexes. A comparison of the results in these solutions can show whether the groundwater anions are an important influence on the actinide solubility or whether oxide and hydroxide formation are the principal factors that control solubility.

Another task of this program is to investigate the effect of temperature change on the solubilities and oxidation-state distribution of the aforementioned actinide solutions by performing measurements at 25°C, 60°C, and 90°C. Furthermore, the experimental data can be used to validate solubilities calculated with the EQ 3/6 chemical equilibrium code, which is used to model waste-element solubilities in the NNWSI project. If necessary, thermodynamic data derived from the experiment will be used to correct and upgrade the existing EQ 3/6 data base.

PROGRESS DURING FISCAL 1986

The solubilities are studied under supersaturated conditions, which allows the determination of an upper limit for the material of interest. Numerous samples are required to study the solubility of the different actinide ions over the desired pH range. Since the solubilities are highly sensitive to pH and temperature changes, close control of these parameters is necessary. During the first weeks of the experiment, the pH of a solution tends to deviate substantially from its target value as a result of precipitation and redissolution effects. Inside the controlled-atmosphere glove box in which the experiments are performed, frequent pH measurements and adjustments become very labor intensive. First, a computer-controlled data acquisition and feedback control system (pH-stat) was designed and manufactured to perform this task. Second, a thermostat system was built to maintain the experimental temperatures (25° to 90°C) inside the radioactive controlled atmosphere in a safe manner over the required long time periods. Third, a gas pressure system was developed to maintain the experimental solutions (i.e., well waters) at their nominal CO_2 pressure at

elevated temperatures without evaporative loss of the actinide test solution. Experiments were started for $^{237}NpO_2^+$, $^{239}Pu^{4+}$, and $^{243}Am^{3+}$ at 60°C with water from well J-13 at pH values of 6, 7, and 8.5.

The determination of steady-state solution concentrations is made by nuclear counting. Because of the rather low ^{239}Pu concentrations, a procedure was developed to determine the concentration indirectly by use of gamma- and *L* X-ray spectroscopy (Lee et al., 1987). The effectiveness and sorption behavior on a variety of filter materials were studied to determine a reliable method for the separation of the solution phases from the solids (Standifer et al., 1987). A scheme was developed to determine quantitatively the oxidation states of plutonium ions in the supernatant solution at equilibrium (Nitsche et al., 1987). Detailed results of all of the above areas of research are published in quarterly and topical reports.

ACKNOWLEDGMENT

This work is supported by the Nevada Nuclear Waste Storage Investigations (NNWSI) Project, which is managed by the Waste Management Project Office of the U.S. Department of Energy, Nevada Operations Office.

REFERENCES

Kerrisk, J.F., 1985. Solubility experiments for the Nevada Nuclear Waste Storage Investigations project. Los Alamos National Laboratory Report LA-10560-MS.

Lee, S.C., Gatti, R.C., and Nitsche, H., 1987. Indirect determination of plutonium at trace levels by use of gamma- and *L* X-ray spectroscopy. Presented at the 193rd American Chemical Society Meeting, Denver, Colorado, April 5–10, 1987. Lawrence Berkeley Laboratory Report LBL-23379.

Nitsche, H., Lee, S.C., and Gatti, R.C., 1987. Determination of plutonium oxidation states of trace levels pertinent to nuclear waste disposal. Presented at the International Conference on Methods and Applications of Radioanalytical Chemistry, Kona, Hawaii, April 5–10, 1987. Lawrence Berkeley Laboratory Report LBL-23158.

Standifer, E.M., Lee, S.C., and Nitsche, H., 1987. Separation of soluble transuranium species from particulates in groundwater by ultrafiltration. Presented at the 193rd American Chemical Society Meeting, Denver, Colorado, April 5–10, 1987. Lawrence Berkeley Laboratory Report LBL-23378.

Air and Groundwater Alteration of UO_2 and Its Subsequent Reaction with Zirconium Alloy

D.L. Perry

During the last several decades, much interest has been expressed in uranium(IV) oxide as a fuel for electrical power generators and research reactors. This interest has spanned all facets of research involving the compound, including its mechanical, thermal, and chemical properties. Detailed knowledge in these areas of uranium dioxide technology is important, both for studying its performance and durability as a fuel and for understanding its chemical reactions as an escaped nuclear waste material migrating through the surrounding biosphere.

Of equal interest is the interaction between uranium(IV) oxide and the zirconium alloy cladding of the nuclear fuel package. The dissolution of UO_2 under nuclear processing conditions has been studied by several workers with the purpose of trying to understand the kinetics and mechanism of the process. Similar studies of the interaction of UO_2 and Zircaloy with cooling water at elevated temperatures have been conducted from a metallurgical point of view, and wettability studies of various solid/liquid systems (such as UO_2/U and UO_2/Zircaloy) were carried out to measure the interfacial energy and

work of adhesion of various combinations of the materials formed in the interaction between UO_2 and Zircaloy-4. The corrosion of spent UO_2 fuel in synthetic groundwater has been studied by other workers.

The research summarized here has dealt with the reaction of UO_2 with air and groundwater, followed by its soluble-form reaction with Zircaloy-4 alloy. The dry-form reaction has been conducted at relatively low temperatures to study the film layers of uranium species brought about on the UO_2 surface by these reactions. Knowledge of these species will yield information about the effect of uranium chemistry on the groundwater chemistry and the nature of the uranium species that will undergo dissolution and enter into the solution chemistry of such a system.

Although uranium(IV) oxide is a refractory compound with a high melting point (1865°C), it is quite susceptible to oxidation. Oxygen or air oxidation of UO_2 at elevated temperatures yields U_3O_8, which is attained through a variety of several intermediate oxides such as UO_{2+x} and U_4O_9; the exact route and mechanism are dependent on the oxygen pressure and temperature. Thermal studies of bulk UO_2, for example, have shown that the oxidation of UO_2 and U_4O_9 occurs through a U_3O_7 intermediate. Even surface oxidation of UO_2 at room temperature is known to occur, with the oxidation products again consisting of U_4O_9 and mixed oxides of the type UO_{2+x} (x = 0–0.25). Several workers have reported an extensive study of the room-temperature oxidation of air-reacted UO_2, and others have reported the surface oxidation of commercially available UO_2.

The data obtained for the initial air-reacted UO_2 used in this study indicate a high degree of surface oxidation (Fig. 1, top). The uranium $4f_{7/2}$ binding energy of 381.3 eV is considerably higher than the 380.3 eV reported by Allen for UO_2; rather, it is more indicative of uranium(IV) that has been oxidized further. The oxide U_3O_8, for example, has been shown to exhibit a binding energy of 381.1 eV for the principal $4f_{7/2}$ photoelectron line, a value that is compatible with that observed for the starting UO_2 material used in this research.

Two other observations concerning the x-ray photoelectron spectra support a strong oxidation of the UO_2 starting material. The UO_2 exhibits a line width of 3.1 eV (FWHM, the full width at half maximum), half a volt wider than that reported for stoichiometric UO_2; the present UO_2 sample also underwent differential charging. These facts are contrary to previous reports that UO_2 is a moderately good conductor at room temperature and gives no evidence of charging during the x-ray photoelectron experiment. Furthermore, the satellites located at 6.7 and 16.1 eV and 6.8 eV to the high-binding side of the main $4f_{5/2}$ photoelectron line that have been reported by previous investigators are not present. Instead, a rather broad, weak, and diffuse satellite spanning the 6.0–8.0 eV region on the high-binding-energy side of the $4f_{5/2}$ peak is observed. This type of satellite structure in uranium compounds is many times indicative of a noncrystalline species with a poorly defined lattice system, characteristic of a heterogeneous oxide mixture. It should also be remembered that the line broadening (3.1 eV) referred to above has been shown by other researchers to parallel the oxidation of stoichiometric UO_2.

However, the spectrum of uranium in Fig. 1 (bottom) illustrates quite a different situation. Here uranium that has dissolved in the groundwater has been reductively plated out on the Zircaloy-4 as a uranium(IV) oxide species. This is evident from the lowered binding energy of the uranium $4f_{7/2,5/2}$ photoelectron lines that are shown; these lowered binding energies are in excellent agreement with those of

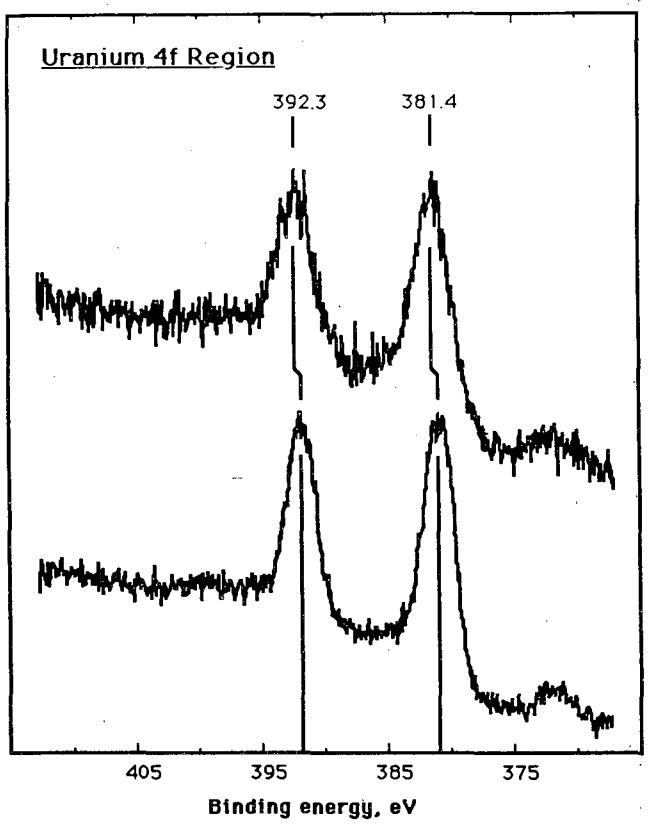

Figure 1. The uranium $4f_{7/2,5/2}$ x-ray photoelectron spectra of air-oxidized UO_2 (**top**) and a Zircaloy-4 surface reacted with UO_2-saturated groundwater at 100°C for 144 hours (**bottom**). [XBL 8610-3611]

uranium(IV) species that have been published previously.

Complex reactions of the kind demonstrated here are indicative of reactions that can occur when alloys like those of zirconium interact with uranium dioxide in groundwater. These chemical reactions and mechanisms have a strong bearing on the migration of both the uranium species in the ground and any zirconium species that might be leached from the alloy.

Reaction of Uranium with Zeolites

D.L. Perry

Studies of zeolites and their interaction with uranium are extremely important in elucidating the reaction mechanisms between uranium and some geologic materials. Zeolites, for example, are a constituent of tuff, a pyroclastic rock that is under consideration as a storage medium for nuclear waste repositories. For any real understanding of the movement of radionuclides such as uranium through this material, a detailed knowledge of the types of chemical reactions, products, and reaction kinetics is necessary.

Uranyl (UO_2^{2+}) glasses also have been studied as solar energy devices. Uranyl-exchanged zeolites and other aluminosilicates have recently been used as photooxidation catalysts. In general, these photooxidations have involved the oxidation of organic substrates like isopropyl alcohol, methanol, diethyl ether, and ethyl alcohol. The selectivity of the uranyl aluminosilicate catalysts depends on the structure of the aluminosilicate. For instance, well-ordered zeolites are more selective than clay catalysts.

The exact mechanism for these photooxidations is not clearly understood. It has been suggested on the basis of electron paramagnetic resonance, luminescence, and x-ray photoelectron spectroscopy (XPS) experiments that the UO_2^{2+} ions are regenerated after photolysis by oxygen, since there is little loss of activity when oxygen is present. XPS experiments do show that a reduced UO_2^{+} species can be observed in certain cases as an intermediate after extended photolysis times.

The research conducted in our laboratory this past year has addressed the chemical states of uranium(VI) that has been reacted with a variety of zeolites. Figure 1 shows the uranium $4f_{7/2,5/2}$ x-ray photoelectron spectra of the surfaces of three

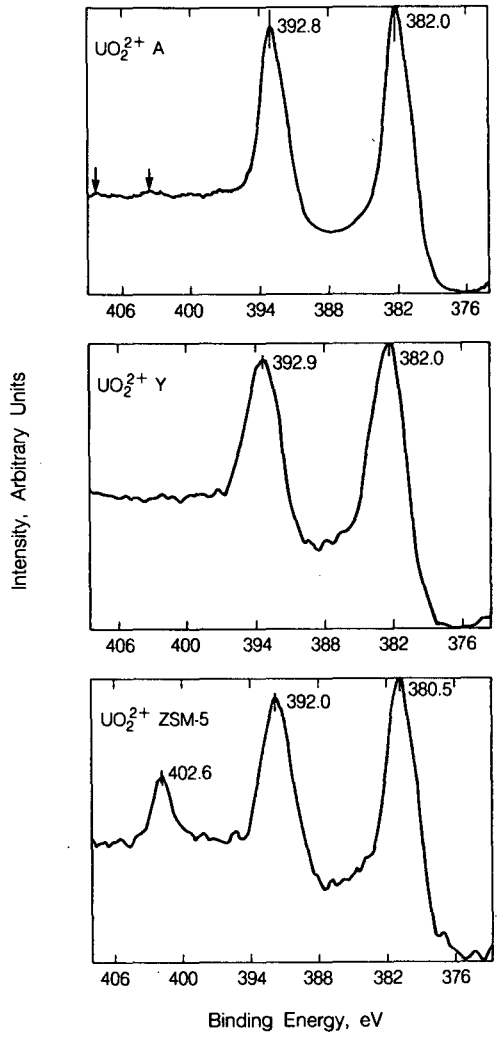

Figure 1. The uranium $4f_{7/2,5/2}$ x-ray photoelectron spectra of zeolites A, Y, and ZSM-5 reacted with 0.01 $UO_2(NO_3)_2 \cdot 6H_2O$ for 24 hours at 25°C. [XBL 862-10599]

zeolites—designated A, Y, and ZSM-5—with which uranium(VI) has been reacted. The upper spectrum clearly reflects the uranium in the hydrated uranium(VI) oxide state. This is altered from the initial $UO_2(NO_3)_2 \cdot 6H_2O$ reactant, which would yield large satellite peaks in the regions marked by the arrows. The same uranium-zeolite surface-chemical condition is observed for the Y zeolite. In the lower spectrum, however, one observes the peak at 402.6 eV, indicating the incorporation of the NO_3^- into the surface. Moreover, the lowered binding energy of the uranium indicates the partial x-ray beam photoreduction of the uranium(VI); this is merely one effect observed using this experimental technique and is studied as part of the overall investigation.

The research is being expanded to include reactions that are effected at elevated temperature and pressure for comparison with those reactions conducted at 25°C and atmospheric pressure. The high-temperature/pressure reactions will result in the formation of new uranium silicate phases—phases that will be documented by spectroscopy and x-ray diffraction techniques and serve as useful experimental models for uranium-zeolite reaction systems.

Thermodynamics of NaCl in Steam

K.S. Pitzer and R.T. Pabalan

At high temperatures and pressures NaCl-bearing steam has an important role in certain geologic processes, such as the formation of porphyry copper deposits, volcanic fumaroles, and boiling geothermal systems, as well as in steam power generation. Although the solubility of NaCl in steam is slight at low temperatures and pressures, it becomes significant at pressures and temperatures above the critical point of water and provides for important transport of NaCl. Because experimental data are lacking in certain temperature and pressure regions relevant to geologic systems, it is important to have a chemical model that predicts the solubility in those regions. This article summarizes a paper (Pitzer and Pabalan, 1986) that (1) presents a theoretically based equation whose empirical parameters represent selected experimental data on the solubility of solid NaCl in steam through 600°C and (2) provides reliable predictions to higher temperatures. When combined with thermodynamic data for pure NaCl and for concentrated liquid solutions, the predictions extend to the vapor + liquid field of the phase diagram in the range up to 500 bars and above 600°C.

THEORY AND EQUATIONS

The basic theory for a two-component imperfect gas developed on a rigorous basis from the grand partition function (Hill, 1960) yields series expansions in terms of the fugacities of the components for the pressure and for the densities ρ_1 and ρ_2 of the two components. The cluster integrals in these series can be regarded as equilibrium constants for the hydration reactions

$$NaCl + jH_2O = NaCl(H_2O)_j, \qquad (1)$$

where NaCl represents the anhydrous NaCl gas. It is preferable to recast this into a series of successive additions of single water molecules:

$$NaCl(H_2O)_{j-1} + H_2O = NaCl(H_2O)_j. \qquad (2)$$

The equilibrium constants K_j for these additions of one H_2O molecule are expected to be of similar magnitude but decreasing gradually with increasing j. The constant K_j at temperature T, assuming ΔC_p° is a constant independent of temperature, is given by

$$\ln K_j(T) = \Delta S^\circ(T_R)_j/R - \Delta H^\circ(T_R)_j/RT + \Delta C_p^\circ [\ln(T/T_R) - 1 + T_R/T], \qquad (3)$$

where T_R is a reference temperature here selected to be 500 K.

The working equation for the total concentration of all NaCl species is

$$\Sigma C/C_0 = (SO) = 1 + K_1 f_1 + K_1 K_2 f_1^2 + K_1 K_2 K_3 f_1^3 + \cdots, \qquad (4)$$

where ΣC and C_0 are the densities or concentrations of all NaCl-containing species and of anhydrous NaCl gas, respectively, in moles per unit volume. C_0 is calculated from the well-known thermodynamic properties of pure NaCl (Stull and Prophet, 1971), and f_1, the fugacity of water, is calculated from the equations of Haar et al. (1984). The mean hydration number is given by

$$\langle j \rangle = \Sigma jC/\Sigma C$$

$$= [K_1 f_1 + 2K_1K_2 f^2 + 3K_1K_2K_3 f^3 + \cdots]/(SO). \quad (5)$$

NaCl SOLUBILITY DATA

There are many published reports on the solubility of NaCl in steam: Olander and Liander (1950), Styrikovich et al. (1955), Sourirajan and Kennedy (1962), Martynova (1964), Styrikovich et al. (1966), and Galobardes et al. (1981). In addition there are the very recent measurements of Bischoff et al. (1986) to 503°C on the three-phase line. Figure 1 shows the various results for the three-phase line. Up to 400°C there is good agreement among the different sets of data for the three-phase line, but at higher temperatures the data of Sourirajan and Kennedy differ significantly from the other data.

Figure 2 shows the data over the full range of pressure for 450°C. Near 100 bars the results of Galobardes and others generally agree well with those of various Russian investigators, but there are substantial differences at lower pressures. We have chosen to accept the more recent Galobardes values at the lower pressures. At other temperatures the pattern is similar to that of Fig. 2, but the range of pressure is more limited.

EVALUATION OF PARAMETERS

Kebarle (1977) gave equilibrium constants for successive hydration reactions of Na^+ and Cl^- in steam (based on mass spectrometric measurements) and the ΔH_j and ΔS_j values that yield the temperature dependencies of those reactions. In the case of the neutral NaCl molecule, such detailed information is absent. However, we expect the ΔS_j values for the NaCl ion pair to be about the same as those for the Na^+ and Cl^- ions, as, indeed, they are for various other ions (Kebarle, 1977). Thus we adopt $-\Delta S_j/R$ values of 11.0 for all j at a reference temperature of 500 K, which is the mean temperature of the mass spectrometric measurements.

Similarly it is not feasible to determine each ΔH_j individually for the ion pair, but these are expected to be smaller than those for the ions and to decrease for successive additions of H_2O. Consequently the ΔH_j were selected with the same value assigned to the first three steps and successively smaller values for groups of three j-values: 4–6, 7–9, etc. Initially

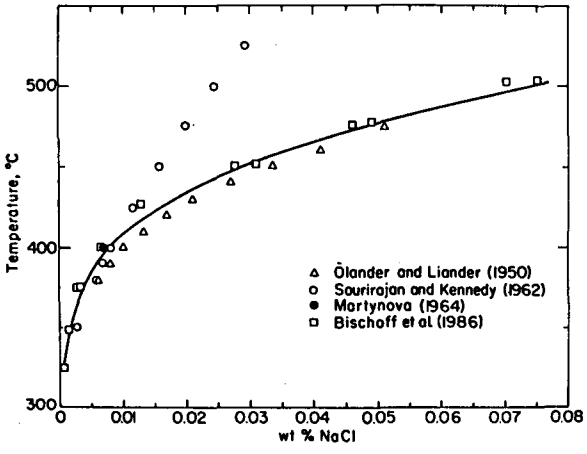

Figure 1. Vapor-phase compositions in the H_2O–NaCl system along the three-phase line as a function of temperature. The solid curve is calculated from the model. [XBL 871-410]

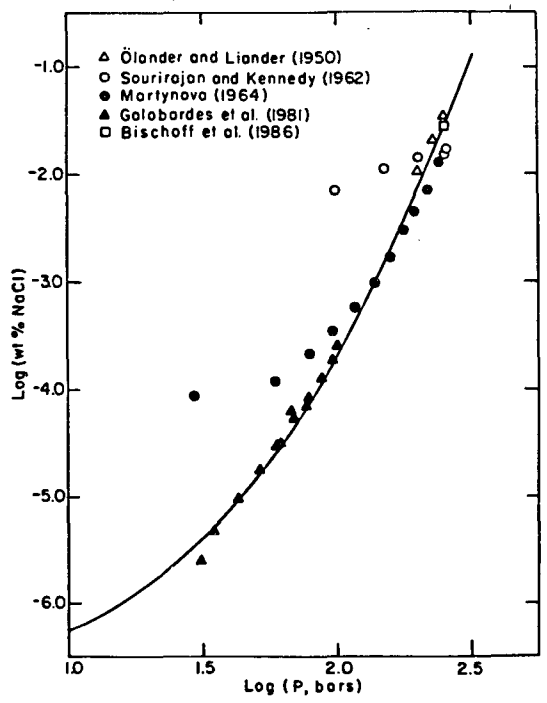

Figure 2. Vapor-phase compositions at 450°C as a function of pressure. The solid curve is calculated from the model. [XBL 8511-6779]

these values were adjusted to fit the calculated wt% of NaCl in steam to experimental data at 450°C, where there is the widest array of points.

Since we wish to deal with a wide range of temperatures, we must also consider the change in heat capacity ΔC_p for the reaction. From theoretical considerations we estimate $\Delta C_p/R$ to be greater than +2. NaCl solubility data at other temperatures and pressures were included in an overall fit by testing integral values of $\Delta C_p°/R$ and fine-tuning the $\Delta H°$ values initially chosen from the data for 450°C. A value of 3 was found to be optimum for $\Delta C_p°/R$ and is fully consistent with theoretical expectations. Table 1 gives the parameters for successive hydration of NaCl in steam.

Since the highest mean hydration number reached along the three-phase line is less than 12.0, the enthalpies for higher steps cannot be determined from the data considered so far. The progression of values for $\Delta H°/R$ for steps after 12 was selected to approximate the Gibbs energy of hydration obtained by Pitzer and Li (1984) for the NaCl ion pair at 550°C and critical pressure.

Figures 1 and 2 include the calculated curves. In general, there is good agreement of calculated values with the measurements of Olander and Liander (1950), Galobardes et al. (1981), and Bischoff et al. (1986), including those not shown in Figs. 1 and 2. The agreement with the Russian measurements is acceptable, but less precise, in the range above 100 bars at all temperatures. Below 100 bars, the Russian values are much higher than those of Galobardes.

Table 1. Parameters for successive hydration of NaCl in steam.[a]

Steps	$\frac{\Delta H_j°/R}{kK}$
1–3	6.39
4–6	4.90
7–9	4.30
10–12	3.95
13–15	3.90[b]

Note: $\Delta S°/R = -11.0$; $\Delta C_p°/R = 3.0$.

[a]All values are for $T = 500$ K.

[b]For higher steps, decrease by 0.05 per three steps.

CALCULATED VALUES FOR HIGHER TEMPERATURES

The mean hydration number decreases with increase of temperature at constant pressure. Thus extrapolation upward in temperature from the highest Bischoff measurements at 503°C should be quite reliable because the results depend on the parameters for the lower hydration stages, which are well-determined. The calculated solid solubilities in the vapor and the three-phase vapor compositions are shown in Fig. 3. The sharp break in the three-phase line just below 800°C arises as steam pressure drops to low values comparable to the vapor pressure of pure NaCl. Below 550°C the vapor–liquid curves of Fig. 3 are based on the experimental measurements of various investigators. At 100 and 200 bars these curves originate at zero wt% NaCl on the vapor–liquid curve for pure H_2O. The vapor–solid curves are calculated.

At higher temperatures (above 550°C), we calculated the NaCl activity for the vapor–liquid equilibria from the liquid compositions given by Bodnar et al. (1985) and the NaCl activity coefficient in the liquid from Gunter et al. (1983).

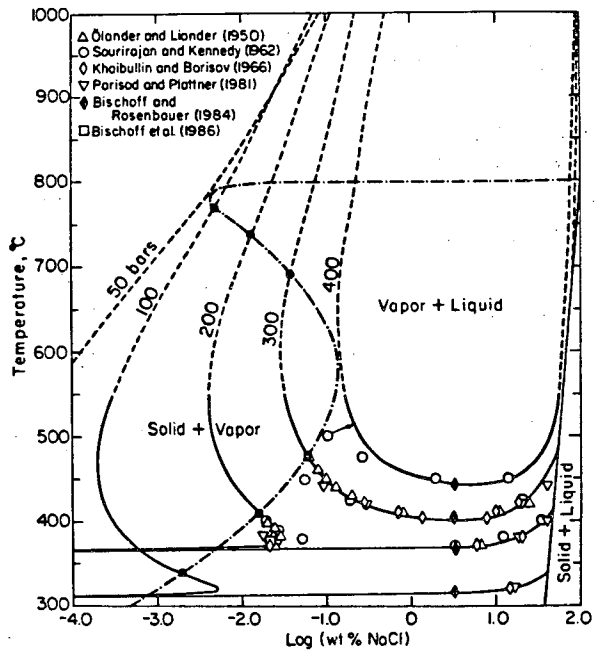

Figure 3. Calculated vapor-phase compositions in the system NaCl–H_2O along several isobars as a function of temperature. These curves are dashed outside the region of experimental data. Curves in the vapor + liquid region are based on experimental data. Shown dotted-dashed is the three-phase line; its real intersections with isobars are indicated with solid circles. Other, apparent intersections are at different pressures. [XBL 8511-6782]

Bodnar et al. (1985) recently measured equilibrium vapor compositions in synthetic fluid inclusions created by healing fractures in quartz in the presence of NaCl–H_2O in vapor–liquid equilibrium. Bodnar reports 0.4 wt% for 500 bars and 800°C, with the same value for 825°C and 500 bars. Our equation yields 0.33 and 0.35 wt% for 800 and 825°C, respectively, values that are in good agreement with Bodnar's data considering the various uncertainties.

Figure 4 presents a constant-composition diagram for the NaCl–H_2O system based on selected experimental data and on our model for the dilute, low-density vapor. Additional diagrams are given in the full report.

GEOLOGIC IMPLICATIONS

The generation of one or two aqueous phases during the intrusion and crystallization of a granitic magma is generally accepted as important in the formation of porphyry copper deposits. If the aqueous phase is formed at a pressure near or above that of the P–T critical line for the NaCl–H_2O system, only a single phase will arise. If there is another volatile component, such as CO_2, then the three-component critical line is the criterion. If the pressure is substantially below critical, however, both vapor and liquid phases may be formed. It is in this lower-pressure range that the results of this research yield different predictions from those of Sourirajan and Kennedy (1962).

The minimum melting curve of a granitic magma (Tuttle and Bowen, 1958) is shown schematically in Fig. 4, with points A and B representing the lowest pressures at which the magma can retain 4 and 2 wt% dissolved H_2O, respectively. Thus aqueous fluids with initial salinities of a few to about 20 wt% NaCl equivalent (Burnham, 1979) separating from a magma with water contents within this range fall within the vapor + liquid region of the simple NaCl–H_2O system and will therefore immediately separate into two phases, a dilute vapor and a concentrated brine. This is consistent with the discussion of Bodnar et al. (1985) and the characteristic occurrence of vapor-rich and halite-bearing inclusions in porphyry copper deposits.

Physical separation of these two fluids of highly different densities provides the basis for the vapor-plume model discussed by Henley and McNabb (1978) and may account for the generation of saline brines from magmatic fluids, almost irrespective of the initial concentrations of salt and water dissolved in the magma.

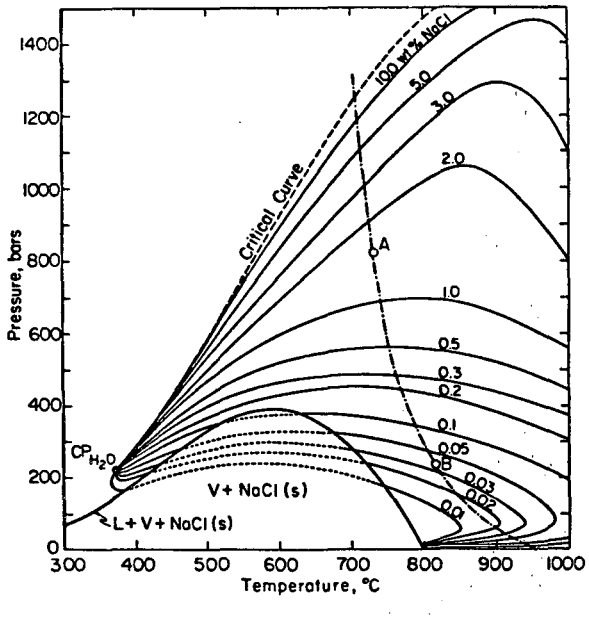

Figure 4. Isoplethal P–T projections for several vapor-phase compositions in the vapor + liquid region of the NaCl–H_2O binary. The isopleths are dotted in the vapor + NaCl(s) field. The critical curve is shown by dashed lines, and the critical point of pure water is shown by the solid circle. Also shown by the dotted-dashed line is the granite minimum melting curve from Tuttle and Bowen (1958), with points A and B representing the lowest pressures at which granitic magma can retain 4 and 2 wt% dissolved water, respectively. [XBL 8512-6880]

REFERENCES

Bischoff, J.L., Rosenbauer, R.J., and Pitzer, K.S., 1986. A note on the system NaCl–H_2O: Relations of vapor-liquid near the critical temperature of water and of vapor–liquid–halite from 300° to 500°C. Geochim. Cosmochim. Acta, v. 50, p. 1437–1444.

Bodnar, R.J., Burnham, C.W., and Sterner, S.M., 1985. Synthetic fluid inclusions in natural quartz. III. Determination of phase equilibrium properties in the system H_2O–NaCl to 1000°C and 1500 bars. Geochim. Cosmochim. Acta, v. 49, p. 1861–1873.

Burnham, C.W., 1979. Magmas and hydrothermal fluids. *In* H.L. Barnes (ed.), Geochemistry of Hydrothermal Ore Deposits (2nd ed.). Wiley, New York, p. 71–136.

Galobardes, J.F., Van Hare, D.R., and Rogers, L.B., 1981. Solubility of sodium chloride in dry steam. J. Chem. Eng. Data, v. 26, p. 363–366.

Gunter, W.D., Chou I-M., and Girsperger, S., 1983. Phase relations in the system NaCl–KCl–H_2O. II: Differential thermal analysis of the halite liquidus in the NaCl–H_2O binary above 450°C. Geochim. Cosmochim. Acta, v. 47, p. 863–873.

Haar, L., Gallagher, J.S., and Kell, G.S., 1984. NBS/NRC Steam Tables: Thermodynamic and Transport Properties and Computer Programs for Vapor and Liquid States of Water in SI Units. Hemisphere Publishing, Washington, D.C., p. 318.

Henley, R.W., and McNabb, A., 1978. Magmatic vapor plumes and ground-water interaction in porphyry copper emplacement. Econ. Geol., v. 73, p. 1–20.

Hill, T.L., 1960. An Introduction to Statistical Thermodynamics. Addison-Wesley, Reading, Maryland, p. 508.

Kebarle, P., 1977. Ion thermochemistry and solvation from gas phase ion equilibria. Ann. Rev. Phys. Chem., v. 28, p. 445–476.

Khaibullin, I. Kh., and Borisov, N.M., 1966. Experimental investigations of the thermal properties of aqueous and vapor solutions of sodium and potassium chloride at phase equilibrium. High Temperature, v. 4, p. 489–494.

Martynova, O.I., 1964. Some problems of the solubility of involatile inorganic compounds in water vapour at high temperatures and pressures. Russian J. Inorganic Chem., v. 38, p. 587–592.

Olander, A., and Liander, H., 1950. The phase diagram of sodium chloride and steam above the critical point. Acta Chem. Scand., v. 4, p. 1437–1445.

Parisod, C.J., and Plattner, E., 1981. Vapor–liquid equilibria of the NaCl–H_2O system in the temperature range 300–440°C. J. Chem. Eng. Data, v. 26, p. 15–20.

Pitzer, K.S., and Li, Y., 1984. Critical phenomena and thermodynamics of dilute aqueous sodium chloride to 823 K. Proc. Nat. Acad. Sci. USA, v. 81, p. 1268–1271.

Pitzer, K.S., and Pabalan, R.T., 1986. Thermodynamics of NaCl in steam. Geochim. Cosmochim. Acta, v. 50, p. 1445–1454.

Sourirajan, S., and Kennedy, G.C., 1962. The system H_2O–NaCl at elevated temperatures and pressures. Am. J. Sci., v. 260, p. 115–141.

Stull, D.R., and Prophet, H., 1971. JANAF thermochemical tables (2nd ed.). Nat. Stand. Ref. Data Serv., U.S. Nat. Bur. Stand. v. 37, p. 1141.

Styrikovich, M.A., Khaibullin, I.Kh., and Tschvirashvili, D.G., 1955. Solubility of salts in high pressure steam. Dokl. Akad. Nauk. SSSR, v. 100, p. 1123–1126 (in Russian).

Styrikovich, M.A., Martynova, O.I., and Mingulina, E.I., 1966. The dependence of the coordination number of weak electrolytes on the density of the solvent water. Dokl. Akad. Nauk. SSSR, v. 171, p. 783–786 (English translation).

Tuttle, O.F., and Bowen, N.L., 1958. Origin of granite in the light of experimental studies in the system $NaAlSi_3O_8$–$KAlSi_3O_8$–SiO_2–H_2O. Geol. Soc. Am. Memoir, v. 74, p. 153.

Mechanisms of Mobility Control with Foams

K.S. Udell and C.J. Radke

Establishing mobility control is crucial in all enhanced oil-recovery schemes. A concerted effort is needed to find inexpensive, effective, and controllable mobility-control fluids. The objective of the work summarized here is to elucidate and quantify the microscopic mechanisms underlying foam flow in porous media for the purpose of establishing foam as a generic mobility-control fluid in all enhanced oil recovery.

Foams consist of a high fraction of internal phase (e.g., CO_2, steam, nitrogen, hydrocarbon) dispersed in a continuous aqueous-surfactant phase. Because foam in a porous medium is not a continuum fluid, straightforward application of Darcy's law is unwarranted for describing foam flow. Indeed, the bulk viscosity of foam is irrelevant to porous-media flow. Rather, flow resistance arises from interactions between bubbles and pore walls.

Our approach is to deal with the texture and microrheology of foam at the pore level. This leads to a micro or scalable apparent viscosity. Our program is divided into four parts: (1) foam generation, (2) foam breakage, (3) foam flow, and (4) foam displacement.

The most pronounced factor controlling foam mobility in porous media is texture (i.e., the size of the bubbles, their size distribution, and the fraction of discontinuous gas phase). To control the texture

or type of foam in a foam drive, it is crucial to understand how the foam is generated, shaped, and regenerated in porous media.

This work elucidates the mechanisms of foam generation and foam shaping in porous media, and establishes how factors such as flow rate and permeability affect the relative importance of these mechanisms. Physical insight is provided by experiments in transparent glass bead packs. Two types of experiments were performed: visual and quantitative. In the visual experiments highly magnified movies were taken to view the foam-generation processes at the pore level. In the quantitative studies gas-phase relative permeabilities and liquid saturations were monitored to determine the effect of various parameters on the foam-generation processes.

Three pore-level mechanisms of foam generation were observed in the visual experiments. We call these mechanisms "leave behind," "snap-off," and "lamella division." These mechanisms are thought to be general to all types of porous media.

As shown in Fig. 1, the most significant result from the quantitative studies is that there exists a critical capillary number in homogeneous bead packs above which snap-off and lamella division become the dominant generation mechanisms, causing a strong foam to be formed. Below this critical velocity, the generated foam is weaker and is due to the leave-behind mechanism. Increasing the fractional flow of the liquid increases this critical capillary number slightly. In addition we find that snap-off occurs at all velocities when gas flows from a low-permeability region into a high-permeability region. Finally, surfactant structure strongly influences the relative importance of the foam-generation mechanisms.

The concept of "germination sites," which meet the static, geometric criterion for snap-off, is the crucial aspect of a proposed theory for the generation of strong foam in porous media. Three criteria must be met for a germination site to be active: the site must be entered by the gas, a dynamic flow-back criterion for snap-off must be met, and there must be sufficient liquid present for snap-off to occur. Therefore, the number of active germination sites, and hence the relative importance of the snap-off mechanism, depends on the pore geometry, fluid properties, and capillary and viscous fores. The germination-site model predicts a critical capillary number of 8 for the onset of snap-off. As seen in Fig. 1, this agrees quantitatively with the observed snap-off behavior in homogeneous bead packs over a range of bead size (0.25–1.0 mm), gas velocities (0.001–0.3 cm/s), and gas-phase fractional flow (0.6–1.0).

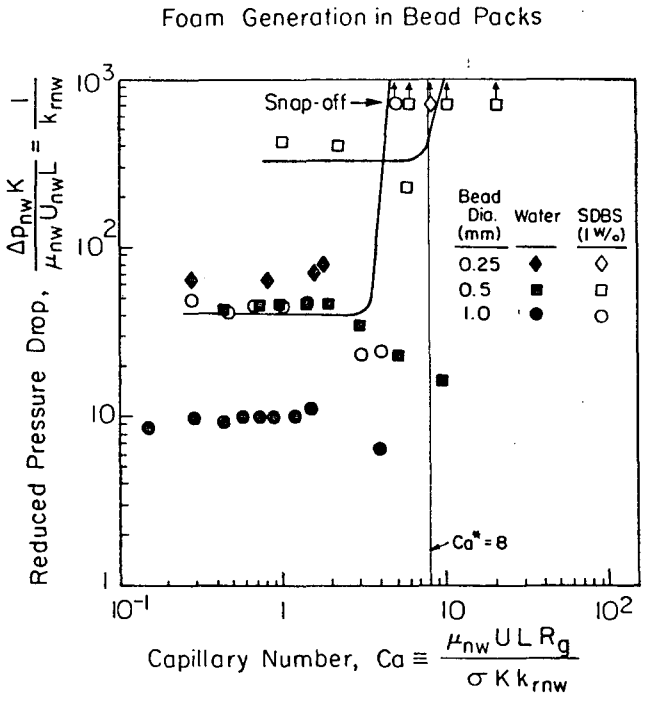

Figure 1. Experimental data for the steady-state, gas-phase, viscous pressure drop across an initially liquid-filled bead pack as a function of flow rate. Data are presented in the form of an inverse relative permeability against a capillary number. "Snap-off" points represent capillary numbers at which snap-off dominates the foam-generation process. In the experiments the injected fractional flow of gas is 1.0; the liquid phase is either deionized, distilled water or 1 wt% sodium dodecyl benzene sulfonate (SDBS); and the nominal bead size is 0.25, 0.5, or 1.0 mm. The germination-site theory predicts $C_a^* = 8$ for onset of snap-off. [XBL 875-2248]

The importance of snap-off in a porous medium is directly proportional to the number of active germination or snap-off sites. Previously, the number of sites has been assumed to be a constant, independent of any process or porous-medium parameters. Our work has shown that this assumption is an unrealistic one, and it provides a basic model that can be used to determine the dependence of the number of active germination sites on various parameters, such as capillary number and porous-matrix geometry. Details on this work may be found in Ransohoff and Radke (1986).

REFERENCE

Ransohoff, T.C., and Radke, C.J., 1986. Mechanisms of foam generation in glass bead packs. Paper SPE 15441 presented at the 1986 Annual Technical Conference and Exhibition, New Orleans, LA, October 5–8, 1986.

Selenium at Kesterson Reservoir: Hydrologic, Geochemical, and Ecological Appraisal

O. Weres, S.M. Benson, A.F. White, T.K. Tokunaga, A. Horne, J. Roth,* A. Yee, and H.A. Wollenberg*

Kesterson Reservoir, situated at the terminus of the San Luis Drain, became the focus of attention in 1983, when a high incidence of deaths and deformities was noted in the young of several species of birds that breed there. Before 1978 most of the water flowing into Kesterson was surface runoff. From that time on the flow contained gradually increasing amounts of subsurface drain water as more and more farm drainage systems were connected to the San Luis Drain. By 1981 most of the flow to Kesterson consisted of subsurface agricultural drain water. Two years later, investigations revealed that selenium was present in high concentrations in the reservoir. The selenium was found to originate in the soils and shallow groundwater of the irrigated lands of the Panoche fan on the west side of the San Joaquin Valley. Irrigation raised the water table in this area, so that water drained from the soil and transported to Kesterson by the San Luis Drain contained salts plus some selenium and boron.

Lawrence Berkeley Laboratory (LBL) began studies at Kesterson early in 1985, when some 40 groundwater samples were collected from wells drilled in the reservoir and analyzed for selenium and other constituents. Although the water ponded in Kesterson contained 200−300 ppb (parts per billion by weight) dissolved selenium at that time, most groundwater samples contained less than 5 ppb selenium (the EPA drinking water standard for selenium is 10 ppb). In its salinity and major ion composition, the groundwater is similar to water ponded in the reservoir, indicating that groundwater is derived from reservoir water that has percolated down through the sediment at the bottom of the reservoir. Later work verified that most of the selenium accumulates in the top 2 inches of sediment and remains there. Apparently, chemical or microbial processes remove the selenium from the water as it percolates through the bottom sediment. The geologic setting of Kesterson Reservoir and the earlier work done there by LBL are described in Weres et al. (1985).

A broader LBL research program devoted to Kesterson and supported by the U.S. Bureau of Reclamation (USBR) began in August of 1985. This article summarizes the results of the first year of this program and describes plans for continued work. Also included here is a brief description of a separately funded but related LBL project with the aim of developing an economical method of water treatment for selenium removal.

DESCRIPTION OF KESTERSON RESERVOIR

The reservoir (Fig. 1) consists of 12 ponds totaling about 1200 acres, located within the much larger Kesterson National Wildlife Refuge. The ponds are separated from one another by earth berms topped with unpaved roads. The San Luis Drain defines the reservoir's northeastern boundary and ends at its northern tip. Historically, most of the drain water has entered the reservoir through pond 2. From

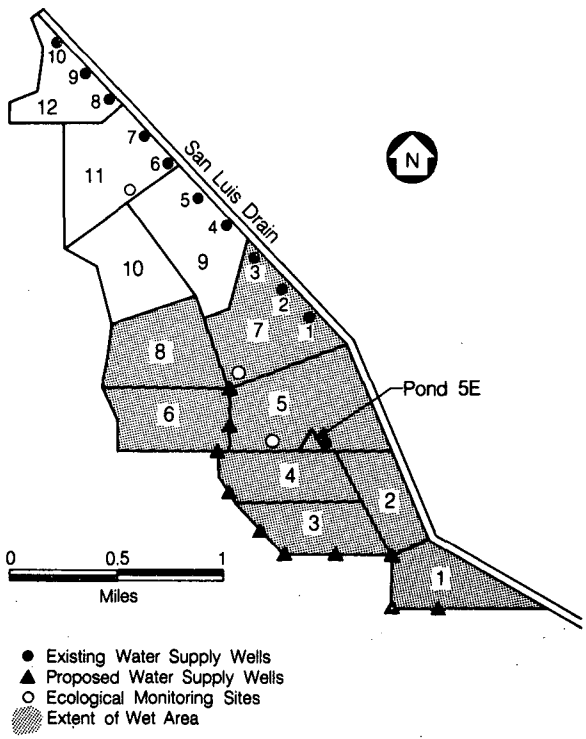

Figure 1. Map of Kesterson Reservoir, showing the 12 ponds and the locations of existing and proposed water supply wells and other features. [XBL 872-9904]

*Sanitary Engineering and Environmental Health Research Laboratory, University of California, Berkeley.

pond 2 the water is distributed to the other ponds through a series of connecting weirs. A triangular 1-acre test pond (pond 5E) was created on the southern edge of pond 5 by building an earth berm in early 1986. Pond 5E is supplied with low-selenium saline well water.

There are four major terrains within Kesterson, as shown in Fig. 2. They correspond to four distinct water regimes, vegetation types, and sediment profiles; the distribution of these terrains in the 12 ponds of the reservoir is summarized in Table 1.

Because most of the selenium within Kesterson is contained in the superficial sediment in the terrains dominated by the large alga *Nitella* and cattails, our research to date has focused mainly on these areas. *Nitella* and cattails overwhelmingly dominate their respective terrains. The predominance of cattails and *Nitella* is very fortunate. *Nitella* attaches itself to the bottom using anchors that are not true roots and do not take water, nutrients, or selenium from the sediments. Cattails have true roots and may extract selenium from the sediments. However, few animals eat cattails, and any selenium taken up by the cattails would eventually return to the sediments. Thus the selenium in the sediments is unavailable to most of the ecosystem. However, the *Nitella*, the diatoms and other phytoplankton, the zooplankton, and the various insect larvae and mosquito fish that live in the pond water probably take up their selenium from the pond water; these organisms make up the food chain that supports the birds.

RECENT FINDINGS

Surface Water

Selenium levels in surface water have dropped rapidly since the flow of high-selenium water from the San Luis Drain was stopped in early August of 1986 and was replaced by low-selenium water pumped from wells. By early fall the selenium concentration of surface water at most sampling sites had dropped well below 25 ppb (Fig. 3), with isolated higher values in stagnant water bodies. The selenium concentration in test pond 5E, which has been receiving low-selenium well water since late

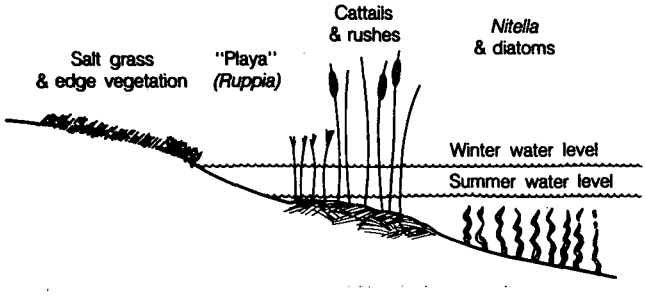

Figure 2. The major terrains within Kesterson Reservoir. [XBL 871-9833]

Table 1. Distribution of terrains at Kesterson Reservoir.

Pond	Terrains	Classification
1	Playa, CT	Wet
2	CT, Water	Wet
3	Playa, CT, SG	Wet
4	CT, Playa, Water	Wet
5	Water, CT	Wet
6	Playa, CT, SG	Wet
7	Playa, CT, Water	Wet
8	Playa, CT, SG	Wet
9	Playa, SG, CT	Dry
10	SG, Playa	Dry
11	SG, Playa	Dry
12	SG, Playa	Dry

Notes:
"Water" = standing water year round.
"CT" = cattails and similar emergent vegetation.
"Playa" = areas flooded in winter, dry and barren in summer.
"SG" = areas dominated by salt grass and other terrestrial vegetation.

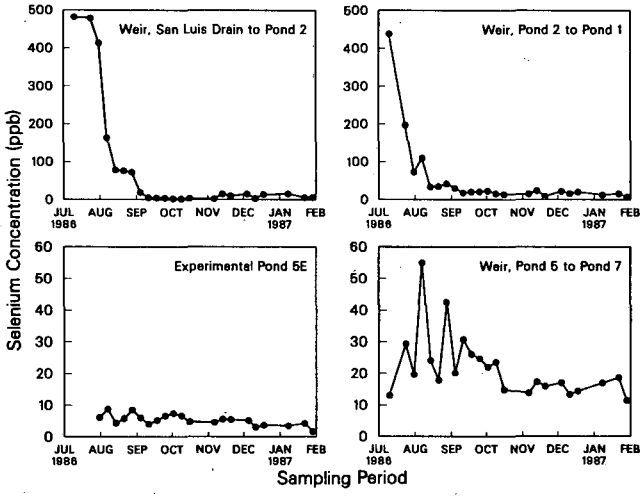

Figure 3. The variation with time of selenium concentrations at some surface water sampling sites. [XCG 872-6744]

May, has dropped to 3−5 ppb. These observations strongly suggest that selenium levels throughout most of the reservoir will drop below 10 ppb within months. Selenium concentrations in the algae in pond 5E have dropped rapidly during this period, suggesting that the selenium present in the water there may be coming from a finite accumulation in the standing biomass, which will soon be exhausted.

Improved analytical methods are being developed to identify and measure organic selenium compounds that may be present in surface water or groundwater. So far, only dimethylselenide (i.e., volatile selenium) definitely appears to be present, usually in association with decaying vegetation and always in amounts subordinate to those of inorganic selenium in the water.

Selenium Immobilization in Shallow Sediment

Continued work has confirmed that most of the selenium within Kesterson Reservoir is confined to the top few inches of organic-rich sediment in the cattail and *Nitella* (i.e., deep-water) terrains of the reservoir. The situation is not so simple in the playa areas, which are dry and practically devoid of vegetation and organic matter during the summer and early fall. Selenium is taken up by the aquatic vegetation that proliferates in the playas during the spring (when they are flooded). During the summer this vegetation becomes desiccated and quickly decays. Some of the selenium is released to the atmosphere in volatile form, but most probably remains as inorganic selenium in the salt crust typical of the playas and in the very shallow sediments. Typically, half of the selenium in the top inch of playa soil during the summer is in the form of highly soluble sodium selenate, which returns to solution immediately upon contact with water. Soil water samples from a depth of 2 feet in the playa areas of pond 1 have been recorded with as much as 1000 ppb selenium, and yet no selenium concentrations greater than 5 ppb have ever been recorded in wells located there. Figure 4 shows the profiles of selenium and boron in shallow groundwater at a particular site in pond 1. Boron is practically constant throughout, demonstrating that this water is derived from ponded surface water. Selenium drops by over 2 orders of magnitude in less than 2 feet. These observations suggest that other geochemical processes remove selenium from the groundwater a few feet down, even in the absence of an organic-rich superficial sediment.

A large field experiment is underway to test this hypothesis in pond 1, which contains extensive playa areas with high selenium levels in the superficial sediment. Pond 1 was deliberately kept dry until early fall, when it began to be flooded with low-selenium well water. Nine field monitoring sites have been established at various elevations and in playa, cattail, and salt grass terrains within pond 1. Baseline profiles of selenium in soil water have already been measured at these sites, and shallow sediment samples have been taken to determine total selenium and the chemical forms of selenium present. The response of selenium profiles in soil water, groundwater, and soil to the infiltrating water will be monitored. These data will show whether selenium extracted from the salt crust and from superficial sediment is in fact removed from the water by reaction with the deeper sediments. To support this test and related work, improved analytical methods are being developed to (1) measure the total selenium in sediments with concentrations of less than 1 ppm, (2) identify the various chemical forms of selenium that may be present, and (3) determine the proportions in which those forms occur.

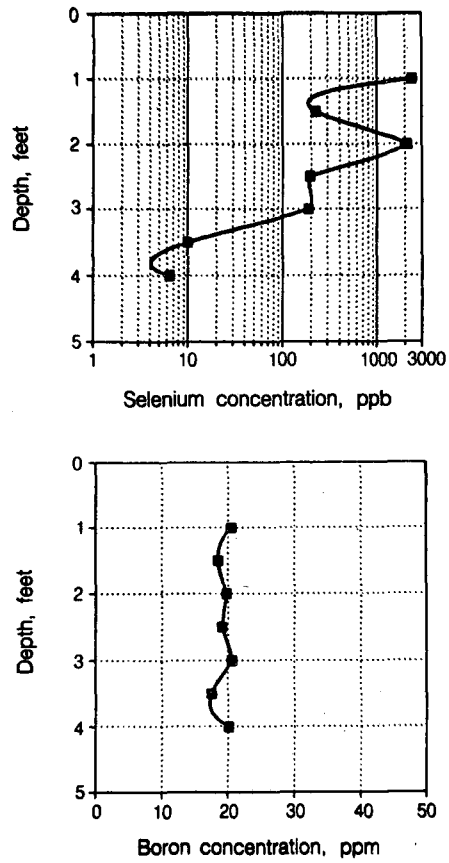

Figure 4. Concentrations of selenium and boron in the pore water at a site in pond 1. [XBL 872-9903]

Groundwater

Selenium concentrations above 5 ppb have been found only in a plume of groundwater beneath pond 2 and the immediately adjacent parts of ponds 1 and 5, which receive water from pond 2. Unlike the groundwater in the rest of the reservoir, where reducing conditions prevail, the groundwater in this area is oxidizing.

The plume of oxidizing groundwater has been well defined in depth and around most of its periphery, except toward the northeast, the direction of groundwater motion. (Access to the land in that direction is denied.) Selenium concentrations are highly variable inside this plume of oxidizing water, reflecting local variations in geochemistry and hydrology (Fig. 5). This plume underlies about 10% of the surface area of the reservoir. We estimate that the total selenium in the groundwater of the plume is about 50 kg, which is approximately the average weekly amount that entered the reservoir from the San Luis Drain during 1985. Groundwater monitoring is continuing at pond 2 to determine the further evolution of the contaminated groundwater plume. A recently constructed berm that extends 600 feet into pond 2 will be used to drill nests of monitoring wells for sampling the groundwater to a depth of 150 feet in the middle of pond 2 and to determine if selenium is still entering the groundwater. Sediment samples taken from the deeper wells will be analyzed for selenium content to see if selenium is being transferred from water to sediment within the plume.

There are indications that the plume of selenium contamination beneath pond 2 is moving slower than the water; as the water flows through the aquifer, selenium may gradually be removed from it by chemical interaction with the sediment. If this is the case, the plume of selenium contamination might not move much farther through the aquifer. This retardation effect is probably the same phenomenon that keeps selenium from entering the groundwater in the playa areas. This hypothesis will be tested in another experiment: water containing a very small amount of selenium and an inert tracer dye will be injected into wells located inside the reservoir, and after a few weeks the wells will be pumped to recover the injected water. This experiment will directly determine if interaction with deeper sediments can remove selenium from percolating groundwater over this period of time. (Less than 20 g of selenium will be injected, and the risk of contaminating groundwater is insignificant.)

It may ultimately be necessary to capture and extract the plume of contaminated groundwater by drilling and pumping wells along the northeastern edge of pond 2. Hydrologic testing and groundwater modeling work have been started to evaluate the feasibility of this remedial action and to identify proper locations and depths for the needed wells. Because the total amount of contaminated groundwater is probably less than 2000 acre-feet, capturing the plume probably will not be very difficult.

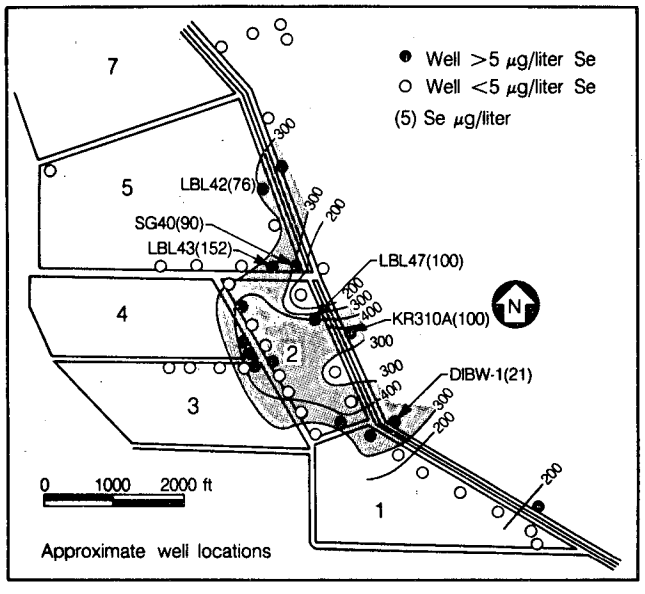

Figure 5. Lateral distribution of Eh relative to the hydrogen reference in groundwater at depths of 20–40 feet. Well numbers are shown at locations where selenium exceeds 10 μg/L, with concentrations indicated in parentheses. [XBL 869-12601]

Ecological Research

Experiments conducted in the laboratory using 5-gallon aquaria stocked with mud, water, plants, and mosquito fish from Kesterson have given an early indication of the ecological effects of keeping low-selenium water over contaminated sediment versus keeping high-selenium water over contaminated sediment. Selenium levels rapidly decreased in the high-selenium water and slowly increased in the low-selenium water until concentrations became roughly equal, indicating equilibrium with the sediment. Selenium levels in vegetation decreased by about half in both cases. These experiments demonstrated that selenium is transferred from surface water to sediment even without replacing contaminated water with clean water and showed that selenium levels in vegetation will decrease as waterborne selenium decreases.

Selenium in the water of experimental pond 5E dropped to 3−5 ppb after it received low-selenium

water for about 7 months. Over the same period of time the selenium content of *Nitella* and diatoms growing in this pond dropped by about 75% (Fig. 6), and the selenium content of diatoms dropped by about 60%. Monitoring of selenium levels in the water, plants, and animals of pond 5E will continue through winter and spring.

Ponds 1 to 8 (the wet subarea of the reservoir) are supplied with low-selenium well water, hence the experiment of pond 5E is being repeated on a grand scale. Long-term monitoring sites have been established in three places in Kesterson: a *Nitella*-filled deep-water area in pond 5 and two seasonally flooded playa areas in ponds 7 and 11 (Fig. 1). Initial collections of vegetation and many insect species have been completed, and baseline selenium levels in the food chain have been established. These collections will be repeated periodically to determine the rates of decline of selenium in plant and animal tissues now that no more selenium is entering the reservoir.

The Northern Ponds

The relatively dry northern subarea of the reservoir has received much less selenium-contaminated San Luis Drain water and has much less selenium in sediment and soil. However, baseline biological monitoring indicates that plants and insects in the dry subarea contain as much selenium as their counterparts in the wet subarea, and many migratory birds are known to visit seasonally flooded parts of the dry subarea.

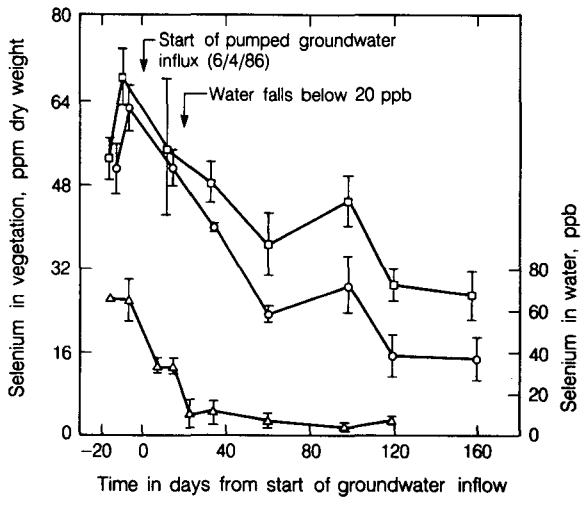

Figure 6. Changes in selenium in water and vegetation in the 1-acre experimental enclosure (pond 5E) during the first 160 days after the introduction of pumped groundwater. Circles: *Nitella*. Squares: aufwuchs (attached diatoms, filamentous algae, etc.) on *Nitella*. Triangles: water. All points are means of three values; error bars show standard deviation. [XBL 872-9905]

Long-term ecological monitoring at established playa sites in ponds 7 and 11 will show the effect of adding no more selenium to the system. Analysis of selenium and determination of selenium species in dry subarea soils will continue. The previously described study of selenium transport in playa areas will also apply to the dry subarea, which includes extensive playas.

Water Treatment for Selenium Removal

Microbial reactions effectively remove selenium from water percolating through the pond-bottom sediments at Kesterson, and it should be possible to utilize the same microbial processes to remove selenium from drainage water in an engineered water-treatment facility (Fig. 7). With internal LBL support, this idea has been successfully tested in the laboratory and in a small-scale pilot plant.

Experiments done in small glass columns have confirmed that selenium is, in fact, removed from drainage water that is allowed to percolate through pond-bottom sediment from Kesterson Reservoir. However, the nitrate in the water oxidizes the sediment, ultimately destroying its ability to sequester selenium (as is suspected to occur in pond 2). Adding glucose to the water protects and enhances the sediment's ability to sequester selenium. To duplicate this microbial process by using glucose or other organic matter in an external system would be impractical. Ecological work at Kesterson has demonstrated that the deep-water ecosystem there is highly productive. In principle, vegetation growing in the ponds should supply enough organic matter to maintain anaerobic conditions in the sediment, as it does at Kesterson.

The complete process, including algae culture, has been successfully operated outdoors in a 150-gallon plastic tank for 10 weeks. At percolation rates of 50 and 100 feet/year, selenium removal has averaged 94%, with 2% conversion to volatile dimethyl selenide. An average percolation rate of 50 feet/year would allow the entire water-treatment requirement of the San Luis Drain to be satisfied by a 160-acre pond. This process is very simple and may prove very economical. The technology is appropriate for use by any irrigation district, and many farmers should be able to build such a treatment facility and operate it effectively. The process lends itself to installations of widely varying capacity, including single-farm or even single-field treatment units.

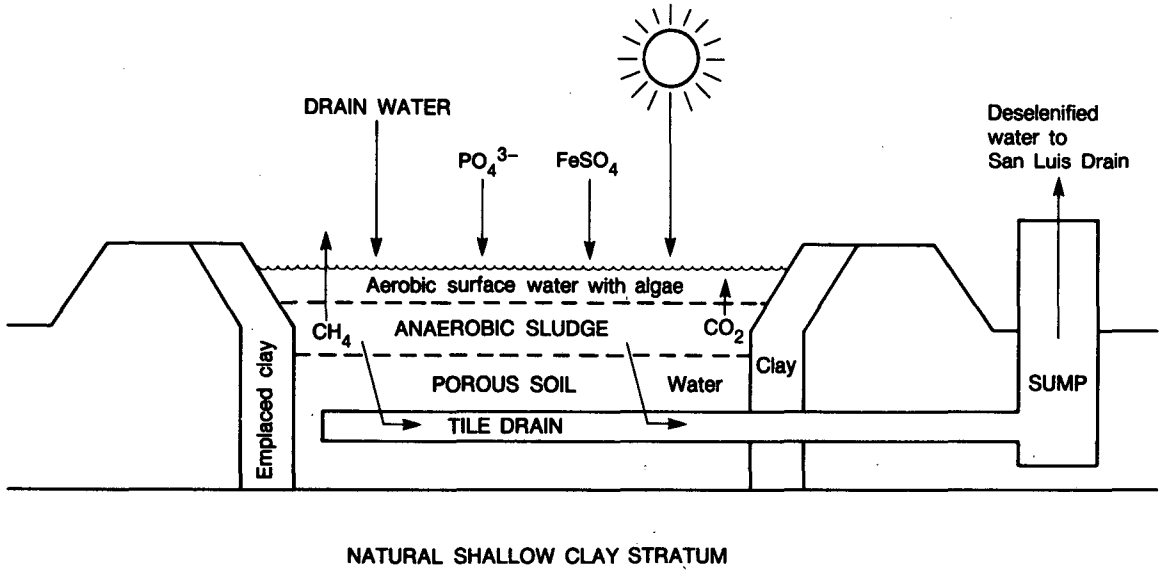

Figure 7. A percolation pond for removing selenium and nitrate from agricultural drainage water. [XBL 859-10729]

CONCLUSION

Research at Kesterson has increased knowledge of the environmental chemistry, groundwater transport, and ecological effects of selenium. This knowledge will find application in related areas; for example, the design of environmentally sound and effective waste-water-treatment systems and the application of hydrological and geochemical methods employed at Kesterson to the larger problem of agricultural drainage in the San Joaquin Valley.

ACKNOWLEDGEMENTS

The Kesterson research program was supported by the United States Bureau of Reclamation. The work on water treatment for selenium removal was supported by the Director's Development Fund.

REFERENCES

USBR, 1986. Preliminary final closure and post-closure maintenance plan, Kesterson Program. U.S. Bureau of Reclamation, Mid-Pacific Region, November 1986.

Weres, O., White, A.F., Wollenberg, H.A. and Yee, A., 1985. Geochemistry of selenium at Kesterson Reservoir: Possible remedial measures. Earth Sciences (Lawrence Berkeley Laboratory PUB-431), v. 8, no. 3, p. 1–8.

Application of Chemical-Reaction-Path Models in Estimating Groundwater Ages at the Nevada Test Site

A.F. White and N.J. Chuma

Determination of groundwater sources and ages in arid environments is often difficult because of the significant variations in the patterns and extent of recharge under past climatic conditions and because of chemical modification during long residence times in the aquifer. One site-specific area where application of ^{14}C age dating of water has proven difficult is at the Nevada Test Site (NTS), at Yucca Mountain in southern Nevada. Estimates of groundwater ages and travel times are critical in this system because it is being studied as a possible site for a nuclear waste repository (Fig. 1). The recharge age of groundwater can be calculated from the radioactive decay of carbon-14 dissolved in water during recharge by the relationship (Mook, 1980)

$$t = -8270\left[\left(\frac{\ln \delta^{14}C}{1000} - 1\right) - \ln Q\right], \quad (1)$$

where t is time in years, $\delta^{14}C$ is the current ^{14}C content of groundwater in parts per million relative to modern water, and Q is a correction factor that accounts for the fact that initial carbon recharged principally as soil gas CO_2 can react with carbonate rocks in an aquifer and thereby dilute the ^{14}C source and increase the apparent age. The principal sources of such carbon at NTS are soil-zone caliche and Paleozoic carbonates underlying the principal tuff aquifer.

The Q correction factor is normally based on the ^{13}C compositions of the initial soil gas, C_{soil}; the calcium carbonate phase, C_{CaCO_3}; and the groundwater, δC_{H_2O}, by the relationship (Pearson, 1965)

$$Q_1 = \delta^{13}C_{H_2O} - \delta^{13}C/\delta^{13}C_{soil} - \delta^{13}C_{CaCO_3}, \quad (2)$$

The use of the above equation has proven difficult in the tuff aquifer because of uncertainties in estimating the initial ^{13}C soil input during past climatic conditions and in estimating the potential ^{13}C inputs from Paleozoic marine carbonates and caliche. Table 1 gives calculated Q values and corrected ^{14}C ages for groundwater in several wells along Fortymile Canyon east of Yucca Mountain. These results are based on the assumption that $\delta^{13}C_{CaCO_3} = 1.4\%$ and $\delta^{13}C_{soil} = -11.3\%$.

An alternate approach to age corrections as suggested by Fritz et al. (1978) is to model the major aqueous geochemistry. Excess Ca^{2+} and HCO_3^- concentrations will indicate extraneous carbonate sources. A reaction-path model controlled by irreversible dissolution of a vitric-tuff phase and soil-zone CO_2 was proposed by Claassen and White (1979). The present study incorporated this approach into a quantitative reaction path code using EQ3NR/EQ6 (Wolery, 1978).

The initial carbon is fixed by the starting CO_2 pressure and is redistributed under closed-system conditions as bicarbonate ions during silicate hydrolysis and carbonate dissolution. An initial P_{CO_2} range

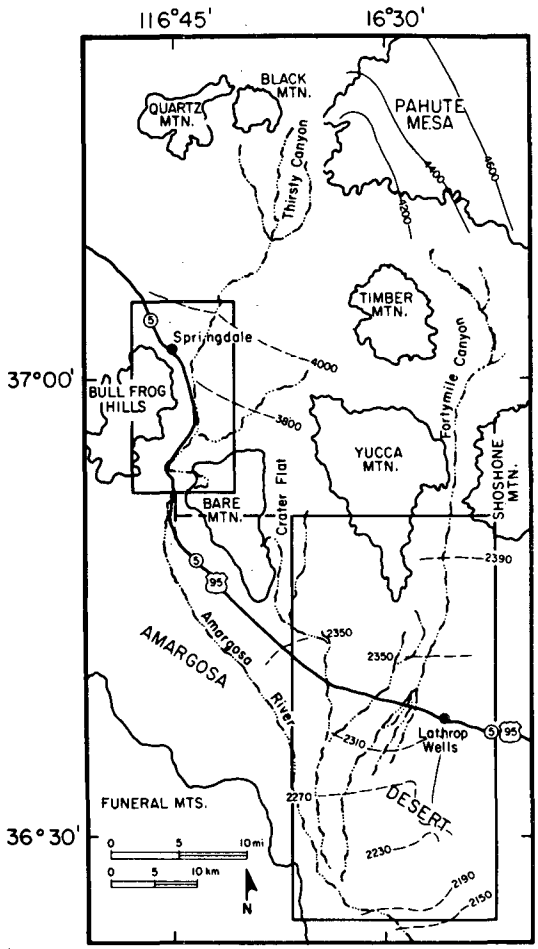

Figure 1. Map of the Oasis Valley-Fortymile Canyon drainage basin. Approximate water-level elevation contours are shown in meters. [XBL 814-2933B]

Table 1. Selected age dates and associated chemical parameters of groundwater in the tuffaceous aquifer.

Site	Location	Total carbon as HCO_3^- (mmoles/L)	^{14}C uncorrected age (y.b.p.)	Isotopic correction factor Q_1	Isotopic corrected age (y.b.p.)	IAP_{CaCO_3} correction factor Q_2	IAP_{CaCO_3} corrected age (y.b.p.)
Fortymile Canyon							
23	J-12	2.03	9,700	0.73	7,100	0.77	7,500
24	J-13	1.93	10,200	0.69	7,100	0.78	8,100
25	UE-29aH2a	1.86	3,900	1.0	3,900	0.79	2,000
26	UE-29aH2b	1.80	4,200	1.0	4,200	0.80	2,400
TE							

of 0.03–0.10 atm produces P_{CO_2}, pH, and HCO_3 reaction simulations that bracket chemical trends observed for groundwater in tuff at NTS (Fig. 2). Present P_{CO_2} pressures currently measured in the unsaturated zone beneath Yucca Mountain are generally an order of magnitude lower, suggesting a greater CO_2 flux during past pluvial periods.

The ionic activity products (IAP) of $MgCO_3$ and $CaCO_3$ for NTS waters, in addition to calcite, dolomite, and magnesite mineral stability fields, are plotted in Fig. 3. The extent of saturation of groundwater can be compared with saturation conditions generated by the closed-system model as indicated by the reaction paths (lines a–f) for mole fractions of variable calcite dissolution $N_{calcite}$ and mole fractions of extraneous carbon produced, N_{carbon}.

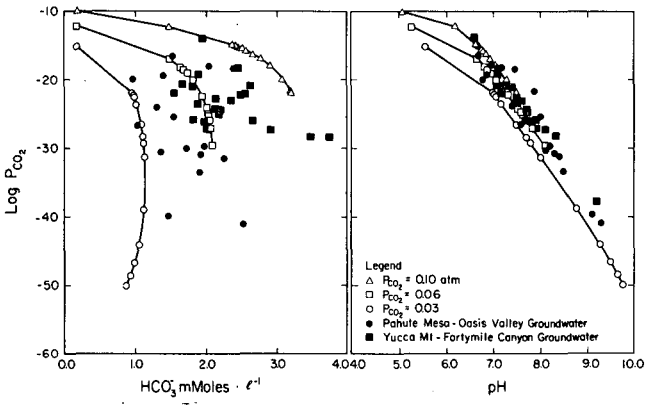

Figure 2. Comparisons of CO_2 partial pressures versus bicarbonate and pH for groundwaters in tuff and for computer simulations reacting glass at varying initial CO_2 pressures. [XBL 8512-12700]

An alternative method of correcting ^{14}C age dates in Eq. (1) is to employ both the calculated IAP_{CaCO_3} and N_{carbon} generated by the model. The corresponding correction factor will be

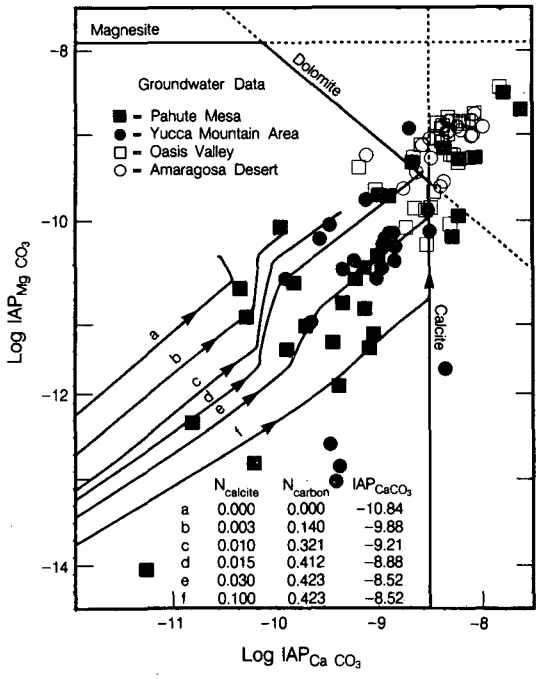

Figure 3. Ionic activity products of calcium carbonate versus magnesium carbonate with indicated mineral stability fields. Reaction paths (lines a–f) are for initial P_{CO_2} = 0.06 atm and for varying mole fractions of calcite reacted (N_{CaCO_3}) and carbon generated (N_C). Solid symbols are for groundwater in tuff, and open symbols are for groundwater in alluvium. [XBL 8611-12731]

$$Q_2 = 1 - N_{carbon}$$

$$= 1 - \left[\frac{\log IAP_{CaCO_3} + 10.836}{5.504} \right], \quad (3)$$

where the right-hand side of Eq. (3) is the approximate linear relationship between N_{carbon} and IAP_{CaCO_3} produced by the simulations (Fig. 3). The resulting Q_2 and adjusted ^{14}C ages are calculated for Fortymile Canyon groundwater and presented in Table 1.

A reasonably good correlation exists between the isotopic and chemical correction factors Q_1 and Q_2 and between adjusted ^{14}C ages. The discrepancy in correction factors for UE-29a2 arises for $\delta^{13}C$ values that are lighter than the assumed soil water $\delta^{13}C$. The uncertainty as to whether these different $\delta^{13}C$ contents actually reflect variable amounts of calcite dissolution or different soil-gas isotopic inputs illustrates the difficulty in making precise age corrections on the basis of unknown but assumed soil ^{13}C contents. In contrast, the total dissolved carbon, pH, and IAP_{CaCO_3} are similar for the Fortymile Canyon wells. These parameters, coupled with similar correction factors based on the chemical-dilution model, indicate small but consistent amounts of carbon dilution in Fortymile Canyon.

REFERENCES

Claassen, H.C., and White, A.F., 1979. Application of kinetic data to ground water systems. A tuffaceous-rock system in southern Nevada. *In* E.A. Jemne (ed.), Chemical Modeling in Aqueous Systems. American Chemical Society Symposium Series 93, p. 771–793.

Fritz, P., Reardon, E.J., Baker, J., Brown, R.M., Cherry, J.A., Killey, W.D., and McNaughton, D., 1978. The carbon isotope geochemistry of a small ground water system in Northeastern Ontario. Water Resour. Res. v. 14, p. 1059–1067.

Mook, W.G., 1980. Carbon-14 in hydrogeological studies. *In* P. Fritz and J. Ch. Fontes (eds.), Handbook of Environmental Isotope Geochemistry. Elsevier, Amsterdam, p. 47–71.

Pearson, F.J., Jr., 1965. $^{13}C/^{12}C$ ratios to correct radiocarbon ages of materials initially diluted by limestone. *In* Proceedings, Sixth International Conference on Radiocarbon and Tritium Dating, Pullman, Washington, USAEC Conf. 650652.

Wolery, T.J., 1978. Calculation of chemical equilibrium between aqueous solutions and minerals. The EQ3/EQ5 software package. Lawrence Livermore Laboratory Report UCRL-52658.

A Core Hole in the Southwestern Moat of the Long Valley Caldera: Early Results

H.A. Wollenberg, M.L. Sorey, C.D. Farrar,† A.F. White, S. Flexser, and L.C. Bartel‡*

The Long Valley caldera (Fig. 1) is the focus of intensive investigations of its volcanic petrology, seismic and volcanic hazards, geothermal resource potential, and potential for energy resource recovery from relatively shallow magma bodies. With respect to the last item of interest, attention has focused on the area underlain by the resurgent dome (Rundle et al., 1986). The present-day hydrothermal system appears to be most strongly influenced by heat sources west of the resurgent dome, perhaps associated with the recently active (550–650 years) Inyo volcanic chain of dikes, craters, and flows described by Miller (1985). However, the western and southwestern parts of the caldera remain the least explored of all. An understanding of the hydrothermal regime of the western moat is considered the key to understanding the origin and circulation of the present-day hydrothermal system within the Long Valley caldera.

Concepts of the Long Valley hydrothermal circulation system have been described by Sorey (1985) and Blackwell (1985). Temperature reversals observed in wells suggest that hot water flows laterally in a continuous zone beneath the south

*U.S. Geological Survey, Menlo Park, California.

†U.S. Geological Survey, Santa Rosa, California.

‡Sandia National Laboratories, Albuquerque, New Mexico.

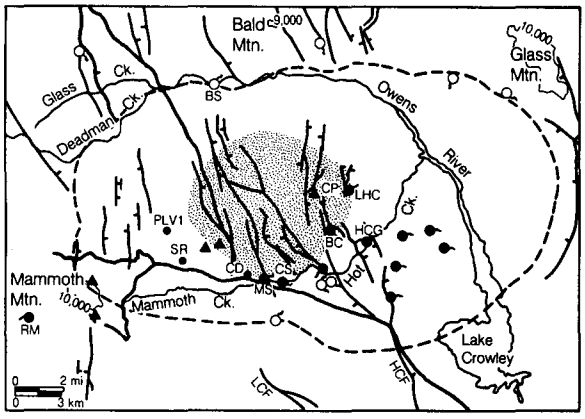

Figure 1. Map of Long Valley caldera, showing outline of caldera floor (broken line), faults (HCF = Hilton Creek fault, LCF = Laurel-convict fault), active thermal springs (filled circles with tails), nonthermal springs (open circles with tails), fumaroles (triangles) and areas of hydrothermal alterations: CP = Clay Pit, LHC = Little Hot Creek, BC = Blue Chert outcrop, HCG = Hot Creek Gorge. PLV-1, SR (Shady Rest), and CD (Casa Diablo) are drill holes discussed in the text. The stippled area represents the resurgent dome. Geologic base from Bailey and Koeppen (1977). [XBL 868-10959]

moat from Casa Diablo (CD in Fig. 1) eastward at an altitude of approximately 2100 m. The temperature in this zone decreases from about 170°C in wells that supply the geothermal electric power plant at Casa Diablo Hot Springs to less than 70°C near Lake Crowley. Before drilling the Shady Rest hole, which is described here, only the high temperature gradient in the bottom part of well PLV-1 suggested the presence of a deeper (> 1 km) hot-water reservoir beneath the west moat. This reservoir may contain water at temperatures above 200°C, as estimated from chemical geothermometer calculations based on Casa Diablo fluids, and may be continuous with the deeper flow zone delineated by the temperature reversal at an altitude of ~1500 m in well M-1, drilled through caldera fill to metamorphic bedrock at Casa Diablo Hot Springs. A portion of the flow in this deeper reservoir may move upward along fault-zone conduits west of Casa Diablo to charge the shallow hot-water flow zone around the south side of the resurgent dome. Fluid in the deeper reservoir may be heated by hot intrusive rocks associated with the southern extension of the ~600-year-old Inyo Craters dike system.

With this concept in mind, it became evident that one or more new drill holes were needed in the caldera's western moat to provide confirmation of the models of the present-day hydrothermal system proposed by Sorey (1985) and Blackwell (1985). The essence of these models is that the hydrothermal system is dominated by zones of lateral flow of thermal water in aquifers located within and above the welded Bishop Tuff. The most likely source of heat for this system is associated with intrusive bodies beneath the west and southwest moat areas. Drill-hole information from the resurgent dome area indicates that zones of deep fluid circulation no longer exist beneath the resurgent dome and that hot springs and fumaroles on or around the dome are fed from relatively shallow aquifers that are connected by lateral flow to a source reservoir within the Bishop Tuff beneath the western moat.

These considerations suggest (1) that if a residual magma chamber is in place beneath the central part of the caldera, it does not represent a significant heat source for the present-day hydrothermal system and (2) that if magma is present at depths as shallow as 4–5 km beneath the resurgent dome, it has not been in place long enough to influence the overlying groundwater system. In contrast, evidence of intrusive and extrusive magmatic activity along the Inyo volcanic chain as recently as 550–650 years ago lends support to the conclusion that the heat source for the present-day hydrothermal system is magma associated with the Inyo-Mono system beneath the west moat. A southern projection of the Inyo-Mono system terminates at Mammoth Mountain—a large, predominantly rhyodacite volcanic dome on the caldera's southwestern rim.

Given this hydrogeologic setting it was proposed to drill a hole near the Shady Rest Campground to provide information on the presence of a hot-water reservoir within the Bishop Tuff beneath the southwest moat. Such information would take the form of a high-temperature gradient, as encountered in well PLV-1, located 2.5 km to the northwest of Shady Rest (Fig. 1). Data from a 155-m test hole drilled in 1984 near Shady Rest for the Mammoth County Water District (Guacci and McCann, 1984) suggested that additional zones of thermal water occur above the welded tuff; the source of this water could provide energy for space heating in Mammoth Lakes. For this reason Mono County and the California Energy Commission contributed financially to the Shady Rest drilling effort. Industry interest was also focused on the western moat. Unocal Geothermal was actively exploring the Inyo Craters area, ~6 km northwest of Shady Rest, and drilled test hole (#44–16) to a depth of ~1800 m in the late fall of 1985. This hole intersected a zone of temperatures over 200°C in the Bishop Tuff at depths of 915–1175 m. This hot zone is immediately underlain by a much cooler zone in precaldera volcanic

rocks (E. Suemnicht, 1987). Hence government-sponsored drilling south of the Unocal hole and west of the town of Mammoth Lakes would provide a valuable source of information on the southern extent of hydrothermal circulation in the present-day system and on the sources of heat for that system.

It was the consensus of participants at the 1984 Long Valley workshop (Sorey et al., 1985) that, to resolve the critical question of the flow paths in the hydrothermal system of the west moat area and the location of the associated heat source, an intermediate-depth (1–2 km) hole should be drilled in the vicinity of Mammoth Mountain. In this respect, the Shady Rest hole described here can be considered a "stepout" west of Casa Diablo, to test the rationale for the deeper hole. Though the Shady Rest hole does not penetrate deeply enough to answer the above-noted questions unequivocably, it does confirm the presence of 200°+ water beneath the west moat and provides access to hydrologic and geochemical information otherwise unobtainable until a deeper hole is drilled. Such information will be definitive in siting and determining the depth of the deeper hole.

CORING AND RELATED ACTIVITIES

On June 17, 1986, the continuously cored hole was completed. Its configuration is shown in Fig. 2. The hole was rotary-drilled to 92 m, and a 12.7-cm-diameter surface casing was installed. The hole was then cored by HQ wireline to a total depth of 715 m. Core recovery exceeded 90%. The core now resides at the DOE's repository at Grand Junction, Colorado.

Difficulties were encountered in completing the hole; sloughing, squeezing, and lost circulation prevented installation of casing over the full 715 m depth. Attempts to redrill and recover the part of the hole below 245 m resulted in a "new" hole that diverged from the original at 241 m (Fig. 2). The "new" hole was cored to a depth of 426 m, where *N*-sized casing (6-cm I.D.) was cemented in and filled with water, temporarily configured as a thermal gradient hole.

Following repeated temperature surveys to determine an equilibrium profile, a 3-m section of the cased hole was perforated at a depth of 335 m in the high-temperature zone in mid-October 1986, providing access for fluid sampling of this hot aquifer. Immediately upon perforation, ~2000 L of cold water was pumped into the hole to prevent flashing should communication with the formation cause excessive draw-down of the hole's water column. Flashing did not occur, as the water level initially fell

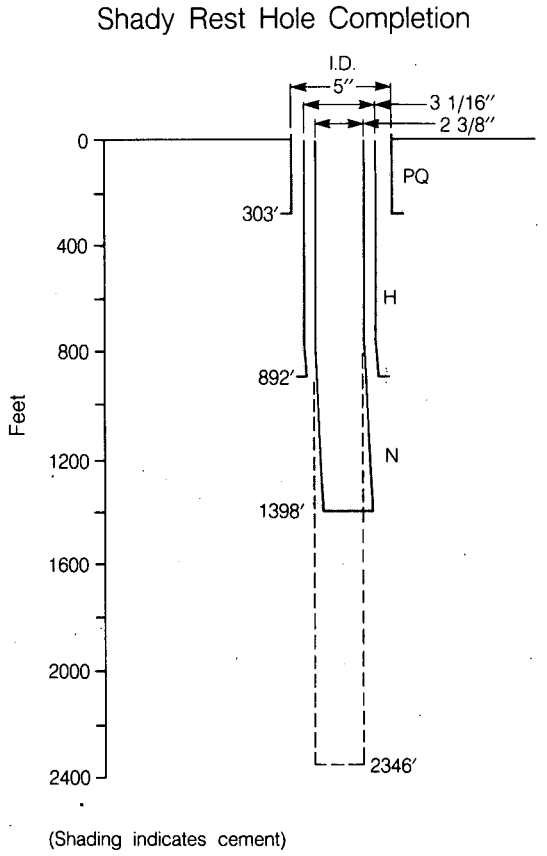

Figure 2. Completion diagram of the Shady Rest hole. [XBL 868-10960]

to a depth of 146 m and then gradually rose to stablize at 134 m. In mid-November 1986, another temperature survey was made. The fluid in the hole was first bailed to ensure the presence of formation water, and then in collaboration with scientists at the Sandia and Los Alamos National Laboratories, fluid samples were obtained at perforation depth by means of a downhole sampler.

EARLY RESULTS

Lithologic units encountered, in descending order, include glacial till to ~65 m; rhyolitic white to light-gray pumiceous tuff, the Moat Rhyolite of Bailey and Koeppen (1977) to ~205 m; harder gray, flow-banded Early Rhyolite, containing a zone of volcanoclastic lake-bed deposits, to 430 m; and ~285 m of predominantly welded ash-flow tuff (the Bishop Tuff) to the bottom of the hole (Fig. 3). Numerous steeply dipping open fractures, lined by quartz and calcite covering sulfide minerals (Fig. 4), are preserved in core from about the lower 400 m of the hole, the high-temperature zone. The elevation of the top of the Bishop in this hole is the highest

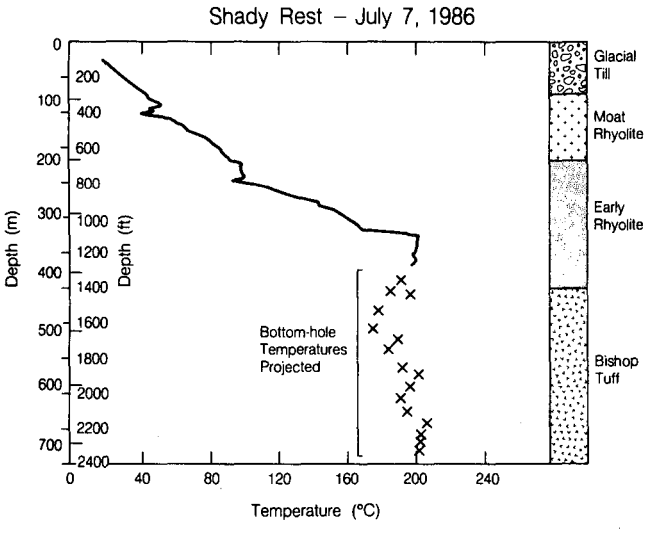

Figure 3. Equilibrium temperature profile (7/7/86) with projected temperatures from bottomhole measurements made during coring, together with a lithologic diagram of the Shady Rest hole. [XBL 868-10961]

encountered in any hole in the caldera, and the temperatures measured are among the hottest reported in any of the holes drilled within the caldera.

An equilibrium temperature profile, together with projected bottomhole temperatures measured during drilling, are plotted in Fig. 3. The temperature increases fairly regularly (interrupted by two zones of apparently cooler water at 120 and 245 m) to ~160°C at a depth of ~330 m. Temperatures then rise abruptly to 202°C at 335 m (a lost-circulation zone in the fractured, silicified Early Rhyolite). Below this zone there is a nearly isothermal pattern, mostly between 190 and 200°C, that extends into the Bishop Tuff and to the bottom of the hole.

The relative position of the Shady Rest thermal profile with respect to those of PLV-1 and the deep test hole at Casa Diablo Hot Springs is shown in Fig. 5. When plotted on the same elevation scale, we see that the upper part of the high-temperature zone at Shady Rest is at nearly the same elevation as the upper high-temperature zone at Casa Diablo, whereas the zone of increasing temperature near the bottom of hole PLV-1 is at a somewhat lower elevation. The similarity in the elevations of the high-temperature portions of the Shady Rest and Casa Diablo profiles suggests that hot water is moving from west to east through that zone, even though its flow path may be interrupted by faults, as shown in the geologic section (Fig. 6). The high-temperature zone at Shady Rest occurs both in the lower part of the Early Rhyolite and in the Bishop Tuff, whereas at Casa Diablo, the high-temperature zone is confined to the Early Rhyolite. The top of the high-temperature zone of Shady rest is ~900 m higher in elevation than that of the high-temperature zone at the Unocal #44-16 hole.

CONTINUING ACTIVITIES

The core has been described in detail. Planned investigations of core include alteration mineralogy, $^{87/86}Sr$ and $^{12/13}C$ ratios of fracture calcite, and oxygen and hydrogen isotope ratios. Uranium-series disequilibrium will be investigated in intervals indicated by gamma-ray logs. At this writing, the hole's casing has been perforated, and the initial fluid samples have been taken. Major and trace chemical constituents of fluid and gases will be analyzed, and stable-element isotope ratios ($^{12/13}C$, H/D, $^{18/16}O$) will be measured. We expect that, as with the fluids

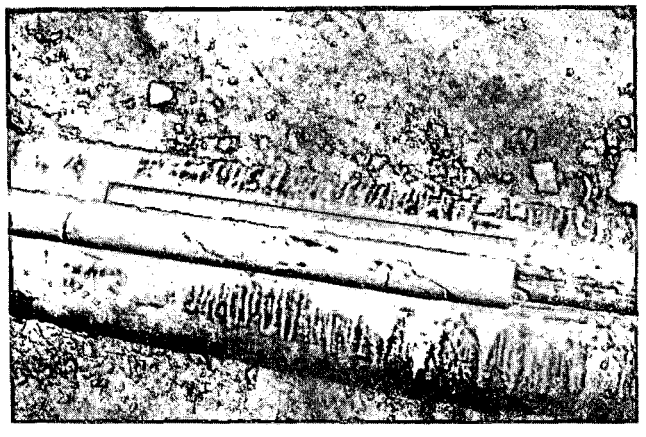

Figure 4. Core from Bishop Tuff section, showing an open fracture lined by calcite-quartz (light) and rimmed by a darker zone of sulfide minerals. [XBC 873-1637]

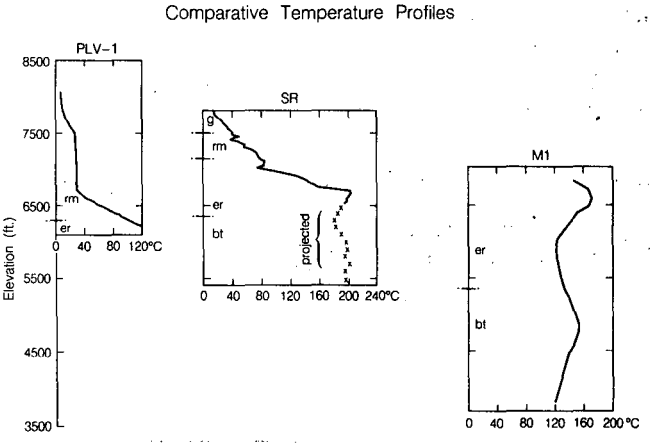

Figure 5. Elevations of thermal profiles at PLV-1, Shady Rest, and the Casa Diablo deep test hole. [XBL 868-10958]

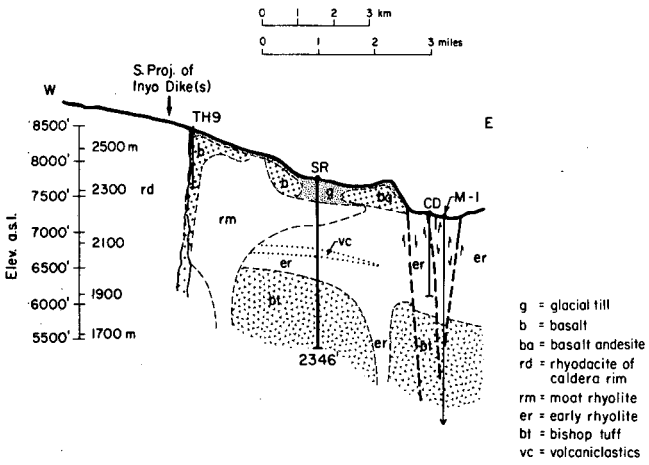

Figure 6. Geologic section from the eastern flank of Mammoth Mountain, through Shady Rest, to Casa Diablo Hot Springs. TH-9 is a water-supply test well drilled by the Mammoth County Water District. [XBL 851-10251]

sampled at Casa Diablo Hot Springs, chemical geothermometer temperatures based on these analyses will indicate that still-hotter conditions will be encountered at depth to the west of Shady Rest. If this expectation holds, there is a good reason for siting a hole—perhaps on the eastern flank of Mammoth Mountain —that would penetrate through caldera fill and into Sierra Nevada basement rock to investigate the source of heat for the hot fluids. The high temperature encountered in the Bishop Tuff in Unocal hole 44-16, together with the immediately underlying relatively cold zone, suggests that conditions of hydrothermal stratification prevail west of Shady Rest. The hot water at 44-16 could be moving northward from the vicinity of Mammoth Mountain, through fractured Bishop Tuff, while colder water, recharged from the Sierra Nevada, moves more easterly in the underlying pre-caldera Tertiary volcanic and Paleozoic metamorphic rocks. In this respect the Mammoth Mountain area remains as a primary location for the next drilling target.

ACKNOWLEDGEMENT

The Shady Rest project is sponsored by the U.S. Department of Energy's Office of Basic Energy Sciences, the California Energy Commission, Mono County, and the U.S. Geological Survey. Drilling, coring, and hole completion were ably accomplished by the Tonto Drilling Company, supervised by personnel of the DOE Geosciences Research Drilling Office at Sandia National Laboratories.

REFERENCES

Bailey, R.A., and Koeppen, R.P., 1977. Preliminary geologic map of Long Valley caldera, Mono County, California. U.S. Geol. Survey Open-File Map 77-468.

Blackwell, D.D., 1985. A transient model of the geothermal system of the Long Valley caldera, California. J. Geophys. Res., v. 90, no. B-13, p. 11229–11241.

Guacci, G., and McCann, D.L., 1984. Exploratory drilling, vicinity of Mammoth Lakes, California for Mammoth County Water District. Internal Report, prepared by LeRoy Crandall and Associates.

Miller, C.D., 1985. Holocene eruptions at the Inyo volcanic chain, California: Implications for possible eruptions in Long Valley caldera. Geology, v. 13, p. 14–17.

Rundle, J.B., Carrigan, C.R., Hardee, H.C., and Luth, W.C., 1986. Deep drilling to the magnetic environment in Long Valley caldera. EOS, Trans. Am. Geophys. Union, v. 67, no. 21, p. 490.

Sorey, M.L., 1985. Evolution and present state of the hydrothermal system in Long Valley caldera. J. Geophys. Res., v. 90, no. B-13, p. 11219–11228.

Sorey, M.L., Farrar, C.D., and Wollenberg, H.A. (eds.), 1985. Proceedings of the Workshop on Hydrologic and Geochemical Monitoring in the Long Valley caldera, Mammoth Lake, California, October 8–10, 1984. Lawrence Berkeley Laboratory Report LBL-20020.

Suemnicht, G.A., 1987. Results of deep drilling in the western moat of Long Valley, California. *In* Proceedings, Twelfth Workshop on Geothermal Reservoir Engineering. Stanford Geothermal Program Report SGP-TR-109, in press.

GEOMECHANICS

The principal thrust of research in the Geomechanics group is to develop a fundamental understanding of the mechanical and hydrologic properties and behavior of rocks under conditions of temperature and pressure pertaining to engineered or natural phenomena in the upper crust. The properties of rocks and their behavior depend upon both the mechanical structure of the rock (pores, microcracks, joints, fractures, and faults) and the physical and chemical interactions between fluids and mineral surfaces.

The research in geomechanics is both theoretical and experimental. Much of it involves applying the principles of linear elastic fracture mechanics to evaluate the effects of microcracks and asperities of contact on the deformation of intact and fractured rock. The effective elastic moduli of rocks containing any populations of cracks and fractures can readily be calculated. By accounting for the initiation, growth, and interaction of cracks, complete stress-strain curves can be derived that exhibit strain hardening, strain softening or slip weakening, dilation, and intrinsic instability under differential compressive stress. Complete stress-strain curves derived explicitly from measured microcrack populations compare well with experimental measurements. For extensively fractured rock masses, an outgrowth of block theory called discontinuous deformation analysis, which incorporates the elastic deformation of both blocks and the contacts between them, is being developed in parallel with physical models.

The growth of microcracks and their coalescence to form fractures is being studied experimentally using Woods metal porosimetry. Woods metal is molten above 90°C, when it resembles mercury, but at room temperature it is solid. Molten Woods metal used as a pore fluid at pressures of 10 MPa penetrates cracks with apertures of as little as a tenth of a micrometer. By solidifying Woods metal in rock specimens deformed to prescribed strains in a stiff, servo-controlled testing machine, it is possible to preserve the deformed crack and fracture geometry in great detail for microscopic study after sectioning. The same technique has been used to study the distribution of the areas of contact and the void spaces between the surfaces of natural fractures in rock.

Important discoveries have been made relating to the geophysical and hydraulic properties of natural fractures. The flow of fluid through natural fractures is much more complex than previously thought, comprising a high-stress component that is very insensitive to the stress across the fracture and a low-stress component that is much more sensitive to stress than indicated by the well-accepted cubic law.

Seismically, fractures can be represented by an elastic-displacement discontinuity. This results in frequency-dependent coefficients for the reflection, transmission, and time delay of seismic waves propagating across a fracture. These changes occur at the fracture for all frequencies and make it possible to locate and characterize fractures using seismic tomography.

Seismic-Wave Properties of Idealized Fractures

D.L. Hopkins, L.R. Myer, and N.G.W. Cook

Seismic methods are currently among the most promising geophysical techniques for characterizing the fracturing at potential repository sites. Until recently the effects of fractures on seismic waves were included implicitly in models by modifying the bulk material properties of the medium. A new theory has now permitted development of models that can explicitly account for the effect of each fracture on the velocity and attenuation of a seismic wave.

A central concept in this new theory is that a fracture, which may be visualized as a nonwelded interface, causes a discontinuity in seismic displacement as the wave crosses the fracture, while seismic stresses remain continuous. Specific stiffness defines the relationship between the applied seismic stress and the displacement discontinuity across the nonwelded interface. For a prescribed stiffness, theory completely specifies the reflection, refraction, and transmission of plane waves incident upon the interface (Schoenberg, 1980).

To validate the theory a series of controlled laboratory experiments has been performed in which seismic waves were propagated across idealized fracture surfaces. In addition a new analytical model has been developed and implemented numerically to calculate the specific stiffness of a fracture.

THEORY

A nonwelded interface may be envisioned as two surfaces that are in contact over a portion of their area. Between the contact areas are voids. Formally, specific stiffness is defined as the average applied stress divided by the displacement across the interface in excess of the displacement that would occur if the load were uniformly distributed across two surfaces in perfect contact. According to this definition, specific stiffness has the desired properties of becoming infinite for a perfectly welded joint and approaching zero for an interface with vanishing contact.

The seismic-wave transmission coefficients are derived on the assumption that stresses are continuous across the joint, whereas displacements are discontinuous by an amount proportional to the specific stiffness of the interface. Making the further assumption that the thickness of the interface is small compared to the incident wavelength, Schoenberg (1980) has derived the general solution to the elastodynamic problem of obliquely incident plane waves.

For normally incident waves and media of the same properties on both sides of the interface, the expressions for the magnitude of the transmission coefficients for compressional (P) and shear (S) waves are:

$$\left|T_P(\omega)\right| = \frac{2(k_z/z_P)}{\sqrt{4(k_z/z_P)^2 + \omega^2}},$$

$$\left|T_S(\omega)\right| = \frac{2(k_x/z_S)}{\sqrt{4(k_x/z_S)^2 + \omega^2}},$$

where $z_P = \rho c_P$, $z_S = \rho c_S$, $c_P = \sqrt{(\lambda + 2\mu)/\rho}$, $c_S = \sqrt{\mu/\rho}$, λ = Lamé's constant, μ = shear modulus, ρ = density, ω = circular frequency, and k_z, k_x = specific stiffness under normal and shear stress, respectively.

RESULTS OF EXPERIMENTS

In a previous series of laboratory experiments, an idealized fracture surface was created by placing thin parallel strips of lead between two steel cylinders. The experimental setup is shown in Fig. 1. For these experiments good agreement was found between observed attenuation and that predicted by theory for both compressional and polarized shear waves and for both dry and saturated conditions (Myer et al., 1985). The present study was designed to extend the experiments to more complex three-dimensional geometries that better represent fracture surfaces in rock. For the current experiments idealized fractures are created by placing thin lead disks of varying diameter between the steel cylinders.

To compare the results of the experiments with those predicted by theory, the stiffness of each idealized fracture was determined using the model described in the following section. The transmission coefficients were then calculated using the equations described in the previous section. Amplitude spectra for each signal were obtained from a Fast Fourier Transform of the received waveform, as described in Myer et al. (1985). To produce predicted spectra for each configuration of disks, the transmission coefficients were applied to the spectra obtained when the two steel cylinders were separated by a solid disk of lead. The solid disk was the same thickness as the

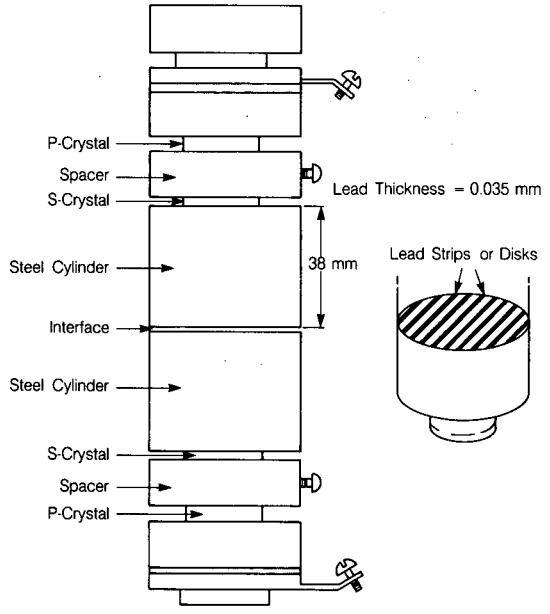

Figure 1. Experimental setup. Thin strips or disks of lead are placed between two steel cylinders to create artificial fracture surfaces. *P*- and *S*-waves are transmitted and received by two pairs of piezoelectric crystals placed at the top and bottom of the stack, respectively. [XBL 8610-12636]

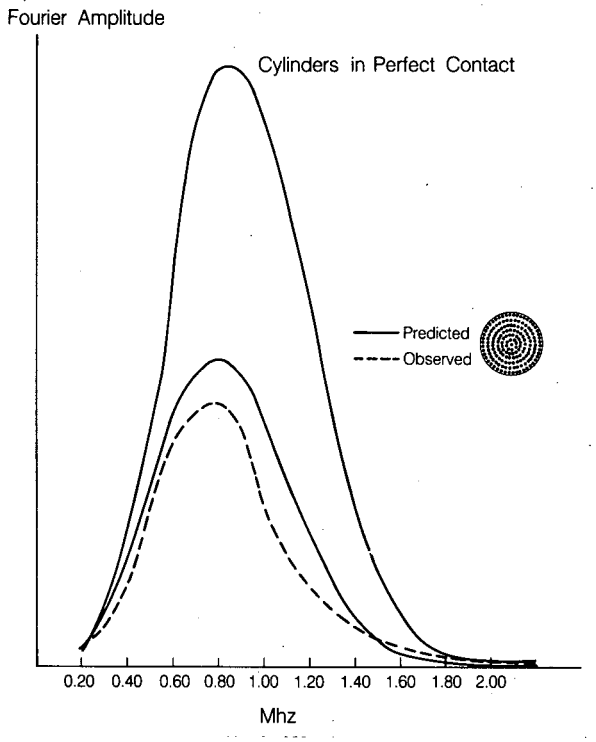

Figure 2. Fourier amplitude spectrum of the predicted signal (solid line) versus the spectrum of the observed signal (broken line) for an arrangement of 165 disks, each 1 mm in diameter. [XBL–8610-12637]

disks of lead used to create the idealized fractures and was used to ensure good contact between the steel cylinders.

Figure 2 shows the predicted amplitude spectrum versus the amplitude spectrum of the observed signal as a function of frequency for an arrangement of 165 1-mm disks. The amplitude spectrum of the signal observed when the steel cylinders were separated by a solid lead disk is included for reference. For these initial experiments the magnitude of the energy transmitted across the interface increased with increasing stiffness, as predicted by theory, but was less than that predicted.

MODELING

The need to calculate the stiffness of the idealized fractures created in the laboratory prompted the development of an analytical model that has been implemented numerically. Models of rough surfaces in contact have been developed by other researchers (e.g., Greenwood and Williamson, 1966; Gangi, 1978; and Brown and Scholz, 1985). In these models fracture stiffness is estimated on the basis of the deformation of the contact areas (asperities) between the opposing fracture surfaces. Our approach differs in that our estimate of stiffness is based on the deformation of the two half-spaces defining the fracture as well as the deformation of the contacts. The difference between the two formulations is illustrated in Fig. 3. Taking account of the deformation of the fracture surfaces leads to a larger average displacement across the fracture and a different value for the volume of the void space than is calculated if only the deformation of the asperities is considered.

Unlike some models, this model is not assumed to have mechanically independent contacts. Rather, the force carried by each asperity depends on its height and the heights and proximity of neighboring asperities. Likewise, the deformation at any point on the half-planes defining the fracture is assumed to be a linear combination of the deformations caused by the forces acting on all asperities in the region. For work done to date, the asperities are modeled as disks, and the deformation of the half-spaces defining the fracture is calculated using the Boussinesq solution for displacement beneath a loaded circle, assuming a constant-stress boundary condition (Timoshenko and Goodier, 1969).

As a first step in assessing the performance of the model, we searched for an alternative method of estimating stiffness that would allow us to compare results from the model with results obtained using an independent solution. For the particular case of an interface defined by a series of parallel strips, we were able to use the methods of linear elastic fracture

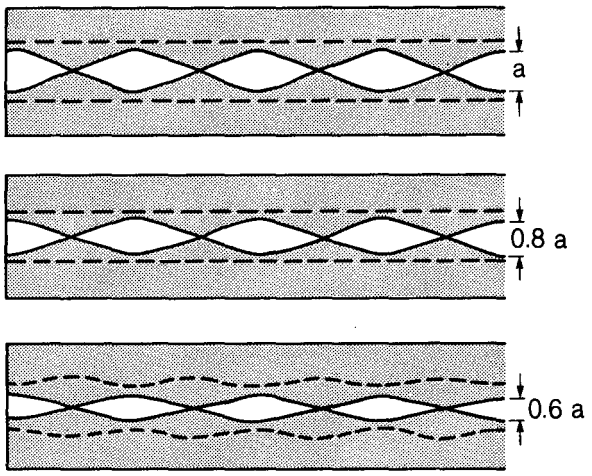

Figure 3. Schematic drawing of displacement across a fracture under two different models. **(Top)** An idealized fracture under zero load. When a normal stress is applied to the fracture, the reference planes (indicated by the broken lines) move closer together. **(Middle)** The difference in displacement and aperture that results when only the deformation of the asperities is considered. **(Bottom)** The difference in displacement and aperture that results when the deformation of the half-planes defining the fracture is considered in addition to the deformation of the asperities. [XBL 8610-12635]

mechanics and Betti's reciprocal theorem to derive the following expression for displacement, which can be used to calculate stiffness:

$$\bar{\delta} = \frac{-8\sigma b(1-\nu^2)[\log\cos(\pi c/2b)]}{\pi E},$$

where σ is the applied stress, ν is Poisson's ratio, E is Young's modulus, $2c$ is the spacing between strips, and $2b$ is the center-to-center distance between strips.

The derivation relies on fracture mechanics to provide an expression for strain energy based on the stress-intensity factor for a row of parallel slits. Betti's reciprocal theorem is then used to derive the relationship between strain energy and displacement. Once the expression for displacement is obtained, stiffness can be calculated as explained previously.

As shown in Table 1, the fracture-mechanics solution and the model yield results that agree well, with the best agreement being for those arrangements where the strips are relatively close together. As an additional check on the model, displacement measurements will be made in the laboratory for a variety of surfaces and compared with those predicted by the model.

In addition to calculating the stiffnesses of the idealized fractures used in the laboratory experi-

Table 1. Comparison of specific stiffness (K_{sp}) calculated using the model described in this article versus the stress-intensity factor solution (SIF) for different ratios of spacing to strip width; e.g., a ratio of 2:1 means the spacing between strips was 2 times the width of the strips.

Ratio of strip spacing : width	K_{sp} (MPa/m)	
	Model	SIF
1 : 1	10.47 E7	10.75 E7
2 : 1	5.25 E7	5.09 E7
3 : 1	3.23 E7	3.00 E7
7 : 1	1.06 E7	0.87 E7

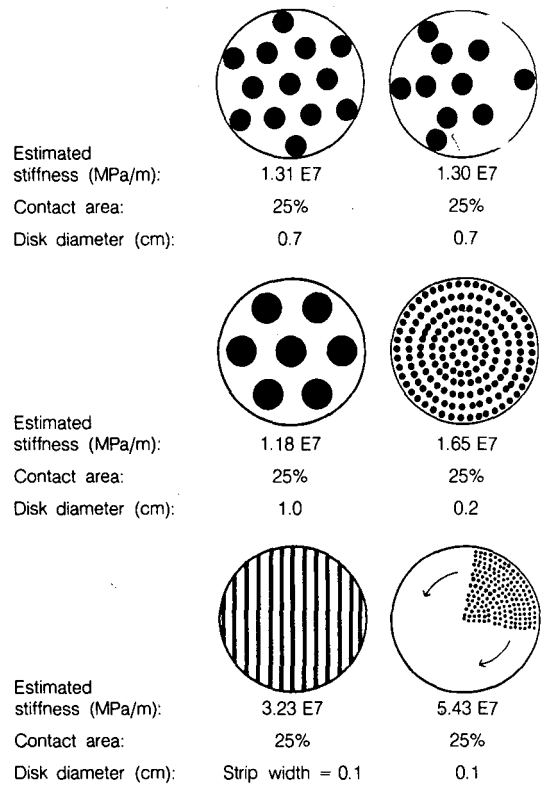

Figure 4. Stiffnesses calculated for different arrangements of disks with nearly identical contact areas. [XBL 871-9889]

ments, the model has been used to study the relationship between contact area, contact geometry, and stiffness. Several different arrangements of disks and strips are shown in Fig. 4. Even though these configurations represent nearly identical contact areas of 25%, stiffnesses vary significantly, demonstrating that stiffness is not uniquely determined by either contact area or geometry.

REFERENCES

Brown, S.R., and Scholz, C.H., 1985. Closure of random elastic surfaces in contact. J. Geophys. Res., v. 90, p. 5531–5545.

Gangi, A.F., 1978. Variation of whole and fractured porous rock permeability with confining pressure. Int. J. Rock Mech. Min. Sci., v. 15, p. 249–257.

Greenwood, J.A., and Williamson, J.B.P., 1966. Contact of nominally flat surfaces. Proc. R. Soc., London, Ser. A, v. 295, p. 300–319.

Myer, L.R., Hopkins, D.L., and Cook, N.G.W., 1985. Effects of contact area of an interface on acoustic wave transmission characteristics. *In* Proceedings, 26th U.S. Symposium on Rock Mechanics, p. 565–572.

Schoenberg, M., 1980. Elastic wave behavior across linear slip interfaces. J. Acoust. Soc. Am., v. 68, no. 5, p. 1516–1521.

Timoshenko, S.P., and Goodier, J.N., 1969. Theory of Elasticity. McGraw-Hill, New York, p. 403–409.

Theoretical Nonlinear Constitutive Relationships for Brittle Rocks

J.M. Kemeny and N.G.W. Cook

Fractures are persistent features in the crustal rocks of the earth and vary in length from microns to kilometers. Fractures in rocks include joints, faults, microcracks, and other planar features across which the displacement field is discontinuous, and fractures are known to alter significantly the mechanical, hydrologic, thermal, chemical, and electrical properties of a rock mass. The work summarized here is concerned with the effect of fractures on the stability of a rock mass, which is important, for instance, in earthquake rupture, stability of underground openings, and acoustic emission in laboratory tests. Experimental work in the 1960s and 1970s revealed that the stability of rock samples tested in compression depends on the interaction of the rock constitutive behavior with the stiffness of the testing machine (Jaeger and Cook, 1979), and these studies also showed a strong correlation between nonlinear constitutive laws for brittle rock and the growth, interaction, and coalescence of microcracks (Wawersik and Brace, 1971; Hallbauer et al., 1973). Recent experimental work with crack-like openings in plexiglass (Horii and Nemat-Nasser, 1985) has shown that the growth of microcracks accounts for most of the nonlinear constitutive behavior of brittle materials rather than the inherent nonlinear behavior of the material surrounding the cracks. This strongly suggests that the instability associated with earthquake rupture may also be related to (1) the nonlinear constitutive relationships that are attributable to the changing microstructure along the fault plane and (2) the interaction of these nonlinear laws with the stiffness of the surrounding ground. It has been suggested (Kanamori, 1986) that earthquakes are due to the breaking of asperities along fault planes. The propagation of cracks in a body and the progressive failure of asperities along a fault zone are complementary features. The same theory can be used to model both of these processes by assuming that asperities are the regions in between a collinear or coplanar distribution of cracks.

Here we describe an analytic method for calculating nonlinear constitutive laws on the basis of crack growth in an otherwise linear elastic material, or the failure of asperities along a fault plane. This approach takes into account the effects of a changing microstructure on the macroscopic behavior of rocks for various types of material heterogeneity. This

method has been applied to the failure of rocks under compressive and tensile stresses, where the heterogeneity consists of randomly located microcracks (Kemeny and Cook, 1986a, 1987). It has also been applied to the frictional response of joints and faults, where the heterogeneity consists of distributions of asperities along the slip surface (Kemeny and Cook, 1986b). In both cases the calculated stress-strain curves and the patterns of energy release during instability correlate well with available experimental data.

ROCK FRACTURE MECHANICS

The basis for the analysis presented here is linear elastic fracture mechanics (Rice, 1968). The crack-tip-stress intensity factor is a measure of the magnitudes of the stresses occurring near the tip of a crack in a linear elastic solid. It is common in crack mechanics to distinguish three types of stress-intensity factors, K_{I}, K_{II}, K_{III}, which relate to the three types of cracking modes, mode I (opening mode), mode II (sliding mode), and mode III (tearing mode). The stresses near the crack tip then have the following form (Rudnicki, 1980):

$$\sigma_{ij} = K_L(2\pi r)^{-1/2} f_{ij}^L(\theta) + \text{nonsingular terms}, \quad (1)$$

where r is the radial distance from the crack tip; θ is the angle measured from the plane of the crack; i and j take on the values 1,2,3 for the three cartesian coordinates; and L takes on the values I, II, III for the three cracking modes. All the details of the loading and crack geometry are contained in the K terms. Equation (1) shows that the singular part of the stress field due to the crack is embedded in the $r^{-1/2}$ term, which contains K as a multiplicative constant, and therefore the solution with only this first term is valid in some neighborhood close to the crack tip.

Much of the usefulness of stress-intensity factors for rock fracture mechanics lies in their exact relation to the strain energy in an elastic solid. The energy release rate, G, is defined as

$$G = \frac{\partial U_e}{\partial c}, \quad (2)$$

where U_e is the elastic strain energy of a solid that contains a crack and $2c$ is the crack length. It has been shown (Irwin, 1957) that the following relationship holds between G and the stress-intensity factors:

$$G = \frac{K_{\mathrm{I}}^2}{E'} + \frac{K_{\mathrm{II}}^2}{E'} + \frac{K_{\mathrm{III}}^2}{E}(1 + \nu), \quad (3)$$

where $E' = E$ for plane stress and $E' = E/(1 - \nu^2)$ for plane strain, E is Young's modulus, and ν is Poisson's ratio. The total additional elastic strain energy due to a crack can be calculated by integrating G from zero to a given crack length. For a two-dimensional solid containing a single crack of length $2c$, the additional strain energy due to the crack is given by

$$U_e = 2\int_0^c \frac{K_{\mathrm{I}}^2}{E'} + \frac{K_{\mathrm{II}}^2}{E'} + \frac{K_{\mathrm{III}}^2}{E}(1 + \nu)\, dc. \quad (4)$$

The strain energy due to a solid containing multiple cracks is given in Kemeny (1986).

Crack extension occurs when the energy-release rate, G, becomes equal to a critical value of the energy-release rate, G_c; i.e.,

$$G = G_c, \quad (5)$$

where G_c represents the energy required for the breakdown process at the crack tip and is a material property (not necessarily constant; see Ouchterlony, 1983), and where G is related to the stress-intensity factors and is a function of crack geometry and the applied stresses and strains.

Finally, we note that the elastic solution for the stresses given in Eq. (1) predicts infinite stresses directly at the crack tip, which is unrealistic, since material will actually yield or fail in a nonlinear fashion at some finite value of stress. However, if the region where the nonlinear behavior occurs is small relative to the region where the K terms dominate, then the stress field predicted by Eq. (1) is still valid. This forms the basis for the use of linear elastic fracture mechanics (LEFM) in rock fracture mechanics.

EFFECTIVE ELASTIC PROPERTIES

A linear elastic material containing cracks, or containing a fault plane made up of asperities, will show linear stress-strain behavior up to the point where cracks begin to propagate, or asperities begin to fail. This linear elastic behavior is different from that of the same material without cracks, or without the fault plane. The effective elastic properties refer to this modified elastic behavior due to the addition

of cracks or faults. For example, for a material containing some configuration of cracks under an applied uniaxial stress, σ, and strain, ϵ, the effective Young's modulus is given by $\bar{E} = \sigma/\epsilon$, where $\bar{E}$ depends on the density, size, orientations, and shapes of the cracks; on the elastic constants for the uncracked material; and on the coefficient of friction for the case of closed cracks (Kemeny and Cook, 1986a). It is sometimes convenient to consider the strain or displacement due only to the cracks or faults, i.e., where the strain due to the uncracked or unfaulted material is subtracted out. For example, for a fault plane containing asperities under shear, the effective shear stiffness is given by $k_s = \tau/\bar{\delta}$, where τ is the applied shear stress and $\bar{\delta}$ is the average displacement due only to the asperities along the fault plane (Kemeny, 1986). Analytic solutions for effective elastic properties can be determined using energy theorems (Betti's reciprocal theorem, Castigliano's theorem). These energy theorems relate the effective elastic properties with the elastic strain energy due to cracks or faults, and thus using Eq. (4), relate the effective elastic properties with the crack-tip stress-intensity factors.

CONSTITUTIVE RELATIONS

Even though the effective elastic properties predict linear stress-strain behavior, the cracks will propagate under high enough stresses, and the material may therefore possess different effective elastic properties. Here we present a procedure for calculating nonlinear constitutive relations based on the growth of cracks in an elastic solid, or the failure of asperities along a slip plane. It turns out that this procedure has a useful graphical interpretation; consider, for example, a material under uniaxial stress σ and strain ϵ that contains some distribution of cracks. We first note that the effective Young's modulus, $\bar{E}$, for a material with a given configuration of cracks plots as a straight line on a diagram of σ versus ϵ. The sequence of changes in $\bar{E}$ for a hypothetical deformation sequence is shown in Fig. 1a. At the start, the body contains an initial configuration of cracks, and the linear behavior for this initial configuration of asperities is shown in Fig. 1a by the effective Young's modulus with the highest slope. The figure also shows that as the material is deformed, the cracks will propagate, and for any of these later crack configurations, the effective Young's modulus will be lower.

Along each of the lines representing an effective modulus for a crack configuration, there will be a critical value of the stress at which crack propagation begins, as shown in Fig. 1b. The critical value of the stress at which crack propagation begins is referred to as the critical stress, σ_c, which is calculated by inverting the formula for the stress-intensity factor for the given crack configuration when $G = G_c$. As the cracks propagate, the effective modulus will always decrease, but the critical stress can either increase or decrease, depending on whether the stress-intensity factor decreases or increases with the changing crack configuration. *The stress-strain path that the body will follow during deformation is the locus of critical points over the sequence of changes in $\bar{E}$ during loading, as shown in Fig. 1c.* Strain hardening is the result of an increasing σ_c as the effective modulus decreases. Figure 1c shows clearly how nonlinear stress-strain curves are produced from the linear model with crack propagation. We also note that this approach applies for any configuration of cracks in both two and three dimensions and also for the failure of asperities along a fault plane.

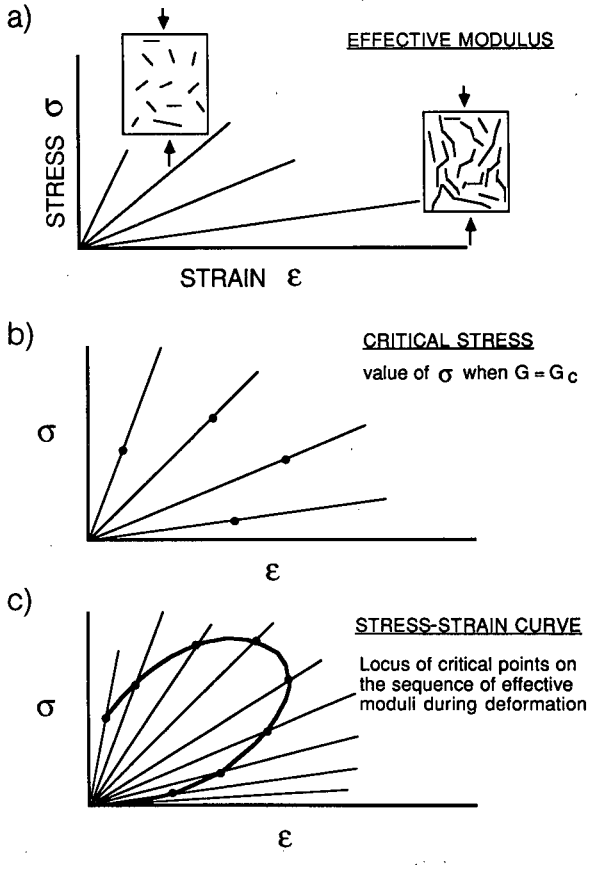

Figure 1. Graphical procedure for calculating nonlinear constitutive laws due to crack growth or asperity failure. [XBL 871-240]

The stress-strain curve as derived above is independent of the stability of the system, and instability will occur at the point where the slope of the stress-strain curve becomes less than the unloading stiffness of the surrounding material. If the boundary conditions consists of applied stress, then the unloading stiffness is horizontal, and all strain-softening slopes will be unstable for this condition. If the boundary condition consists of applied displacements, then the unloading stiffness is vertical, and only those strain-softening slopes that loop back toward the origin will be unstable. In general, the unloading stiffness for ground conditions will fall somewhere in between horizontal and vertical (Li and Rice, 1983).

The deformation sequence for the model developed above is summarized in Fig. 2. This model predicts initial linear loading up to the point where the first cracks start to propagate, nonlinear behavior (strain hardening or strain softening) as the cracks propagate and follow the stress-strain curve, and instability when the slope of the stress-strain curve exceeds the unloading stiffness. The energy released by the unstable event can be calculated from the stress-strain curve and the unloading stiffness. This energy, indicated by the shaded region in Fig. 2, can be released as seismic energy, or it can produce additional crack propagation at other locations or generate other processes (Rice, 1983).

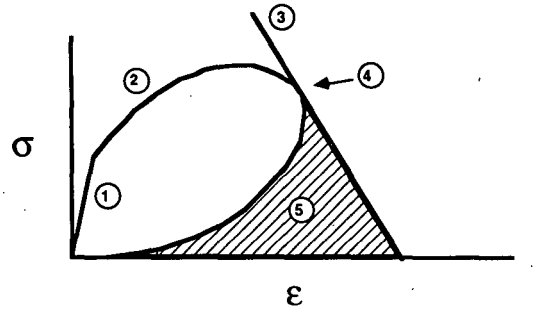

1 - linear loading due to initial crack configuration

2 - nonlinear behavior due to crack growth

3 - unloading stiffness

4 - instability point

5 - energy release during instability

Figure 2. Summary of the deformation sequence for the crack-growth or asperity-failure models. [XBL 871-241]

MULTIPLE INSTABILITIES

Multiple instabilities occur in our models owing to a distribution of cracks of varying sizes that do not extend and coalesce simultaneously. An important consideration here is the overall deformation sequence or global behavior due to a number of instability events. It turns out that the global behavior can be stable even when the individual events are highly unstable, and this explains, for instance, why earthquake faults do not go unstable over their whole length at once. As an example of a situation in which multiple instabilities occur, we consider a joint or fault under shear, where the joint is modeled as a distribution of asperities of varying sizes. Okubo and Dieterich (1984) conducted friction experiments on a saw cut in a large granite specimen, where strain gauges were placed close to the shear surface to detect the onset and propagation of slip. Their results showed that slip does not occur uniformly across the shear plane but, instead, that slip starts at the "weakest link" and propagates outward in a crack-like manner into the field of unbroken asperities. Our model of this experiment is shown in Fig. 3a. We consider a solid containing a collinear row of cracks, where the crack in the center is made slightly larger than the rest. For this configuration of cracks, the stress-intensity factor is always highest at the tips of the large crack, so that crack propagation will start there and will continue to propagate, breaking adjacent asperities and coalescing with the neighboring cracks.

The method described in the previous section has been used to calculate the constitutive behavior due to this sequence of events, as shown in Fig. 3b. Each curve in Fig. 3b represents the stress-strain behavior as the large crack propagates through each set of asperities. The breaking of each set of asperities is highly unstable, and the energy released by each of the individual instabilities is shown by the shaded regions. The global stress-strain behavior for this sequence of events is also shown in Fig. 3b. For this example, the global stress-strain behavior exhibits slip weakening (strength reduction with increasing slip), but the global stress-strain behavior does not loop back toward the origin, as do the individual stress-displacement curves. Thus the global behavior is stable under displacement-controlled boundary conditions (steep unloading stiffness).

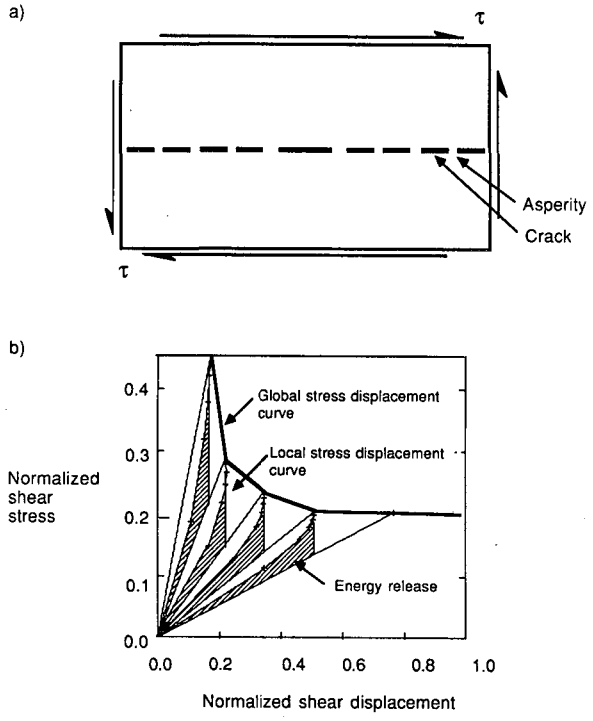

Figure 3. **(a)** Fault model consisting of a row of equal-spaced, equal-sized asperities containing a slightly larger asperity spacing at the center. **(b)** Nondimensionalized stress-displacement behavior showing both individual and global behavior. [XBL 871-242]

REFERENCES

Hallbauer, D.K., Wagner, H., and Cook, N.G.W., 1973. Some observations concerning the microscopic and mechanical behavior of quartzite specimens in stiff, triaxial compression tests. Int. J. Rock Mech. Min. Sci., v. 10, p. 713–726.

Horii, H., and Nemat-Nasser, S., 1985. Compression induced microcrack growth in brittle solids: Axial splitting and shear failure. J. Geophys. Res., v. 90, p. 3105–3125.

Irwin, G.R., 1957. Analysis of stresses and strains near the ends of a crack traversing a plate. J. Appl. Mech., v. 24, p. 361–364.

Jaeger, J.C., and Cook, N.G.W., 1979. Fundamentals of Rock Mechanics. Halstead Press, New York, p. 177–183.

Kanamori, H., 1986. Rupture process of subduction-zone earthquakes. Ann. Rev. Earth Plan. Sci., v. 14, p. 293–322.

Kemeny, J.M., 1986. Frictional stability of heterogeneous surfaces in contact: The mechanics of faulting and earthquake rupture (Ph.D. thesis). University of California, Berkeley.

Kemeny, J.M., and Cook, N.G.W., 1986a. Effective moduli, nonlinear deformation and strength of a cracked elastic solid. Int. J. Rock Mech. Min. Sci. Geomech. Abstr., v. 23, p. 107–118.

Kemeny, J.M., and Cook, N.G.W., 1986b. Frictional stability of heterogeneous surfaces in contact. *In* Proceedings, 27th U.S. Rock Mechanics Symposium, University of Alabama, June 23–25, 1987, p. 40–46.

Kemeny, J.M., and Cook, N.G.W., 1987. Crack models for the failure of rock in compression. *In* Proceedings, Second International Conference on Constitutive Laws for Engineering Materials, Tucson, Arizona, January 5–8, 1987.

Li, V.C., and Rice, J.R., 1983. Preseismic rupture progression and great earthquake instabilities at plate boundaries. J. Geophys. Res., v. 88, p. 4231–4246.

Okubo, P.G., and Dieterich, J.H., 1984. Effects of physical fault properties on frictional instabilities produced on simulated faults. J. Geophys. Res., v. 89, p. 5817–5827.

Ouchterlony, F., 1983. Fracture toughness testing of rock. *In* H.P. Rossmanith (ed.), Rock Fracture Mechanics. Springer-Verlag, New York.

Rice, J.R., 1968. Mathematical analysis in the mechanics of fracture. *In* H. Liebowitz (ed.), Fracture: An Advanced Treatise (Vol. II), p. 191–311.

Rice, J.R., 1983. Consitutive relations for fault slip and earthquake instabilities. Pure Appl. Geophys., v. 121, p. 443–475.

Rudnicki, J.W., 1980. Fracture mechanics applied to the Earth's crust. Ann. Rev. Earth Sci. v. 8, p. 489–525.

Wawersik, W.R., and Brace, W.F., 1971. Post-failure behavior of a granite and diabase. Rock Mech., v. 3, p. 61–85.

Hydrologic Properties of Shale

L.R. Myer, T. Christian, and R. Curtis

In fiscal 1985 Lawrence Berkeley Laboratory began a laboratory study of the hydrologic properties of shale rock under temperatures and pressures representative of the conditions that might prevail in and around a radioactive waste repository. The specific objectives of the study are to compare and contrast intact (matrix) and fracture permeabilities and porosities of different shale mineralogies; evaluate the effect of temperature on intact and fracture permeability; evaluate the effect of effective hydrostatic stress state on intact permeability; and evaluate the effect of normal stress state on fracture permeability.

During fiscal 1986 efforts were centered on accomplishing matrix-permeability measurements. Work proceeded in three stages. In the first stage system-calibration tests were performed using an impermeable (aluminum) sample to evaluate system performance and the effects that fluctuations in confining pressure, ambient room temperature, and pore pressure have on measurements. The second stage of work involved trial testing of expendable samples. Because few shale samples were available, a granite sample was used for this purpose. In the third stage preliminary results were obtained for samples of Green River Shale.

TEST METHODS AND EQUIPMENT

The test technique is a modified version of the transient-pressure-pulse-decay method originally proposed by Brace et al. (1968). In this technique a sample is placed between two fluid volumes, referred to as upstream and downstream fluid reservoirs. While the total fluid volume in the system is kept constant, the pressure in the upstream reservoir is instantaneously increased. Sample hydraulic conductivity can be related to the change in pressure over time between the upstream and downstream reservoirs. Analysis is significantly simplified if the upstream reservoir volume is large compared with the sample pore volume.

Figure 1 is a schematic representation of the experimental apparatus. The hydrostatic confining pressure is maintained by a pressure vessel charged with nitrogen gas. Sample heaters are inside the vessel. The upstream and downstream fluid reservoirs are located outside of the pressure vessel to minimize the effect of nonuniform temperature inside the vessel. The volume vessel was heavily insulated to minimize the effect of fluctuations in room temperature.

Before each measurement, fluid pressures are held constant to achieve pore-pressure equilibrium in the sample. Fluid pressure is then instantaneously increased in the upper reservoir (or decreased in the lower reservoir), and valves are closed on the upstream and downstream reservoirs, completely isolating the pore-fluid system (Fig. 1). Differential pressure changes between the upstream and downstream reservoirs are monitored as a function of time with a differential pressure transducer.

SYSTEM TEST RESULTS

Measurement of fluid permeabilities in the nanodarcy range place extreme demands on system performance because pressure changes are small and test durations long. Of primary concern are the detection of leaks and the effects of ambient temperature variations. Because of the minute fluid volumes involved in these pressure changes, and the superimposed effects of temperature changes, long-term tests were required to assess system performance.

Figure 2 shows the results of a test in which an aluminum plug was substituted for a sample under a pore-fluid pressure of about 1400 psi. The valves on the upstream and downstream reservoirs were closed in order to observe the development of differential pressures due to leaks and temperature changes. The upstream reservoir pressure was monitored independently by a pressure transducer. The downstream reservoir pressure was calculated from the upstream pressure and the differential pressure. These tests showed that the pressurized plumbing required a characteristic "settling-in" time of about 20 hours before differential pressures stabilized. Stabilized differential pressure reflected stabilized pressures throughout the system. Once differential pressure had stabilized, changes in absolute pressures in the fluid reservoirs indicated temperature changes in the volume vessel. Air temperatures are shown in Fig. 2 to illustrate the thermal damping effect of the insulation on the volume vessel.

Over long periods of time, variations in ambient temperature caused perturbations in the differential pressure. A 60-hour test of the entire system with an aluminum plug for a sample yielded an apparent differential pressure correction of 3 psi/°F.

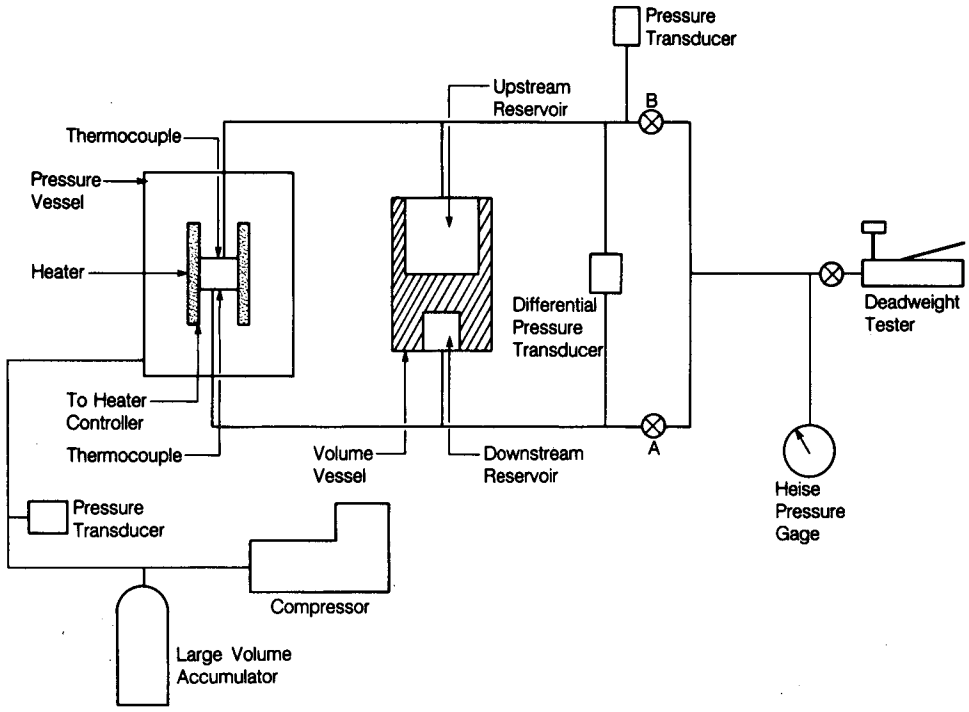

Figure 1. Schematic illustration of experimental apparatus for matrix-permeability measurements. [XBL 859-10751]

GRANITE TEST

The first rock sample to be tested was a sample of Stripa quartz monzonite, 3.27 inches in diameter by 1.5 inches long. Confining pressure was held at approximately 2900 psi throughout the test. The pore-fluid pressure was held constant at approximately 1130 psi for 2 days to allow the system to come to equilibrium. A differential pressure of 88 psi was then placed on the sample, and valves were closed to isolate the pore fluid system. Test duration was about 160 hours. Differential pressure fell, reflecting movement of water from the upstream reservoir to the downstream reservoir. However, after disassembly, a partial blockage was found in a fluid tube leading from the upstream reservoir to the top of the sample. It is not clear how great an error this introduced, but the value of hydraulic conductivity obtained from the data was 1.5×10^{-14} m/s (10^{-9} D). This value is within the range of published values for granitic rocks (Trimmer et al., 1980).

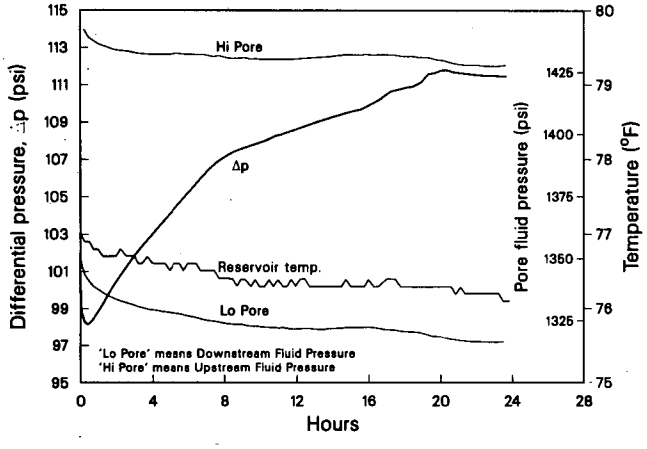

Figure 2. System response test data; entire system with aluminum plug sample with 1400-psi fluid pressure. [XCG 869-12146]

SHALE ROCK TESTS

The first shale samples tested were two samples of Green River Shale. One sample was prepared with the bedding perpendicular to the direction of fluid flow and one with the bedding parallel to that direction. Samples were 3.27 inches in diameter by 1.5 inches long. Because the rock was received in a dried condition, samples had to be saturated under a vacuum before testing. Deionized water was used as the pore fluid.

The first test was performed at a confining pressure of 3000 psi on the sample with its bedding perpendicular to the flow direction. Pore-fluid pressure was held at 1500 psi for 2 days before the start of

measurements. A differential pressure of about 140 psi was then created across the sample, and valves were closed to isolate the pore-fluid system. The differential pressure slowly rose, reflecting a loss of pressure in the downstream reservoir caused by a minute leak. Before disassembly a 655-psi differential pressure was imposed on the sample, but the resulting data showed the same slow increase in differential pressure, amounting to about 50 psi over the 20-hour test duration. The large pressure differential would have caused enough pressure increase in the downstream reservoir to offset effects of the leak, unless the rock permeability was very low. Calculations indicated that the permeability of the sample was in the sub-nanodarcy range.

After the plumbing leak was fixed, the second test was performed at a confining pressure of 3000 psi on the sample with its bedding parallel to the flow direction. Pore-fluid pressure was again held at 1500 psi before the start of measurements. For permeabilities in the sub-nanodarcy range, the rate of change of small differential pressures of 100 psi or less would be difficult to separate from system pressure perturbations caused by fluctuations in ambient temperature. Therefore, a 945-psi differential pressure was imposed on the sample. Results of the test are shown in Fig. 3. Decreasing

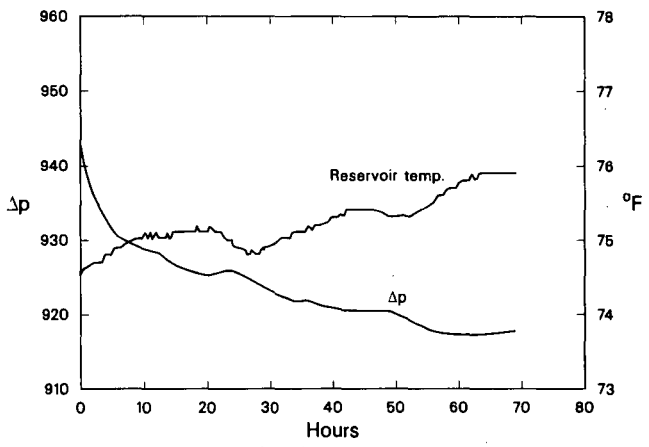

Figure 3. Green River Shale sample permeability test data; bedding parallel to flow direction. [XCG 869-12147]

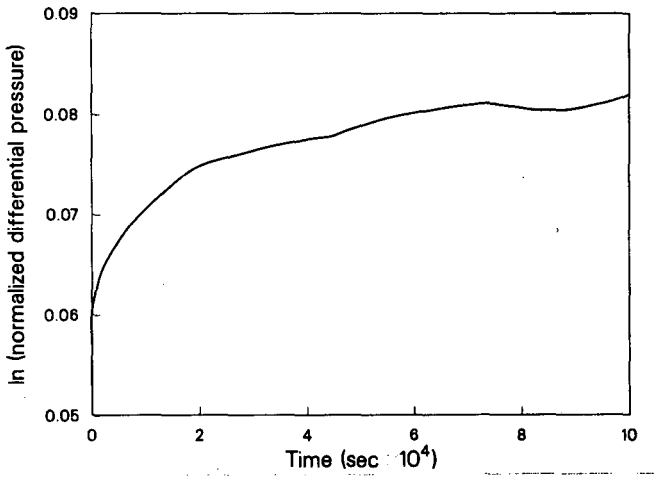

Figure 4. Green River Shale sample differential pressure data plotted as natural logarithm of normalized differential pressure versus time. [XCG 869-12139]

differential pressure reflects the increase in pressure in the downstream reservoir relative to the upstream reservoir and hence the flow of fluid from the high-pressure side to the low-pressure side.

Use of a differential pressure greater than 10% of the pore-fluid pressure resulted in a transient pressure response that included effects of the compressive storage of the sample. This effect is illustrated in Fig. 4, which is a semilog plot of normalized differential pressure change against time. The effect of the sample compressive storage is shown nonlinearily in the curve at times up to about 2×10^4 s. Using pressure from this time onward yielded a hydraulic conductivity of 2.6×10^{-16} m/s (10^{-11} D). The perturbations in the pressure-time curve are due to fluctuations in reservoir temperature.

REFERENCES

Brace, W.F., Walsh, J.B., and Frangos, W.T., 1968. Permeability of granite under high pressure. J. Geophys. Res., v. 73, no. 6, p. 2225–2235.

Trimmer, D., Bonner, B., Heard, H.C., and Duba, A., 1980. Effect of pressure and stress on water transport in intact and fractured gabbro and granite. J. Geophys. Res., v. 85, no. B12, p. 7059–7071.

Deformation of Fractures under Normal Stress

L.R. Myer, L.J. Pyrak-Nolte, and N.G.W. Cook

When the stress state in a rock mass is perturbed, fractures, which may be envisioned as two surfaces in partial contact, experience deformation. Deformations of the areas of contact and the voids between them affect the mechanical, hydrologic, and geophysical properties of the rock mass as a whole. The magnitude of the effect on physical properties is of course related to how much deformation occurs for a particular change in stress. One way to quantify this stress-deformation relationship is to measure the specific stiffness of the fracture. The specific stiffness relates the change in *average* fracture deformation to the change in average stress applied to the fracture surfaces.

This article describes results of a laboratory investigation of the deformation of natural fractures in crystalline rock subjected to normal stress. Deformations of single fractures were measured for stresses up to 85 MPa. Experiments were performed on water-saturated samples at elevated temperatures and on dry samples at room temperature. Specific stiffness values were obtained from the deformation-stress data.

EXPERIMENTAL PROCEDURES

The experimental configuration is shown in Fig. 1. Samples were approximately 52 mm in diameter by 77 mm long. Each contained a single fracture located midway between the ends and oriented orthogonal to the long axis of the sample.

Three donut-shaped collars were attached to the sample, as illustrated in Fig. 1. The inside surface of the collar did not touch the rock surface; each collar was secured to the rock by three pointed set screws. Care was taken to ensure that the collars were parallel and equidistant from one another.

Four precision linear variable differential transformers (LVDTs) (rated repeatability of 4.0 $\times$ 10^{-6} inch) were attached in pairs on diametrically opposite sides of the sample, as shown in Fig. 1. The assembly was placed in a test frame and an axial load applied to the sample. Displacements of the intact rock, as measured by the two upper LVDTs, were subtracted from the displacements measured by the two lower LVDTs to isolate the average displacement of the fracture. Performance of the measurement system was checked by duplicating the experiment using a solid aluminum cylinder in place of the fractured rock.

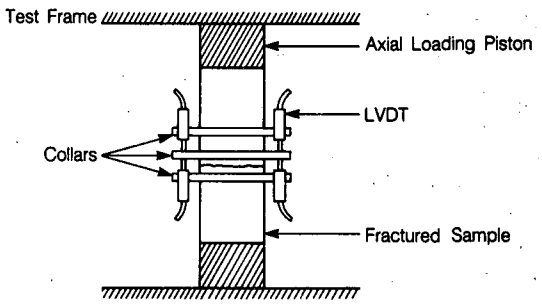

Figure 1. Schematic illustration of experimental setup. [XBL 8611-4373]

To perform a test on a saturated fracture, the sample was enclosed in a rubber sheath, evacuated, and then saturated under a head of about 1 meter of water. With the addition of a sample sheath, the experimental configuration was exactly as illustrated in Fig. 1; the set screws in the collars were driven through the sheath to rest against the rock.

For measurements at elevated temperatures, the sample was wrapped with strip heaters and insulation. Temperature was monitored by a thermocouple strapped to the rock. The system was allowed to equilibrate at constant temperature before measurements were made.

DEFORMATION MEASUREMENTS

Fracture deformation is shown in Fig. 2 as a function of applied normal stress for sample E30.

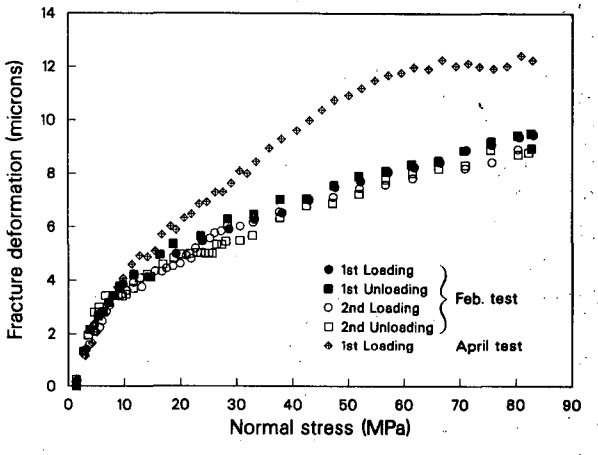

Figure 2. Comparison of deformation test performed in April with earlier test. Sample had been subjected to repeated loading in the interim. [XCG 8610-12156

Data from two different tests are presented. In the first test (February test) the fracture was subjected to two loading/unloading cycles performed sequentially. The second test (April test) was performed 3 months later after the sample had been loaded repeatedly in other testing to 85 MPa.

Though the results are nonlinear, they show essentially no difference in deformation between loading cycles in the February test and very little hysteresis. Deformation of the asperities and voids within the fracture must therefore have been elastic. As will be discussed below, nonlinearity reflects the changing geometry of the areas of asperity contact as load increased. Other investigators (Bandis et al., 1983; Raven and Gale, 1985) have observed significant hysteresis in the initial loading cycle for natural fractures. However, they also observed that the amount of hysteresis—and hence the difference in deformation between cycles—decreases with the number of cycles. Sample E30 had been loaded to 85 MPa on several occasions for various tests before the February test. Thus the observed behavior was consistent with previous studies by other investigators.

Fracture deformations measured in the April test were reversible, showing little hysteresis between loading and unloading cycles. In comparing the deformation behavior of the April and February tests, it is seen in Fig. 2 that more deformation occurred in the April test and that the rate of change of displacement with stress (i.e., compliance of the fracture) was also greater. It is also interesting to note that at high stresses the deformations of the early test appear to approach a constant rate of deformation whereas deformations of the later test approach a constant value. It is believed that the differences in behavior between the February test and the April test are due to the breakage of asperities.

Fracture deformations versus applied normal stress for three different fractures are shown in Fig. 3. Though the magnitude of total deformation varied for the different samples, all samples exhibit decreasing rates of deformation with increasing stress. As will be discussed in the next section, it is believed that this behavior reflects changes in the area of asperity contact between the surfaces.

The inverse of the tangent slope to the curve of deformation versus stress is defined as the specific stiffness of the fracture. Values of specific stiffness for the three fracture-deformation curves in Fig. 3 were determined graphically and plotted in Fig. 4.

Specific stiffness increases rapidly with stress up to about 10 MPa and then increases at a decreasing rate. Though the trend was less for sample E30, the

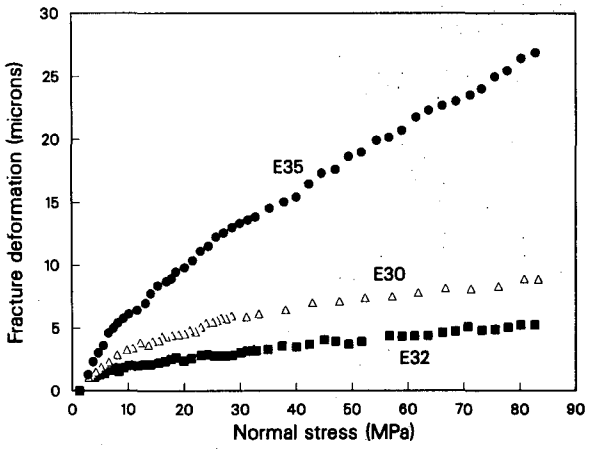

Figure 3. Fracture deformations as a function of normal stress on fracture for three samples. [XCG 8610-12157]

specific stiffness for each fracture appears to approach a constant value. Specific stiffnesses obtained from the April test on E30 exhibit different trends with stress. Specific stiffness increases at about the same rate as in the February test up to about 20 MPa. Thereafter, stiffness in the April test approaches a more constant value up to about 50 MPa and then accelerates to very high values at high stress.

Sample E30 was tested at elevated temperatures while wet and while dry. The wet test was performed under a head of about 2 m of water at a temperature of about 95°C. The temperature of the dry test was about 100°C. Neither the presence of water nor temperatures up to 100°C had any significant effect upon the magnitude of fracture deformations or fracture stiffness.

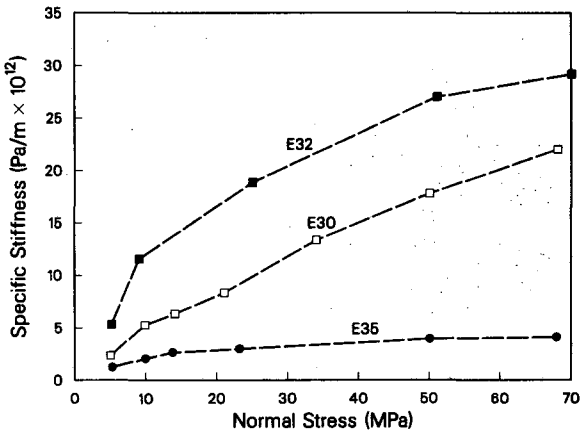

Figure 4. Specific stiffness for the three deformation tests shown in Fig. 3. [XCG 8610-12159]

DISCUSSION

The fracture-deformation behavior described above can be fully explained by assuming that only the changes in fracture geometry and elastic deformation of the voids and asperities need to be taken into account. If deformations are elastic the observed nonlinearity and the change in specific stiffness with load must be due to nonlinear elastic properties of the fracture surfaces or to the changes in the fracture void geometry.

Changes in fracture void geometry as load is increased have been independently confirmed for samples E30 and E32 from tests in which a low-melting-point metal was injected into the fracture (Pyrak et al., 1985). After the metal solidified, separation of the fracture revealed a cast of the void space. Injections performed with the fractures under various normal stresses clearly show an increase in contact area with increasing normal stress. For E32 the injection tests also indicate that the rate of increase in contact area decreases at high stress. In addition, at high stress levels, the amount of void space is still significant in all fractures.

On the basis of these observations it is believed that the observed rapid increases in specific stiffness at low normal stresses are primarily due to increasing numbers of asperities coming into contact. Higher specific stiffness values for E32 than E30 suggest a higher contact area for E32, and this was confirmed by metal-injection tests.

At higher loads the more nearly constant specific stiffness values reflect elastic void deformation and a diminished rate of increase in contact area. The rate of void closure would depend upon the elastic properties of the rock and the distribution, size, and aspect ratio of the voids. The lower stiffness of E35 compared with that of the other samples (Fig. 4) is probably due to the presence of more numerous, larger voids. Similarly, asperity breakage between the February and April tests of E30 created larger voids of higher aspect ratio than had been present before, and, consequently, higher rates of deformation with increasing load.

Elastic void closure cannot continue indefinitely. As more stress is applied, voids will eventually close, with a corresponding increase in contact area and stiffness. The rapid increase in stiffness in the April test of E30 at high stress reflects the limiting condition in which so many voids have closed that there is no further fracture deformation in excess of the intact rock deformation.

CONCLUSIONS

Fracture-deformation measurements as a function of normal stress were completed for three natural granitic fractures. Results from all three fractures illustrate the important influence of geometry, i.e., size and distribution of asperities and voids in the fracture, on mechanical behavior. Deformation seems to take place in three stages. In the first stage at low loads, contact area increases rapidly with load. The second stage is characterized by elastic deformation of voids. As these voids close in the third stage, the specific stiffness of the fracture becomes unbounded.

REFERENCES

Bandis, S.C., Lumsden, A.C., and Barton, N.R., 1983. Fundamentals of rock joint deformation. Int. J. Rock Mech. Min. Sci. Geomech. Abstr., v. 20, no. 6., p. 249–268.

Pyrak, L.J., Myer, L.R., and Cook, N.G.W., 1985. Determination of fracture void geometry and contact area at different effective stress. EOS, Trans. Am. Geophys. Union, v. 66, no. 46, p. 903.

Raven, K.G., and Gale, J.E., 1985. Water flow in a natural rock fracture as a function of stress and sample size. Int. J. Rock Mech. Min. Sci. Geomech. Abstr., v. 22, no. 4, p. 251–261.

Experimental Determination of Fracture-Void Geometry

L.R. Myer, L.J. Pyrak-Nolte, and N.G W. Cook

Rock fractures are commonly modeled as two nominally flat, rough surfaces that, when pressed together, deform elastically at the points of contact. By assigning a statistical distribution to the heights and curvatures of asperities on the two rough surfaces, Greenwood and Tripp (1971) and Brown and Scholz (1985), among others, have developed theories to predict the elastic contact deformations and changes in contact area as the loads are applied normal to the fracture plane. Brown and Scholz (1985) experimentally observed closure of artificial fractures formed from two roughened glass surfaces and compared these results with theoretical predictions based on topographic measurements of these surfaces. Swan (1983) measured the deformation of natural rock fractures and compared these results with a numerical simulation based on topographic measurements of the surfaces.

Few studies have been performed, however, in which the actual geometric distributions of void space and contact area have been studied as a function of normal stress of the fracture. Iwai (1976) and Bandis et al. (1983) obtained impressions of natural fracture contact areas by placing sheets of thin polyester film between the fracture surfaces. Described in this article is a new technique involving injection of a low-melting-point metal into the fracture under controlled stress and fluid-pressure conditions. The result is a three-dimensional cast of the void space in the fracture.

Injections were performed on two natural fractures in crystalline rock under three different normal loads. Samples were 52 mm in diameter by 77 mm in length. Each sample contained a single fracture oriented orthogonal to the long axis of the sample. Fracture surfaces were extensively photographed at several magnifications to reveal flow paths as small as a micron in size. Work began on the development of a method for quantitatively evaluating the geometric properties of the flow paths.

EXPERIMENTAL TECHNIQUE

The metal used for injection is one of a family of bismuth-lead-tin alloys of which Wood's Metal is most commonly recognized. In the liquid phase, these are nonwetting and have an effective surface tension about 0.6 that of mercury (Swanson, 1979). The particular alloy used (Cerrosafe®) has a nominal composition of 0.42 Bi, 0.38 Pb, 0.11 Sn, and 0.08 Cd and a melting point of 160°F to 190°F. The experimental technique is a modification of one previously used by other investigators studying the pore geometry of sandstone cores (Swanson, 1979; Yadov et al., 1984).

A schematic drawing of the injection apparatus is shown in Fig. 1. The sample was held in a triaxial test vessel maintained at a temperature just above the melting point of the alloy. The vessel was placed in the loading frame of a servocontrolled test machine (Myer, 1985), where an axial load was applied normal to the fracture surface. Molten metal was placed in a reservoir connected to the confining-pressure pump of the test machine.

To perform an injection test, the triaxial vessel was evacuated and the desired axial load placed on the sample. While the axial load was kept constant, the molten metal was pumped into the test vessel until the desired pore-fluid pressure was obtained. Both the confining pressure and axial load were maintained until the metal had solidified. After the metal had solidified, the sample was removed from the vessel and the two halves separated, revealing metal casts of the void geometry. Injections were performed on two natural fractures designated E30 and E32 under total normal stresses of approximately 5, 35, and 87 MPa. The injection pressure for all tests was 2 MPa.

ANALYSIS

When the two halves of a sample were separated, metal was found on both fracture surfaces. Because the metal itself did not fracture, the absence of metal at the same relative location on each fracture surface represented an area of contact. Therefore, a composite image created by combining one image from

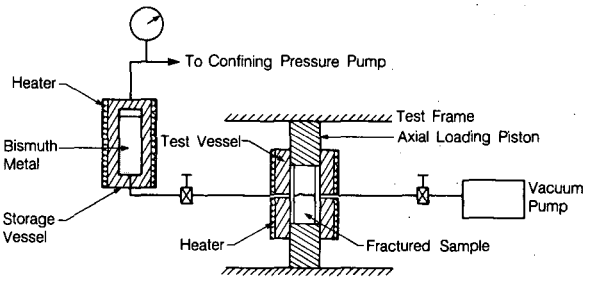

Figure 1. Schematic illustration of apparatus for injecting liquid metal. [XBL 8510-12387]

each of the two mating fracture surfaces was used to study the geometry of the void and contact areas. Images of the individual fracture surfaces were created using both scanning electron microscope (SEM) and standard photographic techniques. Results of both are discussed below.

The average contact area over the entire fracture was estimated from separate photographs of each fracture surface. The photographs were enlarged to provide a magnification of about 4 times. A sheet of acetate was placed first on a photograph of one fracture surface, and the areas containing metal were hand traced onto the acetate. The same procedure was then carried out on the photograph of the mating fracture surface. Composite results for sample E30 at effective stress (total stress minus fluid pressure) levels of 3, 33, and 85 MPa are shown in Fig. 2. Results for sample E32 are shown in Fig. 3 for comparable stress levels. Note that the black areas in these figures are the void spaces.

An image analyzer was used to quantitatively evaluate the contact and void areas on the composites shown in Figs. 2 and 3. The results are plotted in Fig. 4. At an effective stress of 3 MPa, the contact area of E30 was about 8%; it increased to about 15% at 33 MPa and 30% at 85MPa. For E32 the contact area was higher at all stress levels, beginning at about

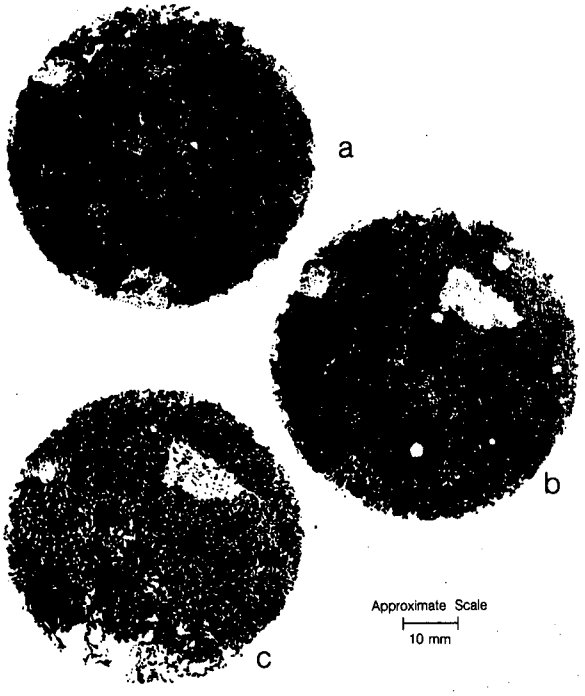

Figure 2. Composite photograph of entire fracture of sample E30 at three effective stress levels: (**a**) 3 MPa; (**b**) 33 MPa; (**c**) 85 MPa (dark regions are metal covered). [XBL 8610-12615]

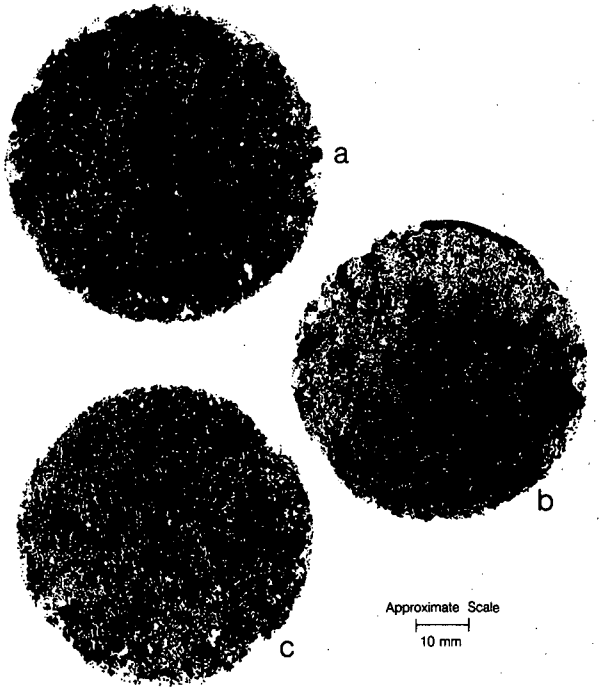

Figure 3. Composite photographs of entire fracture of sample E32 at three effective stress levels: (**a**) 3 MPa; (**b**) 33 MPa; (**c**) 85 MPa (dark regions are metal covered). [XBL 8610-12614]

15% at 3 MPa, increasing to about 42% at 33 MPa, and remaining essentially constant at 85 MPa.

Qualitative relationships were observed between the effects of stress on contact area and the effects of stress on the mechanical and hydrologic properties of the fractures. In general, decreases in fracture deformation and hydraulic conductivity with increasing stress correlate with increases in contact area. In

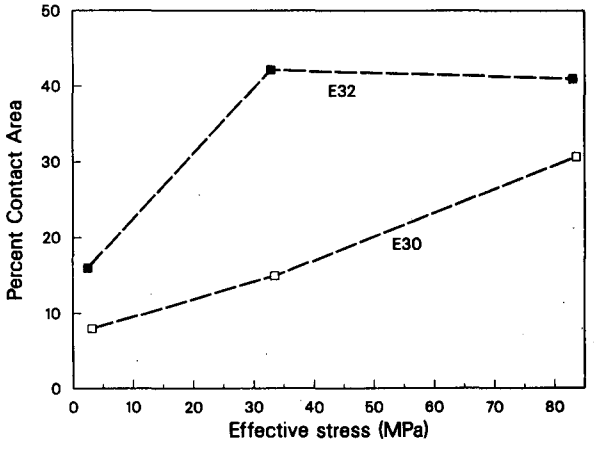

Figure 4. Contact area as a function of effective normal stress for samples E30 and E32; results of image analysis. [XCG 8610-12164]

addition, E32, which had higher contact area than E30, was less permeable and deformed less. Further understanding of the relationship between changing void geometry and physical properties was obtained from detailed SEM images, as described below.

Fracture surfaces to be viewed in the SEM were first coated with approximately 200 Å of aluminum, which provided a conductive layer over the entire surface. The SEM was adjusted using the difference in density between the metal and rock to enhance the contrast between the two materials in the image. This technique was very successful in creating sharp, detailed images of the distribution of metal on a fracture surface.

Composite images from SEM micrographs were made for both samples at three different effective-stress levels. To obtain a composite, an SEM micrograph was first taken of an area on one fracture surface. The corresponding area on the mating fracture surface was located and a micrograph obtained. The negatives from these two images were superimposed to produce the composite image.

Composite images at effective stress levels of 3, 33, and 85 MPa are shown in Fig. 5 for sample E30. Because of difficulties in determining absolute locations on the fracture surfaces in the SEM, the same surface element is not represented at each load level. Comparison of the images at different loads still provides considerable qualitative information about the change in void geometry with stress.

At 3 MPa the dark areas in Fig. 5a (contact areas) appear as isolated "islands" in "oceans" of metal. The void area in the fracture is much greater than the contact area and is freely interconnected. The shape of the contact areas varies from nearly circular to lenticular. The size of the contact areas, roughly scaled from the composite images, ranges from less than 5 μm to 0.1 mm.

Even with an increase in effective stress (Fig. 5b and c), void area remains significant. Contact area increases, but this increase is not uniformly distributed over the surface. The increase is evident in certain localities where contact areas became abundant enough to begin to isolate void areas. In effect, at higher stress levels, the void geometry could be characterized as "lakes" connected by tortuous "streams." Whereas the size of the "lakes" may be measured in millimeters, many of the "streams" are measured in micrometers.

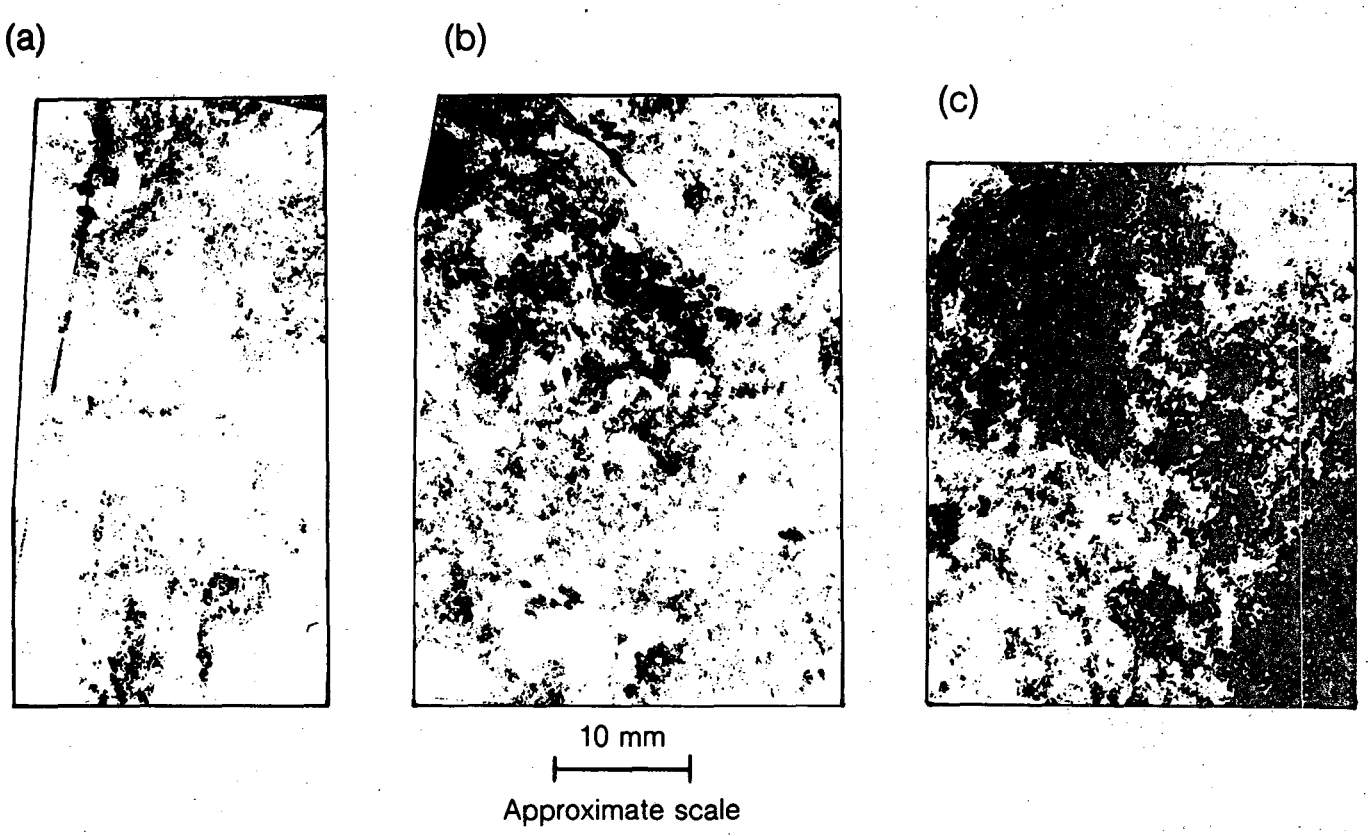

Figure 5. Composite photos of sample E30 at three effective stress levels: (a) 3 MPa; (b) 33 MPa; (c) 85 MPa. White is metal. [XBL 875-10179]

These observations have important implications with respect to the observed mechanical and hydrologic behavior of fractures. As load is applied to a fracture, the number of contacts increases, and fracture deformation increases at a decreasing rate. Above a certain load the data indicate that contact area may become relatively constant. Further fracture deformation is possible but is due only to void deformation and would increase with load at a constant rate. Hydrologically we hypothesize that the decrease in permeability with increasing stress is due to the creation of flow constrictions in the fracture. At high effective stresses the apertures of the large voids continue to close, but the apertures of the constricting channels, being of lower aspect ratio, diminish less rapidly. As a result flow at high effective stresses would approach a constant value.

SUMMARY

A metal-injection technique has been developed that provides, for the first time, quantitative three-dimensional data on how fracture-void geometry changes as a function of normal effective stress. Data have been collected for two natural crystalline rock fractures subjected to three loads. Comparison of this data with mechanical deformation measurements and hydraulic conductivity measurements provide clear, though qualitative, indication of how changes in void geometry affect both mechanical and hydraulic behavior of a fracture. Further work is required to develop techniques for quantitatively evaluating fracture void geometry changes. This will require additional injection tests as well as development of image-analysis techniques.

REFERENCES

Bandis, S.C., Lumsden, A.C., and Barton, N.R., 1983. Fundamentals of rock joint deformation. Int. J. Rock Mech. Min. Sci. Geomech. Abstr., v. 20, no. 6, p. 249–268.

Brown, S.R., and Scholz, C.H., 1985. Closure of random elastic surfaces in contact. J. Geophys. Res., v. 90, no. B7, p. 5531–5545.

Greenwood, J.A., and Tripp, J.H., 1971. The contact of two nominally flat rough surfaces. Proc. Inst. Mech. Eng., v. 185, p. 625–633.

Iwai, K., 1976. Fundamental studies of fluid flow through a single fracture (Ph.D. thesis). University of California, Berkeley.

Myer, L.R., 1985. Electro-servo control system for thermomechanical properties testing. Geotech. Testing J., v. 8, no. 4, p. 171–178.

Swan, G., 1983. Determination of stiffness and other joint properties from roughness measurements. Rock Mech. and Rock Eng., v. 16, no. 1, p. 19–38.

Swanson, B.F., 1979. Visualizing pores and nonwetting phase in porous rock. J. Pet. Technol., v. 31, p. 10–18.

Yadav, G.D., Dullien, F.A.L., Chatzis, I., and MacDonald, I.F., 1984. Microscopic distribution of wetting and non-wetting phases in sandstones during immisible displacements. Paper SPE 13212 presented at the 1984 SPE Annual Meeting, Dallas, Texas, September 16–19, 1984.

Fracture Permeability under Normal Stress

L.J. Pyrak-Nolte, N.G.W. Cook, and L.R. Myer

Understanding fluid flow through fractures is a central issue to many geologic problems. Geologic isolation of nuclear waste, petroleum recovery, and aquifer contamination are just a few of the fields in which knowledge of the fundamentals of fluid flow through single rock fractures is necessary to predict behavior of fluid movements in fractured rock masses.

Several investigations of fluid flow through single fractures have been carried out in the laboratory under varying conditions. Iwai (1976) studied flow as a function of stress through single induced fractures, attaining maximum stresses of only 20 MPa. Engelder and Scholz (1981) studied fluid flow along artificial fractures for effective stresses up to 200 MPa. Raven and Gale (1985) studied the effect of stress on radial fluid flow through natural fractures for samples of various sizes, but the maximum pressure was only 30 MPa. The investigation summarized here was designed to study the effect of

uniaxial effective stress on fluid flow through a natural fracture in a low-permeability granitic rock. Flow measurements in conjunction with fracture-displacement measurements were used to develop an empirical relationship between flow and fracture closure.

EXPERIMENTAL PROCEDURE

Three samples of quartz monzonite (Stripa granite) measuring 52 mm in diameter by 77 mm in length were used in the flow and displacement experiments. Each sample contained a fracture orthogonal to the axis of the core.

A linear-flow technique (quadrant flow) was developed to measure fluid flow. This technique was employed because of sample size. If a radial-flow method had been used, the central borehole would have been very small, and the results would have reflected loss of energy predominately due to flow adjacent to the borehole rather than the effect of the whole fracture.

The fracture was assembled and two diametrically opposed quadrants sealed with silicone sealant. A rubber gasket was stretched thinly over the specimen and a nylon manifold secured around the sample with hose clamps (Fig. 1). Removing the tension from the gaskets caused the rubber jacket to relax and seal the system. Inlet and outlet ports were cut in the gasket after assembly. Flow occurred between the two open quadrants, which are diametrically opposed (Fig. 2). The apparatus was placed in the load frame of a servocontrolled stiff-testing machine to maintain the desired effective stress. An upstream head of 0.4 MPa was applied, and flow measurements were made for one complete loading and unloading cycle plus an additional loading cycle up to a maximum effective stress of 85 MPa. The experimental setup for the displacement measurements is described in the fracture deformation report (Myer et al., 1986a) and will not be described here.

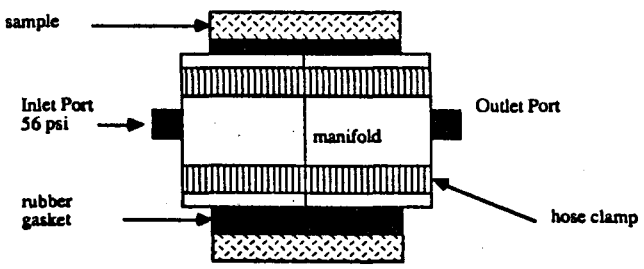

Figure 1. Experimental apparatus for quadrant-flow measurements. [XBL 8610-3880]

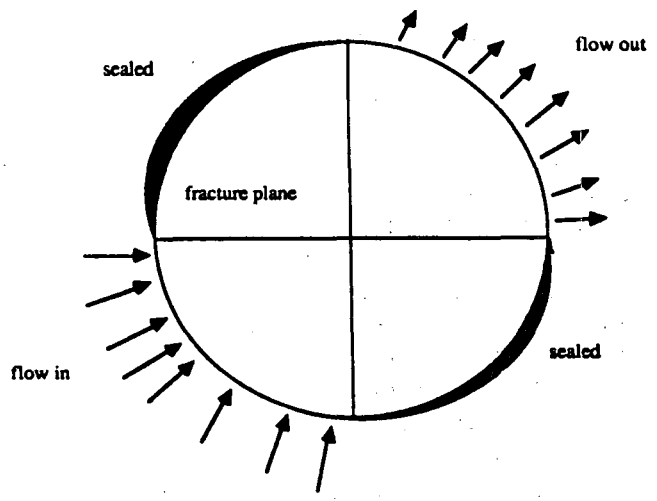

Figure 2. Flow path in quadrant-flow technique. [XBL 8610-3881]

RESULTS

Figure 3 compares fluid-flow data for three fractured samples. Data for samples E30 and E32 were obtained from the first unloading cycle. Data for E35 were obtained from the first loading cycle. Though the magnitude of the flow varies between loading and unloading cycles, the pattern of rapid decrease in flow at low stresses followed by a much more gradual decrease in flow at higher stresses was observed to be independent of the load cycle for all of the specimens. This behavior has also been observed by many other investigators (e.g., Iwai, 1976; Engelder and Scholz, 1981; Raven and Gale, 1985).

For samples E30 and E32, Fig. 3 shows a rapid decrease in flow as stress is increased to about

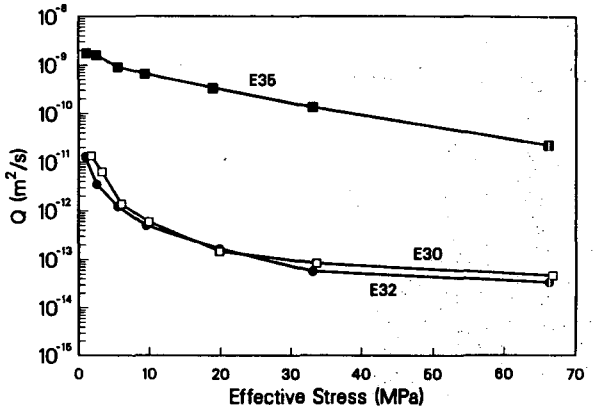

Figure 3. Comparison of flow per unit head drop as a function of effective stress for samples E35, E30, and E32. [XCG 8610-12168]

20 MPa. Above this stress the flow appears to approach a constant value. Though the trend is less pronounced for sample E35, a decrease in flow at higher stresses is still apparent. The small but finite flow in samples E30 and E32 even at 85 MPa is significant in that it suggests that flow approaches an irreducible level at high stresses. Fracture-displacement data for these fractures (Myer et al., 1986a) indicates that the fractures continue to close even at the highest stresses. At high stresses fracture flow is not strongly affected by the average mechanical deformation of the fracture.

Figure 4 shows the flow-test data plotted in the conventional format: logarithm of average fracture closure versus logarithm of flow. The effect of the irreducible flow is seen as a departure from linearity in this plot. The slope of the linear portion of the curves is also not 1/3, as would be expected if the flow followed the commonly accepted "cubic law" relationship. However, it is interesting to note that the slopes are very similar to those obtained by Raven and Gale (1985) for other natural fractures.

To analyze the fracture closure/fluid flow data, a model was proposed that consists of a general power relationship between fracture closure and fluid flow, as well as a constant term representing the irreducible flow. The relationship between flow and average fracture closure is given by

$$Q = Q_\infty + C(d_{max} - d)^n, \qquad (1)$$

where Q = measured value of flow (flow per unit head drop), Q_∞ = irreducible flow, C = fitted constant, d_{max} = maximum value of closure, d = measured value of closure, and n = power relation. A linear least-squares fitting routine applied to the logarithm of the quantities in Eq. (1) (Press et al., 1986) was used to determine Q_∞, d_{max}, C, and n. Table 1 lists the measured values of closure at a stress of 85 MPa and the values of the fitted maximum closure, d_{max}.

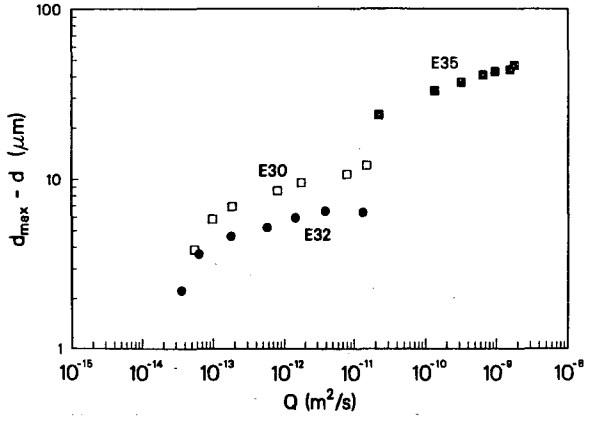

Figure 4. Fracture closure versus flow per unit head drop for samples E35, E30, and E32. [XCG 8610-12166]

Values of d_{max} are estimates of the average closure that might be obtained if the normal stress were increased to a level at which all voids were closed. As seen in Table 1 the difference between the measured closure at 85 MPa and d_{max} varies for the three fractures. These variations are primarily the result of differences in fracture stiffness (Myer et al., 1986a). Fracture E32, having the greatest stiffness, would be expected to experience the least deformation upon complete closure. Fracture E35, on the other hand, having the lowest stiffness, would be expected to deform the most.

When values of irreducible flow Q_∞ are subtracted from the flow data, the result, as shown in Fig. 5, is a power-law relationship between flow and average closure. However, as indicated by the values of n in Fig. 5, the relationship differs greatly from a cubic-law representation.

DISCUSSION

The large values observed for the exponent in Eq. (1) may be explained by the changes in fracture void geometry that occur as stress is increased. The apertures and aspect ratios of the fracture voids are heterogeneous. As stress is applied, the high-aspect-ratio voids close much more rapidly than the average measured value of fracture closure. This rapid closure of some voids is reflected in the rapid increase of displacement and the sharp decrease in flow for low stresses. The high-aspect-ratio fracture voids eventually become barriers to flow as the stress is increased, and the high-aspect-ratio voids become completely closed; the only voids that remain open are small equidimensional pipes. Actual observation of the fracture-void geometry through the use of a metal-injection technique (Myer et al., 1986b) has

Table 1. Values of experimentally determined closure at 85 MPa and maximum closure, d_{max}, determined from the flow equation (1).

Specimen	Closure at 85 MPa (μm)	d_{max} (μm)
E32	4.5	6.6
E30	9.5	12.5
E35	28.1	46.0

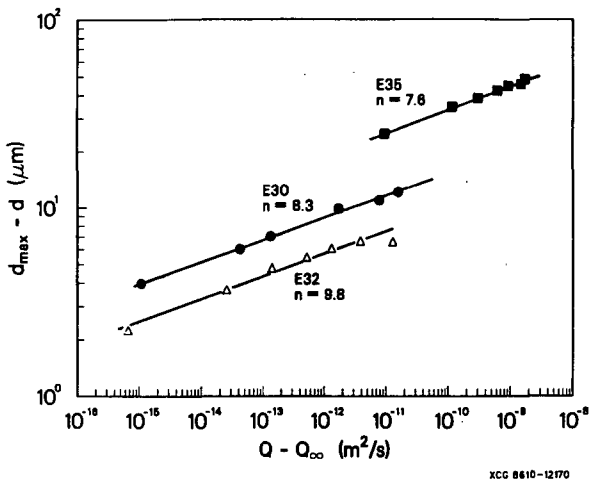

Figure 5. Fracture closure versus flow per unit head drop after subtraction of irreducible flow for samples E35, E30, and E32. [XCG 8610-12170]

shown that the barriers to flow are not randomly distributed but have correlated geometrical arrangements. In injection tests on samples E30 and E32, barriers were found to increase as stress was applied from 3 MPa to 85 MPa, and the flow paths become more tortuous. The difference in the number and distribution of the barriers with increase in stress is evidence that some of the high-aspect-ratio voids closed completely. The irreducible flow observed in the hydrologic tests is believed to be a result of low-aspect-ratio fracture voids that cannot be closed.

CONCLUSIONS

Fluid flow through a natural fracture is controlled by the distribution and number of high-aspect-ratio fracture voids. As stress is applied the high-aspect-ratio voids close first and become barriers to flow. These barriers are not simple point contacts but have geometrical arrangements and are proximate to one another. This result is evident in the rapid increase in displacement at low stresses (which is the closure of high-aspect-ratio voids) and the more gradual increase in closure (the remaining displacement due to low-aspect-ratio voids) at high stresses. The barriers are also evident in contact-area measurements made by Pyrak et al. (1985). Further work needs to be done to explore the distribution of barriers and their formation as stress is increased or decreased.

REFERENCES

Engelder, T., and Scholz, C.H., 1981. Fluid flow along very smooth joints at effective pressures up to 200 Megapascals. *In* Mechanical Behavior of Crustal Rocks. Am. Geophys. Union Monogr. 24, p. 147–152.

Iwai, K., 1976. Fundamentals of fluid flow through a single fracture (Ph.D. thesis). University of California, Berkeley, 280 p.

Myer, L.R., Pyrak-Nolte, L.J., and Cook, N.G.W., 1986a. Deformation of fractures under normal stress. *In* this Annual Report.

Myer, L.R., Pyrak-Nolte, L.J., and Cook, N.G.W., 1986b. Experimental determination of fracture-void geometry. *In* this Annual Report.

Press, W.H., Flannery, B.P., Teukolsky, S.A., and Vettering, W.T., 1986. Numerical Recipes. Cambridge University Press, New York, p. 509.

Pyrak, L.J., Myer, L.R., and Cook, N.G.W., 1985. Determination of fracture void geometry and contact area at different effective stress. EOS, Trans. Am. Geophys. Union, v. 66, no. 46, p. 903.

Raven, K.G., and Gale, J.E., 1985. Water flow in a natural rock fracture as a function stress and sample size. Int. J. Rock Mech. Min. Sci. Geomech. Abstr., v. 22, no. 4, p. 251–261.

Forward Modeling of Block Structures Using Discontinuous Deformation Analysis

G.-H. Shi and R.E. Goodman

A rock mass can be idealized as a three-dimensional mosaic of rock blocks. The behavior of the rock mass depends on (1) the stress/strain relations *within* each block and (2) the contact-force/relative-displacement relations *between* blocks. Discontinuous deformation analysis (DDA) is a novel numerical method for analyzing this idealized block structure.

In a previous publication (Shi and Goodman, 1985), we discussed the use of DDA for backward modeling, in which inverse problems are solved. Given a deformational state, backward modeling was previously capable of determining the corresponding block strains and positions but not the stresses. This article introduces constitutive relations that make it possible to use backward modeling to determine stresses as well.

To perform a forward calculation with discontinuous deformation analysis, the geometry of the block system, the parameters that govern rock deformability, and the interface friction angles are input. Given a specific increment of change in initial conditions, the analysis determines the new stresses and strains in each block, the translations and rotations of each block, and the contact forces, sliding distances, and aperture changes along all interfaces.

A general purpose computer program has been developed that can be applied to the special case of zero friction between blocks. The user directly digitizes the end points of each joint trace; the program then computes the geometry of all of the blocks created by the system of joint traces. The deformed shapes of blocks are computed implicitly and drawn by the computer after each increment of loading or unloading. The input procedures for this discontinuum analysis are no more difficult than for finite-element analysis of a continuum using automatic mesh generation.

To address the essential discontinuous nature of a system of blocks, not only block statics but inter-block kinematics must be respected. The computational steps involve setting up an energy formulation that incorporates constraints prohibiting inter-block penetrations. Minimization of the energy stored in the system yields simultaneous equations constrained by the interpenetration relationships. The sparse but large system of stiffness equations is solved directly with an efficient, novel equation solver.

Block Statics are solved to generate submatrixes describing the stress/strain relationships within individual blocks. The displacements of the points of any block are determined from six unknown parameters contained in the vector $(\alpha) = (u_o, v_o, \omega, \epsilon_x, \epsilon_y, \gamma_{xy})^T$ according to

$$\begin{bmatrix} u \\ v \end{bmatrix} = \begin{bmatrix} 1 & 0 & -(y-y_o) & (x-x_o) & 0 & (y-y_o)/2 \\ 0 & 1 & (x-x_o) & 0 & (y-y_o) & (x-x_o)/2 \end{bmatrix} \begin{bmatrix} u_o \\ v_o \\ \omega \\ \epsilon_x \\ \epsilon_y \\ \gamma_{xy} \end{bmatrix}, \quad (1)$$

where (x,y) and (x_o, y_o) are two points in a block, (u_o, v_o) are parallel translations, ω is rotation, ϵ_x and ϵ_y are normal strains, and γ_{xy} is shear strain.

First we calculate the three contributions to a block's potential energy from each of the stress components acting through the corresponding strain over the area of the block. In this formulation it proves convenient to reserve three additional places for energy contributed by block interactions; accordingly, a 6×6 matrix (k) is established, for each block, as follows:

$$(k) = \frac{EA}{1-\nu^2} \begin{bmatrix} 0 & 0 & 0 & 0 & 0 & 0 \\ 0 & 0 & 0 & 0 & 0 & 0 \\ 0 & 0 & 0 & 0 & 0 & 0 \\ 0 & 0 & 0 & 1 & \nu & 0 \\ 0 & 0 & 0 & \nu & 1 & 0 \\ 0 & 0 & 0 & 0 & 0 & (1-\frac{\nu}{2}) \end{bmatrix}, \quad (2)$$

where E is the modulus of elasticity, ν is Poisson's ratio, and A is the area of the block.

The energy stored in a block will then be given by

$$\text{Energy} = (\alpha)^T(k)(\alpha)12. \quad (3)$$

For a system of n blocks, we next accumulate a system of energy equations like (3) with the *system* matrix (K) being of size $6n \times 6n$, corresponding to the $6n$ unknown deformational mechanisms. The simultaneous equations for determining these mechanisms are derived by differentiating the system energy equations to minimize the energy.

Block Kinematics refers to the condition that sliding and separation of blocks along interfaces cannot produce interpenetrations of blocks. A set of linear inequalities is established to represent this condition, as discussed in Shi et al. (1985). The kinematic constraint inequalities are converted to constraint equations.

Off-On Iteration is then used to solve the essentially nonlinear behavior imposed by the geometric constraints. A subset of the constraint equations is selected as a first trial. Each constraint equation produces four 6×6 submatrixes (termed "penalty matrixes"); each of these is added to the general matrix (K), eliminating some or all of its zeros. After several iterations (typically 3 to 7) the choice of the constraint equation subset will have converged to a final subset; (K) is then a global "stiffness" matrix.

Solution of the $6n \times 6n$ simultaneous stiffness equations is achieved rapidly using a new, highly efficient equation solver that minimizes storage space and computation time. Only nonzero terms are stored. The equations are solved in an almost optimum order using graph theory. Sub-block shifting is eliminated entirely. This method is well suited to the new computers, which have very large addressable memories.

An example is afforded by the 64-block system shown in Figs. 1 through 4. This problem was solved using a microcomputer (HP 9000, series 300) operating in uncompiled Basic; the computation required 10 hours, which corresponds to about 10 minutes on a MicroVax operating in Fortran. The system of blocks contains 16 precompressed springs, producing unequilibrated forces as given by the 16 vectors in the centers of the appropriate blocks (Fig. 1). The existence of these forces infers preconstraint around the outside of the model and attachment of one end of each spring to unspecified reaction points independent of the model. As the computation is begun, the outer margin is free of constraint. The spring loads are divided into 10 equal steps of preload, each relaxation of which is allowed up to 7 iterations. The number of iterations actually required decreased markedly with later load steps.

Figures 2, 3, and 4 show the results of relaxation after the third, seventh, and tenth load steps, respectively. In these figures the vectors of residual spring force approach zero as the system becomes fully relaxed. The consequent block movements and strains are complicated but always appear reasonable. The block shapes show *net strain change* of each block. Note that the solution avoids any interpenetration of blocks.

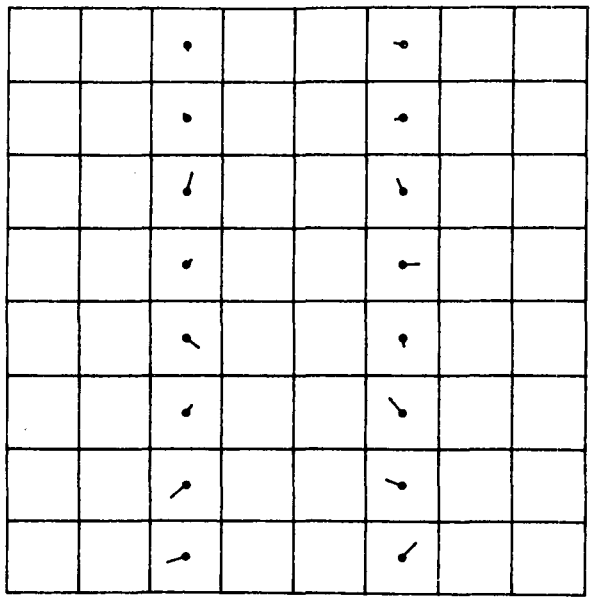

Figure 1. System of 64 blocks in which 10 blocks contain precompressed springs that produce unequilibrated forces represented by the vectors. [XBL 871-243]

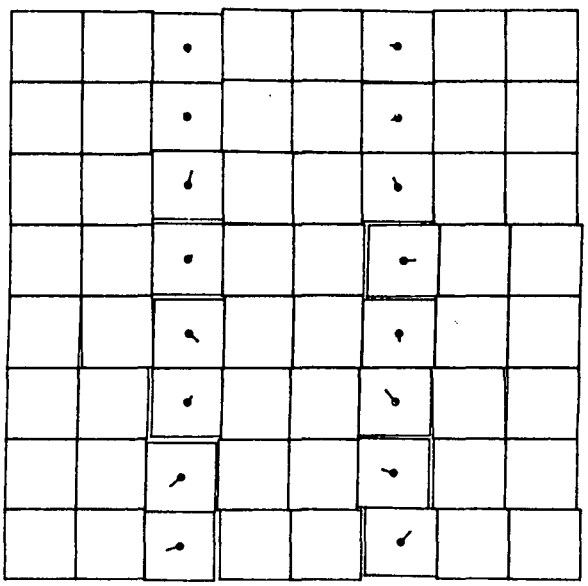

Figure 2. Result of relaxation after the third load step. [XBL 871-244]

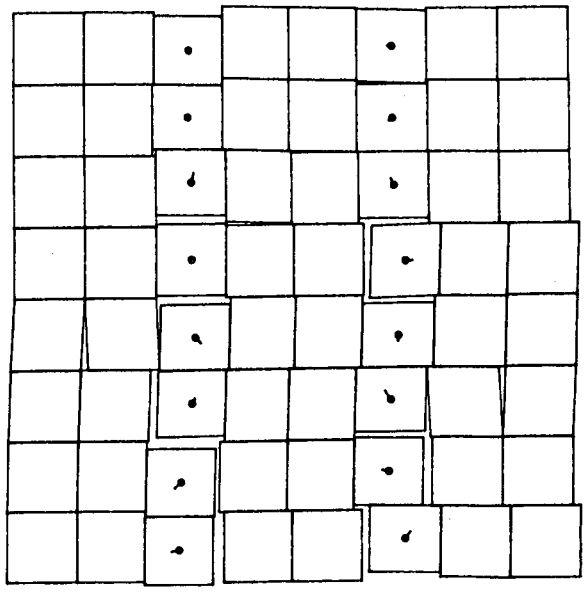

Figure 3. Result of relaxation after the seventh load step. [XBL 871-245]

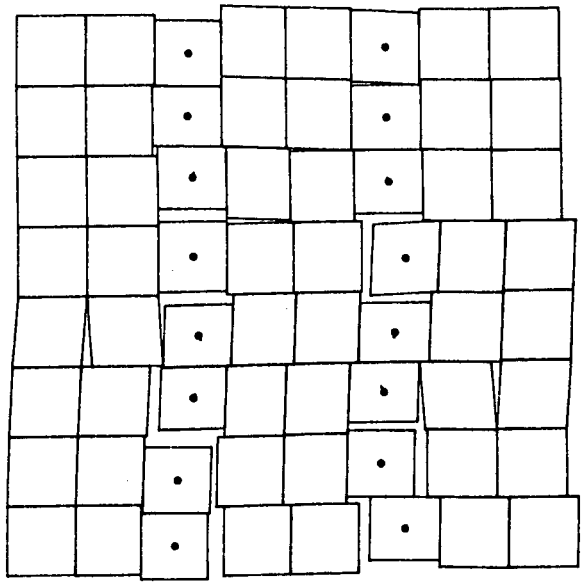

Figure 4. Result of relaxation after the tenth load step. [XBL 871-246]

ACKNOWLEDGEMENT

Work on this model continues in relation to Department of Energy research administered by Battelle Laboratories and monitored by Dr. Ernest Lindner. The computer program being developed will be applied to analysis of excavation monitoring experiments being planned for the Underground Research Laboratory, Lac du Bonnet, Manitoba, in partnership with the Canadian Atomic Energy Company, Ltd., Pinawa, Manitoba.

REFERENCES

Shi, G.-H., and Goodman, R.E., 1985. Two dimensional discontinuous deformation analysis. Int. J. Numer. Anal. Methods Geomech., v. 9, p. 541–556.

Shi, G.-H., Goodman, R.E., and Tinucci, J.P., 1985. The kinematics of joint inter-penetrations. Proceedings, 26th U.S. Symposium on Rock Mechanics, Rapid City, South Dakota, June 26–28, 1985. A.A. Balkema, Boston, p. 121–130.

Borehole Breakout Analysis

Z. Zheng and N.G.W. Cook

Fracture of rock adjacent to the surfaces of underground excavations is of considerable interest in work related to the performance of mined geologic repositories for the disposal of nuclear wastes, to the strength of deep excavations for defense, to safety in underground mining, and to the stability of deep boreholes for gas and oil production or scientific observation.

Boreholes are the most ubiquitous form of underground excavation. Under conditions where the magnitudes of the stresses in the rock are of the same order as the strength of the rock, it has been established that the walls of boreholes fracture, elongating the cross section of the borehole in the direction of the minimum stress orthogonal to its axis (Gough and Bell, 1982; Hickman et al., 1985; Plumb and Hickman, 1985; Zoback et al., 1985).

Gough and Bell (1982) have analyzed the process of fracture that produces wellbore breakouts by applying a Mohr-Coulomb failure criterion to the

distribution of stresses given by the Kirsch solution for a circular hole in an elastic material. They propose that breakouts are produced by two pairs of shear fractures at opposite ends of the above diameter. They argue that these fractures define the pointed, "dog ear" shape of a typical breakout cross section.

Zoback et al. (1985) have also analyzed the process of fracture that results in breakouts, using the Kirsch solution and a Mohr-Coulomb failure criterion. Their method leads to predictions of broad, flat-bottomed breakout cross sections. They then show that the shape of the breakout, in terms of its depth and the angle subtended by it at the center of the borehole, can be used to estimate the ratio of the stresses in the rock orthogonal to the axis of the borehole. They also consider briefly the question of breakout growth. Using a numerical model based on boundary elements, they evaluated the distribution of stresses in an elastic material around a hole, with the cross section given by the initial breakout analysis. The stresses in the rock adjacent to the initial, and succeeding, predicted cross sections become increasingly severe, so that breakouts should propagate indefinitely. They suggest that inelastic processes must provide the stability of breakout cross sections observed in the field.

THE FRACTURE PROCESS

Many rocks are extremely brittle in uniaxial compression. Wawersick and Fairhurst (1970) and Wawersick and Brace (1971) measured complete stress-strain curves on a variety of rocks in uniaxial and triaxial compression. In uniaxial compression, deformation is essentially elastic almost to the maximum ordinate of the stress-strain curve, or the strength of the rock. Beyond this point many rocks are intrinsically unstable (class II, Wawersick and Fairhurst, 1970), in that the stored energy in the rock at the maximum stress exceeds the energy needed to fracture the rock, whereas in other rocks the residual strength diminishes very rapidly with small increases in strain (class I). Fracture occurs mainly by splitting or spalling parallel to the uniaxial compressive stress.

Fracture by axial splitting, or spalling, parallel to the direction of maximum compressive stress has been analyzed by Horii and Nemat-Nasser (1985) and Kemeny and Cook (1986), among others, using linear elastic fracture mechanics. Figure 1 shows the incremental strain associated with the growth of extensile cracks in biaxial compression according to Kemeny and Cook (1986). Stresses and strains have been normalized with respect to the initial length of

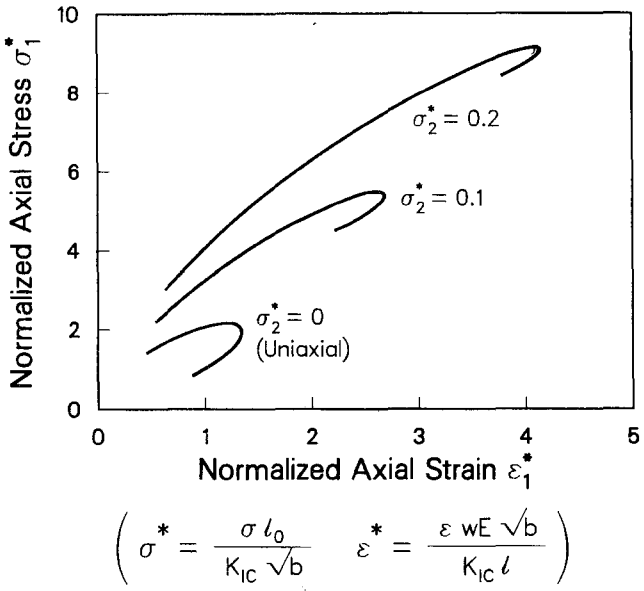

Figure 1. Stress incremental strain curve for failure in biaxial compression by extensile splitting parallel to the direction of the compressive stress. [XCG 8610-12216]

a sliding source crack, $2l$, and the pitch between collinear source cracks, $2b$, as well as the critical stress-intensity factor K_{IC}, for mode I crack propagation (Fig. 2). We use this fracture-mechanics model here for extensile splitting in biaxial compression together

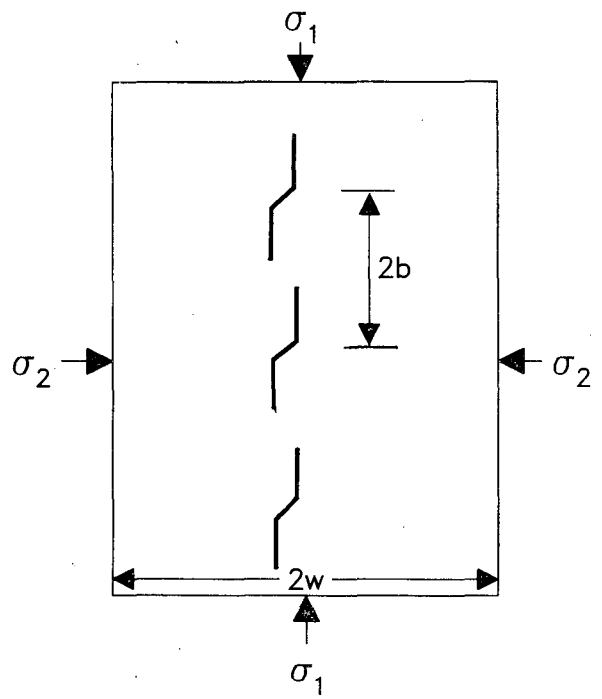

Figure 2. Fracture mechanics model for extensile splitting. [XCG 8710-12217]

with a numerical boundary-element analysis (Crouch and Starfield, 1983) of the distribution of stresses in an elastic material to analyze the formation and stability of wellbore breakouts.

THE BREAKOUT MODEL

When a borehole is drilled, the tangential stress in the rock around the hole is increased near the ends of a diameter parallel to the minimum stress in the rock mass, and the radial stress is reduced to zero in the case of an empty hole or, otherwise, to the value of the fluid pressure in the hole. In the absence of drilling mud or casing, the rock in this region adjacent to the borehole is subjected essentially to a biaxial compressive effective stress. If this stress is sufficiently great in relation to the strength of the rock, given by the maximum ordinate of the stress-strain curve in Figs. 1 or 3, the rock should fail by extensile splitting subparallel to the wall of the borehole. Note that such splitting must occur quite close to the free surface of the borehole, because the radial stress increases rapidly with radial distance into the rock away from the circumference of the borehole, and such confinement inhibits axial splitting very strongly (Fig. 1). Moreover, the extensile splitting becomes intrinsically unstable just beyond the peak of this curve because of its class II character. As a result of the formation of the first spall by extensile splitting, a new free surface is created, and the shape of the cross section of the borehole is changed. In general, the concentration of the tangential stress in the rock adjacent to the elongated portion of the new cross section will be even greater than it was around the initially circular cross section, and the new free surface diminishes the radial stress

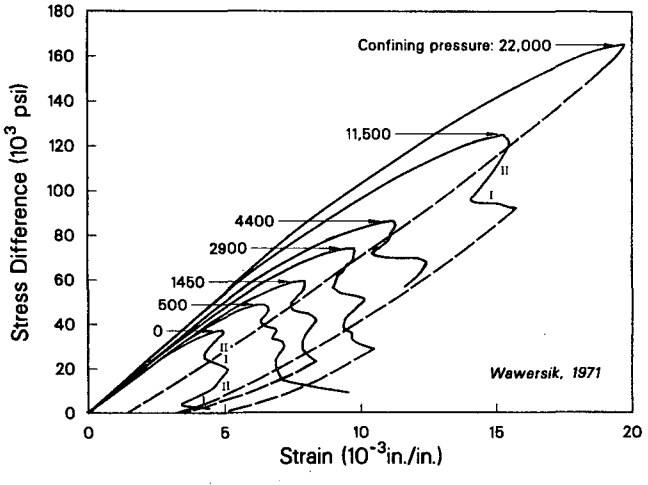

Figure 3. Complete stress-strain curves in biaxial compression (after Wawersik and Brace, 1971). [XCG 8610-12215]

in the rock adjacent to it, so that another extensile fracture should form subparallel to the circumference of the elongated portion of the new cross section. Wellbore breakout is assumed to be the result of a series of episodes of spalling by extensile splitting, like that described above.

Modeling this sequence of changes in cross section by successive spalling requires a method for systematically changing the cross section of the borehole as a result of each episode. This has been done by dividing the rock around an initially circular borehole into a large number of small blocks defined by angular increments of 1.5° and radial increments of 0.067 of a borehole radius. Initially, the boundary-element analysis is used to determine the tangential stress around a circular borehole for values of the rock mass stresses of interest. An annular arc of rock is then removed that extends out 0.067 of the borehole radius and which includes that portion of the borehole circumference within which the tangential stress exceeds the rock strength. The new distribution of stress in the rock around the elongated cross section resulting from this change is now calculated using boundary-element analysis, and another layer of rock is removed from any place on the circumference of the now noncircular cross section where the tangential stress exceeds the compressive strength. The final breakout shape of the borehole is allowed to evolve by a succession of such episodes until the tangential stress is everywhere less than the strength of the rock.

Once the final breakout cross section has been found, the stability of this cross section is verified in two ways. First, the tangential stress around the circumference of the breakout must be everywhere less than the compressive, or tensile, strength of the rock. Second, in the rock outside the borehole, extensile splitting should not occur because that mode of failure is so strongly inhibited by confining stress; however, shear failure may occur. Therefore, the distribution of the stresses everywhere in the rock outside the breakout cross section is compared with a Mohr-Coulomb criterion for the strength of the rock. If the distribution of elastic stresses is everywhere less than that needed to produce failure either by extensile splitting or Mohr-Coulomb shear, the breakout cross section should indeed be stable. The rock will then be in an elastic condition everywhere, so that the stress analysis using boundary elements in an elastic material is valid.

RESULTS

Using the methodology described above, stable wellbore breakout shapes have been determined for a

range of ratios between the principal stresses in the rock mass orthogonal to the axis of a borehole; the range of magnitude of these stresses, relative to the strength of the rock, is illustrated in Fig. 4. The region on the top left of this figure, bounded by the almost circular arc, represents the conditions under which the tangential stress around a circular borehole is not sufficient to result in spalling and produce breakouts. To the right of this are shown stable breakout shapes corresponding to a variety of stress conditions. These results were determined by first applying the stresses to the rock mass and then excavating the borehole. To some extent this represents what occurs when a borehole is drilled, although the full stress concentrations around the hole must actually develop progressively as the hole is drilled beyond the plane where the cross section is being considered.

In laboratory tests of wellbore breakouts, it is much easier to increase the stresses in a specimen of rock in which a predrilled borehole exists (Haimson and Herrick, 1985). We have used a similar methodology to that described above to simulate wellbore breakouts under conditions of progressively increasing stress. The stresses in the rock are increased in small, regular steps from critical values necessary to initiate fracture at the ends of a diameter parallel to the direction of the minimum principal stress in the rock to the desired final values. After each stress increase, the tangential stress around the circumference of the breakout cross section is compared with the strength of the rock. Wherever the tangential stress exceeds this strength, a thin layer of rock is removed to change the cross section. This sequence is repeated until the desired stress values have been reached. The stability of the final breakout cross section is established by showing that the tangential stresses around the entire circumference are less than the strength of the rock and that the elastic stresses everywhere in the rock outside the breakout are less than those necessary to cause shear failure according to a Mohr-Coulomb criterion. The amount of breakout needed to develop a stable cross section is much larger when a hole is created instantly in rock subjected to a pre-existing stress than when the stresses are increased gradually around a pre-existing hole.

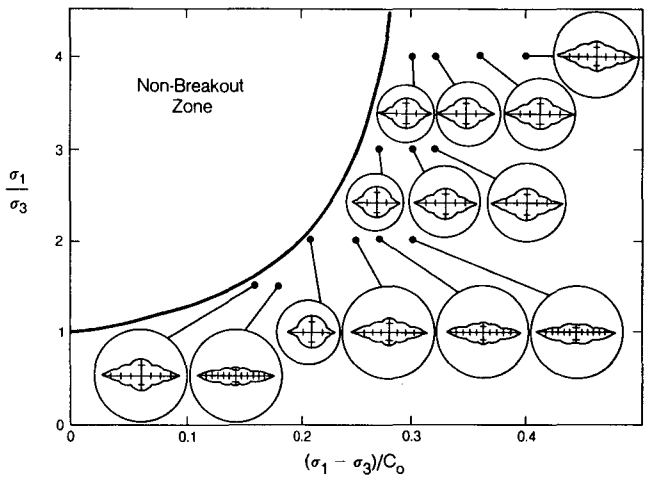

Figure 4. Simulated stable breakout cross sections for different ratios of the horizontal stresses and of the difference between these stresses and the biaxial compressive strength; for the case where a borehole is created instantly in a rock with pre-existing stresses. [XBL 8610-12664]

Laboratory tests in which the stresses in a rock specimen containing a pre-existing hole are progressively increased probably result in breakout cross sections significantly smaller than those that would form as a result of drilling into prestressed rock. Indeed, Mastin (1984) and Haimson and Herrick (1985), who conducted such tests, observed small breakouts and found that the calculated tangential stress needed to produce them was almost twice the uniaxial compressive strength of the rock. The latter observation may be yet another manifestation of the well-recognized, but not well-understood, phenomenon of size effects; the compressive strength of small samples of rock is much greater than that of large samples (Hoek and Brown, 1980).

Wellbore breakouts have been observed in many of the boreholes in the Columbia River basalts at Hanford, Washington (Kim et al., 1986). Some of these have been measured using a seismic televiewer or a downhole television camera. Comparing the shapes of the breakouts with those in Fig. 4 suggests that the ratio between the horizontal stresses must be about 2 and that the ratio of the difference between these stresses and the uniaxial compressive strength is about 0.2. The current best estimates of the horizontal stresses in this region at the depth of this breakout are 60.6 Mpa and 34.5 MPa (Kim et al., 1986), which is only a little less than 2. From the ratio of the stress differences to the compressive strength, a value of about 130 MPa can be inferred for the in situ compressive strength. This is half the uniaxial compressive strength for this basalt as determined from laboratory tests on small specimens taken from cores from the same depth in the borehole as the breakout (K. Kim, personal communication, 1985). The disparity may reflect a real difference between strength determined in laboratory tests and in situ strength. However, it should be pointed out that the absolute values of the stresses are not the real item of interest. It is the magnitude

of the stresses relative to the strength of the rock that is of real concern; and a correct analysis of breakout shapes should provide this information directly.

DISCUSSION

A methodology has been developed to generate wellbore-breakout cross sections in elastic brittle rocks using numerical simulation. There are two particularly interesting results. First, it is shown that the breakout cross section results in a redistribution of the stresses in an elastic rock, so that these stresses become everywhere less than both the biaxial compressive strength and the shear strength given by a Mohr-Coulomb criterion; thus the breakout cross section must be stable. Second, it is shown that the resulting cross section depends upon the stress path. Breakouts are much smaller if they result from a gradual increase in stress than if a hole is created instantly in rock already subjected to stress, yet both cross sections result in stress distributions that do not exceed the strength of the rock.

The predicted breakout cross section should be exact for truly brittle rocks. Many softer rocks exhibit some degree of class I stable strain softening. It is likely that the residual strength of such a rock at a strain exceeding that which corresponds to the peak strength may prevent complete removal of the rock by spalling, as assumed in the above model. Indeed, Plumb and Hickman (1985) report that regions of enhanced electrical conductivity detected at the base of breakouts may be due to porosity increases caused by incomplete spalling and dilatation of the rock in this region. Perhaps rock such as this could be removed by scavenging with high-pressure water jets to reveal the breakout cross section predicted by the elastic brittle spalling model.

REFERENCES

Crouch, S.L., and Starfield, A.M., 1983. Boundary Element Methods in Solid Mechanics. George Allen & Unwin, London.

Gough, D.I., and Bell, J.S., 1982. Stress orientations from borehole wall fractures with examples from Colorado, east Texas, and northern Canada. Can. J. Earth Sci., v. 19, p. 1358–1370.

Haimson, B.C., and Herrick, C.G., 1985. In situ stress evaluation from borehole breakouts experimental studies. *In* E. Ashworth (ed.), Research and Engineering Applications in Rock Masses. A.A. Balkema, Boston, p. 1207–1218.

Hickman, S.H., Healy, J.H., and Zoback, M.S., 1985. In situ stress, natural fracture distribution, and borehole elongation in the Auburn geothermal well, Auburn, New York. J. Geophys. Res., v. 90, no. B7, p. 5497–5512.

Hoek, E., and Brown, E.T., 1980. Underground Excavations in Rock. Institute of Mining and Metallurgy, London.

Horii, H., and Nemat-Nasser, S., 1985. Compression-induced growth in brittle solids: Axial splitting and shear failure. J. Geophys. Res., v. 90, no. B4, p. 3105–3125.

Kemeny, J., and Cook, N.G.W., 1986. Crack models for the failure of rock in compression. *In* C.S. Desai et al. (eds.), Constitutive Laws for Engineering Materials: Theory and Applications. Elsevier, New York, p. 879–887.

Kim, K., Dischler, S.A., Aggson, J.R., and Hardy, M.P., 1986. Characterization of the state of in situ stress by hydraulic fracturing for a nuclear waste repository in basalt. Rockwell International Report RHO-BW-SA-551 P.

Mastin, L., 1984. The development of borehole breakouts in sandstone (M.S. thesis). Stanford University, Stanford.

Plumb, R.A., and Hickman, S.H., 1985. Stress-induced borehole elongation: A comparison between the four-arm dipmeter and the borehole televiewer in the Auburn geothermal well. J. Geophys. Res., v. 90, no. B7, p. 5513–5521.

Wawersik, W.R., and Brace, W.F., 1971. Post-failure behavior of a granite and diabase. Rock Mech., v. 3, p. 61–85.

Wawersik, W.R., and Fairhurst, C., 1970. A study of brittle rock fracture in laboratory compression experiments. Int. J. Rock Mech. Min. Sci., v. 7, p. 561–575.

Zoback, M.D., Moos, D., and Mastin, L., 1985. Wellbore breakouts and in situ stress. J. Geophys. Res., v. 90, no. B7, p. 5523–5530.

GEOPHYSICS

The research program of the Geophysics group is strongly oriented toward detecting and monitoring natural and man-made processes in the subsurface. Coupled to efforts in reservoir engineering and hydrogeology, many of the projects have been designed to investigate the movement of fluid in rocks of the earth's crust and have employed geophysical methods to delineate magma distribution and movement, to detect the mixing of waters of different conductivities, and to locate and characterize natural fractures and hydrofractures. Major emphasis is given to cross-hole tomography and vertical seismic profiling methods for mapping seismic-wave attenuation, velocity, and shear-wave anisotropy. Borehole and surface-based electromagnetic methods are being developed for a number of applications.

In addition to numerical modeling techniques and field experimentation, the program has also emphasized the development of improved field instruments. During 1986 we have continued the development of a high-speed seismic data acquisition and processing system that is based on Motorola 68000 microcomputer technology and which can be used in a wide range of seismic monitoring activities. A novel borehole vibrating seismic source is under development. We have also studied the feasibility of using a transportable magnetohydrodynamic (MHD) generator as a current source for electromagnetic soundings.

The Center for Computational Seismology offers full seismic-reflection-processing software (DISCO plus in-house additions), various synthetic seismograms and ray-tracing modeling programs, and an archive of the Global Digital Seismological Network data. Field capabilities managed through the Geophysical Measurements Facility include a digitally telemetered microearthquake network, P- and S-wave vibrators, electrical and electromagnetic sounding equipment, and much associated hardware.

Division geophysicists are involved actively in several national programs, such as the Continental Scientific Drilling Program, CALCRUST, IRIS, and the Earthquake Prediction Program. Participation of graduate and undergraduate students and faculty from several departments, postdoctoral fellows, and visiting scientists creates a rich scientific environment for a wide range of geophysical research.

Mapping and Monitoring Nuclear Repositories with Subsurface Electrical Resistivity Arrays

T.H. Asch and H.F. Morrison

The siting and future integrity of nuclear waste repositories is critically dependent on the local groundwater regime. Electrical methods seem particularly promising for mapping and monitoring this regime, since the electrical conductivity of rocks depends entirely on the fluid distribution, saturation, and salinity. Electrical methods have conventionally been used just to detect the presence of good electrical conductors (e.g., sulfide orebodies) or to determine the electrical layering in groundwater exploration.

The electrical conductivity of the ground can be measured by injecting current into the ground through pairs of electrodes and then measuring the resulting voltage drops in the vicinity with other pairs of electrodes. Any or all of the electrodes can be placed in the subsurface, although surface arrays have traditionally been employed. Measurements of voltage and current for different electrode geometries are then used to infer the subsurface distribution of conductivity. These methods are indirect but ideally suited to measure the properties of a region for which it is impossible to gain direct access. The resulting interpretation of the conductivity distribution is not unique, nor does it provide high resolution of subsurface features. In many applications the latter property is to our advantage, since the measurements yield bulk average values of the conductivity, which often reveal features that are not discernible in hand specimens or borehole logging measurements.

Surface arrays that measure electrical current and potential have been used for many years to determine the subsurface resistivity. The most important recent developments are the use of two- and three-dimensional numerical models for interpretation and the use of resistivity mapping with subsurface electrodes. The latter yields far greater accuracy and resolution than can be obtained with surface arrays. This new development opens the way to more quantitative analysis of ground conductivity and offers exciting opportunities for mapping and monitoring fluid content, temperature, and fracture distribution at repository sites. To illustrate the power of subsurface-to-surface arrays, we have studied an idealized two-dimensional model of a repository to investigate the responses from conventional and borehole-to-surface arrays.

The model is shown in Fig. 1. We have assumed that during excavation and construction of the repository, the water content of the rocks has been reduced, so that the effective resistivity of a 100-m-thick zone has increased by a factor of 3 over the normal or background value (in this case 200 ohm·m). The results of a standard dipole-dipole surface survey are presented for this model in Fig. 2 as a three-dimensional perspective plot. We are interested in emphasizing the anomaly caused by the repository, or subsequent changes over time in its vicinity, and we have discovered that it is very useful to express the apparent resistivity results as percent differences from the background. The data in Fig. 3 are the percent differences observed in the apparent resistivity relative to the 200-ohm·m halfspace. The anomaly is diffuse and broad but quite large enough to be detected. Our experience in high-accuracy field surveys has shown that it is possible to make apparent resistivity measurements with an accuracy of 0.1%. For time monitoring with fixed surface electrodes, the sensitivity to small changes in the repository resistivity (e.g., as water re-enters the zone) would therefore be quite high.

Resolution can be improved by using subsurface dipole sources and surface-receiver dipoles. As shown in the model (Fig. 1) the current electrodes

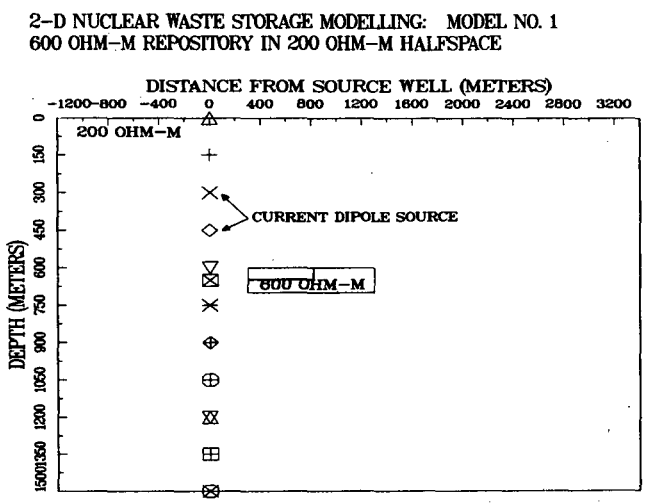

Figure 1. Idealized model of radioactive waste repository site. The symbols represent the location of current electrodes in the subsurface dipole configuration. [XBL 873-691]

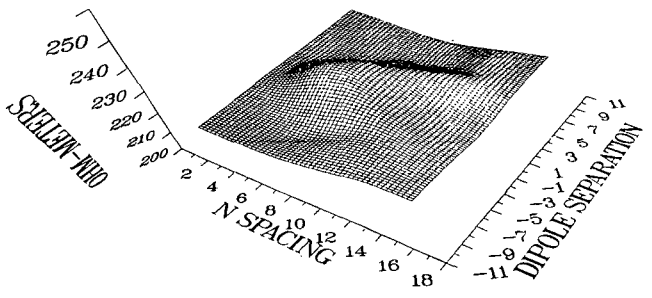

Figure 2. The dipole-dipole apparent resistivities for the model in Fig. 1 presented from a three-dimensional perspective view. The axis labeled "Dipole Separation" refers to the location of the dipoles relative to the center of the model. [XBL 873-690]

are placed every 150 m vertically and are treated as a series of dipole sources. A dramatic definition of the repository boundaries is produced by using percent differences calculated, not on the basis of background half-space resistivity, but on the basis of apparent resistivities observed at a particular depth of the current dipole source. An example is shown in Fig. 4, where all apparent resistivities in the section are compared with the values observed when the center of the dipole source is at a depth of 625 m.

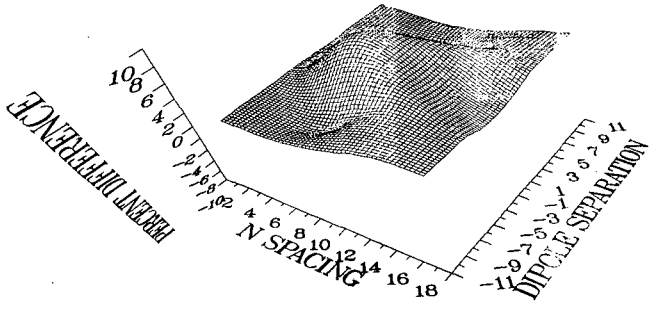

Figure 3. The perspective view of the percent difference between the surface dipole-dipole apparent resistivities for the model in Fig. 1 and the background resistivity, 200 ohm·m. The axis labeled "Dipole Separation" refers to the location of the dipoles relative to the center of the model. [XBL 873-689]

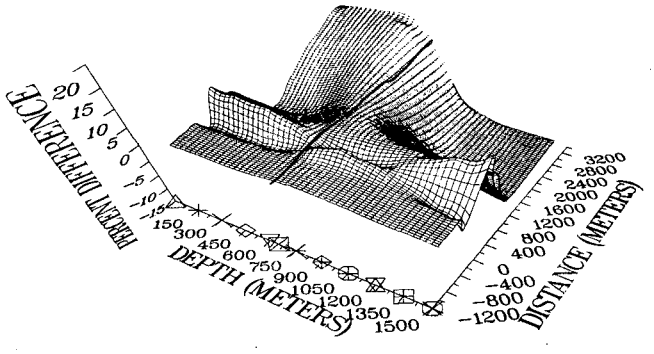

Figure 4. The perspective view of the percent differences for the model in Fig. 1 using borehole dipole sources referenced to the apparent resistivities obtained with the source dipole centered at 625 m depth. [XBL 872-9928]

Finally we have chosen a simple example to show the power of these subsurface methods to detect changes that might occur after the repository is closed. We have considered a case in which the upper left rectangular quadrant of the repository (Fig. 1) resaturates, bringing the resistivity of this zone back down to the normal background resistivity of 200 ohm·m. In Fig. 5 we have plotted the percent difference that this brings about, compared with data from the undisturbed repository. The pseudosection is diagnostic of the zone that has changed, and the changes are well above the accuracy that can be expected for the measurements.

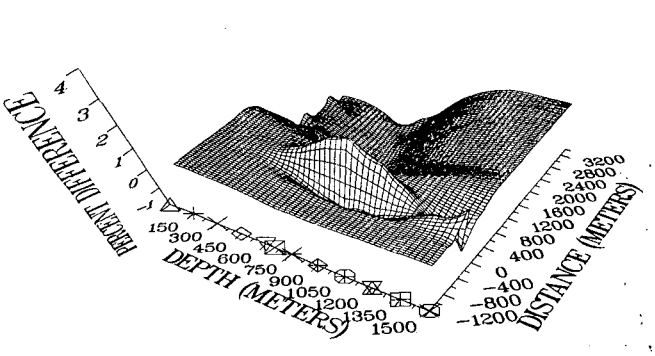

Figure 5. The perspective view of the percent differences for the case when the upper left quadrant of the repository (shown in Fig. 1) has returned to 200 ohm·m. Apparent resistivities are referenced to the undisturbed 600-ohm·m repository. [XBL 872-9929]

In summary, dc resistivity mapping with combinations of surface and subsurface electrodes appears to have great potential for repository mapping and monitoring. Much work remains to be done in selecting the best array geometries for sensitivity in mapping features of interest in site studies.

One of the most exciting possibilities is to investigate the use of these methods to resolve the fracture-induced anisotropy. In the simple illustrations described here we used two-dimensional models with isotropic resistivity. We also have three-dimensional models in which fracture anisotropy could be introduced; the use of such models, coupled with two-dimensional surface arrays of potential electrodes, would undoubtedly greatly improve the resolution of interest in site studies.

A Three-Dimensional Gravity Model of the Structure of Long Valley Caldera

S.F. Carle and N.E. Goldstein

Long Valley caldera is located 30 km south of Mono Lake, on the east side of the Sierra Nevada. The caldera developed around 0.73 Ma, when a volcano explosively ejected about 600 km^3 of magma (Hill and Bailey, 1985), causing an ash flow that formed the Bishop Tuff. Subsequent collapse of the volcano formed an elliptical caldera that measures 32 km east–west by 17 km north–south and has a maximum subsidence of about 3.5 km. The caldera depression has been filled with various sedimentary and volcanic rocks, which primarily consist of (in decreasing order of volume) the Bishop Tuff, early (post-Bishop Tuff) rhyolite tuff, lake sediments, early rhyolite flows, various rhyolitic, rhyodacitic, andesitic, and basaltic flows, moat rhyolites, alluvium, and pumice, up to a cumulative depth of 2.7 km (Bailey et al., 1976). Because most of these fill rocks are less dense than the precaldera "basement" of granite, metasediments, and metavolcanics, a gravity low of about −50 mGals coincides with the caldera.

Several attempts to define and interpret this anomaly have been made in the past using 2-D and 3-D models; none have been definitive. All published 3-D models simplistically assume constant density of fill. All 2-D models suffer from the inherent three-dimensionality of the complicated density structure of Long Valley caldera (Abers, 1985). In addition, previous interpretations have either ignored or lacked access to subsurface data, such as well lithologies and density logs, seismic refraction surveys, and studies of the surface and structural geology. The purpose of this study is to use all available geologic data to constrain a multilayer 3-D density model of Long Valley caldera that produces the anomalous surficial gravity field.

DEFINING THE GRAVITY ANOMALY ASSOCIATED WITH THE CALDERA

The local gravity anomaly is obtained by subtracting the regional component from the terrain-corrected Bouguer gravity field, which has been defined by over 2000 station readings collected and compiled by the U.S. Geological Survey. In the Long Valley caldera area, the principal regional effect is due to isostatic compensation of the crust, causing a strong gravity gradient perpendicular to the strike of the Sierra Nevada and a total gravity change of about −230 mGals. Simpson et al. (1986) removed this part of the regional effect from the Bouguer gravity by applying an isostatic correction based on the Airy-Heiskanen crustal model (assuming a 0.4-g/cm^3 density interface at the Moho). The result is a map of isostatic residual gravity (IRG), and it is these values that we use as the initial gravity data for the study of the caldera (Fig. 1). However, a regional component remains in the IRG, and this component is attributed to lateral density variations in the crust.

In this study the regional component in the IRG was removed by a technique advocated by Skeels (1967). In brief, this method defines the regional component using gravity values sufficiently outside the influence of the local anomaly. The condition for being "sufficiently outside" is that the calculated residual anomalous field should be near zero. This method requires some prior knowledge of the anomalous structure, which in the case of Long Valley caldera has been well documented by detailed geologic mapping, seismic surveys, and some drill-hole information. The stations "sufficiently outside" the anomalous zone constrain the regional field

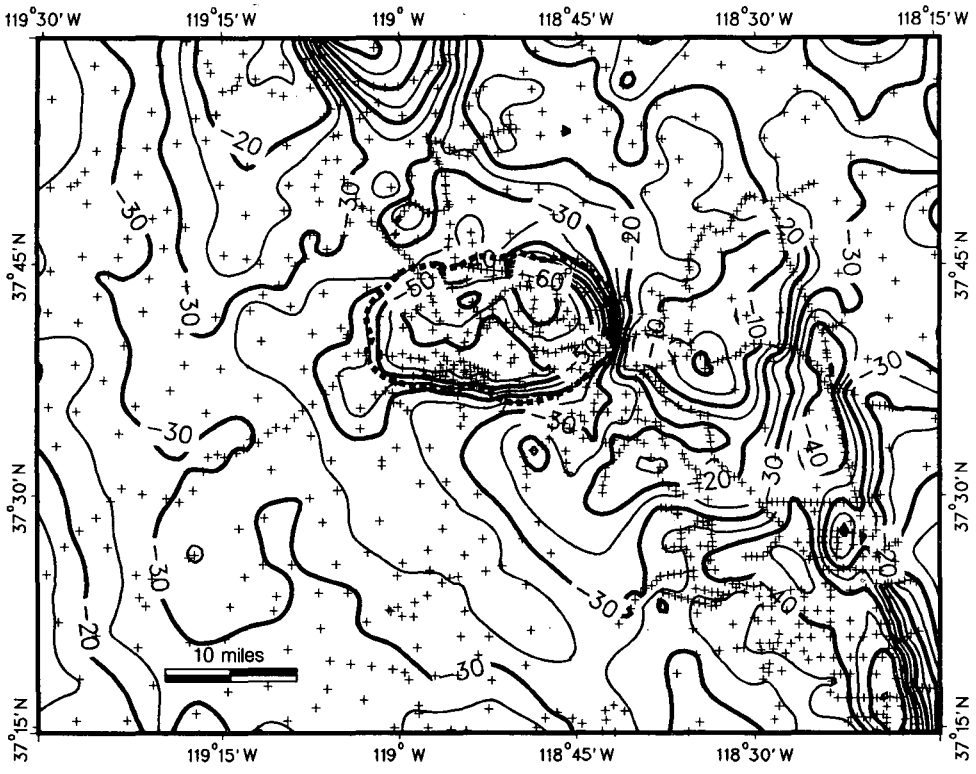

Figure 1. Isostatic residual gravity. Contour interval is 5 mGals. Crosses denote gravity stations. Broken line is caldera boundary. [XBL 873-9960]

within the anomalous zone, which is defined by a surface of minimum curvature (Fig. 2). Subtracting this regional component from the IRG yields the residual gravity anomaly (Fig. 3). An advantage to this method is that the residual gravity anomaly is defined by geology on its edges, so that the model is accordingly plausible. Another advantage is that such a regional component is theoretically reproducible. A disadvantage of this technique is that the regional component in the anomalous zone may be overinfluenced by local features or individual data points. At present, this weakness is considered less critical than the disadvantages of other techniques for removing regional components.

THE MODELING TECHNIQUE

The 3-D gravity inverse problem for a single layer of uniform density over a half-space is unique and can be solved by the method of Cordell and Henderson (1968). In this technique the model is represented by a constant-density 2-D horizontal array of square prisms with variable height above a horizontal reference plane. Each prism height is adjusted iteratively as follows:

$$h(x,y) = h(x,y) \times [\text{gobs}(x,y)/\text{gcalc}(x,y)],$$

where $h(x,y)$ is the height of the prism centered below observation point (x,y), gobs is the observed gravity anomaly, and gcalc is the calculated gravity anomaly. The case of multiple stacked layers is nonunique, although it is routinely solved in two dimensions by forward modeling.

To obtain a multilayer model of the Long Valley caldera in three dimensions, a 3-D modeling program was developed that is an extension of the Cordell-Henderson approach. On the basis of information on geology and rock density, an initial model with 16 discrete density units was defined. The initial model affects the final model by restricting the horizontal extent of the density units. The prism size of 1.4 km was selected to be consistent with gravity station density. Adjustments to the model were made by forward and constrained inverse techniques. Forward modeling was executed by adjusting units after comparing the observed and calculated gravity anomalies and considering plausible geologic reasons for the discrepancy. Inverse modeling of one or more units was executed by the adapted Cordell-Henderson technique:

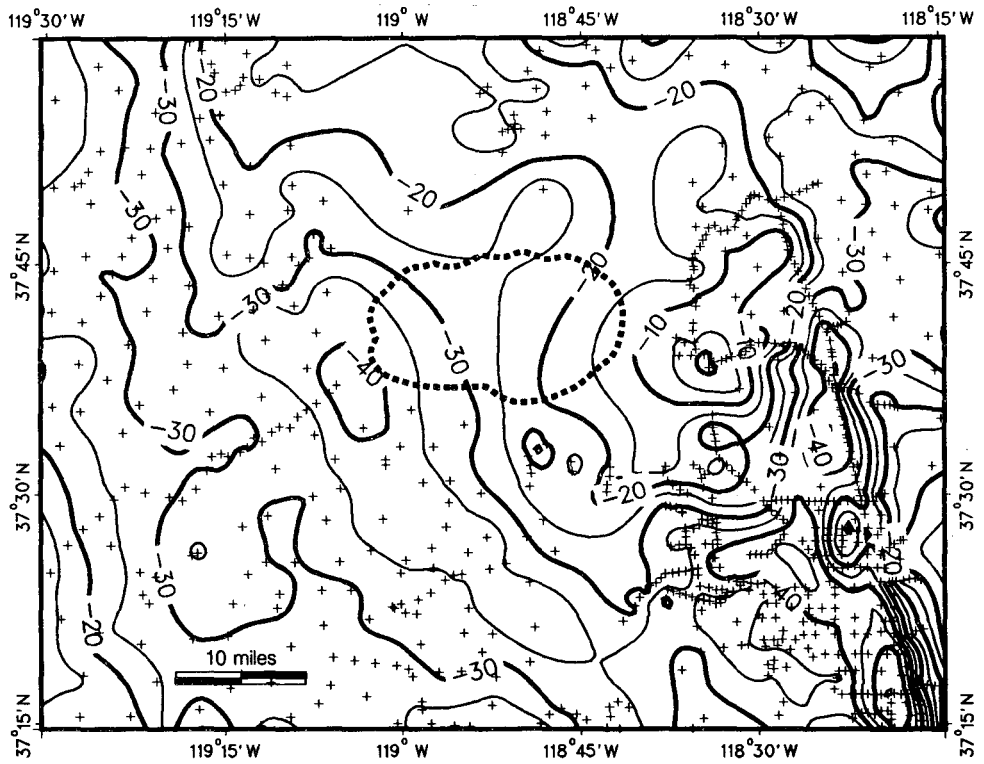

Figure 2. Regional isostatic residual gravity. Contour interval is 5 mGals. Crosses denote gravity stations that are "sufficiently outside" the anomalous zone. Regional surface is defined by minimum curvature. [XBL 873-9961]

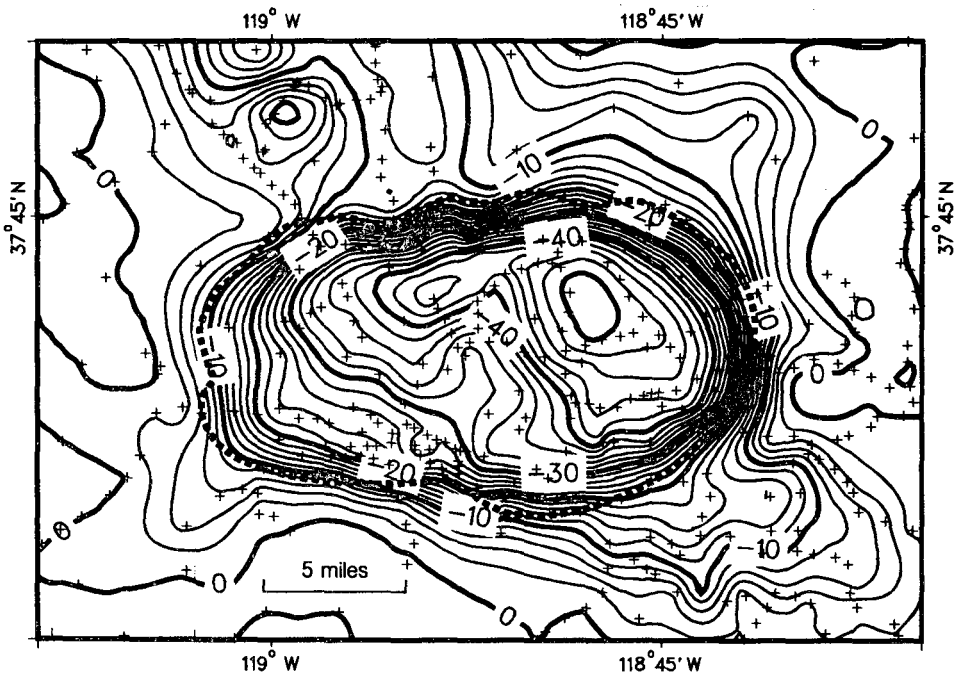

Figure 3. Residual gravity anomaly. Contour interval is 2 mGals. [XBL 873-9959]

$$hv(x,y) = hv(x,y)$$

$$\times [\text{gobs}(x,y) - \sum\text{gcalcr}(x,y)]/\sum\text{gcalcv}(x,y),$$

where hv is the height of one of the variable units, Σgcalcr is the calculated gravity of the restricted units, and Σgcalcv(x,y) is the calculated gravity of the variable units. Thus the scheme used to model the structure of Long Valley caldera in 3-D can be summarized as a multilayer prismatic model that assumes discrete density contrasts and is adjusted iteratively by forward and inverse methods.

The density contrasts chosen for the model units were based on a combination of well logs and laboratory analyses of core samples and surface specimens. Although the assumption of discrete density contrasts for individual geologic units is by no means exact, the assumption appears to be warranted because of the limited data. Nevertheless, modeling multiple geologic units is far more realistic than assuming constant density of fill. For example, the welded Bishop Tuff, which consists of the bottom 1000 to 1500 m of much of the caldera fill, commonly has a density contrast of -0.3 g/cm^3. Some of the upper part of the Bishop Tuff is less welded and commonly has a density contrast of -0.6 g/cm^3. The lake sediments and rhyolite tuffs, which are 200 to 1000 m thick in sum and constitute much of the upper caldera fill, commonly have a density contrast of -0.9 g/cm^3. Because these units vary both in thickness and lateral extent, many of the features of the gravity anomaly can be accounted for by the distribution of units within the caldera fill, rather than by the total depth of fill, and hence the caldera structure.

THE INTERPRETATION

Most of the local gravity anomaly can be accounted for by the Bishop Tuff, early rhyolites, and lake sediments. The other units are thin, or not extensive, near-surface layers whose distribution can be inferred on the basis of surface geology and well data. These units, including moat rhyolites, basalts, till, and alluvium, contribute to the gravity anomaly and cannot be ignored. However, to simplify the interpretation process, we concentrated on varying the thicknesses of the Bishop Tuff, early rhyolites, and lake sediments while holding the other units constant. Some precaldera volcanics, such as the Glass Mountain rhyolites, Tertiary basalt flows, and Quaternary rhyodacites, were modeled because they are associated with specific features in the gravity data. Also investigated was the gravitational influence of a silicic melt body with a configuration proposed by previous geophysical interpretations. Lithologies from three deep holes—Clay Pit, Republic Geothermal #66-29, and Mammoth #1—and from various shallow test holes were used as constraints on results from the density model.

For the initial modeling runs, we assumed no subcaldera density variations in the upper crust, such as a silicic melt body. Cross sections of the resulting 3-D model are shown in Figs. 4 and 5. Because of the coarseness of the prisms (1.4 km), the model lacks the realism of a well-constructed geologic cross section, but it does agree reasonably well with drill-hole lithologies. The model slightly overestimates the depth of fill at all three of the drill holes, suggesting that deeper low-density sources exist. Although many of the detailed features of the model are probably in error, most of the broad features are real. One prominent feature is the uniform demarcation of Bishop Tuff thickness across the Hilton Creek fault zone, from 1000 m in the west to 1500 m in the east, suggesting that there may have been a topographic depression east of the Hilton Creek fault zone prior to the caldera-forming eruption. This confirms the view that the Hilton Creek fault zone predates the caldera. The apparent uniformity of basement depth east of the Hilton Creek fault zone indicates that the subsidence of the eastern floor after the 0.73-Ma eruption was fairly uniform. Another feature is the thickening of early rhyolite tuff to about 900 m in the northwest. The model shows a roughly triangular-shaped wedge of early rhyolite tuff with increasing thickness toward the north moat and a gradual tapering to the southwest and southeast. Apparently a trench existed in the northwest before the eruption of early rhyolite tuff, which apparently blasted in a northerly direction from the resurgent dome area. Other prominent features in the caldera structure are the deepenings along the north and south edges, which appear as extensions of the extensive deepening in the east. These "trenches" are clearly evident in the gravity anomaly (Fig. 6), yet seismic-refraction interpretations have not resolved them. Bailey et al. (1976) suggest that the rhyolites of Glass Mountain and some precaldera basalts were downdropped into the caldera floor after the 0.73-Ma eruption. This idea is supported by the fact that the presence of Glass Mountain rhyolites and precaldera basalts in the model's northeast part of the caldera floor prevents the welded Bishop Tuff from attaining an unreasonable thickness (more than 1700 m).

From the gravity analysis it seems that one could include lower-density basement sources to help get a

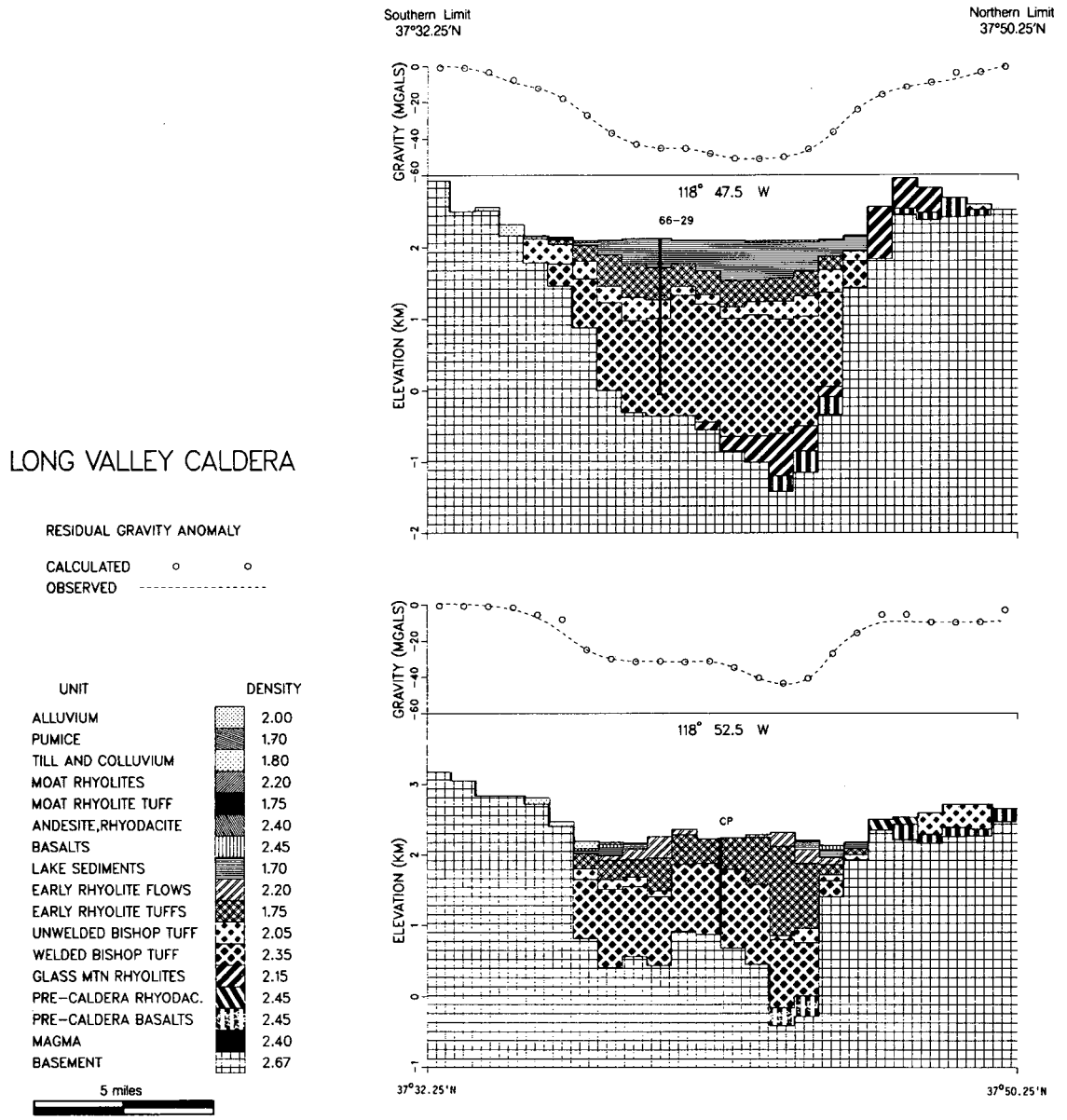

Figure 4. South–north cross sections of the 3-D gravity model along the indicated longitude. Vertical exaggeration is 4:1. [XBL 873-9963]

better match to the drill-hole data, but it seems equally apparent that inclusion of a large, deep low-density source is not essential for modeling the major features of the caldera structure. Although the analysis of the gravity anomaly does not unequivocally confirm the presence of a shallow (< 7 km) magmatic body, it is also true that the analysis cannot refute the presence of such a body. The maximum density contrast between a silicic melt and its solid equivalent could be about -0.27 g/cm^3. This is based on experimental results showing that density contrasts between solid rocks and their melts at deep crustal pressures are less than 10%. Under these conditions a large siliceous melt zone at a depth of 6 km would express itself in the gravity as a broad (7–10 km wavelength) -3 mGal amplitude anomaly. Because the residual gravity anomaly above the postulated melt zone is -25 to -40 mGals, it is difficult to unequivocally attribute so small a perturbation to a deep magmatic source in view of all of the uncertainties in densities and structure in the caldera and the basement.

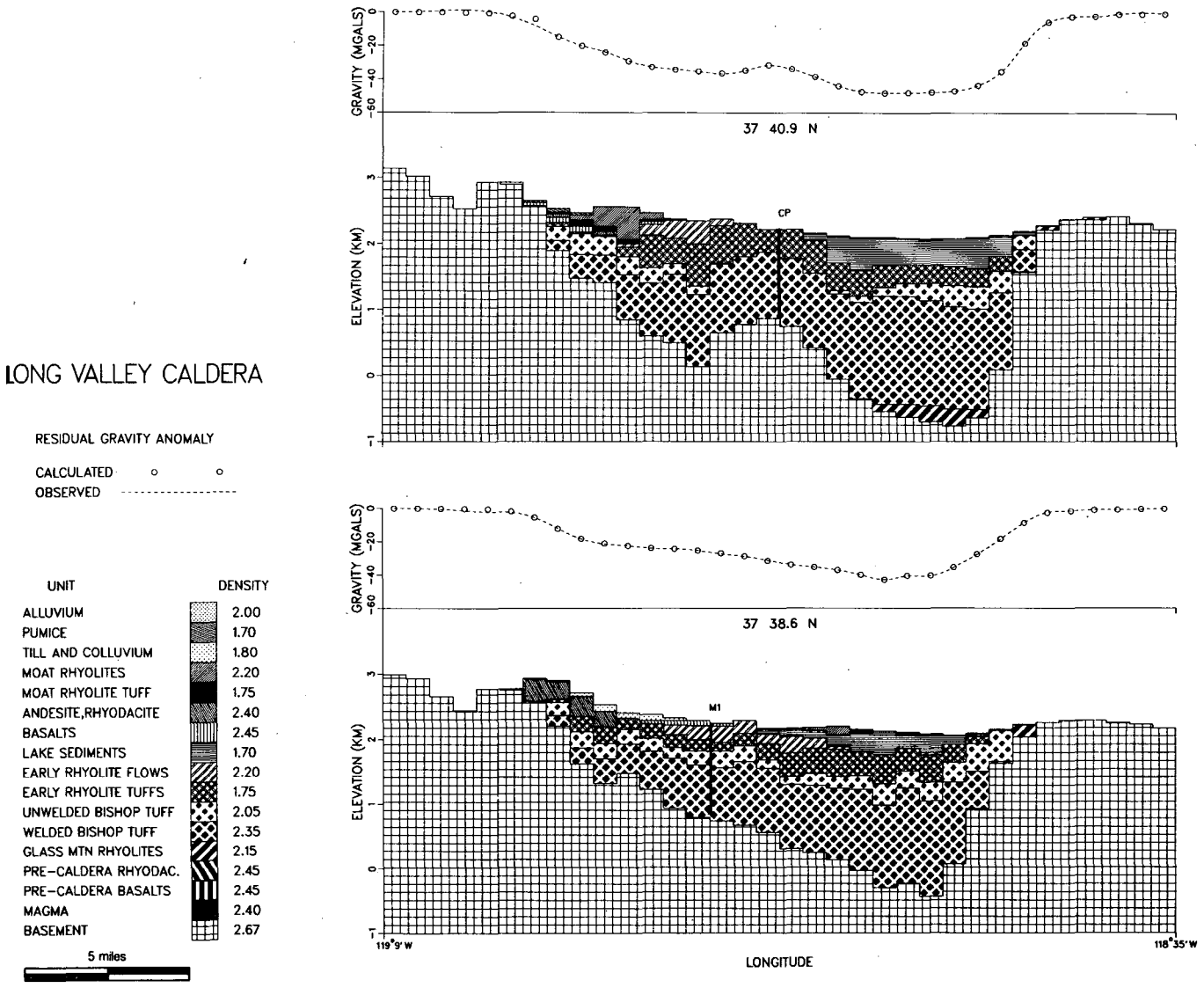

Figure 5. West–east cross sections of the 3-D gravity model along the indicated latitude. [XBL 873-9962]

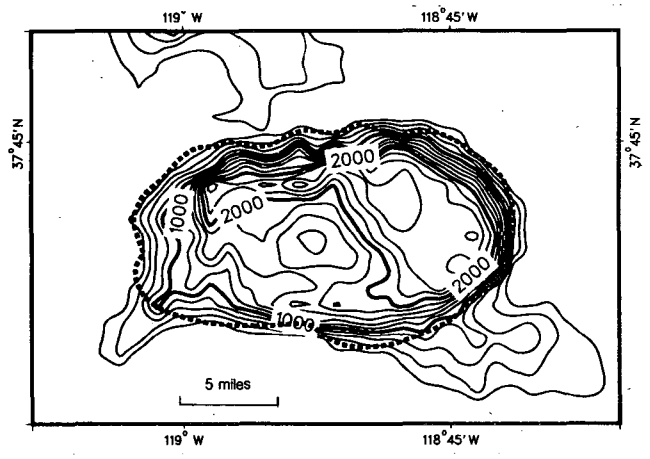

Figure 6. Depth of caldera fill according to the 3-D gravity model. Contour interval is 200 m. [XBL 873-9958]

REFERENCES

Abers, G., 1985. The subsurface structure of Long Valley caldera, Mono County, California: A preliminary synthesis of gravity, seismic, and drilling information. J. Geophys. Res., v. 90 no. B5, p. 3627–3636.

Bailey, R.A., Dalrymple, G.B., and Lanphere, M.A., 1976. Volcanism, structure, and geochronology of Long Valley caldera, Mono County, California. J. Geophys. Res., v. 81, no. B5, p. 725–744.

Cordell, L., and Henderson, R.G., 1968. Iterative 3-D solution of gravity anomaly data using a digital computer. Geophysics, v. 33, no. 4, p. 596–601.

Hill, D.P., and Bailey, R.A., 1985. Active tectonic and magmatic processes beneath Long Valley caldera, eastern California: An overview. J. Geophys. Res., v. 90., no. B13, p. 11,111–11,120.

Hill, D.P., Kissling, E., Luetgert, J.H., and Kradolfer, U., 1986. Constraints on the upper crustal structure of the Long Valley–Mono Craters volcanic complex, eastern California, from seismic refraction measurements. J. Geophys. Res., v. 90, no. B13, p. 11,135–11,150.

Simpson, R.W., Jachens, R.C., Blakely, R.J., and Saltus, R.W., 1986. A new isostatic residual gravity map of the conterminous United States with a discussion on the significance of isostatic residual anomalies. J. Geophys. Res., v. 91, no. B8, p. 8348–8372.

Skeels, D.C., 1967. What is residual gravity? Geophysics, v. 32, p. 872–876.

Use of Gravity Data to Detect Faults Feeding Geothermal Reservoirs

N.E. Goldstein and S.F. Carle

One model that has been used to explain geothermal systems in the Basin and Range Province and in the Salton Trough (Imperial Valley), California, involves the buoyant rise of hot fluids from a deeper source region along a near-vertical fault zone. In some systems the fluids break the surface to create a linear zone of hot springs, travertine deposits, and fumaroles. In other systems there are no visible manifestations of hydrothermal activity; such systems have been identified mainly as a result of the high subsurface temperatures encountered, somewhat fortuitously, in wildcat oil wells. However, one other feature shared by these concealed systems is the presence of small but distinct gravity anomalies. The cause of the gravity anomalies, confirmed by studies on cores and drill cuttings, is the hydrothermal densification of the sediments by the precipitation of authigenic minerals in pores and along fracture surfaces.

One of the well-studied concealed hydrothermal-geothermal systems is the East Mesa geothermal field, which many believe is a fault-charged system tapping a large primary reservoir of hot fluids (Riney et al., 1979; Goyal and Kassoy, 1981). Goyal and Kassoy (1981) developed a model of the system in which thermal water at ~200°C ascends through a system of near-vertical fractures 100–300 m wide. The water is isothermal until it reaches a cooler, impermeable caprock, at which point the water flows laterally into a thick, permeable aquifer.

Hoagland (1976) studied drill cuttings from well 6-2, drilled by the U.S. Bureau of Reclamation to 1830 m near the center of the East Mesa heat-flow anomaly. Figure 1 is a temperature profile taken after a 3-week shut-in period together with the depth ranges and descriptions of the major authigenic (hydrothermal) minerals observed. At a depth of

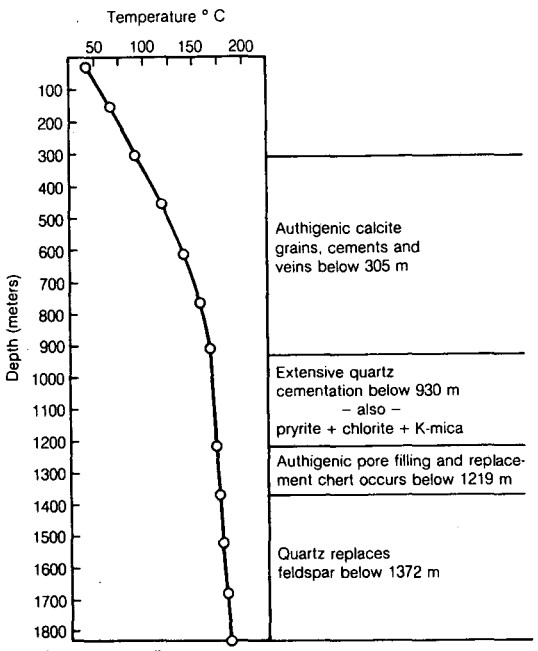

Figure 1. Temperature profile in well 6-2 after 3 weeks of shut-in. Also shown are the depth and types of secondary hydrothermal minerals that occur as pore fillings and replacements of detrital minerals (after Hoagland, 1976). [XBL 865-10801]

about 900 m there is a transition to silicate-sulfide minerals consisting of quartz, pyrite, illite, chlorite, and chert. This transition is regarded as marking the top of the reservoir. The minerals occur as pore fillings and as replacements of detrital minerals. Quartz is the main authigenic mineral, and quartz-cemented rocks are common below 930 m. Hoagland saw evidence for at least three distinct episodes of silica deposition, which would support the widely held contention that these systems must be refractured and reopened by tectonic activity and fluid pressures at many times during their evolution. If not, they would quickly self-seal, and a thermal aquifer would not develop.

On the basis of the γ-γ density log of well 6-2, Hoagland reported that the hydrothermal cementation gradually increases the average rock density from around 1.9 g/cm^3 at 670 m to 2.2 g/cm^3 below 914 m. This density difference is generally believed to cause the 5-mGal residual gravity anomaly that is centered over the geothermal field and which is also roughly coincident with the heat-flow anomaly (Biehler, 1971).

To examine in detail the morphology of the densified zone and to be able to relate this zone to faults and the reservoir region, we developed a method to carry out 3-D inversion of the residual Bouguer anomaly (Goldstein and Carle, 1986).

GRAVITY INTERPRETATION

Our model for the hydrothermal densification associated with the geothermal field is shown schematically in Fig. 2. The normal density section for the southeast corner of the Salton Trough is based on seismic velocities (Fuis et al., 1981), and those densities are shown at the left side of the figure. For a point directly over the thermal and gravity anomalies, the densities of the thermally altered rocks are based on the average bulk density from γ-γ density logs. Notice that densities increase with depth in both sections, but below the caprock the density of the hydrothermally altered section is about 0.1–0.2 g/cm^3 greater than that of the normal section at a comparable depth. TPRZ denotes the top of the poorly reflective zone identified by van de Kamp et al. (1978) as the point below which coherent seismic reflections are lost. Directly over the thermal anomaly the TPRZ is at a depth of 1500 to 1700 m. There is not yet evidence for it, but we show in Fig. 2 the possibility of a deeper central core of higher-temperature hydrothermal minerals where temperatures may have exceeded 250°C.

Because it appears that the density contrast between the altered and unaltered sections below the

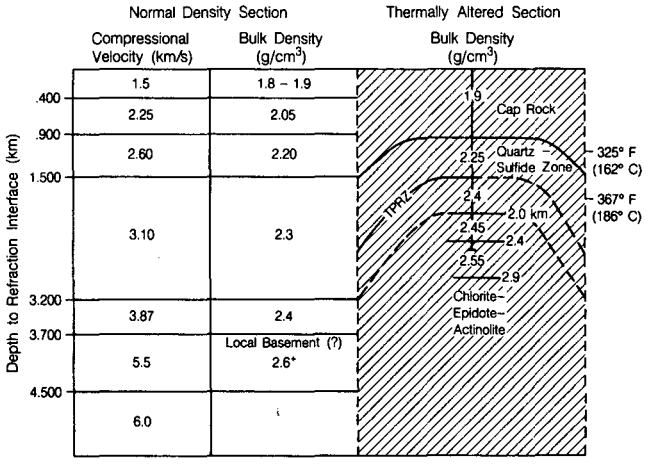

Figure 2. A comparison of bulk densities for both unaltered and thermally altered sections. The unaltered densities are based on seismic velocities (Fuis et al., 1981). The densities within the East Mesa geothermal field are based on geophysical log data. TPRZ is the approximate configuration for the top of the poorly reflective zone (van de Kamp et al., 1978). There is no drill-hole evidence reported yet for a high-temperature chlorite–epidote–actinolite zone. [XBL 865-10797]

caprock is invariant with depth, we can model the residual anomaly (Fig. 3) as an excess mass that consists of a bundle of square prisms of variable height above a reference depth, assumed to be the basement depth of 3.7 km (Fig. 4). The density difference, $\Delta\rho$, between the prisms and the host medium may be specified if that information is available, but in the problem discussed here we solve explicitly for $\Delta\rho$.

To solve for the thickness, T_q, of each prism and the contrast $\Delta\rho$, we use an iterative 3-D inversion procedure based on the approach described by Cordell and Henderson (1968). The residual gravity anomaly in an area measuring 9.5 miles × 10 miles was digitized on a square grid at a station spacing of 0.5 mile. Centers of the vertical prisms coincide with the grid points (Fig. 4). By specifying values for $\Delta\rho$ and the depth, D, to the reference plane, we obtain the gravity effect of the entire bundle of M prisms at the pth grid point:

$$g_p \approx \gamma \sum_{q=1}^{M} f\,(P, Q, T_q; \Delta\rho_1, D), \qquad (1)$$

where P is the pth grid point $P\ (x,y,0)$, Q is the qth prism centered at $Q\ (x',y',0)$, γ is the gravitational constant, T_q is the height of the qth prism, and $\Delta\rho_1$ is the initial value of $\Delta\rho$. Cordell and Henderson (1968) formulated their procedure on the assumption that prism heights go to zero in all perimeter blocks

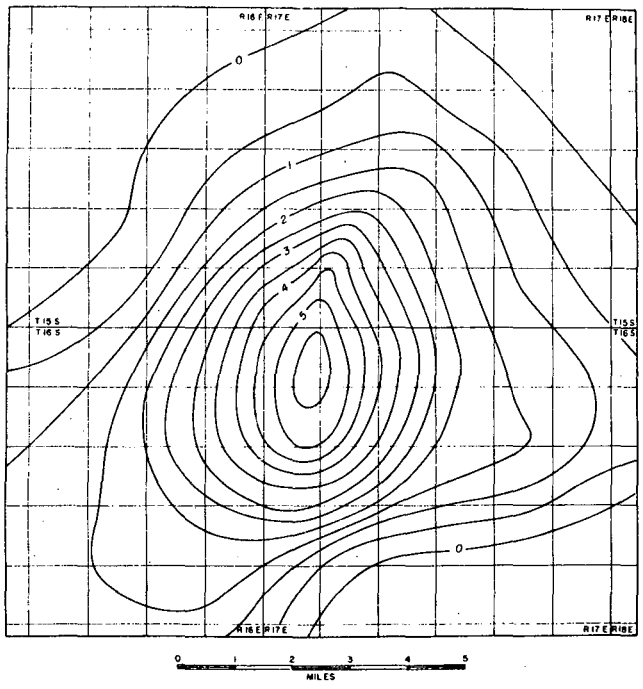

Residual gravity anomalies of the Mesa area, contour interval 0.5 milligals.

Figure 3. Residual Bouguer gravity anomaly of the East Mesa area (Biehler, 1971). Contour interval is 0.5 mGal. [XBL 7810-11720]

around the grid, but this is generally not a safe assumption. For this reason we treat each perimeter block as a slab of nonzero thickness extending to infinity in one direction; the four corner blocks are treated as quarter-space slabs extending to infinity in two directions.

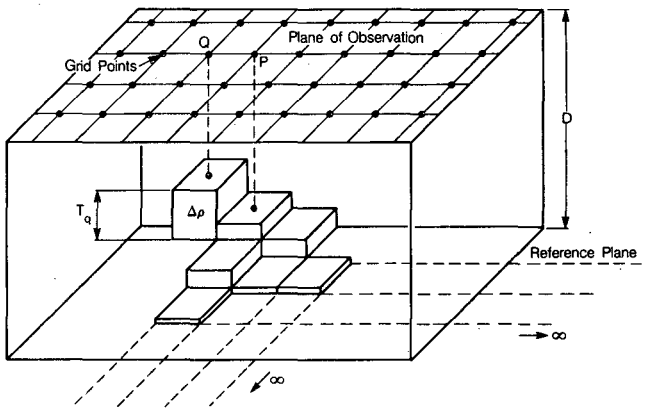

Figure 4. Representation of the densified zone as a bundle of square prisms of variable and unknown height above a reference plane, assumed to be the basement depth of 3.7 km. The prisms have a constant but unknown density contrast, $\Delta\rho$, with respect to the host rocks. [XBL 865-10803]

Following the approach of Cordell and Henderson (1968), we used an iterative procedure such that if $t_{n,q}$ is the height of the prism q at the nth iteration, then

$$\lim_{n\to\infty} t_{n,q} = T_q, \text{ for all } q.$$

The initial guess, $t_{1,q}$, is obtained by using the Bouguer slab formula:

$$t_{1,q} = \frac{g_{obs,q}}{2\pi\gamma\Delta\rho_1}.$$

Using these heights and the appropriate expressions for the gravitational attraction of a finite vertical prism, we calculate the anomalous gravity for each grid point, $g_{calc,1,q}$. Next, we adjust the height of the prisms for the second iteration as follows:

$$t_{2,q} = t_{1,q}\left[\frac{g_{obs,q}}{g_{calc,1,q}}\right]. \quad (2)$$

For subsequent iterations Eq. (2) can be written in a generalized form as

$$t_{n+1,q} = t_{n,q}\left[\frac{g_{obs,q}}{g_{calc,n,q}}\right].$$

After several iterations, usually four, we stop and adjust $\Delta\rho$ by introducing the constraints that one or more prism heights may be known from geophysical well logs, cores, or cuttings. In the East Mesa problem we used the depth to the densified zone in well 6-2 (Hoagland, 1976) to solve for the adjusted density contrast, $\Delta\rho_2$,

$$\Delta\rho_2 = \Delta\rho_1 \frac{t_{m,q}}{T_q}, \quad (3)$$

where $t_{m,q}$ is the calculated height of the prism at the well location after m iterations and T_q is the height of that prism from the drill-hole data. Prism thicknesses are again iterated using $\Delta\rho_2$, and the whole procedure is repeated several times. It was found after six density values, or a total of 24 prism iterations, that every calculated gravity value was within the precision of the corresponding residual anomaly value; i.e., the two values converge to within 0.1 mGal at every grid point.

There are several sources of error in this interpretive approach that limit the accuracy of the densified-zone model away from the drill holes. These include (1) the accuracy of the residual anomaly, (2) the choice of the reference depth, and (3)

the departure from an invariant density contrast. However, all gravity interpretations, regardless of the method used, are limited by errors in the data set or by errors that are introduced by assumptions about the source body.

THE GRAVITY RESULTS

Figure 5 shows the depth (in meters) to the density interface for calculations using gridded data at a 0.5-mile separation. The results show a dominant north–south-trending densified zone whose northern end curves and deepens to the northeast. A small parasitic zone, seemingly disconnected from the main zone, lies to the southeast. The dominant north–south feature appears to be intersected by at least one northwest-trending density structure that we believe is genuine, not an artifact of the numerical procedures.

COMPARISON OF THE DENSITY MODEL WITH OTHER GEOPHYSICAL RESULTS

To obtain a sense of the validity and significance of the 3-D gravity inversion results, we compare the density anomaly with other geophysical data: the trends of possible faults reported on the basis of seismic monitoring, reflection seismic interpretations, self-potential anomalies, and temperature data. Figure 6 shows the relation of the subsurface temperature contours at a depth of 1200 m (G.R. Zebal,

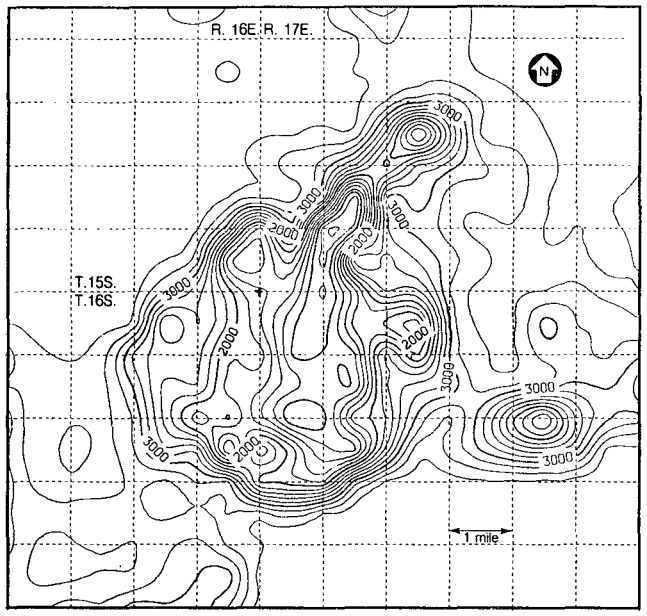

Figure 5. Depth (meters) to the top of the densified zone using gridded data at a 0.5-mile separation. $\Delta\rho$ = 0.14 g/cm^3. [XBL 865-10807]

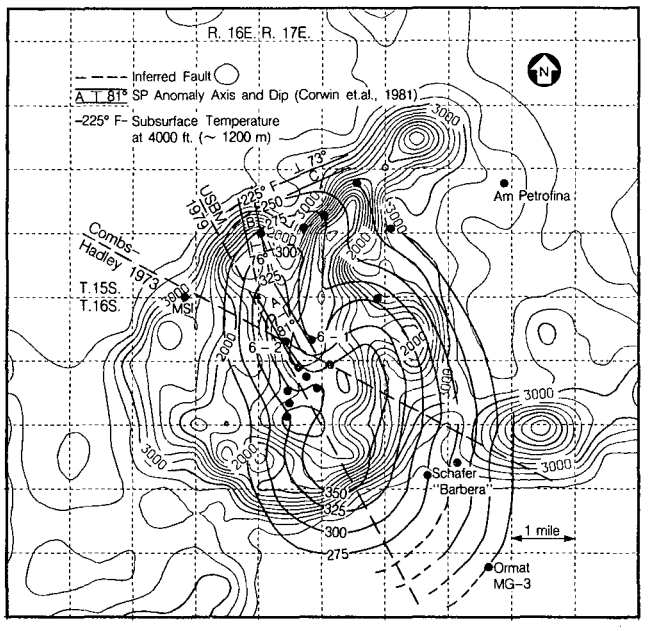

Figure 6. Comparison of the contours on the top of the densified zone (Fig. 5) to temperatures at 1200 m, inferred faults, and self-potential anomalies. The solid circles are wells. [XBL 865-10821]

personal communication, 1984) to the densified zone. Although the isotherms are not too well constrained by subsurface temperature data, there is a reasonably good general correlation between temperature and density. Three main features stand out:

1. The parasitic density anomaly to the southeast and the northern end of the main anomaly are both in areas of declining temperatures. If real, both densified zones may correspond to older, deeper and cooler segments of the hydrothermal system.

2. A double lobe seen on the northern end of the temperature anomaly is related to density features. The more pronounced of these lobes, the northwest one, also correlates very closely with the axis of a dipolar self-potential anomaly (A) and another SP trend (B) as interpreted by Corwin et al. (1981).

3. The zones of maximum temperature do not coincide exactly with the zones of shallowest depth to the densified zone. The two features are slightly displaced. This may indicate a dipping feeder fault.

There does not seem to be any correlation between microseismic activity and the densified zones. For completeness we show two fault trends reported in the literature. Combs and Hadley (1977) identified a right-lateral strike-slip fault (Mesa Fault)

on the basis of 36 locatable earthquakes with epicenters in an elliptical area over the thermal anomaly. The fault labeled USBM 1979, taken from the U.S. Bureau of Reclamation (1979), is an inferred fault aligned with the trend of the surface heat-flow anomaly.

Van de Kamp et al. (1978) found evidence for faults in the reflection seismic data that closely match the trend and location of the northwest temperature-density lobe and the SP anomaly axis (A); we do not show that evidence in Figure 6 because it would overly complicate the map. Figure 7 is an east–west cross section through wells 6-2 and 6-1. The section shows the relationships between the top of the densified zone (TDZ), the 350°F (177°C) and 375°F (190°C) isotherms and faults, and other features observed in the seismic section. Notice that the displaced thermal and density anomalies agree in location with the position of a fault dipping steeply to the west.

CONCLUSIONS

A 3-D inversion of the gravity data, constrained by information from drill-hole logs and a petrographic-alteration study, provides further evidence that the reservoir rocks of the East Mesa geothermal field are being fed by thermal waters ascending along a complex set of faults. The precipitation of a denser suite of authigenic silicate-sulfide minerals along the feeder zones and laterally outward into permeable horizons below a caprock, explain the density contrast and the resulting residual Bouguer anomaly. The slight lateral displacement of the axes of the densified zones from the subsurface temperature maxima suggests that the feeder zones could be dipping in a direction toward the temperature maxima. A feeder zone dipping steeply to the west agrees with the seismic reflection cross section and with the SP interpretation.

When studied along with other geophysical information, the gravity-inversion results indicate that the reservoir has been fed by a complex set of faults, segments of which are in older and presently cooler parts of the hydrothermal system. Whereas the principal part of the density anomaly runs in a north–south direction, curving to the northeast at its northern end, the present-day hydrothermal activity seems to be associated with a northwest-trending lobe. This lobe of the density anomaly also correlates with temperature and SP anomalies and with faults inferred from seismic reflection surveys.

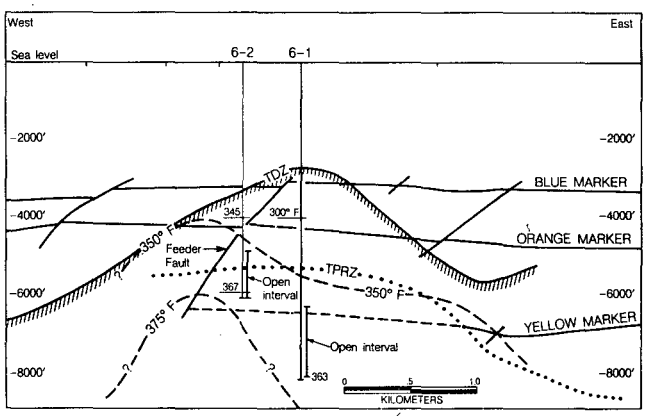

Figure 7. East–west cross section through wells 6-2 and 6-1, showing faults and reflecting horizons (van de Kamp et al., 1978), the 350°F and 375°F isotherms, and the top of the densified zone (TDZ). The shape of the isotherms relative to the TDZ suggest that hydrothermal fluids rise along a fault zone that dips steeply to the west, denoted as the feeder fault. [XBL 865-10798]

REFERENCES

Biehler, S., 1971. Gravity studies in the Imperial Valley. *In* R.W. Rex et al. (eds.), Cooperative Geological-Geophysical-Geochemical Investigations of Geothermal Resources in the Imperial Valley of California. University of California, Riverside, p. 29–41.

Combs, J., and Hadley, O., 1977. Microearthquake investigations of the Mesa geothermal anomaly, Imperial Valley, California. Geophysics, v. 42, p. 17–33.

Cordell, L., and Henderson, R.G., 1968. Iterative three-dimensional solution of gravity anomaly data using a digital computer. Geophysics, v. 33, no. 4, p. 596–601.

Corwin, R.F., De Moully, G.T., Harding, R.S., Jr., and Morrison, H.F., 1981. Interpretation of self-potential results from the East Mesa geothermal field. J. Geophys. Res., v. 86, p. 1841–1848.

Fuis, G.S., Mooney, W.D., Healey, J.H., McMechan, G.A., and Lutter, W.J., 1981. Seismic refraction studies of the Imperial Valley region, California—Profile models, a traveltime contour map, and a gravity model. U.S. Geol. Survey Open-File Report 81-270, 73 p.

Goldstein, N.E., and Carle, S., 1986. Faults and gravity anomalies over the East Mesa hydrothermal-geothermal system. Geoth. Resour. Counc. Trans., v. 10, p. 223–228.

Goyal, K.P., and Kassoy, D.R., 1981. A plausible two-dimensional vertical model of the East Mesa geothermal field, California. J. Geophys. Res., v. 86, no. B11, p. 10719–10733.

Hoagland, J.R., 1976. Petrology and geochemistry of hydrothermal alteration in borehole Mesa 6-2, East Mesa geothermal area, Imperial Valley, California (M.S. thesis). University of California, Riverside, IGPP-UCR-76-12, 90 p.

Riney, T.D., Pritchett, J.W., Rice, L.F., and Gary, S.K., 1979. A preliminary model of the East Mesa hydrothermal system. *In* Proceedings, Fifth Workshop on Geothermal Reservoir Engineering, Stanford Geothermal Program Report SGP-TR-40, p. 211–214.

U.S. Bureau of Reclamation, 1979. Geothermal resource investigations, East Mesa test site, Imperial Valley, California. U.S. Bureau of Reclamation Concluding Report.

van de Kamp, P.C., Howard, J.H., and Graf, A.N., 1978. Section 1: Geology. *In* Geothermal Resources and Reservoir Investigations of U.S. Bureau of Reclamation Leaseholds at East Mesa, Imperial Valley, California. Lawrence Berkeley Laboratory Report LBL-7094, p. 1–32.

Electromagnetic Imaging of Subsurace Conductivity Heterogeneities

K.H. Lee and H.F. Morrison

Mapping the subsurface distributions of electrical conductivity is important in mineral and geothermal exploration. It is also emerging as a useful tool in petroleum exploration in situations where seismic methods do not work and in crustal studies, where conductivity provides vital information on the distribution of water, fracturing, and temperature. In the petroleum and crustal applications, the method has not gained wide acceptance because of the difficulties of presenting and interpreting the electromagnetic response of an inhomogeneous medium. It has not been possible, for example, to obtain images of subsurface reflectors, as can be done with seismic methods. The full power of electromagnetic methods could be utilized if an imaging technique, comparable to those used in reflection seismology, were to be developed. In the research summarized here, we have developed an algorithm that has the potential for greatly improving the resolution of subsurface conductivity discontinuities.

FORMULATION OF PROBLEMS

Maxwell's equations state that the scattered electromagnetic fields satisfy the vector-diffusion equation

$$(\nabla\times\nabla\times + \gamma\mu\frac{\partial}{\partial t})\, u(r,t) = 0, \qquad (1)$$

where the vector u(r) is either the electric or the magnetic field and γ is the conductivity $\sigma(r)$. It is assumed that the displacement current is negligible and that the conductivity is homogeneous in the neighborhood of the point of observation (r). In the frequency domain Eq. (1) becomes

$$(\nabla\times\nabla\times + \iota\omega\gamma\mu)\tilde{u}(r,\omega) = 0. \qquad (2)$$

Changing variables ($\nu^2 = -\iota\omega$) transforms Eq. (2) into

$$(\nabla\times\nabla\times - \nu^2\gamma\mu)\tilde{v}(r,\nu) = 0, \qquad (3)$$

which in turn is associated with a wave equation

$$(\nabla\times\nabla\times + \gamma\mu\frac{\partial^2}{\partial\tau^2})v(r,\tau) = 0. \qquad (4)$$

Our initial objective is to recover the wave field $v(r,\tau)$ and display it in such a way that vital information can be obtained by simple inspection. Note that since the foregoing transformation involves only $t \to \tau$, the space variable r will be dropped henceforth.

The wave field $\tilde{v}(\nu)$ is related to $v(\tau)$ by the Fourier transform

$$\tilde{v}(\nu) = \int_0^\infty v(\tau)e^{-\iota\nu\tau}\, d\tau. \qquad (5)$$

Changing variables ($\tau = e^{-\eta}$ and $\omega = e^{2\xi}$) transforms Eq. (5) into

$$e^{\xi}\,\tilde{v}(\xi) = \int_{-\infty}^{\infty} v(\eta)\, e^{\exp[-\iota 3\pi/4]\exp[\xi-\eta]}\, e^{\xi-\eta}\, d\eta. \qquad (6)$$

Since this is a convolution integral, the solution for $v(\eta)$ can be formally written as

$$v(\eta) = \frac{1}{2\pi} \int_{-\infty}^{\infty} \frac{G(k)}{H(k)} e^{\iota k \eta} \, dk, \tag{7}$$

where

$$H(k) = \int_{-\infty}^{\infty} e^{\exp[-\iota 3\pi/4]\exp[\xi]} e^{\xi} e^{-\iota k \xi} \, d\xi$$

$$= e^{-(\iota+k)\pi/4} \Gamma(1 - \iota k)$$

$$G(k) = \int_{-\infty}^{\infty} e^{\xi} \tilde{v}(\xi) e^{-\iota k \xi} \, d\xi$$

$$= \int_{0}^{\infty} \tilde{v}(\beta) \beta^{-\iota k} \, d\beta. \tag{8}$$

To obtain $v(\eta)$, or $v(\tau)$, the entire process involves two numerical integrals given by Eqs. (7) and (8). The frequency-domain EM data $\tilde{v}(\beta = \sqrt{\omega})$ is Mellin transformed numerically to give $G(k)$, and then the functional $G(k)/H(k)$ is inversely Fourier transformed.

EXAMPLE

Let us consider a simple problem in which the whole space consists of an upper medium of $\gamma = \sigma_1$ and a lower medium of $\gamma = \sigma_2$. An impulse plane wave is excited at $t = 0$, $x = -h$ in the upper medium. The scattered electric field at x reflected by the lower medium is given by

$$\tilde{u}(\omega) = \frac{R}{2} \frac{e^{-\sqrt{\iota\omega\mu\sigma_1}\,(h-x)}}{\sqrt{\iota\omega\mu\sigma_1}}, \quad (h - x) > 0, \tag{9}$$

where the *reflection coefficient* is given by

$$R = \frac{\sqrt{\sigma_1} - \sqrt{\sigma_2}}{\sqrt{\sigma_1} + \sqrt{\sigma_2}}.$$

Fourier transformation of $\tilde{u}(\omega)$ gives

$$u(t) = \frac{R}{2\sqrt{\pi\mu\sigma_1}} \frac{e^{-\mu\sigma_1 (h-x)^2/4t}}{\sqrt{t}}. \tag{10}$$

Equation (7) can be used to obtain the τ-domain wave field as follows. Rewriting Eq. (8) for $G(k)$ gives

$$G(k) = \int_{0}^{\infty} \tilde{v}(\beta) \beta^{-\iota k} \, d\beta$$

$$= \frac{R}{2\sqrt{\iota\mu\sigma_1}} \{\sqrt{\iota\mu\sigma_1}\,(h - x)\}^{\iota k} \Gamma(-\iota k).$$

Substituting this result into Eq. (7) gives, after some manipulation,

$$\frac{\partial}{\partial\tau} v(\tau) = \frac{R}{2\sqrt{\mu\sigma_1}} \frac{\delta\{\tau - \sqrt{\mu\sigma_1}\,(h - x)\}}{\tau}. \tag{11}$$

Note that the strength of the delta function at $\tau = \sqrt{\mu\sigma_1}\,(h - x)$ is proportional to the reflection coefficient R and inversely proportional to the travel "time" τ. Figure 1 shows normalized $u(t)$ and $v'(\tau)$. Obviously it will be a long struggle before one can relate the transient response $u(t)$ to the actual conductivity distribution of the medium. On the other hand, it is clear that knowing the onset of wavelet $v'(\tau)$ and its amplitude will immediately lead us to calculate the distance to the reflecting boundary and the conductivity of the lower medium.

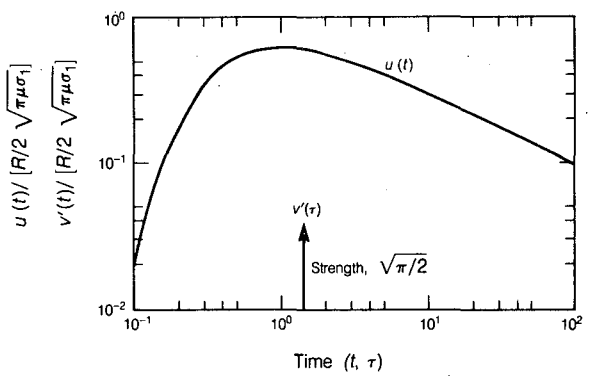

Figure 1. Transient electric field $u(t)$ and transformed wave field $v'(\tau)$ at $(h - x) = \sqrt{2/\mu\sigma_1}$, normalized by $R/2\sqrt{\pi\mu\sigma_1}$. [XBL 871-9890]

Development of the Fast ASP

E.L. Majer and T.V. McEvilly

The ASP concept (McEvilly and Majer, 1982) has served us well, but with the increased availability of off-the-shelf board sets and the dramatic improvement in CPU and memory since 1977, we felt that a new improved version of the ASP was necessary. We wanted the new version not only to be faster (e.g., a sample rate of 500 sam/s at 16 bits rather than 100 sam/s at 12 bits for very detailed microearthquake studies) but to include many features that cannot be attained with CMOS technology, such as waveform saving and F-K processing. It is relatively expensive with CMOS technology to devote a CPU or microcomputer to each channel of data, which is the architectural basis of the original ASP. Therefore, in the fall of 1984 we began designing and building a prototype Fast ASP system. The system is designed to carry out all of the functions of the ASP (McEvilly and Majer, 1982).

During the past year we have built the first version of the Fast ASP. Shown in Fig. 1 is the present configuration of the Fast ASP. The system is designed around the Motorola 68000 series CPUs and a VME/VMX bus. We are currently using 68010s as data acquisition CPUs and a 68020 with a 68881 coprocessor as the event CPU. The 68010s can be easily upgraded with just a few chip changes if the processing power is needed. The first stage of the project was to build a 48-channel, fully operational system. The target parameters for this first-stage system are as follows:

1. 48 channels, 500 samples/s/channel.
2. 12-bit A/D.
3. Storage capacity for up to 100 events (i.e., full waveform data plus processed data).
4. Capability of performing all present ASP processing plus the capability to designate a *P* or an *S* channel (for three-component data).
5. Streaming to disk at high data rates for AE data. The data would be read back at slower rates for full processing.

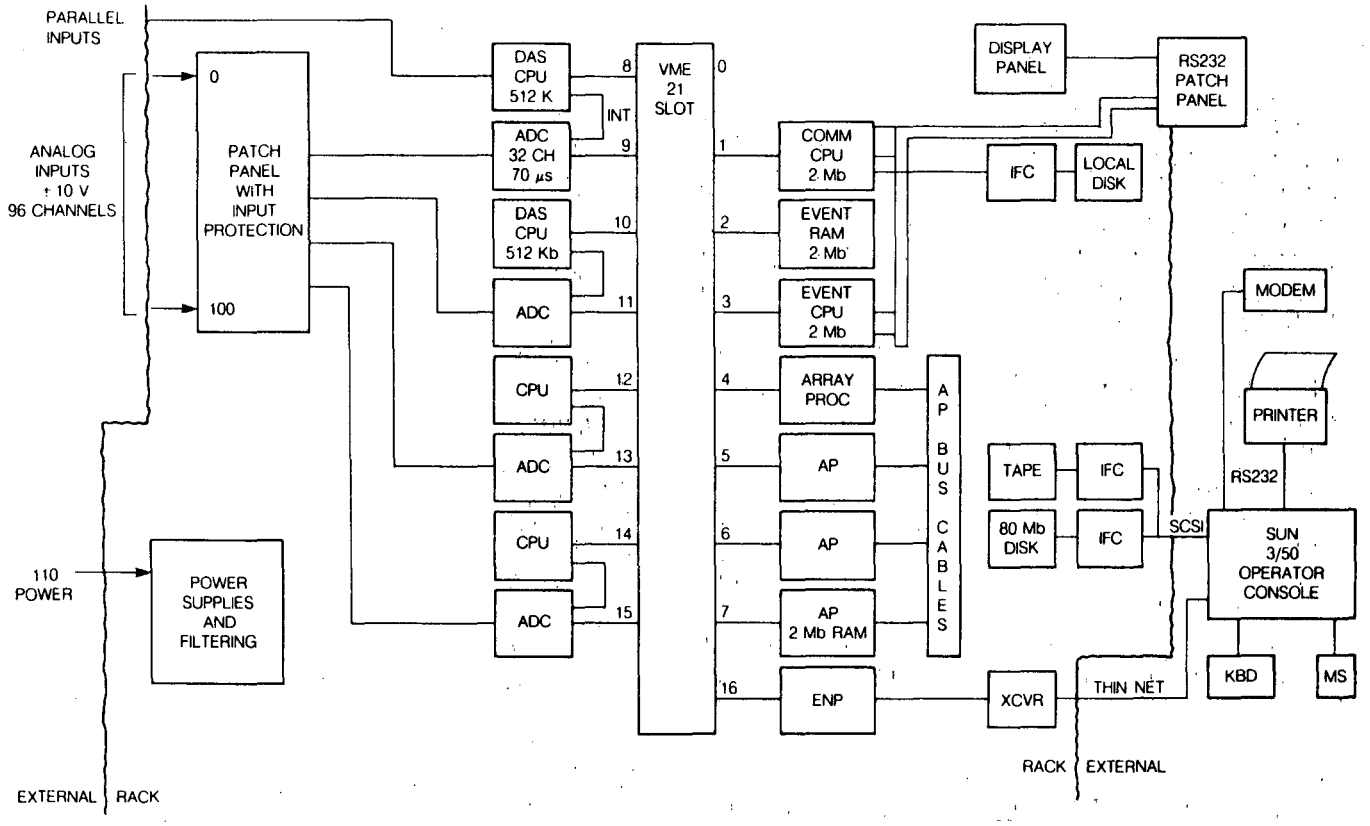

Figure 1. Schematic diagram of Fast ASP. [XBL 871-9896]

6. Enhanced processing for array studies (i.e., F-K analysis, beam forming).

7. Ethernet connection for networking to other systems.

8. Optional waveform saving for later analysis.

Figure 1 shows the present configuration of the Fast ASP. The real-time operating system present in the DAS CPU's is PSOS. The event CPU will be running FORTRAN under PSOS. This will allow easier use of the present FORTRAN programs. The user interface will be a SUN Microsystems 3/50. This provides the ethernet capability to other systems with the TCP/IP protocol. Also included in the system is a Mercury 32/32 array processor. This 8-MFLOP device will do a complex 1024 FFT in 7 ms. It will also be used for matrix manipulations and inversions as well as such operations as correlation and filtering. The tape drives are for program transfer from the development system (also a SUN work station) and data backup. The local disk on the communication CPU (COMM CPU in Fig. 1) is for direct-disk dumps of large blocks of time-series data at high data rates. The 80-Mbyte disk on the SUN 3/50 serves as program storage for system routines and user-interface programs. Having the 3/50 as the user interface also allows much easier program changing in the field.

The Fast ASP system is almost complete. A complete field test remains to be carried out. The next step is to incorporate into the system enhanced software that was not used in the old ASP system. This will be done during fiscal 1987. This system can easily be expanded to include more channels or to accept digital telemetry. Being a true 32-bit system, the processing power with the floating point co-processor chip is several orders of magnitude greater than the old ASP. It is hoped that the Fast ASP will have many more uses than the ASP. The system is much more flexible and powerful and promises to be a valuable research tool.

REFERENCE

McEvilly, T.V., and Majer, E.L., 1982. ASP: An automated seismic processor for microearthquake networks. Bull. Seismol. Soc. Am., v. 72, no. 1, p. 303–325.

CCS: Center for Computational Seismology

E.L. Majer, T.V. McEvilly, and L.R. Johnson

The Center for Computational Seismology (CCS) has now been in existence for 4 years. It has expanded from a several-user facility occupying 10–25% of a VAX-11/780 to a 20- to 30-user community utilizing an equivalent of one to one-and-a-half VAX-11/780s. The purpose of CCS has been to provide a facility with a wide range of computational tools to serve U.S. Department of Energy (DOE) programs in the basic energy sciences and other areas of energy research. Research over the entire spectrum of seismology is carried out at CCS, from basic studies in earthquake-source mechanisms to the applied work of reflection seismology. The software base represents 4 years of our own efforts in coding internal analysis routines in addition to processing tools of DISCO (Digicon inc), INGRES (Relational technology), and the Geoquest Inc. AIMS package. We now have the ability to address research topics that were previously beyond our capabilities. Various DOE seismic research programs, both basic and applied, make up the principal effort. During the past year this has included work for the Office of Basic Energy Sciences (e.g., the Salton Sea project and the Long Valley data synthesis). Geothermal programs constitute another area of work; two examples are vertical seismic profiling (VSP) for fracture detection and microearthquake studies for reservoir management. We are also working on a project that is part of the DOE nuclear waste program; the purpose of the project is to relate the seismic response of fractured media to the hydrologic response. This project will soon require field work, but the present thrust of the study is to develop 2-D and 3-D models for ray tracing *P*-, *SV*-, and *SH*-waves through fractured rock. Our approach is to use seismic tomography for mapping the density, spacing, and orientation of fractures. It is hoped that sufficient resolution can be achieved to aid the hydrologist/reservoir

engineer in predicting fluid flow. Last but not least, we are still carrying out work related to mapping fluid flow in natural and induced (hydrofracture) fractures.

Overall, CCS has grown into a mature research unit carrying out a broad range of research topics. In fact, we will soon have to expand our facilities. During the next year we hope to implement a hardware upgrade that will greatly enhance our computational capabilities. At the present time we are leaning toward a semidistributed system of work stations. In addition to the support given to the DOE and other government programs, on which there are individual reports in this Annual Report, CCS supports student and post-doctoral research. This article includes brief summaries of all ongoing CCS research projects.

A RAY-THEORY-IMAGING ALGORITHM FOR VSP DATA

—F.S. Eastwood, E.L. Majer, and T.V. McEvilly

We have developed a ray-theoretical approach to the imaging of nonzero-offset vertical-seismic-profiling (VSP) data. The method is valid for arbitrary source-receiver geometries, including non-VSP geometries. It is also capable of correctly imaging reflectors in the presence of arbitrary two-dimensional velocity variations. The algorithm is a noncoincident source-and-receiver generalization of "event" or "interface" migration of common-midpoint seismic-reflection data. We are in the process of applying the method to synthetic and real VSP data from a geothermal field in northern Japan in order to image a steeply dipping reflector.

VECTORIZED REFLECTIVITY PROGRAMS

—E.R. Flueh

The calculation of synthetic seismograms on the basis of reflectivity (Fuchs and Mueller, 1971) is the most accurate method in use today. Its application has been restricted, however, because of the large computation time needed. Sandmeier and Wenzel (1986) recently demonstrated that the most time-consuming part of the calculation, the computation of the reflectivity, can be vectorized. Thus, where vector-computers are available, computation time can be decreased significantly, and the calculation of synthetic seismograms for realistic earth models of up to several hundred layers becomes feasible, opening new frontiers for interpreters. The program developed by Sandmeier and Wenzel uses the method described by Kennett (1979) and calculates the response from a reflecting zone beneath a nonreflective zone that contains the source and the receivers. Within this nonreflective zone only the transmissions are considered, so that no surface waves or free surface reveberations are included. This ambiguity has been overcome in another approach by Kind (1978, 1979), whose modified reflectivity program is based on the method described by Harkrider (1964) and is often referred to as "full waveform synthetic seismograms."

Kind's program was reformulated so that portions of it can be vectorized, especially in the most time-consuming subroutine, which calculates the reflectivity matrix. A comparison of computation time for the Sandmeier-Wenzel and the Kind programs between the VAX-11/780 at Lawrence Berkeley Laboratory and the CRAY-XMP at Lawrence Livermore National Laboratory (LLNL) demonstrates that computation time is significantly reduced. For the Sandmeier-Wenzel program the CRAY-XMP was 200 times faster than the VAX-11/780, and for the reformulated Kind program it was 80 times faster. The increased speed of both programs now offers CCS users a resource for extensive modeling of detailed and more realistic earth models in seismic-reflection investigations of the earth's crust.

For example, the calculated synthetic seismograms for the complex crustal structure shown in Fig. 1 are shown in Figs. 2, 3, and 4. The model

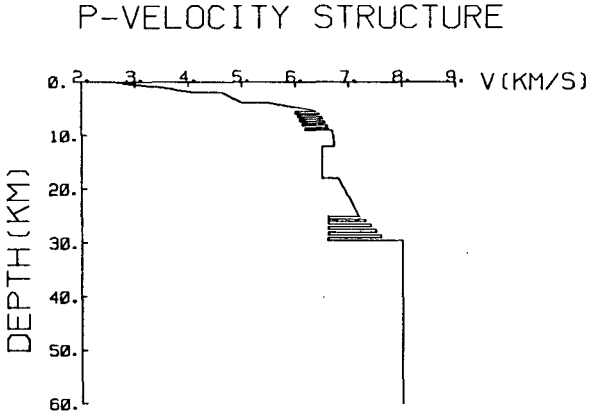

Figure 1. The *P*-wave velocity-depth function used to calculate the synthetic seismograms shown in Figs. 2, 3, and 4. The *S*-wave velocities were assumed to be Vp/1.732. A constant velocity-density relation with $\rho = 1.67 + 0.174Vp$ was used. The *Q*-factor varied with depth, being 200 for *P*-waves and 100 for *S*-waves in the upper 5 km, 400 for both *P*- and *S*-waves in the upper and middle crust to the bottom of the low-velocity zone, and 1000 below. [XBL 871-247]

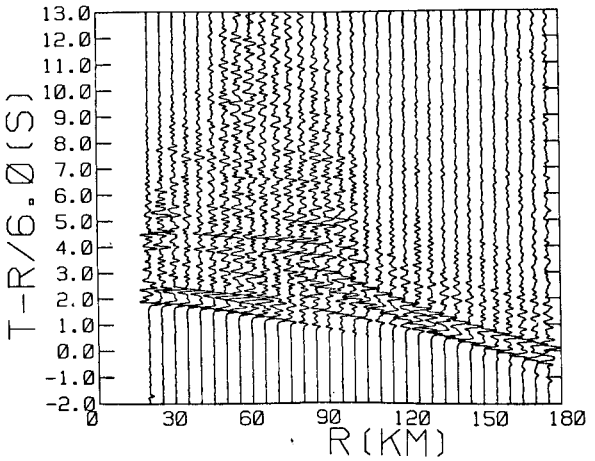

Figure 2. Seismograms in the distance range 20–175 km, calculated using Kind's program. The velocity-depth function was divided into 84 layers. Only phases with velocities greater than 4.9 km/s are considered. Times are reduced by 6.0 km/s. [XBL 871-248]

consists of two sedimentary layers with high velocity gradients. In the upper crust a stack of 10 alternating high- and low-velocity layers is introduced, each 200 m thick with a velocity contrast of 0.4 km/s. The middle crust from 12 to 18 km depth shows a pronounced velocity inversion. The lower-crust/upper-mantle transition is another zone of alternating high- and low-velocity layers, each 500 m thick with a velocity contrast of 0.6–1.0 km/s. Figure 2 shows the synthetic seismograms for offsets from 20 to 175 km, representing a standard crustal

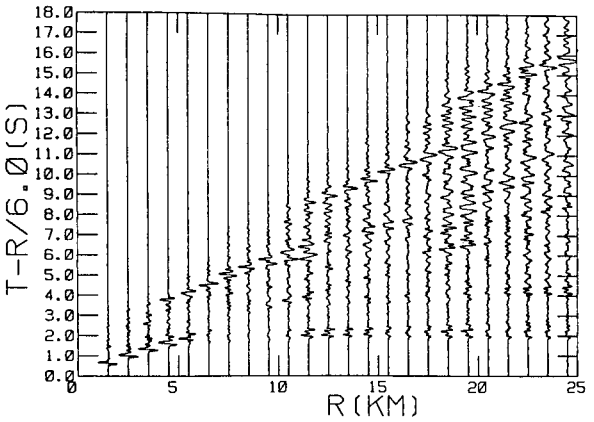

Figure 3. Seismograms in the distance range 1.5–24.5 km calculated using Kind's program. As in Fig. 2, 84 layers were used, but all phases with velocities greater than 1.0 km/s are included. Times are reduced by 6.0 km/s. [XBL 871-249]

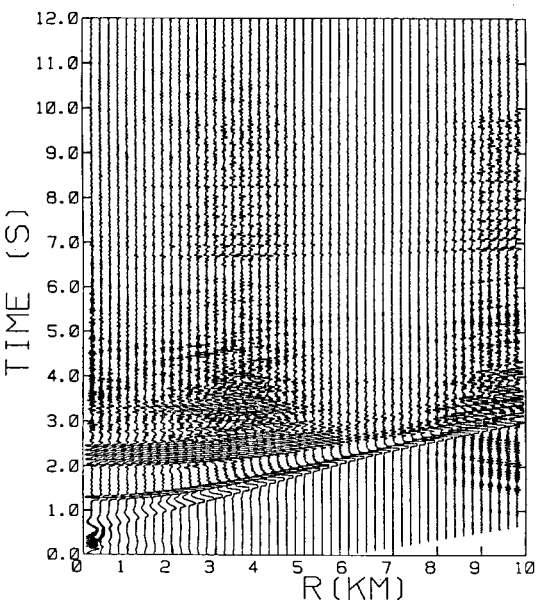

Figure 4. Seismograms in the distance range 0.2–9.8 km calculated using the Sandmeier-Wenzel program. Thirty-seven layers were used, and phase velocities greater 4 km/s were considered. The amplitudes of the first arrivals and the first reflection are clipped to enhance the later arrivals. [XBL 871-250]

refraction profile. Figure 3 shows the offset from 0 to 25 km. Figure 4 shows the offset from 0 to 10 km, corresponding to a standard shotgather for a seismic reflection survey of near-vertical incidence. In all calculations the source was an explosion at a depth of 20 m. All traces are normalized to the maximum amplitude.

REFERENCES

Fuchs, K., and Mueller, G., 1971. Computation of synthetic seismograms with the reflectivity method and comparison with observations. Geophys. J. R. Astr. Soc., v. 23, p. 417–423.

Harkrider, D.G., 1964. Surface waves in multilayered elastic media. 1. Rayleigh and Love waves from buried sources in a multilayered elastic half-space. Bull. Seis. Soc. Am., v. 54, p. 627–679.

Kind, R., 1978. The reflectivity method for a buried source. J. Geophys., v. 44, p. 603–612.

Kind, R., 1979. Extensions of the reflectivity method. J. Geophys., v. 45, p. 373–380.

Sandmeier, K.J., and Wenzel, F., 1986. Synthetic seismograms for a complex crustal model. Geophy. Res. Lett., v. 13, no. 1, p. 22–25.

SEISMOLOGICAL STUIES OF CORE TRANSITION ZONES

—L.R. Johnson, F.E. Followill, and P. Cummins

The high quality and broad bandwidth of the data generated by the Regional Seismic Test Network (RSTN) make possible several new lines of research. The objective of this effort is to use these data to study the transition zones between the outer and inner cores. A proper study of this zone requires that both elastic and anelastic effects be investigated, and the RSTN data are well suited to such studies.

A search was made through the NEIC Event Tape archive at CCS for all deep events in the distance range 105–160 degrees that had good signal quality and relatively simple-source time functions. Twelve events satisfying these criteria were selected (mainly in the Banda and Java Sea regions) during the period 1980–present for which the RSTN recorded a suite of inner-core reflections ranging from pre- to postcritical. Almost all of these events were listed in the ISC catalogs as having moment tensors that favor vertically downward propagation from the source. Fortunately, eight of theses events were recorded by station RSNT at precritical distances, where the pulse should undergo relatively little distortion and does not interfere with the multiple inner-core refractions. We are now using this phase as an empirical source-time series for the Green's function evaluated at greater distances. While this procedure should have the advantage of stripping out the distortion due to the mantle, we are still investigating distortion of the precritical core reflection by velocity gradients at the top of the inner core.

For the past year Cummins and Johnson have worked extensively with a code for generating synthetic seismograms via the well-known "full-wave" technique. Within the constraints imposed by the requirement of an analytic velocity profile in the inner core, this method is capable of modeling all of the various frequency-dependent phenomena encountered by body waves interacting with the inner-core boundary, and we are now capable of accurately calculating the body-wave pulse shapes associated with critical and grazing incidence on the inner-core boundary (e.g., PREM model) as well as diffraction by the B caustic for frequencies up to 5 Hz. Use of the "full-wave" theory for seismogram modeling does, however, require that velocity models consist of a few layers with velocity given by an analytic function of radius. Moreover, it does not account for the coupling between P- and S-waves that occurs in regions of high velocity gradient. Since a region of anomalously high velocity gradients is exactly the type of structure we would like to use as a model for the top of the inner core, we felt that a more complete method for seismogram computation was needed.

The reflectivity method is one way of generating complete seismograms, but its use for high-frequency core phases involves an earth-flattening approximation with a very large number of layers, and the run time for such an algorithm would be prohibitively long even on LLNL's CRAY computer. We therefore developed a hybrid method that would use the full-wave theory in the mantle and outer core but use the reflectivity algorithm in a zone 500–1000 km thick encompassing the inner core boundary, where the more complete calculations are needed. Accuracy checks against both the exact solution for a homogeneous earth and the full-wave solution for the PREM model indicate that the new algorithm is accurate to within a few percent.

MAGNITUDE ESTIMATION FROM INITIAL-WAVEFORM ANALYSIS

—J.E. Scheiner

The intriguing possibility that the final size of a seismic source may be estimated by examination of the developing initial P waveform has important implications for earthquake early-warning systems (EEWS). Furthermore, the workings of such a discriminant bear on our understanding of the rupture process at the source, since source theory does not predict the method. Rather, the ability of the early waveform to predict the source size during nucleation suggests that the rupture process itself is somehow different for large and small earthquakes, a notion that is not indicated in our theoretical understanding. Preliminary observations yield interesting and encouraging results.

Analysis of 20 broadband recordings of 15 earthquakes recorded at regional distances in central and northern California indicate that the time rate of change during the initial waveform reception of the low-frequency spectral amplitude ($\Omega_0(t)$) of the initial P-wave may provide an EEWS discriminant. A series of Fourier amplitude spectra are calculated for windows that begin on the P-wave onset and that increase in length with time, simulating a real-time process. The slope of the resultant $\Omega_0(t)$ versus time (i.e., $d(\Omega_0(t))/dt$) is examined as a function of magnitude. In this preliminary study the slopes were

found to increase in an almost linear fashion with magnitude. Only two recordings of an anomalous earthquake failed statistically to fit the linear trend, and this earthquake was located such that the two recording sites were on nodes for *P*-wave propagation and in the opposite direction as rupture propagation.

Analysis of earthquake recordings from LLNL's broadband array in Nevada and eastern California is underway in an effort to increase the total data set. Finally, the inclusion of regionally recorded seismograms from underground explosions is also anticipated, as these may have different propagation characteristics with respect to the time rate of change of Ω than those for earthquakes.

ESTIMATION OF TRAVEL TIMES FOR SOURCE LOCATION IN A LATERALLY HETEROGENEOUS EARTH

—D.M. Tralli and L.R. Johnson

A method has been developed to obtain travel times from estimates of tectonically regionalized *P*-wave tau functions and slowness-dependent source and receiver corrections. A quadratic programming algorithm interpolates the tau estimates constrained by the analytical properties of tau and the statistical uncertainties. The regionalized travel-time estimates are used to locate seismic sources in the epicentral distance range 15 to 95 degrees. Since all the information on lateral velocity variations is contained in the tau functions, seismic sources in a laterally heterogeneous earth are located without explicitely defining a laterally varying velocity model. The formulation is efficient in that the travel-time estimates and corrections are obtainable for any source and receiver pair on the globe and requires minimal computation time.

The *P*-wave travel-time data are provided by the Bulletin of the International Seismological Center. Twenty-eight disclosed nuclear explosions at Nevada Test Site (NTS) allow estimation of a travel-time baseline bias. Azimuthal corrections for NTS events are also obtained. Nuclear explosions at NTS are then located, as are events in Eastern Kazakh and Novaya Zemlya in the Soviet Union and in the Tuamotu Archipelago in French Polynesia. Three earthquakes along the San Andras fault zone in west-central California are also relocated for comparison with hypocentral parameters provided by local seismographic networks. All events are also located using the Jeffreys-Bullen (J-B) *P* Tables and PREM with a set of azimuthal station corrections. A comparison of the reduction in sample variances of travel-time residuals provides a measure of the ability of tectonically regionalized tau functions to characterize lateral variations in mantle and crustal *P* velocities. Mean epicentral mislocations for NTS events are about 3 km, whereas mislocations using J-B and PREM are about 7 km. For NTS, and particularly, Eastern Kazakh, the tau formulation yields consistently smaller sample variances, with a mean reduction of 30% compared with results obtained using J-B and 15% compared with results obtained using PREM.

CONSTRAINTS ON MOMENT TENSOR COMPONENTS

—D.W. Vasco

A major problem in seismology is the determination of the nature of seismic sources. The analysis of earthquake waveform data is the chief method of observing the faulting process. Other methods, such as deep drilling and surface-strain measurement, are more expensive and time consuming. Furthermore, they do not offer a dynamic picture of the faulting process. Therefore, one must turn to the elastic-wave radiation for details of the faulting process.

The connection between the source parameters and the elastic-wave radiation is in terms of equivalent body forces. This is a force system that would produce displacements of the earth's surface equivalent to those from faulting. Commonly this body-force distribution is expanded in a Taylor series about a subsurface point ξ_0. Furthermore, only the first-order term is usually considered. This results in a linear equation relating the observed surface displacements to the convolution of the equivalent force moments about the point ξ_0 and a Green's function that accounts for elastic-wave propagation in the region. Assuming the Green's function is correct, one takes the Fourier transform of the convolution to obtain a linear relationship between the moment-tensor components and the observed waveforms. This linear system of equations may be solved by the generalized inverse. This approach works best when there are many data and few unknowns. Even in this case, however, there are tradeoffs between resolution and reliability of the solution.

Because of the above difficulties an alternative method is being explored. The calculation of bounds on model parameters does not suffer from the difficulties mentioned previously. These constraints on the equivalent force moments are efficiently computed by the linear-programming method. This

method works well on underdetermined problems. The effects of errors can also be incorporated into the inversion. Preliminary work has included the calculation of moment-tensor time functions, which minimize the l^1 norm of the residuals—i.e., the sum of the absolute values of the differences between the predicted seismograms and the observed seismograms. Future work will include general bounds on linear combinations of the moment-tensor components. It is hoped that the method will make the evaluation of higher-order moment-tensor components possible. This has important implications for the determination of possible fault models. The computed parameter bounds could be used to eliminate certain fault models that exceed the bounds.

EXTREMAL INVERSION OF TRAVEL-TIME RESIDUALS

—D.W. Vasco

A technique has been developed that determines bounds on velocity structure from travel-time residuals. The problem was first linearized and then discretized using a series-expansion method. The solutions derived are extremal in that they minimize or maximize a property of the model. For a given data set the solutions are unique to the linearized problem. The method has been tested by computing bounds on a test problem. The method also provides a mapping from bounds on the data to bounds on the velocity distribution. Furthermore, the technique is applicable to one-, two- or three-dimensional velocity distributions.

As an example, the technique was applied to a set of teleseismic relative residuals recorded at Long Valley caldera, California. Two methods have been examined to deal with negative travel-time residuals. Lower bounds and upper bounds are placed on velocity perturbations at depth (Figs. 1 and 2, respectively). The upper bounds indicate that teleseismic residuals cannot adequately constrain the velocity structure in Long Valley caldera. Lower bounds indicate where velocity perturbations must occur. The presence of a region of low velocity in the northwest portion of Long Valley caldera at a depth of 15 to 20 km has been supported. A minimum width of 18 km was derived for any anomalous body that could give rise to the observations.

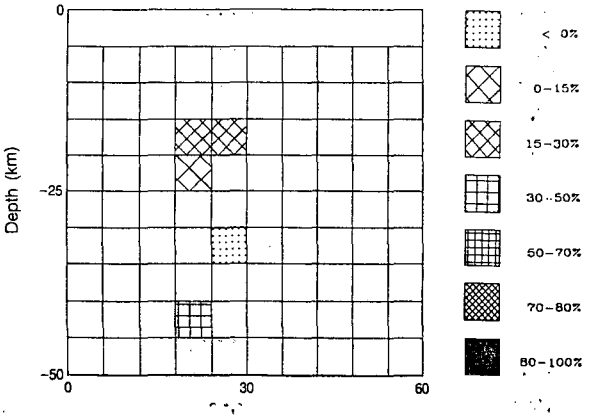

Figure 1. Lower bounds on velocity decreases in each pixel. [XBL 871-251]

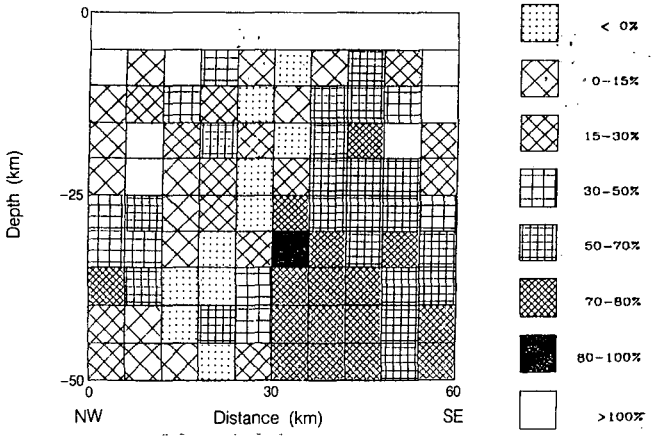

Figure 2. Upper bounds on velocity decreases in each pixel. Unpatterned pixels contained decreases in velocity that were greater than background velocity. [XBL 871-252]

THE VELOCITY STRUCTURE BENEATH XIAGUAN EXPERIMENTAL SITE, WESTERN YUNNAN, CHINA

—C. Wang and T.V. McEvilly

The State Seismological Bureau of the Peoples Republic of China established in 1980 the Xiaguan Experimental Site in Western Yunnan. A number of investigations of earthquakes, tectonics, and crustal structure are underway in this seismically active region as part of a concentrated study of earthquake-prediction methods. The velocity struc-

ture in the area has been determined from the refraction data of two profiles conducted in 1982 combined with 73 earthquakes that were recorded between 1982 and 1985 by the Kunming Telemetry Network of the Seismological Bureau of Yunnan Province and the China-U.S. cooperative seismic network in Western Yunnan. The progressive inversion method, beginning with the refraction-derived model, was used to refine the upper-crustal velocity structure on the basis of *P*- and *S*-wave arrivals for the earthquakes. Hypocenter locations were improved in the process in an iterative manner. Epicenters generally became more clustered in the process, their depths falling in the range 5–15 km. The velocity model is perturbed measurably in the inversion.

THE INTERPRETATION OF SEISMIC-REFRACTION PROFILES IN YUNNAN PROVINCE, CHINA

—C. Wang and T.V. McEvilly

From November 1982 through January 1983, three long seismic-refraction profiles were conducted in Yunnan province, southwestern China, an area of active tectonics. The twelve shots fired at four shot points on each profile were recorded by 196 seismic recorders with an average station spacing of about 2 km. The crustal velocity structure was determined on the basis of refraction data obtained along the profile from Eryuan to Jiangchuan (line 1) and the profile from Zhefang to Binchuan (line 2). The final model consists of three layers: (1) the upper crust, with a high-gradient transition in the basement and a weaker-gradient transition in the crystalline base; (2) the middle crust, with low velocity; and (3) the lower crust, with an upper section of low gradient and a lower section of normal gradient. The majority of the *P*-wave arrivals on the record sections were modeled as diving waves. The MOHO discontinuity dips toward north from 38 km to 45 km. The average crustal velocity is 6.25 km/s along line 1 and 6.30 km/s along line 2. The velocity at the top of the upper mantle varies from 7.80 to 8.10 km/s. The Red River Fault is considered as the boundary of the Indian and Eurasian plates. However, from both profiles, we could not obtain significant evidence about the change of velocity or about the MOHO interface across the northern end of the Red River Fault.

The Development of Seismological Techniques for the Real-Time Mapping of Grout Injections

E.L. Majer and J.T. Nelson

The problem of tracing a grout, or any viscous fluid as it is being injected into the ground, has long been the concern of many different disciplines. Most of the work done on tracing fluid injections into the ground has been in the area of hydraulic fracturing, a method that has been used mostly in the petroleum industry. Hydraulic fracturing was first used in the 1940s for stimulating unproductive oil wells and has grown in popularity ever since. A very sophisticated technology has developed around hydrofracturing; associated with defining the fluid path, this technology is based mainly on computer modeling and theoretical studies. Only recently, however, have researchers addressed the problems of hydrofracture detection and model verification with remote-sensing or geophysical techniques. Today, the injection of fluids into the ground is also a major concern of the waste industry, both toxic and nuclear. It is critical in the waste isolation industry to know the location and path of fluids that are being injected into the ground and to know the effects of naturally circulating groundwaters on waste canisters stored in underground repositories. Last, but certainly not least, is the problem associated with grout injection in the construction or repair of man-made structures. It is obviously very important to know the grout geometry, both for volume control and economy of operation. Moreover, in some cases the extent of the natural fractures is unknown, and knowledge of the grout path would be very valuable.

In almost all of these cases of fluid injection there has been some detectable form of seismic energy release. This is not surprising when one considers the physics of the situation. Energy is being expended to place the fluids into the ground. Often thousands of horsepower are used for deep oil-field hydrofracture jobs. As the fluid travels out into the ground, it must overcome the in situ stress. If the formation is very impermeable in spots, the fluid must also overcome the tensile strength of the rock. Depending upon the depth of injection and the rock type, this may occur quite rapidly and cause a stress or seismic wave to travel out from the sources, i.e., an acoustic emission—if the barriers or asperities are large enough, then the failure may be big enough to be detected at long distances, i.e., a microearthquake. Tensile failure may be accompanied by shear failure, which occurs when the stress state is such that one of the three principal stress magnitudes overcomes the shear strength of the rock and the other minor stress magnitudes. The most common demonstration of this process is an earthquake, in which case stress is increased by an outside force, such as overburden stress or plate-tectonic pressure. However, shear failure may also occur when the confining stress is reduced. This in essence increases the other stresses, and if the effect is large enough, shear failure will result. This can occur when the fluid pressure in a saturated environment is increased by some means. A well-documented example of induced failure is when water is impounded behind a dam; the resulting increase in fluid pressures at depth reduce the confining pressure and thus induce shear failure. Induced seismicity is often observed when dams are filled, especially in areas where high differential stresses already prevail, as in California. It is obvious that injecting grout or any other fluid into the ground could also have the same effect of locally reducing the effective stress, thus causing microseismic behavior around the zone of fluid injection.

Various other phenomena have been observed when fluid is injected into the ground. Seismic energy may be radiated from the path of the fluid as the fracture resonates. This is especially likely to occur if the fluid being injected is very viscous. Fracture-wall resonance may be caused by pressure drops due to variation in the pumping rate or by the leak-off of fluid due to diffusion or fracture extension. The acoustic properties of the fluid may cause the invaded area to act as a wave guide. The frequency content and amplitude of the guided wave may be characteristic of the dimensions of the invaded zone. The amount of energy and frequency content of the resonance and the guided-wave process will depend upon the pressure changes in the fracture zone, its geometry, and the acoustic impedance mismatch between the solid and the fluid. Depending on how fast the grout sets up, and on the size of the grout zone, there may also be a longer-period signal generated in association with the actual deformation of the solid due to the volume increase. A good example of this phenomenon are the tilt anomalies associated with hydrofracture operations. Although there will probably be no detectable tilt anomalies in grout jobs of relatively small volume, there may be signals in frequency ranges that have not been previously recognized—e.g., the high-frequency tilt anomalies associated with hydrofracture operations. Until a few people had the foresight to look in the frequency range several orders of magnitude less than the bandwidth of the microseismic energy, these signals were never detected or recognized as significant. It now appears that these signals may be a very valuable diagnostic tool in cases when it is logistically difficult to detect the higher-frequency microseismic activity.

Shown in Fig. 1 is the experimental field setup that is being used to monitor the seismic signals generated by the pumping of grout into the ground. This work is being conducted at McNary Dam, near Umatilla, Oregon, a project of the U.S. Army Corps of Engineers Waterways Experimental Station. The

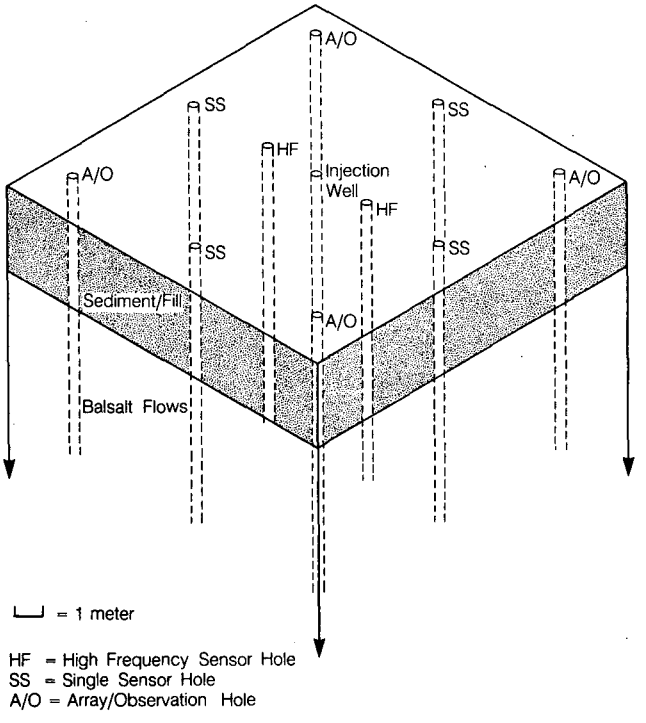

Figure 1. Grout-injection experiment, McNary Dam, near Umatilla, Oregon. [XBL 868-10957]

rock type is a fractured basalt. Complete hydrologic testing of the holes was carried out prior to the injection of grout.

To accomplish the goal of mapping the path of the grout, we are using a wide-band monitoring system that captures signals from 1 to 30 kHz. This is the same system we have used in past laboratory and small-scale experiments. Basically, a 3-D array of piezoelectric sensors is placed around a potential grout zone. The sensors are placed at distances ranging from a few meters to tens of meters away from the grout-injection hole. The purpose of this spacing is to investigate the attenuation and velocity changes with distance. Some sensors are aligned with the suspected grout direction and others perpendicular to it so that we can determine velocity and attenuation anomalies in the grout zone and compare them with those outside the zone. This is important for determining the applicability of the resonance and guided-wave techniques as well as for calibration of the array. Four of the sensors were grouted into holes in the rock (SS holes, Fig. 1) to insure good seismic coupling. Arrays of sensors were placed in the remaining holes (A/O holes) within packers for retrievability. The two modes of placement allowed us to compare the difference between grouted-in and retrievable sensors. These holes were also open to the formation and were used as grout-observation holes. Once the arrays were in place, we monitored several grout injections while varying the rate and pressure of grouting and the viscosity of the grout. Two distinct types of signals have been observed, discrete acoustic emission (AE) signals and harmonic tremor signals. The observed frequency range of these signals varies from 1 to 10 kilohertz. These signals are observable at distances up to 10 m away at pressures of 50 psig and flow rates of 2 to 4 L/min.

There are basically two areas of investigation:

1. The primary purpose is to monitor the discrete seismic activity associated with the grout as it is pumped into the rock. It is necessary to determine how much tensile and shear failure occurs from the near surface to depths of several hundred meters and the relative amount of each. Moreover, it is necessary to determine the range of frequency content in these signals and the amount of energy release. Locating the discrete AE events would potentially be the most straightforward technique to use. The acoustic-emission/microseismic (AE/MS) activity will be the most useful while the grout is in the process of extending fractures. Techniques have already been developed by us as well as others to map AE/MS activity.

2. If there is not a sufficient amount of discrete seismic activity associated with the propagation of the grout, it may be possible to use the signals generated by the resonance of the grout or the waves guided along it to characterize the extent of the grout invasion. This may not provide the resolution obtainable by mapping the discrete seismic activity, but if the stress and fluid conditions are not adequate for the generation of individual events, then this may offer an easy and fast approximation of the grout geometry. This is the most likely case in the flow of grout through open fissures or joints.

To date we have seen that both types of signal, AE and continuous, are generated during the injection of grout. The bandwidth of the signals varies from 1000 to 15,000 Hz. Noise due to pumping can easily be filtered out from the desired signals. AE activity is most pronounced during high pumping rates (1 gal/min or more) and high differential pressures (100 psi or more). The continuous signals occur at the higher viscosities (greater than 40 s, marsh funnel viscosity). The AE signals are used for mapping the detailed path of the grout, and the continuous signals are used for mapping the general areas of fluid flow. At present we have analyzed in detail only a small amount of data from three field tests. The next step is to analyze further the data from the field tests and to determine an implementation scheme for real-time mapping of grout in the field.

VSP/Tomographic Studies for Fracture Detection and Characterization

E.L. Majer, J.E. Peterson, T.V. McEvilly, and J.C.S Long

Vertical-seismic-profiling (VSP) techniques are becoming increasingly popular for defining detailed subsurface structure. In addition to the more conventional uses of VSP, Lawrence Berkeley Laboratory is investigating the use of three-component VSPs for fracture detection and characterization. Fracture detection using *P*- and *S*-waves in VSP studies is not a new idea (Stewart et al., 1981). It is becoming increasingly apparent, however, that to utilize the full potential of VSP, three-component data should be acquired. Crampin has pointed out the importance of using three-component data in VSP work, particularly for fracture detection (Crampin, 1978, 1981, 1984a,b, 1985). These authors and others have pointed out the phenomenon of shear-wave splitting and the effects of anisotropy on the *SH*- and *SV*-waves in addition to *P*-wave anisotropy (Leary and Henyey, 1985). In addition to Crampin's theoretical work on shear-wave splitting (1978, 1985), some recent laboratory work (Myer et al., 1985) and theoretical work Schoenberg (1980, 1983) has been done that explains shear-wave anisotropy in terms of "fracture stiffness." The fracture-stiffness theory differs from Crampin's theory in that at a fracture, or a nonwelded interface, the displacement across the surface is not required to be continuous as a seismic wave passes; only the stress must remain continuous. This displacement discontinuity is taken to be linearly related to the stress through the stiffness of the discontinuity.

The implication of the fracture-stiffness theory is that very thin discontinuities, such as fractures, can have a significant effect upon the propagation of a wave. Usually one thinks of seismic resolution in terms of the wavelength in relation to the thickness and lateral extent of a bed or other feature. In the stiffness theory the lateral extent is still important, but if the fracture stiffness is adequate, the thickness of the feature can be much less than the seismic wavelength. This stiffness theory is also attractive from several other points of view. Schoenberg (1980,1983) shows that the ratio of the seismic-wave velocities perpendicular and parallel to a set of stiffness discontinuities is a function of the spacing of the discontinuities as well as the stiffness. Thus, given the stiffness and the velocity anisotropy, one could determine the average fracture spacing or density. Alternatively, given independent information on fracture density, one could determine the fracture stiffness and, it is hoped, relate this stiffness to actual fracture characteristics (e.g., whether they are filled or open) and to such properties as hydraulic conductivity. In any case, there is sufficient reason to expect fracture content and properties to be reflected in the velocity, amplitude, and polarization of the shear waves.

In addition to describing structure and fracture content, we are also hoping to relate the seismic response of the rock mass to the hydrologic response. The idea is to map the variation in the *P*-, *SV*-, and *SH*-wave properties tomographically and relate the resulting anomalies to the actual fracture density, orientation, and spacing. An example of this approach is depicted in Fig. 1. Shown are ray paths through a model of fractured rock. This fracture model was actually generated by modifying a code that is used to model the hydrologic response of fractured media. In this way we can compare the seismic response to the hydrologic response. In a conventional approach to ray tracing, the fractures would have little or no effect on the ray parameters because of their very small width. The programs that we have developed incorporate the effect of fracture stiffness (Myer et al. 1985) in addition to the

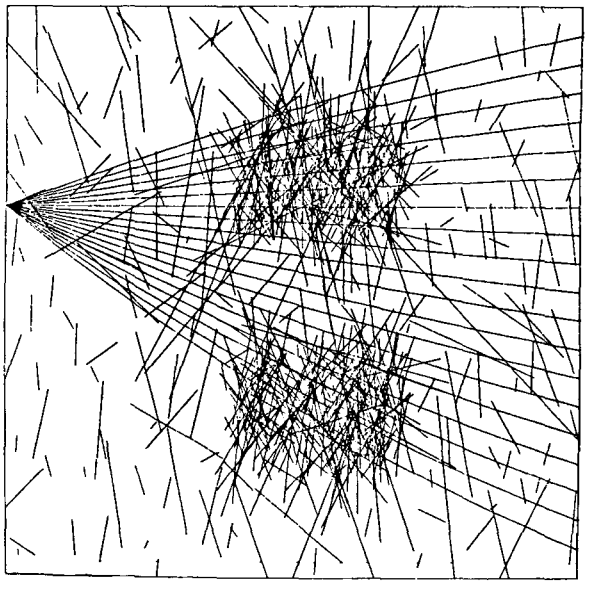

Figure 1. FMGRAY model showing fracture pattern and ray paths. [XBL 871-253]

effect of the bulk-rock properties. The fractures in Fig. 1 have zero thickness but finite stiffness. The area modeled in Fig. 1 is 1 km by 1 km. Figures 2 and 3 show the resulting waveforms from 4-Hz and 40-Hz wavelets, respectively. As can be seen the stiffness has a significant effect on the seismic energy. Shown in these figures are *P*-waves. We also have the capability to model *SV*- and *SH*-waves as well. The aim is to use the times, amplitudes, and polarizations of the *P*-, *SV*-, and *SH*-waves to map fracture properties.

A significant question that remains to be answered is the scale effect of stiffness. If we use stiffnesses of fractures that have been measured in the laboratory in our kilometer-size model, we see no effect on the seismic waves. To see an effect we must assume that stiffness scales as the square of the length of the fracture. We have observed in field cases effects of fractures at kilometer-size scales (Majer et al., 1988). Therefore we assume that there must be a scale effect.

In a field study at the Salton Sea deep hole, we observed another interesting effect of fractures. Shown in Figs. 4 and 5 are the *P*-wave VSPs from a near offset (300 ft) and a far offset (4000 ft), respectively. The depth covered in detail in the well was from 5600 to 2000 ft. In the near-offset data (Fig. 4) we see a clean waveform with good first arrivals and no secondary arrivals until the converted *S*-waves appear over a second later. In the far offset this is not the case. The data in Fig. 5 have been dip filtered slightly, but there is still significantly more energy directly after the first arrival in the far offset than in the near offset. This difference may be due to fractures. Available core and well-log data suggest

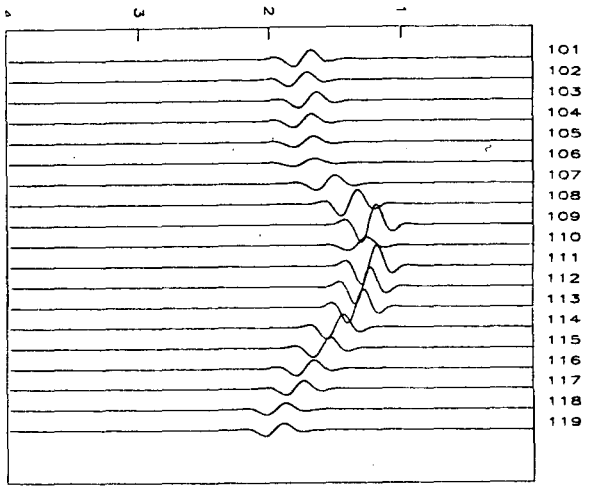

Figure 2. The synthetic seismograms generated from the model in Fig. 1 using a 4-Hz wavelet. [XBL 871-254]

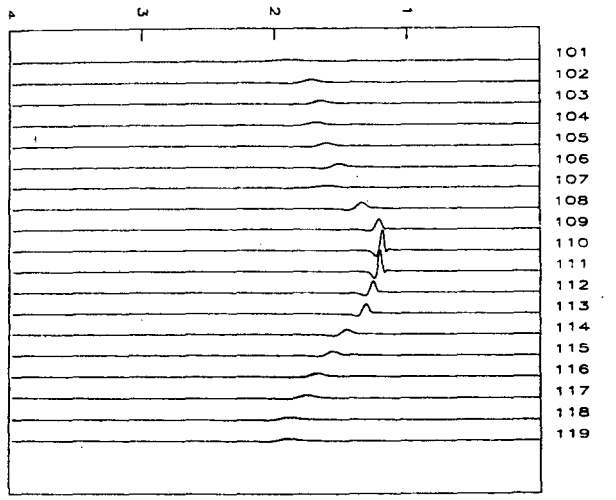

Figure 3. The synthetic seismograms generated from the model in Fig. 1 using a 40-Hz wavelet. [XBL 871-255]

the presence of significant vertical fractures in this section of the well. In the near-offset case the waves will be almost at vertical incidence, hence vertical fractures would have little effect on the waves. In the far-offset case, the waves propagate in a more horizontal orientation; thus, if they intersect a vertical feature, there would be an effect on the wave, which is what we observe. In the far offset we are probably observing diffraction from the vertical fracture sets. This may be the reason why the secondary arrivals travel away from the fracture zone up and down the well. The shear-wave data also are complicated, indicating significant fracture content.

In another field study in a less complicated environment, we performed a multioffset/

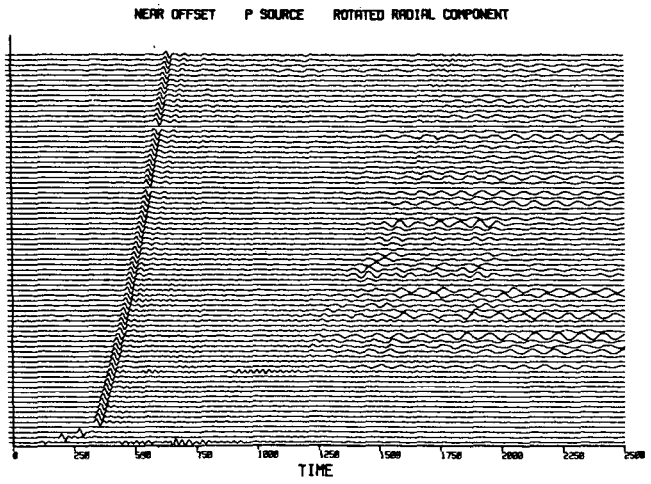

Figure 4. *P*-wave data from the near offset (300 ft) at the Salton Sea well. The depth ranges from 7000 to 500 ft. [XBL 871-256]

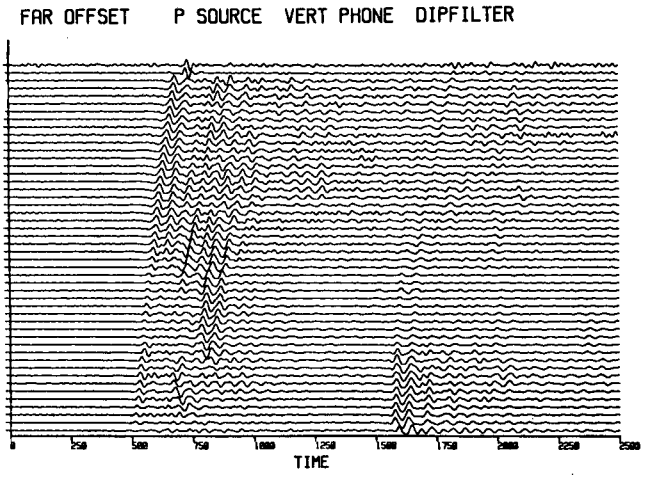

Figure 5. *P*-wave data from the far offset (4000 ft) at the Salton Sea well. The depth ranges from 7100 to 1500 ft. Compare with Fig. 4, and note the complexity of the first arrivals compared with the near offset. [XBL 871-257]

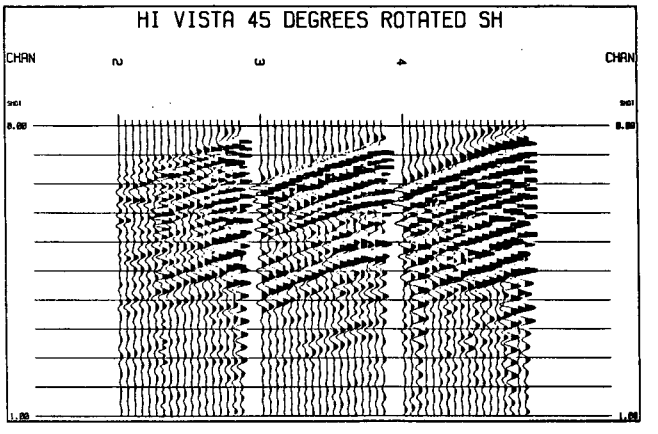

Figure 7. Three-component data that have been rotated. Channel 2 is the *P*-wave component, channel 3 the *SV* component, and channel 4 the *SH* component. The data are from a shear-wave vibrator oriented such that the base-plate motion is 45 degrees to the inferred fracture direction. [XBL 871-259]

multisource VSP. As in the case of the Salton Sea we used *P*- and *S*-wave vibrators. The zone covered in the well was from 300 to 1800 ft. At each offset (each being 300 ft from the well) we turned the *S*-wave vibrator parallel and perpendicular to the ray path connecting the well and the vibrator. In effect we had a compressional wave source (*P*-wave vibrator), and an *SH*-wave source (shear-wave vibrator perpendicular to the well), and an *SV*-wave source (shear-wave vibrator parallel to the well). The well that we used is in a tight, relatively unfractured granite about 30 miles east of the San Andreas Fault near Lancaster, California. Hydrofracturing had been carried out in the well to determine the stress information. There were some fractured regions at the bottom of the well, but the rock was mostly unfractured, especially compared with a geothermal environment. The plan of the experiment was to generate waves vibrating at 0, 45, and 90 degrees to the fracture direction inferred from the hydrofracture data. It seemed unlikely that we would detect the short fractures from the hydrofracture data, but we were interested in determining if we could detect a preferred fabric or overall microfracturing of the rock. Differences were detected in the *SH*- and *SV*-components from the various shear-wave sources as

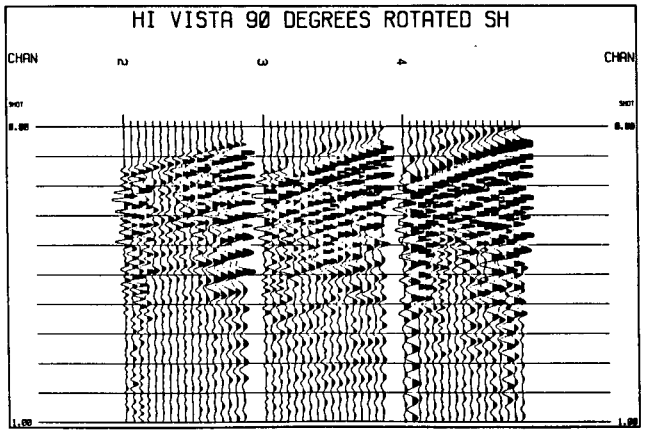

Figure 6. Three-component data that have been rotated. Channel 2 is the *P*-wave component, channel 3 the *SV* component, and channel 4 the *SH* component. The data are from a shear-wave vibrator oriented such that the base-plate motion is perpendicular to the inferred fracture direction. [XBL 871-258]

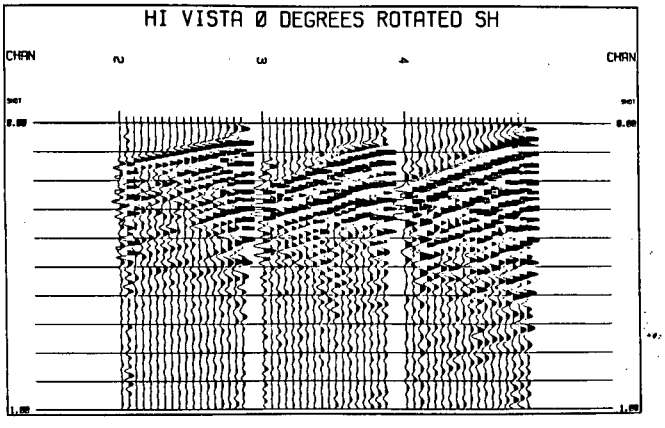

Figure 8. Three-component data that have been rotated. Channel 2 is the *P*-wave component, channel 3 the *SV* component, and channel 4 the *SH* component. The data are from a shear-wave vibrator oriented such that the base-plate motion is parallel to the inferred fracture direction. [XBL 871-260]

a function of azimuth. Although the differences are subtle and difficult to demonstrate at the scale available in this report, they amount to 5–10% velocity anisotropy. Shown in Figs. 6 to 8 are the three-component data from the *SH* source at 0, 45, and 90 degrees, respectively, to the fracture directions that have been rotated into the plane of propagation of the *P*-wave. That is, channel 2 is the particle-motion component along the ray path (*P*), channel 3 is vertical (*SV*) to the ray path, and channel 4 is horizontal (*SH*) to the ray path. From these figures one can at least see the relative amount of energy arriving at the different positions of the source and receiver. Even in this relatively isotropic environment, we do see effects of fractures.

In conclusion, we are carrying out field and modeling studies to determine the effect of fractures on the propagation of seismic waves. the goal is to be able to map the orientation, density, and spacing of fracture sets in the field and to be able to give the hydrologist/reservoir engineer useful information. To date we have seen that fractures do have a significant effect on seismic waves. Through modeling and controlled field experiments, we hope to quantify this effect.

REFERENCES

Crampin, S., 1978. Seismic-wave propagation through a cracked solid: Polarization as a possible dilatancy diagnostic. Geophys. J. R. Astron. Soc., v. 53, p. 467–496.

Crampin, S., 1981. A review of wave motion in anisotropic and cracked elastic media. Wave Motion, v. 3, p. 343–391.

Crampin, S., 1984a. Effective anisotropic propagation through a cracked solid. *In* S. Crampin, R.G. Hipkin, and E.M. Chesnokov (eds.), Proceedings, First International Workshop on Seismic Anisotropy. Geophys. J. R. Astron. Soc., v. 76, p. 135–145.

Crampin, S., 1984b. Anisotropy in exploration seismics. First Break, v. 2, p. 19–21.

Crampin, S., 1985. Evaluation of anisotropy by shear wave splitting: Geophysics, v. 50, no. 1, p. 142–152.

Leary, P.C., and Henyey, T.L., 1985. Anisotropy and fracture zones about a geothermal well from *P*-wave velocity profiles. Geophysics, v. 50, no. 1, p. 25–36.

Majer, E.L., McEvilly, T.V., Eastwood, F.S., and Myer, L.R. 1988. Fracture detection Using *P*- and *S*-wave VSP's at The Geyers geothermal field. Geophysics, in press.

McLaughlin, R.J., 1981. Tectonic setting of pre-Tertiary rock and its relation to geothermal resources in The Geyers-Clear Lake area. U.S. Geol. Survey Prof. Paper 1141, p. 3–23.

Myer, L.R., Hopkins, D.L., and Cook, N.G.W., 1985. Effects of an interface in partial contact on attenuation of acoustic waves. Geophysics, in press.

Schoenberg, M., 1980. Elastic wave behavior across linear slip interfaces. J. Acoust. Soc. Am., v. 68, no. 5, p. 1516–1521.

Schoenberg, M., 1983. Reflection of elastic waves from periodically stratified media with interfacial slip. Geophys. Prospect., v. 31, p. 265–292.

Stewart, R.R., Turpenning, R.M., and Toksöz, M.N., 1981. Study of a subsurface fracture zone by vertical seismic profiling. Geophys. Res. Lett., v. 8, p. 1132–1135.

Hydraulic Fracturing: Acoustic and Elastic-Wave Propagation in Hydraulically Fractured Rock Layers

J.T. Nelson and E.L. Majer

Downhole monitoring of hydraulically induced seismicity is an attractive and potentially economical method for real-time mapping of the azimuth and extent of hydraulic fractures. This potentially useful method of monitoring has been frustrated to some extent by the presence of tube waves, which may be related to transient acoustic waves emanating from the fracture.

A specialized tool has been developed for measuring downhole acoustic pressure signatures

over a bandwidth of 0–10 KHz using an absolute-pressure transducer. To date, however, measurements of downhole acoustic pressures and correlation with out-of-fracture-plane seismic arrivals have not been performed because of a lack of field testing opportunities. Field testing is being pursued with governmental and industrial organizations.

Modeling efforts are aimed at studying acoustic- and elastic-wave arrivals in both the fractured and unfractured regions. Specifically, dynamic Green's functions for dislocation sources within hydraulically fractured layers are being sought to aid interpretation of seismic and fluid-pressure signatures observed during downhole monitoring.

PROBLEMS CONSIDERED THUS FAR

Viscous Fluid Layer

The propagation of pressure waves in a viscous fluid layer confined between two rigid boundaries has been studied using the computer model SALE (Amsden et al., 1980) and an exact analytical model based on potential theory. Both of these models employ two-dimensional plane-strain representations. The program SALE was used to model the evolution of a propagating pressure drop of magnitude equal to the static pressure of the fluid. Typical fractures were 4 mm in aperture and 1–2 m in length. Fluid properties were similar to those of water but with viscosities of 1, 10, and 100 CP. The results indicated little change in the shape of the propagating wave front except for the case with viscosity 100 CP. The study of far-field behavior was inhibited by model size and computer-memory limitations.

The analytical model was developed during the initial study to provide some insight into attenuation of the acoustic wave with distance in a thin viscous fluid layer. Biot (1956) actually considered an approximation of this problem, describing essentially similar results. For fracture widths on the order of a few millimeters, the attenuation with distance is on the order of a few decibels per meter, depending strongly on viscosity. Thus relatively large pressure amplitudes generated by rapid or virtually instantaneous fracture extensions might be expected at the borehole.

Viscous Fluid Layer between Two Semi-Infinite Elastic Media

Bernard Chouet's 2-D numerical finite-difference model (Chouet and Julien, 1984) was run on the CRAY computers at Lawrence Livermore National Laboratory to model the propagation of waves along a viscous fluid layer between two semi-infinite elastic layers. Limitations were encountered in modeling a very long thin crack, including the ability to determine the attenuation with distance of acoustic and psuedo-Rayleigh waves. The model does describe the response of the system to fracture extension.

The analytical model developed for a viscous fluid layer between rigid boundaries was extended to model the propagation of acoustic waves in a viscous fluid layer between two semi-infinite elastic regions. Again, low rates of attenuation—a fraction of a decibel per meter for waves within a layer of water 1 mm thick—are predicted, implying that relatively significant pressure signatures at audio frequencies might be observed at the fracture mouth. Model fluids were required to be highly viscous or to be present in thin layers in order to produce high rates of attenuation and thus reduce fluid pressure at the fracture mouth. A problem with the 2-D model is that for the fundamental mode at long wavelengths, the phase velocity of the acoustic wave decreases with increasing wavelength—a relationship that is probably not realistic for a fracture of finite dimensions.

CURRENT WORK

The data on extent and distribution of fractures suggest that modeling a saturated fracture as a discrete fluid layer with well-defined boundaries is perhaps not realistic. Accordingly, we began to develop a model of wave propagation within a poroelastic medium using the method of Biot (1956). To gain familiarity with the poroelastic problem, we first used a constant-porosity model of a hydraulically fractured layer to determine rates of attenuation and propagation velocities of acoustic waves within the medium. This work formed the basis for the development of a model of a fractured region with a poroelastic layer of variable porosity. Both of these models are discussed below.

Saturated Porous Layer between Two Semi-Infinite Media

An analytical model of a constant-porosity layer bounded by two semi-infinite elastic media was developed using potentials and Biot's representation for poroelastic waves (Biot, 1956). In order to implement the Biot model, the shear and bulk moduli of the fractured region were estimated using the equations discussed by Bruner (1976). The mass coupling parameter, ρ_{12}, initially proposed by Biot and discussed by Plona and Johnson (1984), was estimated

by averaging the kinetic energy for an "ad hoc" fracture geometry and found to be roughly 10% to 20% of the average fluid density for a porosity on the order of 10%. The corresponding "tortuosity" (Plona and Johnson, 1984) is roughly 1.1 to 1.3. Similarly, Biot's "sinuosity" coefficient (Biot, 1956), estimated by averaging the dissipated power within a given volume element, has about the same magnitude as the "tortuosity" coefficient.

Parametric evaluations of layer thickness and microfracture height were carried out. The dispersion of phase velocity and attenuation rates with frequency were studied for the fundamental "normal-mode" acoustic wave propagating within a saturated layer of fractured material corresponding very roughly to granite. Three values of fluid viscosity were considered: 1 CP (water), 10 CP, and 100 CP, with a fractured-layer width of 1 m and a microfracture height of 1 mm. The dispersion curves were calculated by numerically searching for zeros of the determinantal equation that results from satisfying the boundary conditions. The numerical searches were performed on the VAX-11/780 computer in the Center for Computational Seismology (CCS), Lawrence Berkeley Laboratory.

The results of this cursory investigation indicate that the phase velocity for the fundamental mode of the "slow" acoustic wave for water at normal viscosity and 10 times normal viscosity is generally flat above 100 Hz. The actual velocity depends on the elastic matrix moduli but is less than the acoustic velocity for the fluid alone, consistent with Biot's theory.

The attenuation with distance of the slow "acoustic mode" is less than a decibel per meter for water at normal viscosity and about 1 dB/m for water at 10 times normal viscosity. Only if the fluid viscosity were about 100 times that of water would the attenuation rate exceed 5 dB/m at acoustic frequencies for the arbitrary fracture parameters considered. These results are similar to those predicted by the models of viscous fluid layers. The phase velocity and attenuation rate tend to zero as the frequency tends to zero, approaching diffusion at very low frequencies.

For a microfracture height of 100 μ, the phase velocity and attenuation rate for water at 1 CP would be on the order of those shown for water at 100 CP in Figs. 1 and 2, since the frictional effects scale as

$$\frac{\mu}{\omega h_f^2 \rho_f},$$

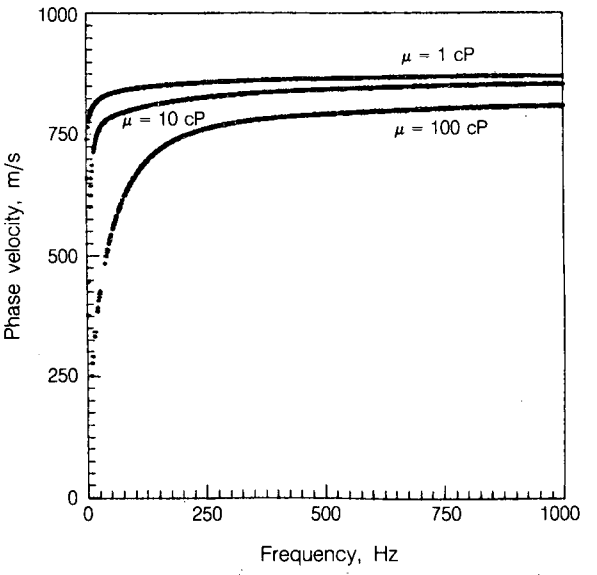

Figure 1. Phase velocity versus frequency for second-mode pressure wave in homogeneous fluid-saturated fractured layer. [XBL 871-9803]

where μ is the fluid viscosity, h_f the microfracture height, ρ_f the fluid density, and ω the radian frequency. (High-frequency effects, not included in the above formula, were included in the model.)

As with our earlier investigations, these results suggest that, for a fracturing fluid such as water, the rate of acoustic wave attenuation with distance along the fractured layer may be low and that acoustic pressure signatures at the fracture mouth may be

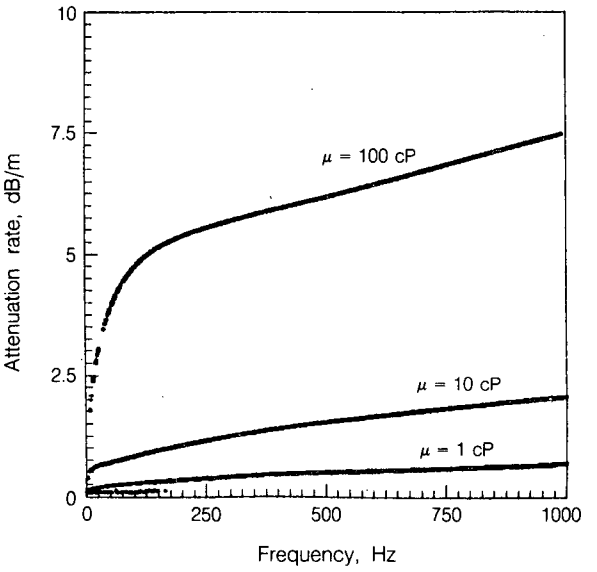

Figure 2. Attenuation rate versus frequency for second-mode pressure wave in homogeneous fluid-saturated fractured layer. [XBL 871-9802]

substantial, depending on source strength. The pressure signatures may also be rich with information. For instance, comparing the relative arrival times and spectral energies for elastic waves detected outside the fracture plane with those for the acoustic signatures may provide an independent measure of average microfracture height and density, since the fluid viscosity is presumably known. Moreover, by increasing the fluid viscosity, the generation of tube waves at the fracture mouth in the borehole might be effectively controlled to reduce interference with the detection of shear- and dilatational-wave arrivals generated during fracture extension, thus simplifying mapping.

Because fluid shear is neglected in the Biot model (represented only through the friction arising from relative motion of the fluid and porous matrix), the fundamental mode of propagation of the slow-acoustic mode is approximately a plane wave across the height of the layer. Reducing the layer height does not significantly alter the slow-wave velocity or the attenuation rate. On the other hand, the velocity and attenuation rate are very sensitive to microfracture height, which, together with the microfracture height-to-width ratio and fracture density, determine the porosity.

Variable-Porosity Layer

A model of a variable-porosity layer between two semi-infinite elastic regions is now being developed to study the basic features of the response both inside and outside of the fractured region to an arbitrary seismic moment acting on the porous matrix. Some work has been performed by Yamamoto (1983) to study porous layers with variable parameters using a displacement-stress representation for a vertically heterogeneous porous layer. Yamamoto does not actually provide for variable porosity but considers only the reflection and transmission of waves through the layer.

Model description

The fractured region is represented by a vertically heterogeneous porous layer, with relatively high porosity at the center, decreasing smoothly to a small but finite porosity at the fracture boundaries. The model includes the effects of porosity, fluid viscosity, fracture height, porosity profile, microfracture height, and location of the fracture event on the observed fluid-pressure and elastic-wave responses. Depending on practicality, a grout may be included within the model fluid to represent certain fracturing fluids more accurately. The variable porosity layer is more realistic than a constant-porosity layer, since a region of relatively high porosity may be used to represent the fracture proper, with regions of decreasing porosity on either side to represent rock layers structurally weakened by the hydraulic-fracturing process. Dislocation sources can be included at various positions across the porous layer, including the extreme edge of the porous layer, to model seismicity at the boundary between the weakened rock and the competent rock.

A displacement-stress representation and direct integration of the displacement-stress vector to obtain the propagator matrix is used to model wave motion in the porous region. The approach is a direct extension of the methods described by Aki and Richards (1980). The displacement-stress vectors are coupled with potentials for the elastic region at the boundaries of the fractured layer. Dislocation sources acting on the porous matrix are situated at various points across the layer, including the extreme edge of the layer, and Green's functions are calculated. The spectral responses to dislocations of the porous matrix are then computed by direct numerical inversion of Hankel transforms. The temporal responses are computed by Fourier syntheses of time-dependent solutions. These results can be combined with a general seismic-moment tensor to compute the response to an arbitrary dislocation source.

The equations discussed by Bruner (1976) are used to estimate the bulk and shear moduli for the fractured region for the "drained" condition as a function of porosity and an assumed constant microfracture aspect ratio and size distribution. The Biot parameters are computed from intrinsic relations that must hold for the porous region in the static case, according to Biot and Willis (1957). Input parameters include maximum porosity of the layer, porosity-profile parameters, various moduli, fluid viscosity, densities, microfracture aspect ratios, layer thickness, source positions, and various control parameters.

A moment tensor may eventually be used for modeling shear and tension failures of the elastic matrix. At present, a seismic moment for the porous matrix, including fluid flow, remains to be studied and developed. Norris (1985) has derived Green's functions for a porous, saturated medium, has shown these to be equivalent to those of Burridge and Vargas (1981) and has developed an analog of Betti's reciprocal theorem for a saturated porous material.

Development to date

A displacement-stress representation for an isotropic vertically heterogeneous porous layer has been developed at CCS for modeling *P-SV* and *SH*-waves

in three dimensions. For the *SH* case, the representation is similar to that for an elastic region, but includes dissipation due to fluid motion relative to the porous matrix. In the *P-SV* case, the representation involves six independent solutions, rather than four as in the elastic case. The additional two solutions result from including the fluid displacement normal to the layer boundaries and the partial fluid pressure.

Convergence problems were encountered when attempting a Hankel transform of the displacements and fluid-stress responses within the source layer. The problem is particularly severe when the source and receiver are on the same horizontal plane. To develop some useful information with the present model, initial efforts were directed to calculating the elastic-wave responses within the elastic regions bounding the porous layer. These are relatively easy to compute, since the Hankel transform integrals converge rapidly for wave numbers in excess of the shear-wave number for the elastic region.

The more interesting problem of computing the fluid-pressure responses to dislocation sources within the porous layer remains to be solved without excessive use of computer resources. Rather than attempt a direct Hankel transform of the porous-layer responses, a more fruitful approach may be to compute branch-line integrals and evaluate the residues corresponding to the most significant propagating modes. This approach would involve searching for complex poles using Mueller's method with some means of avoiding branch cuts.

The CPU time required to compute the propagator matrices for the layer to 4 significant figures is on the order of 3 s using double precision on the CCS VAX-11/780 computer and a standard Runge-Kutta integration routine to integrate the displacement-stress vectors used in forming the propagators. Significant reductions of time have been obtained recently by simultaneous integration of independent displacement stress vectors across the layer. The model has also been adapted for use on the CRAY computers at Lawrence Livermore National Laboratory. Recent test runs indicate that elastic-wave responses outside the layer can be computed with 1–2 hours of CRAY computer time.

RELATED PROBLEMS

Models of variable- or constant-porosity layers are relevant to a number of other areas of research.

VSP studies

Vertical seismic profiling is an effective tool for mapping hydraulically fractured layers. The propagator matrix for a fluid-saturated fractured porous layer can be used directly for computing reflection and transmission coefficients and can possibly be extended to the case of anisotropic materials with only a moderate amount of generalization.

Partial-melt problems

Wave propagation through a partially melted region is of interest to many seismologists. In this case, however, fluid shear may have to be included, since the porosity may be allowed to approach unity, and the "friction" due to fluid flowing through the elastic matrix would no longer be the dominant source of dissipation.

Fault models

Fault zones might be modeled as heavily fractured fluid-saturated regions. In this case, "long-period" motions could be studied with respect to fluid flow. The fractured porous layer with dislocation sources can be used directly for modeling downhole seismicity associated with acoustic emissions from a faulted region, emissions that may be precursors to failure or rupture and which may provide a means for early warning of earthquake motion.

Propagation of vibration in soils

The propagator representation developed for saturated fractured layers could be adapted to modeling the response of layered porous saturated soils to surface or subgrade sources. Many modern manufacturing and research endeavors require virtually vibration-free facilities, typified by the semiconductor and aerospace industries. The ability to predict vibration in soils and building foundations is increasing in importance, and much of the research conducted since Biot first developed the theory of porous media can be incorporated directly into such a model as discussed above. However, the effective-medium theories developed for approximating the dissipative mechanism of fluid motion relative to the porous matrix may be more appropriate.

REFERENCES

Aki, K., and Richards, P.G., 1980. Quantitative Seismology (Vol. I). W.H. Freeman, San Francisco, p. 267–315.

Amsden, A.A., Ruppel, H.M., Hirt, C.W., 1980. SALE: A simplified ALE computer program for fluid flow at all speeds. Los Alamos Scientific Laboratory Report No. LA-8095.

Biot, M.A., 1956. Theory of propagation of elastic waves in a fluid-saturated porous solid. I. Low-frequency range. J. Acoust. Soc. Am., v. 28, no. 2, p. 168–178.

Biot, M.A., and Willis, D.G., 1957. The elastic coefficients of the theory of consolidation. J. Appl. Mech., v. 24, p. 594–601.

Burridge, R., and Vargas, C.A., 1981. The fundamental solution in dynamic poroelasticity. Geophys. J.R. Astron. Soc., v. 58, p. 61–90.

Bruner, W.M., 1976. Comment on "Seismic velocities in dry and saturated cracked solids" by Richard O'Connell and Bernard Budionsky. J. Geophys. Res., v. 81, no. 14, p. 2573–2576.

Chouet, B., and Julien, B.R., 1984. Dynamics of an expanding fluid filled crack. J. Geophys. Res., v. 90, no. B13, p. 11,187–11,198.

Norris, A.N., 1985. Radiation from a point source and scattering theory in a fluid-saturated porous solid. J. Acoust. Soc. Am., v. 77, no. 6, p. 2012–2023.

Plona, T.J., and Johnson, D.L., 1984. Acoustic properties of porous systems: I. Phenomenological Description Physics and Chemistry of Porous Media, AIP Conference Proceedings Number 107 (Schlumberger-Doll Research), Ed. D.L. Johnson, and P.N. Sen, Publ. American Inst. of Physics.

Yamamoto, T., 1983. Propagator matrix for continuously layered porous seabeds. Bull. Seismol. Soc. of Am., v. 73, no. 6, p. 1599–16201.

Constraints on Volume Expansion in Long Valley Caldera, California, Derived from Vertical Displacements, 1975 to 1985

D.W. Vasco and N.E. Goldstein

Many numerical methods have been proposed and used to determine the nature of surface deformation at Long Valley caldera, which has been attributed to magma injection. Unfortunately, most methods rely on local linearization about some assumed source geometry. Thus these methods are highly dependent on the form of the model fit. If this form is not general enough to include all possible source types or multiple sources, then the results may be misleading. The purpose of our work is to present a stable way to invert surface displacement and strain for deformation at depth without assuming an initial source model. This was done by characterizing the three-dimensional distribution of strains by six linear combinations of strain components. The distribution is discretized using a series-expansion method, and a linear-inverse problem is derived without local linearization. This problem can then be solved by a least-squares algorithm. Unfortunately, each term of the series expansion involves nine unknowns, so that the parameters are too numerous for a reasonable order of expansion. For most problems this results in an underdetermined inverse problem. For this reason we have also used an extremal-inversion technique to study the constraints on the volume change beneath the resurgent dome area of Long Valley caldera. We used a set of vertical leveling measurements to derive bounds on the depth to the top of any possible magma intrusion in the caldera. We also derived the upper bounds on the total volume change within the caldera and examined the changes of the depth bound and volume-change bound over the period 1975 to 1985. The method is applicable to a wide variety of other geodetic data sets, such as the recent set of Global Positioning System (GPS) measurements and the frequent trilateration observations made at Parkfield, California.

THE METHOD

The displacement at any observation point on the surface $\vec{x}$ due to a point-force combination at $\vec{\xi}$ has a representation as a combination of the six double forces. Hence the displacement at $\vec{x}$ due to a distribution of forces at depth may be written as

$$u_m(\vec{x}) = \int\int\int_V \epsilon_{kl}(\vec{\xi}) W_{kl}^m(\vec{x},\vec{\xi}) dV,$$

where $\epsilon_{kl}(\vec{\xi})$ may be considered as a weighting function of the double forces at source point $\vec{\xi}$. Because of the symmetry of $\epsilon_{kl}(\vec{\xi})$ only six independent values exist. $W_{kl}^m(\vec{x},\vec{\xi})$ is a function that relates strain at the source point to surface displacement at the station at $\vec{x}$. The importance of the representation above is that it is linear and may be interpreted in terms of six physically meaningful source types. This interpretation will allow the determination of the distribution of principal strains and principal axes. The linearity simplifies questions involving uniqueness and resolution.

For computational purposes it is necessary to expand the distribution of strain nuclei in a three-dimensional orthonormal series. This is advantageous in that the data still depend linearly on the parameters. Introducing a set of N orthonormal basis functions, $\beta_j(\vec{\xi})$, $j = 1,..., N$, restricts the model space to those six model perturbations $\epsilon_{kl}(\vec{\xi})$ that may be described as a linear combination of the N basis functions,

$$u_m(\vec{x}) = \sum_{j=1}^{N} b_j^m \beta_j(\vec{\xi}).$$

The b_j^m can be thought of as generalized Fourier coefficients. This results in a linear representation in terms of $6 \times N$ coefficients of the basis functions,

$$u_m(\vec{x}) = \sum_{I=1}^{6 \times N} b^I G_m^I,$$

or, in matrix form,

$$\mathbf{u} = \mathbf{Gb}.$$

The resulting linear system of equations may be solved by any of the methods commonly used in geophysics, such as the generalized inverse, damped least squares, or Backus-Gilbert method (Backus and Gilbert, 1968).

Nonuniqueness may lead to a search for bounds on model properties of interest. These bounds may be used to characterize the range of possible solutions. Specifically, let us consider model properties that are linear functions of the model perturbations,

$$A = \mathbf{a}^t \mathbf{b}.$$

Many useful properties of the model can be put in this form. For example, bounds on the total volume change that gives rise to a set of observations can be determined by choosing a to be a column vector of 1's. Similarly, bounds can be placed on any nth-order moment of the strain model about a point in space, ξ_0. Higher-order moments, $n = 2,3$, represent compactness and skewness of the solution about ξ_0.

Linear optimization problems, subject to the linear equality and inequality constraints described above, are easily solved using linear programming techniques. The simplex method, the standard solution algorithm, is very efficient and can solve problems involving thousands of variables and thousands of constraints. It will be used below to determine bounds on the magma intrusion in Long Valley caldera.

CONSTRAINTS ON THE VOLUME EXPANSION IN LONG VALLEY CALDERA

Over the period 1975–1985 up to 47 cm of vertical displacement has been measured within Long Valley caldera. The measurements were taken principally along two lines within the caldera (Fig. 1). Four surveys from this period, those made in 1982, 1983, 1984, and 1985, are examined relative to a survey from 1975. Because prior leveling detected little or no displacement, the 1975 survey serves as a base for subsequent measurements. The magnitude of the uplift and the associated earthquake activity have prompted the explanation that magma is intruding within the caldera. The presence of a magma chamber is supported by other lines of geophysical

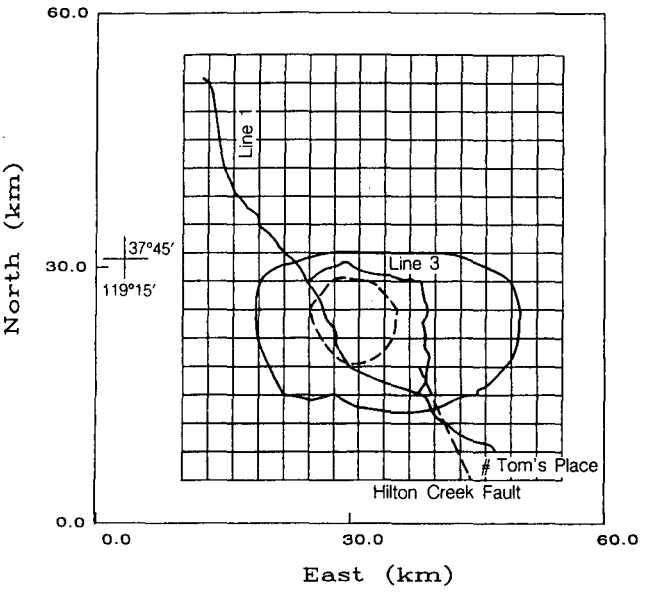

Figure 1. Location map of the Long Valley caldera region, showing the outline of the caldera (solid oval), leveling lines 1 and 3, the Hilton Creek Fault, the resurgent dome (broken circular outline within caldera), and the grid used in the derivation of the extremal bounds. [XBL 872-9924]

evidence, such as P-wave teleseismic delays (Steeples and Iyer, 1976), S-wave attenuation (Sanders and Ryall, 1983), and P-wave tomography (Kissling et al., 1984).

A variety of models have been proposed to account for the observed deformation. For example, various point-source models with source depths of 4 to 12 km have been proposed by Savage and Clark (1982), Castle et al. (1984), and Rundle and Whitcomb (1984) to explain the vertical displacements at various times. Furthermore, Savage and Cockerham (1984) proposed two dipping dike models to account for the 1975–1983 deformation. Unfortunately, surface displacements, like potential data, do not determine a unique source model. Given the limited number and distribution of leveling measurements and the necessity of considering all possible intrusion shapes, the problem is highly underdetermined. Furthermore, it may not even be necessary to invoke magma at depth as a source of the uplift; other modes of strain may have produced the observed uplift. Because of this ambiguity it is appropriate to ask what the vertical-displacement data actually reveal about the strain occurring below Long Valley caldera. Such a question is appropriately addressed by the extremal-inversion methods.

To derive constraints on the possible magma intrusion in the region, it will be assumed that the uplift is due only to volume expansion. The effects of faulting and regional shear will be accounted for through modelling and the addition of error terms. What will be examined are the bounds on the depth to the top of any intrusion satisfying the data and the total volume change associated with the intrusion. Temporal changes in these limits will be examined for the years 1982, 1983, 1984, and 1985. Figures 2 and 3 show the vertical displacement that occurred between each of these years and 1975.

To find the constraints using extremal inversion, we discretized the distribution of strain nuclei using the series-expansion method. The requirement that the data are satisfied within errors σ_i and that only intrusion is occurring results in a linear system of inequalities,

$$u_i - \sigma_i \leqslant \sum_{n=1}^{N} k_{i,n} \Delta\theta_n \leqslant u_i + \sigma_i \qquad i = 1,2,3,...,M$$

$$\Delta\theta_n \geqslant 0 \qquad n = 1,2,3,...,N.$$

Here $\Delta\theta$ is the fractional volume change, and u_i is the uplift at the ith station. As is often the case there are many sources of error. Two principle sources will be considered: leveling errors and errors

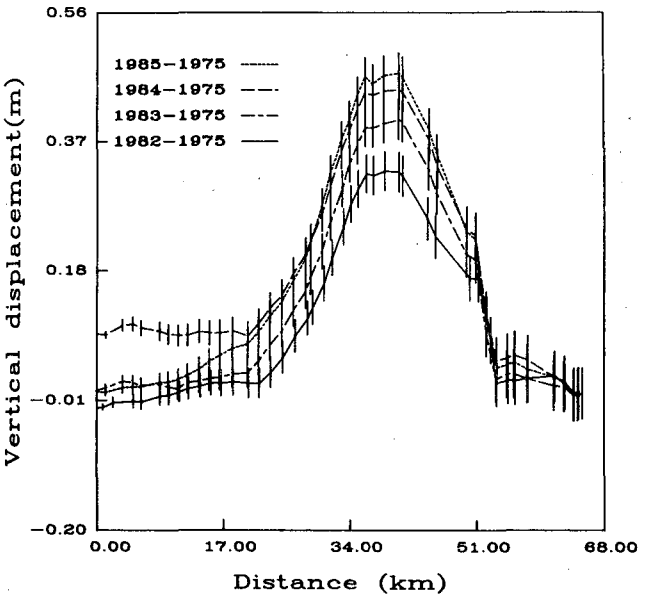

Figure 2. Vertical displacement for the periods 1982–1975, 1983–1975, 1984–1975, and 1985–1975 for leveling line 1. Error bars of two standard errors are also shown. [XBL 8611-4728]

due to the occurrence of faulting during the time period. The errors in leveling have been examined; they tend to be random and are described by the formula (Castle et al., 1984)

$$\sigma_i = \gamma L_i^{1/2},$$

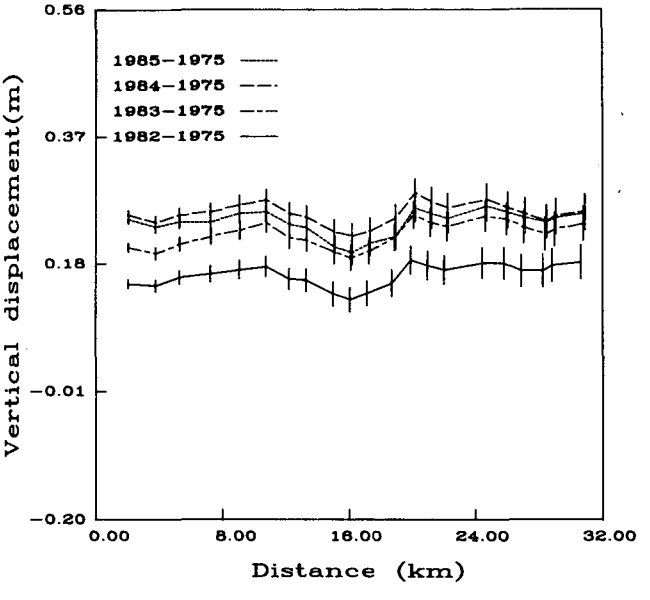

Figure 3. Line 3 displacements for the four time periods shown in Fig. 1. [XBL 8611-4727]

where γ is a constant and L_i is the distance between the ith station and the base bench mark. For the single-run first-order leveling surveys of 1982, 1983, and 1985, $\gamma = 2.0$ mm/km$^{1/2}$. For the double-run first-order leveling survey of 1975, $\gamma = 1.5$ mm/km$^{1/2}$. The lower-precision value $\gamma = 2.0$ mm/km$^{1/2}$ was considered as a measure of the error in the 1975–1982, 1975–1983, and 1975–1985 data. Movement along the Hilton Creek Fault occurred between the initial survey in 1975 and the subsequent surveys. It appears in the data shown in Fig. 2 as sudden large changes in the vertical displacement. To take these effects into account, we modeled the fault that gave rise to the changes. We used the fault model of Castle et al. (1984), which is a dip-slip fault dipping 60° to the east with 0.12 m of slip, and varied the dip, location, and slip somewhat to attempt an improved fit. Their model yields the smallest discontinuity in the vertical displacement. The effect of the fault along line 1 is shown in Fig. 4. The way in which this disturbance was incorporated into the inversion was through the error bounds. The displacement due to faulting at each station was considered to be part of the data errors. Therefore, it was added to the errors given above. The data and resultant error bounds are shown in Fig. 2. Similarly, Fig. 3 shows the data and the resulting error bounds for line 3.

Now we are in a position to ask how deep an intrusive body must be in order to satisfy the data within the specified error. To do this we consider the generalized moment A for the rectangular constant basis functions and when only volume change is occurring,

$$A = \sum_{n=1}^{N} \alpha_n \Delta\theta_n,$$

where $\Delta\theta_n$ is the fractional volume change averaged over the nth block R_n,

$$\Delta\theta_n = \int_{R_n} \Delta\theta(\vec{\xi}) dV(\vec{\xi}),$$

and

$$\alpha_n = \begin{cases} 1, & \xi \text{ in } U \\ 0, & \xi \text{ not in } U, \end{cases}$$

where U is a subregion of V; i.e., some collection of pixels R_i. Thus the minimization of A would find a solution in which the minimum total volume change occurs in the region U while satisfying the data. Note that by letting U be a specified pixel R_n, this α_n can be used to place bounds on the possible expansion within the nth pixel.

By choosing the region U to be between the surface and a given depth, it is possible to find the minimum volume change needed above this depth. By varying this region, a depth can be found above which no volume change need occur and below which some expansion must occur. This is the least upper bound on the depth to the magma body. The result of applying this procedure to all time intervals is shown in Fig. 5. In this figure it is seen that for

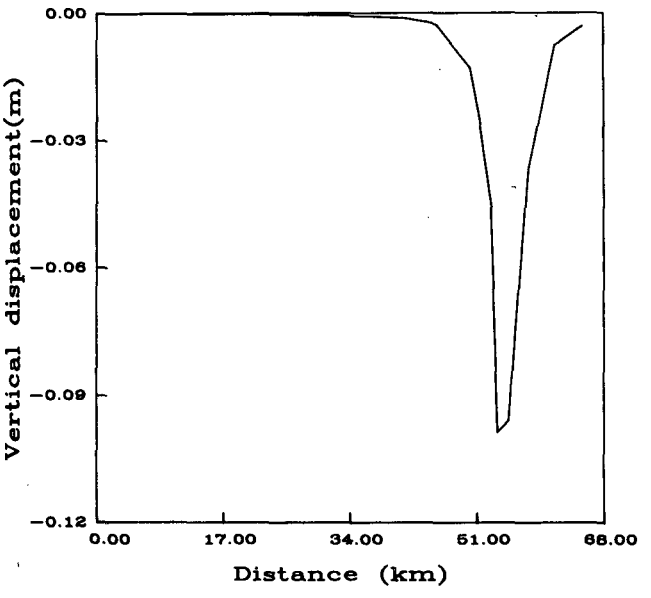

Figure 4. Displacement caused by faulting along line 1. [XBL 8611-4741]

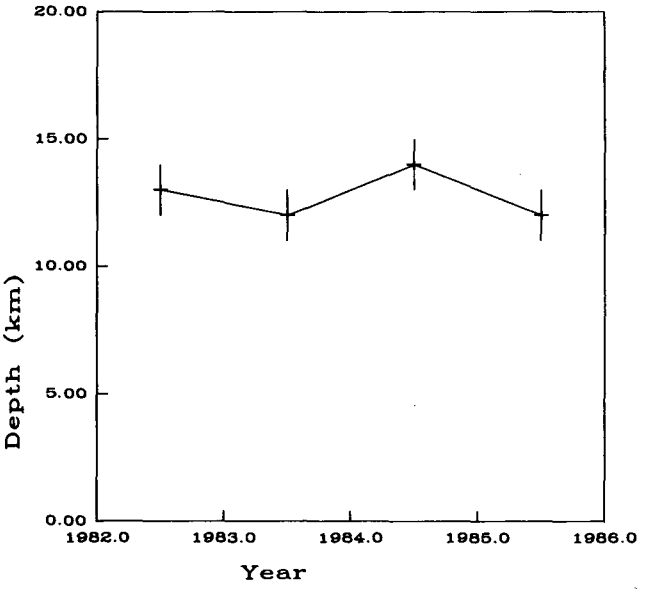

Figure 5. Depth bounds derived for the years 1982, 1983, 1984, and 1985. The bounds are in kilometers. [XBL 8611-4738]

the period 1982–1975 some intrusion must have occurred above 13 km. This bound does not change significantly after that period. This does not mean that magma has not moved toward the surface. However, it might be suspected that such motion would cause the bounds to move also.

Another property of interest is the amount of magma intruding at depth. Constraining the total volume change associated with an uplift episode can be done by choosing α_n to be the initial volume of the nth block. Then the generalized moment A represents the total volume change in the region studied. Applying this to the uplift shown in Figs. 2 and 3 gives the results shown in Fig. 6. In this figure we see a slight increase in upper bound for the period 1983–1975, followed by a major increase for the period 1984–1975. This increase might be due to a systematic error that is thought to have occurred in the 1984 leveling data (J. Savage, personal communication, 1986). The subsequent volume change for 1985–1975 returns to the value for 1983–1985.

CONCLUSIONS

The problem of determining the deformation at depth from surface displacements may be discretized through an expansion of the displacement-nuclei distribution into orthonormal basis functions. The resulting problem may be solved by a least-squares inverse method or by extremal inversion. The advantage of this approach is that no initial source geometry need be assumed. In some cases it may be more correct to treat a fault zone as a region of shear rather than slip over an infinitesimal plane. Unfortunately, the choice of basis functions and the number of basis functions to use remains unspecified. The number of basis functions to use will depend on the scale of the anomaly and on the station spacing. The type of basis functions will depend on the properties to be bounded or determined. Useful basis functions include the rectangular constant functions and spherical harmonics.

Applying these ideas to the uplift observed at Long Valley caldera results in a temporal record of the constraints on the possible intrusion of magma. The analysis reveals that the top of the postulated magma chamber must be shallower than 13 km. This depth constraint may be compared with the 6- to 8-km depth suggested by other lines of geophysical evidence. No significant changes have occurred in the constraints on the depth of any magma body satisfying the data. Moreover, if one ignores the period 1984–1975 because of bias, the upper bounds on the volume of intrusion change little. This may be evidence that little magma movement has occurred following the initial activity in the period 1982–1975.

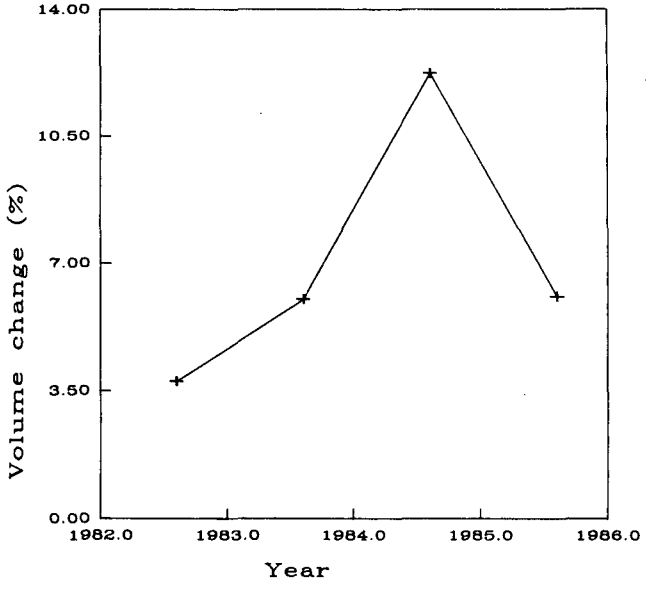

Figure 6. Upper bounds on total volume change in percent for the same time intervals as Fig. 4. [XBL 8611-4739]

REFERENCES

Backus, G.E., Gilbert, J.F., 1968. The resolving power of gross earth data. Geophys. J. R. Astron. Soc., v. 16, p. 169–205.

Castle, R.O., Estrem, J.E., Savage, J.C., 1984. Uplift across Long Valley caldera, California. J. Geophys. Res., v. 89, p. 11,507–11,515.

Kissling, E., Ellsworth, W.L., and Cockerham, R.S., 1984. Three-dimensional structure of the Long Valley caldera, California, region by geotomography. *In* Proceedings, Workshop XIX, Active Tectonic and Magmatic Processes beneath Long Valley caldera, Eastern California, January 24–27, 1984. U.S. Geol. Survey Open-File Report 84-939 (Vol. 1), p. 188–220.

Rundle, J.B., Whitcomb, J.H., 1984. A model for deformation in Long Valley, California, 1980–1983. J. Geophys. Res., v. 89, p. 9371–9380.

Sanders, C.O., Ryall, F., 1983. Geometry of magma bodies beneath Long Valley, determined from anomalous earthquake signals. Geophys. Res. Lett., v. 10, p. 690–692.

Savage, J.C., Clark, M.M., 1982. Magmatic resurgence in Long Valley caldera, California: Possible cause of the 1980 Mammoth Lakes earthquakes. Science, v. 217, p. 531–533.

Savage, J.C., Cockerham, R.S., 1984. Earthquake swarm in Long Valley caldera, California, January 1983: Evidence for dike inflation. J. Geophys. Res., v. 89, p. 8315–8324.

Steeples, D.W., and Iyer, H.M., 1976. Low-velocity zone under Long Valley as determined from teleseismic events. J. Geophys. Res., v. 81, p. 849–860.

Fracture Detection Using a Grounded Subsurface Vertical Electric Dipole

Q. Zhou, K.H. Lee, N.E. Goldstein, H.F. Morrison, and A. Becker

A practical problem encountered in geothermal reservoir exploration and development, as well as in other site-characterization studies, is the detection and characterization of any possible major water-filled fracture zone that lies close to but was missed by a drill hole. In the geothermal case it is not uncommon to drill a well on the basis of geologic information with the purpose of intersecting a specific fluid-producing fault or fracture zone. If the zone is not encountered the questions to be answered are: (1) Is the zone locally sealed? or (2) Was the well incorrectly placed to intersect the permeable zone?

Having at least one hole available in the area of interest, one can use borehole electromagnetic techniques for detecting possible major water-filled fractures (or fracture zones) missed by the holes. The implied assumptions are that the zone is a good reflector of electromagnetic waves, that the zone is embedded in a less conductive but otherwise homogeneous region, and that in situ thermal and chemical conditions are not so severe that they would prevent the use of suitably engineered in-hole sources and/or receivers. To date, most of the electromagnetic studies for fracture detection have considered a downhole VHF radar source using directional source and receiver antennas in the borehole (Chang et al., 1984; Chang, 1986; Olsson et al. 1986). Although this technique seems promising, it requires a steerable, directional antenna and a transmitter with sufficient power to offset the high attenuation of the VHF waves in rock, yet the probe must be sufficiently small to operate within the confines of a drill hole.

As part of our ongoing study to evaluate numerically the applicability of various electromagnetic techniques for detecting a "missed" fracture zone, we have considered the use of a very simple downhole source—a grounded vertical electric dipole (G.V.E.D.)—in combination with magnetic field observations made at the surface. The fracture zone is approximated by a thin, conductive three-dimensional sheet with variable conductance and dip. The G.V.E.D. is an interesting and important source because in the absence of the thin-sheet conductor the magnetic field is everywhere zero on and above the surface of a layered half-space. Variable parameters included sheet conductance, sheet dip, overburden thickness, and frequency of excitation (10 Hz–10 kHz). The purpose of the study was to determine whether diagnostic information on the location and dip of the sheet can be extracted from the shapes of the anomaly curves.

FORMULATION OF THE PROBLEM

The physical model studied is shown in Fig. 1. The fracture zone is simulated by a rectangular thin sheet with a conductance of τ siemens (S) located in an otherwise homogeneous, porous, and water-saturated half-space with resistivity ρ_2. The fractured half-space is concealed by an overburden layer with resistivity ρ_1 and thickness D. The upper edge of the sheet is horizontal and lies at a depth H ($H > D$) below the surface. The thin sheet is assigned a range of conductances τ (conductivity-thickness products) representative of natural conditions. The G.V.E.D. may be placed anywhere in the earth except very close to the sheet conductor and has a moment $I\delta l$ (A·m) that oscillates harmonically at angular frequency $\omega = 2\pi f$. The G.V.E.D. moment is taken as unity in all calculations and in the figures.

Other sheet parameters specified in this problem are sheet strike length L_a, dip length L_b, dip angle β, and the angle γ between sheet strike and the line of

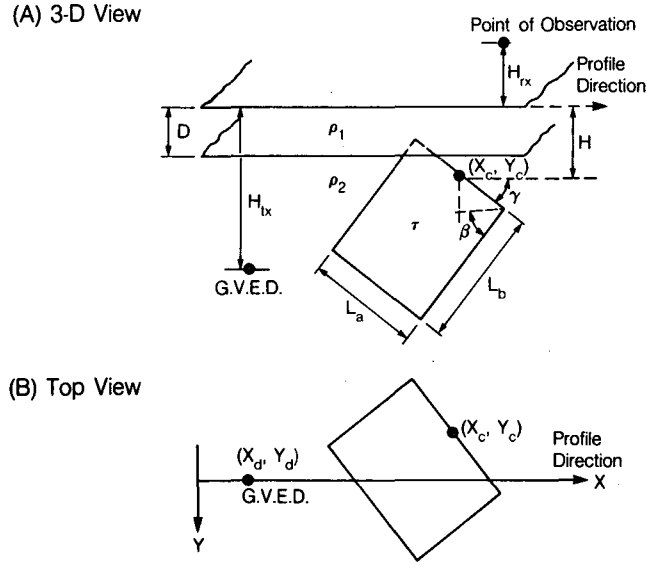

Figure 1. A conductive thin sheet buried in a conductive half-space (resistivity ρ_2) with an overburden (resistivity ρ_1) of thickness D. The rectangular thin sheet is characterized by its conductance (τ), strike length (L_a), dip extent (L_b), dip angle (β), and strike (γ). The coordinate of the center of the top edge of the sheet is (x_c, y_c, H). The medium is excited by a grounded vertical electric dipole located at (x_d, y_d, H_{tx}), and the resultant magnetic field is measured at (x, 0, H_{rx}) on or above the ground. [XBL 869-10985]

observations, or profile line, on the surface. H_{tx} and H_{rx} are the vertical distances of the transmitter below and the receivers above the ground planes, respectively.

The approach we have used to calculate the scattered (i.e., secondary) magnetic fields at the surface is based on the algorithm developed by Weidelt (1981). In our modified version of the code SHEET we have included a G.V.E.D. source embedded in the conductive medium. Weidelt (1981) derived the following two integral equations using the thin-sheet approximation (Price, 1949)

$$\mathbf{E_s(r_0)} = \mathbf{E_{ns}(r_0)} - i\omega\mu \int_S \tau\,(\mathbf{r}) g(\mathbf{r_0/r}) \cdot \mathbf{E_s(r)} ds \quad (1)$$

on the sheet and

$$\mathbf{H(r_0)} = \mathbf{H_n(r_0)} + \int_S \tau\,(\mathbf{r}) \mathbf{E_s(r)} \cdot \nabla_0 \times g(\mathbf{r_0/r}) ds \quad (2)$$

everywhere. $\mathbf{E_s}$ is the total tangential electric field on the sheet, and $\mathbf{E_{ns}}$ is the primary (incident) tangential electric field on the sheet. $\mathbf{H}$ is the magnetic field at the point of interest, $\mathbf{H_n}$ is the primary magnetic field, and $g(\mathbf{r_0/r})$ is the Green's dyadic function relating the tangential current distribution on the sheet with the electric fields everywhere. (Throughout the analysis μ is set equal to the free-space permeability μ_0.)

To modify Weidelt's SHEET program for a G.V.E.D. source buried in the conductive medium, we only have to change the primary tangential field $\mathbf{E_{ns}}$ on the sheet. The primary magnetic field $\mathbf{H_n}$ in the air will be zero, assuming that the displacement current is negligible.

SOME NUMERICAL RESULTS

A few numerical checks were made to ensure the desired performance of the algorithm. For example, the primary electric fields at low frequencies closely agree with the dc fields inside the conductive medium. Another numerical check was made by setting the overburden resistivity equal to the host-rock resistivity and then making the computation for a two-layered earth. Keeping the source position fixed, we varied the thickness of the overburden, which is equivalent to placing the source in the overburden or in the host rock. The results obtained for different thicknesses of the overburden have been found to be the same, which shows that the program is at least self-consistent. Other checks, such as reciprocity, duality, and symmetry, also show that the results are acceptable.

Some model results are presented to demonstrate the characteristics of the anomalous fields from the G.V.E.D. and its advantages over the vertical magnetic dipole (V.M.D.) source. The model parameters held fixed in this study are listed in Table 1. The center of the top edge of the sheet (x_c,y_c) is located directly below the line of observations, which is also the x axis for these calculations. In the cases studied we allowed parameters τ, f, β, and ρ_1 to vary, changing only one at a time to find its effect on the anomaly.

The first model considered is a vertical ($\beta = 90°$) sheet in a uniform half-space, $\rho_1 = \rho_2 = 100$ ohm·m, with varying conductance; τ = 0.5, 1, 3, 5, and 10 S. The real and imaginary components of the horizontal magnetic field (H_y) at 1000 Hz (in units of A/m) are plotted in Fig. 2. Contrary to what one might expect, the real component decreases with increasing sheet conductance from 0.5 to 3 S and crosses zero between 3 and 5 S. However, as the conductance increases further, the real component of H_y changes sign and increases in amplitude. The imaginary component of the anomaly is better behaved, varying little over the range of sheet conductances used. This phenomenon can be explained in the following way. For the real component of the total current in the sheet, the current channeling is dominant when τ is small. As τ increases, the

Table 1. Fixed model parameters used in the G.V.E.D. study.

Parameter	Parameter symbol	Value
Sheet strike length	L_a	100 m
Sheet dip length	L_b	60 m
Coordinate of the center of the top edge of the sheet	(x_c, y_c, H)	(200, 0, 60) m
Source coordinate	(x_d, x_d, y_d, H_{tx})	(100, 0, 100) m
Height of the receiver above surface	H_{rx}	1 m
Overburden thickness	D	10 m
Host-rock resistivity	ρ_2	100 ohm·m
Strike angle	γ	90°

induced current on the sheet increases and finally dominates. Since the two parts of the current flow in opposite directions on the upper edge of the sheet conductor, the real component of the total current on the upper part of the sheet changes sign as τ increases. This explains why the real component of the magnetic field (H_y) changes sign as τ increases. As for the imaginary component of the current, the two parts of the current are in the same direction on the upper part of the sheet, and therefore there is no sign change for the imaginary component of the magnetic field as τ increases.

Figure 3 shows the behavior of the magnetic field (H_y) at different excitation frequencies. The model is a vertical thin sheet (τ = 1.0 S) buried in a uniform half-space; $\rho_1 = \rho_2$ = 100 ohm·m. The real and imaginary components of the responses are plotted for frequencies of 10, 100, 1000, 3000, and 10,000 Hz. The effect of the increasing frequency on the observed magnetic field anomaly is similar to that of the increasing conductance of the sheet. At low frequencies the real component is dominant, but at higher frequencies the imaginary component becomes larger. The responses for the real component at 10 and 100 Hz are essentially equal and cannot be differentiated in the figure. At higher frequencies, the responses of the real component change

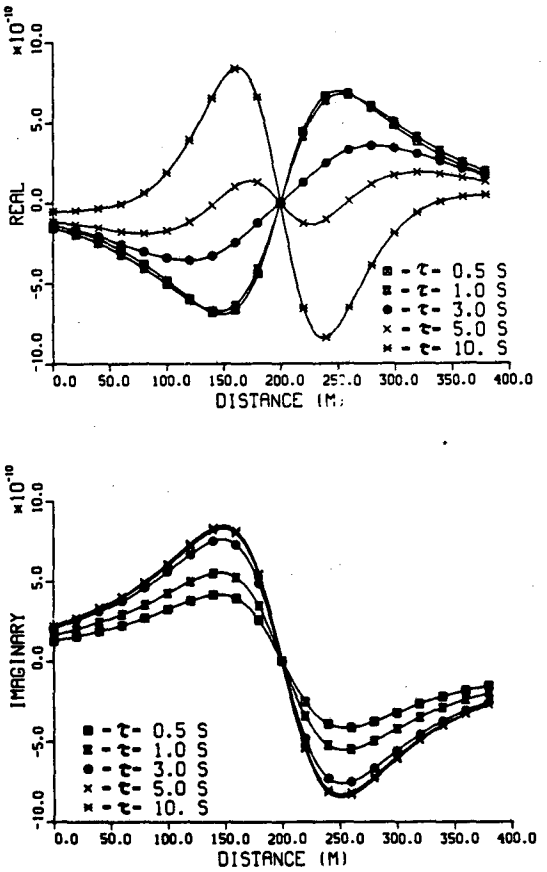

Figure 2. The magnetic field (H_y) anomaly in A/m for varying sheet conductance; τ = 0.5, 1, 3, 5, 10 S. The sheet is vertical (β = 90°) and is buried in a uniform half-space of resistivity $\rho_1 = \rho_2$ = 100 ohm·m. The frequency used is 1000 Hz. [XBL 869-3567]

sign as in the case of increasing sheet conductance. For a G.V.E.D. source there always exists current channeling and its associated magnetic fields, even if the frequency goes to zero because of the conduction current from the source. On the other hand, for a magnetic dipole source, both the real and imaginary components of the secondary field would vanish as the frequency goes to zero.

The next model studied is the same as the previous one, except that the resistivity of the 10-m-thick overburden is varied and the frequency used is held at 1000 Hz. The four curves in Fig. 4 are for overburden resistivity (ρ_1) of 1, 3, 10, and 100 ohm·m. It was found, as expected, that the amplitude of the anomaly, both the real and the imaginary components, decreases as the overburden resistivity decreases. At lower values of ρ_1, more conduction current from the source and more of the current induced in the host rock would flow into the overburden, with the result that less current is channeled

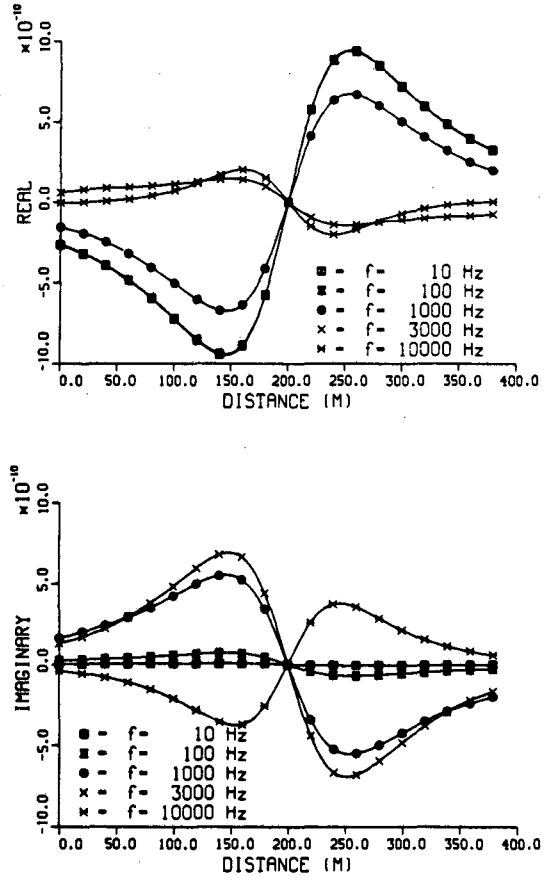

Figure 3. The magnetic field (H_y) anomaly for varying frequency; f = 10, 100, 1000, 3000, 10000 Hz. The sheet is vertical (β = 90°), and is buried in a uniform half-space of resistivity $\rho_1 = \rho_2$ = 100 ohm·m. The sheet conductance used is 1.0 S. [XBL 869-3571]

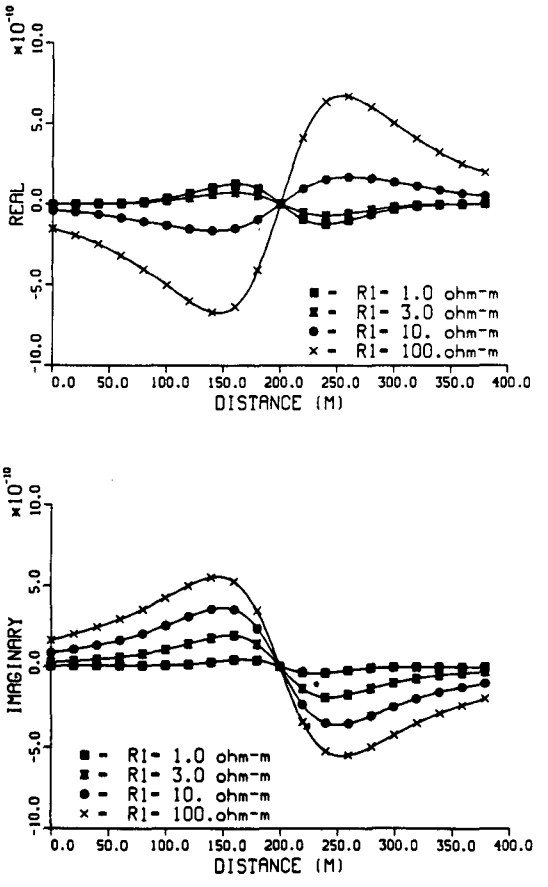

Figure 4. The magnetic field (H_y) anomaly for varying overburden resistivity; ρ_1 = 1, 3, 10, 100 ohm·m, with fixed thickness of D = 10 m. (For $R1$ in figure, read ρ_1.) The sheet is vertical (β = 90°) and is buried in the lower half-space of resistivity of ρ_2 = 100 ohm·m. The sheet conductance used is 1.0 S, and the frequency used is 1000 Hz. [XBL 869-3572]

into the sheet. For ρ_1 = 1 and 3 ohm·m, for example, the current channeled into the sheet is insignificant, and consequently the anomaly decreases rapidly. The induced current within the sheet seems to have contributed most of the anomaly, if any, in this case.

One of the important parameters involving the study of sheet response is the dip angle (β). The plots in Fig. 5 show the magnetic field anomaly for a dipping sheet with β = 90°, 75°, 60°, 45°, and 30°. The model is a thin sheet of conductance 1.0 S buried in a uniform half-space of 100 ohm·m. The frequency used is again fixed at 1000 Hz. Major changes in the shape of the anomaly occur as the sheet dips away from the vertical position; the zero crossing disappears, and the anomaly sharply increases with a sudden phase reversal at smaller dip angle (β = 30° in this case). The increase in anomaly is caused by the clockwise rotation of the sheet, which brings the bottom edge of the sheet closer to the source and to the surface. In addition, the current in the dip direction is no longer vertical in this case, so that it contributes increasingly more to the magnetic fields as the dip angle decreases. The abrupt phase reversal of the anomaly is directly related to the position of the G.V.E.D. source with respect to the plane that contains the sheet. The current in the sheet, especially the conduction current, reverses its direction depending upon the position of the source relative to that of the sheet plane, which in turn results in the observed phase reversal in the magnetic field. If a sufficient number and density of surface measurements are made with respect to one or more source positions, we may then be able to deduce some of the important geometrical parameters of the sheet, such as its strike length, strike angle, and dip angle.

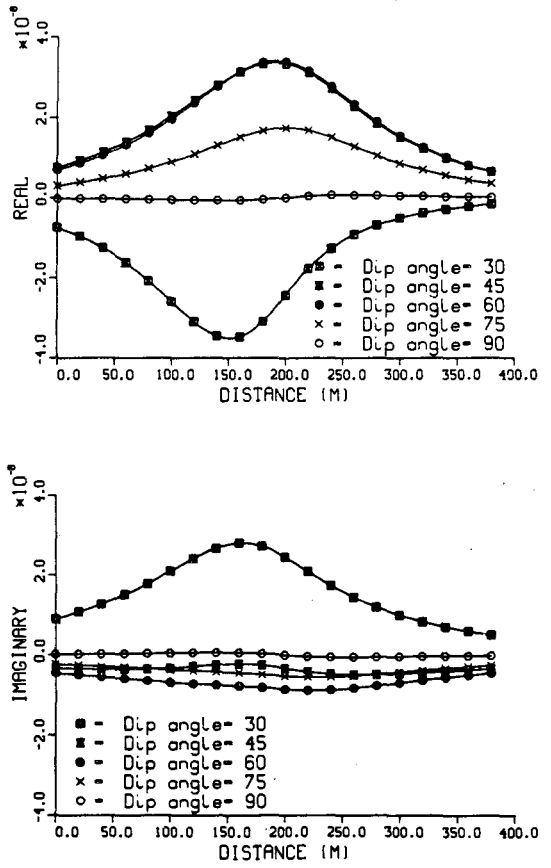

Figure 5. The magnetic field (H_y) anomaly for varying dip angle; β = 30°, 45°, 60°, 75°, 90°. The sheet is buried in a uniform half-space of resistivity $\rho_1 = \rho_2$ = 100 ohm·m. The sheet conductance used is 1.0 S, and the frequency used is 1000 Hz. [XBL 869-3573]

CONCLUSIONS

In our evaluation of surface-to-borehole electromagnetic methods for detecting a major fracture zone in a geothermal reservoir, we have analyzed and presented a numerical study involving the use of the G.V.E.D. source in the frequency domain. Particular attention was paid to the effect of the changing sheet conductance. The effect of the changing frequency is similar to that of the changing conductance, as long as the product of the conductance and the frequency remains small.

The anomalous currents contained in a vertical sheet conductor generate surface magnetic fields whose profile is either symmetric or antisymmetric in shape. This information is of great value in diagnosing a vertical fracture, since no other 2-D or 3-D lateral inhomogeneities can produce such an anomaly when a fixed source is used. In the case of a dipping fracture, including a horizontal one, the symmetry in the anomaly disappears, and, without further comprehensive analysis of the subject, it cannot be said whether the shape of the anomaly is distinguishable from those caused by other types of inhomogeneities. Within the context of the models studied, however, the dip angle and the location of the down-dip portion of the sheet with respect to the G.V.E.D. source may be approximately deduced by examining the phase and the amplitude of the anomalous magnetic field on the surface.

We also found that the G.V.E.D. source has certain advantages over the vertical magnetic dipole (V.M.D.) source (Zhou and Becker, 1985). The main reason is that the magnetic field of a G.V.E.D. measured in the air is caused only by the presence of a lateral inhomogeneity. This should make them more diagnostic than V.M.D. anomalies but, by the same token, more difficult to interpret.

For the cases studied the numerical results show that a unit moment G.V.E.D. produces surface magnetic field anomalies on the order 10^{-9} to 10^{-10} A/m or 10^{-6} to 10^{-7} nT in practical SI units. Since dipole moments of at least 10^2 A·m should be possible with borehole systems, the surface signals should have maximum amplitudes in the range 10^{-4} to 10^{-5} nT and thus would be discernible from natural field and other noise only if extremely careful signal-detection and noise-cancellation procedures were allowed. Extrapolating the surface anomaly to one for a deep fracture zone at a depth of, say, 1 km is best done by direct calculation. However, because the geometric decay of the secondary magnetic field must be at least as rapid as a $1/R$ function, the surface magnetic fields would be no larger than 10^{-6} to 10^{-7} nT unless much larger source moments can be created. Because of these extremely low signal strengths, the argument can be made for the use of cross-hole techniques in which the receivers are placed in a second nearby borehole and a large-moment G.E.V.D. source is created.

REFERENCES

Chang, H-T., 1986. A downhole system for fracture detection. Geotherm. Resour. Counc., Trans., v. 10, p. 217–222.

Chang, H-T., Suhler, S.A., and Owen, T.E., 1984. Evaluation of borehole electromagnetic and seismic detection of fractures. Sandia National Laboratories Report SAND 84-7109, 75 p.

Olsson, O., Forslund, O., Lundmark, L., Sandberg, E., and Falk, L., 1986. Borehole RADAR—A new technique for investigation of large rock volumes. Sveriges Geologiska AB, ID-NR: IRAP86292, 12 p.

Price, A.T., 1949. The induction of electric currents in nonuniform thin sheets and shells. Q. J. Mech. Appl. Math., v. 2, p. 283–310.

Weidelt, P., 1981. Report on Dipole Induction by a Thin Plate in a Conductive Half-space with an Overburden. Federal Institute for Earth Science and Raw Materials, Hannover, Germany.

Zhou, Q., and Becker, A., 1985. Distortion of electromagnetic waves by geological structure. Engineering Geosciences, University of California, Berkeley, Interim report submitted to Electronic Engineering Department of Lawrence Livermore National Laboratory.

Controlled-Source Electromagnetic Investigations: Field Test of an MHD Generator

R. Zollinger and H.F. Morrison

During September 1986 we conducted field tests of a controlled-source electromagnetic sounding system powered by a transportable magnetohydrodynamic (MHD) generator. The transmitter was a horizontal square loop measuring 200 m × 250 m with a resistance of 0.07 Ω and an inductance of 800 μH. The generator delivered two current pulses with peak currents of 6500 and 7250 A, and we recorded the radial, tangential, and vertical magnetic fields with SQUID magnetometers at sites 1.2 and 21 km from the center of the loop.

The maximum magnetic moment generated in this experiment was 3.6×10^{-8} A·m^2. The maximum primary vertical magnetic field 1.2 km from the transmitter was 46 nT. Extremely high 60-Hz levels, up to 0.2 nT, were recorded at the 1.2-km base site, and 0.01–0.08 nT of 60-Hz noise contaminated the 21-km remote site. The maximum expected primary B_z at the remote was ~0.005 nT, too small to be resolved in the noise.

THE MHD GENERATOR

The MHD generator developed by STD Research Corporation (Maxwell and Demetriades, 1986) is self-excited and uses high-electrical-conductivity plasmas to generate short pulses of very high current in low-resistance loads. The device generates highly conductive plasmas (~100 S/m) by using cesium-seeded combustion products from a subscale hybrid rocket combustor. The ionically charged exhaust flows through a segmented channel, perpendicular to a strong magnetic field supplied by a conventional air-core electromagnet. This creates a large voltage difference across the channel, and the presence of the ionized plasma in the channel allows current to flow across it. The current then flows through a low-resistance load (~60 mΩ) and through the electromagnet. As the current increases, the magnetic field increases, which further increases the current; thus the generator is self-exciting. An initial magnetic field of 0.45 T is created with a bank of batteries in order to start the self-excitation process.

A schematic diagram of the MHD generator is shown in Fig. 1. The low-resistance load is the 200-m × 250-m transmitting loop of the electromagnetic sounding system used in this experiment. A 200-mΩ resistance was connected in parallel with the transmitter loop during the second half of the experiment, reducing the percentage of total generator current supplied to the loop but increasing the generator efficiency with a well-matched load resistance.

At the beginning of an MHD pulse, shorting switches 1 and 2 are both closed. The batteries provide enough current to create an initial field of 0.45 T in the magnet. When the combustor is ignited, the voltage across the channel begins to rise. When it exceeds the battery voltage (~70 V), the battery-protection diode removes the batteries from the circuit. When the generator reaches full power, shorting switch 2 is opened, and all of the current begins flowing through the low-resistance load. At the end of the pulse, shorting switch 2 is closed, immediately removing the load from the generator. The fuel supply is then shut off, and the current in the generator gradually falls to zero.

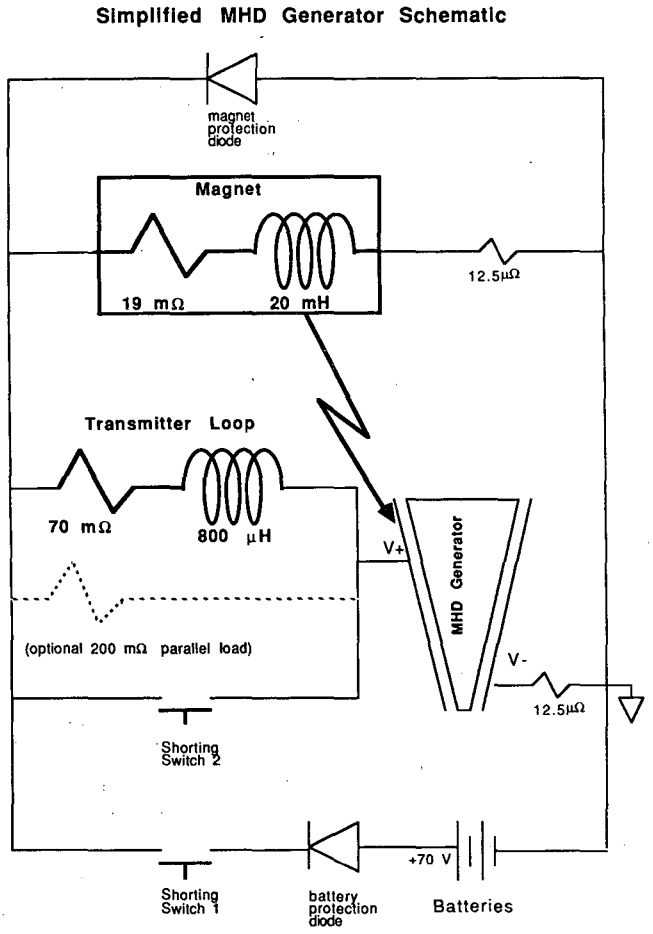

Figure 1. Schematic diagram of the MHD generator. [XBL 877-3111]

THE CONTROLLED-SOURCE ELECTROMAGNETIC SOUNDING SYSTEM

The time-domain electromagnetic sounding system developed by UC Berkeley and Lawrence Berkeley Laboratory consists of a horizontal-loop transmitter and two three-component SQUID magnetometer receivers. One of the receiver sites is located 20–30 km from the transmitter loop and serves as a remote reference for removing natural field noise from data recorded at the other receivers. The other receivers are located in the middle of the transmitter loop when making central-induction soundings or at some distance from the transmitter loop when making offset soundings.

Central-induction soundings are desirable because they are minimally contaminated by lateral inhomogeneities in the earth, but they are difficult to make because of the large dynamic range required. This problem worsens as the loop size gets smaller. Short-offset soundings, where the receiver is a short distance from the transmitter loop, are almost equivalent to central-induction soundings at late times but require significantly less dynamic range when making measurements. Selection of the central or short-offset receiver site is made on the basis of the expected primary and secondary field magnitudes inside and outside of the transmitter loop.

Electric-dipole receivers were installed at the receiver sites in order to make magnetotelluric (MT) measurements. The MT data may be used to infer much deeper structure when the controlled-source data are used to constrain the conductivity structure of the first 5–10 km of the crust.

The magnetic and electric signals are sent to the data-acquisition system 200 m away through line drivers. A schematic diagram of the data-acquisition system is shown in Fig. 2. All of the signals coming in are multiplexed by the scanner and are then fed into the voltmeter. The maximum sampling speed of the voltmeter at the base is 200 Hz; therefore, the maximum sampling frequency of each component of electric or magnetic field depends on the total number of components recorded. When recording only the three components of magnetic field (B_z, B radial, and B tangential), each component is sampled at 66.6 Hz. At the remote, the maximum sampling speed of the voltmeter is 50 Hz; therefore, when recording three components, the effective sampling frequency is 16.6 Hz.

In addition to the continuous sampling of the fields by the scanner/voltmeter, we also use a Nicolet digital oscilloscope to record at extremely high sampling rates for short periods. This is primarily used to obtain an accurate record of the current in the transmitting loop during the pulse. The current may be monitored inductively, which appears to be noisier and less precise, or resistively, which requires

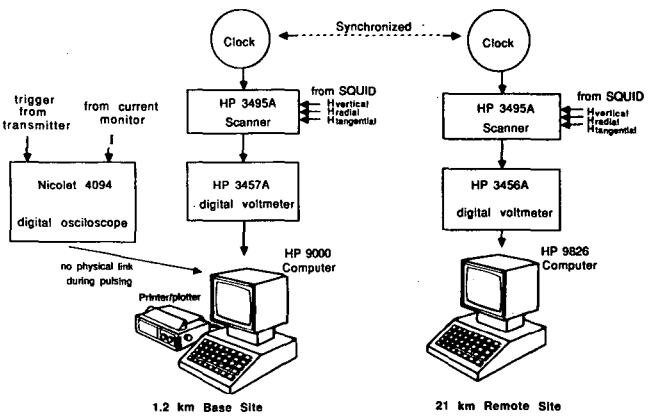

Figure 2. Schematic diagram of the data-acquisition system configured for recording transmitter pulse. [XBL 877-3109]

optical isolation to protect the oscilloscope from the high-inductive voltage spikes generated in the loop. The current-monitor output is then sent by line drivers to the data-acquisition system over a kilometer away. The oscilloscope is triggered to begin acquiring a high-frequency sweep of data by another signal sent from the transmitter just before the pulsing. After the pulsing is complete, the oscilloscope is connected to the computer by an interface bus, and the data are transferred to the storage disk. Thus the data-acquisition system is completely isolated from the high voltages of the transmitter loop during the time that the current pulse flows into the loop.

FIELD TEST

The field test was conducted at an approved site near the town of Rialto in southern California, where STD Research Corporation has tested the MHD generator for several years. This site has extremely high levels of cultural noise, most notably that due to a network of high-voltage power lines surrounding the area. A major power plant and switching station is located 7 km from the site, and several industrial plants are located nearby.

A 200-m × 250-m square transmitter loop made up of 50 parallel turns of #10 copper wire was connected to the MHD generator in place of the 60-mΩ load resistor used in previous tests. The transmitter loop had a resistance of 70 mΩ and an inductance of 800 μH. A 10-μΩ resistor was connected in series with the loop, and the current was monitored by measuring the voltage drop across this resistor.

The base receiver was located 1.2 km northeast of the transmitter loop, and the remote receiver was 21 km northwest of the loop. Two SQUID magnetometers and two sets of orthogonal-electric-field dipoles were installed at the base, and one magnetometer and one set of electric dipoles were installed at the remote. Natural magnetotelluric fields were recorded for several days at both base and remote. Applying remote-reference noise-cancellation techniques between the remote and base revealed that high levels of uncorrelated 60-Hz noise at both stations and powerline transient bursts at the base prevented any significant reduction of noise in the base signal over the short time periods of interest in a controlled-source sounding. The 60-Hz noise at the base had peak-to-peak amplitudes of 0.2 nT, whereas the remote had highly variable levels of 60-Hz noise, from 0.01 to 0.08 nT peak to peak. The secondary magnetic fields expected at the base begin around 0.4 nT and decay quickly to values much smaller than the high-frequency noise level. The noise level at the remote is higher even than the expected primary vertical magnetic field of 0.006 nT.

Pulse 1: The first current pulse lasted 1.25 s, starting at a peak value of 6500 A and decaying to 1400 A before shorting switch 2 was opened. The current in the loop then began decaying with a time constant of 0.01 s (Fig. 3). The primary vertical magnetic field at the 1.2-km base site is proportional to the current. For the geometry used in this experiment, the vertical field B_z (nT) at 1.2 km from the loop was $6.6 \times 10^{-3} \times A$, where A is the loop current in amperes. This is more than twice as high as it would be if the transmitter were a true magnetic dipole of equivalent moment. For this short-offset sounding, the geometry and size of the loop still have a strong effect on the magnitude of the primary field at the receiver.

The first pulse was recorded using only 100-Hz low-pass filters on the magnetometers at the base and remote sites. This distorts the received pulse very little but passes the high 60-Hz noise unattenuated. Because of the high 60-Hz noise, the small secondary fields are not immediately detectable in the data. It will first be necessary to first try removing the high-frequency signal, possibly through predictive filtering.

The recorded loop current and vertical magnetic field are shown in Fig. 3. The radial and tangential magnetic fields are shown in Fig. 4. The observed radial field is caused by slight misorientations of the transmitter and receiver. The interesting tangential field appears to be caused by a nearby lateral inhomogeneity, possibly the San Andreas Fault, which is located only a few kilometers northeast of the receiver site.

Pulse 2: The second current pulse lasted 1.5 s, starting at a peak value of 7250 A and decaying to 5180 A before shorting switch 2 was opened to remove the loop from the generator. The current in the loop amounted to only 74% of the current produced by the MHD generator during this run. The other 26% of the current was dissipated in a 200-mΩ resistor placed in parallel with the transmitter loop to provide better load matching and increase the generator efficiency. The primary vertical magnetic fields measured during the two pulses are compared in Fig. 5.

The second pulse was recorded using 100-Hz and 5-Hz low-pass filters and 60-Hz notch filters at the base and remote sites. This significantly distorted the high-frequency character of the square pulse, and the strong 60-Hz noise was still very evident in the data.

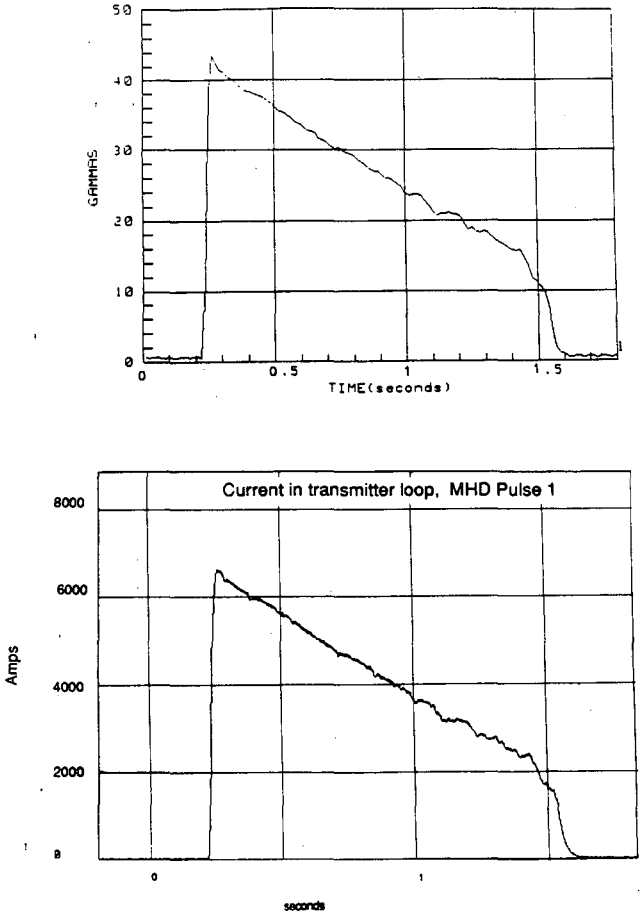

Figure 3. **(Top)** Vertical magnetic field (top) recorded 1.2 km from the transmitting loop. **(Bottom)** Current flowing in the loop during MHD Pulse 1. [XBL 877-3107]

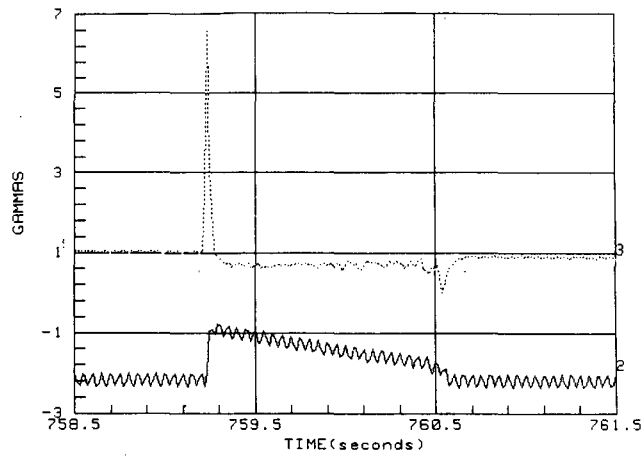

Figure 4. Radial (solid line) and tangential (dotted line) magnetic fields measured 1.2 km from the transmitting loop during MHD Pulse 1. [XBL 877-3108]

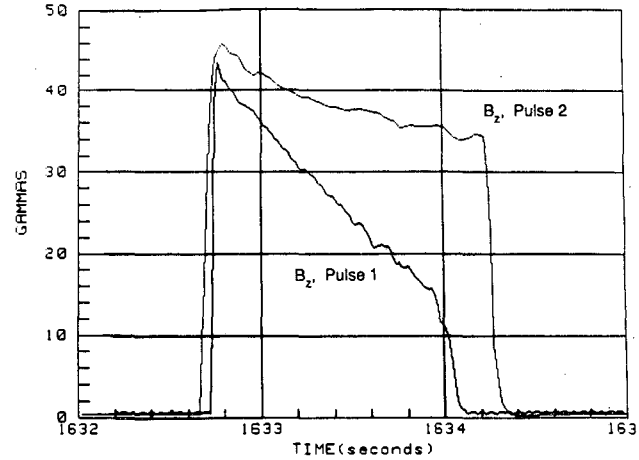

Figure 5. Comparison of the vertical magnetic field recorded 1.2 km from the transmitter loop during the two MHD generator pulses. [XBL 877-3110]

CONCLUSIONS AND RECOMMENDATIONS

The MHD generator was able to supply high instantaneous power to the loop and provide a moderately long-period high-amplitude current waveform. This waveform is a little noisy, but these fluctuations are generally less than 4% of the total amplitude. The current in the loop is best monitored resistively with good optical isolation between the loop and a high-frequency data acquisition system.

The MHD generator provides very high power and current, but in the present state of development it can only generate about 10 pulses for the purpose of stacking. Therefore, other means must be used to reduce noise that cannot be removed by remote-reference cancellation techniques. Predictive filtering may provide a means of removing some cultural noise that remains consistent over short periods of time. Small portable MHD sources may be very useful in areas where the electromagnetic noise is primarily due to natural telluric fields that correlate over 20–30 km.

When using an MHD generator to power the transmitter, matching the impedance of the loop to that of the generator ensures that the maximum power and current may be delivered to the loop. In this experiment, 26% more current would have been supplied to the transmitter loop during the second pulse if 10 more parallel turns of #10 gauge wire could have been added to the loop. This, in turn, means that 52% more energy would have been stored in the magnetic field created by the transmitter at the time of turn off.

An important requirement in the use of the available MHD generator is that the transmitter loop have a very low resistance. This, in turn, generally implies that small-diameter loops with a large amount of copper, hence weight, are best suited to the purpose. These loops are awkward to deploy in most field environments, although they are ideal in areas where topography or other barriers prevent the use of large loops. Small loops also place much greater dynamic-range requirements on any central induction or short-offset sounding system. This is not an inherent limitation; an MHD generator could easily be built with higher internal impedances for use in powering more resistive loads.

REFERENCE

Maxwell, C.D., and Demetriades, S.T., 1986. Initial tests of a lightweight, self-excited MHD power generator. J. Propulsion Power, v. 2, no. 5.

APPENDIXES

APPENDIX A: ABSTRACTS OF JOURNAL ARTICLES

Benson, S.M., and Bodvarsson, G.S., 1986
Nonisothermal effects during injection and falloff tests
SPE Formation Evaluation, v. 1, no. 1, p. 53–63 (LBL-14270)

Numerically simulated pressure transients during injection and falloff tests are analyzed to develop methods for obtaining the correct permeability/thickness of the reservoir and the skin factor for the well. The results show that to analyze correctly the pressure transients governed by a moving thermal front, the fluid-property values must correspond to the temperature of the injected fluid. For pressure falloff tests and for injection tests conducted in a well cooled by previous injection or drilling, however, the physical properties of the in-situ reservoir fluids must be used. The application of conventional isothermal methods for calculating skin values from injection and falloff data will give erroneous results. A new method is presented for calculating skin values from injection and falloff data that accurately corrects for nonisothermal effects. Examples are given to illustrate this analysis method. The technique is applied to the analysis of injection test data from a well located in the East Mesa geothermal field in southern California.

Benson, S.M., and Lai, C.H., 1986
Analysis of interference data in a highly heterogeneous naturally fractured geothermal reservoir
SPE Formation Evaluation, v. 1, no. 3, p. 236–248 (LBL-17450)

An approach consisting of a combination of composite and naturally fractured reservoir models has been proposed to interpret pressure-transient data from an 11-well interference test in a highly heterogeneous geothermal reservoir. The approach leads to an integrated interpretation that accounts for all of the salient features of the data.

An initial appraisal of the data indicates excellent agreement with theoretical results for double-porosity reservoirs. For some of the wells, however, the bulk storativity, calculated with the double-porosity model, differs significantly from the average value of this parameter. Furthermore, it increases systematically as the distance between the active and observation wells decreases. To explain this peculiar result, an alternative method of analyzing data from composite reservoirs is presented. The method demonstrates that local permeability variations can result in enormous variations in the apparent storativity without causing variations in the apparent permeability-thickness of the reservoir. A simple graphical technique, based on analyzing systematic variations in the apparent storativity, has been developed to determine the size of the region and the mobility contrast between different regions of the reservoir. By using this technique, we show that the observed variations in the storativity are the result of a small, high-permeability region that surrounds the pumped well and is penetrated by several of the observation wells.

Bodvarsson, G.S., Pruess, K., and Lippmann, M.J., 1986
Modeling of geothermal systems
J. Pet. Technol., v. 38, no. 10, p. 1007–1021 (LBL-18268)

During the last decade, the use of numerical modeling for geothermal resource evaluation has grown significantly, and new modeling approaches have been developed. In this paper, we present a summary of the current status in numerical modeling of geothermal systems, emphasizing recent developments. Different modeling approaches are described and their applicability discussed. The various modeling tasks—including natural-state, exploitation, injection, multicomponent, and subsidence modeling—are illustrated with geothermal field examples.

Carnahan, C.L., 1986
Thermal osmosis near a buried heat source
Int. Commun. Heat Mass Transfer, v. 13, p. 659–664 (LBL-21918)

Phenomenological equations for fluxes of heat and volume and balance equations for mass, temperature and pressure are stated for a water-saturated porous medium near a heat source. Previous work is discussed, and the behavior of the system is examined, in the light of the correct governing equations.

Chun, K.-Y., and McEvilly, T.V., 1986
Crustal structure in Tibet: High seismic velocity in the lower crust
J. Geophys. Res., v. 91, no. B10, p. 10,405–10,411 (LBL-18186)

A least squares procedure is used to extract pure path Tibetan group velocities in the period range 8–100 s from fundamental mode Rayleigh and Love waves recorded along 50 mixed paths. The crustal model derived from these dispersion data reveals that the lower half of the very thick (74 ± 10 km) Tibetan crust has a shear velocity similar to those found in the lower crust beneath stable continental and shield regions. A second interesting feature of the model is the presence of a prominent low-velocity channel at midcrustal depth. The uniqueness of the Tibetan crustal structure places the plateau region in a class by itself among tectonic provinces characterized by high heat flow and/or widespread recent volcanism, setting stringent constraints on tectonic models of the Tibetan Plateau.

D'Amore, F., and Pruess, K., 1986
Correlations between steam saturation, fluid composition and well decline in vapor-dominated reservoirs
Geothermics, v. 15, no. 2, p. 167–183 (LBL-18899)

A large body of field data from Larderello and other vapor-dominated geothermal reservoirs shows striking temporal correlations between (1) decline of well flow rate, (2) gas/steam ratio, (3) chloride concentration, (4) degree of superheat and (5) vapor fraction. The latter is inferred from concentrations of non-condensible gases in samples of well fluid, using chemical phase equilibrium principles. Observed temporal changes in the vapor fraction can be interpreted in terms of a "multiple source" model, as suggested by D'Amore and Truesdell (1979, Models for steam chemistry at Larderello and The Geysers. Proc. 5th Workshop Geothermal Reserv. Engng., Stanford, California, pp. 283–297). This provides clues to the dynamics of reservoir depletion and to the evaluation of well productivity and longevity.

Javandel, I., and Tsang, C.F., 1986
Capture-zone type curves: A tool for aquifer cleanup
Ground Water, v. 24, no. 5, p. 616–625 (LBL-19843)

Currently a common method of aquifer cleanup is to extract the polluted ground water and, after reducing the concentration of contaminants in the water below a certain level, the treated water is either injected back into the aquifer, or if it is environmentally and economically feasible, released to a surface-water body. The proper design of such an operation is very important, both economically and environmentally. In this paper a method is developed which can assist in the determination of the optimum number of pumping wells, their rates of discharge and locations, such that further degradation of the aquifer is avoided. The complex potential theory has been used to derive the equations for the streamlines separating the capture zone of one, two, or more pumping wells from the rest of the aquifer. A

series of capture-zone type curves are presented which can be used as tools for the design of aquifer cleanup projects. The use of these type curves is shown by an hypothetical field case example.

Jensen, J.A., Gillis, J.V., and Radke, C.J., 1986
Dispersion attendant sodium/hydrogen ion exchange in reservoir sands
SPE Formation Evaluation, v. 1, no. 6, p. 607–610 (LBL-20111)

Chromatographic lag observed upon injection of dilute alkali into reservoir sands is now well explained in terms of sodium/hydrogen ion exchange. However, the spread of the eluting hydroxide is more extreme than that associated with axial dispersion. We postulate an additional mass-transfer resistance caused by molecular diffusion in a microporous clay fraction. A quantitative model for this diffusion resistance is presented that compares favorably with experimental hydroxide histories from a water-saturated Berea sandstone. Both thin-section and scanning electron microscope (SEM) examination of the Berea rock confirm the presence of microporous regions of clay fines.

Kan, R.-J., Hu, H.-X., Zeng, R.-S., Mooney, W.D., and McEvilly, T.V., 1986
Crustal structure of Yunnan Province, People's Republic of China, from seismic refraction profiles
Science, v. 234, p. 433–437 (LBL-19997)

Seismic refraction profiles in Yunnan Province, southwestern China, define the crustal structure in an area of active tectonics on the southern end of the Himalaya-Burma arc. The crustal thickness ranges from 38 to 46 kilometers, and the relatively low mean crustal velocity indicates a crustal composition compatible with normal continental crust and consisting mainly of meta-sedimentary and silicic intrusive rocks, with little mafic or ultramafic component. This composition suggests a crustal evolution involving sedimentary processes on the flank of the Yangtze platform rather than the accretion of oceanic island arcs, as has been proposed. An anomalously low upper-mantle velocity observed on one profile but not on another at right angles to it may indicate active tectonic processes in the mantle or seismic anisotropy.

Kemeny, J., and Cook, N.G.W., 1986
Effective moduli, non-linear deformation and strength of a cracked elastic solid
Int. J. Rock Mech. Min. Sci. Geomech. Abstr., v. 23, no. 2, p. 107–118 (LBL-20522)

Utilizing the principles of Linear Elastic Fracture Mechanics (LEFM), the effective elastic moduli, the stability, and the strength of a solid containing a random distribution of interacting cracks is calculated. In order to account for the effects of interacting cracks, the "external crack" model is introduced, as a high crack density complement to non-interacting crack models. The behaviour of rock may be seen as progressing from the non-interacting crack models to the external crack model as cracks extend, interact, and coalesce. In rock mechanics, it is more common to encounter boundary conditions other than pure load controlled, and therefore we utilize the Griffith locus, which can determine the onset of fracture and the manner in which fractures extend, under any combination of load-controlled and displacement-controlled boundary conditions. Stress intensity factors are also calculated for random distributions of interacting cracks under displacement-controlled boundary conditions. The external crack model is found to exhibit sub-critical strain softening behaviour, and this gives a mechanism, not found in the non-interacting crack models, for the ultimate failure of brittle rock.

Lai, C.H., Bodvarsson, G.S., and Witherspoon, P.A., 1986
Second-order upwind differencing method for nonisothermal chemical transport in porous media
Numer. Heat Transfer, v. 9, p. 453–471 (LBL-19998)

A second-order upwind differencing method for convection-diffusion type equations in porous media has been developed. The method utilizes explicit monotonized upwind/central differencing and operator splitting. Various test cases have been considered to verify the accuracy of the numerical method. The results show that the present method greatly reduces numerical diffusion errors and gives no oscillations near fronts for high Peclet numbers.

The method has been applied to natural convection in a porous slab. The results indicate that the overall heat transfer (Nusselt number) is not strongly affected by relaxing the Boussinesq approximation. However, the mass flux and temperature distributions in the medium are significantly affected by the temperature- or pressure-dependent fluid properties.

Lange, R.A., Carmichael, I.S.E., and Stebbins, J.F., 1986
Phase transitions in leucite ($KAlSi_2O_6$), orthorhombic $KAlSiO_4$, and their iron analogues ($KFeSi_2O_6$, $KFeSiO_4$)
Am. Mineral., v. 71, p. 937–945 (LBL-21731)

The heat capacities of natural and synthetic samples of leucite ($KAlSi_2O_6$), orthorhombic $KAlSiO_4$, and their iron analogues, $KFeSi_2O_6$ and $KFeSiO_4$, have been measured between 400 and 1000 K by differential scanning calorimetry. For the various phase transitions that occur, temperatures of transition and associated changes in enthalpy and entropy have been determined. The tetragonal-cubic transition in leucite spans 122 to 176 deg, depending upon the sample studied, and is characterized by two peaks on a C_P heating curve. Heat treatment of a natural leucite for one week at 1673 K lowers the transition by 24 deg. Two distinct peaks in the C_P curve, enhanced by heating, suggest that an intermediate phase exists that is stable over 17 deg. A space group of $I4_{1/acd}$ has been assigned to this phase because it can be related to the low-temperature tetragonal leucite phase ($I4_{1/a}$) by merohedric twinning and the high-temperature cubic leucite phase ($Ia3d$) by pseudomerohedric twinning, both of which are found in leucite. In contrast, $KFeSi_2O_6$ (leucite structure) has a single, sharp C_P peak at a lower transition temperature. A natural leucite consisting of 88 wt% $KAlSi_2O_6$ and 12 wt% $KAlSi_3O_8$ has an X-ray pattern that indicates tetragonal symmetry, yet appears to be without twinning when viewed optically. The C_P data indicate a very small transition effect which may, however, be spread out in temperature above the limit of the DSC (1000 K). The orthorhombic polymorph of $KAlSiO_4$ undergoes one transition at 695 and one at 817 K, whereas its iron analogue, orthorhombic $KFeSiO_4$, has a single transition at 729.5 K. The enthalpy and entropy data indicate that the single transition in orthorhombic $KFeSiO_4$ is approximately equivalent to the sum of the two transitions in $KAlSiO_4$.

Majer, E.L., and Doe, T.W., 1986
Studying hydrofractures by high frequency seismic monitoring
Int. J. Rock Mech. Min. Sci. Geomech. Abtsr., v. 23, no. 3, p. 185–199 (LBL-19767)

Two experiments were carried out in salt and granite to address several questions regarding the utility of seismological techniques for monitoring the propagation of a hydrofracture. More specifically, could techniques developed for earthquake analysis be used to characterize the detectable acoustic emission (AE) activity associated with the hydrofracture process, and could the AE activity be used to define the geometry of the hydrofracture, and characterize its manner of propagation? To answer these and other questions, 3-D arrays of piezoelectric sensors were placed around the immediate hydrofracture zones in a small scale laboratory experiment (300 × 300 × 450 mm triaxially confined salt block) and a shallow, 35 m, field experiment (5 × 5 × 5 m granite mine). Confirmation of the seismic techniques was provided by using dyed fluids for the hydrofracture experiments and later visually inspecting the hydrofracture zones by breaking the salt block apart and mining back the rock in the granite mine. Results of the experiments show that there is abundant detectable discrete seismic activity, and that high frequency seismicity can be very useful for determining the path and geometry of the hydrofracture. Tensile failure "events" can be directly related to the actual path of the hydrofracture, whereas the shear failures are not as closely related to the actual fracture path, but are nevertheless related to the overall dimensions of the hydrofracture. Source sizes of individual events as inferred from the seismic data varied from 5 to 7 mm in the salt block experiment (average grain size = 5 mm) to 5 to 10 cm in the granite field experiment. Energy release of the events averaged 10^2 N-m $(10)^9$ dyne-cm) in the laboratory and 10^3 N-m (10^{10} dyne-cm) in the field experiment. All events in the laboratory test were primarily tensile failure in nature as inferred from the waveform radiation patterns; however, in the field experiment, there were shear events as well as "harmonic tremor" type events in addition to the tensile failure. The occurrence rate, spatial, and temporal distribution of the events indicate that the hydrofracture growth pattern, at least for these two cases, is not symmetrical and does not follow the often assumed symmetric paths. The data indicate that the hydrofracture process is a complicated phenomenon and that the "fracture" is actually made up of a network of fractures which forms a zone around a main fracture. The overall direction of the hydrofracture and the surrounding zone is strongly influenced by rock inhomogeneities and anisotropy as well as the stress directions.

Mozley, E.C., Goldstein, N.E., and Morrison, H.F., 1986
Magnetotelluric investigations at Mount Hood, Oregon
J. Geophys. Res., v. 91, no. B11, p. 11,596–11,610 (LBL-19547)

Magnetotelluric data, with both electric and magnetic field references for noise cancellation, were collected at accessible locations around and as close as possible to the Mount Hood andesite-dacite volcano. The purpose of the study was to identify and map conductive features and to relate them to the thermal regime of the region. Several conductors could be discerned. The shallowest, at a depth of around 500 m below the surface, was identified as a flow of heated water moving away from the summit; the deepest (~50 km) might be a melt zone in the upper mantle. Of particular interest is an elongate conductor that strikes N10° W and extends from a depth of 12 km down to 22 km. Because the conductor strike is close to the trend of the chain of Cascade volcanoes and because of the high conductive thermal gradients reported for the area, this feature was initially believed to be a zone of partial melt following the volcanic axis. However, because no teleseismic *P* wave velocity anomaly has been found, the cause of the conductor is more problematic. While the existence of small zones of melt cannot be ruled out, it is possible that the conductor is caused by a large volume of intensely deformed rocks with brine-filled microfractures.

Narasimhan, T.N., and Dreiss, S.J., 1986
A numerical technique for modeling transient flow of water to a soil water sampler
Soil Sci., v. 141, no. 3, p. 230–236 (LBL-19756)

The soil water sampler is a widely used device for collecting water from the vadose zone. Previous users attempting to mathematically model the fluid flow around a sampler have treated the sampler as a prescribed potential (Dirichlet) boundary condition. Physically, the sampler is a finite volume of space in which the air pressure changes (as dictated by the gas law) as the water level rises within. This change in air pressure can be a dominant factor that controls the transient flow of water into the sampler. An important consequence of the air-pressure effect is that the volume of sample that can be collected and the radius of influence of the sampler are both functions of the void volume of the sampler. A numerical technique in the context of the integral finite different method (IFDM) is proposed to simulate the behavior of a pneumatically sealed soil water sampler that extracts water from a partially saturated soil. A detailed parametric analysis of the problem will be the subject of a future paper.

Narasimhan, T.N., White, A.F., and Tokunaga, T., 1986
Groundwater contamination from an inactive uranium mill tailings pile. 2. Application of a dynamic mixing model
Water Resour. Res., v. 22, no. 13, p. 1820–1834 (LBL-19800)

At Riverton, Wyoming, low pH process waters from an abandoned uranium mill tailings pile have been infiltrating into and contaminating the shallow water table aquifer. The contamination process has been governed by transient infiltration rates, saturated-unsaturated flow, as well as transient chemical reactions between the many chemical species present in the mixing waters and the sediments. In the first part of this two-part series [White et al., 1984] we presented field data as well as an interpretation based on a static mixing model. As an upper bound, we estimated that 1.7% of the tailings water had mixed with the native groundwater. In the present work we present the results of numerical investigation of the dynamic mixing process. The model, DYNAMIX (DYNAmic MIXing), couples a chemical speciation algorithm, PHREEQE, with a modified form of the transport algorithm, TRUMP, specifically designed to handle the simultaneous migration of several chemical constituents. The overall problem of simulating the evolution and migration of the contaminant plume was divided into three sub problems that were solved in sequential stages. These were the infiltration problem, the reactive mixing problem, and the plume-migration problem. The results of the application agree reasonably with the detailed field data. The methodology developed in the present study demonstrates the feasibility of analyzing the evolution of natural hydrogeochemical systems through a coupled analysis of transient fluid flow as well as chemical reactions. It seems worthwhile to devote further effort toward improving the physicochemical capabilities of the model as well as to enhance its computational efficiency.

Perry, D.L., 1986
Detection of uranium in aqueous media using x-ray photoelectron spectroscopy
Spectrosc. Int. J., v. 1, p. 38–40 (LBL-20584)

A method has been developed to use x-ray photoelectron spectroscopy, normally used for solid samples, to detect uranium in aqueous samples in which uranium is present at concentration levels of 10^4 *M* or higher. Contaminants in natural water samples did not interfere with XPS analysis of uranium at this concentration.

Perry, D.L., and Taylor, J.A., 1986
X-ray photoelectron and Auger spectroscopic studies of Cu_2S and CuS
J. Mater. Sci. Lett., v. 5, p. 384–386 (LBL-20521)

Cu_2S (chalcocite) and CuS (covellite) have been studied by x-ray photoelectron and x-ray induced Auger spectroscopy. Binding energies for the copper $2p_{3/2,1/2}$ photoelectron lines, coupled with the absence of strong paramagnetically-induced "shake-up" structure, confirm both compounds to be copper(I) sulfides. The lineshapes of both the copper $2p_{3/2,1/2}$ photoelectron and L_3VV Auger lines are identical to one another and are also consistent with copper(I) species. The difference between the copper $2p_{3/2}$ and sulfur $2p_{3/2}$ core levels [Cu $2p_{3/2}$ − S $2p_{3/2}$] is 770.9 eV for Cu_2S and 769.9 eV for CuS, thus offering the most effective way for differentiating the compounds spectroscopically. The modified Auger parameter, using the copper $2p_{3/2}$ photoelectron line and the copper L_3VV Auger line, is 1849.9 eV for Cu_2S and 1850.3 eV for CuS.

Phutela, R.C., and Pitzer, K.S., 1986
Densities and apparent molar volumes of aqueous magnesium sulfate and sodium sulfate to 473 K and 100 bar
J. Chem. Eng. Data, v. 31, no. 3, p. 320–327 (LBL-20350)

Densities of aqueous solutions of $MgSO_4$ and Na_2SO_4 have been measured up to 473 K, 100 bar, and 1 *m* ionic strength. The derived apparent molar volumes along with the available literature data on these substances have been analyzed by using the ion-interaction (Pitzer) approach, $\overline{V}_2^0$ for $MgSO_4$ is obtained indirectly from values for $MgCl_2$, Na_2SO_4, and NaCl. The term in $\beta^{(2)}$ represents adequately the ion-association effect in $MgSO_4$ up to 473 K. The present results yield the pressure effect on various thermodynamic properties.

Phutela, R.C., and Pitzer, K.S., 1986
Heat capacity and other thermodynamic properties of aqueous magnesium sulfate to 473 K
J. Phys. Chem., v. 90, no. 5, p. 895–901 (LBL-20041)

Measurements are reported for the heat capacity of aqueous $MgSO_4$ from 348 to 473 K. Ion-interaction (Pitzer) equations are fitted to these data with additional guidance for $\overline{C}_{p2}^o$. The last quantity is obtained indirectly from literature data for $MgCl_2$, Na_2SO_4, and NaCl; we have made a new analysis for $MgCl_2$ but used published expressions for the sodium compounds. Literature data on the osmotic coefficient and the enthalpy of $MgSO_4$ solutions are used to complete a comprehensive thermodynamic treatment. Since all of the other major components of natural waters and sea water have been treated with the same set of equations and over a wide temperature range, the present results for $MgSO_4$ complete the basic data set required for prediction of most thermodynamic properties of these systems. The effectiveness of a special second-virial-coefficient term in representing the ion pairing in $MgSO_4$ is considered in some detail.

Phutela, R.C., and Pitzer, K.S., 1986
Thermodynamics of electrolyte mixtures. Enthalpy and the effect of temperature on the activity coefficient
J. Soln. Chem., v. 15, no. 8, p. 649–662 (LBL-21140)

The temperature dependence of the parameters for symmetrical mixing of ions of the same sign in the virial-coefficient (Pitzer) system are evaluated from literature data on heats of mixing in the presence of a common ion for 20 systems. The higher-order limiting law for symmetrical mixing is used in the form of an expression for the ionic strength dependence of the binary mixing parameter. Heats of mixing of the MX-NY type (without common ion) are calculated for eight systems from these parameters and found to be in excellent agreement with experimental values. Since pure-electrolyte parameters are required for the non-common-ion calculations, these are calculated as needed from recently published data.

Pitzer, K.S., 1986
Theoretical considerations of solubility with emphasis on mixed aqueous electrolytes
Pure Appl. Chem., v. 58, no. 12, p. 1599–1610 (LBL-21961)

The theoretical bases for prediction of solubilities are provided by thermodynamics and statistical mechanics. In many cases statistical mechanics

yields the chemical potential as an equation including several terms. While one or more terms may be fully determined theoretically, the parameters in other terms must be evaluated empirically at present. Then the solubility is obtained by equating the chemical potential for each species in different phases or by minimizing the total Gibbs energy at constant pressure and temperature. As an example of a recent major advance, the problem of the solubility of salts, including complex minerals, in multicomponent aqueous solutions is discussed in some detail. The status of predictive calculations for 25°C is described and new results for higher temperatures are reported. Brief comments are added concerning theories for other types of solubility systems.

Pitzer, K.S., and Pabalan, R.T., 1986
Thermodynamics of NaCl in steam
Geochim. Cosmochim. Acta, v. 50, p. 1445–1454 (LBL-20779)

On the basis of the statistical mechanics of a two-component imperfect gas, a successive hydration model is developed for the NaCl ion-pair molecule in steam which fits satisfactorily an extensive array of experimental solubility data including the measurements of Bischoff et al. (1986) at the three-phase pressure from 300° to 503°C and other concordant measurements extending to 600°C at 290 bars. Some published experimental results depart substantially from the concordant set here selected. The theoretical basis of this model should make it useful for estimates at higher temperatures provided the mean hydration number and the total fluid density remain within the range corresponding to the fitted data. The measurements of Bodnar et al. (1985) at 500 bars and 800°C provide a test and the agreement with model predictions is good.

Pitzer, K.S., and Simonson, J.M., 1986
Thermodynamics of multicomponent, miscible, ionic systems: Theory and equations
J. Phys. Chem., v. 90, no. 13, p. 3005–3009 (LBL-21756)

Equations of a type which has proven successful for binary and pseudo-binary ionic systems miscible from dilute solution in polar solvent to the fused salt are extended to an indefinite number of components. The underlying theory is discussed as well as the optimum form for empirical terms. In brief, the equations comprise an ideal term, an extended Debye-Hückel term, and a Margules expansion. The latter is carried out to the three-suffix level but could be extended. Relationships between molality and mole-fraction standard states are given. Examples are given showing the extent to which parameters measured for binary systems determine the properties of more complex systems.

Saluja, P.P.S., Pitzer, K.S., and Phutela, R.C., 1986
High-temperature thermodynamic properties of several 1:1 electrolytes
Can. J. Chem., v. 64, p. 1328–1335 (LBL-20208)

Comprehensive equations for the thermodynamic properties of aqueous NaI, CsF, CsCl, CsI, $NaIO_3$, KIO_3, $CsIO_3$, $KClO_4$, and HCl are generated by combining the heat capacity and density measurements reported by the first author with literature data for the enthalpy and Gibbs energy, or activity, as a function of molality at 298 K. The composition dependence is represented by the equations of Pitzer, which combine a theoretical form and Debye-Hückel terms with empirically evaluated parameters for short-range ion interactions. Temperature dependencies are presented by simple empirical equations, which should be reliable to 413 K or a little higher.

Simonson, J.M., and Pitzer, K.S., 1986
Thermodynamics of multicomponent, miscible ionic systems: The system $LiNO_3$—KNO_3—H_2O
J. Phys. Chem., v. 90, no. 13, p. 3009–3013 (LBL-20207)

Vapor pressures of water over KNO_3–H_2O and $LiNO_3$–KNO_3–H_2O (50.34 cation % Li) are reported in the temperature range $373 \leq T/K \leq 436$. Water activities calculated from these vapor pressures and other available results are fitted to an equation appropriate for multicomponent electrolyte solutions which are miscible to fused salts. The resulting equation gives the excess Gibbs energy over the complete composition range of the three-component system. Parameters for the binary fused salt mixture are determined from aqueous solution data and compared with approximate values calculated from phase diagrams. Excess thermodynamic properties, including solute activity coefficients and excess enthalpies, are calculated from the model.

Tralli, D.M., and Johnson, L.R., 1986
Estimation of travel times for source location in a laterally heterogeneous earth
Phys. Earth Planet. Inter., v. 44, p. 242–256 (LBL-21454)

A method is presented to obtain travel times from estimates of tectonically regionalized *P*-wave tau functions and slowness-dependent source and receiver corrections (Tralli and Johnson). A quadratic programming algorithm interpolates the tau estimates constrained by the analytical properties of tau and the statistical uncertainties. The regionalized travel-time estimates are used to locate seismic sources in the epicentral distance range 15–95°. Since all the information on lateral velocity variations is contained in the tau functions, seismic sources in a laterally heterogeneous Earth are located without explicitly defining a laterally varying velocity model. The formulation is efficient in that the travel-time estimates and corrections are obtainable for any source and receiver pair on the globe and require minimal computation time.

The *P* travel-time data are provided by the *Bulletin of the ISC*. Twenty-eight disclosed nuclear explosions at Nevada Test Site (NTS) allow estimation of a travel-time baseline bias. Azimuthal corrections for NTS events are also obtained. Nuclear explosions at NTS are then located, as are events in Eastern Kazakh and Novaya Zemlya in the Soviet Union, and in the Tuamotu Archipelago in French Polynesia. Three earthquakes along the San Andreas fault zone in west central California are also relocated for comparison with hypocentral parameters provided by local seismographic networks. All events are also located using the Jeffreys-Bullen *P* Tables and PREM (Dziewonski and Anderson) with a set of azimuthal station corrections (Dziewonski). A comparison of the reduction in sample variances of travel-time residuals provides a measure of the ability of tectonically regionalized tau functions to characterize lateral variations in mantle and crustal *P* velocities. Mean epicentral mislocations for NTS events are about 3 km whereas mislocations using J-B and PREM are about 7 km. For NTS and particularly Eastern Kazakh, the tau formation yields consistently smaller sample variances, with a mean reduction of 30% compared to using J-B and 15% compared to using PREM.

Vasco, D.W., 1986
Extremal inversion of travel-time residuals
Bull. Seismol. Soc. Am., v. 76, no. 5, p. 1323–1345 (LBL-21351)

A technique is presented which determines bounds on velocity structure from travel-time residuals. The problem is first linearized and then discretized using a series expansion method. The solutions derived are extremal in that they minimize or maximize a property of the model. For a given data set, the solutions are unique to the linearized problem. Examples are presented in which bounds are placed on the total velocity anomaly and on the extent of the anomalous body. The method also provides a mapping from bounds on the data to bounds on the velocity distribution. Furthermore, the technique is applicable to one-, two-, or three-dimensional velocity distributions.

As an example, the technique is applied to a set of teleseismic relative residuals recorded at Long Valley caldera, California. Two methods are proposed to deal with negative travel-time residuals. Upper bounds and lower bounds are placed on velocity perturbations at depth. The upper bounds indicate that teleseismic residuals cannot adequately constrain the velocity structure in Long Valley caldera. Lower bounds indicate where velocity perturbations must occur. The presence of a region of low velocity in the northwest portion of the Long Valley caldera, at a depth of 15 to 20 km, is supported. Also a minimum width of 16 km is derived for any anomalous body which could give rise to the observations.

Weres, O., and Tsao, L., 1986
Activity of water mixed with molten salts at 317°C
J. Phys. Chem., v. 90, p. 3014–3018 (LBL-20156)

We have determined the activity of water in extremely concentrated solutions of individual salts and common ion ternary mixtures in the system Na^+–K^+–OH^-–acetate–Cl^-–H_2O at 317°C. The sodium salts of boric acid, phenol, propionic acid, benzoic acid, and toluenesulfonic acid were also studied. These solutions are relevant to water chemistry and corrosion control in the steam generator of a nuclear power plant. Our data have been fitted by using the thermodynamic model of very concentrated salt solutions recently proposed by Pitzer and Simonson. The model is able to successfully represent the data in all cases, and allows salt activity coefficients to be calculated.

White, A.F., 1986
Chemical and isotopic characteristics of fluids within the Baca geothermal reservoir, Valles Caldera, New Mexico
J. Geophys. Res., v. 91, p. 1855–1866 (LBL-19341)

Geochemical and isotopic fluid data from 10 wells completed in the Baca geothermal reservoir indicate the presence of both a normal enthalpy, lower chloride fluid and an excess-enthalphy, higher-chloride fluid. This chemical difference, along with enrichment of deuterium and oxygen-18 in the excess-enthalpy fluid, can be explained by adiabatic cooling or boiling at 170°C during upward convection along the central fault system in the reservoir followed by conductive reheating during downward movement. Chemical modeling using the EQ3NR computer code indicates chemical stability with the mineral assemblage quartz, albite, K-mica, epidote, chlorite, calcite, anhydrite, and pyrite, which is in agreement with observed minerals in well cuttings. This correlation, along with chemical geothermometers, implies a constant temperature range of 260° to 320° during evolution of the reservoir.

Williams, C.F., Narasimhan, T.N., Anderson, R.N., Zoback, M.D., and Becker, K., 1986
Convection in the oceanic crust: Simulation of observations from Deep Sea Drilling Project hole 504B, Costa Rica rift
J. Geophys. Res., v. 91, no. B5, p. 4877–4889 (LBL-18564)

Three-dimensional modeling of convection in the oceanic crust at Deep Sea Drilling Project site 504B using an integral finite difference model reasonably duplicates underpressures, surface heat flow, down-hole temperature profiles, and fluid drawdown rates observed by in situ measurements in the borehole. The major constraint to produce such good fits is the permeability versus depth function, a quantity which was actually measured in the borehole. Pronounced "underpressuring" (fluid pressures less than hydrostatic) occurs throughout the convection cell if and only if a tight, nearly impermeable cap rock (chert) exists over the cell. The computed flow rates of water from the ocean through the borehole into the basalt agree closely with the measurements carried out 65, 720, and 1280 days after drilling. The model predicts an inflow rate of 50-60 L/h during the expected next occupation of the site by mid-1986. Numerical modeling has confirmed that an active hydrothermal convection cell exists in the region of hole 504B and that a very low permeability cap rock is necessary for the existence of the convection cell. Convective hydrothermal cells in the oceanic crust can explain observed periodic heat flow variations in suboceanic crust.

Witherspoon, P.A., 1986
Flow of groundwater in fractured rocks
Bull. Int. Assoc. Eng. Geol., v. 34, p. 103–115 (LBL-21622)

A pervasive problem in dealing with fractured rocks is the importance of the flow of groundwater through the discontinuities. This paper describes the results of recent work in this laboratory to investigate this problem. A much better understanding of the physics of fluid flow in a natural fracture from a sample of granite has been obtained from metal casts of the complex topography of the surfaces of the fracture as it is subjected to normal stresses up to 85 MPa. Contact area within the deforming aperture increases up to 30 percent and produces a flow regime that cannot be described by the cubic law. An investigation of flow in a network of fractures using a new numerical technique has been carried out to determine the effect of length and density of fractures on permeability. Networks with shorter fracture lengths and higher density will have lower permeabilities and will behave less like porous media than networks with longer fracture lengths and lower density. As fracture length increases, permeability approaches a maximum that can be predicted on the basis of infinite length fractures. A new analytical solution for transient flow to a borehole that penetrates a fracture dominated rock mass is summarized. A new derivative method of analyzing pressure transients from this solution is discussed and enables one to distinguish a fracture dominated system from one that exhibits double-porosity behavior.

Wollenberg, H.A., and Flexser, S., 1986
Contact zones and hydrothermal systems as analogues to repository conditions
Chem. Geology, v. 55, p. 345–359 (LBL-18587)

Radioactive waste isolation efforts in the U.S.A. are currently focused on examining basalt, tuff, salt and crystalline rock as candidate rock types to encompass waste repositories. As analogues to near-field conditions, the distributions of radio- and trace elements have been examined across contacts between these rocks and dikes and stocks that have intruded them. The intensive study of the Stripa quartz monzonite in Sweden has also offered the opportunity to observe the distribution of U and its daughters in groundwater and its relationship to U associated with fracture-filling and alteration minerals.

Investigations of intrusive contact zones to date have included: (1) a Tertiary stock into Precambrian gneiss; (2) a stock into ash flow tuff; (3) a rhyodacite dike into Columbia River basalt, Washington, and (4) a kimberlite dike into salt. With respect to temperature and pressure, these contact zones may be considered "worst-case scenario" analogues. Results indicate that there has been no appreciable migration of radioelements from the more radioactive intrusives into the less radioactive country rocks, either in response to the intrusions or in the fracture-controlled hydrologic systems that developed following emplacement. In many cases, the radioelements are locked up in accessory minerals, suggesting that artificial analogues to these would make ideal waste forms.

Emphasis should now shift to examination of active hydrothermal systems, studying the distribution of key elements in water, fractures, and alteration minerals under pressure and temperature conditions most similar to those expected in the near-field environment of a repository.

APPENDIX B: LBL REPORTS, BOOKS, CONFERENCES, PROCEEDINGS

LBL REPORTS

LBL-12670 (SAC-54)
Binnall, E., and McEvoy, M., 1985. Assessment of thermocouple temperature measurements during in situ heater experiments at Stripa, Sweden.

LBL-13327 (SAC-53)
Lingle, R., Nelson, P.H., DuBois, A., and Sellden, H., 1984. Performance of borehole deformation gauges and vibrating wire stressmeters at Stripa.

LBL-14875 (SAC-52)
Rouleau, A., 1985. Characterization of the fracture system at Stripa with emphasis on the ventilation drift.

LBL-19429
Ahn, J., Chambré, P.L., and Pigford, T.H., 1985. Nuclide migration through a planar fissure with matrix diffusion.

LBL-19430
Chambré, P.L., Pigford, T.H., Lee, W. W.-L., Ahn, J., Kajiwara, S., Kim, C.L., Kimura, H., Lung, H., Williams, W.J., and Zavoshy, S.J., 1985. Mass transfer and transport in a geologic environment.

LBL-19918
Pigford, T.H., and Chambré, P.L., 1985. Mass transfer in a salt repository.

LBL-20387 (NUREG/CR-4582)
Nitsche, H., 1985. Temperature effects on the solubility and speciation of selected actinides.

LBL-20553
Rulon, J., Bodvarsson, G.S., and Montazer, P., 1986. Preliminary numerical simulations of groundwater flow in the unsaturated zone, Yucca Mountain, Nevada.

LBL-20594
Verma, A.K., 1986. Effects of phase transformation of steam-water relative permeabilities.

LBL-21022
Wang, J.S.Y., and Narasimhan, T.N., 1986. Hydrologic mechanisms governing fluid flow in fractured welded units and porous nonwelded units at Yucca Mountain.

LBL-21025
Lai, C.H., Pruess, K., and Bodvarsson, G.S., 1986. On the accuracy of the MINC approximation.

LBL-21171
Lai, C.-H., 1985. Mathematical models of thermal and chemical transport in geologic media (Ph.D. thesis).

LBL-21313
Hellström, G., Tsang, C.-F., and Claesson, J., 1986. Motion of a two-fluid interface in a porous medium: Analytical studies.

LBL-21439
Long, J.C.S., and Billaux, D.M., 1986. The use of geostatistics to incorporate spatial variability in the modeling of flow through fracture networks.

LBL-21442
Karasaki, K., 1986. Well test analysis in fractured media (Ph.D. thesis).

LBL-21498
Peterson, J.E., Jr., 1986. The application of algebraic reconstruction techniques to geophysical problems (Ph.D. thesis).

LBL-21596
Tralli, D.M., 1986. Lateral variations in mantle P velocity for a tectonically regionalized earth (Ph.D. thesis).

LBL-21806
Chambré, P.L., Lee, W. W.-L., Kim, C.L., and Pigford, T.H., 1986. Steady-state and transient radionuclide transport through prentrations in nuclear waste containers.

BOOKS

Javandel, I., 1986. Applications of capture-zone type curves for aquifer cleanup. *In* R.M. Khanbilvardi and J. Fillos (eds.), Groundwater Hydrology, Contamination, and Remediation. Scientific Publications Co., Washington, D.C.

Perry, D.L., 1986. Applications of surface techniques to chemical bonding studies of minerals (Chapter 18). *In* J.A. Davis and K.F. Hayes (eds.), Geochemical Reactions at Mineral Surfaces (ACS Symposium Series, No. 323). American Chemical Society, Washington, DC, p. 389–402 (LBL-20225).

White, A.F., Benson, L.V., and Yee, A., 1986. Chemical weathering of the May 18, 1980, Mount St. Helens ash fall and the effect on the Iron Creek watershed, Washington (Chapter 14). *In* S.M. Colman and D.P. Dethier (eds.), Rates of Chemical Weathering of Rocks and Minerals. Academic Press, New York, p. 351–375 (LBL-17661).

CONFERENCES AND PROCEEDINGS

Benson, S.M., 1986. Computerized data acquisition system for production, injection, and interference tests. Presented at the Geothermal Resources Council Annual Meeting, Palm Springs, California, September 29–October 1, 1986 (LBL-21727).

Bodvarsson, G.S., and Cox, B.L., 1986. Numerical studies of gravity effects in two-phase reservoirs. Presented at the Geothermal Resources Council Annual Meeting, Palm Springs, California, September 29–October 1, 1986 (LBL-21935).

Bodvarsson, G.S., and Gaulke, S., 1986. Effects of noncondensible gases on fluid recovery in fractured geothermal reservoirs. Presented at the Society of Petroleum Engineers 56th Annual California Regional Meeting, Oakland, California, April 2–4, 1986 (LBL-21112).

Bodvarsson, G.S., Pruess, K., Lippmann, M.J., 1986. Numerical models for the evaluation of geothermal systems. Presented at the International Meeting on Geothermics and Geothermal Energy, Guarujá, State of Sao Paulo, Brazil, August 10–14, 1986 (LBL-22047).

Calore, C., Pruess, K., and Celati, R., 1986. Modeling studies of cold water injection into fluid-depleted, vapor-dominated geothermal reservoirs. Presented at the 11th Workshop on Geothermal Reservoir Engineering, Stanford, California, January 21–23, 1986 (LBL-21252).

Carnahan, C.L., 1986. Simulation of uranium transport with variable temperature and oxidation potential: The computer program THCC. Presented at the Materials Research Society Fall Meeting, Symposium L: Scientific Basis for Nuclear Waste Management X, Boston, Massachusetts, December 1–4, 1986 (LBL-21639).

Carnahan, C.L., 1986. A simulator of solute transport in saturated porous media incorporating variable temperature and oxidation potential. Presented at the 1986 Fall Meeting of the American Geophysical Union, San Francisco, California, December 8–12, 1986 (LBL-22134A).

Chambré, P.L., Kang, C.H., and Pigford, T.H., 1986. Flow of ground water around buried waste. Presented at the 1986 Annual Meeting of the American Nuclear Society, Reno, Nevada, June 15–19, 1986. Trans. Am. Nucl. Soc., v. 52, p. 77 (LBL-20900).

Chambré, P.L., Kang, C.H., Lee, W. W.-L., and Pigford, T.H., 1986. Mass transfer of soluble species into backfill and rock. Presented at the 1986 Winter Meeting of the American Nuclear Society, Washington, D.C., November 16–20, 1986. Trans. Am. Nucl. Soc., v. 53, p. 136 (LBL-21807).

Chambré, P.L., Lee, W. W.-L., Kim, C.L., and Pigford, T.H., 1986. Radionuclide transport through penetrations in nuclear waste containers. Presented at the 1986 Winter Meeting of the American Nuclear Society, Washington, D.C., November 16–20, 1986. Trans. Am. Nucl. Soc., v. 53, p. 135 (LBL-21809).

Chambré, P.L., Lee, W. W.-L., Kim, C.L., and Pigford, T.H., 1986. Transient and steady state radionuclide transport through penetrations of nuclear waste containers. Presented at the Materials Research Society Fall Meeting, Symposium L: Scientific Basis for Nuclear Waste Management X, Boston, Massachusetts, December 1–4, 1986 (LBL-21697).

Chambré, P.L., Lung, H.C., and Pigford, T.H., 1986. Mass transfer of a radioactive chain through backfill. Presented at the 1986 Annual Meeting of the American Nuclear Society, Reno, Nevada, June 15–19, 1986. Trans. Am. Nucl. Soc., v. 52, p. 78 (LBL-20901).

Cox, B.L., and Bodvarsson, G.S., 1986. Preliminary studies of two-phase effects on pressure transient data. Presented at the 11th Workshop on Geothermal Reservoir Engineering, Stanford, California, January 21–23, 1986 (LBL-21249).

Goldstein, N.E., 1986. Perspective and trends: Future of geothermal exploration technology. Presented at the Geothermal Resources Council Symposium on the Future of Geothermal Energy, San Diego, California, November 17–18, 1986 (LBL-22487).

Goldstein, N.E., and Carle, S., 1986. Faults and gravity anomalies over the East Mesa hydrothermal-geothermal system. Presented at the Geothermal Resources Council Annual Meeting, Palm Springs, California, September 29–October 1, 1986 (LBL-21459).

Goldstein, N.E., and Iovenitti, J.L., 1986. Fracture detection and mapping. Presented at the 11th Workshop on Geothermal Reservoir Engineering, Stanford, California, January 21–23, 1986 (LBL-21254).

Halfman, S.E., Lippmann, M.J., and Bodvarsson, G.S., 1986. Quantitative model of the Cerro Prieto field. Presented at the 11th Workshop on Geothermal Reservoir Engineering, Stanford, California, January 21–23, 1986 (LBL-20523).

Halfman, S.E., Manón, A., and Lippmann, M.J., 1986. Update of the hydrogeologic model of the Cerro Prieto field based on recent well data. Presented at the Geothermal Resources Council Annual Meeting, Palm Springs, California, September 29–October 1, 1986 (LBL-21499).

Jacobsen, J.S., and Carnahan, C.L., 1986. Chemical osmosis near a heat source buried in a saturated semi-permeable medium. Presented at the 1986 Fall Meeting of the American Geophysical Union, San Francisco, California, December 8–12, 1986 (LBL-22121A).

Lee, W.W.-L., Kim, C.L., Chambré, P.L., and Pigford, T.H., 1986. Cumulative releases of radionuclides from uncontained waste packages. Presented at the 1986 Winter Meeting of the American Nuclear Society, Washington, D.C., November 16–20, 1986. Trans. Am. Nucl. Soc., v. 53, p. 134 (LBL-21808).

Lippmann, M.J., and Bodvarsson, G.S., 1986. Convective heat transport in geothermal systems. Presented at the International Meeting on Geothermics and Geothermal Energy, Guarujá, State of Sao Paulo, Brazil, August 10–14, 1986 (LBL-21984).

Nir, A., Doughty, C., and Tsang, C.-F., 1986. Seasonal heat storage in unsaturated soils: Example of design study. Presented at the 21st Intersociety Energy Conversion Engineering Conference, San Diego, California, August 25–29, 1986 (LBL-21026).

Pitzer, K.S., 1986. Theoretical considerations of solubility with emphasis on mixed aqueous electrolytes. Presented at the IUPAC 2nd International Symposium on Solubility Phenomena, Newark, New Jersey, August 11–15, 1986 (LBL-21961).

Ransohoff, T.C., and Radke, C.J., 1986. Mechanisms of foam generation in glass bead packs. Presented at the 1986 SPE Annual Technical Conference and Exhibition, New Orleans, Louisiana, October 5–8, 1986 (LBL-21845).

Solbau, R., Weres, O., Hansen, L., and Dudak, B., 1986. Description of a high temperature downhole fluid sampler. Presented at the Geothermal Resources Council Annual Meeting, Palm Springs, California, October 29–31, 1986 (LBL-21495).

Sorey, M.L., Farrar, C.D., and Wollenberg, H.A. (eds.), 1986. Proceedings of the Second Workshop on Hydrologic and Geochemical Monitoring in the Long Valley Caldera, Mammoth Lakes, California, July 15–17, 1986 (LBL-22852).

Truesdell, A.H., and Lippmann, M.J., 1986. The lack of immediate effects from the 1979–80 Imperial and Victoria earthquakes on the exploited Cerro Prieto geothermal reservoir. Presented at the Geothermal Resources Council Annual Meeting, Palm Springs, California, September 29–October 1, 1986 (LBL-21711).

Verma, A., and Pruess, K., 1986. Enhancement of steam phase relative permeability due to phase transformation effects in

porous media. Presented at the 11th Workshop on Geothermal Reservoir Engineering, Stanford, California, January 21–23, 1986 (LBL-21027).

Weres, O., Jun, C.H., and Tsao, L., 1986. New three phase equilibrium model (oil–gas–brine) used to interpret production of liquid hydrocarbons from a geopressured gas well. Presented at the Society of Petroleum Engineers 56th Annual California Regional Meeting, Oakland, California, April 2–4, 1986 (LBL-20806).

Wu, Y.-S., and Pruess, K., 1986. A multiple-porosity method for simulation of naturally fractured petroleum reservoirs. Presented at the Society of Petroleum Engineers 56th Annual California Regional Meeting, Oakland, California, April 2–4, 1986 (LBL-21111).

☆ U.S. GOVERNMENT PRINTING OFFICE: 1987— 789-001/79263

LAWRENCE BERKELEY LABORATORY
TECHNICAL INFORMATION DEPARTMENT
UNIVERSITY OF CALIFORNIA
BERKELEY, CALIFORNIA 94720